(2)

Acoustic Coupling Phenomena Between Hydrodynamic Pressure Fluctuations in Boundary Layers and Elastic Layered Media

J.A. Domaradzki, M. Dravinski
University of Southern California

October 2, 1992

Final Report for the period 01/01/1988 - 09/30/1992
ONR Contracts No. N00014-88-K-0157 and N00014-91-J-4163

1 Summary of the Research Results

The following goals have been accomplished in the course of this research:

1. We have developed an analytic Green's function method for pseudo-spectral numerical simulations of boundary layer and channel flows (Domaradzki 1990). The new method reduces number of Poisson and Helmholtz equations that must be solved numerically in classical pseudo-spectral Navier-Stokes solvers, bringing significant savings in computer time needed to perform direct numerical simulations for such flows. The method has been implemented in boundary layer and Rayleigh-Benard convection solvers used at USC.

2. The numerical code was used to simulate burst-like events in a laminar boundary layer. Localized bursts were obtained by applying appropriately chosen suction/blowing boundary conditions at the wall and large scale features of the flow were modeled by finite amplitude travelling wave states in boundary layer flows over rigid walls. Conclusions from the simulations were as follows. Applied suction/blowing mechanism at the wall induced desired burst-like flow structures and large scale structures could be effectively modeled through nonlinear finite amplitude Tollmien-Schlichting waves. The low amplitude wall forcings resulted in viscously damped perturbations and higher amplitudes led quickly to turbulence. None of these behaviors reproduces desired time-behavior of natural turbulent bursts and we had to conclude that the selected numerical methodology was unable to provide a realistic model of a burst, in particular its finite life-span.

3. We have developed four models of a wall-pressure associated with a turbulent burst. Three of these models are purely analytical and one was obtained using results of direct numerical simulations of turbulent, three-dimensional boundary layer performed by Spalart at NASA-Ames. The last model is a single high pressure region on a rigid wall underneath turbulent boundary layer. The pressure pulse evolves in time changing its strength, shape and location. To capture the pulse and its evolution all other neighbouring high pressure regions present in the simulations are selectively suppressed and the results for the remaining pulse given on a finite mesh in the (x,y) plane and for a finite number of time steps are interpolated to provide a continuous function of the spatial variables (x,y) and time t with the results of the fitting procedure stored on a tape.

4. A theoretical investigation was conducted of the process of sound generation by a deterministic pressure pulse in a fluid flowing over a compliant coating containing a small inhomogeneity with the results described in detail in a paper by Domaradzki et al. (1992).

   To leading order the void inhomogeneity can be treated as a monopole source, its strength determined by the detailed form of the pressure at the interface between the fluid and the coating. Four different models of the pressure pulse were employed to specify the monopole strength. For three of these models, a concentrated force advected

with constant velocity U_c, the pressure field of an advected vortex, and the wall pressure of a turbulent burst, pressure values are strictly positive. In all these three cases the frequency dependence of the monopole strength exhibits the same, generic behaviour: a large, almost constant plateau in the range of subconvective frequencies $\omega h/U_c \leq 1$, followed by a fairly rapid decrease in the range $1 \leq \omega h/U_c$. The remaining model satisfies the Kraichnan-Phillips condition and the associated monopole strength differs from those computed for the other three models only by exhibiting a maximum at a finite, instead of zero, frequency.

The far field acoustic pressure in the fluid and in the coating due to the inhomogeneity has been calculated. In the interesting case of water flow over a particular rubber-like coating the sound has dipole character in the fluid, whereas in the coating there is a gradual change from monopole to dipole radiation when the radiation direction changes from the normal to the tangent to the interface. Also, in this case the coating always captures most of the sound energy scattered by the inhomogeneity.

A comparison was made between the sound generated by a single pressure pulse and the sound generated by the scattering of the statistically stationary turbulent boundary layer pressures by the inhomogeneity. Only those events in the boundary layer which contribute to the convective peak in the wall pressure spectrum were taken into account. For the particular set of the parameters considered in this paper, in the range of high acoustic frequencies, the average intensity of the radiation induced by the individual pressure pulses can exceed the averaged intensity of the sound induced by the turbulent boundary layer by 10-40 dB. It is thus expected that the presence of deterministic pressure pulses in the turbulent boundary layer will result in *bursts of acoustic radiation with the intensities substantially greater than those predicted by the statistical approach.*

5. Diffraction of elastic waves by multiple dipping layers of arbitrary shape for two and three dimensional models in the absence of fluid for incident plane P, SV, SH and Rayleigh waves was investigated. Both steady state and transient results were obtained. We found that the presence of irregularity greatly changes local response of the media. In addition, we found that for highly irregular scatterers the importance of three dimensional nature of the problem cannot be accurately described with two dimensional model. In particular, the SH to P/SV mode conversion is found to be significant in many cases. This conversion cannot be accounted with two dimensional models.

6. Diffraction of elastic waves in a multilayered plate with an inclusion of arbitrary shape submerged in fluid is the second class of problems which have been completed in this project. Steady state and transient solutions were obtained for both two dimensional and three dimensional models. Parametric studies were performed in order to gain understanding of the wave amplification at the fluid-solid interface for a wide range of parameters present in the problem such as the angle of incidence and frequency of incident wave, impedance contrast of the materials, and the geometry of the inclusion. To our knowledge these solutions are the most general ones available in literature at the present time.

2 Publications/Presentations

Refereed Journals

1. Domaradzki, J.A. (1990), An analytic Green's functions method for pseudo-spectral Navier-Stokes solver for boundary layer and channel flows, *J. Comput. Phys.* 88, 232-242.

2. Domaradzki, J.A., Shah, K., and Crighton, D.G., (1992), Scattering of hydrodynamics pressure pulses on coating inhomogeneities, to appear in *J. Acoust. Soc. Am.*, Nov. 1992.

3. Eshraghi, H., and M. Dravinski (1989a). Transient scattering of elastic waves by dipping layers of arbitrary shape. Part 1. Antiplane strain model, *Earthquake Eng. Struct. Dyn.*, Vol. 18, No. 3, pp. 397-415.

4. Eshraghi, H., and M. Dravinski (1989b). Transient scattering of elastic waves by dipping layers of arbitrary shape, Part 2. Plane strain model, *Earthquake Eng. Struct. Dyn.*, Vol. 18, No. 3, pp. 417-434.

5. Eshraghi, H., and M. Dravinski (1989c). Scattering of plane harmonic SH, SV, P, and Rayleigh waves by non-axisymmetric three dimensional canyons: A wave function expansion approach, *Earthquake Eng. Struct. Dyn.*, Vol. 18, pp. 983-998.

6. Mossessian, T. K., and M. Dravinski (1989a). Scattering of elastic waves by three dimensional surface topographies, *Wave Motions*, Vol. 11, pp. 579-592.

7. Eshraghi, H., and M. Dravinski (1989b). Scattering of elastic waves by non-axisymmetric three dimensional dipping layer, *Num. Meth. Part. Diff. Eqns.*, Vol. 5, pp. 327-345.

8. Mossessian, T.K., and M. Dravinski (1990a). Amplification of elastic waves by a three dimensional valley, Part 1: Steady-state response, *Earthq. Eng. Struct. Dyn.*, Vol. 19, 667-680.

9. Mossessian, T. K., and M. Dravinski (1990b). Amplification of elastic waves by a three dimensional valley, Part 2: Transient response, *Earthq. Eng. Struct. Dyn.*, Vol. 19, 681-691.

10. Eshraghi, H., and M. Dravinski (1991). Scattering of elastic waves by three dimensional non-axisymmetric dipping layers, *Int. J. Num. Methds. Engng.*, Vol. 31, 1009-1026.

11. Mossessian, T. K., and M. Dravinski (1992). A hybrid approach for scattering of elastic waves by three dimensional irregularities of arbitary shape, *J. Phys. Earth*, Vol. 40, No. 1, 241-261.

12. Mossessian, T.K., and M. Dravinski (1992). Transient response patterns for a 3D canyon in a viscoelastic half-space for different incident waves, *J. Geol. Soc. China*, Vol. 35, No. 2, 153-172.

13. Keshavamurthy, R., and M. Dravinski (1991). Elastic wave scattering by an inclusion in a multilayered media submerged in fluid, submitted to *Wave Motion.*

14. Keshavamurthy, R. and M. Dravinski (1992). Elastic wave scattering by an inclusion in a multilayered medium submerged in fluid: Three dimensional model, submitted to *Wave Motion.*

Conference Proceedings/Abstracts

1. Domaradzki, J.A., Shah, K., and Crighton, D.G., (1990), Scattering of localized boundary layer pressures by coating inhomogeneities, *Bull. Am. Phys. Soc.* **35**, 2263.

2. Rossi, M., Domaradzki, J.A., and Tadepalli, S., (1991), Finite amplitude states in boundary layers, *Bull. Am. Phys. Soc.* **36**, 2700.

3. T. K. Mossessian and M. Dravinski (1990). Resonant motion of three-dimensional alluvial basins, *Proceedings of Fourth U.S. National Conference on Earthquake Engineering*, U.C. Irvine, May 20-24, 1990, 525-534.

4. H. Eshraghi and M. Dravinski (1990). Amplification of ground motion by three-dimensional sedimentary basins of arbitrary shape, *Proceedings of Fourth U.S. National Conference on Earthquake Engineering*, U.C. Irvine, May 20-24, 1990.

5. Eshraghi, H., and M. Dravinski (1988). Transient scattering of SH, P, SV, and Rayleigh waves by subsurface irregularities,to be presented at the Annual Meeting of the Seismological Society of America, Honolulu, Hawaii, May 24-27, 1988.

6. T. K. Mossessian and M. Dravinski (1989). Transient Scattering of elastic waves by three dimensional basins. A boundary integral equation approach, Annual Meeting of the Seismological Society of America, April 19-21, 1989, Victoria, British Columbia.

7. H. Eshraghi and M. Dravinski (1989). Transient scattering of elastic plane SH, SV, and P waves by non-axisymmetric three dimensional multiple dipping layers of arbitrary shape, Annual Meeting of the Seismological Society of America, April 19-21, 1989, Victoria, British Columbia.

Invited Talks

1. Domaradzki, J.A., Scattering of localized boundary layer pressures by coating inhomogeneities, Department of Mechanical Engineering, University of Maryland, College Park, Maryland, 05/92.

Statement A per telecon, Dr. Purtell
ONR/Code 1132F. Arlington, VA

10/28/92 JK

3 Research Personnel

1. J.A. Domaradzki (co-Principal Investigator), Associate Professor, Department of Aerospace Engineering, University of Southern California, Los Angeles, CA 90089-1191. Dates supported: 01/01/88 - 09/30/92.

2. M. Dravinski (co-Principal Investigator), Associate Professor, Department of Mechanical Engineering, University of Southern California, Los Angeles, CA 90089-1453. Dates supported: 01/01/88 - 09/30/92.

3. P. Huerre (co-Principal Investigator), Professor, Department of Aerospace Engineering, University of Southern California, Los Angeles, CA 90089-1191. Dates supported: 01/01/88 - 08/31/89.

4. T. K. Mossessin (Graduate Student), Department of Mechanical Engineering, University of Southern California, Los Angeles, CA 90089-1453. Dates supported: 01/01/88 - 12/31/88.

5. H. Esharghi (Graduate Student), Department of Mechanical Engineering, University of Southern California, Los Angeles, CA 90089-1453. Dates supported: 01/01/88 - 12/31/88.

6. R. Keshavamurthy (Graduate Student), Department of Mechanical Engineering, University of Southern California, Los Angeles, CA 90089-1453. Dates supported: 09/01/90 - 09/31/92.

7. K. Shah (Graduate Student), Department of Aerospace Engineering, University of Southern California, Los Angeles, CA 90089-1191. Dates supported: 09/01/88 - 08/31/90.

8. S. Tadepalli (Graduate Student), Department of Aerospace Engineering, University of Southern California, Los Angeles, CA 90089-1191. Dates supported: 09/01/90 - 08/31/92.

Our research had a collaborative character and during its course we have collaborated with the following scientists:

1. D. Crighton (Consultant), Professor, Department of Applied Mathematics and Theoretical Physics, University of Cambridge, Cambridge CB3 9EW, England. Dates supported: 07/31/89 - 08/11/89, and 05/20/91 - 06/04/91.

2. M. Rossi (Consultant), Professor, Laboratory of Modeling and Mechanics, University of Paris VI, 75252 Paris, Cedex 05, France. Dates supported: 05/09/91 - 05/30/91.

This collaboration is reflected in joint authorship of papers, either published or submitted for publication, and in presentations.

4 Degrees Granted

1. Tomi K. Mossessin, Ph.D., (December, 1988), Diffraction of Elastic Waves by Non-axisymmteric Three Dimensional Subsurface Inhomogenieties Using a Boundary Integral Equation Method and a Hybrid Technique, Department of Mechanical Engineering, USC.

2. Hossein Esharghi, Ph.D., (December, 1988), Elastic Waves Scattering by Two and Three Dimensional Near Surface Irregularities of Arbitrary Shape, Department of Mechanical Engineering, USC.

3. Ramdass Keshavamurthy, Ph.D., (September, 1992), Elastic Waves Scattering by an Inclusion in a Multilayered Media Submerged in Fluid, Department of Mechanical Engineering, USC.

4. K. Shah, M.S., (December, 1990), Department of Aerospace Engineering, USC.

5. S. Tadepalli, M.S., (May, 1992), Department of Aerospace Engineering, USC.

5 Honors/Awards/Promotions

1. J.A. Domaradzki, Promotion to Associate Professor of Aerospace Engineering (with tenure), 1991.

2. J.A. Domaradzki, Northrop Junior Faculty Research Award, University of Southern California, School of Engineering, 1991.

3. J.A. Domaradzki, Alexander von Humboldt Research Award for Senior U.S. Scientists, Alexander von Humboldt Foundation, Germany, 1992.

6 Research Results

This section consists of published/accepted journal papers and one unpublished report, which provide detailed information about research results summarized in section 1.

Reprinted from JOURNAL OF COMPUTATIONAL PHYSICS
All Rights Reserved by Academic Press, New York and London

Vol 88, No 1, May 1990
Printed in Belgium

Note

An Analytic Green's Functions Method in Pseudo-Spectral Navier–Stokes Solvers for Boundary Layer and Channel Flows

In pseudo-spectral simulations of a flow between rigid parallel plates with periodic boundary conditions in the horizontal directions, a number of different numerical methods are currently in use. These methods are briefly reviewed by Gottlieb *et al.* [1]. The differences among the methods amount essentially to different ways of imposing the incompressibility condition on the flow and this in turn is directly related to their efficiency in terms of computer storage and time required to perform simulations with a given spatial and temporal resolution. All these methods [2–8] treat the nonlinear terms in the Navier–Stokes equations explicitly and the pressure and viscous terms implicitly. The implicit part must be solved by inverting matrices resulting from spatial discretization of the pressure and viscous terms.

The most efficient methods in terms of computer time and storage are based on expansions of the velocity field into divergence free basis functions [4, 5]. Their disadvantage is that the basis functions must be constructed individually for each flow geometry and the inversion of the resulting matrices may require new algorithms for each geometry. For that reason, methods that can be reduced to solving sequences of standard Poisson and Helmholtz equations are more popular. Among these methods the most efficient is the full time splitting method of Orszag and Kells [8] that requires inversion of four N by N matrices for each horizontal wavenumber (k_x, k_y), where N is the number of mesh points between the plates. The matrices result from a sequence of four Poisson and Helmholtz equations and a variety of numerical schemes exist to acomplish inversions efficiently. The disadvantage of this method is that it violates incompressibility in a numerical boundary layer of thickness $O((\nu\,\Delta t)^{1/2})$ at the plates [6] and for this reason it is not used very frequently.

Incompressibility may be enforced by using the capacitance matrix algorithm of Kleiser and Schumann [7] or the equivalent Green's functions method of Marcus [3]. The Green's functions method of Marcus [3] may be implemented also with four Poisson solvers but ensures incompressibility at the expense of increasing storage requirements by two auxiliary arrays of size N^3. However, such storage is usually not available in high resolution numerical simulations and in commonly used Green's functions methods storage requirements are reduced to those in the full time splitting method, but required computer time increases since six instead of four Poisson equations must then be solved. Orszag *et al.* [6] discuss

0021-9991/90 $3.00

such a Green's functions method for a channel flow that requires six Poisson solvers. The capacitance matrix algorithm of Kleiser and Schumann [7] also requires six Helmholtz solvers. In essence, the Green's functions methods use either more computer time or storage than the full time splitting method. This additional work or storage is a consequence of a need to enforce incompressibility violated by the full time splitting method.

The purpose of this note is to demonstrate that for channel and for flat plate boundary layer flow the Green's functions method may be implemented with only four instead of six Poisson solvers per time step. The savings come from the observation that two of six Poisson equations may be solved analytically in terms of elementary functions. The implementation of the method is straightforward and existing pseudo-spectral computer codes may be easily modified bringing savings in the computer time. The modifications are described for both a channel and a boundary layer code.

Fluid is contained between two rigid parallel plates (channel flow) or above one horizontal plate (boundary layer flow). The z axis of the frame of reference is perpendicular to the plates. The velocity field is decomposed into a prescribed time-independent mean velocity $\mathbf{V}(z) = (U(z), 0, 0)$ in the x direction and a perturbation velocity $\mathbf{v}(x, y, z) = (u, v, w)$. The mean velocity is chosen to satisfy the boundary conditions for the entire flow, e.g., $U(z)$ is the Blasius profile for the boundary layer flow or a parabolic profile for the channel flow. Therefore the perturbation velocity satisfies homogeneous boundary conditions at the horizontal boundaries. With this decomposition the Navier–Stokes equations are

$$\frac{\partial \mathbf{v}}{\partial t} = \left[\mathbf{v} \times \boldsymbol{\omega} - w \frac{\partial \mathbf{V}(z)}{\partial z}\right] - U(z) \frac{\partial \mathbf{v}}{\partial x} - \nabla \Pi + \nu \nabla^2 (\mathbf{v} + \mathbf{V}(z)) \tag{1a}$$

$$\nabla \cdot \mathbf{v} = 0, \tag{1b}$$

where $\boldsymbol{\omega} = \nabla \times \mathbf{v}$ is the vorticity and $\Pi = p/\rho + 1/2\mathbf{v}^2$ is the pressure head where p is the pressure, ρ is the density, and ν is the kinematic viscosity.

Equations (1) are solved by the following pseudo-spectral time splitting method consisting of three separate fractional steps which advance flow velocities from time t_n to t_{n+1}. In Eq. (1a) the nonlinear term is separated into two components. In the first fractional step, the component in the square brackets is calculated pseudo-spectrally and advanced in time using the explicit Adams–Bashforth scheme. In the second fractional step, the advection part of the nonlinear term is diagonalized by Fourier expansion and is solved by the implicit Crank–Nicolson scheme to reduce the convective stability restrictions due to the large mean flow $U(z)$. The intermediate velocities resulting from application of these two fractional steps will be denoted by asterisks. In the third fractional step, pressure and viscous terms with incompressibility (1b) are solved by the Green's functions method as described by Marcus [3] for Couette flow and outlined by Orszag *et al.* [6] for channel flow

leading to the final velocities at time t_{n+1}. Using Fourier expansions in the horizontal directions for the dependent variable

$$\mathbf{v}(x, y, z, t) = \sum_{|m| < M} \sum_{|n| < N} \hat{\mathbf{u}}(k_x, k_y, z, t) \exp(ik_x x) \exp(ik_y y), \tag{2}$$

where $k_x = 2\pi m/L_x$, $k_y = 2\pi n/L_y$ are the horizontal wavenumbers and L_x and L_y are the periodicity lengths, the following equations in spectral space are obtained from the pressure and the viscous terms at the last fractional step

$$\frac{\partial \hat{u}}{\partial t} = -ik_x \hat{\Pi} + \nu \left(\frac{\partial^2}{\partial z^2} - k_x^2 - k_y^2 \right) (\hat{u} + \hat{U}(z)) \tag{3a}$$

$$\frac{\partial \hat{v}}{\partial t} = -ik_y \hat{\Pi} + \nu \left(\frac{\partial^2}{\partial z^2} - k_x^2 - k_y^2 \right) \hat{v} \tag{3b}$$

$$\frac{\partial \hat{w}}{\partial t} = -\frac{\partial}{\partial z} \hat{\Pi} + \nu \left(\frac{\partial^2}{\partial z^2} - k_x^2 - k_y^2 \right) \hat{w}, \tag{3c}$$

where $\hat{U}(z)$ is the horizontal Fourier transform of the mean velocity $U(z)$, which is nonzero only for $(k_x, k_y) = 0$. The continuity equation (1b) becomes

$$ik_x \hat{u} + ik_y \hat{v} + \frac{\partial \hat{w}}{\partial z} = 0. \tag{4}$$

Equations (3) are discretized in time using the Crank–Nicolson method for the viscous term and the full implicit method for the pressure term. Eliminating $\hat{\Pi}$ from (3a) and (3b), and using the incompressibility condition (4) we get an equation for $\hat{w}^{n+1}$, *the vertical component of the velocity* at time t_{n+1},

$$(D^2 - k^2) \left(D^2 - k^2 - \frac{2}{\nu \Delta t} \right) \hat{w}^{n+1}(k_x, k_y, z) = g(k_x, k_y, z), \tag{5}$$

where

$$g(k_x, k_y, z) = \left(D^2 - k^2 + \frac{2}{\nu \Delta t} \right) [D(ik_x \hat{u}^* + ik_y \hat{v}^*) + k^2 \hat{w}^*]. \tag{6}$$

In (5) and (6) $k^2 = k_x^2 + k_y^2$, $D = \partial/\partial z$ and velocities denoted by asterisks are the results of the first two fractional steps. Note that these velocities do not satisfy incompressibility since this condition is imposed only at the last fractional step, so that the velocity is divergence free after the full time step. Equation (5) must be solved for each horizontal wavenumber (k_x, k_y) with the boundary conditions $\hat{w}^{n+1} = 0$ and $D\hat{w}^{n+1} = 0$. The latter condition follows from (4). In boundary layer

flow this condition is used only at the lower boundary $z=0$. Once $\hat{w}^{n+1}$ is found then the expression for $\hat{\Pi}^{n+1}$ is

$$\hat{\Pi}^{n+1} = -\frac{\nu}{2k^2}\left[(D^2-k^2)(ik_x\hat{u}^* + ik_y\hat{v}^* - D\hat{w}^{n+1}) + \frac{2}{\nu\,\Delta t}(ik_x\hat{u}^* + ik_y\hat{v}^* + D\hat{w}^{n+1})\right]. \tag{7}$$

The horizontal velocity components are obtained from the following Helmholtz equations

$$\left(D^2 - k^2 - \frac{2}{\nu\,\Delta t}\right)\hat{u}^{n+1} = \frac{2}{\nu\,\Delta t}[ik_x\,\Delta t\hat{\Pi}^{n+1} - \hat{u}^*] - (D^2-k^2)(\hat{u}^* + 2\hat{U}(z)) \tag{8}$$

$$\left(D^2 - k^2 - \frac{2}{\nu\,\Delta t}\right)\hat{v}^{n+1} = \frac{2}{\nu\,\Delta t}[ik_y\,\Delta t\hat{\Pi}^{n+1} - \hat{v}^*] - (D^2-k^2)\,\hat{v}^*. \tag{9}$$

In what follows let us assume that we have efficient numerical solvers for the channel and the boundary layer flow geometry for the Poisson equation

$$(D^2-k^2)\,f(k_x, k_y, z) = g(k_x, k_y, z) \tag{10a}$$

and the Helmholtz equation

$$\left(D^2 - k^2 - \frac{2}{\nu\,\Delta t}\right)f(k_x, k_y, z) = g(k_x, k_y, z) \tag{10b}$$

with homogeneous Dirichlet boundary conditions. With these solvers it is a straightforward task to solve Eqs. (8) and (9) for $\hat{u}^{n+1}$ and $\hat{v}^{n+1}$. Equation (5) will be solved by a modified Green's functions method.

Boundary Layer Flow

Equation (5) must be solved for all pairs of horizontal wavenumbers (k_x, k_y) in the domain $z \in [0, \infty)$ with the boundary conditions

$$\hat{w}(0) = \hat{w}(\infty) = D\hat{w}(0) = 0. \tag{11}$$

Note that in (11) and in all subsequent formulae explicit dependence of various functions on k_x, k_y is often omitted if it does not lead to confusion. The solution of (5) is obtained as

$$\hat{w}(z) = b_- w_-(z) + w_0(z), \tag{12}$$

where w_0 is obtained by solving the sequence of equations

$$\left(D^2-k^2-\frac{2}{\nu\,\Delta t}\right)\zeta_0(z)=g(z);\qquad \zeta_0(0)=\zeta_0(\infty)=0 \tag{13a}$$

$$(D^2-k^2)\,w_0(z)=\zeta_0(z);\qquad w_0(0)=w_0(\infty)=0 \tag{13b}$$

and $w_-(z)$ is obtained by solving

$$\left(D^2-k^2-\frac{2}{\nu\,\Delta t}\right)\zeta_-(z)=0;\qquad \zeta_-(0)=1,\ \zeta_-(\infty)=0 \tag{14a}$$

$$(D^2-k^2)\,w_-(z)=\zeta_-(z);\qquad w_-(0)=w_-(\infty)=0. \tag{14b}$$

Constant b_- is determined in such a way that the boundary condition (11) for $D\hat{w}(z)$ is satisfied,

$$b_- = -Dw_0(0)/Dw_-(0). \tag{15}$$

In the Green's functions method described in [6] if the function w_- (the Green's function for this problem) is found in the preprocessing step and is stored, the solution of (5) requires solution of the two equations (13a) and (13b). If storage is limited only the boundary values $Dw_-(0)$ are stored. To get $\hat{w}$, after finding w_0 from (13) and b_- from (15) Eqs. (13) are solved once more with the following boundary conditions:

$$\hat{\zeta}(0)=b_-,\qquad \hat{\zeta}(\infty)=0;\qquad \hat{w}(0)=0,\qquad \hat{w}(\infty)=0. \tag{16}$$

Thus finding $\hat{w}$ is equivalent to solving numerically *four Poisson equations.*

A simplification of the Green's function method discussed here is based on the observation that Eqs. (14) for the Green's functions may be solved analytically. Indeed, the solution to Eq. (14a) is

$$\zeta_-(z)=\exp(-\kappa z), \tag{17}$$

where $\kappa=(k^2+2/(\nu\,\Delta t))^{1/2}$. A solution to Eq. (14b) is sought as

$$w_-(z)=Ae^{-\kappa z}+Be^{-kz}. \tag{18}$$

Equation (14b) and the boundary conditions are satisfied if

$$A=-B=\nu\,\Delta t/2. \tag{19}$$

The derivative of w_- at the boundary needed in (15) is

$$Dw_-(0)=0.5\nu\,\Delta t(k-\kappa). \tag{20}$$

After numerically solving the two equations (13a) and (13b), the complete solution $\hat{w}(z)$ is found from (12), (15), and (18)–(20). The work required is therefore equivalent to solving numerically only two Poisson equations.

Channel Flow

In the case of the channel flow, Eq. (5) must be solved in the domain $z \in [-1, +1]$ with the following boundary conditions

$$\hat{w}(-1) = \hat{w}(+1) = D\hat{w}(-1) = D\hat{w}(+1) = 0. \tag{21}$$

In the Green's functions approach [6] this is done by representing the solution $\hat{w}$ as

$$\hat{w}(z) = b_- w_-(z) + b_+ w_+(z) + w_0(z), \tag{22}$$

where w_0 is obtained from Eqs. (13) with zero boundary conditions at $z = \pm 1$, and the functions $w_\pm$ are solutions of the following sequence of equations

$$\left(D^2 - k^2 - \frac{2}{\nu\,\Delta t}\right)\zeta_\pm(z) = 0; \qquad \zeta_-(-1) = \zeta_+(+1) = 1; \qquad \zeta_+(-1) = \zeta_-(+1) = 0; \tag{23a}$$

$$(D^2 - k^2)\, w_\pm = \zeta_\pm(z); \qquad w_\pm(\pm 1) = 0. \tag{23b}$$

Constants $b_\pm$ will be determined from the boundary conditions for $D\hat{w}(\pm 1)$ (Eq. (21)).

As in the case of the boundary layer flow Eqs. (23) may be solved analytically. The solution of (23a) is

$$\zeta_\pm(z) = A_\pm e^{-\kappa z} + B_\pm e^{+\kappa z}, \tag{24}$$

where $\kappa = (k^2 + 2/(\nu\,\Delta t))^{1/2}$, and

$$A_- = \frac{1}{e^{\kappa} - e^{-3\kappa}}, \qquad B_- = \frac{1}{e^{-\kappa} - e^{3\kappa}}, \qquad A_+ = B_-, \qquad B_+ = A_-. \tag{25}$$

A solution to Eq. (23b) is sought in the following form

$$w_\pm(z) = C_\pm e^{+\kappa z} + D_\pm e^{-\kappa z} + E_\pm e^{+kz} + F_\pm e^{-kz}. \tag{26}$$

The constants in (26) are determined from Eq. (23b) and its boundary conditions

$$C_- = \frac{\nu\,\Delta t/2}{e^{-\kappa} - e^{3\kappa}}, \qquad D_- = \frac{\nu\,\Delta t/2}{e^{\kappa} - e^{-3\kappa}} \tag{27a), (27b)}$$

$$E_- = -\frac{\nu\,\Delta t/2}{e^{-k} - e^{3k}}, \qquad F_- = -\frac{\nu\,\Delta t/2}{e^{k} - e^{-3k}} \tag{27c), (27d)}$$

$$C_+ = D_-, \qquad D_+ = C_-, \qquad E_+ = F_-, \qquad F_+ = E_-. \tag{27e}$$

The boundary conditions (21) are used to get a system of linear equations for $b_\pm$,

$$b_+ Dw_+(\pm 1) + b_- Dw_-(\pm 1) = -Dw_0(\pm 1). \tag{28}$$

Using symmetries (27e) we get

$$Dw_-(\pm 1) = -Dw_+(\mp 1) \tag{29}$$

and the explicit expression for $b_\pm$ is obtained from (28)

$$b_\pm = \frac{(-Dw_+(\pm 1)\,Dw_0(+1) + Dw_+(\mp 1)\,Dw_0(-1))}{(Dw_+(+1)^2 - Dw_+(-1)^2)}. \tag{30}$$

Expressions for $Dw_+(\pm 1)$ are gotten from (26),

$$Dw_+(-1) = \frac{1}{2}\nu\,\Delta t\left[\frac{2\kappa}{e^{2\kappa} - e^{-2\kappa}} - \frac{2k}{e^{2k} - e^{-2k}}\right] \tag{31a}$$

$$Dw_+(+1) = \frac{1}{2}\nu\,\Delta t\left[\kappa\left(\frac{1}{1-e^{-4\kappa}} - \frac{1}{1-e^{4\kappa}}\right) - k\left(\frac{1}{1-e^{-4k}} - \frac{1}{1-e^{4k}}\right)\right]. \tag{31b}$$

Note that the solution procedure must be modified for the wavenumber $k = 0$, since in this case a solution to (23b) is

$$w_\pm(z) = C_\pm e^{\kappa z} + D_\pm e^{-\kappa z} + E_\pm z + F_\pm. \tag{32}$$

In (32) the constants $C_\pm$, $D_\pm$ are given by (27a), (27b), and (27e) and

$$E_- = -F_- = \tfrac{1}{4}\nu\,\Delta t, \qquad E_+ = F_+ = -\tfrac{1}{4}\nu\,\Delta t. \tag{33}$$

The complete solution is determined by Eq. (22), where w_0 is obtained by numerically solving the two equations (13), $w_\pm$ are given by (26) (or (32) for $k = 0$), and constants $b_\pm$ are given by Eq. (30). Formula (30) involves derivatives of the exact solution w_+ and the solution w_0 which are calculated numerically with necessarily finite accuracy. For the vertical resolution $N < 32$ modes combining derivatives of the analytical and the numerical solutions led to slight errors in the constants $b_\pm$. In such a case it is advisable to use in (30) boundary derivatives of the function w_+ computed numerically in the pre-processing step. This results in cancellation of errors and improved accuracy for the constants $b_\pm$. For $N > 64$ this method does not improve accuracy any further and formulas (30) and (31) should be used.

TABLE I

Comparison between Growth Rates of the Tollmien–Schlichting Waves Obtained from the Orr–Sommerfeld Equation (ω_{OS}) and from the Navier–Stokes Solver (ω_{NS}).

Re	ω_{OS}	ω_{NS}	ε
1500	−0.0010049	−0.0010048	10^{-4}
1800	−0.0000991	−0.0000990	10^{-3}
2100	+0.0005267	+0.0005269	3×10^{-4}

Note. The relative error $\varepsilon = (\omega_{NS} - \omega_{OS})/\omega_{OS}$.

Numerical Example

To test the above method a pseudo-spectral boundary layer code used previously by Domaradzki and Metcalfe [9] was modified according to these ideas. The code used in [9] was derived from the channel code of Orszag and Kells [8] and uses the full time splitting method which is known to violate the incompressibility condition. For this reason it generally produces results that are significantly less accurate than results obtained by numerical codes that satisfy incompressibility. A standard test of the accuracy of a boundary layer and a channel flow code is made by comparing growth rates of modes calculated from the Orr–Sommerfeld equation with growth rates of the same modes predicted by the Navier–Stokes code.

We have performed such tests for the modified code. The Navier–Stokes simulations were initialized with the velocity fields obtained from the most unstable mode of the Orr–Sommerfeld equation for a wavenumber $\alpha = 1.0$ and three different Reynolds numbers (based on the boundary layer thickness defined as $\delta = 6.02(\nu x/U_0)^{1/2}$). The amplitude of the wave was chosen as 10^{-5} of the free stream velocity U_0, so that the nonlinear effects were small. Simulations were two-dimensional with 65 mesh points in the vertical and 8 points in the horizontal direction. In Table I the comparison is presented between growth rates of the Tollmien–Schlichting waves obtained from the Orr–Sommerfeld solver and results of numerical solution of the Navier–Stokes equation after 50 time steps. For all three cases the growth rates predicted by the Navier–Stokes solver agree with the growth rates calculated from the Orr–Sommerfeld equation up to six significant figures. This accuracy matches the accuracy of results obtained by Marcus [3] in a similar test problem for his divergence free code for Couette flow (see Table I in [3]). Also the relative error ε is generally about two orders of magnitude less than the error observed in simulations performed with the full time splitting method used in [9] for the boundary layer and in [8] for the channel flow.

In Table II timings for the analytical and numerical Green's functions methods are presented for the boundary layer code run with a resolution of 64^3 modes on

TABLE II

CPU Timings (in Seconds) for Different Implementations of the Green's Functions Method

Method	Full step	3rd step	Poisson solver
NA	12.20	9.37	0.50
AA	11.03	8.25	0.50
NF	19.26	16.34	1.64
AF	15.40	12.58	1.58

Note. NA-numerical with an assembly Poisson solver; AA-analytical with an assembly Poisson solver; NF-numerical with a Fortran Poisson solver; AF-analytical with a Fortran Poisson solver. Timings are for the full time step, the third fractional step (the pressure and viscous step), and the Poisson solver.

the Cray X-MP. Using the analytical Green's functions reduces required CPU time by about 10% (time needed to solve two Poisson equations) as compared with the methods discussed in [6, 7] which solve all Poisson equations numerically. The above estimate should be considered as a lower bound since we used a highly optimized Poisson solver coded in the Assembly language on the Cray X-MP. For the same Poisson solver coded in Fortran savings in computer time are about 20% when using the analytical Green's functions method instead of the numerical one, since two Poisson solvers saved constitute larger portion of the full time step than in the previous case. Similar savings were also observed after applying the analytical Green's functions methods to modify the numerical code used by Domaradzki and Metcalfe [10] to simulate Rayleigh-Benard convection between two rigid plates. The numerical Navier–Stokes solver in [10] uses the Green's functions method of reference [6]. How much time will precisely be saved in any particular case depends on details of a numerical code since savings are equivalent to time needed to solve two Poisson equations and this time may vary among different codes. In high resolution numerical simulations an increase by 10–20% in an efficiency of a numerical code may translate into hours of supercomputer time saved per run.

The incompressibility was checked by comparing individual terms $\partial u/\partial x$, $\partial v/\partial y$, $\partial w/\partial z$ with their sum, which should be equal to zero. At the first mesh point away from the boundary $z = 0.00018\delta$ the relative error is 2%, dropping to 0.03% at the second mesh point $z = 0.0007\delta$, and to 0.001% at the third point $z = 0.0017\delta$. This error in the divergence at the boundary is caused entirely by an inaccuracy of the order 10^{-10} in the numerical calculation of the z-derivative in that region. Close to the boundary derivatives of the velocity are all of the order 10^{-8} so that the absolute error of the order 10^{-10} has an appreciable effect on the accuracy of the divergence. The relative error in the divergence becomes uniformly less than 10^{-8} for $z > 0.015\delta$.

CONCLUSIONS

We have shown that the Green's functions method [3, 6, 7] for the channel and the flat plate boundary layer flow may be modified by solving analytically several equations that are usually solved numerically. This modification reduces from six to four the number of Poisson and Helmholtz equations that must be solved numerically at each time step. For a typical pseudo-spectral Navier–Stokes solver this modifications saves about 10% of computer time as compared with the original method that solves all equations numerically. The amount of required computer time may be reduced even further as follows. If the vertical component of velocity w is known and one of the horizontal components of velocity (u) is determined from (8) then the other horizontal component may be obtained from the incompressibility condition instead of Poisson Eq. (9). This reduces to three the total number of Poisson solvers needed per time step. The implementation of the Green's functions method described in this note is especially attractive in modifying existing pseudo-spectral codes that use either the Green's functions method [6] or the equivalent capacitance matrix technique [7]. It may also be attractive in the development of new codes since an algorithm to solve efficiently Eqs. (1) may be constructed from standard numerical building blocks: Fast Fourier Transform subroutines to calculate the nonlinear terms and Poisson and Helmholtz solvers (with homogeneous Dirichlet boundary conditions) to treat viscous and pressure effects. The existence of the analytical Green's functions in Navier–Stokes solvers for simple flat plate and channel flow geometry also suggests that their existence in more complicated geometries should be investigated.

ACKNOWLEDGMENTS

This research was supported by the Office of Naval Research Contract N00014-88-K-0157 and a Research Initiation Grant from the Powell Foundation. Computer time on Cray X-MP was provided by the San Diego Supercomputer Center.

REFERENCES

1. D. GOTTLIEB, M. Y. HUSSAINI, AND S. A. ORSZAG, in *Spectral Methods for Partial Differential Equations*, edited by R. G. Voigt *et al.* (SIAM, Philadelphia, 1984), p. 1.
2. P. MOIN AND J. KIM, *J. Comput. Phys.* **35**, 381 (1980).
3. P. S. MARCUS, *J. Fluid Mech.* **146**, 45 (1984).
4. R. D. MOSER, P. MOIN, AND A. LEONARD, *J. Comput. Phys.* **52**, 524 (1983).
5. P. R. SPALART, NASA Technical Memorandum 88222 (1986).
6. S. A. ORSZAG, M. ISRAELI, AND M. O. DEVILLE, *J. Sci. Comput.* **1**, 75 (1986).
7. L. KLEISER AND U. SCHUMANN, in *Spectral Methods for Partial Differential Equations*, edited by R. G. Voigt *et al.* (SIAM, Philadelphia, 1984), p. 141.

8. S. A. ORSZAG AND L. C. KELLS, *J. Fluid Mech.* **96**, 159 (1980).
9. J. A. DOMARADZKI AND R. W. METCALFE, *Phys. Fluids* **30**, 695 (1987).
10. J. A. DOMARADZKI AND R. W. METCALFE, *J. Fluid Mech.* **193**, 499 (1988).

RECEIVED: June 6, 1988; REVISED: April 14, 1989

J. ANDRZEJ DOMARADZKI

Department of Aerospace Engineering,
University of Southern California,
Los Angeles, California 90089-1191

Printed by Catherine Press, Ltd., Tempelhof 41, B-8000 Brugge, Belgium

NUMERICAL SIMULATIONS FOR BOUNDARY LAYER FLOW OVER A FLAT PLATE

by

J. A.Domaradzki and Srinivas Tadepalli
Department of Aerospace Engineering
University of Southern California, Los Angeles,
CA 90089-1191

ONR Contract N00014-91-J-4163
Computer time provided by SDSC

Abstract: We have obtained finite amplitude states for boundary layer flow over a flat plate initializing simulations with the most unstable Tollmien-Schlicting(T-S) waves and advanced until the amplitudes of all excited modes were found to be saturated. The eigen-functions of the transverse velocity modes as well as the streamwise velocity modes were observed to be preserving in shape. However the mean flow correction was observed to be not stabilizing. The response of this finite amplitude state to a localized perturbation is investigated. Low amplitude forcing (1% of free stream velocity) led to no significant interaction between the large scales and the small scale perturbations, but resulted in viscously damped perturbations. Qualitatively, different behavior was observed in the energy growth rate by varying the amplitude of forcing for both T-S and finite amplitude state initializations. A 50% distribution of Chebyshev points in the vertical direction in the boundary layer could best resolve the transverse eigen functions and their derivatives.

I. Introduction. A sizeable scientific community agrees that the turbulent burst cycle is the single most important event for wall bounded flows. There are a large number of models pertaining to the appearance and the activities of these structures and their role in the flow properties. Bursts are rare, intense hydrodynamic events in turbulent boundary layers and result in high wall pressure peaks which advect with the mean flow and may serve as sources of acoustic radiation. The most important feature of natural bursts in turbulent boundary layers is their random occurrence. Apart from the difficulties associated in resolving the vortex structures over a large range of length scales (typically 10^7), the long memory of the flow complicates the understanding between the observed effects and external stimuli. According to Acarlar and Smith,(JFM 1987, Vol-175, pp. 43-83) artificially creating an inflectional profile yield similar flow structures and behavior as observed in a turbulent boundary layer. Controlled experiments would be useful in understanding turbulent flow structures. However, it is essential to note that by considering artificial bursts large scale turbulent structures responsible for terminating bursts are removed. The evolution of pairs of counter rotating vortices (figure-1) generated by suction-blowing mechanism gave the required structure for study, as a model problem.

II. Details of Numerical simulations

Nonlinear stability analysis of laminar boundary layer flow predicts existence of finite amplitude time periodic waves for supercritical Reynolds numbers in the vicinity of the lower branch of the stability curve(figure-2). We have attempted to perform pseudospectral numerical simulations for finite amplitude states in a boundary layer and study their interaction with T-S waves and wall forcing. Crank Nicolson time stepping is used. Pressure and viscous terms are handled implicitly and nonlinear terms are handled using Adams-Bashforth explicit scheme. Mean flow diffusion term was switched off to prevent boundary layer growth in the computational cell.

Breuer's Initialization(JFM 1990 Vol 220, pp595-621): The initial disturbance used is comprised of two pairs of counter rotating vortices defined by the following velocity field at t=0. Figures 3(a) and 3(b) show the streamwise and spanwise perturbation field in the horizontal and vertical planes at the end of first time step.

$$u = 0$$

$$v = -0.2xy\,(3z^2 - 2z^4)\,e^{-(x^2+y^2+z^2)}$$

$$w = 0.2xz^3\,(1-2y^2)\,e^{-(x^2+y^2+z^2)}$$

where $x=x/L_x$, $y=y/L_y$ and $z=z/L_z$, where x, y, z are the cartesian coordinates, $L_x = 5.0\delta_d^*$, $L_y = 6.0\delta_d^*$, $L_z = 1.2\delta_d^*$ and δ_d^* is the displacement thickness of the boundary layer.

This initial field gives a peak-peak value of w about 7% of free stream velocity at $(\sqrt{\frac{1}{2}}, 0, \sqrt{\frac{3}{2}})$. The size of the computational box is 100 δ_d^* by 50 δ_d^*. Reynolds number based on the boundary layer thickness is 3325.

Poisson Equation for Pressure head:
A Poisson equation for pressure head is obtained by taking the divergence of N-S equations and is given by

$$(D^2 - k^2)\,\Pi^{n+1} = ik_x\,(v\times\omega)_x^n + ik_y\,(v\times\omega)_y^n + \frac{\partial}{\partial z}(v\times\omega)_z^n - ik_x U'(z)\,w^n$$
$$+ k_x^2 U(z)\,u^n + k_x k_y U(z)\,v^n - ik_x U(z)\frac{\partial}{\partial z}w^n$$

where $D=\frac{d}{dz}$. This is solved with the boundary condition

$$\frac{\partial \Pi}{\partial z} = \nu\frac{\partial^2 w}{\partial 2}$$

where u,v,$w$and Π are in spectral space.
The expression for the pressure head employing Green's function method (Domaradzki, J. Comput. Phys. 1990, vol. 88) in spectral space is

$$\Pi^{n+1}(z) = \frac{e^{-kz}}{k}\,(\Pi_n'(0) - \nu w''(0)) + \Pi_n(z)$$

where $\Pi_n(z)$ satisfies

$$(D^2 - k^2)\,\Pi_n = g(z), \Pi_n(0) = 0, \Pi_n(\infty) = 0$$

where

$$g(z) = ik_x(v\times\omega)_x^n + ik_y(v\times\omega)_y^n + \frac{\partial}{\partial z}(v\times\omega)_z^n - ik_xU'(z)w^n$$
$$+ k_x^2U(z)u^n + k_xk_yU(z)v^n - ik_xU(z)\frac{\partial}{\partial z}w^n$$

This method when used as a diagnostic gave the correct structure for the pressure field. Alternatively,

$$(D^2-k^2)\Pi^{n+1} = \frac{\nu}{2}(D^2-k^2+\frac{2}{\nu\Delta t})(ik_xu^* + ik_yv^* + Dw^*)$$

where u^*, v^*, w^* are the fractional step streamwise, spanwise and vertical velocities. This is solved with the following boundary conditions ((a) and (b))

$$\text{(a) } D\Pi^{n+1}\Big|_b = \frac{\nu}{2}D^2(w^{n+1}+w^*)$$

$$\text{(b) } D\Pi^{n+1}\Big|_b = \nu D^2w^{n+1}$$

This gives

$$\text{(a) } \Pi^{n+1}(z) = \frac{1}{k}\left(\frac{d}{dz}\Pi_n - \frac{\nu}{2}\left(\frac{d^2}{dz^2}w^{n+1} + \frac{d^2}{dz^2}(w)^*\right)\right)_b \Pi_0(z) + \Pi_n(z)$$

$$\text{(b) } \Pi^{n+1}(z) = \frac{1}{k}\left(\frac{d}{dz}\Pi_n - \nu\frac{d^2w}{dz^2}^{n+1}\right)_b \Pi_0(z) + \Pi_n(z)$$

However the pressure head was found to be not sensitive to the type of boundary condition imposed ((a) or (b)). Though this method gave the correct vertical structure of pressure, it could not preserve incompressibility. Figures 4(a) and 4(b) depict pressure head in the vertical and horizontal planes respectively in the first few steps.

An alternate numerical scheme for the explicit handling of nonlinear terms for the equations written in the spectral space using the fractional time splitting method:

$$\frac{\partial u}{\partial t} = -wU' - ik_xuU$$
$$\frac{\partial v}{\partial t} = -ik_xUv$$
$$\frac{\partial w}{\partial t} = -ik_xUw$$

is given by:

$$u^n = \frac{(1+ik_xU\frac{\Delta t}{2})}{(1-ik_xU\frac{\Delta t}{2})}u^* + U'\frac{\Delta t}{2}(w^*+w^n)$$

$$v^n = \frac{(1 + ik_x U\frac{\Delta t}{2})}{(1 - ik_x U\frac{\Delta t}{2})} v^*$$

$$w^n = \frac{(1 + ik_x U\frac{\Delta t}{2})}{(1 - ik_x U\frac{\Delta t}{2})} w^*$$

where u, v, w and U are in spectral space and u^*, v^*, w^* are the intermediate results of velocity in x, y, z directions respectively.
However, the implementation of this scheme did not lead to any improved accuracy.

Vertical Mapping:
The distribution of Chebyshev points by an analytical mapping in the vertical direction controls the grid growth ratios of successive points. We observe that the accuracy of the numerical derivatives computation is strongly dependent on the uniformity of the grid growth ratios especially close to the boundary. The present mapping was found to be better than other algebraic functions explored. For T-S wave initializations, 50% distribution of vertical points in the boundary layer resolved the transverse velocity modes accurately. The analytical mapping used has the matrix elements:

$$GF(z) = \frac{ab}{(b+z)^2}$$

Finite Amplitude State:
Finite amplitude state is obtained by 2-D temporal simulations of the most unstable T-S wave initialization for Re=2170 (based on boundary layer thickness). The point corresponding to z=10 in the physical space is used for normalizing the equilibrium amplitude to A_e=0.0023. Temporal simulations are continued until all the higher modes were saturated.
The governing equation at equilibrium for transfer of energy between spectral modes for finite amplitude states is given by:

$$\nu\frac{d^2u_0}{dz^2} = w_1\frac{du_1^*}{dz} + w_1^*\frac{du_1}{dz}$$

where u_0 and u_1^* refer to the zero mode and complex conjugate of first mode of the streamwise velocity respectively in the spectral space.
These finite amplitude states when perturbed by blowing and suction led to large energy growth during the first phase of blowing. The maximum perturbation measured from the entire flow field was observed to be periodic in time.

LOCATION OF THE SLIT FOR THE BLOWING-SUCTION

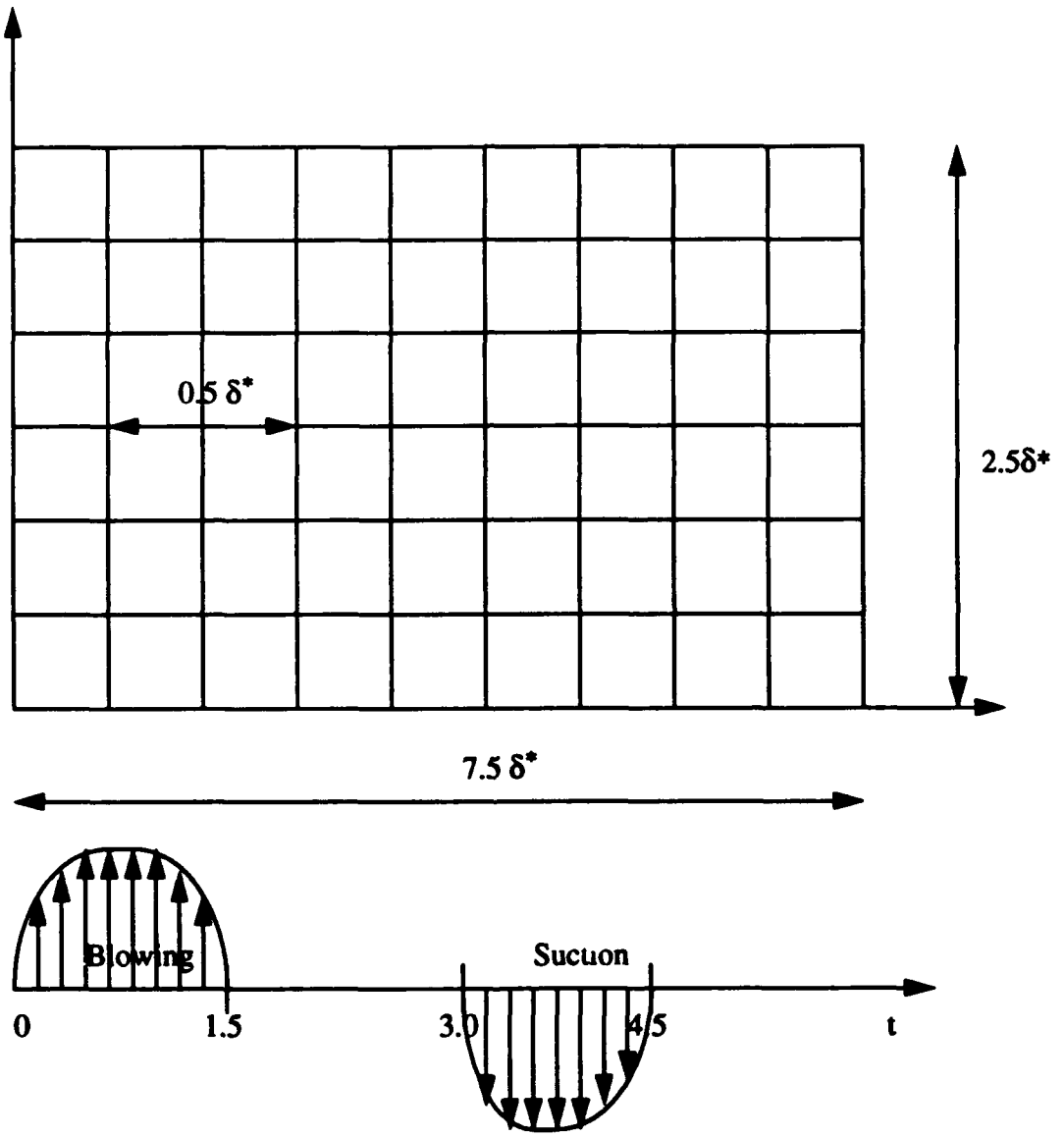

Mechanism of Blowing & Suction: A slit is made on the boundary at the mid -spanwise location of width half a boundary layer thickness in the computational box of size $7.5\delta^*$ and $2.5\delta^*$ in the streamwise and spanwise directions respectively. The blowing is continued until t=1.5 and suction is enforced after 1.5 units of time.

III. Qualitative features

(i)The transverse eigen modes and streamwise eigen modes preserve their shape in the temporal simulations. Figures 10(a)&(b), 11(a)&(b) show the normalized streamwise first mode real and imaginary parts at t=0 and t=400 in spectral space. Figures 12(a)&(b) show the transverse fourth mode real part at t=100 and t=200.

(ii)The transverse eigen modes and their derivatives were observed to be smooth and best resolved for 50% distribution of vertical Chebyshev points in the boundary layer.

(iii)The energy set in the first mode remains approximately constant while higher modes gain energy by nonlinear interactions and saturate after a certain time. Figures 8(a)&(b) and 9(a)&(b) depict the streamwise first and fourth velocity modes evolution and their maximum amplitude.

(iv)The structure generated by the wall forcing in the boundary layer advects in the temporal simulations. Figures 5(a)&(b) show the streamwise velocity u in the vertical plane at t=10 and t=25. The flow is from left to right and the structure advects downstream.

(v)Viscous decay of the perturbations occurred for 1.5% boundary layer forcing. Figures 6(a)&(b) are the contour plots of spanwise velocity v at t=10 and t=25 in the horizontal plane for boundary layer forcing alone. Figures 13(a)-(d), 14(a)&(b) are the contour plots of streamwise velocity u in the vertical plane starting from t=0 to t=25. Figures 15(a)&(b) are the contour plots of spanwise velocity v in the horizontal plane at t=5 and t=25.

(vi)An enormous energy growth rate occurred at 5% wall forcing with T-S wave initialization while this occurred at 1.25% wall forcing with finite amplitude initialization.

(vii)The maximum streamwise perturbation recorded for the entire flow decays with time, while perturbation energy growth rate decays at an increasing rate for boundary layer forcing generated by blowing-suction mechanism (Figures 7(a)&(b)).

(viii)Large scale structures can be effectively modeled through nonlinear, finite amplitude Tollmien-Schlicting waves.

Data Visualization:

The following color templates, coded on the magnitude of the variable plotted are available from the authors upon request. They depict a pair of counter rotating vortices localized in the boundary layer with periodic boundary conditions. They can be observed to be diffusing in time.

Template-1 shows the surface plot of the initial condition for streamwise perturbation obtained from the most unstable T-S wave initialization.

Template-2 shows the streamwise perturbation surface plot at t=400.

Template-3 is a contour plot of the evolution of a set of counter rotating vortices in the 2-D simulation at intermediate time t=50.

Template-4 depicts the diffusion of the counter rotating vortices at t=200.

Template-5 is a contour plot of streamwise perturbation in x-z plane(Finite Amplitude state).

The table-1 given below shows the amplitude limits, CPU time and minimum required resolution for different types of runs as shown below.

Table-1

Type of run	physical time before blow up	Amplitude of forcing	CPU time per iteration	Min. vertical resoln.*
B.L. forcing	-----	**1.5%**	**11 sec**	**65**
B.L. forcing + T.S. waves		5% before blow up	28sec	129
B.L. forcing + FAST**	.85sec 1.25 sec	1.5% 1.25%	29sec	129

Conclusions:

(a)Applied suction/blowing mechanism at the wall induces desired flow structures.

(b)Low Amplitude forcing (1.5%U_∞) results in viscously damped perturbations.

(c)Large Scale structures can be effectively modeled through nonlinear finite amplitude T-S waves.

(d)No significant interaction between large scales and a small scale perturbation at the low level of forcing. (up to 1.5%U_∞)

(e)The transverse eigen modes and streamwise eigen modes preserve their shape in the temporal simulations.

*-To resolve the eigen functions and their derivatives accurately.

**-Finite Amplitude state

figure -1

Artificial Burst

Pseudospectral numerical code for boundary layer flows employing analytical Green's functions method (JAD,*J. Comput. Phys.***88**, (1990))

Suction-blowing boundary conditions to induce two pairs of counter-rotating vortices (after Breuer, Haritonidis and Landahl JFM **220**, 1990).

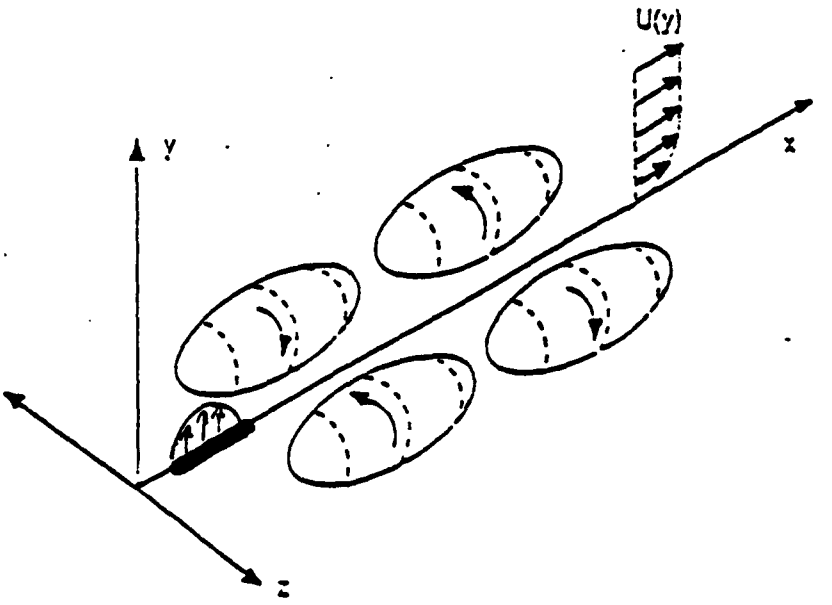

Large Scale Structure

Nonlinear, finite amplitude Tollmien-Schlichting wave in a laminar boundary layer flow (Sen and Vashist, Proc. R. Soc. Lond. A**424**, 1989)

figure -2

P. K. Sen and T. K. Vashist

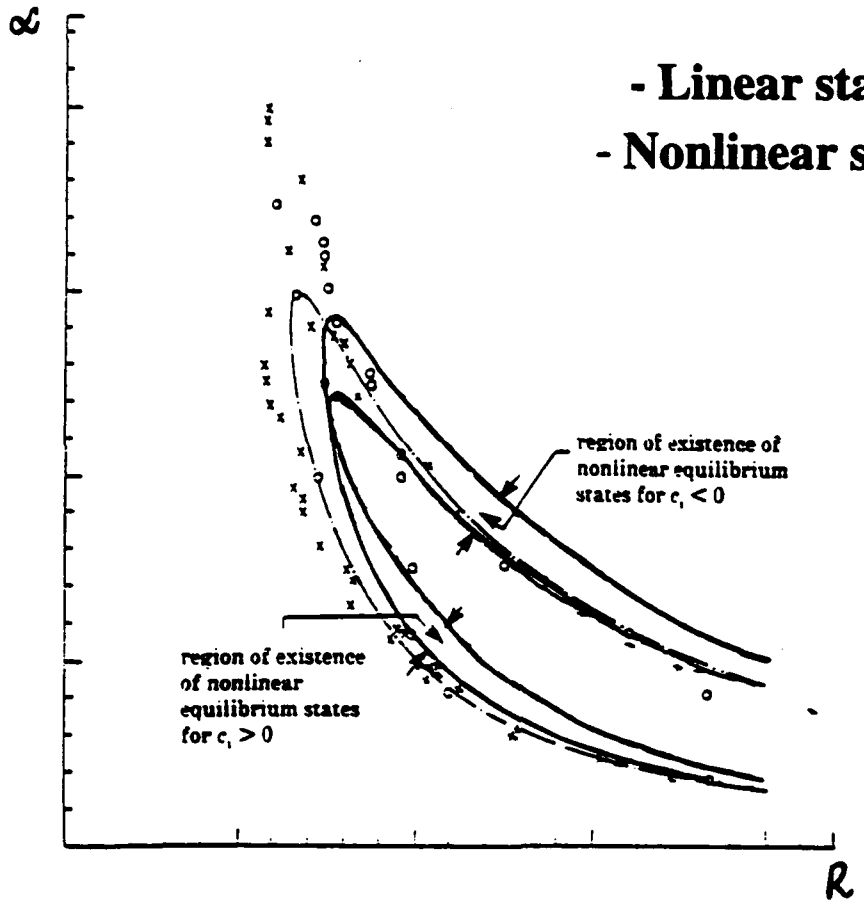

$$\mathbf{u}(x,z,t) = \sum_{n=0}^{4} \mathbf{A}_n(z,t) e^{in\alpha(x-ct)}$$

Linear Tollmien-Schlichting wave: n=1.

figure -3(a)

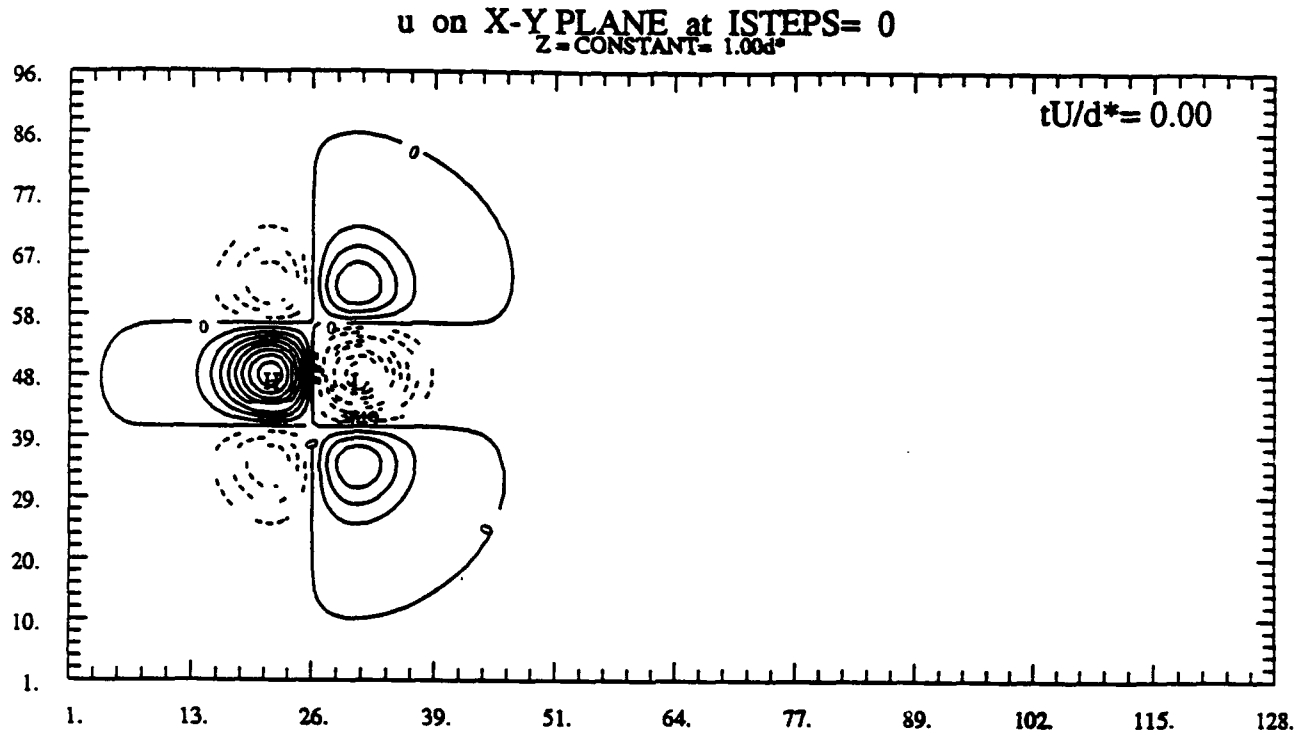

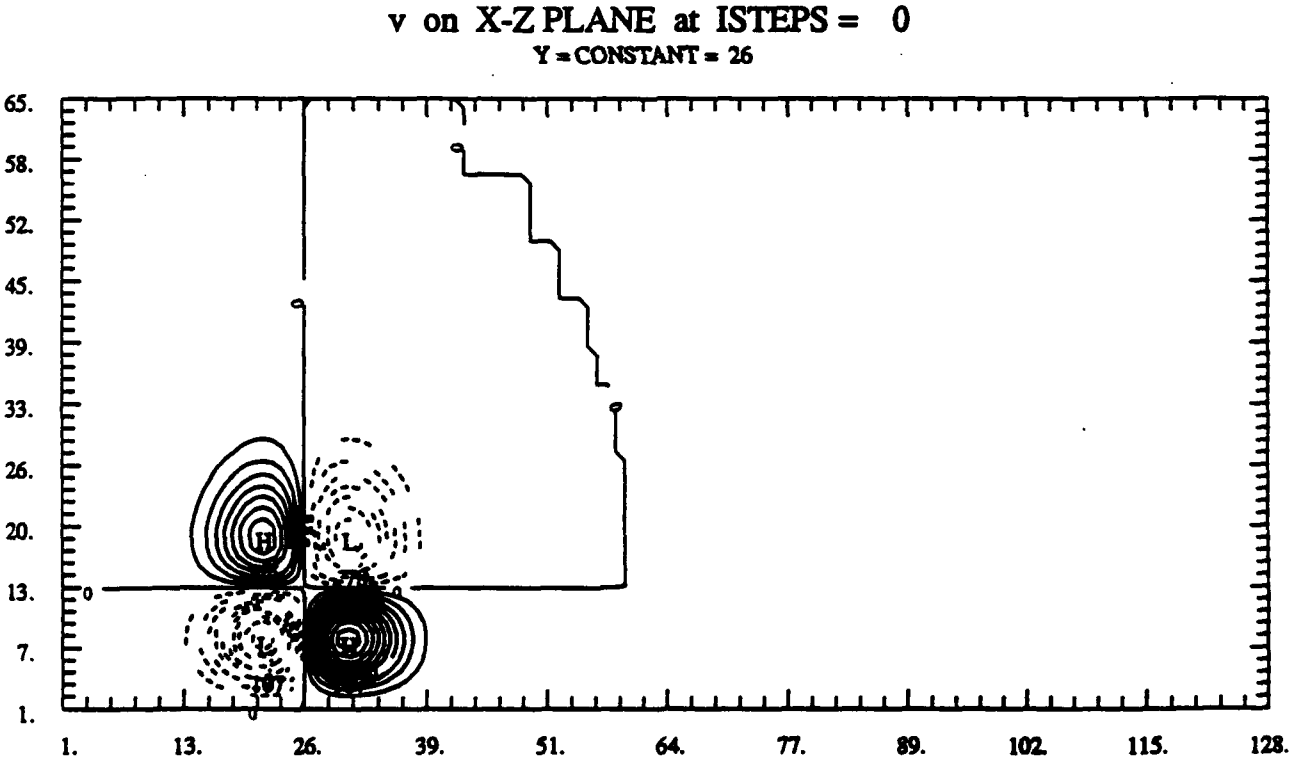

figure -3(b)

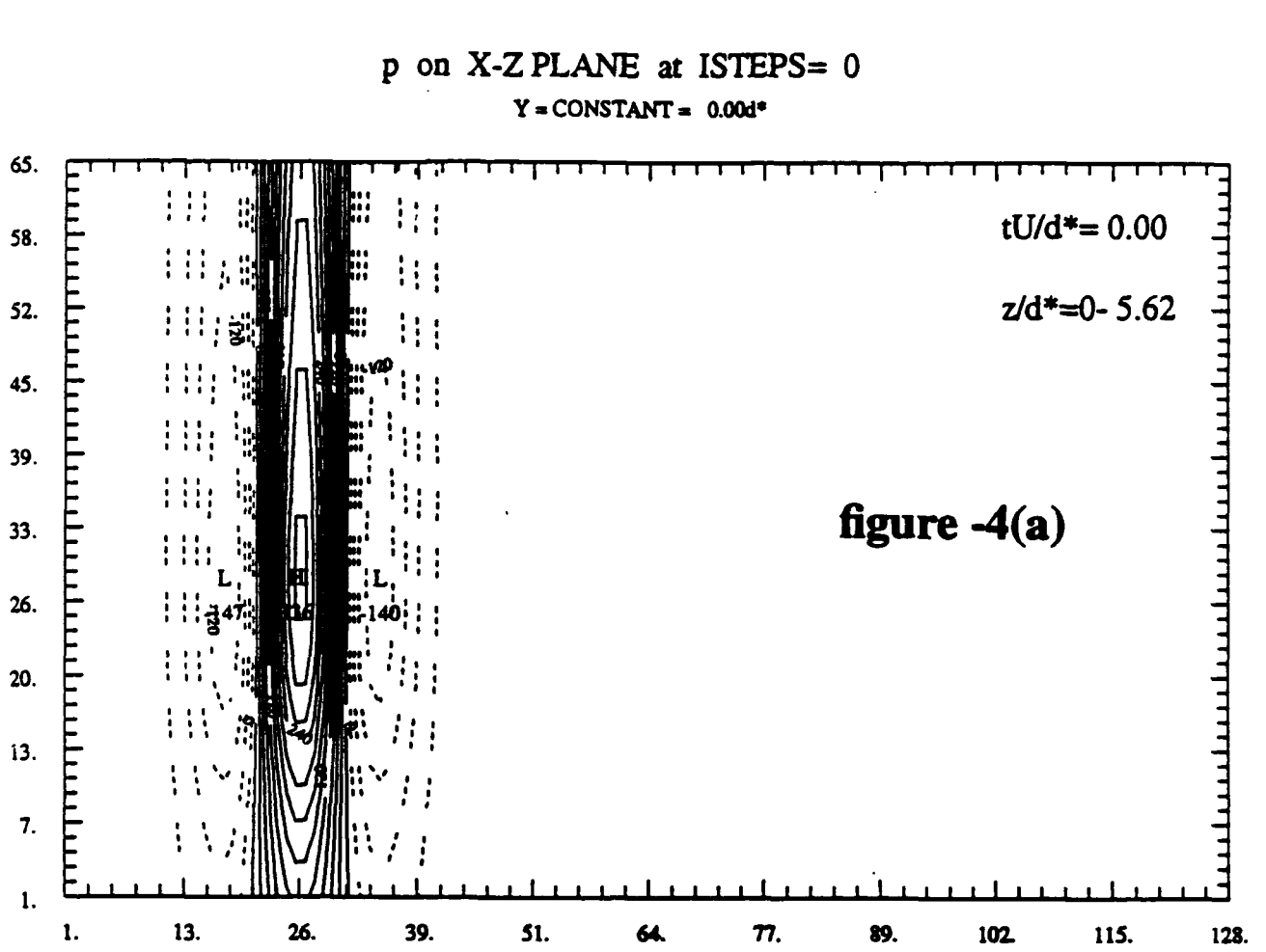

figure -4(a)

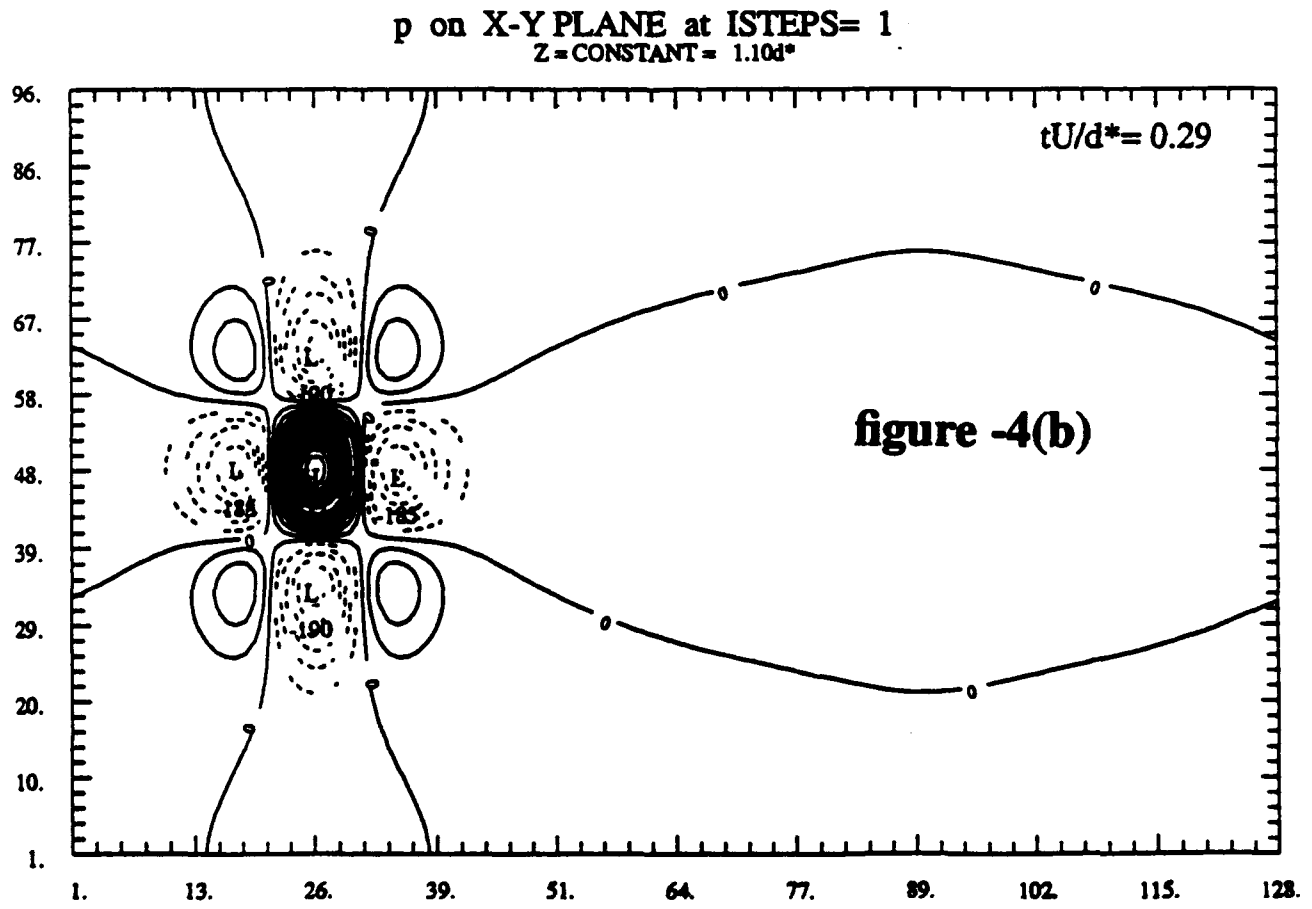

figure -4(b)

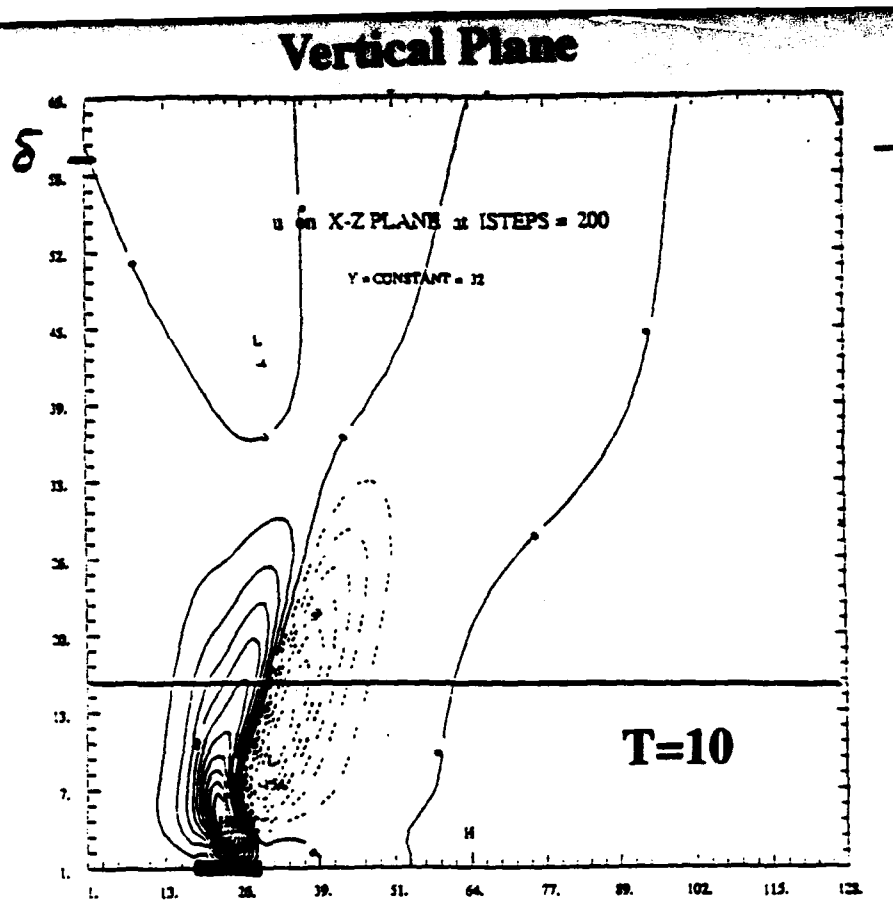

contour plot of streamwise velocity u

figure -5(a)

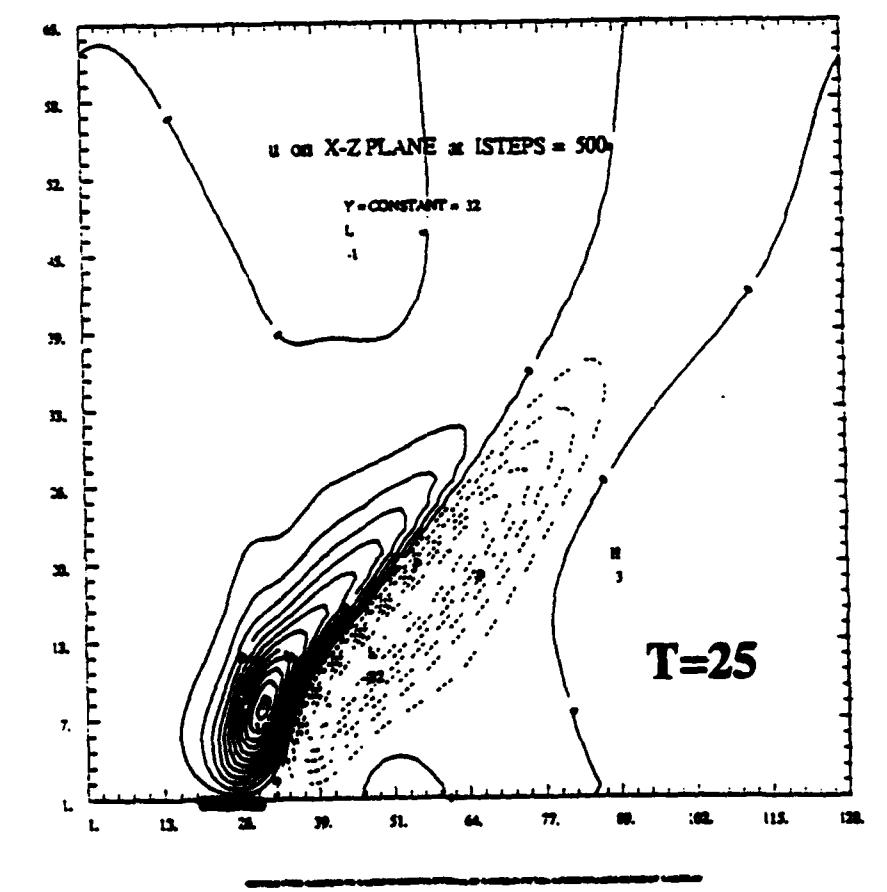

figure -5(b)

Horizontal Plane

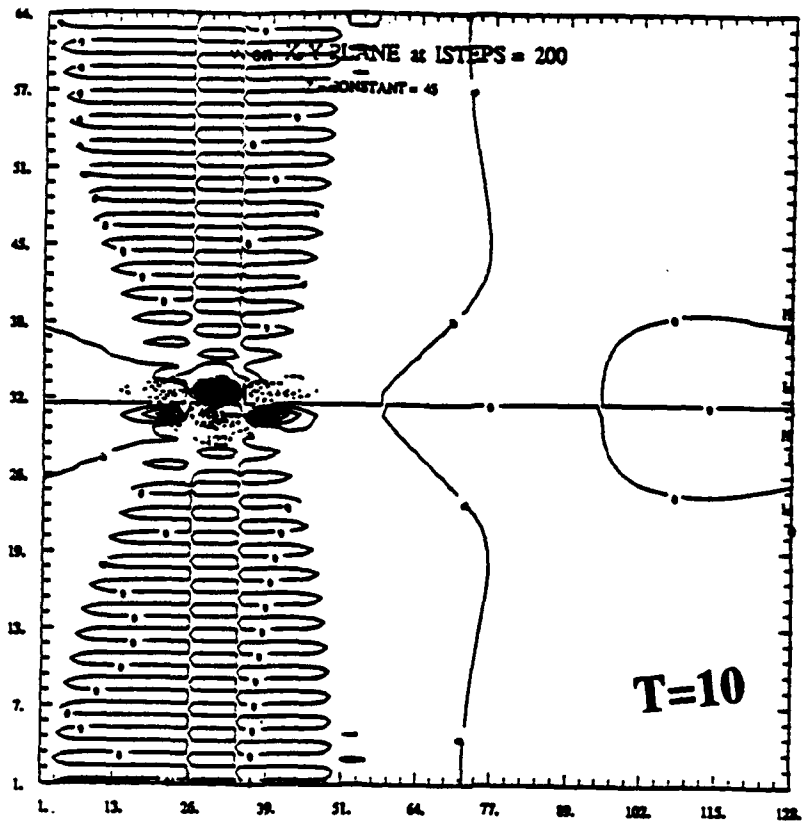

Flow

contour plot of spanwise velocity v

figure -6(a)

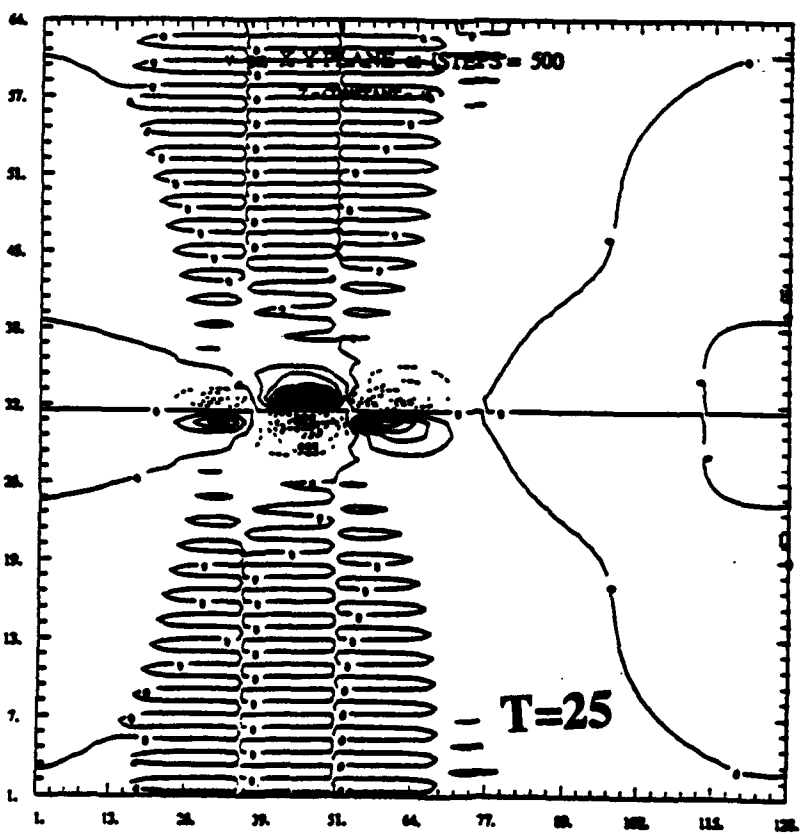

figure -6(b)

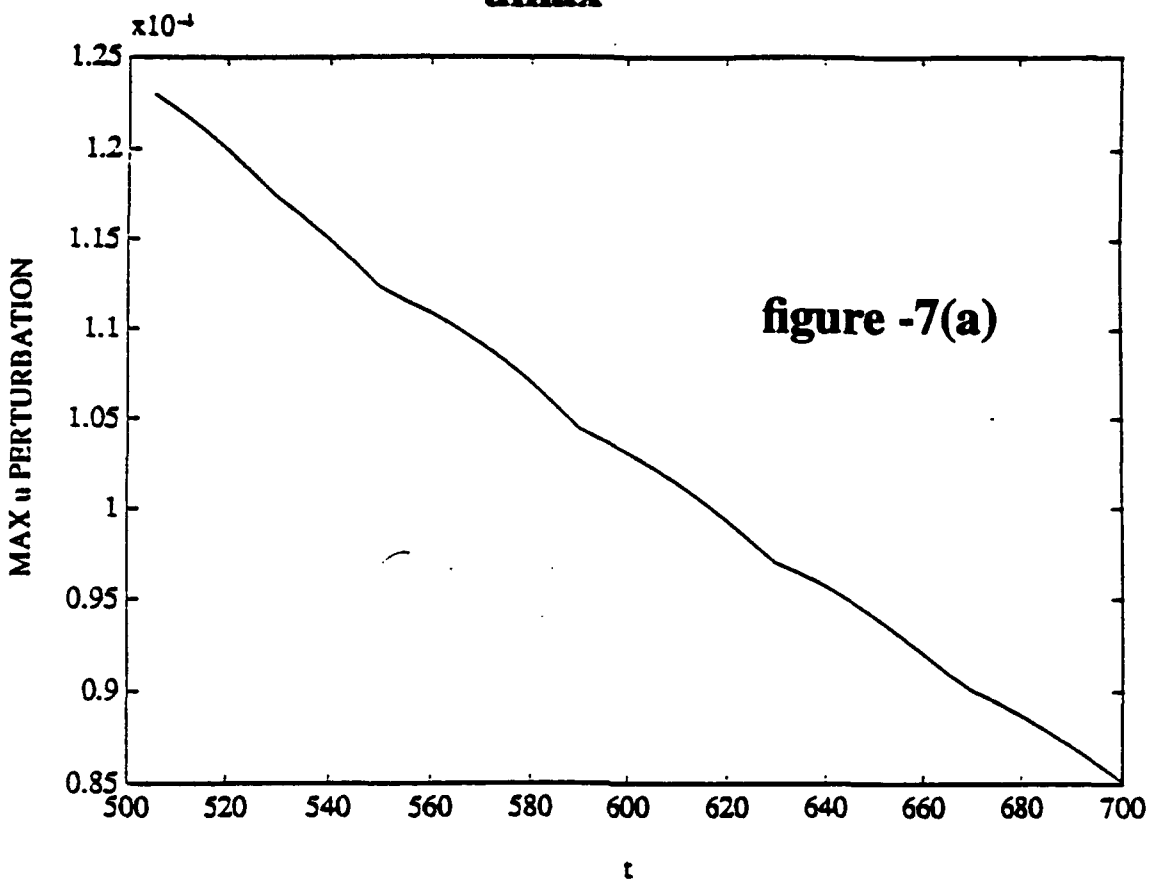

figure -7(a)

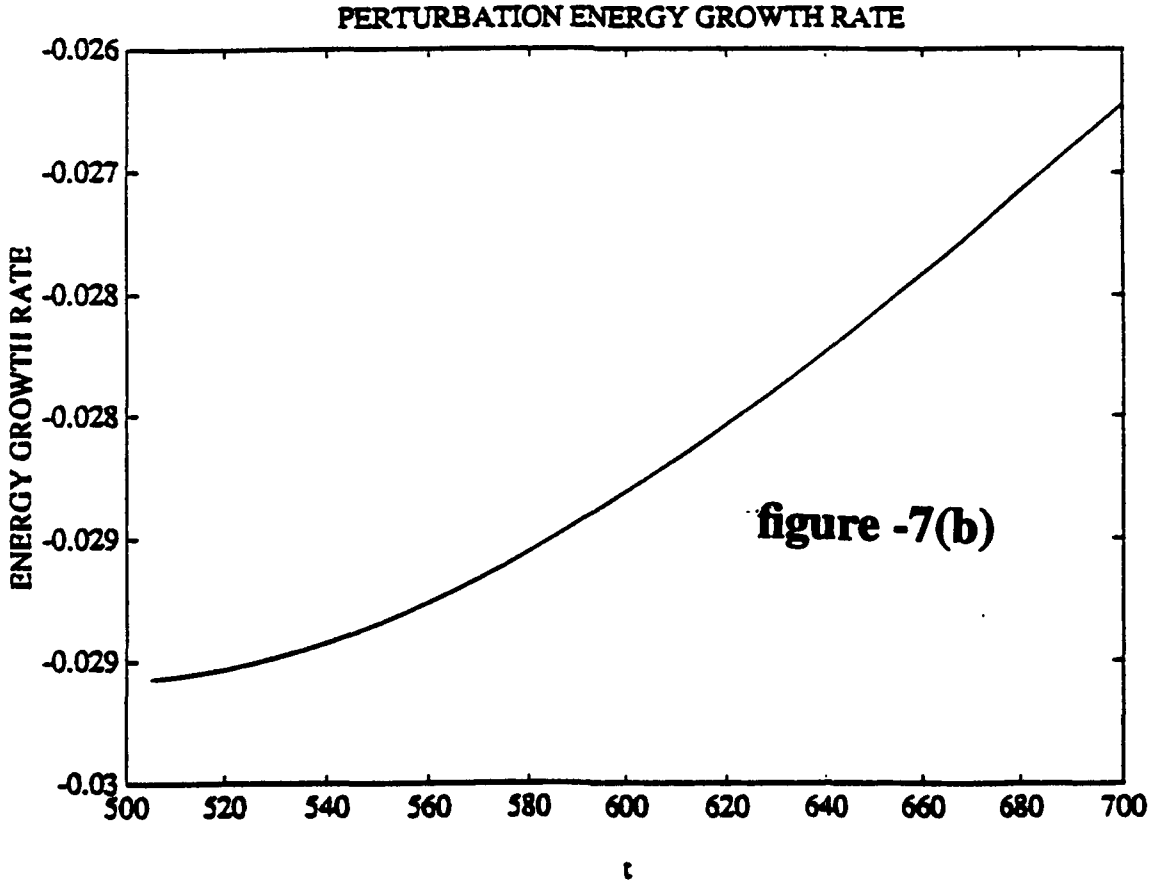

figure -7(b)

Mode n=1

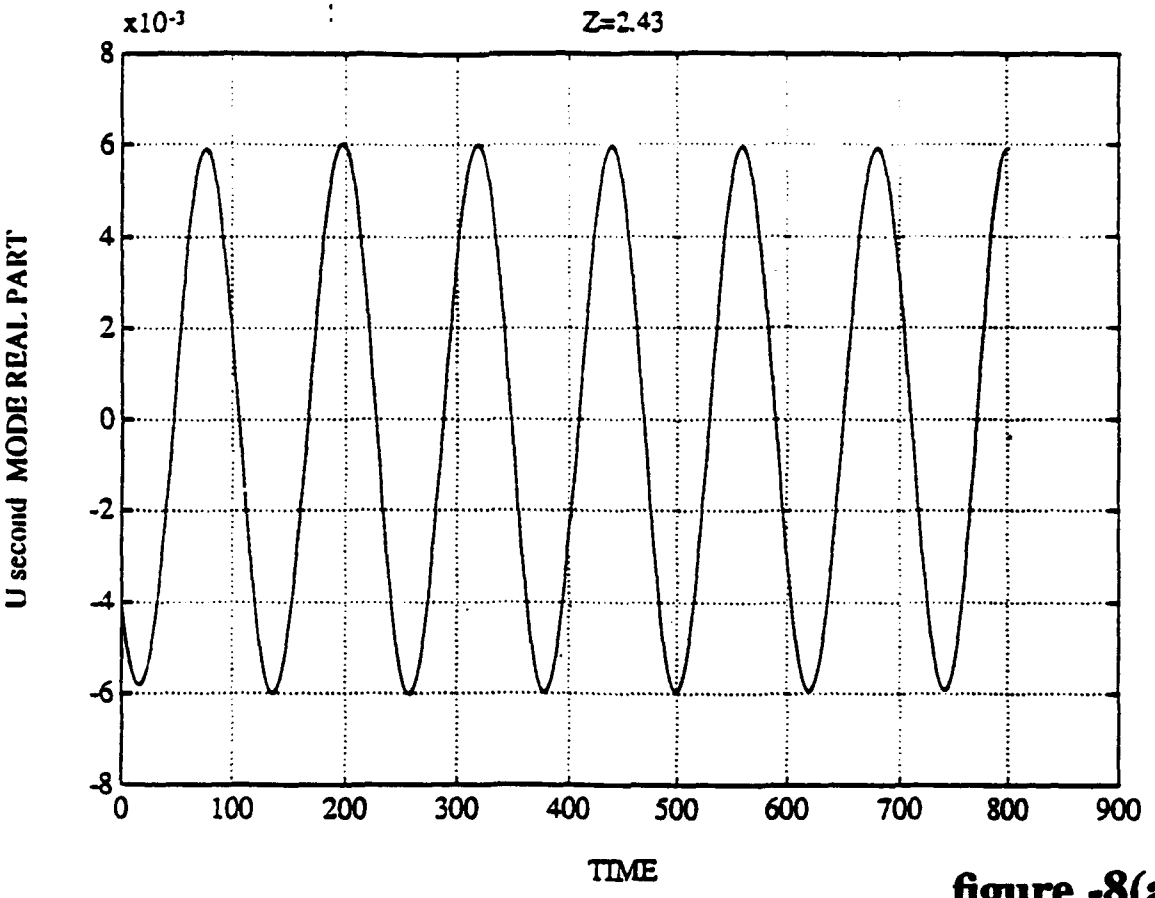

figure -8(a)

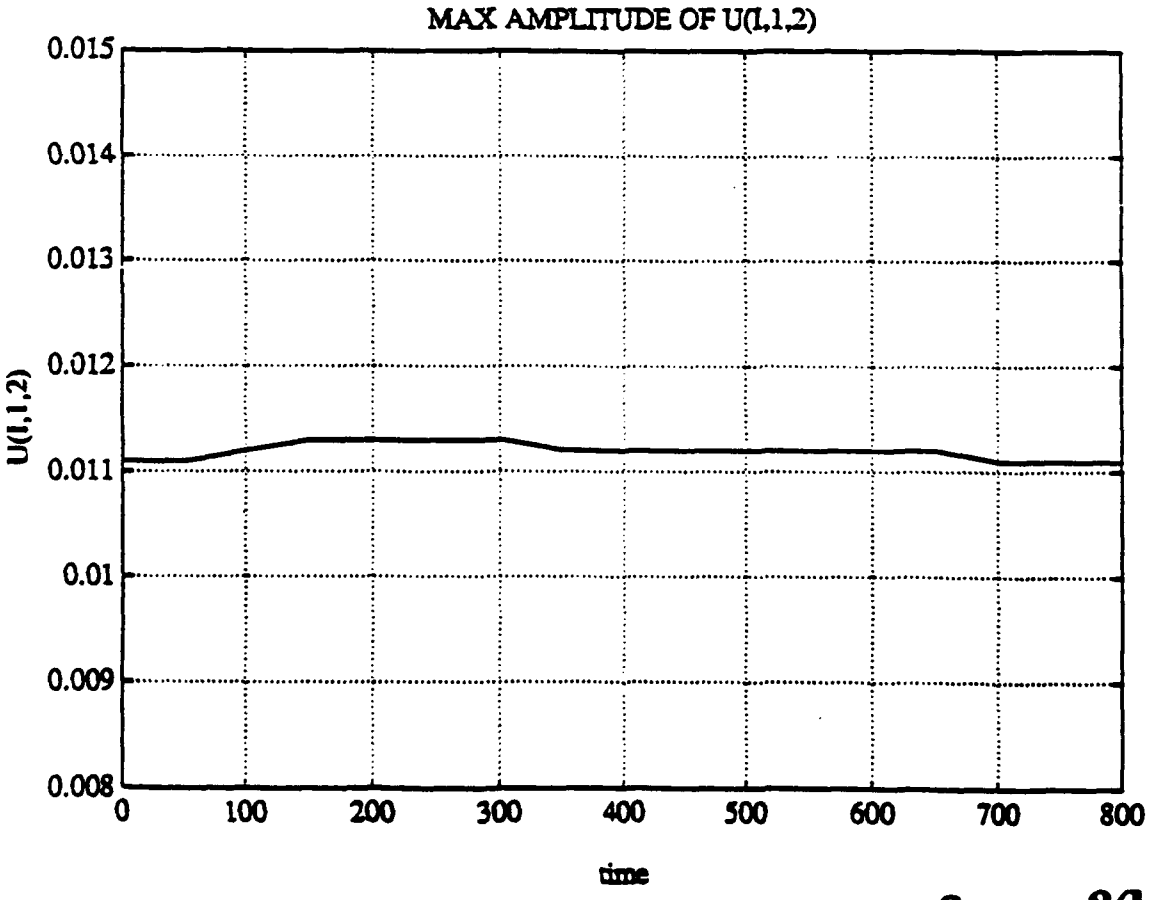

figure -8(b)

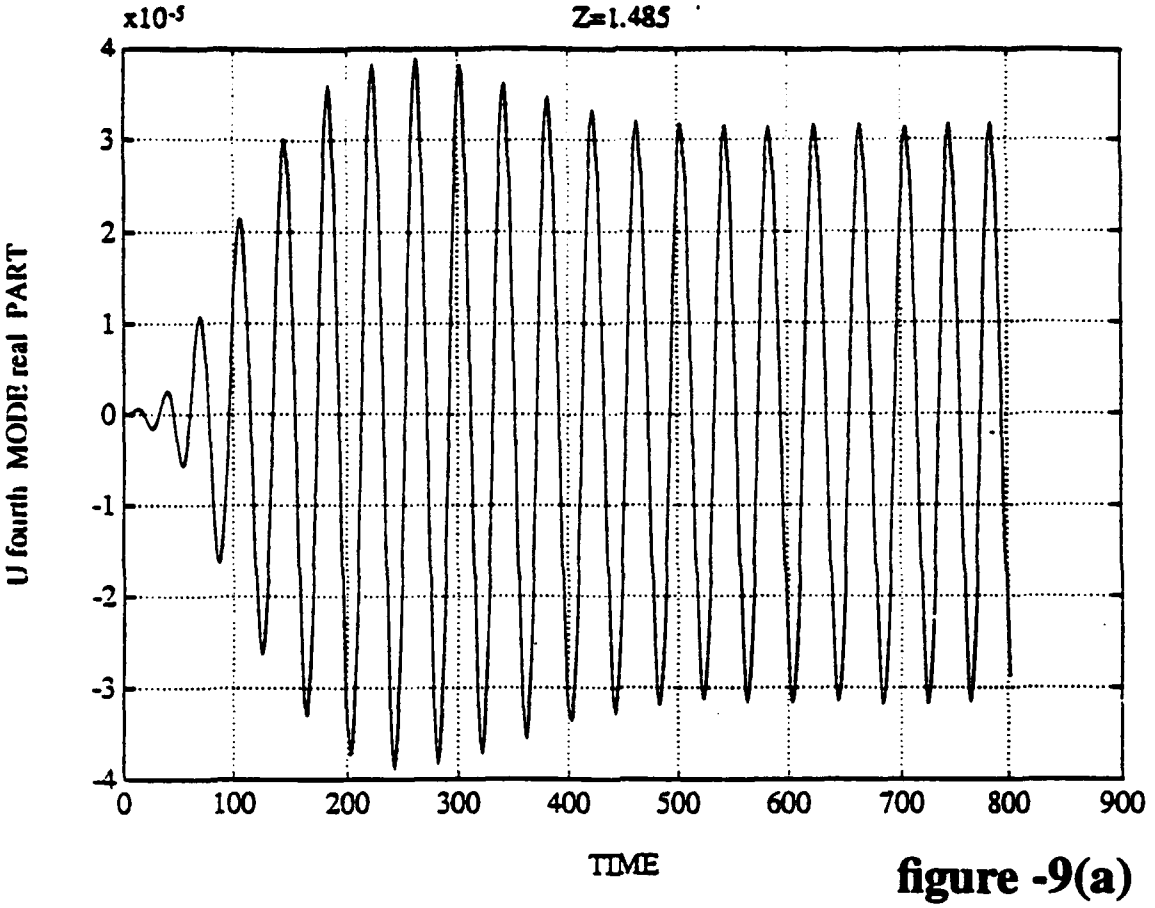

figure -9(a)

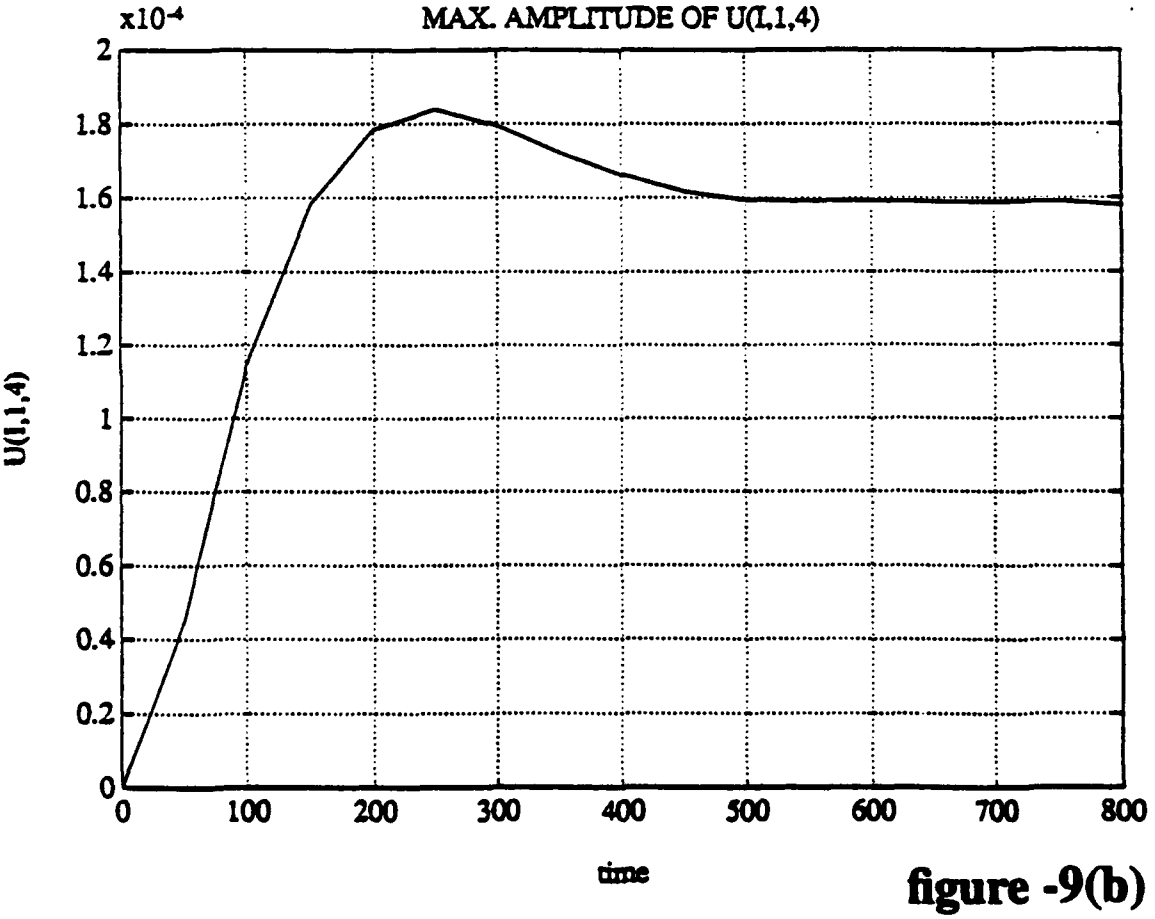

figure -9(b)

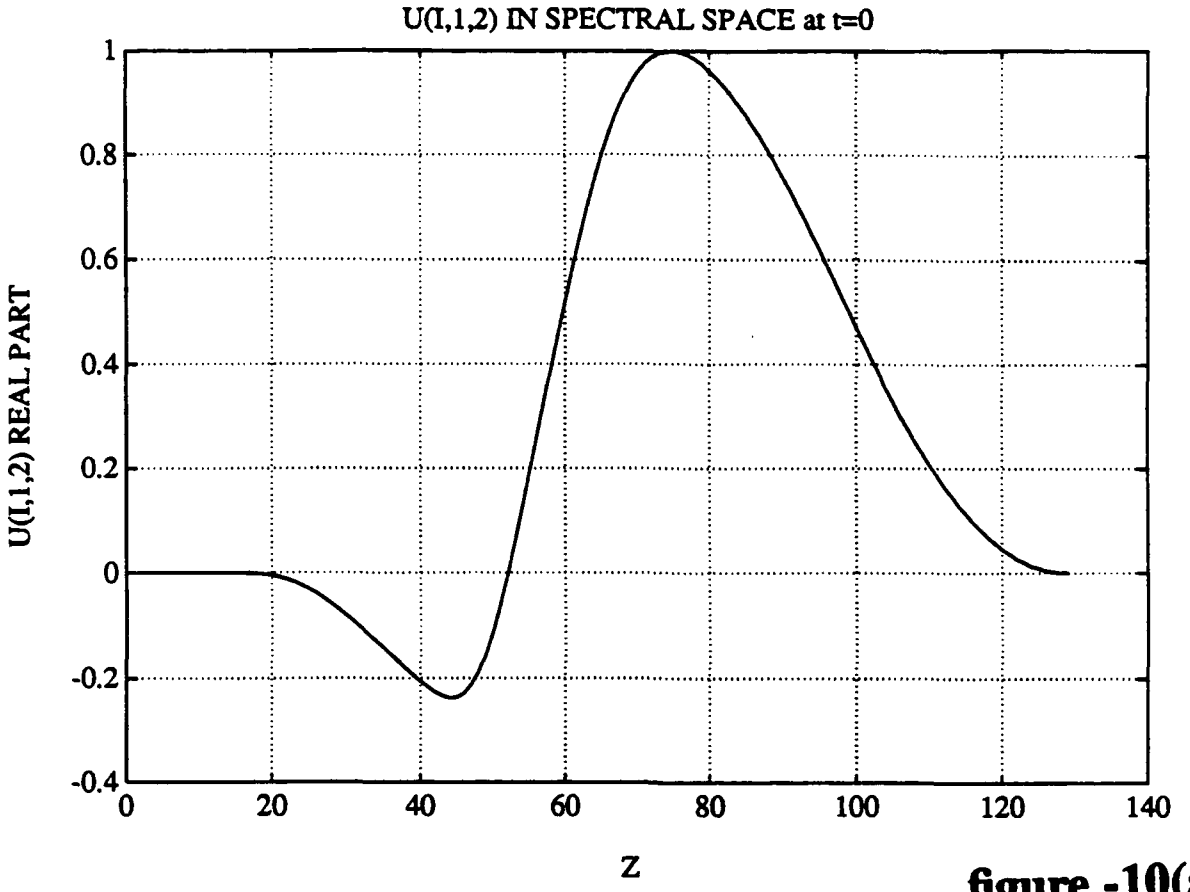

figure -10(a)

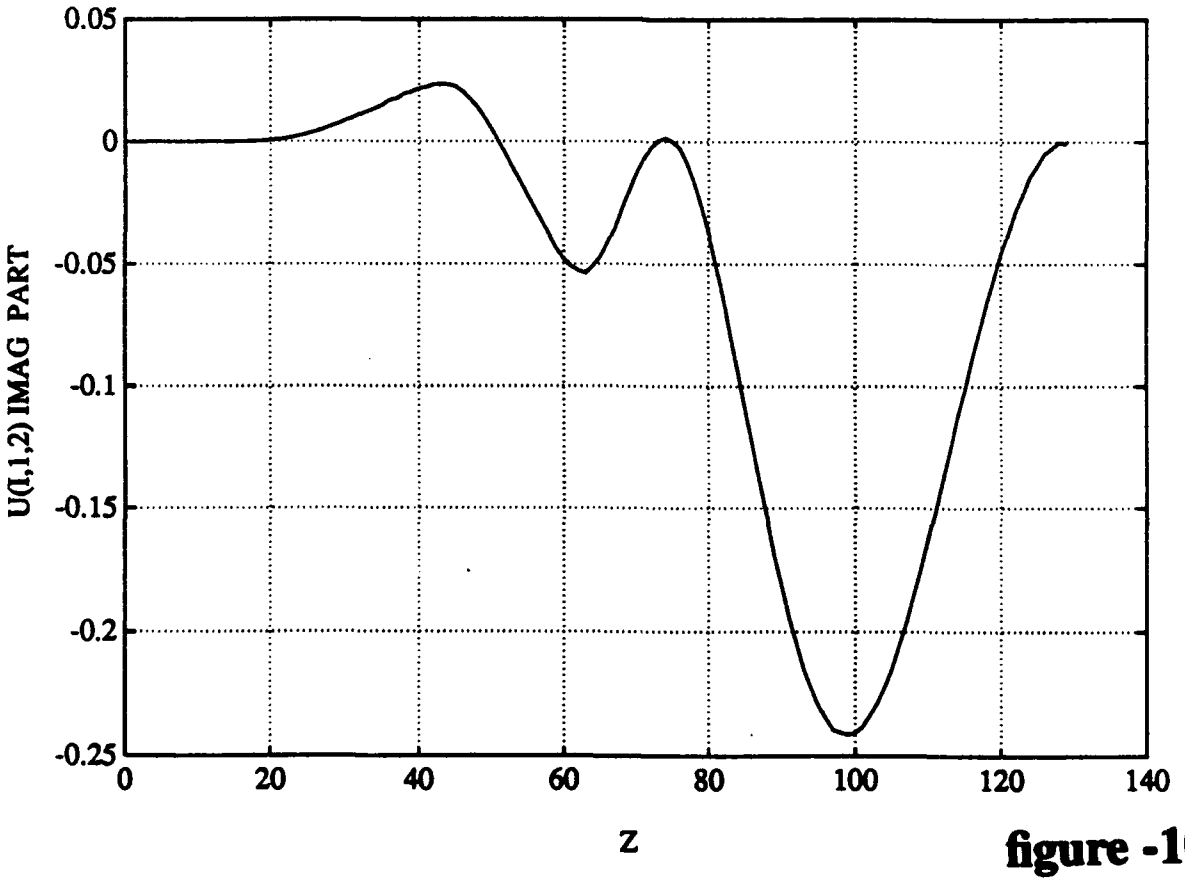

figure -10(b)

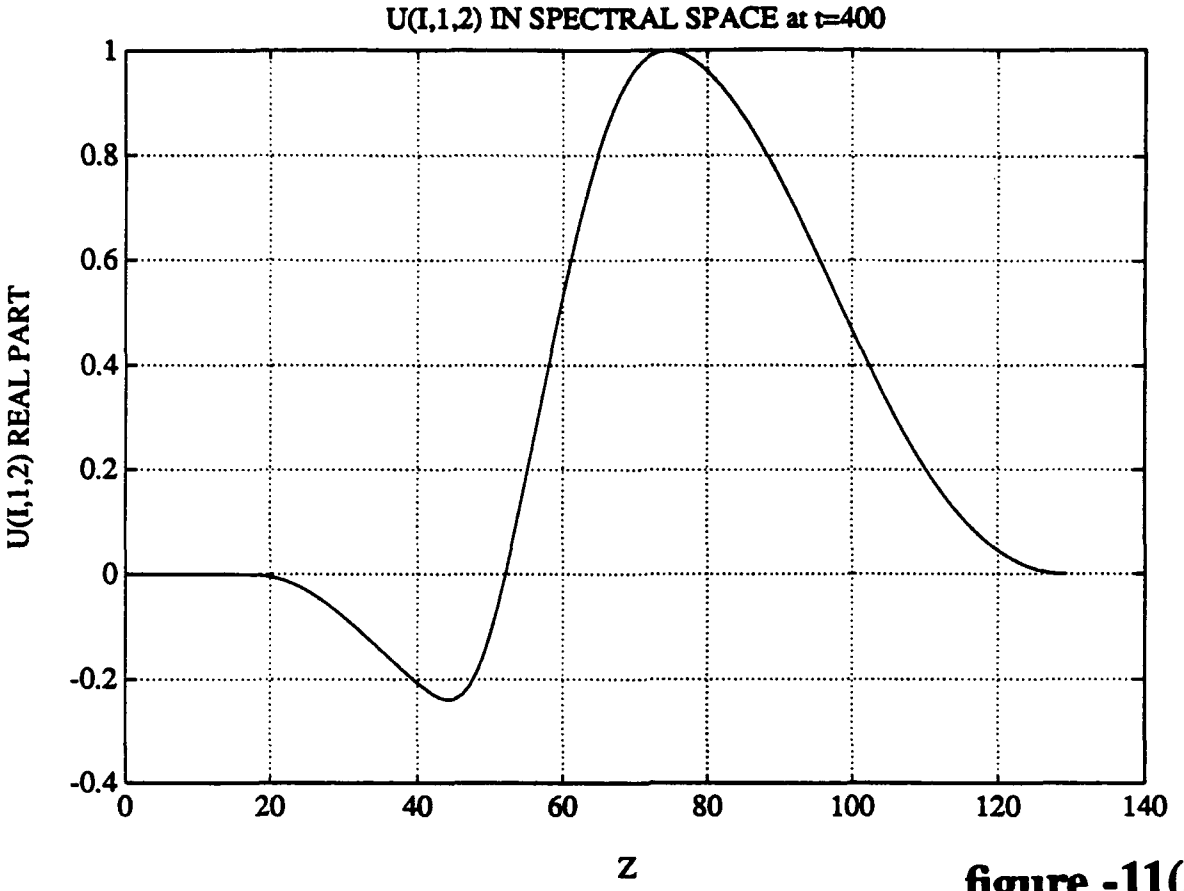

figure -11(a)

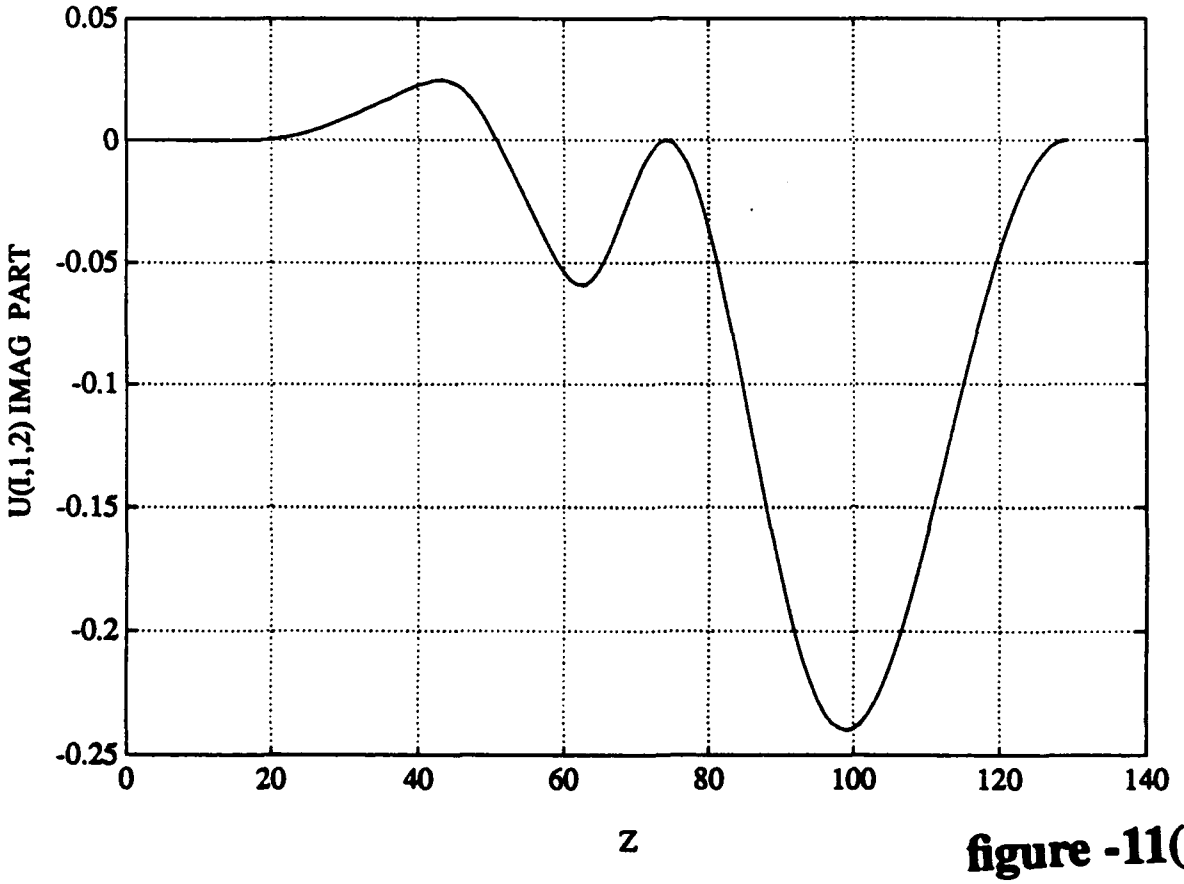

figure -11(b)

Mode n=4

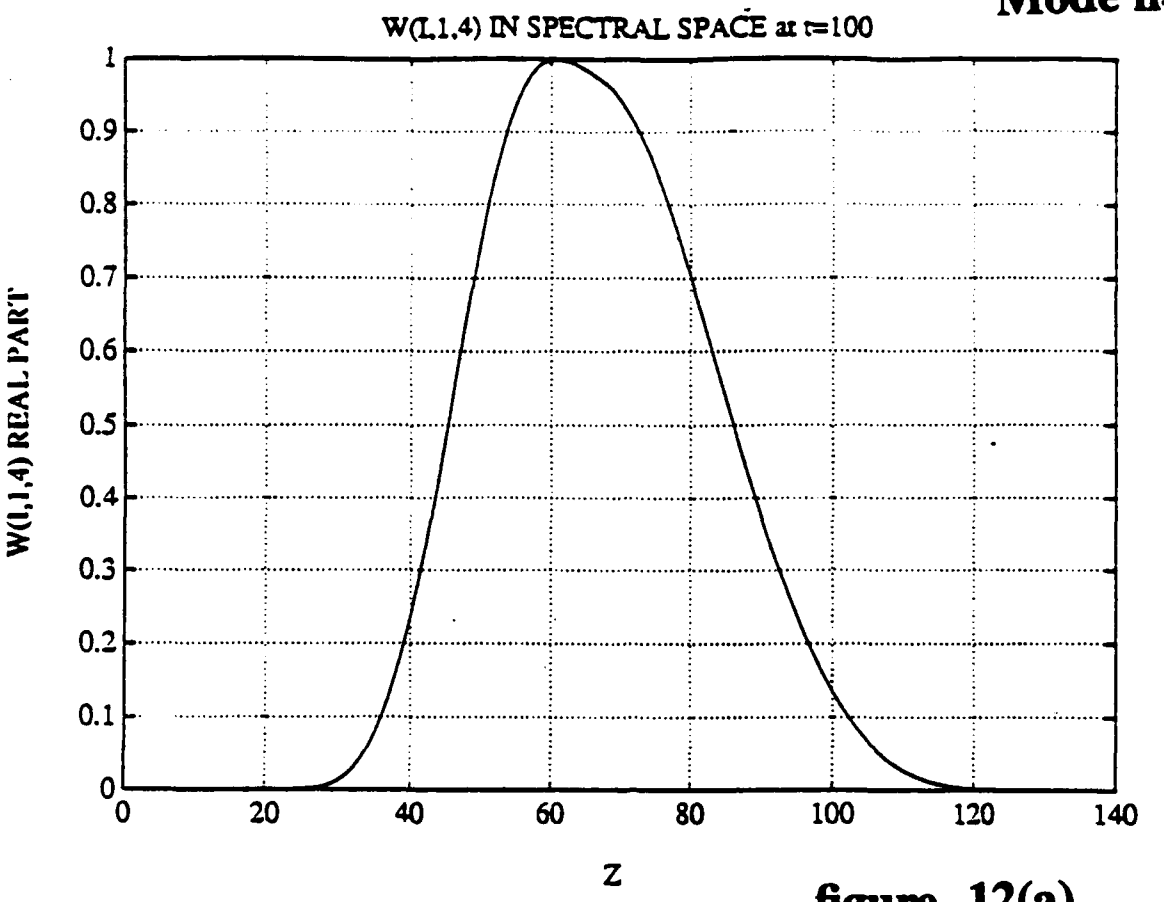

figure -12(a)

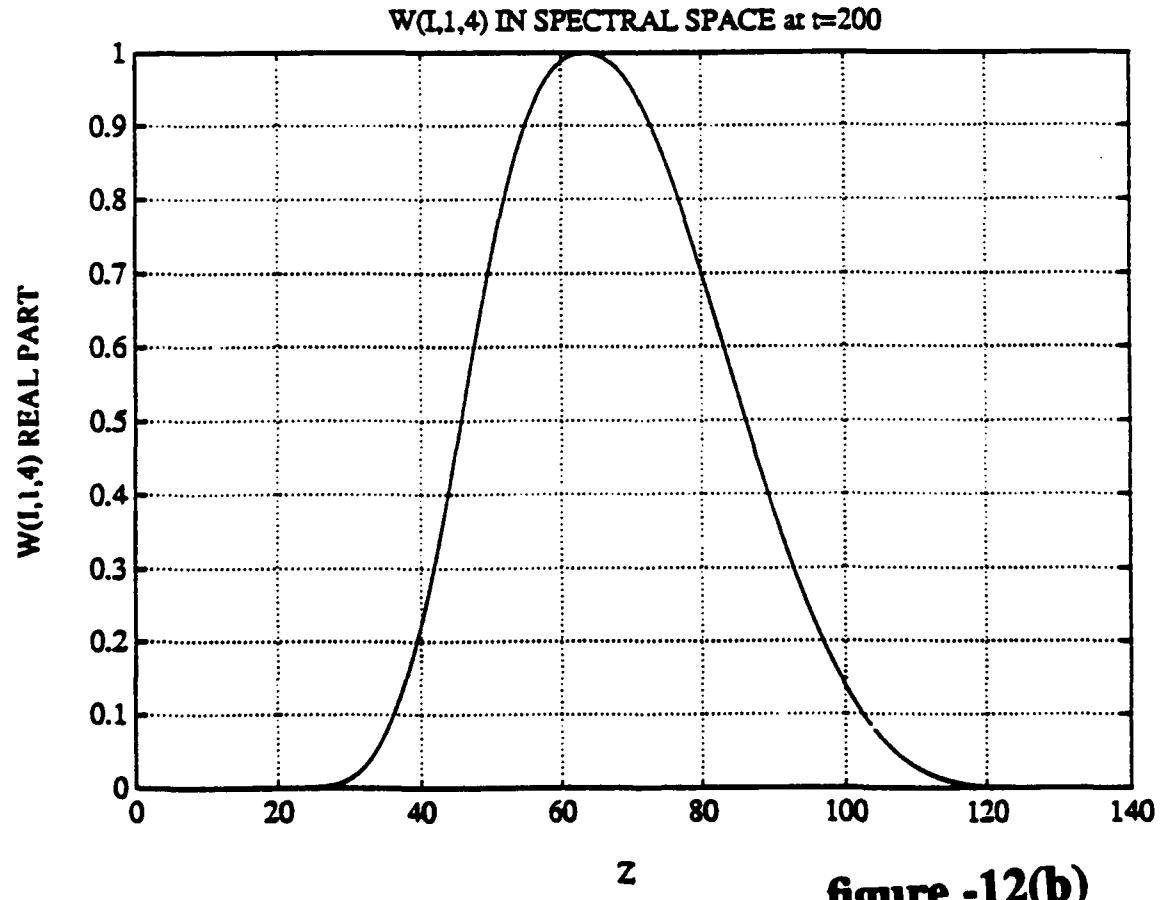

figure -12(b)

streamwise velocity u
Vertical Plane
Flow

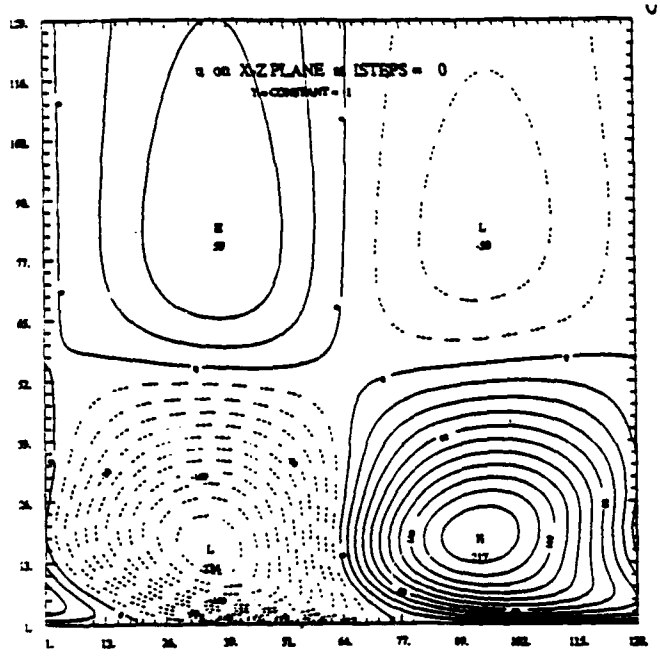

figure -13(a)

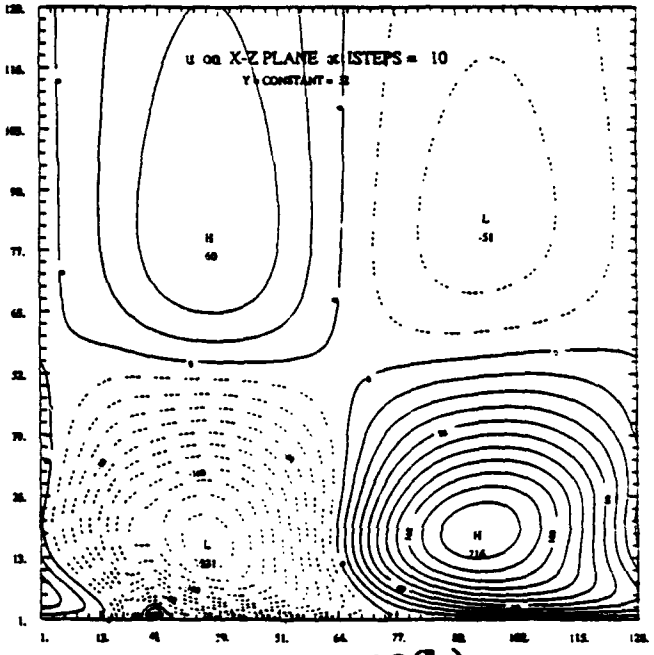

figure -13(b)

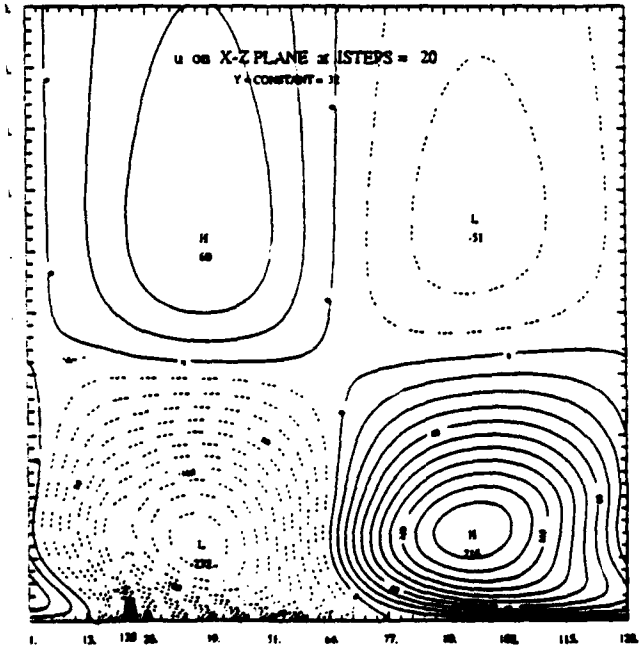

figure -13(c)

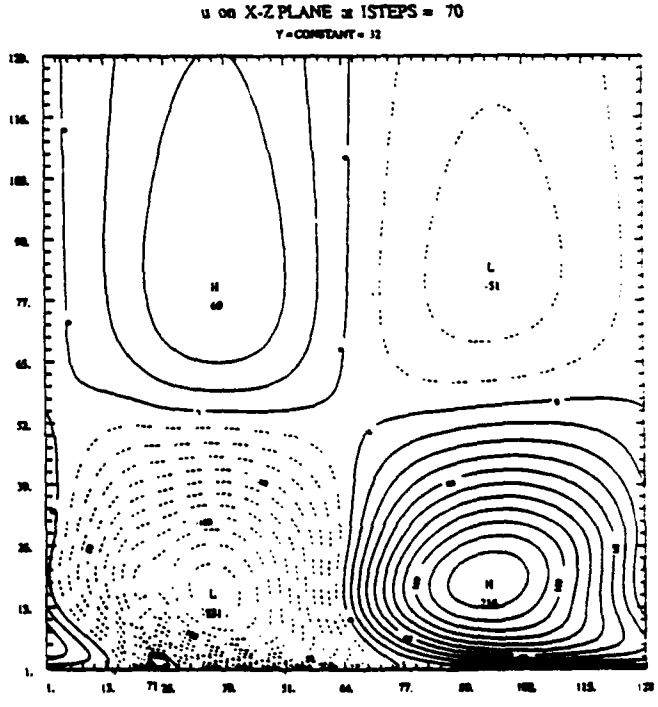

figure -13(d)

figure -14(a)

δ

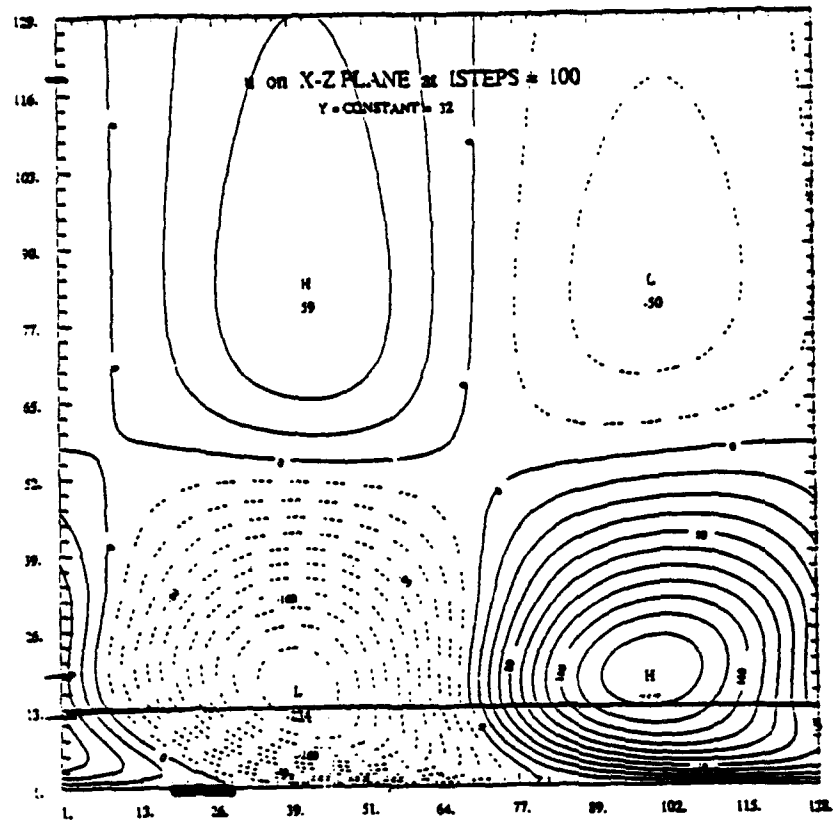

T=5

umax=2% U_∞

figure -14(b)

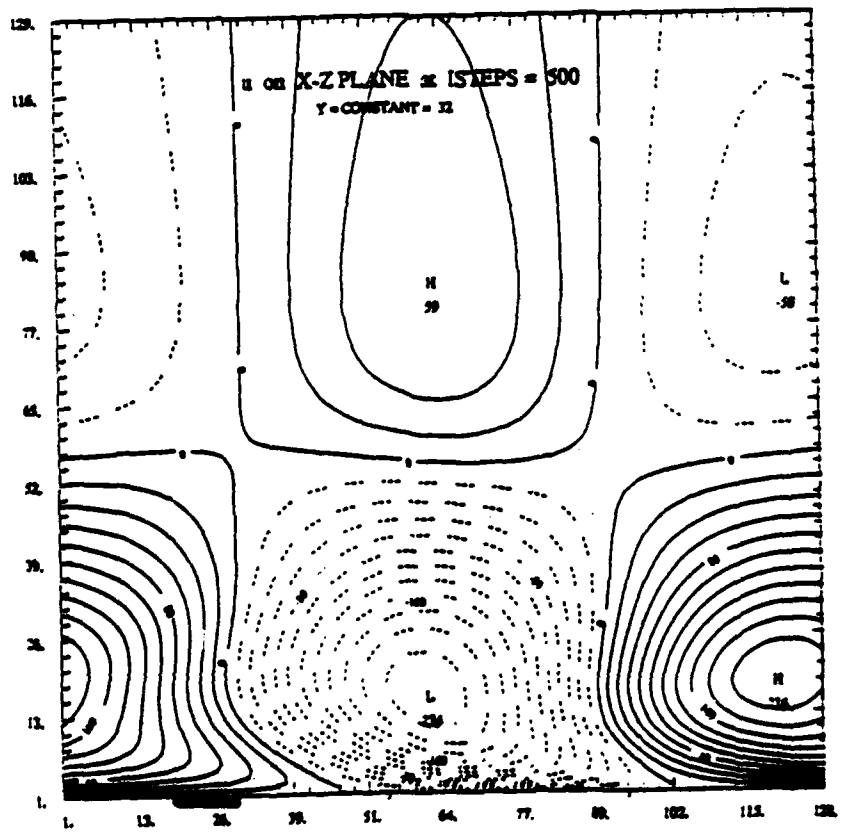

T=25

Horizontal Plane

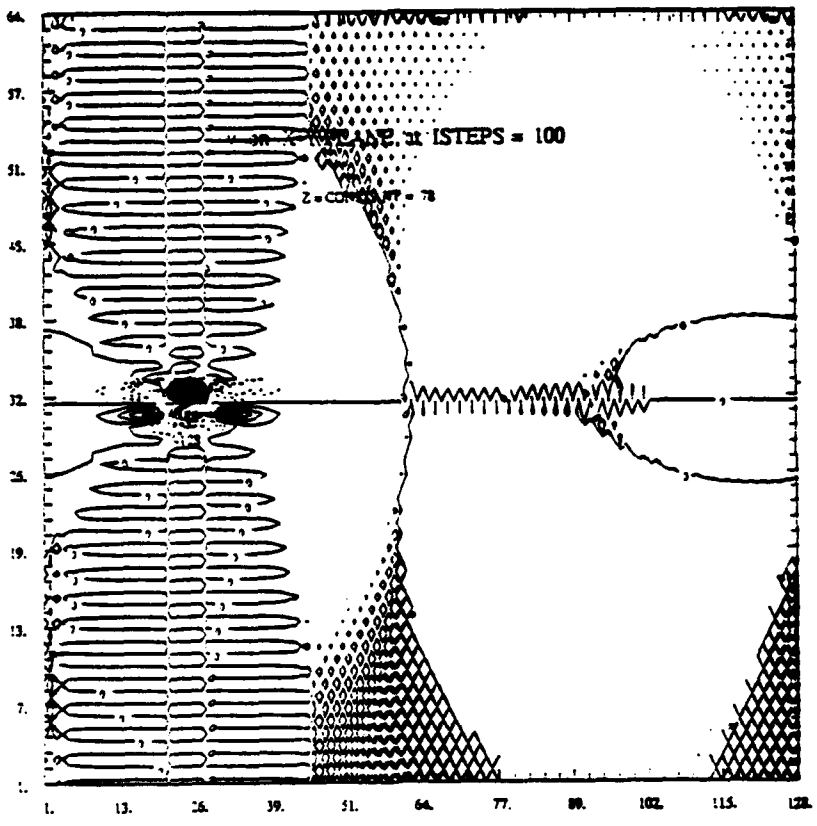

Spanwise velocity v

figure -15(a)

T=5

vmax=0.1% U_∞

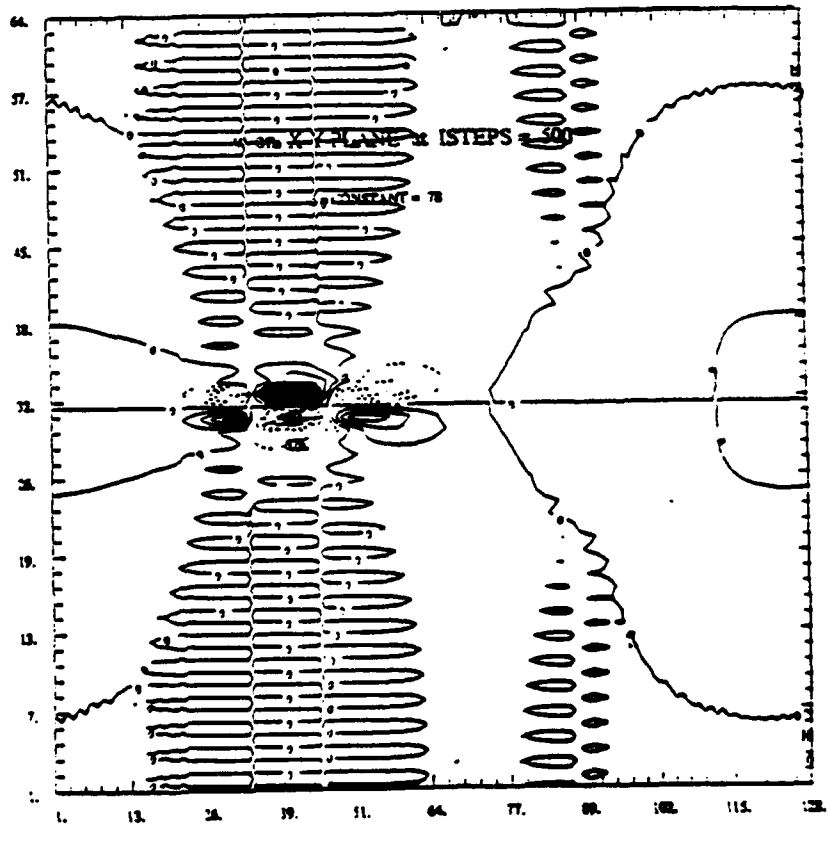

figure -15(b)

T=25

044211JAS = 044211JAS
Running Title: Scattering of pressure pulses

J. Acoust. Soc. Am., Nov. 1992

Scattering of hydrodynamic pressure pulses by coating inhomogeneities

J. Andrzej Domaradzki and Kishan Shah
Department of Aerospace Engineering, University of Southern California, Los Angeles, California 90089-1191

David G. Crighton
Department of Applied Mathematics and Theoretical Physics, University of Cambridge, Cambridge CB3 9EW, England

(Received 26 December 1991; revised 10 June 1992; accepted 1 July 1992)

Sound generation by a deterministic, hydrodynamic pressure pulse in a fluid flowing over a compliant coating with an embedded void inhomogeneity is investigated. The inhomogeneity is represented by an acoustic monopole and its strength is found for several models of the pressure pulse. The far-field acoustic pressure is calculated for all models and is compared with the sound generated by a statistically stationary turbulent boundary layer. It is found that for certain parameters of the coating, the intensity of scattered sound generated by a deterministic pulse may exceed by 10–40 dB the intensity of sound estimated for the statistical turbulent boundary layer forcing.

PACS numbers: 43.20.Fn

INTRODUCTION

A turbulent boundary layer flow at low Mach number over a rigid, uniform plate radiates sound that is determined by a distribution of quadrupoles resulting from the velocity fluctuations in the boundary layer.[1] In practical applications, the assumption of the rigid, uniform plate is usually untenable since various inhomogeneities in the plate are introduced by manufacturing processes, and for structural reasons, often nonrigid, compliant plates are desirable. In a number of papers, Howe[2-6] has shown that inhomogeneities in compliant plates will be responsible for acoustic radiation with intensity levels which may considerably exceed the intensity levels of the background quadrupole radiation. The mechanism that generates this intense sound has been identified as a scattering by inhomogeneities of the strong hydrodynamic pressure fluctuations from the convective region of the wall pressure spectrum. Quantitative results for the intensity of the scattered sound are usually arrived at by employing the phenomenological formulas of Chase[7] for the rigid wall pressure spectrum, which represents the effect of the wall pressure fluctuations averaged over the ensemble of statistically stationary turbulent boundary layers. However, the statistical representation of the wall pressures masks the presence of strong, deterministic events in turbulent boundary layers known as *bursts*. Bursts in turbulent boundary layers have been identified as relatively rare, spatially localized, short-lived events, with amplitudes considerably larger than the corresponding statistically averaged quantities.[8-10] Despite their rare occurrence, these events contribute significantly to the Reynolds stress production and drag in the boundary layers. It also appears that turbulent bursts are responsible for the generation of localized, high wall pressures beneath turbulent boundary layers. Recently, extensive investigations of the wall pressure properties in turbulent boundary layers have been conducted at the Catholic University of America. These investigations clearly identified the presence of large amplitude wall pressure events[11] and correlated them with turbulent bursts observed in the boundary layers.[12] The wall pressures associated with bursting events are larger than the rms wall pressure values and despite their rare occurrence contribute significantly to global quantities. Johansson *et al.*[13] report that pressure peaks with amplitudes larger than $2.5p_{rms}$ occur during about 6% of the total time but contribute about 20% to the long time rms value of pressure p_{rms}. Karangelen *et al.*[14] observe much stronger effects, claiming that pressure peaks greater than $3p_{rms}$ contribute 49% to the rms pressure.

The importance of bursts in the Reynolds stress production and in generation of the high wall pressure peaks points to their possible acoustical importance. In this paper, we examine a generic problem of scattering of a hydrodynamic pressure pulse, attributable to a turbulent burst in a fluid, by an inhomogeneity in a surface coating which lies under the fluid. The intensities of sound produced by a deterministic burst are compared with estimates provided for the same problem by the standard statistical approach.

I. FORMULATION OF THE PROBLEM

We consider the problem of generation of acoustic waves by a boundary layer flow over a coating containing a localized inhomogeneity. Inviscid fluid with density ρ_0 and speed of sound c_0 occupies the upper half-space $x_3 > 0$. The coating occupies the lower half-space $x_3 < 0$, and is itself modeled as a static, inviscid fluid with density ρ_1 and speed of sound c_1. The inhomogeneity is modeled as a spherical void of radius a centered at the point $\mathbf{r}_0 = (0,0,-h)$ (Fig. 1). Acoustic waves are generated by the flow either directly (e.g., a turbulent boundary layer will produce quadrupole radiation in the presence of a homogeneous coating) or indirectly through the process of scattering of hydrodynamic

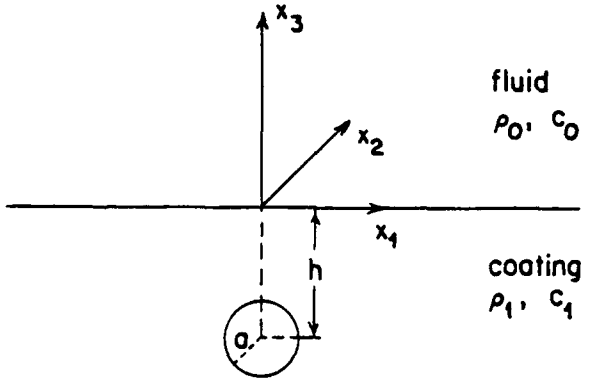

FIG. 1. Schematic view of the physical situation.

pressures by the coating inhomogeneity. The void is assumed to be acoustically compact for all significant hydrodynamic frequencies; i.e.,

$$\omega a/c_0, \omega a/c_1 \ll 1. \tag{1}$$

Therefore, the inhomogeneity may be treated as equivalent to a concentrated monopole. With these assumptions, Lighthill's aeroacoustic equation determining the acoustic pressure at point $\mathbf{r} = (x_1, x_2, x_3) = (x, y, z)$ is

$$\left(\nabla^2 - \frac{1}{c_0^2}\frac{\partial^2}{\partial t^2}\right) p(\mathbf{r},t) = T(\mathbf{r},t), \quad \text{for } x_3 > 0, \tag{2}$$

$$\left(\nabla^2 - \frac{1}{c_1^2}\frac{\partial^2}{\partial t^2}\right) p(\mathbf{r},t) = M(\mathbf{r},t), \quad \text{for } x_3 < 0, \tag{3}$$

where $p(\mathbf{r},t)$ is the pressure field, $T(\mathbf{r},t)$ is the Lighthill quadrupole source term, and $M(\mathbf{r},t)$ is a monopole concentrated at $\mathbf{r}_0 = (0,0,-h)$,

$$M(\mathbf{r},t) = Q(t)\delta(x)\delta(y)\delta(z+h). \tag{4}$$

The monopole strength $Q(t)$ will be determined in the course of the calculations.

Solutions of Eqs. (2) and (3) must satisfy the radiation conditions of outgoing waves at large distances from the interface, $x_3 \to \pm\infty$, and the pressure $p(\mathbf{r},t)$ and normal velocity (or the acceleration $(1/\rho)[\partial p(\mathbf{r},t)/\partial x_3]$) must be continuous at the interface $x_3 = 0$. It is assumed that deformations of the interface by the pressure forces are small and the interface may be treated as being flat. All propagation effects associated with the very low Mach number mean flow have been neglected.

II. SOLUTION OF THE GOVERNING EQUATIONS

Equations (2) and (3), with the boundary conditions specified at the end of the previous section, are conveniently solved using a Fourier representation. Definitions of the Fourier transform $\hat{F}(\mathbf{k},x_3,\omega)$ of a function $F(\mathbf{x},x_3,t)$ and the inverse relation used in this paper are

$$\hat{F}(\mathbf{k},x_3,\omega) = \int\int\int F(\mathbf{x},x_3,t)e^{i(\mathbf{k}\cdot\mathbf{x}+\omega t)}\,dx_1\,dx_2\,dt, \tag{5}$$

$$F(\mathbf{x},x_3,t) = \frac{1}{(2\pi)^3}\int\int\int \hat{F}(\mathbf{k},x_3,\omega) \times e^{-i(\mathbf{k}\cdot\mathbf{x}+\omega t)}\,dk_1\,dk_2\,d\omega, \tag{6}$$

where $\mathbf{k} = (k_1,k_2)$ is the two-dimensional wave-number vector parallel to the interface, $\mathbf{x} = (x_1,x_2)$ is the projection of the radial vector $\mathbf{r}$ on the interface, and ω is the circular frequency. Analogous formulas for quantities which are functions of time only are

$$\hat{f}(\omega) = \int f(t)e^{i\omega t}\,dt, \tag{7}$$

$$f(t) = \frac{1}{2\pi}\int \hat{f}(\omega)e^{-i\omega t}\,d\omega. \tag{8}$$

Fourier transforming Eqs. (2) and (3) gives

$$\left(\frac{\partial^2}{\partial z^2} - \gamma_0^2\right)\hat{p}(\mathbf{k},z,\omega) = \hat{T}(\mathbf{k},z,\omega), \quad \text{for } z>0, \tag{9}$$

$$\left(\frac{\partial^2}{\partial z^2} - \gamma_1^2\right)\hat{p}(\mathbf{k},z,\omega) = \hat{Q}(\omega)\delta(z+h), \quad \text{for } z<0, \tag{10}$$

where z now denotes the vertical coordinate x_3, and

$$\gamma_0 = \sqrt{k_1^2 + k_2^2 - \omega^2/c_0^2} = \sqrt{k^2 - \omega^2/c_0^2}, \tag{11}$$

$$\gamma_1 = \sqrt{k_1^2 + k_2^2 - \omega^2/c_1^2} = \sqrt{k^2 - \omega^2/c_1^2}. \tag{12}$$

For real k such that $k > |\omega|/c_i$ $(i = 0,1)$ γ_i is real and taken as positive. For k such that $k < |\omega|/c_i$, to satisfy the radiation condition γ_i must be taken as negative imaginary if $\omega > 0$ and positive imaginary if $\omega < 0$.

Solutions of (9) and (10) satisfying either radiation conditions for $|z| \to \infty$ if $k < |\omega|/c_i$, or decaying to zero if $k > |\omega|/c_i$, are then as follows:

$$\hat{p}(\mathbf{k},z,\omega) = -\frac{1}{2\gamma_0}\int_0^\infty \hat{T}(\mathbf{k},z',\omega)e^{-\gamma_0|z-z'|}\,dz' + Ae^{-\gamma_0 z}, \quad \text{for } z>0, \tag{13}$$

$$\hat{p}(\mathbf{k},z,\omega) = -\frac{1}{2\gamma_1}\hat{Q}(\omega)e^{-\gamma_1|z+h|}dz' + Be^{-\gamma_1|z|}, \quad \text{for } z<0. \tag{14}$$

Boundary conditions at the interface provide equations for A and B:

$$A - \frac{\tilde{T}(\mathbf{k},\omega)}{2\gamma_0} = B - \frac{\tilde{Q}(\mathbf{k},\omega)}{2\gamma_1}, \tag{15}$$

$$-\frac{\gamma_0}{\rho_0}A - \frac{\tilde{T}(\mathbf{k},\omega)}{2\rho_0} = \frac{\gamma_1}{\rho_1}B + \frac{\tilde{Q}(\mathbf{k},\omega)}{2\rho_1}, \tag{16}$$

where

$$\tilde{T}(\mathbf{k},\omega) = \int_0^\infty \hat{T}(\mathbf{k},z,\omega)e^{-\gamma_0 z}\,dz, \tag{17}$$

$$\tilde{Q}(\mathbf{k},\omega) = \hat{Q}(\omega)e^{-\gamma_1 h}. \tag{18}$$

The solution to this system of equations is

$$A = -\frac{\tilde{T}(\mathbf{k},\omega)}{2\gamma_0}\frac{\rho_1\gamma_0 - \rho_0\gamma_1}{\rho_1\gamma_0 + \rho_0\gamma_1} - \frac{\tilde{Q}(\mathbf{k},\omega)}{2\gamma_1}\frac{2\rho_0\gamma_1}{\rho_1\gamma_0 + \rho_0\gamma_1}, \tag{19}$$

$$B = -\frac{\tilde{T}(\mathbf{k},\omega)}{2\gamma_0}\frac{2\rho_1\gamma_0}{\rho_1\gamma_0+\rho_0\gamma_1} - \frac{\tilde{Q}(\mathbf{k},\omega)}{2\gamma_1}\frac{\rho_0\gamma_1-\rho_1\gamma_0}{\rho_1\gamma_0+\rho_0\gamma_1}. \tag{20}$$

Using the above formulas, we get explicit expressions for the pressure field as a function of position $\mathbf{r}$ and frequency ω:

$$p(\mathbf{r},\omega) = \frac{1}{(2\pi)^2}\int d^2k\, e^{-i\mathbf{k}\cdot\mathbf{x}}\left(-\frac{1}{2\gamma_0}\int_0^\infty \hat{T}(\mathbf{k},z',\omega) \times e^{-\gamma_0|z-z'|}\,dz'\right) + \frac{1}{(2\pi)^2}\int d^2k\, e^{-i\mathbf{k}\cdot\mathbf{x}-\gamma_0 z} \times\left(-R_T\frac{\tilde{T}(\mathbf{k},\omega)}{2\gamma_0} - P_Q\frac{\tilde{Q}(\mathbf{k},\omega)}{2\gamma_1}\right), \quad z>0, \tag{21}$$

$$p(\mathbf{r},\omega) = -\frac{1}{(2\pi)^2}\frac{\hat{Q}(\omega)}{2}\int d^2k\,\frac{e^{-i\mathbf{k}\cdot\mathbf{x}-\gamma_1|z+h|}}{\gamma_1} + \frac{1}{(2\pi)^2}\int d^2k\, e^{-i\mathbf{k}\cdot\mathbf{x}-\gamma_1|z|}\left(-P_T\frac{\tilde{T}(\mathbf{k},\omega)}{2\gamma_0} - R_Q\frac{\tilde{Q}(\mathbf{k},\omega)}{2\gamma_1}\right), \quad z<0, \tag{22}$$

where P and R are, respectively, the transmission and reflection coefficients for the boundary layer (subscript T) and the monopole (subscript Q) radiation:

$$P_T = \frac{2\rho_1\gamma_0}{\rho_1\gamma_0+\rho_0\gamma_1}, \quad P_Q = \frac{2\rho_0\gamma_1}{\rho_1\gamma_0+\rho_0\gamma_1}, \tag{23}$$

$$R_T = \frac{\rho_1\gamma_0-\rho_0\gamma_1}{\rho_1\gamma_0+\rho_0\gamma_1}, \quad R_Q = \frac{\rho_0\gamma_1-\rho_1\gamma_0}{\rho_1\gamma_0+\rho_0\gamma_1}. \tag{24}$$

III. DETERMINATION OF THE MONOPOLE SOURCE

Pressure fields (21) and (22) are formally determined by the hydrodynamic forcing T and the monopole source Q. Physically, however, pressure is generated entirely by the hydrodynamic forces; the monopole source Q is not an independent quantity and must be expressed in terms of T. The relation between the strength of the monopole and the hydrodynamic forces is found by assuming that the void acts only as a passive scatterer of the hydrodynamic pressures, such that the pressure in the void remains at all times constant. Since we are representing the void to leading order simply as a monopole, we must ignore pressure fluctuations in the void associated with shape variations, and must require that the pressure $p(\mathbf{r},\omega)$ averaged over the surface of the void $x_1^2+x_2^2+(x_3+h)^2=a^2$ vanishes; i.e., the "monopole component" of the pressure at the void surface is zero. Thus averaging (denoted by $\langle\ldots\rangle$) Eq. (22) over the surface of the void will provide the required relation between Q and T.

The first term in (22) is the direct field of the monopole in the absence of the interface and thus its contribution is known to be

$$p_1(\mathbf{r},\omega) = -\hat{Q}(\omega)\frac{e^{i\omega|\mathbf{r}-\mathbf{r}_0|/c_1}}{4\pi|\mathbf{r}-\mathbf{r}_0|}. \tag{25}$$

By virtue of the condition $\omega a/c_1 \ll 1$ [Eq. (1)], its average over the sphere of radius a centered at $\mathbf{r}-\mathbf{r}_0$ is

$$\langle p_1(\mathbf{r},\omega)\rangle \approx -\hat{Q}(\omega)/4\pi a. \tag{26}$$

The second term in Eq. (22) contains contributions from both the hydrodynamic forces T and from the monopole Q. The factor $\tilde{T}(\mathbf{k},\omega)$, for given ω, is heavily concentrated around the convective wave number $(k_1,k_2)=(\omega/U_c,0)$, where U_c is the convection velocity which, in practical underwater situations, is always much less than the speed of sound. Therefore, in the term involving $\tilde{T}$, we have $k=\sqrt{k_1^2+k_2^2} \gg \omega/c_1$ and the factor γ_1 may be approximated by k. This approximation results in the dependence of the integral on spatial coordinates through $\exp(-ik_1x_1-ik_2x_2-\sqrt{k_1^2+k_2^2}\,|z|)$ which implies that the contribution $p_2(\mathbf{r},\omega)$ to total pressure coming from the hydrodynamic forces is a harmonic function. Since the average of any harmonic function over a sphere is equal to the value of the function at the center of the sphere (e.g., Tikhonov and Samarski[15]), we get the following result:

$$\langle p_2(\mathbf{r},\omega)\rangle \approx -\frac{1}{(2\pi)^2}\int d^2k\, e^{-\gamma_1 h}P_T\frac{\tilde{T}(\mathbf{k},\omega)}{2\gamma_0} \approx -\frac{1}{(2\pi)^2}\frac{\rho_1}{\rho_0+\rho_1}\int d^2k\, e^{-kh}\frac{\tilde{T}(\mathbf{k},\omega)}{k}. \tag{27}$$

The final term, denoted as $p_3(\mathbf{r},\omega)$, describes the contribution from the monopole radiation reflected from the interface. Averaging this term over a sphere will involve variations in the variable z of the order $a \ll \omega/c_1$. Using this fact and representing $|z|$ as $h+\Delta z$, where $-a<\Delta z<+a$, we get the following approximation for the quantity $\gamma_1|z|$:

$$\gamma_1|z| \approx \gamma_1 h + k\,\Delta z = k|z| + (\gamma_1-k)h. \tag{28}$$

Thus for variations of z over a scale a, the term $p_3(\mathbf{r},\omega)$ is a harmonic function and its spherical average is its value at the center of the sphere:

$$\langle p_3(\mathbf{r},\omega)\rangle \approx -\frac{1}{(2\pi)^2}\frac{\hat{Q}(\omega)}{2}\int d^2k\, e^{-2\gamma_1 h}\frac{R_Q(\mathbf{k},\omega)}{\gamma_1}. \tag{29}$$

Since the sum of expressions (26), (27), and (29) is to be set to zero, we get the following result for the strength of the monopole in terms of the hydrodynamic forces:

$$\hat{Q}(\omega) = -\left(\frac{\rho_1}{\rho_0+\rho_1}\int d^2k\, e^{-kh}\frac{\tilde{T}(\mathbf{k},\omega)}{k}\right) \times\left(\frac{\pi}{a}+\frac{1}{2}\int d^2k\, e^{-2\gamma_1 h}\frac{R_Q(\mathbf{k},\omega)}{\gamma_1}\right)^{-1}. \tag{30}$$

Further simplification of formula (30) is achieved employing the assumption that deformations of the interface by the pressure forces are small. Thus the Lighthill source term T may be approximated by the equivalent source for a flow over a flat, rigid plate. In this case, the pressure field for $z>0$ is determined by Eq. (2), solved with the boundary condition $\partial p/\partial z = 0$ at the interface $z=0$. Solution is given by Eq. (21) with reflection coefficient $R_T=1$ and transmission coefficient $P_Q=0$:

$$p(\mathbf{r},\omega)=\frac{1}{(2\pi)^2}\int d^2k\, e^{-i\mathbf{k}\cdot\mathbf{x}}\times\left(-\frac{1}{2\gamma_0}\int_0^\infty \hat{T}(\mathbf{k},z',\omega)e^{-\gamma_0|z-z'|}\,dz'\right)+\frac{1}{(2\pi)^2}\int d^2k\, e^{-i\mathbf{k}\cdot\mathbf{x}-\gamma_0 z}\left(-\frac{\tilde{T}(\mathbf{k},\omega)}{2\gamma_0}\right),\quad z>0. \tag{31}$$

In particular, at $z=0$,

$$p(\mathbf{x},0,\omega)=-\frac{1}{(2\pi)^2}\int d^2k\, e^{-i\mathbf{k}\cdot\mathbf{x}}\frac{\tilde{T}(\mathbf{k},\omega)}{\gamma_0}. \tag{32}$$

The last equation allows us to express the hydrodynamic forcing $\tilde{T}$ in terms of the wall pressure transform (spectrum) $P_0(\mathbf{k},\omega)$ on the rigid plate:

$$\tilde{T}(\mathbf{k},\omega)=-\gamma_0\hat{p}(\mathbf{k},0,\omega)=-\gamma_0 P_0(\mathbf{k},\omega). \tag{33}$$

In Eq. (30) defining $\hat{Q}(\omega)$, the main contribution to the integral containing $\hat{T}$ comes from wave numbers k such that $k=\sqrt{k_1^2+k_2^2}\gg\omega/c_0$. Therefore, $k\approx\gamma_0$ and the strength of the monopole can be expressed in terms of the rigid wall pressure spectrum as

$$\hat{Q}(\omega)=\left(\frac{\rho_1}{\rho_0+\rho_1}\int d^2k\, e^{-kh}P_0(\mathbf{k},\omega)\right)\times\left(\frac{\pi}{a}+\frac{1}{2}\int d^2k\, e^{-2\gamma_1 h}\frac{R_Q(\mathbf{k},\omega)}{\gamma_1}\right)^{-1}. \tag{34}$$

The integrals defining $\hat{Q}(\omega)$ may be further simplified. Let us introduce the following parameters: acoustic wave numbers for both media, $\kappa_0=|\omega|/c_0$, and $\kappa_1=|\omega|/c_1$; distance of the inhomogeneity from the interface in acoustic wavelength units, $\epsilon=h|\omega|/c_1=h\kappa_1=2\pi h/\lambda_1$; ratio of acoustic wave numbers $\kappa=\kappa_0/\kappa_1=c_1/c_0$; density ratio $\sigma=\rho_1/\rho_0$.

Using the definitions (5) and (6) of the Fourier transforms, we can write the integral containing $P_0(\mathbf{k},\omega)$ in the following form:

$$I_p(\omega)=\int d^2k\, e^{-kh}P_0(\mathbf{k},\omega)=\int_{-\infty}^{+\infty}dt\int d^2x\, e^{i\omega t}p_0(\mathbf{x},t)\left(\int d^2k\, e^{i\mathbf{k}\cdot\mathbf{x}}e^{-kh}\right), \tag{35}$$

where $p_0(\mathbf{x},t)$ is the rigid wall pressure distribution. In the above equation, the Fourier transform of e^{-kh} is calculated in polar coordinates as

$$\int d^2k\, e^{i\mathbf{k}\cdot\mathbf{x}}e^{-kh}=2\pi\int_0^\infty dk\, e^{-kh}kJ_0(k|\mathbf{x}|)=\frac{2\pi h}{(h^2+|\mathbf{x}|^2)^{3/2}}, \tag{36}$$

where J_0 is the Bessel function of zero order and the last equality is found from a table of integrals.[16] Therefore, the integral $I_p(\omega)$ is the Fourier transform, in the time domain, of the wall pressure averaged with the weight function (36):

$$I_p(\omega)=2\pi h\int_{-\infty}^{+\infty}dt\, e^{i\omega t}\left(\int d^2x\,\frac{p_0(\mathbf{x},t)}{(h^2+x_1^2+x_2^2)^{3/2}}\right). \tag{37}$$

The remaining integral in formula (30) is again simplified using a cylindrical system of coordinates:

$$I_R(\omega)=\frac{1}{2}\int d^2k\, e^{-2\gamma_1 h}\frac{R_Q(\mathbf{k},\omega)}{\gamma_1}=-\pi\int_0^\infty k\,dk\,\frac{e^{-2\gamma_1 h}}{\gamma_1}\left(\frac{\sigma\gamma_0-\gamma_1}{\sigma\gamma_0+\gamma_1}\right). \tag{38}$$

For problems of interest in this paper $c_0>c_1$ and thus $\kappa_0<\kappa_1$. With this ordering of acoustic wave numbers the integral (38) is split into three parts, involving integration over k with limits from 0 to κ_0, from κ_0 to κ_1, and from κ_1 to infinity. Changing the variable of integration k to $u=\sqrt{\kappa_1^2-k^2}$ in the first two integrals, and to $u=\sqrt{k^2-\kappa_1^2}$ in the last one, we get

$$I_R(\omega)=-i\pi\int_0^s du\, e^{-2ihu}\left(\frac{\sigma\sqrt{s^2-u^2}-u}{\sigma\sqrt{s^2-u^2}+u}\right)-i\pi\int_s^{\kappa_1}du\, e^{-2ihu}\left(\frac{\sigma\sqrt{u^2-s^2}-u}{\sigma\sqrt{u^2-s^2}+u}\right)+\pi\int_0^\infty du\, e^{-2hu}\left(\frac{\sigma\sqrt{s^2+u^2}-u}{\sigma\sqrt{s^2+u^2}+u}\right), \tag{39}$$

where $s^2=(\kappa_1^2-\kappa_0^2)=\kappa_1^2(1-\kappa^2)$. An additional change of variables $u=\kappa_1 v$, and introduction of the nondimensional parameter ϵ, give

$$\frac{I_R(\omega)}{(\kappa_1\pi)}=-i\int_0^1 dv\, e^{-2i\epsilon v}\left(\frac{\sigma\sqrt{|v^2-(1-\kappa^2)|}-v}{\sigma\sqrt{|v^2-(1-\kappa^2)|}+v}\right)+\int_0^\infty dv\, e^{-2\epsilon v}\left(\frac{\sigma\sqrt{v^2+(1-\kappa^2)}-v}{\sigma\sqrt{v^2+(1-\kappa^2)}+v}\right), \tag{40}$$

where the dependence on ω is through the parameter ϵ. Therefore, the expression for $\hat{Q}$ becomes

$$\hat{Q}(\omega)=-\frac{\sigma}{\sigma+1}\frac{I_p(\omega)}{\pi/a+I_R(\omega)}, \tag{41}$$

where the integrals $I_p(\omega)$ and $I_R(\omega)$ are given by Eqs. (37) and (40), respectively. Note that the strength of the monopole in this equation is expressed entirely through the wall pressure distribution $p_0(\mathbf{x},t)$. Exact frequency dependence of $\hat{Q}$ must be obtained through numerical computation of these integrals for particular $p_0(\mathbf{x},t)$ and prescribed values of the nondimensional parameters.

IV. MODELS OF PRESSURE PULSE

We consider in this section four different models of localized, wall pressure distributions to evaluate the integral (37). The simplest model that allows analytical evaluation of (37) is a concentrated force moving with a constant convection velocity U_c, which is a fraction of the mean free stream velocity U_0, along the x_1 axis:

$$p_0(\mathbf{x},t) = P_c\delta(x_1 - U_c t)\delta(x_2). \tag{42}$$

For this model, which we will refer to as the concentrated force model, Eq. (37) becomes

$$I_p(\omega) = 2\pi h \int_{-\infty}^{+\infty} dt\, e^{i\omega t} \frac{P_c}{U_c^3} \frac{1}{[(h/U_c)^2 + t^2]^{3/2}}$$

$$= \frac{4\pi P_c}{hU_c}\left(\frac{h\omega}{U_c}\right) K_1\left(\frac{h\omega}{U_c}\right), \tag{43}$$

where K_1 is the modified Bessel function of the second kind, of order unity. Employing directly formula (35), with $P_0(\mathbf{k},\omega)$ calculated as the Fourier transform of (42), gives the same result, which serves as an independent check of the transformations leading from (35) to (37). The intensity of the acoustic radiation at any frequency will be proportional to the square of the absolute value of (43). A plot of this quantity, normalized by its peak value, is shown in Fig. 2. The function has its maximum at $h\omega/U_c = 0$, is relatively large at subconvective frequencies $h\omega/U_c \leq 1$ (where here "subconvective" implies reference to a wave number of order h^{-1}), and decays rapidly to zero for $h\omega/U_c > 5$.

A model of a wall pressure distribution associated with a burst in a turbulent boundary layer was proposed by Duncan.[17] It has the form of the wall pressure generated by a two-dimensional vortex moving with velocity U_c parallel to the x axis, at a distance d from the wall:

$$p_0(\mathbf{x},t) = P_D g(t) \frac{d^2}{d^2 + (x - U_c t)^2}, \tag{44}$$

where the function $g(t)$ accounts for the fact that the amplitude of the burst varies in time, with maximum $P_D = 0.0055\rho_0 U_0^2$, and $U_c = 0.8U_0$ chosen to match the experimental results of Willmarth.[9] In this model, subsequently referred to as the Duncan model, the function $g(t)$ is

$$g(t) = \begin{cases} 3.7856\exp(-2t/3)\sin(\pi t/6), & 0 \leq t \leq 6, \\ 0, & \text{otherwise.} \end{cases} \tag{45}$$

where time is nondimensionalized with δ/U_c, where δ is the boundary layer thickness, and $d = \delta/2$.

In what follows, we assume that the distance of the inhomogeneity from the interface is close to the boundary layer thickness. This choice of h is motivated by the fact that our most realistic model, discussed next, is obtained for the boundary layer flow at $\mathrm{Re}_\theta \approx 600$, where Re_θ is Reynolds number based on the momentum thickness. For the flow of water (kinematic viscosity $\nu = 0.01\ \mathrm{cm}^2/\mathrm{s}$) with typical free stream velocity $U_0 = 10$ m/s, the boundary layer thickness is $\delta \approx 1$ mm at this Reynolds number. This last value seems to be a realistic distance of possible inhomogeneities from the interface. In any event, inhomogeneities further away than δ from the interface will not be effective as scatterers because the exponential factors in Eq. (34) put them out of range of the most energetic pressure fluctuations. For $h \approx \delta$ Eq. (37) can be written as follows:

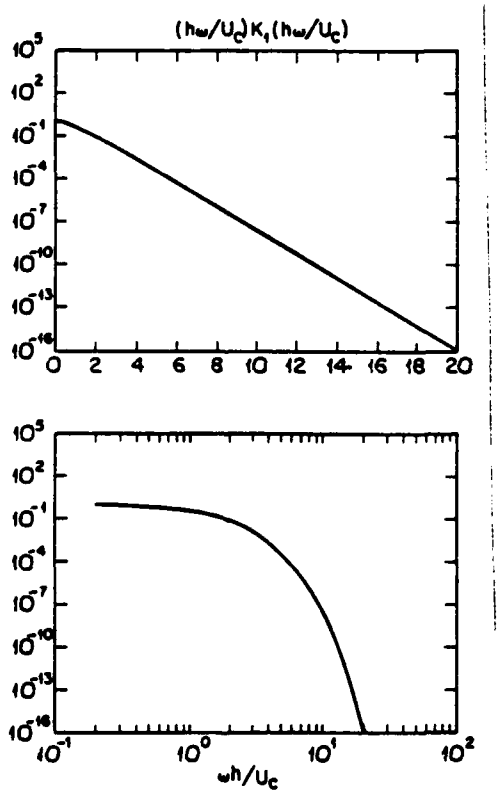

FIG. 2. Frequency dependence of the monopole intensity $|\hat{Q}(\omega)|^2$ for the concentrated force model, on log–linear and log–log scales.

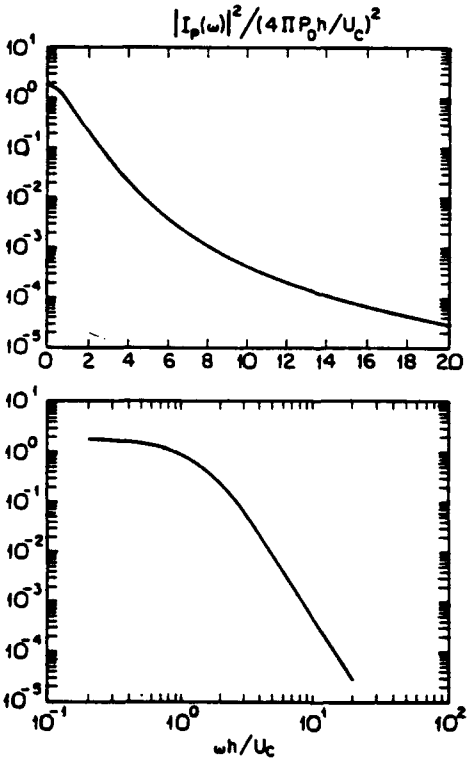

FIG. 3. Frequency dependence of the monopole intensity $|\hat{Q}(\omega)|^2$ for the Duncan model, on log–linear and log–log scales.

$$I_p(\omega) = \frac{4\pi P_0 h}{U_c} \int_0^\infty dt \exp\left(i \frac{h\omega}{U_c} t\right) g(t) e(t), \qquad (46)$$

where

$$e(t) = \int_{-\infty}^{+\infty} \frac{dx}{[1 + 4(x-t)^2](1+x^2)}. \qquad (47)$$

Integral (46) has been evaluated numerically and the square of its normalized absolute value is shown in Fig. 3. Very much as in the case of the concentrated force, it is largest at subconvective frequencies $h\omega/U_c \leqslant 1$ and decays fairly rapidly for $h\omega/U_c > 1$. Note, however, that the decay rate is smaller than for the case of the concentrated force.

In order to obtain the most realistic model of a localized wall pressure distribution $p_0(\mathbf{x},t)$ we have used the results of direct numerical simulations of a turbulent boundary layer. The pressure values were calculated by Robinson[18] from the results of numerical simulations of a three-dimensional, turbulent boundary layer over a flat plate performed and described in detail by Spalart.[19] Data employed in our work are characterized by the following principal parameters: Reynolds number, based on the momentum thickness, $\mathrm{Re}_\theta = 640$; friction velocity u_τ as a fraction of the free stream velocity U_0, $u_\tau/U_0 = 0.0484$; time extent of the data in wall time units, $T^+ = Tu_\tau^2/\nu = 72$; streamwise and spanwise dimensions of the plate in wall length units,

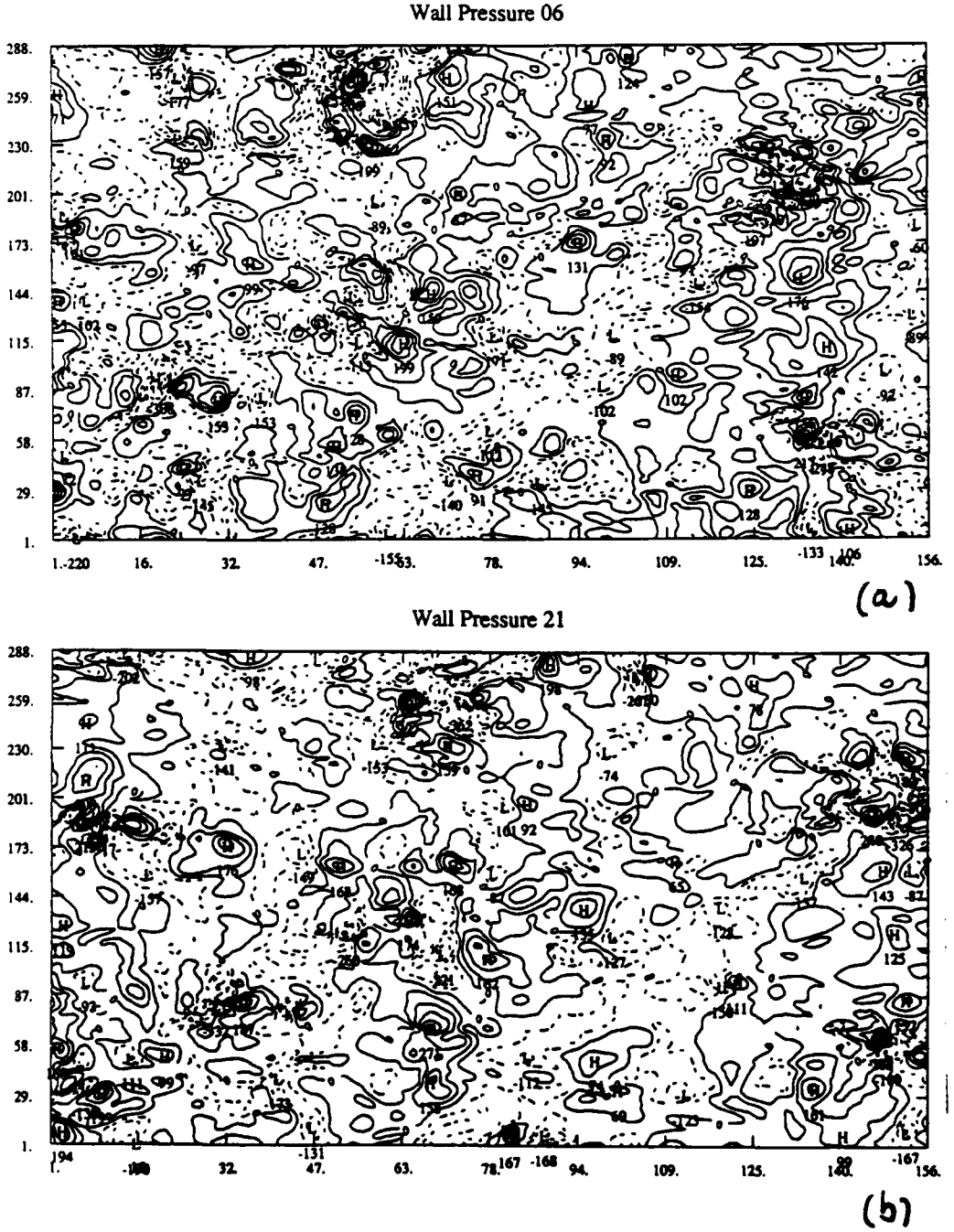

FIG. 4. Wall pressure contours from direct numerical simulations. Solid lines correspond to positive values and broken lines to negative values. The mean flow is from left to right. (a) $t^+ = 6$, and (b) $t^+ = 21$.

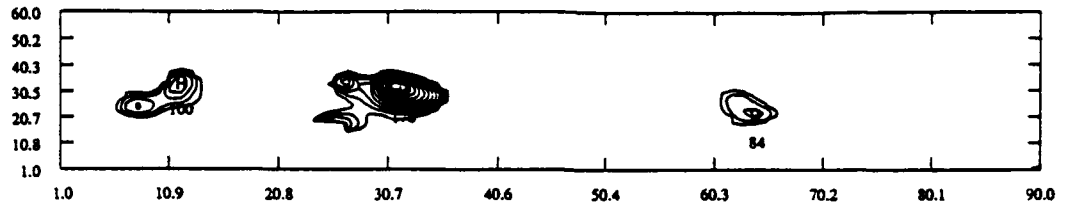

FIG. 5. Contours of wall pressures for a single burst at three different times $t^+ = 6$, 21, and 51. The mean flow is from left to right.

$L_x^+ = L_x u_\tau/\nu \approx 2000$ and $L_y^+ = L_y u_\tau/\nu \approx 1230$, respectively. The wall-pressure data made available to the authors of this paper have the form of 24 distinct datasets, each for a different time t^+ which is an integer multiple of $\Delta t^+ = 3$. Each dataset gives normalized pressure $p/(\rho_0 U_0^2)$ on a rectangular mesh with 156 points in the streamwise x direction, and 288 points in the spanwise y direction. Typical appearance of the instantanous wall pressure at two different times is shown in Fig. 4(a) and (b). The wall pressure has a spotty character, with a number of localized high-pressure regions. In Fig. 4, the mean flow direction is from left to right, and comparison of Fig. 4(a) with (b) reveals that the individual high-pressure regions move in that direction, and at the same time change in strength and spatial extent. The convection velocity U_c of high-pressure regions varies between 0.6 U_0 and 0.8 U_0.

Our primary task was to identify a few pressure pulses that could serve as useful representations of pressures associated with the presence of localized, energetic events in turbulent boundary layers. We will focus our attention on one such pulse that displayed the desired behavior. The selected pulse initially was very weak, grew subsequently in strength, and eventually decayed. Moreover, throughout its evolution it remained isolated from other high- and low-pressure regions, thus preserving its identity.

After the selection was made, all other pressure pulses present in the data had to be suppressed. This was achieved by specifying a point inside the high-pressure region of interest and finding a contour around this point where pressure values had fallen to a certain specified threshold level. Once this limit contour was reached, all the other pressure values beyond it were set to zero. This procedure was incorporated in a numerical routine and performed for each of 24 datasets. Finally, a three-dimensional fit of discrete data obtained in this procedure was carried out using a BS3IN routine from the IMSL package of mathematical routines, in order to get a representation continuous in space and in time, of a single-pressure pulse. Cubic splines were used for the x and y variables, and a linear fit for the time t. The large number of fitting coefficients ($\approx 10^4$) precludes the manual use of data. The coefficients are stored on tape and a computer program is used to provide a pressure value at a given spatial location, $0 < x^+ < 2000$, $0 < y^+ < 1230$, and given time, $0 < t^+ < 72$. In Fig. 5, we plot the high-pressure region obtained from this procedure at three different times. The amplitude of this pressure pulse was set to zero for $t^+ = 0$, it gradually reached its maximum at $t^+ \approx 20$, and decayed to zero at $t^+ \approx 70$. These results may be considered as a realistic model, which will be referred to as the numerical simulation model, of a localized wall pressure pulse in a turbulent boundary layer. Note, however, that the individual pressure pulses vary in strength and spatial extent, and the results obtained for the particular one chosen here are subject to similar variations.

Integral (37) has been computed using the above representation of $p_0(\mathbf{x},t)$, assuming $U_c = 0.8\ U_0$, and $h^+ = hu_\tau/\nu = 300$. This last value is approximately equal to the boundary layer thickness δ, which for water at this Reynolds number is about 1 mm. For the purpose of computations the integral (37) is rewritten using wall units, as

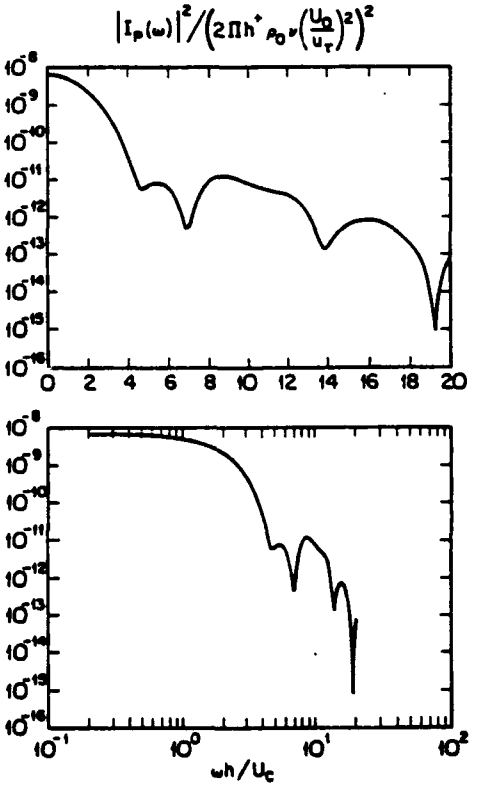

FIG. 6. Frequency dependence of the monopole intensity $|\hat{Q}(\omega)|^2$ for the numerical simulation model, on log–linear and log–log scales.

$$I_p(\omega^+) = 2\pi h^+ \rho_0 \nu \left(\frac{U_0}{u_\tau}\right)^2 \int_{-\infty}^{+\infty} dt^+ e^{i\omega^+ t^+} \times \left(\int d^2x^+ \frac{p_0(\mathbf{x}^+, t^+)/(\rho U_0^2)}{(h^{+2} + x_1^{+2} + x_2^{+2})^{3/2}} \right). \tag{48}$$

In Fig. 6, we plot the square of the absolute value of (48), normalized by the multiplicative factor in front of the integral, with frequencies ω^+ converted to nondimensional units $\omega h/U_c = \omega^+ h^+ u_\tau / U_c$. As in the previous case, the function is approximately constant for the subconvective frequencies $\omega h/U_c < 1$, and decays rapidly for $\omega h/U_c > 1$.

The strength of the monopole $\hat{Q}(\omega)$ is proportional to the integral $I_p(\omega)$, and modified by the ω-dependent expression in the denominator in (41). This expression can be rewritten as follows:

$$\frac{\pi}{a} + I_R(\omega) = \kappa_1 \pi \left(\frac{h}{a} \frac{1}{\epsilon} + \frac{I_R(\omega)}{\kappa_1 \pi} \right), \tag{49}$$

where the integral $J(\epsilon) = I_R(\omega)/(\kappa_1 \pi)$ is given by formula (40). This integral is easily computed numerically and the results of such integration, in the limit of interest $\kappa \ll 1$ and $\sigma \approx 1$, are gathered in Table I for a few values of the parameter ϵ. It is seen that the value of the integral is always much less than $1/\epsilon$ for $\epsilon \leq 1/4$. Therefore, for a large range of values of ϵ, to good approximation

$$\hat{Q}(\omega) \approx -\frac{\sigma}{\sigma + 1} \frac{a}{\pi} I_p(\omega), \tag{50}$$

and the frequency dependence of $\hat{Q}(\omega)$ is the same as that of the function $I_p(\omega)$.

For all models of a localized pressure pulse considered so far, this frequency dependence exhibits the same generic features: a large, almost constant plateau in the range of subconvective frequencies $\omega h/U_c < 1$, followed by a fairly rapid decrease for $1 \leq \omega h/U_c$.

The above models of pressure pulses are strictly of positive sign. In experiments, Johansson *et al.*[13] and Karangelen *et al.*[14] find that conditionally averaged high-pressure events are indeed predominantly of one sign, either positive or negative. Use of the negative pressure models will result in a trivial change of sign in the previous formulas containing the wall pressure function. Therefore, the pressure pulse models used in our work are consistent with the experimental observations.

TABLE I. Absolute values of integral (40) as a function of $\epsilon = h|\omega|/c_1$, for $\sigma = 1$ and $\kappa = 0.05$.

ϵ	$1/\epsilon$	$\lvert J(\epsilon)\rvert$
1.0	1.0	0.36095
0.63	1.6	0.41087
0.40	2.5	0.46036
0.25	4.0	0.50894
0.16	6.3	0.55331
0.10	10.0	0.59123
0.063	15.8	0.62230
0.040	25.0	0.64621
0.025	40.0	0.65137
0.016	62.5	0.61286
0.010	100.0	0.52459

However, according to the Kraichnan–Phillips theorem[20,21] the instantaneous surface integral of the unsteady wall pressure under an incompressible turbulent boundary layer is zero. This result has recently been reinforced by the analysis of Howe[22] who showed that any localized hydrodynamic event will produce a nonvanishing net normal force on the wall only by virtue of edge effects and in the absence of such effects (an infinite plate) the net force will be zero. In experimental situations, the Kraichnan–Phillips condition will be satisfied if positive wall pressure bursts are balanced by negative ones in other regions of the wall, or weaker negative pressure regions covering a larger wall area.

In evaluation of the integral (37), the wall pressure $p_0(\mathbf{x},t)$ is integrated with the weight function (36) which strongly limits contributions that wall pressures from outside the immediate vicinity of the inhomogeneity can make to the integral. Thus the presence of this weight function in (37) implies that if the positive pressure event over the inhomogeneity is balanced by a negative pressure event of equal strength (to satisfy the Kraichnan–Phillips condition) away from the inhomogeneity, the monopole strength $\hat{Q}(\omega)$ will be determined primarily by the positive pressure peak.

The above argument does not apply to the case of a high, positive pressure region surrounded by a region of weaker, negative pressure values. Even though such events are less likely to occur than localized bursts of predominantly one sign, it may be instructive to investigate them in some detail since such an analysis may shed more light on the importance of the Kraichnan–Phillips theorem in the context of sound generation by localized hydrodynamic forcings.

We will consider the following pressure model:

$$p_0(\mathbf{x},t) = P_D g(t) \left[5\left(\frac{x - U_c t}{\delta/2}\right)^4 - 6\left(\frac{x - U_c t}{\delta/2}\right)^2 + 1 \right], \quad \text{for } \left|\frac{x - U_c t}{\delta/2}\right| < \frac{\delta}{2}, \tag{51}$$

where the pressure amplitude P_D and the function $g(t)$ are the same as for the Dyson model (44), δ is the boundary layer thickness, and $U_c = 0.8U_0$ is the convection velocity. Formula (51) describes a pressure distribution which at all times t has a finite spatial extent δ and contains a strong positive central peak and two smaller, negative side minima. The constants are chosen such that the pressure integrated over the wall is zero for all times t and therefore we will refer to this model as the zero net force model. Integral (37) for this pressure pulse model is easily reduced to the form (47), with function $e(t)$ given by

$$e(t) = \int_{t-1/2}^{t+1/2} [80(x-t)^4 - 24(x-t)^2 + 1] \frac{dx}{1+x^2}. \tag{52}$$

A numerical integration of (47) for this model has been performed and the square of its normalized absolute value, which is proportional to $|\hat{Q}(\omega)|^2$, is plotted in Fig. 7. The main qualitative difference between this case and previously

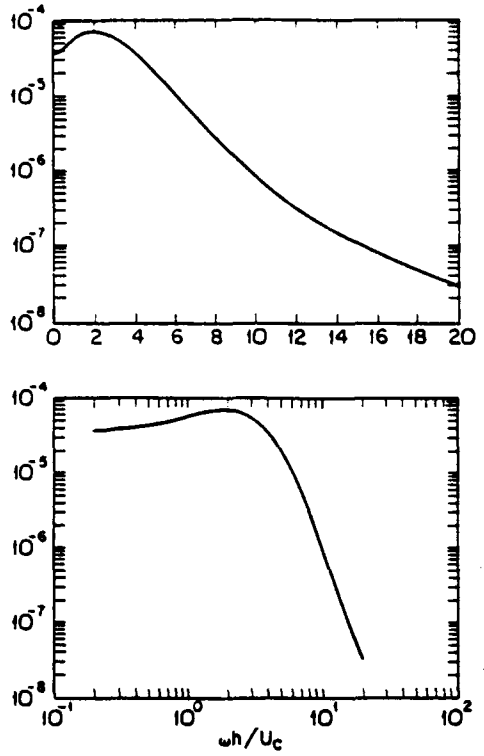

FIG. 7. Frequency dependence of the monopole intensity $|\hat{Q}(\omega)|^2$ for the zero net force model satisfying the Kraichnan–Phillips condition, on log–linear and log–log scales.

considered models is observed in the low-frequency regime. Whereas for positive pressure pulses the monopole strength reaches its maximum for $\omega \to 0$, for the current model satisfying the Kraichnan–Phillips condition it has a maximum at a finite value $\omega h/U_c \approx 1$.

V. ACOUSTIC RADIATION FROM THE MONOPOLE SOURCE

It has been shown by Howe[2-6] that the intensity of sound produced by scattering of the boundary layer pressure fluctuations by an inhomogeneity exceeds substantially the intensity of sound radiated directly by the boundary layer flow. We may thus expect that the acoustic radiation from the monopole source will also dominate in our case. In what follows, we will concentrate our attention on the evaluation of the far-field acoustic pressure resulting from the presence of the monopole.

In Eq. (21), the monopole contribution $p_m(\mathbf{r},\omega)$ to the total pressure $p(\mathbf{r},\omega)$ for $z>0$ is

$$p_m^{>}(\mathbf{r},\omega) = -\frac{\hat{Q}(\omega)}{(2\pi)^2}\int d^2k\,\frac{e^{-i\mathbf{k}\cdot\mathbf{x}-\gamma_0 z-\gamma_1 h}}{\sigma\gamma_0+\gamma_1}. \tag{53}$$

In the integral (53), when $z\to\infty$ only the wave numbers from the radiating acoustic domain $k_1^2+k_2^2\le\kappa_0^2$ will contribute. Using the radiation condition, for $\omega>0$, this integral is written as follows:

$$I^{>}(\mathbf{r},\omega) = \int_{k_1^2+k_2^2<\kappa_0^2} dk_1\,dk_2\,\exp(-ik_1x_1-ik_2x_2 + i\sqrt{\kappa_0^2-k_1^2-k_2^2}\,z)F(k_1,k_2), \tag{54}$$

where $F(k_1,k_2)=e^{-\gamma_1 h}/(\sigma\gamma_0+\gamma_1)$. Projection of the vector $\mathbf{r}$ onto the Oxz plane is denoted by $\mathbf{R}$, and the angle between $\mathbf{R}$ and the x axis is denoted by α. With this notation, the integral over k_1 in (54) is

$$I_1^{>}(\mathbf{r},k_2,\omega) = \int_{-K}^{+K} dk_1\,\exp[iR(-k_1\cos\alpha + \sqrt{K^2-k_1^2}\sin\alpha)]F(k_1,k_2), \tag{55}$$

where $K^2=\kappa_0^2-k_2^2$. Using the method of stationary phase, the asymptotic form of this integral for large R is

$$I_1^{>}(\mathbf{r},k_2,\omega) \approx (2\pi K/R)^{1/2}\exp(iKR-i\pi/4) \times\sin\alpha F(-K\cos\alpha,k_2). \tag{56}$$

Integrating the above function over k_2 with limits $-\kappa_0\le k_2\le+\kappa_0$, and using once again the method of stationary phase, provides the following asymptotic expression for $I^{>}(\mathbf{r},\omega)$ at large r:

$$I^{>}(\mathbf{r},\omega) \approx (2\pi\kappa_0/r)\exp(i\kappa_0 r-i\pi/2) \times\cos\theta F(-\kappa_0\sin\theta\cos\phi,-\kappa_0\sin\theta\sin\phi), \tag{57}$$

where θ and ϕ are polar angles of the position vector $\mathbf{r}$ in the far field in spherical coordinates with θ measured from the z axis and ϕ measured from the x axis. Thus the explicit form of the far-field acoustic pressure for large positive z, due to the monopole, is

$$p_m^{>}(r,\theta,\phi,\omega) = -\hat{Q}(\omega)(\kappa/2\pi r) \times\frac{\exp[i(\kappa_0 r+\kappa_1\sqrt{1-\kappa^2\sin^2\theta}\,h)]}{\sigma\kappa\cos\theta+\sqrt{1-\kappa^2\sin^2\theta}}\cos\theta. \tag{58}$$

The monopole contribution $p_m^{<}(\mathbf{r},\omega)$ to the total pressure $p(\mathbf{r},\omega)$ in the coating ($z<0$) is, according to Eq. (22),

$$p_m^{<}(\mathbf{r},\omega) = -\frac{\hat{Q}(\omega)}{(2\pi)^2}\left(\int d^2k\,\frac{e^{-i\mathbf{k}\cdot\mathbf{x}-\gamma_1|z+h|}}{2\gamma_1} - \int d^2k\,\frac{e^{-i\mathbf{k}\cdot\mathbf{x}-\gamma_1(|z|+h)}}{2\gamma_1}\,\frac{\sigma\gamma_0-\gamma_1}{\sigma\gamma_0+\gamma_1}\right). \tag{59}$$

In spherical coordinates with the axis in the negative z direction the first integral in (59) is calculated exactly as

$$I_1^{<}(\mathbf{r},\omega) = -\hat{Q}(\omega)\,\frac{e^{i\kappa_1|\mathbf{r}-\mathbf{r}_0|}}{4\pi|\mathbf{r}-\mathbf{r}_0|}, \tag{60}$$

where $\mathbf{r}_0$ is the location of the center of the inhomogeneity. Therefore, as expected, we get the expression for the direct monopole radiation. The second integral in (59) has the following asymptotic form for large negative values of z:

$$I_2^{<}(\mathbf{r},\omega) = \hat{Q}(\omega)\,\frac{e^{i\kappa_1|\mathbf{r}+\mathbf{r}_0|}}{4\pi|\mathbf{r}+\mathbf{r}_0|}\,\frac{\sigma\sqrt{\sin^2\theta_1-\kappa^2}+i\cos\theta_1}{\sigma\sqrt{\sin^2\theta_1-\kappa^2}-i\cos\theta_1}, \tag{61}$$

where θ_1 is the angle measured between the negative z axis and the vector $(\mathbf{r}+\mathbf{r}_0)$ giving location $\mathbf{r}$ with respect to the image of $\mathbf{r}_0$; i.e., $-\mathbf{r}_0=(0,0,h)$. Thus the far-field acoustic pressure in the coating due to the monopole is

$$p_m^{<}(r,\theta_1,\phi,\omega) = -\frac{\hat{Q}(\omega)}{4\pi}\left(\frac{e^{i\kappa_1|\mathbf{r}-\mathbf{r}_0|}}{|\mathbf{r}-\mathbf{r}_0|} - \frac{e^{i\kappa_1|\mathbf{r}+\mathbf{r}_0|}}{|\mathbf{r}+\mathbf{r}_0|} \times \frac{\sigma\sqrt{\sin^2\theta_1 - \kappa^2} + i\cos\theta_1}{\sigma\sqrt{\sin^2\theta_1 - \kappa^2} - i\cos\theta_1}\right). \quad (62)$$

Formulas (37), (40), (41), (58), and (62) constitute a complete solution to the problem of the far-field acoustic radiation produced by scattering of the boundary layer pressures by a localized inhomogeneity in the coating.

For certain values of the nondimensional parameters, these expressions for the far-field acoustic pressure have a simple physical interpretation. One case of interest is the situation when $\kappa = c_1/c_0 \ll 1$ and $\sigma \approx 1$, corresponding to the flow of water ($c_0 \approx 1500$ m/s) over vulcanized rubber ($c_1 \approx 50$ m/s according to Resnick and Halliday[23]). In this limit, sound scattered in the upper medium has dipole characteristics arising from the interaction between the monopole and its image:

$$p_m^{>}(r,\theta,\phi,\omega) \approx -\hat{Q}(\omega)\left(\frac{1}{2\pi r}\right)\left(\frac{c_1}{c_0}\right)e^{i(\kappa_0 r + \kappa_1 h)}\cos\theta. \quad (63)$$

The leading order cancelation between the monopole and its image comes about because the surface reflection coefficient is -1 in this limit.

In the same limit, the sound scattered in the lower medium is

$$p_m^{<}(r,\theta_1,\phi,\omega) = -\frac{\hat{Q}(\omega)}{4\pi}\left(\frac{e^{i\kappa_1|\mathbf{r}-\mathbf{r}_0|}}{|\mathbf{r}-\mathbf{r}_0|} - \frac{e^{i\kappa_1|\mathbf{r}+\mathbf{r}_0|}}{|\mathbf{r}+\mathbf{r}_0|}\frac{\sin\theta_1 + i\cos\theta_1}{\sin\theta_1 - i\cos\theta_1}\right). \quad (64)$$

For small angles θ_1 the last equation gives monopole radiation

$$p_m^{<}(r,\theta_1 \approx 0,\phi,\omega) \approx -\hat{Q}(\omega)\left(\frac{1}{2\pi r}\right)e^{i\kappa_1 r}, \quad (65)$$

whereas for directions almost tangent to the interface one gets from (64) dipole radiation:

$$p_m^{<}\left(r,\theta_1 \approx \frac{\pi}{2},\phi,\omega\right) \approx -\hat{Q}(\omega)\left(\frac{1}{2\pi r}\right)(\kappa_1 h)e^{i\kappa_1 r}\cos\theta_1. \quad (66)$$

Note that the ratio of intensities of scattered sound in directions normal to the interface is

$$\frac{(1/\rho_0 c_0)|p_m^{>}|^2}{(1/\rho_1 c_1)|p_m^{<}|^2} \approx \kappa^3 \ll 1, \quad (67)$$

and for directions tangent to the interface is

$$\frac{(1/\rho_0 c_0)|p_m^{>}|^2}{(1/\rho_1 c_1)|p_m^{<}|^2} \approx \frac{\kappa^3}{\epsilon^2}. \quad (68)$$

In the last equation, both κ and ϵ are small and their ratio will depend on the exact values of these quantities. However, for a typical value $\kappa \approx 0.05$ at the physical conditions in mind, the above ratio can be controlled only by changing ϵ, i.e., by adjusting the distance h of the inhomogeneity from the interface. Assuming that $h < \delta$, where δ is the boundary layer thickness, which at typical speeds $U_0 \approx 10$ m/s and Reynolds numbers $\mathrm{Re}_\delta = U_0\delta/\nu \approx 10^4$ is less than 1 mm, the typical value of $\epsilon = h\omega/c_1$ for acoustic frequencies is of the order 1. The distance h cannot be less than the radius a of the inhomogeneity. Assuming that a is no less than 0.1δ, the minimum value of ϵ is about 0.1. Thus the maximum value of the ratio (68) is about 0.01 and we may conclude that, in general, for the flow of water over such a rubberlike compliant plate, the intensity of sound scattered by the inhomogeneity into the fluid is at least two orders of magnitude smaller than the intensity of sound scattered into the compliant medium. However, it should be noted that often for other rubberlike materials the longitudinal-wave speed is comparable to the sound speed in water and, consequently, the above conclusions will not apply to such coatings.

VI. COMPARISON WITH STATISTICALLY STATIONARY AND HOMOGENEOUS BOUNDARY LAYER FORCING

Localized high-pressure bursts occur in turbulent boundary layers randomly in space and time, and have different amplitudes and durations. Thus, in practical situations, boundary layer forcing must be treated statistically. In this section, we compare the scattered sound produced by statistically stationary and homogeneous boundary layer forcing with sound produced by a single, deterministic pressure pulse.

The acoustic intensity averaged over the turbulence ensemble is

$$I_l(\mathbf{r}_l,t) = \frac{1}{\rho_l c_l}\langle p^2(\mathbf{r}_l,t)\rangle = \frac{1}{\rho_l c_l}\frac{1}{(2\pi)^2}\int\int d\omega\, d\omega' \langle \hat{p}(\mathbf{r}_l,\omega)\hat{p}^*(\mathbf{r}_l,\omega')\rangle \times e^{-i(\omega-\omega')t}, \quad l = 0,1 \quad (69)$$

where index l serves to distinguish between the upper and the lower medium. According to (53) and (59)

$$\langle \hat{p}(\mathbf{r}_l,\omega)\hat{p}^*(\mathbf{r}_l,\omega')\rangle = G_l(\mathbf{r}_l,\omega)G_l^*(\mathbf{r}_l,\omega')\langle \hat{Q}(\omega)\hat{Q}^*(\omega')\rangle, \quad (70)$$

where $G_l(\mathbf{r}_l,\omega)$, $l = 0,1$, denote deterministic functions of $\mathbf{r}$ and ω that multiply $\hat{Q}(\omega)$ in (53) and (59). Using formula (34) for $\hat{Q}(\omega)$, expressed in terms of the Fourier transform $P_0(\mathbf{k},\omega)$ of the rigid wall pressure, the last equation becomes

$$\langle \hat{p}(\mathbf{r}_l,\omega)\hat{p}^*(\mathbf{r}_l,\omega')\rangle = \frac{\sigma^2}{(\sigma+1)^2}\left|\frac{1}{\pi/a + I_R(\omega)}\right|^2 G_l(\mathbf{r}_l,\omega)G_l^*(\mathbf{r}_l,\omega') \times \int\int d^2k\, d^2k' \langle P_0(\mathbf{k},\omega)P_0^*(\mathbf{k}',\omega')\rangle. \quad (71)$$

If the turbulence is stationary in time and homogeneous in horizontal planes parallel to the interface, then

$$\langle P_0(\mathbf{k},\omega)P_0^*(\mathbf{k}',\omega')\rangle = (2\pi)^3\delta(\mathbf{k}-\mathbf{k}')\delta(\omega-\omega')S_p(-\mathbf{k},-\omega), \quad (72)$$

where $S_p(\mathbf{k},\omega)$ is the wave-number-frequency surface pressure power spectral density. Defining the frequency spec-

trum $S_s(\mathbf{r}_l,\omega)$ of the acoustic intensity at a point $\mathbf{r}_l$ resulting from the statistical forcing such that

$$I_l(\mathbf{r}_l) = \int_{-\infty}^{+\infty} d\omega\, S_s(\mathbf{r}_l,\omega), \tag{73}$$

taking the complex conjugate of (72) and using the previous formulas, we get

$$S_s(\mathbf{r}_l,\omega) = \frac{2\pi}{\rho_l c_l}\frac{\sigma^2}{(\sigma+1)^2}\left|\frac{G_l(\mathbf{r}_l,\omega)}{\pi/a + I_R(\omega)}\right|^2 \times \int d^2k\, e^{-2kh} S_p(\mathbf{k},\omega). \tag{74}$$

Note that for the stationary forcing the acoustic intensity at a point $\mathbf{r}$ does not depend on time.

For a deterministic pressure pulse of finite duration, we introduce the sound intensity averaged over time

$$I_d(\mathbf{r}_l) = \frac{1}{T}\int_0^T dt\,\frac{p^2(\mathbf{r}_l,t)}{\rho_l c_l}, \tag{75}$$

where T is the duration of the pulse which started at time $t=0$. The intensity (75) is rewritten using Parseval's equality:

$$I_d(\mathbf{r}_l) = \frac{1}{2\pi T\rho_l c_l}\int_{-\infty}^{+\infty} d\omega |p(\mathbf{r}_l,\omega)|^2 = \frac{1}{2\pi T\rho_l c_l}\frac{\sigma^2}{(\sigma+1)^2} \times \int_{-\infty}^{+\infty} d\omega \left|\frac{G_l(\mathbf{r}_l,\omega)}{\pi/a + I_R(\omega)}\right|^2 |I_p(\omega)|^2. \tag{76}$$

Therefore, the appropriate frequency spectrum of a deterministic pressure pulse to be used for comparison with the frequency spectrum (74) of statistical forcing is

$$S_d(\mathbf{r}_l,\omega) = \frac{1}{2\pi T\rho_l c_l}\frac{\sigma^2}{(\sigma+1)^2}\left|\frac{G_l(\mathbf{r}_l,\omega)}{\pi/a + I_R(\omega)}\right|^2 |I_p(\omega)|^2. \tag{77}$$

The main quantity of interest is the ratio of (77) and (74) calculated at the same point $\mathbf{r}$:

$$R(\omega) = \frac{S_d(\mathbf{r},\omega)}{S_s(\mathbf{r},\omega)} = \frac{1}{(2\pi)^2 T}\frac{|I_p(\omega)|^2}{I_S(\omega)}, \tag{78}$$

where

$$I_S(\omega) = \int d^2k\, e^{-2kh} S_p(\mathbf{k},\omega). \tag{79}$$

The integral $I_p(\omega)$ has already been calculated in the previous section for four different models of a pressure pulse. The integral $I_S(\omega)$ will be calculated using a phenomenological representation of $S_p(\mathbf{k},\omega)$ proposed by Chase,[7]

$$S_p(\mathbf{k},\omega) = (2\pi)^3 C_m \rho_0^2 u_\tau^3 k_1^2\left[\left(\frac{\omega - U_c k_1}{H u_\tau}\right)^2 + (k_1^2 + k_2^2) + \frac{1}{(b\delta)^2}\right]^{-5/2}. \tag{80}$$

In the above equation, the nondimensional constants are $b = 0.75$, $C_m = 0.1553$, and $H = 3$. There is an additional factor $(2\pi)^3$ in (80) as compared with Chase[7] resulting from different definitions of Fourier transforms. Chase's model takes into account the presence of strong pressure fluctuations in turbulent boundary layers, whose deterministic models were discussed in the Sec. IV. Since high-pressure regions are advected in the mean stream direction with the convection velocity U_c, the function $S_p(\mathbf{k},\omega)$ has a strong maximum in the vicinity of $k_1 \approx \omega/U_c$, $k_2 \approx 0$. Representation (80) is valid for $k_1 \gg \omega/c_0$.

Using (80), the integral (79) can be written as follows:

$$I_S(\omega) = (2\pi)^3 C_m \rho_0^2 u_\tau^3 \int dK_1\, dK_2\, \frac{K_1^2 \exp(-2\sqrt{K_1^2+K_2^2})}{[(1/H^2)(U_c/u_\tau)^2(\omega h/U_c - K_1)^2 + (K_1^2+K_2^2) + (h/b\delta)^2]^{5/2}}, \tag{81}$$

where $K_1 = hk_1$, $K_2 = hk_2$ are the nondimensional wave numbers. The above integral has been computed numerically for $h = \delta$ and a typical value of the ratio $U_c/u_\tau = 20$, with the results of the calculations shown in Fig. 8. The curve peaks in the range of convective frequencies $\omega h/U_c \approx 1$. In contradistinction to the case of a positive deterministic pressure pulse, it is about one order of magnitude less at $\omega h/U_c = 0$ than its peak value at $\omega h/U_c = 1$. This feature is similar to the low-frequency behavior of the zero net force model (51) satisfying the Kraichnan–Phillips condition. This suggests that the low-frequency behavior of (81) may be explained by the presence of cancellation effects among positive and negative pressure pulses accounted for in the statistical description but neglected in the strictly positive pulse models.

The ratio (78) for all four models of the pressure pulse is plotted in Fig. 9. Expression (46) was used for the Duncan model (44) and the zero net force model (51). Equation (48) was used for the numerical simulation model. In the expression (43) for the concentrated force model, the amplitude P_c was set to $\pi d^2 P_D$, with parameters d and P_D and the duration T of the pulse taken from the Duncan model. In all cases, the ratio (78) has a local maximum for $\omega h/U_c = 0$, followed by a gradual decrease by about 10 dB in the range $0 < \omega h/U_c < 1$. Subsequently, the curves begin to increase before reaching a plateau for $\omega h/U_c > 10$. The exception is the curve for the concentrated force model, which decreases rapidly for $\omega h/U_c > 10$. Note that the range $\omega h/U_c \approx \omega\delta/U_c > 5$ (for the typical values used here, $\delta \approx 1$ mm and $U_c \approx 10$ m/s), corresponds to important acoustic frequencies $f = \omega/(2\pi) > 10^4$ Hz.

The curve for the Duncan model follows rather closely the curve for the model obtained from the direct numerical simulations; however, its level is consistently about 20 dB higher. The variations in the range 10–20 dB for the intensity of sound produced by the individual pressure pulses are expected because of variations in their strength and size. For instance, an increase in the linear dimensions of the pressure

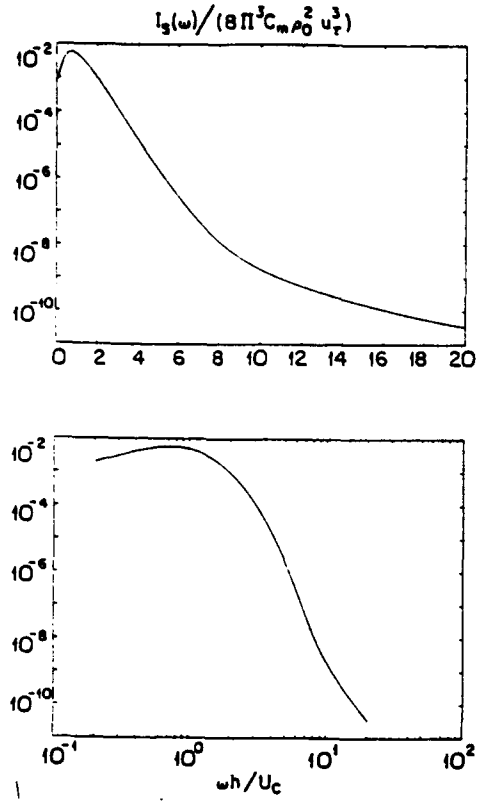

FIG. 8. Frequency dependence of the monopole intensity $I_S(\omega)$ for the stationary turbulent boundary layer model, on log–linear and log–log scales.

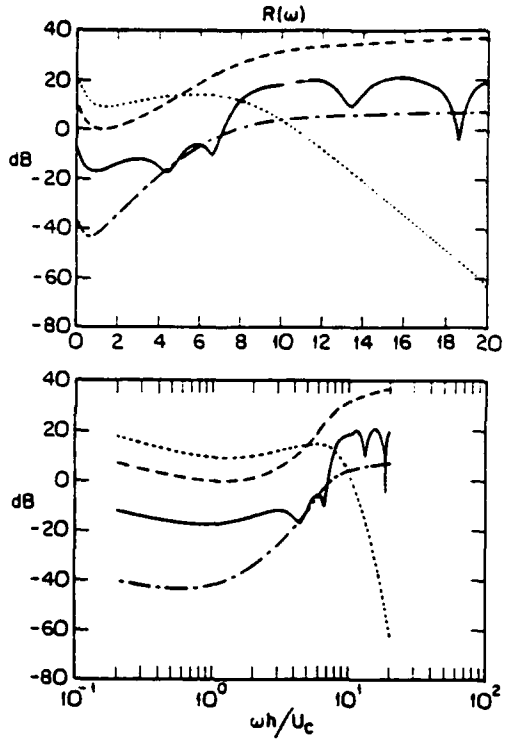

FIG. 9. Sound intensities for the concentrated force model (dotted line), the Duncan model (dashed line), the zero net force model (dashed-dotted line), and the numerical simulation model (solid line). All curves normalized by the sound intensity of the stationary turbulent boundary layer model.

footprint by a factor of 3 would increase the intensity level by close to 10 dB. Results presented in Fig. 4 indicate that pulses significantly larger than the one investigated in this paper exist in the boundary layer. Therefore, it could be expected that the intensity levels associated with these pulses will be comparable or greater than for the Duncan model.

In the range of acoustic frequencies $\omega h/U_c > 10$ the intensity of radiation induced by the zero net force model (51) is about 10 dB greater than the averaged acoustic intensity calculated for a stationary turbulent boundary layer forcing. It is, however, less by over 20 dB than the intensity estimated for a purely positive pressure model of the advected vortex (44) (the Duncan model). Acoustic intensity in the range of frequencies $\omega h/U_c < 5$ is substantially lower (20–40 dB) for this pressure model than for the boundary layer forcing. We may conclude that enforcing the Kraichnan–Phillips condition for the high-amplitude pressure events by surrounding positive peaks by negative pressure regions will result in decreased levels of radiation as compared with the case of strictly positive pressure distributions. Nevertheless, these decreased intensities are still larger in the range of acoustic frequencies than the corresponding intensities induced by the boundary layer forcing.

The most striking feature of these results are consistently higher levels of sound generated in the range of acoustic frequencies $\omega h/U_c > 10$ by the individual pressure pulses than by the boundary layer. This feature is not unexpected. Indeed, the average sound intensity of the burst (75) is calculated by averaging over only the small period of time in which a burst is active. During this time the pressure is much higher than the pressure associated with low-level activity preceding and following the bursting event. Since in the classical statistical description (e.g., Chase[7]) the averaging time covers both bursts and the low-level activity periods, the result of the averaging is necessarily less than in the previous case. In order to recover the classical estimate of radiated sound, we should increase the averaging period T in (75) to the mean time between bursts. According to Karangelen *et al.*,[14] the bursting events with large amplitudes (3–4 p_{rms}) occur about 1%–5% of the recording time. This implies that the ratio (78) plotted in Fig. 9 would be 10 to 20 dB lower if the averaging period T were equal to the time between bursts rather than the duration of a single burst. Such a change would bring the results obtained by both approaches into much closer agreement for frequencies $\omega h/U_c > 10$, indicating that there is no fundamental contradiction between them. However, it must be stressed that that a recorded acoustic signal would reflect the wall pressure evolution exhibiting periods of radiation with intensities substantially greater than could be predicted by the statistical approach.

In the range $\omega h/U_c < 10$, radiation levels generated by bursts may be either lower or higher, depending on the model employed, than statistical estimates. However, in all cases considered, the ratio (78) has a minimum in this range implying a relatively lower content of the low-frequency modes in the radiation induced by the deterministic bursts than by the stationary turbulent boundary layer.

VII. CONCLUSIONS

We have investigated the process of sound generation by a deterministic pressure pulse in a fluid flowing over a compliant coating containing a small inhomogeneity.

To leading order, the void inhomogeneity can be treated as a monopole source, its strength determined by the detailed form of the pressure at the interface between the fluid and the coating. Four different models of the pressure pulse were employed to specify the monopole strength. For three of these models, a concentrated force advected with constant velocity U_c, the pressure field of an advected vortex, and the wall pressure of a turbulent burst, pressure values are strictly positive. In all these three cases, the frequency dependence of the monopole strength exhibits the same generic behavior: a large, almost constant plateau in the range of subconvective frequencies $\omega h / U_c \leqslant 1$, followed by a fairly rapid decrease in the range $1 \leqslant \omega h / U_c$. The remaining model satisfies the Kraichnan–Phillips condition and the associated monopole strength differs from those computed for the other three models only by exhibiting a maximum at a finite, instead of zero, frequency.

The far-field acoustic pressure in the fluid and in the coating due to the inhomogeneity has been calculated. In the interesting case of water flow over a particular rubberlike coating, the sound has dipole character in the fluid, whereas in the coating there is a gradual change from monopole to dipole radiation when the radiation direction changes from the normal to the tangent to the interface. Also, in this case, the coating always captures most of the sound energy scattered by the inhomogeneity.

A comparison was made between the sound generated by a single pressure pulse and the sound generated by the scattering of the statistically stationary turbulent boundary layer pressures by the inhomogeneity. Only those events in the boundary layer that contribute to the convective peak in the wall pressure spectrum were taken into account. For the particular set of the parameters considered in this paper, in the range of high acoustic frequencies, the average intensity of the radiation induced by the individual pressure pulses can exceed the averaged intensity of the sound induced by the turbulent boundary layer by 10–40 dB. It is thus expected that the presence of deterministic pressure pulses in the turbulent boundary layer will result in *bursts of acoustic radiation with the intensities substantially greater than those predicted by the statistical approach.*

ACKNOWLEDGMENTS

The authors would like to thank Dr. S. K. Robinson for providing the numerical wall pressure data employed in this work. This research has been supported by the Office of Naval Research under Contracts No. N00014-88-K-0157 and N00014-91-J-4163. Computer time was provided by the San Diego Supercomputer Center.

[1] M. J. Lighthill, "On Sound Generated Aerodynamically. I. General Theory," Proc. R. Soc. London, Ser. A 211, 564–587 (1952).
[2] M. S. Howe, "Production of Sound by Turbulent Flow over an Embedded Strut," IMA J. Appl. Math. 39, 99–120 (1987).
[3] M. S. Howe, "The Influence of an Elastic Coating on the Diffraction of Flow Noise by an Inhomogeneous Plate," J. Sound Vib. 116, 109–124 (1987).
[4] M. S. Howe, "Diffraction of Flow Noise by a Flexible Seam," J. Sound Vib. 125, 291–304 (1988).
[5] M. S. Howe, "Diffraction Radiation Produced by Turbulent Flow over an Inhomogeneous Compliant Coating," J. Sound Vib. 136, 289–304 (1990).
[6] M. S. Howe, "Scattering by a Surface Inhomogeneity on an Elastic Half-Space, with Application to Fluid-Structure Interaction Noise," Proc. R. Soc. London, Ser. A 429, 203–226 (1990).
[7] D. M. Chase, "The Character of the Turbulent Wall Pressure Spectrum at Subconvective Wavenumbers and a Suggested Comprehensive Model," J. Sound. Vib. 112, 125–147 (1987).
[8] S. J. Kline, W. C. Reynolds, F. A. Shraub, and P. W. Runstadler, "The Structure of Turbulent Boundary Layers," J. Fluid Mech. 30, 741–773 (1967).
[9] W. W. Willmarth, "Structure of Turbulence in Boundary Layers," Adv. Appl. Mech. 15, 159–254 (1975).
[10] B. J. Cantwell, "Organized Motion in Turbulent Flow," Annu. Rev. Fluid Mech. 13, 437–515 (1981).
[11] C. C. Karangelen, "Temporal and Spectral Features of Wall Pressure Fluctuations Beneath a Turbulent Boundary Layer," Ph.D. dissertation, The Catholic University of America, Washington, DC (1991).
[12] V. Wilczynski, "Organized Turbulent Structures and Their Induced Wall Pressure Fluctuations," Ph.D. dissertation, The Catholic University of America, Washington, DC (1992).
[13] A. V. Johansson, J. Y. Her, and J. H. Haritonidis, "On the Generation of High-Amplitude Wall-Pressure Peaks in Turbulent Boundary Layers and Spots," J. Fluid Mech. 175, 119–142 (1987).
[14] C. C. Karangelen, V. Wilczynski, and M. J. Casarella, "Large Amplitude Wall Pressure Events Beneath a Turbulent Boundary Layer," in *Proceedings of the Symposium on Flow Noise, Modeling, Measurement, and Control*, edited by T. M. Farabee, W. L. Keith, and R. M. Lueptow (ASME, Atlanta, GA, 1991).
[15] A. N. Tikhonov and A. A. Samarski, *Equations of Mathematical Physics* (Moscow, 1953).
[16] I. S. Gradshteyn and I. M. Ryzhik, *Table of Integrals, Series, and Products* (Academic, San Diego, 1980).
[17] J. H. Duncan, "The Response of an Incompressible, Viscoelastic Coating to Pressure Fluctuations in a Turbulent Boundary Layer," J. Fluid Mech. 171, 339–363 (1986).
[18] S. K. Robinson, "Kinematics of Turbulent Boundary Layer Structure," Ph.D. dissertation, Stanford University (1990).
[19] P. R. Spalart, "Direct Simulation of a Turbulent Boundary Layer up to $Re_\theta = 1410$," J. Fluid Mech. 187, 61–98 (1988).
[20] R. H. Kraichnan, "Pressure Fluctuations in Turbulent Flow Over a Flat Plate," J. Acoust. Soc. Am. 28, 378–390 (1956).
[21] O. M. Phillips, "On the Aerodynamic Surface Sound from a Plane Turbulent Boundary Layer," Proc. R. Soc. London, Ser. A 234, 327–335 (1956).
[22] M. S. Howe, "A Note on the Kraichnan–Phillips Theorem," J. Fluid Mech. 234, 443–448 (1992).
[23] R. Resnick and D. Halliday, *Physics for Students of Science and Engineering* (Wiley, New York, 1963), Table 20-1.

EARTHQUAKE ENGINEERING AND STRUCTURAL DYNAMICS, VOL. 18, 397-415 (1989)

TRANSIENT SCATTERING OF ELASTIC WAVES BY DIPPING LAYERS OF ARBITRARY SHAPE. PART 1: ANTIPLANE STRAIN MODEL

HOSSEIN ESHRAGHI and MARIJAN DRAVINSKI

Department of Mechanical Engineering, University of Southern California, Los Angeles, California 90089-1453, U.S.A.

SUMMARY

Scattering of elastic waves by two dimensional multilayered dipping sediments of arbitrary shape embedded in an elastic half-space is investigated by using a boundary method. The displacement field is evaluated throughout the elastic media for both steady state and transient incident SH waves. The unknown scattered field is expressed in terms of wave functions which satisfy the equation of motion, traction-free boundary condition and appropriate radiation conditions. The transient response is constructed from the steady state solution by using the fast Fourier transform technique.

The numerical results presented demonstrate that scattering of waves by subsurface irregularities may cause locally very large amplification of surface ground motion. The motion can be affected greatly by the scattered surface waves in the sediments. The results clearly indicate that the surface ground motion depends upon a number of parameters present in the problem, such as frequency and the angle of incidence of the incoming wave, impedance contrast between the layers and location of the observation point.

INTRODUCTION

Damage analysis after large earthquakes often shows that strong ground motion can be highly localized. For example, during the Michoacon, Mexico earthquake of 1985, great damage occurred to the structures atop the alluvium of the Mexico City sedimentary basin while the damage to the buildings atop the base rocks at the outskirts of the basin was considerably smaller.[1] If one takes into account that most of the damage occurred in Mexico City, which is more than 350 km away from the earthquake's epicentre, the role of the site effect in the amplification of strong ground motion appears to be of considerable importance to seismologists and engineers. During the Lima, Peru earthquake of November 9, 1974, ground motion accelerograms recorded at two sites with nearly the same epicentral distance display pronounced dissimilarities.[2] The first site (Instituto Geofisico del Peru) in central Lima, which is located atop weakly horizontally varying subsurface structure, experienced only minor shaking. The second site, atop the La Molina sediment-filled valley, was subjected to severe shaking during the same earthquake. This phenomenon was observed during previous earthquakes as well.[2] Similarly, during the Niigata, Japan earthquake of 1964, severe damage occurred to the buildings within Niigata city located atop the deepest part of a sedimentary basin while the shaking at the rock sites was considerably smaller.[3] From all these examples it is evident that there is a need to explain in detail how the site effects influence the ground motion during an earthquake. In order to explore this subject further, two models for scattering of elastic waves by subsurface irregularities are considered: An antiplane strain model is presented in this paper and a plane strain one in the companion paper.

The site amplification phenomena have been the subject of several theoretical studies in the past.[4-10] Field measurements by Tucker and King[11] and King and Tucker[12] show specific resonance patterns of the ground surface caused by the presence of sediments. Bard and Bouchon[13] studied these resonance effects extensively for simple alluvial valleys. Dravinski[14] and Dravinski and Mossessian[15] extended the analysis to valleys with multiple dipping layers of arbitrary shape. Still, investigation of local amplification of ground motion is confronted with several major difficulties. Some of these are (i) lack of data for detailed modelling and

0098-8847/89/030397-19$09.50

Received 29 April 1988
Revised 16 August 1988

implementation of realistic soil properties and geometry of the actual alluvial valleys. (ii) problems associated with large characteristic length of the sedimentary basins and (iii) experimental verification of the results.

Modelling half-space problems with irregular geometry of the scatterers requires application of various numerical techniques. There are basically two numerical approaches: (i) approximate methods and (ii) exact methods.

A typical representative of the approximate technique is the ray method. This method is based on asymptotic techniques in approximation of the wave field.[16] It has been successfully applied in many seismological studies.[17,18] This technique is suitable for calculation of response at high frequencies. Recently, Moczo *et al.*[19] extended the ray method to include moderate frequencies as well.

The exact numerical techniques such as finite element, finite difference and boundary integral equation (BIE) methods are suitable for calculation of low frequency response. These problems are considered in the present study.

Modelling the scattering of seismic waves by realistic subsurface irregularities using standard numerical methods, finite elements and finite differences appears to be ineffective for geophysical problems. The required discretization of the entire solution domain of the model leads to a vast computational grid for problems with large characteristic length.[20] In addition, finite element and finite difference methods do not completely satisfy the radiation condition at infinity.[21]

Boundary integral equation (BIE) methods formulate the problem in terms of boundary values and possibly internal sources.[22,23] In this approach, the radiation condition at infinity is satisfied exactly. Discretization may be applied to the boundary of the scatterers only. This reduces greatly the number of unknown variables in the discretization procedure. Still, use of the BIE methods may require an unacceptable amount of computation because these methods require evaluation of the corresponding Green functions. Calculation of these functions often requires a large amount of computational effort.[24] Consequently, the BIE methods appear less efficient for transient problems with complex geometry.

In general, the BIE methods are not suitable for analysing inhomogeneous media. On the other hand, the finite element and finite difference methods are very versatile in handling a medium with varying material properties.[20] This prompted development of the so-called hybrid methods. Hybrid methods combine, say, finite elements with the BIE methods. They are good alternatives for reducing the shortcomings of both of these methods. The advantage of such an approach is that it utilizes the versatility of the finite element method for detailed modelling of the near field and the effectiveness of the BIE methods in the far field.[21] Still, these hybrid techniques require evaluation of the Green functions. In order to avoid the use of the Green functions, Shah *et al.*[25] proposed another hybrid method which combines the finite element method with the wave expansion technique. The interior region is modelled by the finite elements and the wave function expansion is used in the exterior unbounded medium.

Most of the papers cited so far dealt with steady state problems. For solution of transient problems using the exact methods there are basically two formulations: (i) direct methods and (ii) indirect methods.

In direct methods, the solution to scattering problems is formulated as a function of space and time. The main difficulty with these methods has been the accumulation of errors with increase of time.[26] Smith[20] used the finite element approach and Boore *et al.*[5] used the finite difference technique to solve the antiplane strain problem directly in the time domain.

For indirect methods, the transient response is obtained from the steady state solution through use of the Fourier or the Laplace transforms. Niwa *et al.*[27] used the Fourier transform technique and the BIE approach for calculation of transient response for completely embedded irregularities subjected to incident P and SV waves. Bard and Bouchon[8,9,13] used the Fourier transform technique to extend the Aki–Larner method to transient analysis of alluvial valleys for antiplane and plane strain models. Still, at the present time the transient solutions for scattering of elastic waves by general three dimensional irregularities have not been fully developed. The main reason for this is the prohibitive amount of computation required for solving the problems of interest in strong ground motion seismology and earthquake engineering. Thus, it is necessary to develop a method which would reduce the required computational effort.

For that reason, another type of the boundary method is investigated in the present paper. The method utilizes the wave function expansion technique. This approach originates in the works of Herrera and

Sabina[28] and Herrera.[29] The method has the advantage of not requiring evaluation of the Green functions. These wave functions in general do not satisfy the traction-free boundary conditions on the surface of the half-space and therefore the boundary conditions must be imposed locally. Sanchez-Sesma *et al.*[30,31] and Moeen-Vaziri[32] used this approach to solve the scattering of SH, P, SV and Rayleigh waves for two dimensional problems. Dravinski *et al.*[33] used a similar wave expansion technique to study the response of an alluvial valley subjected to an incident plane harmonic SH wave.

The purpose of the present study is first to extend this approach to problems involving diffraction of plane SH waves by multiple dipping layers of arbitrary shape embedded within an elastic half-space and to transient results. In the companion paper[34] the antiplane strain model is generalized to the plane strain one to include incident P, SV and Rayleigh waves.

STATEMENT OF THE PROBLEM

The geometry of the problem is depicted by Figure 1. The problem model consists of an elastic half-space with a finite number of elastic dipping layers of arbitrary shape. The layer interfaces are considered to be smooth, with no sharp corners. Throughout the paper the following conventions are understood. Subscript j corresponds to either layer domains D_j ($j = 0, 1, \ldots, R$) or to the interfaces C_j ($j = 1, \ldots, R$). Domain D_0 denotes the half-space layer while C_1 denotes the interface between the half-space and the first layer, etc. Summation over repeated indices is understood. Underlined indices indicate that the summation is being suppressed. Material of the media is assumed to be linearly elastic, homogeneous and isotropic. The half-space is subjected to an incident plane SH wave. Therefore, the two dimensional antiplane strain model is considered in this paper.

For each domain of this model the steady state equation of motion reduces to a single scalar wave equation[35]

$$(\nabla^2 + k_{\underline{j}}^2) w_{\underline{j}}(\mathbf{x}, \omega) = 0, \quad j = 0, 1, \ldots, R \tag{1}$$

$$\nabla^2 = \partial^2/\partial x^2 + \partial^2/\partial y^2, \quad \mathbf{x} = (x, y)$$

where w_j is the only non-zero component of the displacement field of the jth layer acting along the z-axis, $\mathbf{x}$ is a position vector, ω is the circular frequency and k_j denotes the shear wavenumber. The stress field is specified by

$$\sigma_{zxj} = \mu_j \partial w/\partial x \tag{2a}$$

$$\sigma_{yzj} = \mu_j \partial w/\partial y, \quad j = 0, 1, \ldots, R \tag{2b}$$

where μ_j is the shear modulus of the jth layer. The stress-free boundary conditions along the surface of the half-space can be written as

$$\sigma_{yz}(\mathbf{x}, \omega) = 0, \quad y = 0 \tag{3a}$$

Perfect bonding along the layer interfaces requires continuity of displacement and traction fields according to

$$w_{\underline{j}-1}^{+}(\mathbf{x}, \omega) = w_{\underline{j}}^{-}(\mathbf{x}, \omega) \tag{3b}$$

$$\mu_{\underline{j}-1} \partial w_{\underline{j}-1}^{+}(\mathbf{x}, \omega)/\partial n = \mu_{\underline{j}} \partial w_{\underline{j}}^{-}(\mathbf{x}, \omega)/\partial n \quad \mathbf{x} \in C_j, \quad j = 1, \ldots, R \tag{3c}$$

where $\mu_{\underline{j}} \partial w_{\underline{j}}/\partial n$ is a σ_{nzj} component of the stress tensor and $\mathbf{n}_j$ is the outward unit normal on interface C_j. The $+$ and $-$ supercripts denote that the interface is being approached from the outside and the inside, respectively (see Figure 1).

The incident SH wave is assumed to be of the form

$$w^{\text{inc}} = \exp\{-\mathrm{i}(k_0 x \sin\theta_0 - k_0 y \cos\theta_0 - \omega t)\} \tag{4}$$

where θ_0 is the angle of incidence. This completes the statement of the problem. The steady state solution of the problem is considered next.

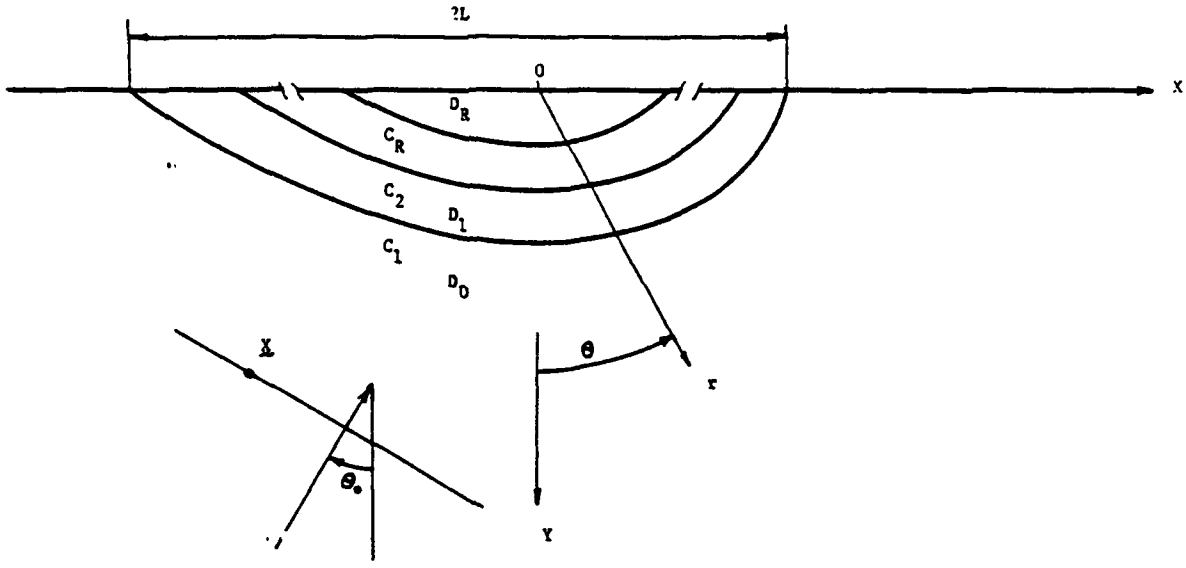

Figure 1. Problem model

STEADY STATE SOLUTION

As the incident wave strikes the interface C_1, it is partially reflected back into the half-space D_0 and partially transmitted into layer D_1. This process continues from one layer to another as the waves propagate throughout the layered media. Consequently, the wave field in the half-space consists of the free field and the scattered field, while the wave field inside each dipping layer consists of the scattered wave field only. The displacement field can be written in the following form:

$$w_0 = w^{ff} + w_0^s, \quad x \in D_0 \tag{5a}$$

$$w_j = w_j^s, \quad x \in D_j, \quad j = 1, \ldots, R \tag{5b}$$

where the superscripts s and ff denote the scattered and the free field, respectively. The scattered wave field in this model can be expressed as a linear combination of the wave functions

$$\begin{aligned} w_0^s = {} & a_{2m} H_{2m}^{(2)}(k_0 r)\cos(2m\theta) \\ & + a_{2m+1} H_{2m+1}^{(2)}(k_0 r)\sin(2m+1)\theta, \quad x \in D_0 \end{aligned} \tag{6a}$$

$$\begin{aligned} w_j^s = {} & b_{2m} H_{2m}^{(2)}(k_j r)\cos(2m\theta) \\ & + c_{2m} H_{2m}^{(1)}(k_j r)\cos(2m\theta) \\ & + b_{2m+1} H_{2m+1}^{(2)}(k_j r)\sin(2m+1)\theta \\ & + c_{2m+1} H_{2m+1}^{(1)}(k_j r)\sin(2m+1)\theta \\ & j = 1, \ldots, R-1, \quad x \in D_j \end{aligned} \tag{6b}$$

$$\begin{aligned} w_R^s = {} & d_{2m} J_{2m}(k_R r)\cos(2m\theta) \\ & + d_{2m+1} J_{2m+1}(k_R r)\sin(2m+1)\theta \\ & x \in D_R, \quad m = 0, 1, 2, \ldots, M \end{aligned} \tag{6c}$$

where r and θ are the polar coordinates defined in Figure 1, a, b, c and d are unknown coefficients, M is the order of approximation, $H_m^{(1)}$ and $H_m^{(2)}$ correspond to Hankel functions of the first and second kind,

respectively, and J_m denotes a Bessel function of the first kind.[36] As indicated earlier, summation over repeated indices is understood. The wave functions in equations (6a–c) are solutions of the equation of motion [equation (1)] and they satisfy the Sommerfeld radiation condition at infinity as well as the traction-free boundary condition along the surface of the half-space. It is interesting to observe that the scattered wave field within the half-space is chosen to consist of the outgoing waves only, while the waves within the dipping layers $D_1 - D_{R-1}$ incorporate both the incoming and outgoing waves. The scattered wave field within the innermost layer D_R consists of the standing waves only.

At this point more about the nature of the wave functions used to formulate the scattered waves should be stated. These functions belong to a class of functions known as the c-complete functions. The theory of these functions has been developed by Herrera and Sabina[28] and Herrera[29] using algebraic theory. The concept of c-completeness allows constructing systems of solutions which are complete with respect to general boundary values independently of the specific region of consideration.[31] Sanchez-Sesma *et al.*[30] used this approach to study diffraction of plane SH waves by subsurface irregularities. Existence and uniqueness of the c-complete functions for other models is still the subject of ongoing research in algebraic theory. Detailed analysis of these theories is beyond the scope of this paper. For further study of this subject the reader is referred to Herrera.[29]

Once the scattered wave field is expressed as a series of the wave functions, it is necessary to determine the unknown expansion coefficients in these series. Substitution of the scattered wave field [equations (6a–c)] into the total displacement field [equations (5a, b)] and then into the continuity conditions [equations (3b, c)] at N_j points along the layer interfaces C_j leads to a system of linear equations of the form

$$\mathbf{Gc} = \mathbf{f} \tag{7}$$

where vector c contains the unknown expansion coefficients, vector f corresponds to the free field displacement and stress fields along the layer interfaces, and matrix G contains the wave functions and their normal derivatives. The size of matrix G is $(S \times K)$, where $S > K$ in order to solve equation (7) in the least-squares sense.[37] Once the expansion coefficients are known, the displacement and stress fields can be evaluated throughout the elastic medium. This concludes the steady state analysis for the displacement field. The corresponding transient problem is considered next.

TRANSIENT SOLUTION

To find a transient response of an elastic medium due to an incident wave signal $f(\mathbf{x}, t)$ this function must be broken into corresponding simple harmonic components by means of the Fourier integral[38]

$$f(\mathbf{x}, t) = 1/(2\pi) \int_{-\infty}^{\infty} F(\mathbf{x}, \omega) e^{i\omega t} \, d\omega \tag{8}$$

where $F(\mathbf{x}, \omega)$ is the temporal Fourier transform of $f(\mathbf{x}, t)$. Function f is assumed to be a casual function. A plane SH wave, propagating in the direction of unit vector $\mathbf{n}$ with phase velocity c can be described by

$$\mathbf{u}^{inc}(\mathbf{x}, t) = \mathbf{u}^0 f[t - \mathbf{n} \cdot (\mathbf{x} - \mathbf{x}_0)/c] \tag{9}$$

where

$$\mathbf{n} \cdot (\mathbf{x} - \mathbf{x}_0) = (x - x_0)\sin\theta_0 - (y - y_0)\cos\theta_0$$

Here, θ_0 is the angle of incidence, $\mathbf{x}_0$ denotes an arbitrary reference point at time $t = 0$ [see Figure (1)], and $\mathbf{u}^0 = (0, 0, 1)$ is a unit vector which represents direction of motion. For plane shear waves $\mathbf{u}^0 \cdot \mathbf{n} = 0$. If the incident wave of the form $\mathbf{u}^0 \exp(i\omega(t - \mathbf{x} \cdot \mathbf{n}/c))$ results in the response of the half-space $\mathbf{u}^0 \chi(\mathbf{x}, \omega) \exp(i\omega t)$, it is easy to show that transient response $\mathbf{u}(\mathbf{x}, t)$ of the half-space due to an arbitrary plane SH wave input $\mathbf{u}^{inc}(\mathbf{x}, t)$, specified by equation (9), is given by

$$\mathbf{u}(\mathbf{x}, t) = 1/(2\pi) \int_{-\infty}^{\infty} \mathbf{U}(\mathbf{x}, \omega) e^{i\omega t} \, d\omega \tag{11}$$

where

$$\mathbf{U}(\mathbf{x}, \omega) = \mathbf{u}^0 \chi(\mathbf{x}, \omega) \exp(i\mathbf{x}_0 \cdot \mathbf{n}\omega / c) F(\omega) \tag{12}$$

The result specified by equation (11) is exactly the inverse Fourier transform of $\mathbf{U}(\mathbf{x}, \omega)$.

An efficient way for numerical calculaton of equation (11) is by means of the fast Fourier transform (FFT). There are several important parameters which are required in this technique, such as sampling time interval Δt, cut-off frequency ω_c and number of samples P. The sampling time interval is determined according to Reference 39 as $\Delta t = 1/(2f_{max})$, where f_{max} corresponds to the maximum frequency. These parameters are mentioned here only for the sake of completeness, since they must be specified for the numerical evaluation of the results, which is considered next.

NUMERICAL RESULTS

Steady state response

To assess the numerical accuracy of the proposed method, a few problems with known solutions are considered next. First, diffraction of a plane harmonic SH wave by a stack of semi-elliptical dipping layers embedded in a half-space is investigated. For one dipping layer the results are compared with those of Wong and Trifunac.[6] For two and three dipping layers the results are compared with those of Dravinski.[14] Before proceeding with a comparison of the results a few conventions regarding the numerical calculations are introduced. All spatial variables are normalized with respect to the half-width of the innermost dipping layer. The shear modulus and shear wave speed for the material of the half-space are assumed to be unity, and a dimensionless frequency Ω is introduced as the ratio of the total width of the outermost dipping layer to the wavelength of the incident wave ($\Omega = 2L/\lambda^{inc}$, see Figure 1).

For one dipping layer subjected to an incident plane SH wave the corresponding results are shown by Figure 2. In this figure the amplitude and the phase of surface displacement are presented for four angles of incidence. These results are in complete agreement with those of Wong and Trifunac.[6]

Surface displacement results for two and three dipping layers displayed by Figures 3–6 are in excellent agreement with those of Dravinski.[14] Excellent agreement between the results of Dravinski[14] and this study is obtained for different frequencies, ratios of the principal axis and angles of incidence as well. For the sake of reducing the number of figures these additional comparisons are omitted in this paper.

At this point it is of interest to elaborate further about some numerical aspects of the solution. It is found that, in solving the steady state problem for low and moderate frequencies, only a few expansion terms [M in equations (6a–c)] and observation points [N_j, defined in the paragraph preceding equation (7)] are needed. Evaluation of these wave functions numerically is very fast. For higher frequencies, say $\Omega > 2$, the required number of expansion terms and observation points needed for convergence of the displacement field increases substantially. This results in a more extensive computation. However, even for high frequencies the evaluation of wave functions is still very fast. What makes the computation expensive is the inversion of relatively large matrices in solving the least-squares problem [see equation (7)]. It was observed that the method converges faster for deeper valleys than for the shallow ones. The following criterion has been used to establish the convergence of the results: as the number of expansion terms and observation points increases the results are accepted as the final ones if the difference between two successive calculations is sufficiently small.

Transient response

This section deals with the transient response of an alluvial valley embedded in an elastic half-space when subjected to an incident plane SH wave. Two types of incident signal are considered: half-sine and Ricker wavelet. The half-sine wavelet is of the form

$$f(t) = \begin{cases} \sin(pt), & 0 < t < T \\ 0, & t > T \end{cases} \tag{13}$$

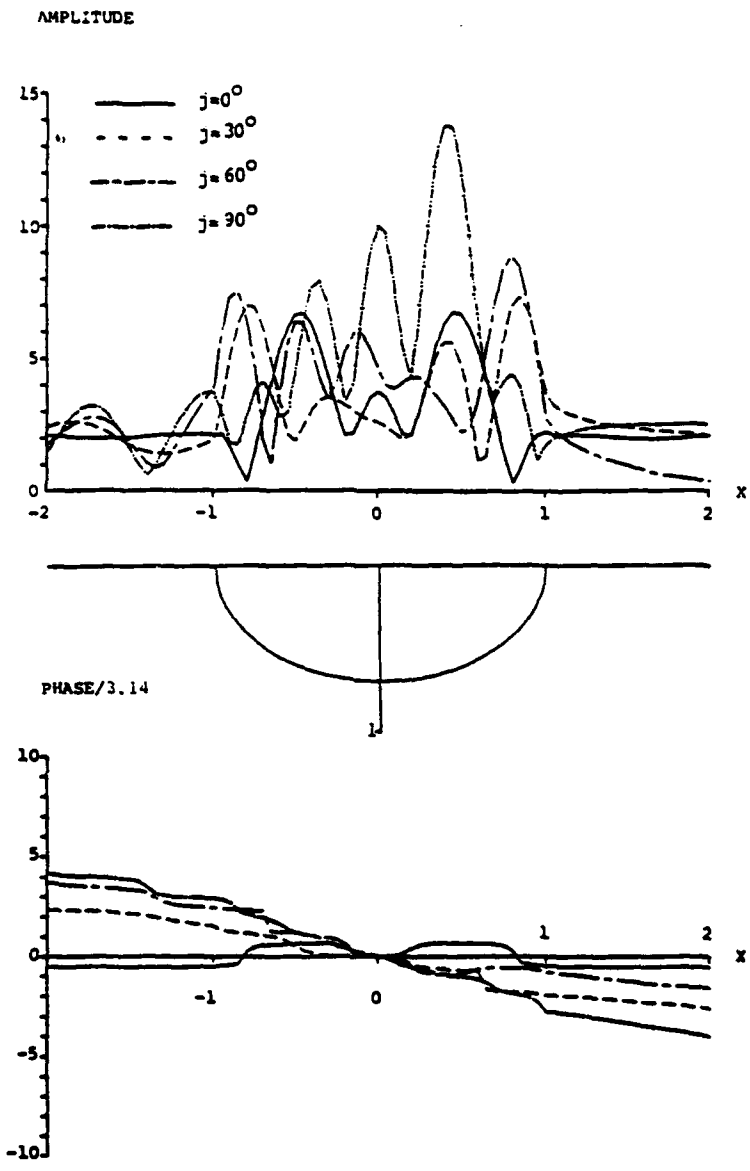

Figure 2. Amplitude and phase of surface displacement spectra for four angles of incidence of a plane harmonic SH wave incident upon a semi-elliptical alluvial valley. Dimensionless frequency $\Omega = 1{\cdot}5$. Unless stated differently, the following parameters are assumed: $\mu_0 = \beta_0 = 1$, $\mu_1 = 0{\cdot}167$, $\beta_1 = 0{\cdot}5$, $A_2/A_1 = 0{\cdot}7$ (ratio of the minor and major axis of the ellipse), $M = 15$, $N = 40$ (M and N correspond to the number of the expansion and nodal points, respectively)

where t corresponds to time, T is the time period of the signal and p is given.

The Ricker wavelet is defined to be the same one used by Bard and Bouchon:[8]

$$f(t) = (\sqrt{\pi}/2)(\alpha - 0{\cdot}5)e^{-\alpha}, \quad \alpha = (\pi(t - t_s)/t_p)^2 \tag{14}$$

where t_s corresponds to the peak amplitude in the time domain and t_p corresponds to angular frequency $\omega_p (= 2\pi/t_p)$ which is associated with the peak amplitude in the Fourier transform domain.

As a test case, a problem previously studied by Bard and Bouchon[8] is reconsidered. The input wave is

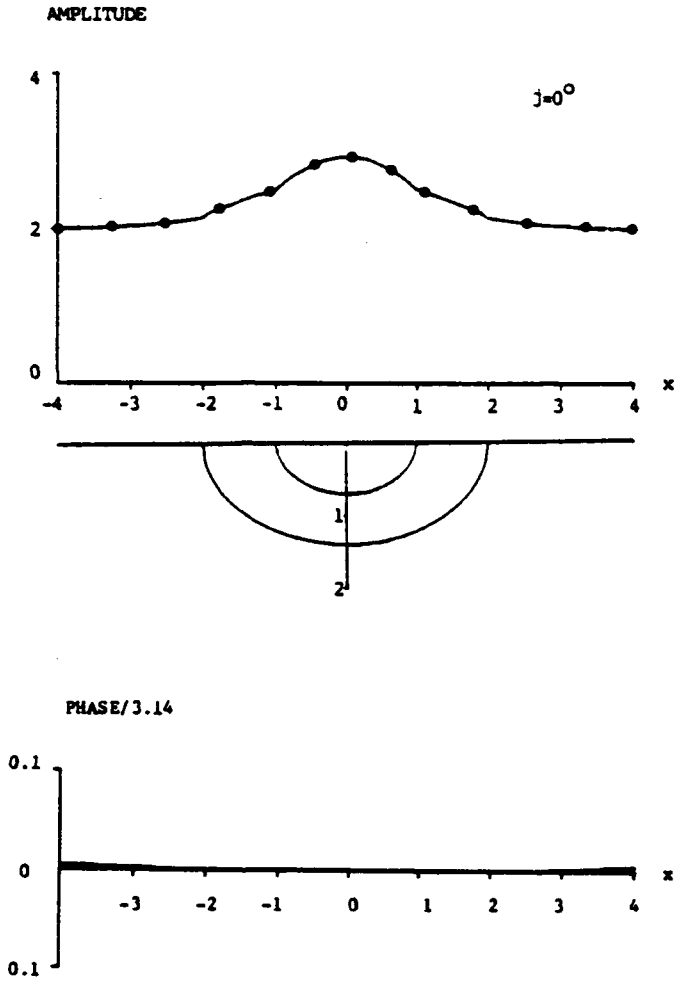

Figure 3. Amplitude and phase of surface displacement spectra for a vertically incident SH wave for two semi-elliptical dipping layers. $\Omega = 0{\cdot}5$, $A_2/A_1 = 0{\cdot}7$ (for both interfaces), $\mu_1 = 0{\cdot}6$, $\beta_1 = 0{\cdot}8$, $\mu_2 = 0{\cdot}3$, $\beta_2 = 0{\cdot}6$, $M = 8$, $N = 17$

assumed to be a vertically propagating SH Ricker wavelet, incident upon an interface defined by

$$C_1: y = \begin{cases} (h/2)(1 + \cos \pi x/D), & -D < x < D \\ 0, & x < -D \text{ or } x > D \end{cases} \tag{15}$$

The results of this comparison are displayed by Figure 7. Apparently, the present results are in good agreement with those of Bard and Bouchon.[8]

For a semi-elliptical dipping layer subjected to an incident SH half-sine wavelet the seismograms along the surface of the alluvial valley are shown for vertical and grazing incidences by Figures 8 and 9, respectively. For a vertically incident wave (Figure 8), the surface displacement field consists of signals associated with direct arrival of the incident wave and disturbances due to scattered surface waves. Three stations on the half-space (A, B and C) indicate clearly the arrival of the undisturbed incident signal at expected times. However, the two stations atop the valley (D and E) display a significant amplification of the incident signal (for $t < 6$). The amplification is mainly due to interference of the scattered field with the incoming incident signal (this phenomenon can be also observed in the steady state response, as indicated by Figure 2). After the passage of

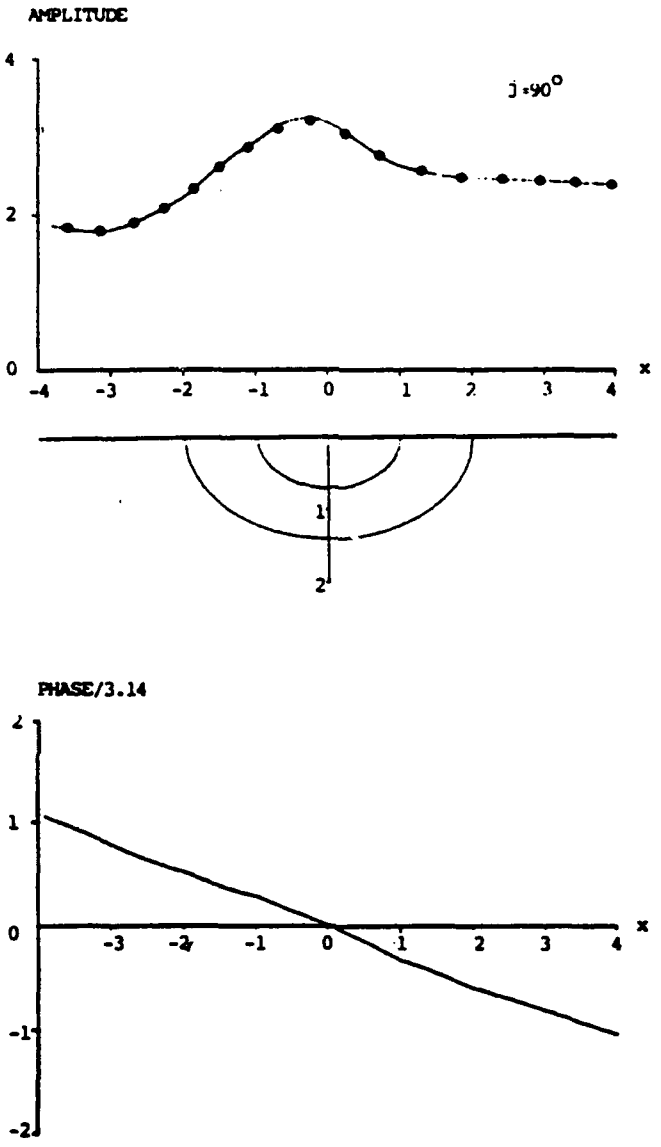

Figure 4. Amplitude and phase of surface displacement spectra for a grazing incident SH wave for two semi-elliptical dipping layers. $\Omega = 0{\cdot}5$, $A_2/A_1 = 0{\cdot}7$ (for both interfaces), $\mu_1 = 0{\cdot}6$, $\beta_1 = 0{\cdot}8$, $\mu_2 = 0{\cdot}3$, $\beta_2 = 0{\cdot}6$, $M = 8$, $N = 17$

the direct incident signal, the wave field atop of the valley consists mainly of the surface waves which are generated by the two edges of the valley. These waves interact constructively (destructively) within the valley. Particularly large amplification can be observed at the centre of the valley at station E (for $t > 6$). After passing each other, the surface waves strike the opposite edges of the valley, regenerating new surface waves which partially reflect back into the valley. The initial and reflected surface waves on the half-space are clearly shown along lines AA and BB of Figure 8. Each one of these lines tracks a particular wave as it moves from one station to another.

An interesting feature in these results is the arrival of the main disturbance prior to the direct arrival of the incident signal. This is clearly evident in the case of grazing angle of incidence (Figure 9). For the seismograph at station C the arrival time of the main disturbance is at time $t = 9{\cdot}3$. This is quite different from the expected

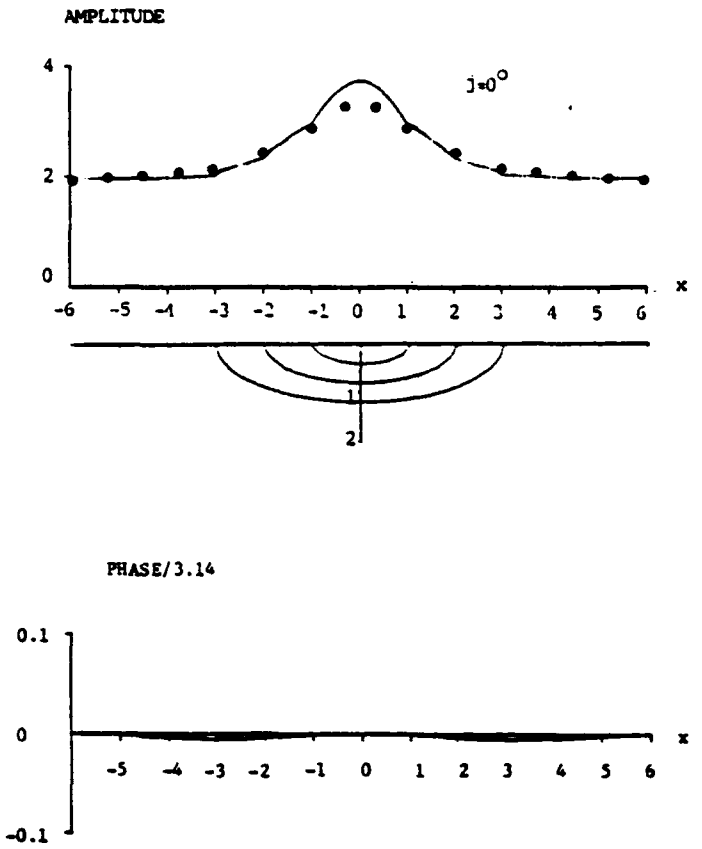

Figure 5. Amplitude and phase of surface displacement spectra for a vertically incident SH wave for three semi-elliptical dipping layers. $\Omega = 0{\cdot}75$, $A_2/A_1 = 0{\cdot}4$ (for all interfaces), $\mu_1 = 0{\cdot}6$, $\beta_1 = 0{\cdot}8$, $\mu_2 = 0{\cdot}3$, $\beta_2 = 0{\cdot}6$, $\mu_3 = 0{\cdot}1$, $\beta_3 = 0{\cdot}4$, $M = 12$, $N = 29$

time $t = 13$, which corresponds to the direct arrival of the incident signal. However, considering that the wave travelling beneath the valley is scattered by the bedrock, the arrival time $t = 9{\cdot}3$ at station C seems quite reasonable (the minimum arrival time for the same station for a homogeneous half-space is $t = 9$). The arrival of the incident signal along the surface of the half-space (indicated by a dashed line in seismograph C) can be seen clearly at about $t = 13$.

For the two dipping layer model corresponding surface displacement results are depicted by Figures 10 and 11 (to reduce the number of figures only vertical and grazing angles of incidence are considered). For a vertically incident wave, for most of the stations away from the centre of the valley, the surface response is basically caused by direct arrival of the incident signal, and not much of the lateral propagation of the surface waves can be observed. However, at the centre of the valley, the scattered surface waves play a much more important role. The amplification of scattered surface waves at the centre of the valley for a vertically incident wavelet was also observed in the simpler one dipping layer model (Figure 8). In particular, for grazing incidence (Figure 11), the lateral propagation of surface waves is much more significant. This is due to direct transformation of the obliquely incident SH wave into Love waves. This effect was also observed by Bard and Bouchon.[8]

For the three dipping layer model and vertical (grazing) incidence the results are shown by Figure 12 (Figure 13). Both figures demonstrate clearly generation and propagation of the surface waves as observed along lines AA. The slopes of these lines give the average phase velocity of these surface waves. This velocity is about 1 in both cases, suggesting propagation of surface waves of the same nature, independent of the angle

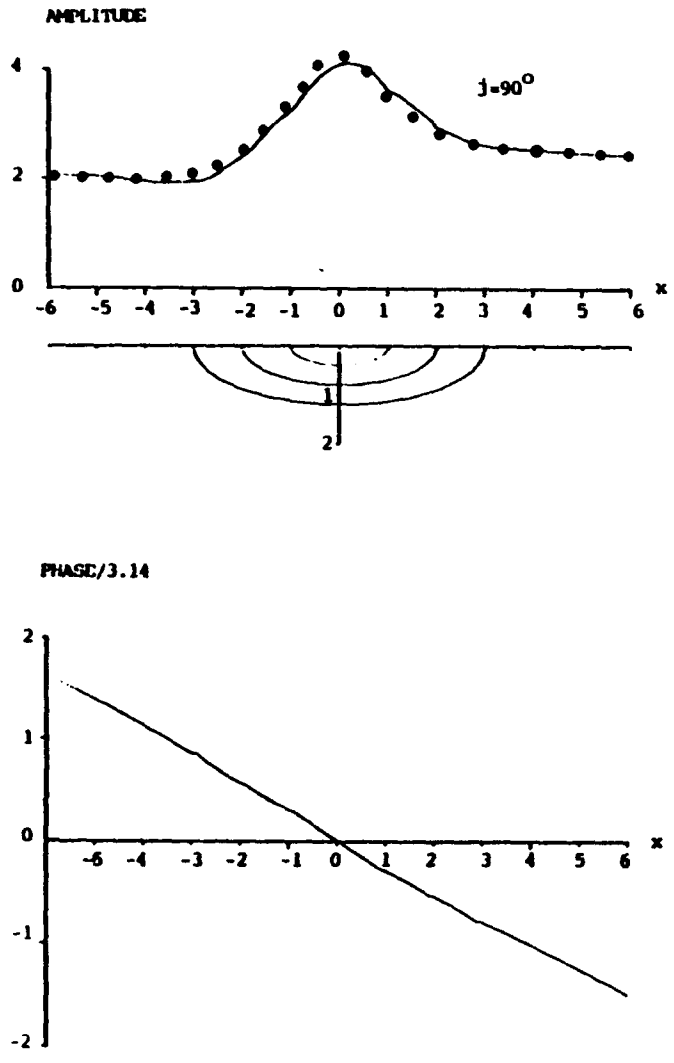

Figure 6. Amplitude and phase of surface displacement spectra for a grazing incident SH wave for three semi-elliptical dipping layers. $\Omega = 0{\cdot}75$, $A_2/A_1 = 0{\cdot}4$ (for all interfaces), $\mu_1 = 0{\cdot}6$, $\beta_1 = 0{\cdot}8$, $\mu_2 = 0{\cdot}3$, $\beta_2 = 0{\cdot}6$, $\mu_3 = 0{\cdot}1$, $\beta_3 = 0{\cdot}4$, $M = 12$, $N = 29$

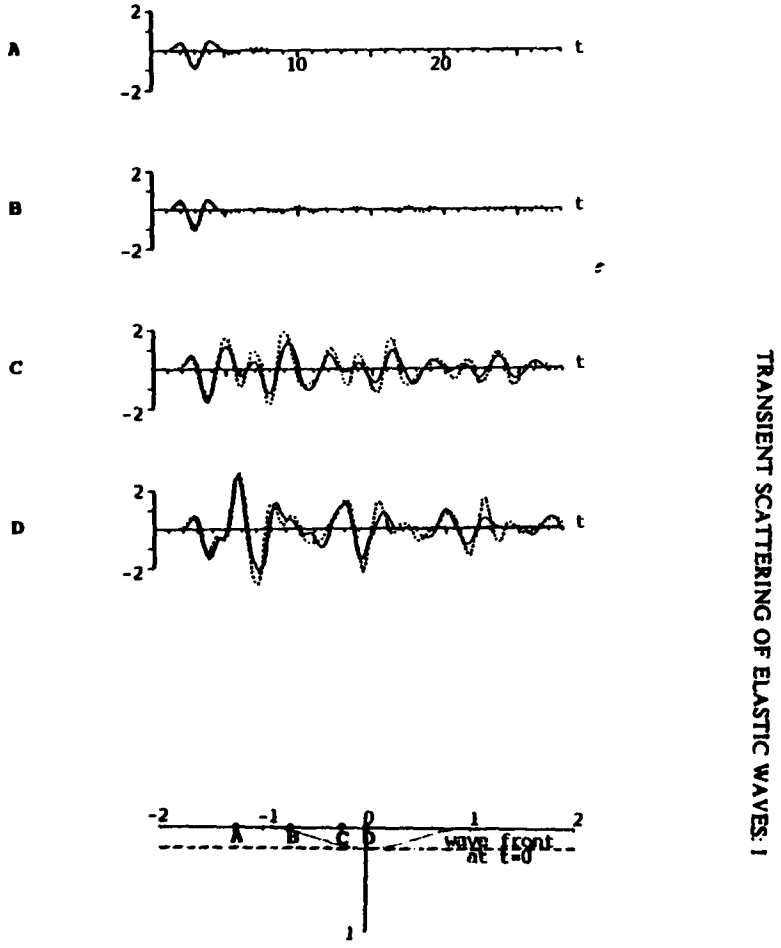

Figure 7. Transient surface response of a cosine type valley (with half-width of 1 and maximum depth of 0·2) to a vertically incident SH Ricker wavelet of characteristic period $t_p = 2{\cdot}562$ ($t_s = 2{\cdot}8$). Stations A to D are located at $x = -1{\cdot}24$, $-0{\cdot}72$, $-0{\cdot}24$ and 0. $\mu_0 = \beta_0 = 1{\cdot}0$, $\mu_1 = 0{\cdot}02424$, $\beta_1 = 0{\cdot}2$. The parameters used in the fast Fourier transform (FFT) are: $P = 256$ (number of samples) $\Delta t = 0{\cdot}2$ (sampling time intervals) and $\omega_c = 7{\cdot}85$ (cut off frequency). Solid lines correspond to the result of this investigation while dots correspond to results of Figure 7 of Bard and Bouchon.[6] The geometry of the problem, location of seismographs and wave front at time equal to zero (dashed line) are shown at the bottom of the figure

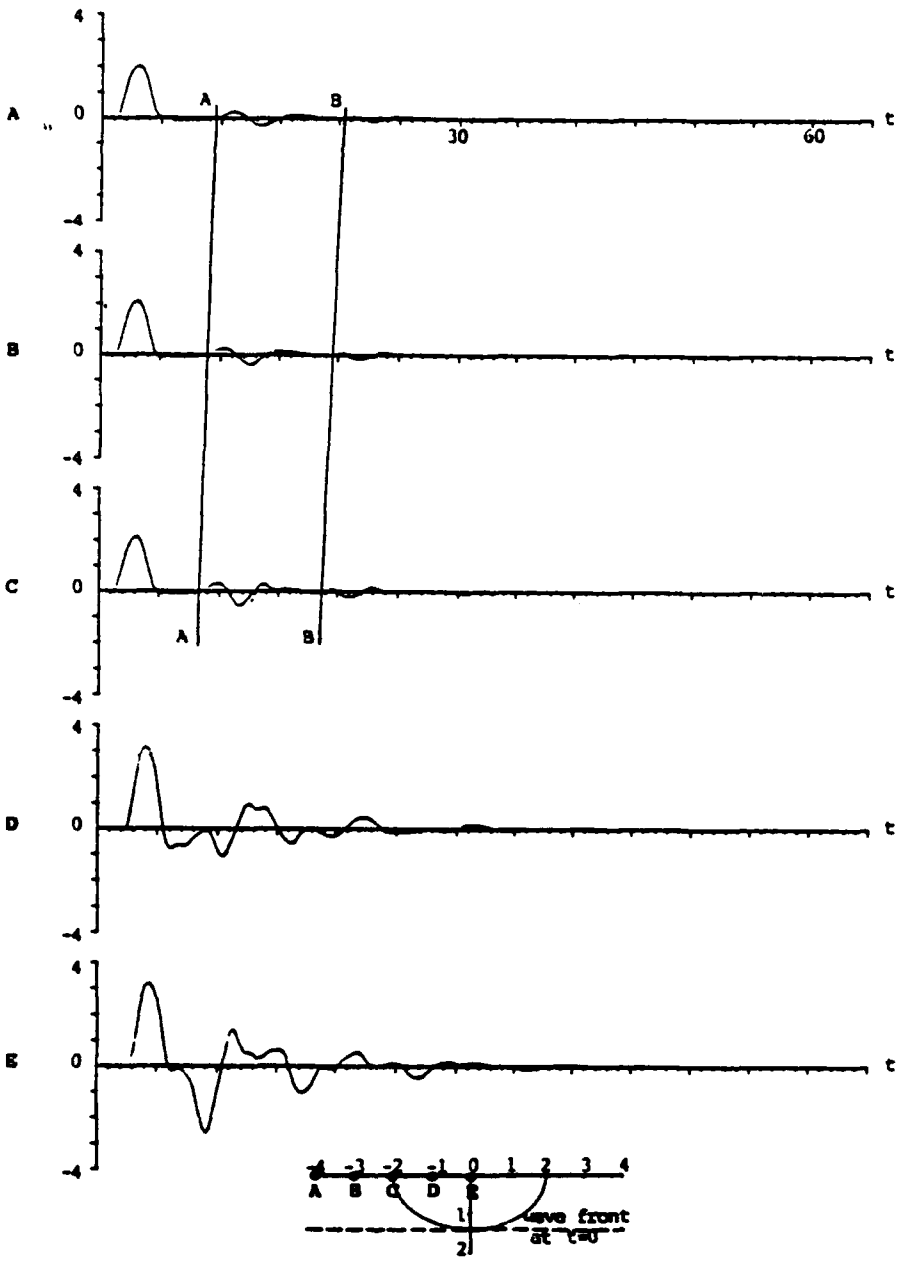

Figure 8. Transient surface response of a semi-elliptical dipping layer to a vertically incident SH half-sine wavelet with a time period of 3·14. Stations A to E are located at $x = -4, -3, -2, -1$ and 0. $A_2/A_1 = 0{\cdot}7$, $\mu_1 = 0{\cdot}167$, $\beta_1 = 0{\cdot}5$, $P = 256$, $\Delta t = 0{\cdot}25$, $\omega_e = 4{\cdot}673$

of incidence. For grazing incidence (Figure 13), the scattered waves (by the bedrock) reach station G at time $t = 16$ prior to the arrival of the direct incident signal which can be detected by a sudden change in the slope of the seismograph at $t = 23{\cdot}3$ (indicated by a dashed line). The minimum arrival time for the same station for a homogeneous half-space is $t = 13{\cdot}6$. Very likely, owing to the much more complex pattern of the scattered waves, the arrival of the incident signal is less clearly displayed here than in the simpler model of a one dipping layer (Figure 9). As expected, for vertical incidence the main disturbance is basically due to the arrival of the direct incident signal (Figure 12).

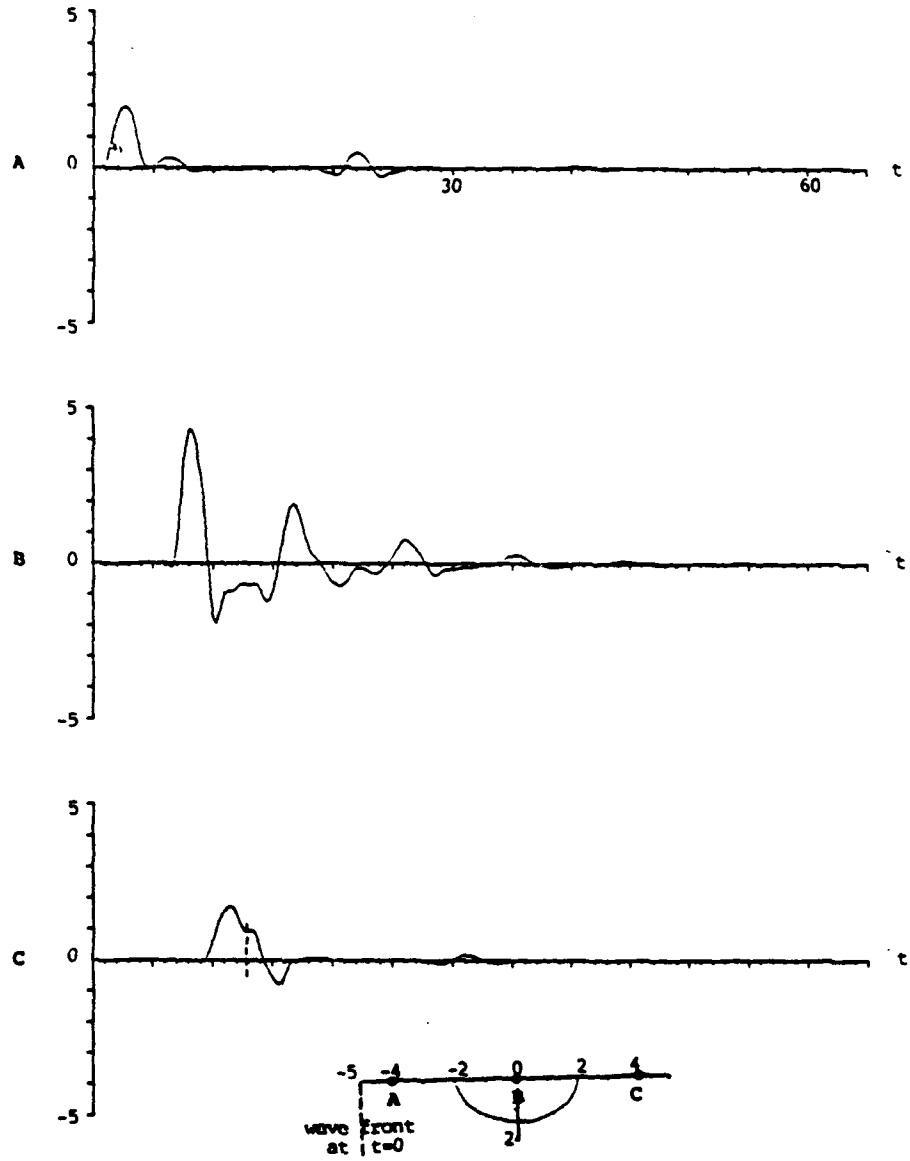

Figure 9. Transient surface response of a semi-elliptical dipping layer to a grazing incident *SH* half-sine wavelet with a time period of 3·14. Stations A to C are located at $x = -4$, 0 and 4. $A_2/A_1 = 0{\cdot}7$, $\mu_1 = 0{\cdot}167$, $\beta_1 = 0{\cdot}5$, $P = 256$, $\Delta t = 0{\cdot}25$, $\omega_c = 4{\cdot}673$

The geometric complexity of multilayer models precludes more detailed examination of the corresponding transient responses. Nevertheless, the results presented offer sufficient information for reaching a basic understanding of the scattering phenomenon by alluviums subjected to incident SH waves. Apparently, amplification of surface ground motion is very sensitive to the presence of subsurface irregularities, the nature of the incident wave, impedance contrast between the layers and the location of the observation station. In addition, surface waves generated by the edges of the layer play a particularly important role in the resulting motion atop the deeper parts of the sediments.

This concludes the transient analysis of the antiplane strain problem.

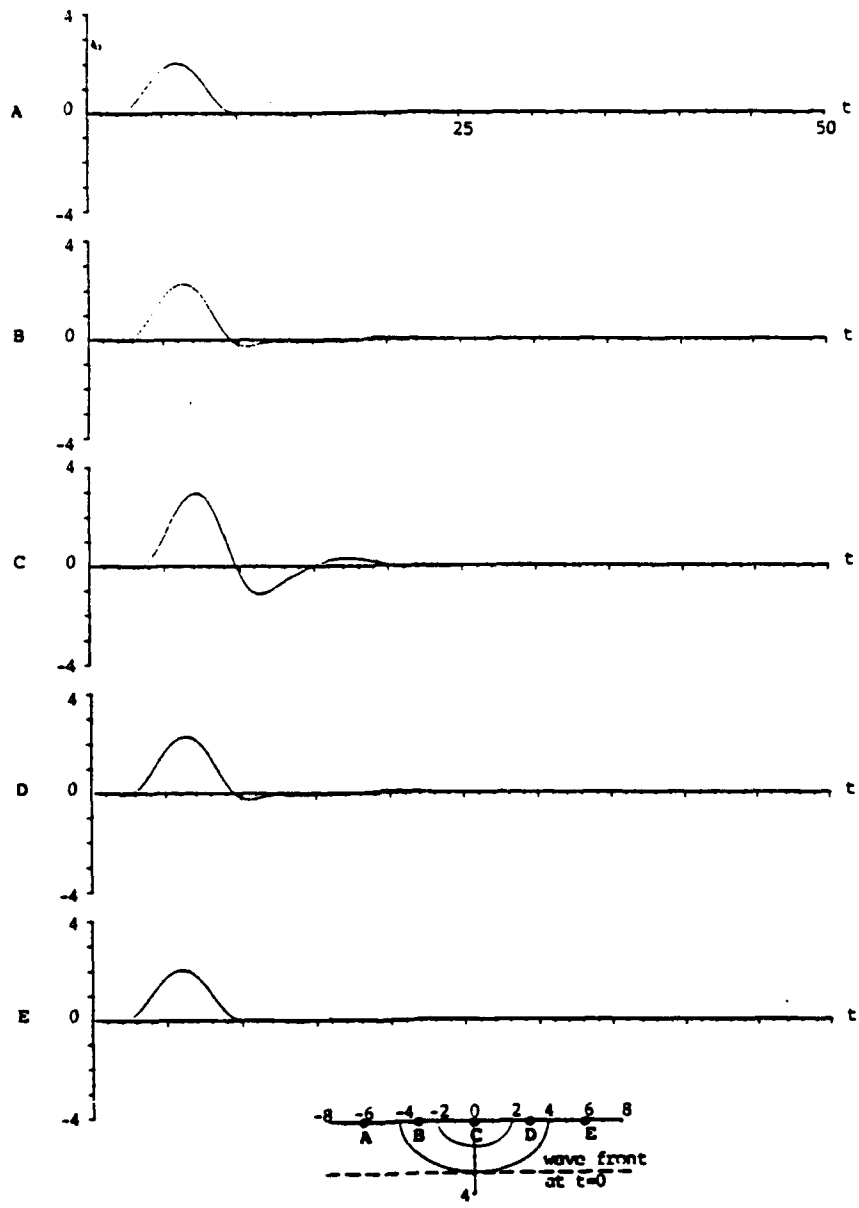

Figure 10. Transient surface response of two semi-elliptical dipping layers ($A_2/A_1 = 0{\cdot}7$) to a vertically incident SH half-sine wavelet with a time period of 6·28. Stations A to E are located at $x = -6, -3, 0, 3$ and 6. $\mu_1 = 0{\cdot}6$, $\beta_1 = 0{\cdot}8$, $\mu_2 = 0{\cdot}3$, $\beta_2 = 0{\cdot}6$, $P = 256$, $\Delta t = 0{\cdot}25$, $\omega_c = 1{\cdot}940$

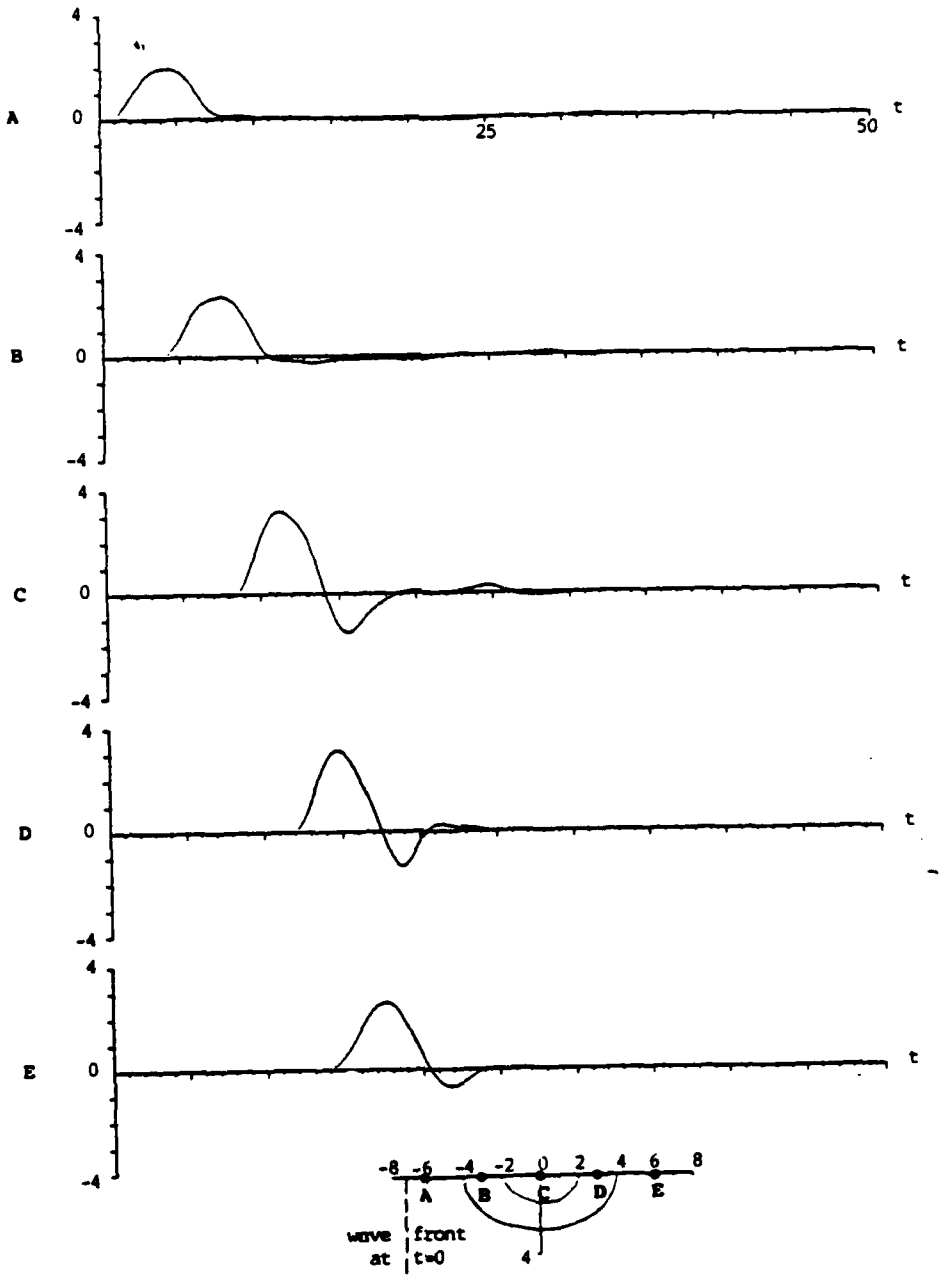

Figure 11. Transient surface response of two semi-elliptical dipping layers to a grazing incident SH half-sine wavelet with a time period of 6·28. Stations A to E are located at $x = -6, -3, 0, 3$ and 6. $A_2/A_1 = 0{\cdot}7$, $\mu_1 = 0{\cdot}6$, $\beta_1 = 0{\cdot}8$, $\mu_2 = 0{\cdot}3$, $\beta_2 = 0{\cdot}6$, $P = 256$, $\Delta t = 0{\cdot}25$, $\omega_c = 2{\cdot}337$

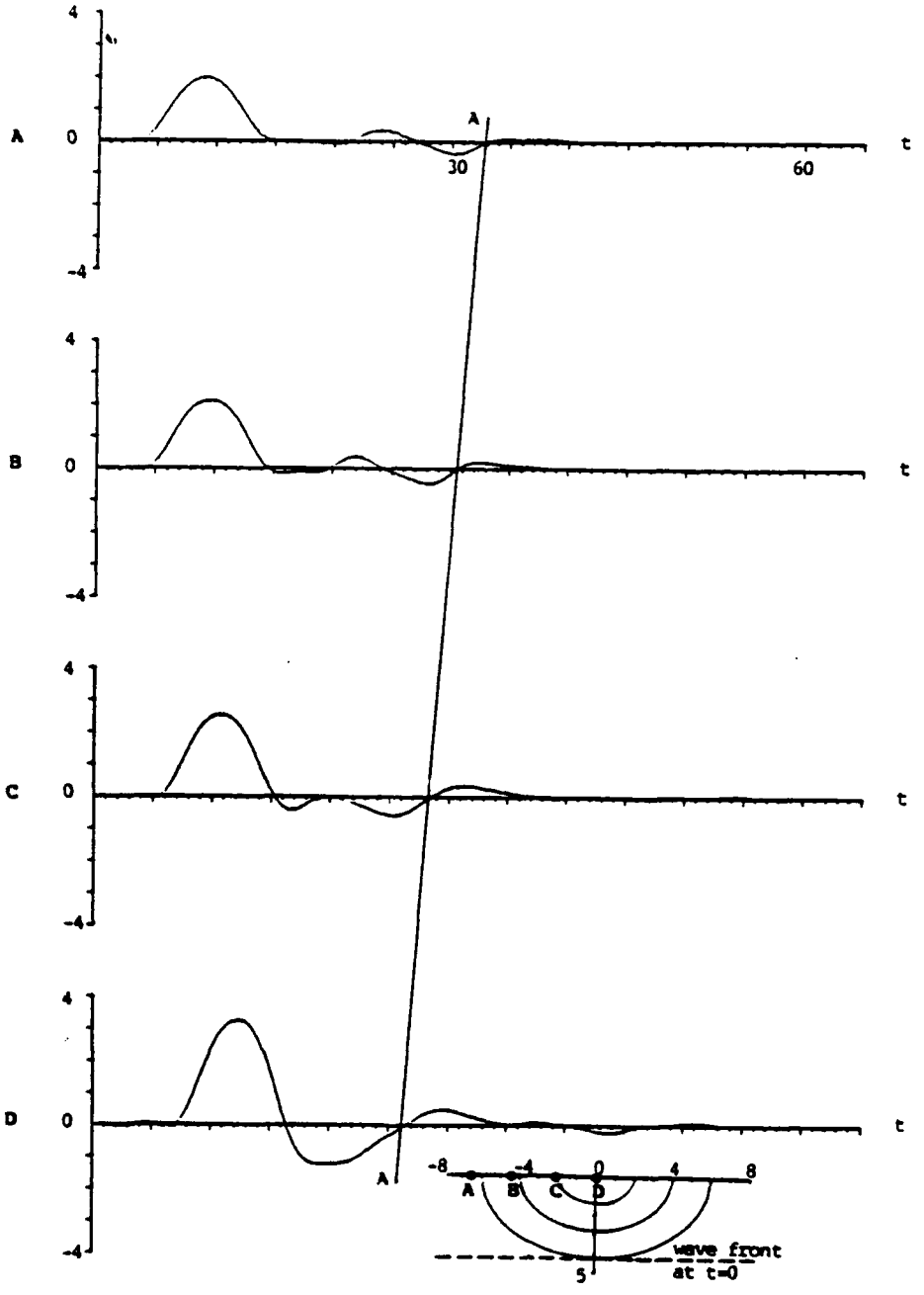

Figure 12. Transient surface response of three semi-elliptical dipping layers ($A_2/A_1 = 0{\cdot}7$) to a vertically incident SH half-sine wavelet with a time period of 9·42. Stations A to D are located at $x = -6{\cdot}6, -4{\cdot}4, -2{\cdot}2$ and 0. $\mu_1 = 0{\cdot}6$, $\beta_1 = 0{\cdot}8$, $\mu_2 = 0{\cdot}4$, $\beta_2 = 0{\cdot}6$, $\mu_3 = 0{\cdot}2$, $\beta_3 = 0{\cdot}4$, $P = 256$, $\Delta t = 0{\cdot}25$, $\omega_c = 1{\cdot}427$

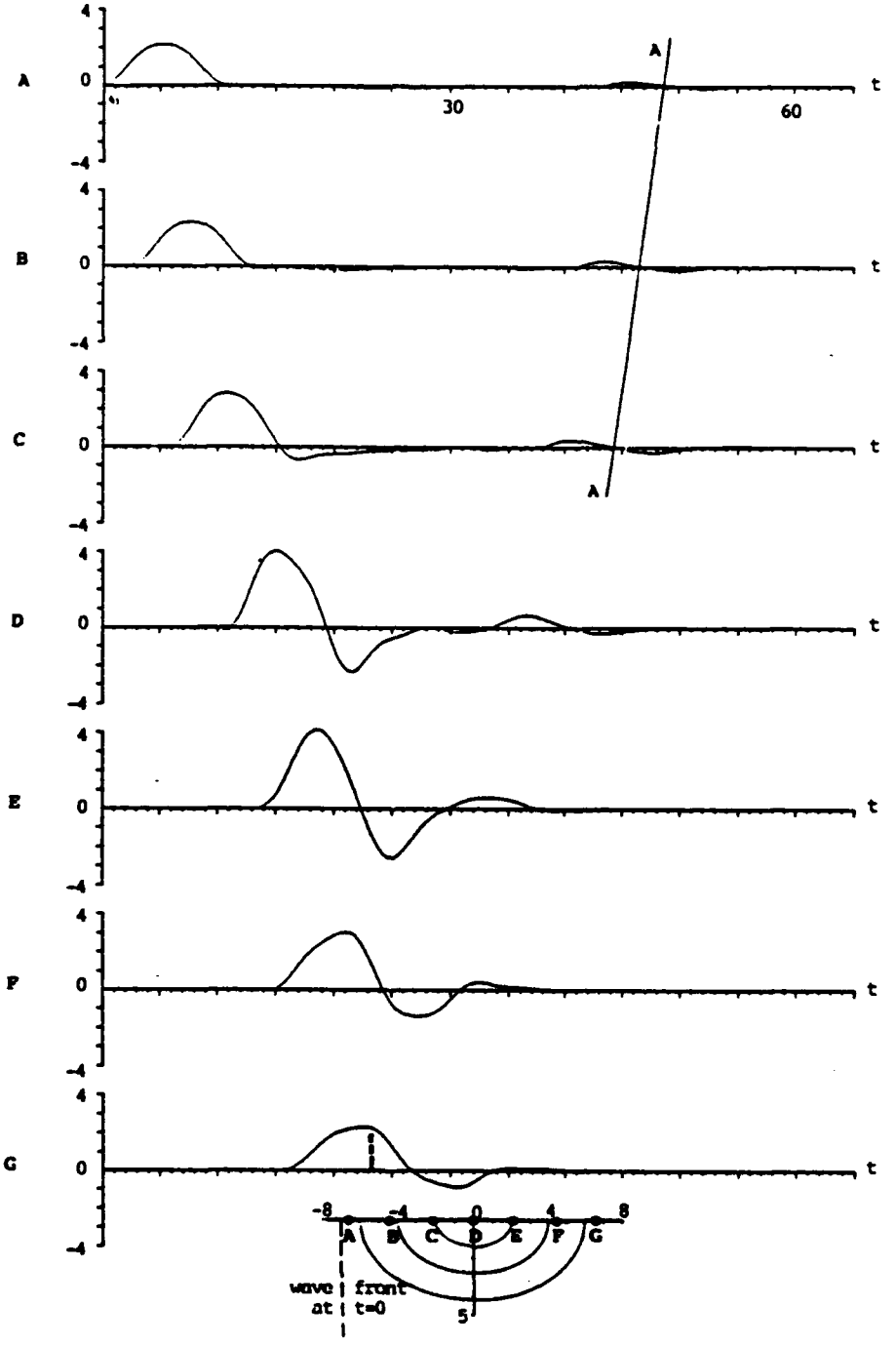

Figure 13. Transient surface response of three semi-elliptical dipping layers to a grazing incident SH half-sine wavelet with a time period of 9·42. Stations A to G are located at $x = -6{\cdot}6, -4{\cdot}4, -2{\cdot}2, 0, 2{\cdot}2, 4{\cdot}4$ and $6{\cdot}6$. $A_2/A_1 = 0{\cdot}7$, $\mu_1 = 0{\cdot}6$, $\beta_1 = 0{\cdot}8$, $\mu_2 = 0{\cdot}4$, $\beta_2 = 0{\cdot}6$, $\mu_3 = 0{\cdot}2$, $\beta_3 = 0{\cdot}4$, $P = 256$, $\Delta t = 0{\cdot}25$, $\omega_c = 1{\cdot}558$

CONCLUSIONS

Amplification of incident plane SH waves by two dimensional dipping layers of arbitrary shape is investigated by using a boundary method. Both harmonic and transient incident wave fields are considered.

The steady state response for various types of valley is obtained by using a wave function expansion technique. The continuity conditions are imposed at a number of points along the interfaces. Transient response is constructed from the steady state solution by using the fast Fourier transform technique. The results presented indicate that the presence of sediments may change substantially the local amplification of the strong ground motion. This amplification is very sensitive to the nature of incident wave, type of subsurface irregularity and the location of the observation station at the surface of the alluvium. It is shown that surface waves generated by the edges of the layers play a very important role in the resulting displacement patterns atop the deeper parts of the sediments.

ACKNOWLEDGEMENT

This material is based upon work supported in part by the National Science Foundation under Grant No. 53-4519-3792 and in part by the Office of Naval Research under Contract No. N00014-88-K-0157.

REFERENCES

1. J. G. Anderson, P. Bodin, J. N. Brune, J. Prince, S. K. Singh, R. Quaas and M. Onate, 'Strong ground motion from the Michoacan, Mexico, earthquake', *Science* 233, 1043–1049 (1986).
2. J. Zahradnik and F. Hron, 'Seismic ground motion of sedimentary valleys—Example La Molina, Lima, Peru', *J. geophys.* 62, 31–37 (1987).
3. H. Kagami, C. M. Duke, G. C. Liang and Y. Ohata, 'Observation of 1 to 5 second microtremors and their application to earthquake engineering. Part II. Evaluation of site effect upon seismic wave amplification due to extremely deep soil deposits', *Bull. seism. soc. Am.* 72, 987–998 (1982).
4. K. Aki and L. Larner, 'Surface motion of a layered medium having irregular interface due to incident plane SH waves', *J. geophys. res.* 75, 933–954 (1970).
5. D. M. Boore, K. L. Larner and K. Aki, 'Comparison of two independent methods for the solution of wave-scattering problems: Response of a sedimentary basin to vertically incident SH waves', *J. geophys. res.* 76, 558–569 (1971).
6. H. L. Wong and M. D. Trifunac, 'Surface motion of a semielliptical alluvial valley for incident plane SH waves', *Bull. seism. soc. Am.* 64, 1389–1408 (1974).
7. F. J. Sanchez-Sesma and J. A. Esquivel, 'Ground motion on alluvial valleys under incident plane SH waves', *Bull. seism. soc. Am.* 69, (1979).
8. P.-Y. Bard and M. Bouchon, 'The seismic response of sediment-filled valleys. Part 1. The case of incident SH waves', *Bull. seism. soc. Am.* 70, 1263–1286 (1980).
9. P.-Y. Bard and M. Bouchon, 'The seismic response of sediment-filled valleys. Part 2. The case of incident P and SV waves', *Bull. seism. soc. Am.* 70, 1921–1941 (1980).
10. H. L. Wong, 'Diffraction of P, SV, and Rayleigh waves by surface topographies', *Bull. seism. soc. Am.* 72, 1167–1184 (1982).
11. B. E. Tucker and J. L. King, 'Dependence of sediment-filled valley response on the input amplitude and the valley properties', *Bull. seism. soc. Am.* 74, 153–165 (1984).
12. J. L. King and B. E. Tucker, 'Observed variations of earthquake motion across a sediment-filled valley', *Bull. seism. soc. Am.* 74, 137–151 (1984).
13. P.-Y. Bard and M. Bouchon, 'The two-dimensional resonance of sediment-filled valleys', *Bull. seism. soc. Am.* 75, 519–541 (1985).
14. M. Dravinski, 'Scattering of plane harmonic SH wave by dipping layers of arbitrary shape', *Bull. seism. soc. Am.* 73, 1303–1319 (1983).
15. M. Dravinski and T. K. Mossessian, 'Scattering of plane harmonic P, SV, and Rayleigh waves by dipping layers of arbitrary shape', *Bull. seism. soc. Am.* 77, 212–235 (1987).
16. V. Cerveny and R. Ravindra, *Theory of Seismic Head Waves*, University of Toronto Press, Toronto, 1971.
17. T. L. Hong and D. V. Helmberger, 'Glorified optics and wave propagation in nonplanar structure', *Bull. Seism. soc. Am.* 68, 1313–1330 (1978).
18. J. J. Lee and C. A. Langston, 'Wave propagation in a three dimensional circular basin', *Bull. seism. soc. Am.* 73, 1637–1653 (1983).
19. P. Moczo, P.-Y. Bard and I. Psencik, 'Seismic response of two dimensional absorbing structures by the ray method', *J. geophys.* 62, 38–49 (1987).
20. W. D. Smith, 'The application of finite element analysis to body wave propagation problems', *Geophys. j. Roy. astr. soc.* 42, 747–768 (1975).
21. T. K. Mossessian and M. Dravinski, 'Application of a hybrid method for scattering of P, SV and Rayleigh waves by near surface irregularities', *Bull. seism. soc. Am.* 77, 1784–1803 (1987).
22. D. M. Cole, D. D. Kosloff and J. B. Minster, 'A numerical boundary integral equation method for elastodynamics', *Bull. seism. soc. Am.* 68, 1331–1357 (1978).
23. Y. Niwa, T. Fukui, S. Kato and K. Fujiki, 'An application of the integral equation method to two dimensional elastodynamics', *Theor. appl. mech. (Tokyo)*, 28, 281–290 (1980).

24. M. Dravinski and T. K. Mossessian, 'An evaluation of the Green functions for harmonic line loads in an elastic half-space', *Int. j. numer. methods. eng.*, **26**, 823–841 (1988).
25. A. H. Shah, K. C. Wong and S. K. Datta, 'Diffraction of plane SH waves in a half-space', *Earthquake eng. struct. dyn.* **10**, 519–528 (1982).
26. F. J. Rizzo, D. J. Shippy and M. Rezayat, 'A BIE method for radiation and scattering of elastic waves in three dimensions', *Int. j. numer. methods eng.* **21**, 115–129 (1985).
27. Y. Niwa, S. Horose and M. Kitahara, 'Application of the boundary integral equation (BIE) method to transient response analysis of inclusions in a half-space', *Wave motion*, **8**, 77–91 (1986).
28. I. Herrera and F. J. Sabina, 'Connectivity as an alternative to boundary integral equations: Construction of bases', *Proc. natl. acad. sci. U.S.A.*, **75**, 2059–2063 (1978).
29. I. Herrera, 'Boundary methods: A criterion for completeness', *Proc. natl. acad. sci. U.S.A.* **77**, 4395–4398 (1980).
30. F. J. Sanchez-Sesma, I. Herrera and J. Aviles, 'A boundary method for elastic wave diffraction: Application to scattering of SH waves by surface irregularities', *Bull. seism. soc. Am.* **72**, 473–490 (1982).
31. F. J. Sanchez-Sesma, M. A. Bravo and I. Herrera, 'Surface motion of topographical irregularities for incident P, SV, and Rayleigh waves', *Bull. seism. soc. Am.* **75**, 263–269 (1985).
32. N. Moeen-Vaziri, 'Investigation of scattering and diffraction of plane seismic waves through two dimensional inhomogeneities', *Ph.D. Thesis*, Department of Civil Engineering, University of Southern California, Los Angeles, 1984.
33. M. Dravinski, H. Eshraghi and F. J. Sabina, 'Scattering of SH waves by an alluvial valley of arbitrary shape: A boundary integral approach', *Proc. 3rd U.S. natl. conf. earthquake eng.* (1986).
34. H. Eshraghi and M. Dravinski, 'Transient scattering of elastic waves by dipping layers of arbitrary shape. Part 2. Plane strain model', *Earthquake eng. struct. dyn.*, **18**, 417–434 (1989).
35. K. Aki and P. G. Richards, *Quantitative Seismology, Theory and Methods*, Vol. 1, W. H. Freeman, San Francisco, 1980.
36. M. Abramowitz and I. A. Stegun, *Handbook of Mathematical Functions*, Dover, New York, 1972.
37. C. L. Lawson and R. J. Hanson, *Solving Least Squares Problems*, Prentice-Hall, Englewood Cliffs, N.J., 1974.
38. Y.-H. Pao and C. C. Mow, *Diffraction of Elastic Waves and Dynamic Stress Concentrations*, New York, Crane, Russak, 1973.
39. E. O. Brigham, *The Fast Fourier Transform*, Prentice-Hall, Englewood Cliffs, N.J., 1974.

EARTHQUAKE ENGINEERING AND STRUCTURAL DYNAMICS, VOL. 18, 417-434 (1989)

TRANSIENT SCATTERING OF ELASTIC WAVES BY DIPPING LAYERS OF ARBITRARY SHAPE. PART 2: PLANE STRAIN MODEL

HOSSEIN ESHRAGHI AND MARIJAN DRAVINSKI

Department of Mechanical Engineering, University of Southern California, Los Angeles, California 90089-1453, U.S.A.

SUMMARY

Scattering of elastic waves by dipping layers of arbitrary shape embedded within an elastic half-space is investigated for a plane strain model by using a boundary method. Unknown scattered waves are expressed in the frequency domain in terms of wave functions which satisfy the equations of motion and appropriate radiation conditions at infinity. The steady state displacement field is evaluated throughout the elastic medium for different incident waves so that the continuity conditions along the interfaces between the layers and the traction-free conditions along the surface of the half-space are satisfied in the least-squares sense. Transient response is constructed from the steady state one through the Fourier synthesis.

The results presented show that scattering of waves by dipping layers may cause locally very large amplification of surface ground motion. This amplification depends upon the type and frequency of the incident wave, impedance contrast between the layers, component of displacement which is being observed, location of the observation station and the geometry of the subsurface irregularity. These results are in agreement with recent experimental observations.

INTRODUCTION

This paper is an extension of the study by Eshraghi and Dravinski[1] in which scattering of plane SH waves by dipping layers of arbitrary shape was considered. The present paper extends the analysis to the plane strain model of the problem. A detailed literature review of the problem can be found in the companion paper by Eshraghi and Dravinski[1] and it will not be repeated here.

As discussed in the paper dealing with the antiplane strain model,[1] calculation of strong ground motion due to subsurface irregularities may require a great amount of computation time. Consequently, this paper considers a method which appears to be computationally very effective in comparison to the standard numerical techniques such as finite elements and finite difference. In this method, the unknown scattered wave field is expressed in terms of the wave functions which satisfy the equations of motion and appropriate radiation conditions at infinity. However, these functions do not satisfy the stress-free boundary conditions along the surface of the half-space. This idea originates in works of Herrera and Sabina[2] and Herrera[3] and it has been successfully applied to problems of scattering of elastic waves by Sanchez-Sesma *et al.*[4,5] and Dravinski *et al.*[6]

STATEMENT OF THE PROBLEM

The geometry of the problem is depicted by Figure 1 of the paper by Eshraghi and Dravinski[1]. The problem model consists of an elastic half-space with a finite number of elastic dipping layers of arbitrary shape. The layer interfaces are considered to be smooth, with no sharp corners. The conventions are the same as in the paper dealing with the antiplane strain model.[1] Subscript j corresponds to either layer domains D_j ($j = 0, 1, \ldots, R$) or to the interfaces C_j ($j = 1, \ldots, R$). Domain D_0 denotes the half-space layer while C_1 denotes the interface between the half-space and the first layer, etc. Summation over repeated indices is understood. Underlined indices indicate that the summation is being suppressed. The material of the media is assumed to

0098-8847/89/030417-18$09.00

Received 29 April 1988
Revised 16 August 1988

: linearly elastic, homogeneous and isotropic. The half-space is subjected to an incident P, SV or Rayleigh ave. In this model the displacement field $\mathbf{u} = (u, v, 0)$ is related to the displacement potentials according to[7]

$$\mathbf{u}_j = \nabla\phi_j + \nabla \times (0, 0, \psi_j), \quad j = 0, 1, \ldots, R \tag{1}$$

here ϕ_j and ψ_j are P and SV wave potentials of the jth layer, respectively. The steady state equations of otion are specified by

$$(\nabla^2 + h_j^2)\psi_j(\mathbf{x}, \omega) = 0, \tag{2a}$$

$$(\nabla^2 + k_j^2)\psi_j(\mathbf{x}, \omega) = 0, \quad \mathbf{x} = (x, y) \in D_j, \quad j = 0, \quad 1, \ldots, R \tag{2b}$$

ere, h_j and k_j denote the dilatational and equivoluminal wavenumbers, respectively, of the jth layer. The oundary conditions on the surface of the half-space are given by

$$\sigma_{xyj}(\mathbf{x}, \omega) = 0, \quad y = 0 \tag{3a}$$

$$\sigma_{yyj}(\mathbf{x}, \omega) = 0, \quad y = 0, \quad \mathbf{x} \in D_j, \quad j = 0, 1, \ldots, R \tag{3b}$$

ontinuity conditions along the layer interfaces are assumed to be

$$u_{j-1}^{+}(\mathbf{x}, \omega) = u_j^{-}(\mathbf{x}, \omega) \tag{4a}$$

$$v_{j-1}^{+}(\mathbf{x}, \omega) = v_j^{-}(\mathbf{x}, \omega) \tag{4b}$$

$$\sigma_{nnj-1}^{+}(\mathbf{x}, \omega) = \sigma_{nnj}^{-}(\mathbf{x}, \omega) \tag{4c}$$

$$\sigma_{nnj-1}^{+}(\mathbf{x}, \omega) = \sigma_{nnj}^{-}(\mathbf{x}, \omega), \quad \mathbf{x} \in C_j, \quad j = 1, 2, \ldots, R \tag{4d}$$

here u_j and v_j are components of the displacement vector field along the x and y directions, respectively, and $_j$ and σ_{nnj} are the components of the stress tensor along interface C_j with unit normal $\mathbf{n}_j$ and tangent vector , respectively. Incident P and SV waves are assumed to be of the form

$$\phi^{\text{inc}} = A \exp\{-\mathrm{i}(h_0 x \sin\theta_0 - h_0 y \cos\theta_0 - \omega t)\} \tag{5a}$$

$$\psi^{\text{inc}} = B \exp\{-\mathrm{i}(k_0 x \sin\theta_0 - k_0 y \cos\theta_0 - \omega t)\} \tag{5b}$$

here ϕ and ψ are P and SV wave potentials, respectively. It is customary to distinguish the angle of cidence for a P wave from that of SH and SV waves. Therefore, $\theta_0 = i$ corresponds to incident P waves hile $\theta_0 = j$ corresponds to incident SV waves. The Rayleigh wave is considered to be of the form

$$\phi^{\text{inc}} = A \exp(-b_1 y) \exp\{-\mathrm{i}(\kappa_0 x - \omega t)\} \tag{6a}$$

$$\psi^{\text{inc}} = B \exp(-b_2 y) \exp(-\mathrm{i}(\kappa_0 x - \omega t)\} \tag{6b}$$

$$b_1 = \kappa_0[1 - (c_0/\alpha_0)^2]^{1/2}$$

$$b_2 = \kappa_0[1 - (c_0/\beta_0)^2]^{1/2}$$

$$\kappa_0 = \omega/c_0$$

ere, c_0 is the half-space Rayleigh wave velocity, κ_0 is the corresponding wavenumber, α_0 and β_0 are ngitudinal and shear velocities, and A and B are known amplitudes. This completes the statement of the oblem. Solution of the problem is considered next.

SOLUTION OF THE PROBLEM

s the incident wave strikes the interface C_1, it is partially reflected back into the half-space D_0 and partially ansmitted into layer D_1. This process continues from one layer to another as the waves propagate roughout the layered media. Consequently, the wavefield in the half-space consists of the free field and the attered field, while the wave field inside each dipping layer consists of the scattered wave field only. The splacement field can be written in the following form:

$$\mathbf{u}_0 = \mathbf{u}^{\text{ff}} + \mathbf{u}_0^{s}, \quad \mathbf{x} \in D_0 \tag{7a}$$

$$\mathbf{u}_j = \mathbf{u}_j^s, \quad \mathbf{x} \in D_j, \quad j = 1, \ldots, R \tag{7b}$$

where $\mathbf{u} = (u, v)$, $\mathbf{x} = (x, y)$, and the superscripts s and ff denote the scattered field and the free field, respectively.

The stress and displacement fields in polar coordinates (defined by Figure 1 of Eshraghi and Dravinski[1]) can be expressed in terms of potentials according to

$$u_r = \partial\phi/\partial r - 1/r\,\partial\psi/\partial\theta \tag{8a}$$

$$u_\theta = 1/r\,\partial\phi/\partial\theta + \partial\psi/\partial r \tag{8b}$$

$$\sigma_{rr} = \lambda\nabla^2\phi + 2\mu[\partial^2\phi/\partial r^2 - \partial/\partial r(1/r\,\partial\psi/\partial\theta)] \tag{8c}$$

$$\sigma_{\theta\theta} = \lambda\nabla^2\phi + 2\mu[1/r(\partial\phi/\partial r + 1/r\,\partial^2\phi/\partial\theta^2) - 1/r(1/r\,\partial\psi/\partial\theta - \partial^2\psi/\partial r\partial\theta))] \tag{8d}$$

$$\sigma_{r\theta} = \mu\{2[1/r\,\partial^2\phi/\partial\theta\partial r - 1/r^2\,\partial\phi/\partial\theta] - [1/r^2\,\partial^2\psi/\partial\theta^2 - r\partial/\partial r(1/r\partial\psi/\partial r]\} \tag{8e}$$

where λ and μ are the Lamé constants and the subscript j is suppressed for simplification. The scattered wave fields are assumed to be of the form

$$\phi_0^s = a_m H_m^{(2)}(h_0 r)\cos m\theta + b_m H_m^{(2)}(h_0 r)\sin m\theta \tag{9a}$$

$$\psi_0^s = a_m^* H_m^{(2)}(k_0 r)\cos m\theta + b_m^* H_m^{(2)}(k_0 r)\sin m\theta \tag{9b}$$

$$\mathbf{x} \in D_0$$

$$\phi_j^s = c_m H_m^{(2)}(h_j r)\cos m\theta + d_m H_m^{(1)}(h_j r)\cos m\theta + e_m H_m^{(2)}(h_j r)\sin m\theta + f_m H_m^{(1)}(h_j r)\sin m\theta \tag{9c}$$

$$\psi_j^s = c_m^* H_m^{(2)}(k_j r)\cos m\theta + d_m^* H_m^{(1)}(k_j r)\cos m\theta + e_m^* H_m^{(2)}(k_j r)\sin m\theta + f_m^* H_m^{(1)}(k_j r)\sin m\theta \tag{9d}$$

$$\mathbf{x} \in D_j, \quad j = 1, 2, \ldots, R-1$$

$$\phi_R^s = g_m J_m(h_R r)\cos m\theta + l_m J_m(h_R r)\sin m\theta \tag{9e}$$

$$\psi_R^s = g_m^* J_m(k_R r)\cos m\theta + l_m^* J_m(k_R r)\sin m\theta \tag{9f}$$

$$\mathbf{x} \in D_R, \quad m = 0, 1, 2, \ldots, M$$

where a_m to l_m^* are unknown coefficients, M is the order of approximation, J_m is a Bessel function, and $H_m^{(1)}$ and $H_m^{(2)}$ are Hankel functions of the first and second kind, respectively.[8] All the wave functions in equations (9a–f) are solutions of the equations of motion [equations (2a, b)]. Analogously to the antiplane strain model, the scattered wave field within the half-space consists of outgoing waves only, thus satisfying the radiation conditions at infinity. Scattered waves within the layers $D_1 - D_{R-1}$ incorporate both incoming and outgoing waves, while the scattered wave field within the inner most layer D_R consists of standing waves only. It can be seen that the wave functions for the scattered wave field in this model do not satisfy the stress-free boundary conditions along the surface of the half-space. These conditions will be imposed locally, as discussed in the next section.

EVALUATION OF THE EXPANSION COEFFICIENTS

Once the scattered wave field is expressed as a series of the wave functions, it is necessary to determine the unknown expansion coefficients in these series. First, the scattered wave field [equations (9a–f)] is substituted into the continuity conditions [equations (4a–d)] at N_j points along the layer interfaces C_j. Then, the boundary conditions [equations (3a, b)] are imposed locally at L_j points along the surface of the half-space.

This results in a system of linear equations of the form

$$Gc = f \tag{10}$$

where vector c contains the unknown expansion coefficients, vector f corresponds to the free field displacement, and stress fields along the layer interfaces and matrix G contains the wave functions and their normal derivatives. The size of matrix G is $(S \times K)$, where $S > K$ is order to solve equation (10) in the least-squares sense. Once expansion coefficients are known, the displacement and stress fields can be evaluated throughout the elastic medium according to equations (8a–e).

This concludes the steady state analysis for the displacement field. Corresponding transient displacements are evaluated through the Fourier synthesis analogously to the antiplane strain model.[1] Numerical results are discussed next.

NUMERICAL RESULTS

Steady state response

Response of a canyon and alluvial valleys subjected to incident plane harmonic P, SV and Rayleigh waves is discussed in this section. As in the case of the antiplane strain model,[1] the shear wave velocity and the shear modulus of the half-space are chosen to be equal to unity, and Poisson's ratio for all the materials is taken to be 1/3. Spatial variables are normalized with respect to the half-width of the innermost dipping layer. The dimensionless frequency Ω is defined as the ratio of the total width of the outer most dipping layer to the wavelength of the half-space shear wave.

First, for testing purposes, surface displacement field results are compared with the ones obtained in some earlier studies. For a canyon, the results by Wong,[9] Dravinski and Mossessian[10] and Mossessian and Dravinski[11] are used to test the accuracy of the present method. These studies are referred to as papers I, II, and III, respectively. For one and two dipping layer models only studies II and III are applicable for the comparison. It should be pointed out that, although the results of study II are evaluated for small attenuation, they are still suitable for testing purposes. Present results include also the phase of the surface displacement field which has not been considered in the previous investigations.

For a semicircular canyon subjected to incident P waves the surface displacement fields are depicted by Figures 1 and 2. It is evident from these figures that the present results are in complete agreement with those obtained previously by other methods.

For a semicircular dipping layer and incident SV wave corresponding results are shown by Figures 3 and 4, and for an incident Rayleigh wave by Figure 5. These results are in excellent agreement with the ones obtained in studies II and III. The small difference from the results of study II could be attributed to the weakly anelastic nature of the material used in that investigation. Excellent agreement between the results obtained by the present method and the results of studies II and III is obtained for incident P and Rayleigh waves for a range of different parameters (frequency, angle of incidence, etc.) as well, but the latter are omitted here for the sake of reducing the number of figures.

The two dipping layer model is constructed by adding one layer to the one dipping layer model. This produces a more gradual transition from the stiff half-space to the soft top layer. Results pertinent to this model are depicted by Figure 6 for a vertically incident P wave. These results are in excellent agreement with those of papers II and III.

At this point it is of interest to elaborate further some numerical aspects of the solution. The wave functions used in this study are similar to the ones used in the antiplane strain model.[1] However, these wave functions do not satisfy the stress-free surface boundary conditions. These conditions must be imposed locally at several points placed uniformly along the surface of the half-space on both sides of the irregularity. In particular, if the maximum width of the irregularity is denoted by $2L$, then these additional points are located within the interval $-3L < x < 3L$. Similarly to the antiplane strain model, more observation points [N_j and L_j, defined in the paragraph prior to equation (10)] and higher order of expansion [M, see equations (9a–f)] are required at higher frequencies in this model as well. The convergence of the results has been

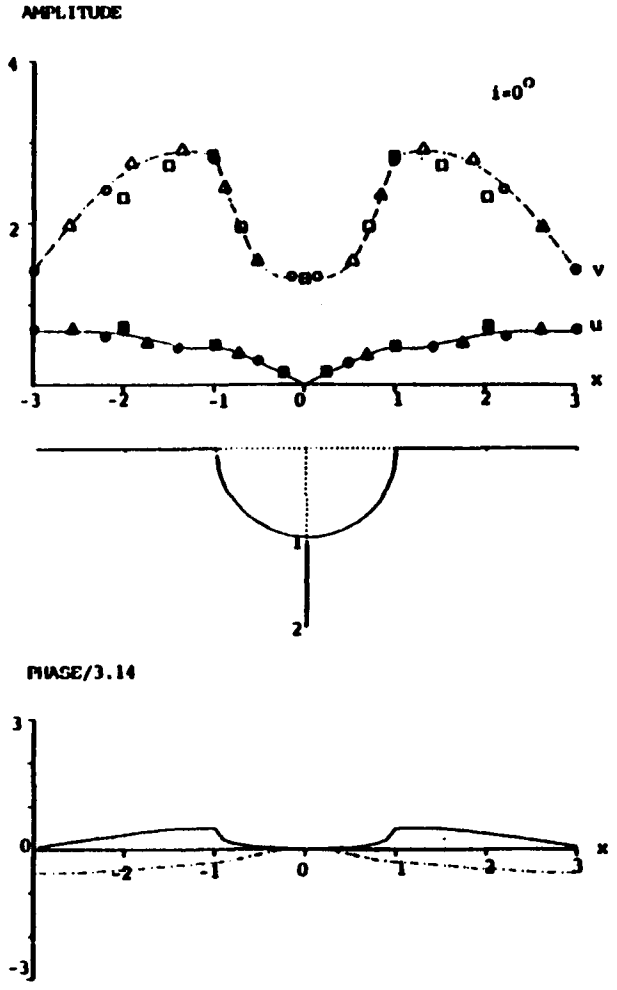

Figure 1. Amplitude and phase of surface displacement spectra for a semicircular canyon subjected to a vertically incident P wave for $\Omega = 0.5$. Unless stated differently, $\mu_0 = \beta_0 = 1$, $\alpha_0 = 2$. Radius of the canyon $R_1 = 1$. Number of expansion terms for each one of the potentials $M = 15$, number of nodal points on the surface of canyon $N = 20$ and on the free surface of the half-space $L_0 = 16$. Throughout Figures 1 to 7, solid and dashed lines correspond to results of this investigation (they correspond to horizontal and vertical components of displacement, respectively). Squares represent the results of Wong[9], triangles and circle correspond to results of Dravinski and Mossessian[10] and Mossessian and Dravinski,[11] respectively

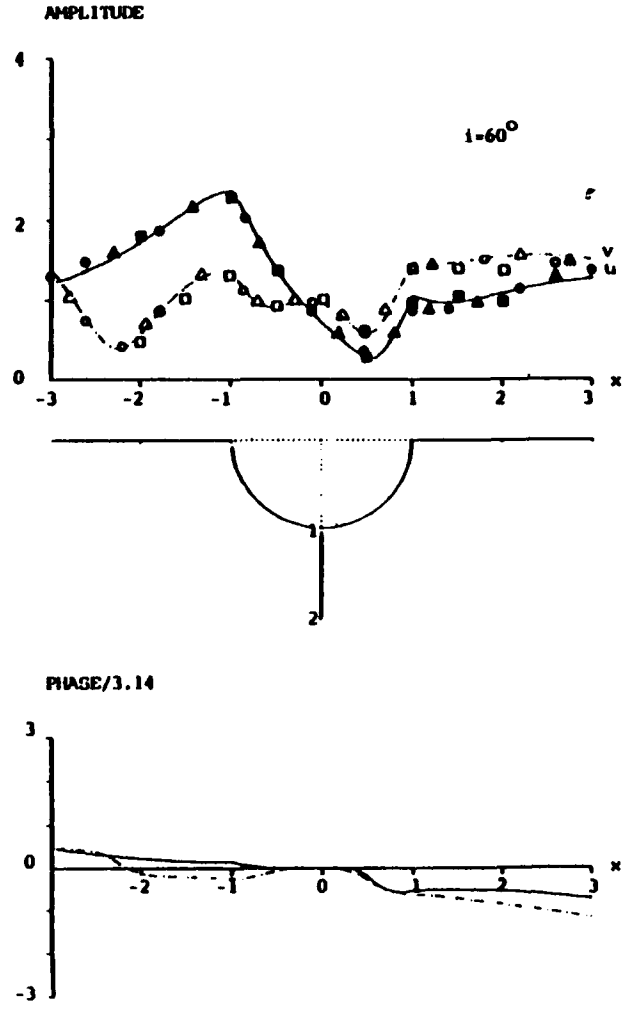

Figure 2. Amplitude and phase of surface displacement spectra for a semicircular canyon subjected to an incident P wave and $i = 60°$. $\Omega = 0.5$, $R_1 = 1$, $M = 15$, $N = 20$, $L_0 = 16$

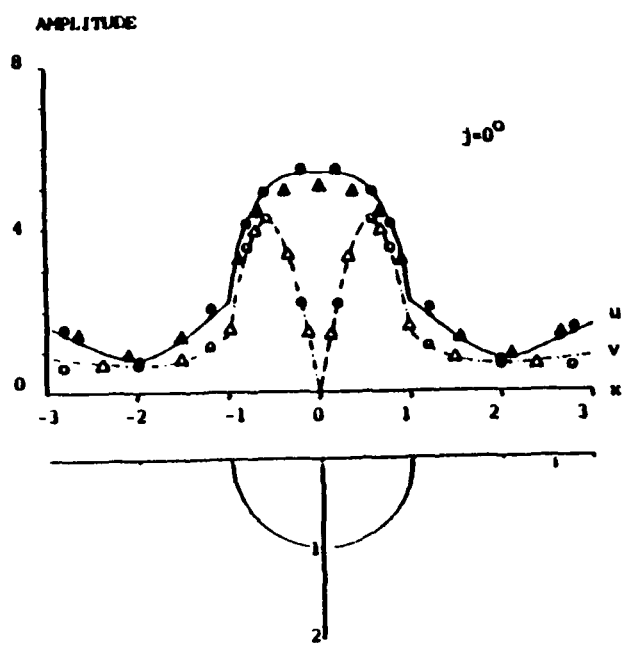

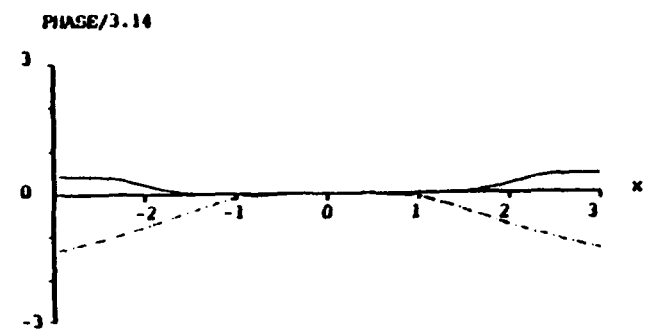

Figure 3. Amplitude and phase of surface displacement spectra for a semicircular dipping layer subjected to a vertically incident SV wave. $\Omega = 0.5$, $R_1 = 1$, $M = 15$ (for both materials), $N = 20$, $L_0 = 16$, $L_1 = 8$ (the number of nodal points atop of the alluvium). $\mu_1 = 0.167$, $\beta_1 = 0.5$, $\alpha_1 = 1$

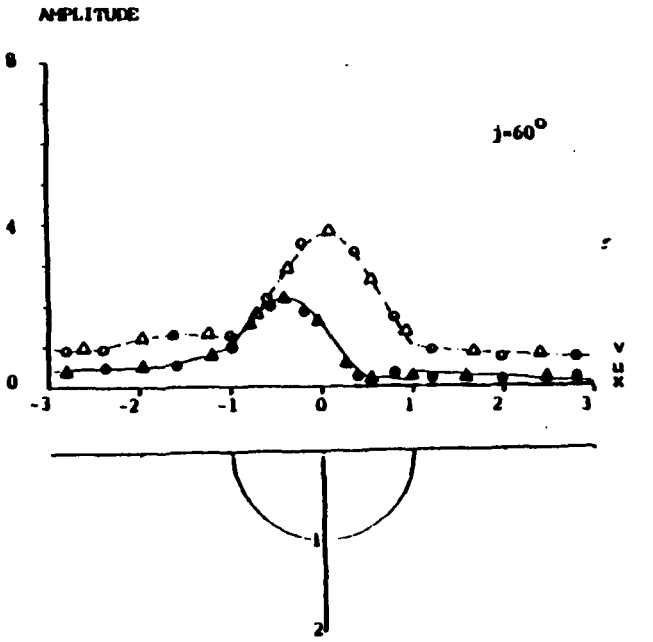

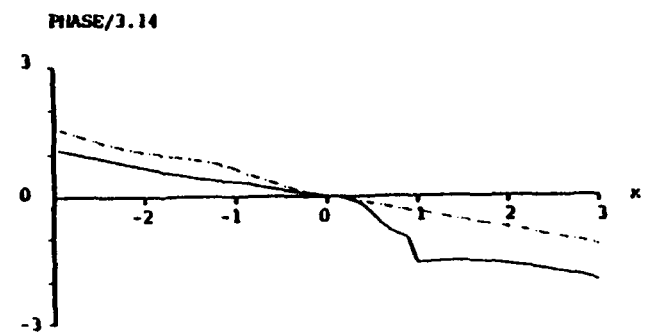

Figure 4. Amplitude and phase of surface displacement spectra for a semicircular dipping layer subjected to an incident SV wave and $j = 60°$. $\Omega = 0.5$, $R_1 = 1$, $M = 15$, $N = 20$, $L_0 = 16$, $L_1 = 8$, $\mu_1 = 0.167$, $\beta_1 = 0.5$, $\alpha_1 = 1$

$l=0^{o}$

tablished by observing the stability of the displacement field as the number of expansion terms and bservation points increases. The numerical results are accepted as the final ones if the difference between wo successive calculations is judged to be sufficiently small.

Overall, the numerical results indicate that the proposed method provides an accurate displacement field r a wide range of parameters present in the problem and that the solution exhibits very fast convergence.

ransient response

Transient surface reponse to an incident P or SV Ricker wavelet is investigated next. For definition of the icker wavelet used in this study the reader is referred to the paper by Eshraghi and Dravinski.[1]

First, for testing purposes, the predominant component of the displacement field for a cosine type valley is aluated for a vertically incident P wave. This problem has been investigated earlier by Bard and ouchon.[12] The results are shown by Figure 7. Very good agreement between the two methods can be bserved for all four stations at the surface of the half-space. After this verification of the algorithm for the aluation of transient response, several additional transient problems are considered as follows.

For a semicircular canyon and vertically incident SV wave the results are presented by Figures 8 and 9. As pected, the predominant motion of the valley takes place in the horizontal direction (Figure 8). This

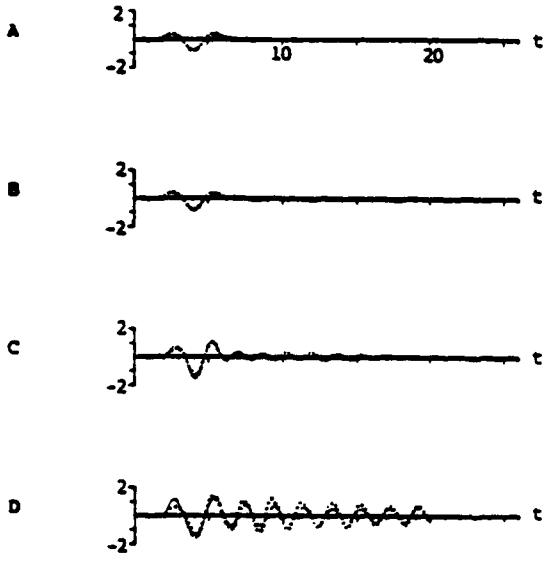

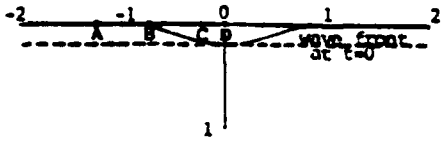

gure 7. Vertical component of displacement for transient surface response of a cosine type valley to a vertically incident P Ricker velet with characteristic period $t_p = 3{\cdot}556$ ($t_s = 3{\cdot}886$). Stations A to D are located at $x = -1{\cdot}2, -0{\cdot}72, -0{\cdot}24$ and 0. $\mu_0 = 1$, $\beta_0 = 1$, $= 1{\cdot}731$ (only for this figure), $\mu_1 = 0{\cdot}02424$, $\beta_1 = 0{\cdot}2$, $z_1 = 0{\cdot}4$, $P = 256$, $\Delta t = 0{\cdot}2$, $\omega_c = 7{\cdot}697$. Solid lines correspond to this method while dots correspond to the results of Figure 13 of Bard and Bouchon[12]

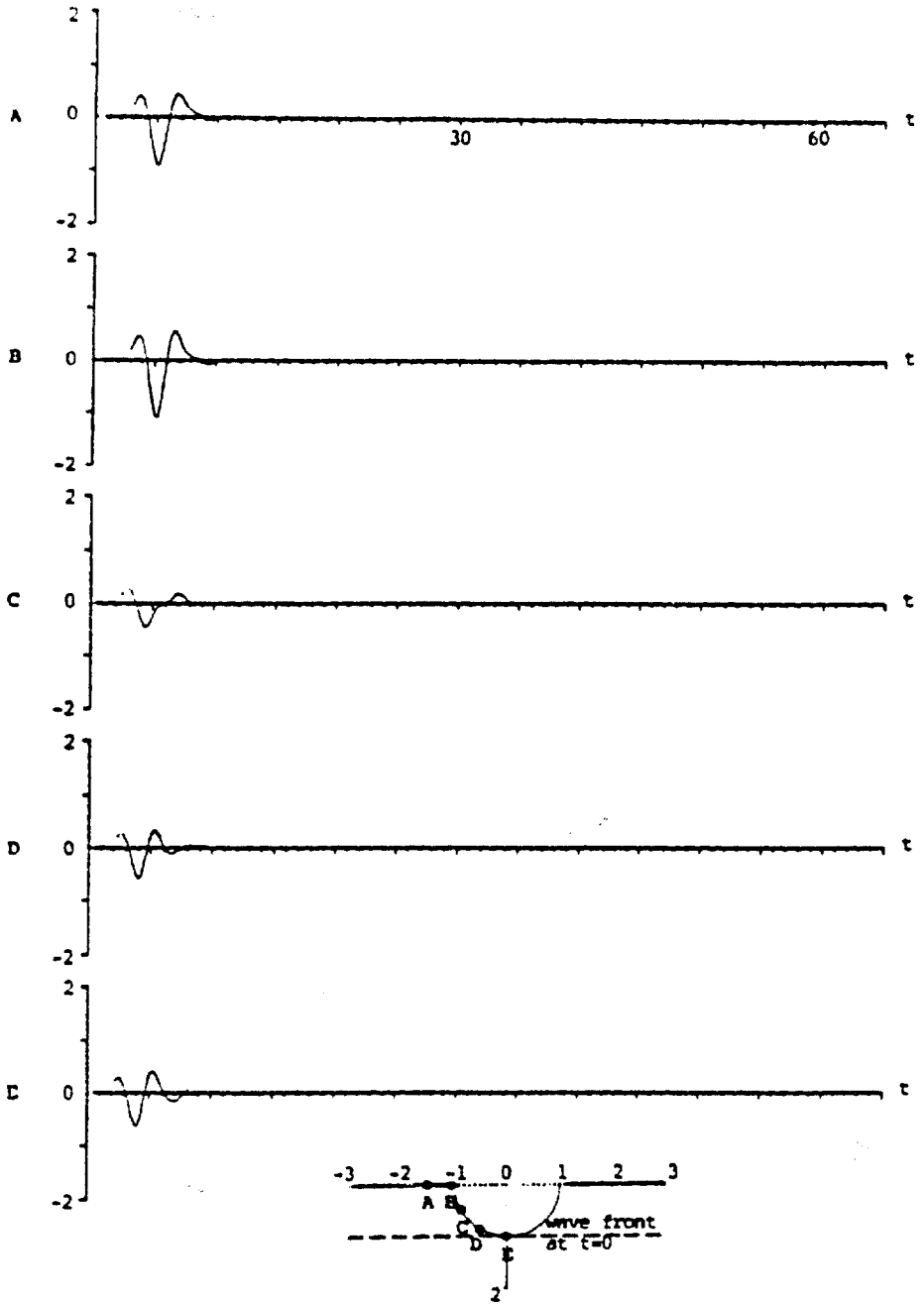

Figure 8. Horizontal component of transient surface response of a semicircular canyon to a vertically incident SV Ricker wavelet with characteristic period $t_p = 3{\cdot}66$ ($t_s = 4$). Stations A to E are located at $x = -1{\cdot}6$, $-1{\cdot}2$, $-0{\cdot}8$, $-0{\cdot}4$ and 0. $R_1 = 1$, $P = 256$, $\Delta t = 0{\cdot}25$, $\omega_c = 8{\cdot}561$, $\mu_0 = \beta_0 = 1$, $\alpha_0 = 2$ (for rest of figures)

component of motion consists of both incident and scattered waves, while the vertical or non-predominant component of the displacement field (Figure 9) consists of the scattered waves only. In Figure 9 line AA tracks a particular wave as it moves from station B to station A. The slope of line AA in Figure 9 gives the phase velocity of the propagating surface waves slightly less than one, suggesting that these waves are Rayleigh waves which originate at the edge of the canyon and are travelling along the soil surface. The

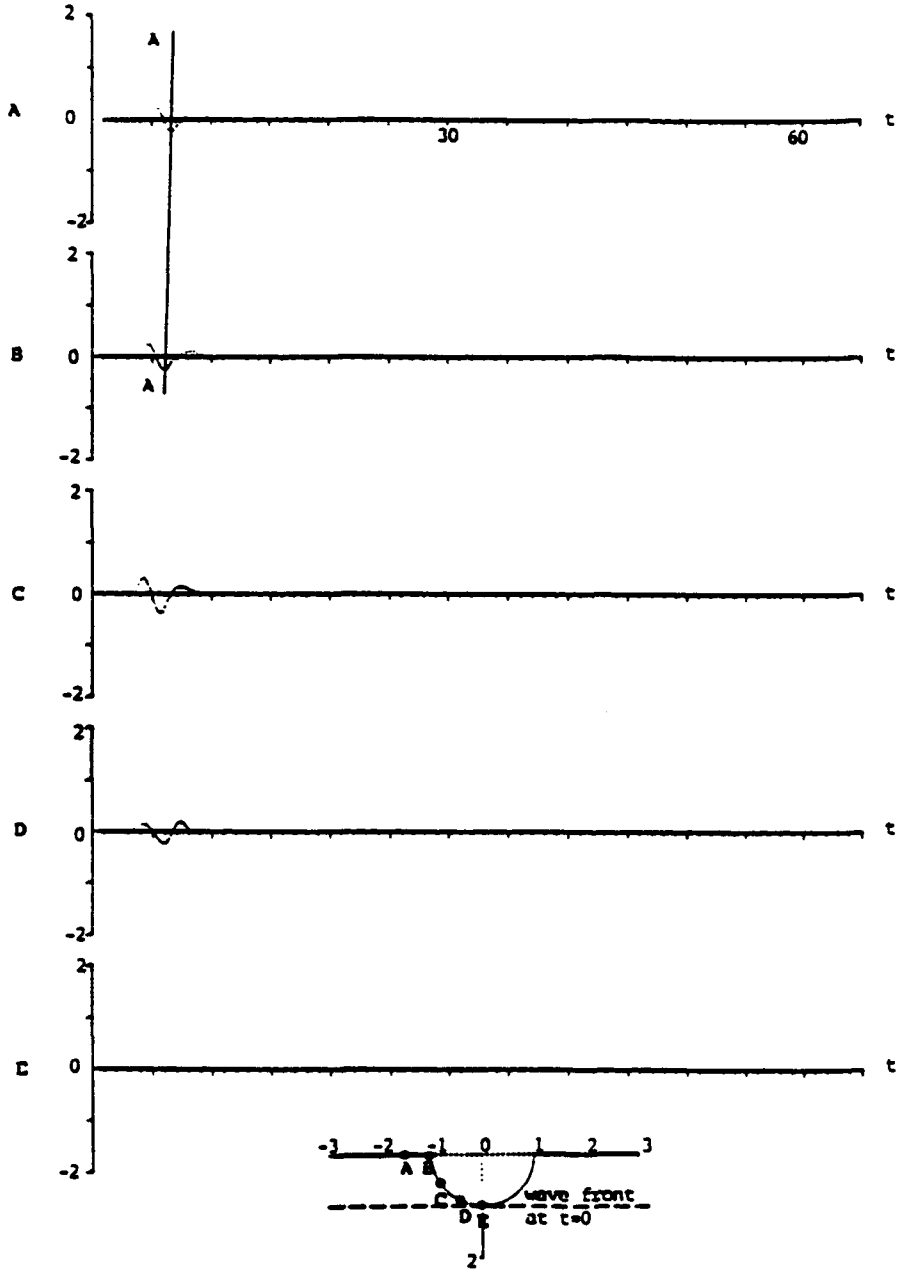

Figure 9. Vertical component of transient surface response of a semicircular canyon to a vertically incident SV Ricker wavelet with characteristic period $t_p = 3{\cdot}66$ ($t_s = 4$). Stations A to E are located at $x = -1{\cdot}6, -1{\cdot}2, -0{\cdot}8, -0{\cdot}4$ and 0. $R_1 = 1$. $P = 256$. $\Delta t = 0{\cdot}25$. $\omega_c = 8{\cdot}561$

seismograph at the centre of the canyon shows no vertical disturbance because of the symmetry of the model. The appearance of the direct incident signal at expected times at each station for the predominant component of the displacement field provides further confidence in the accuracy of the results (Figure 8). It is interesting to observe a delay in wave arrival for the vertical (non-predominant) displacement component (Figure 9) in comparison to the arrival time of the horizontal displacement component (Figure 8): the scattered field for

vertical motion consists mainly of the surface waves generated at the edges of the canyon, therefore, an extra time for their arrival at an observation station must be taken into account.

For the one layer model, the seismographs displayed by Figures 10 to 13 show propagation patterns of the displacement field for various stations atop of the alluvial valley. Figures 10 and 11 correspond to a vertically incident P wave. The predominant motion takes place in the vertical direction. In that direction, the response consists of both incident and scattered wave fields, as indicated by Figure 11. Large amplification of the

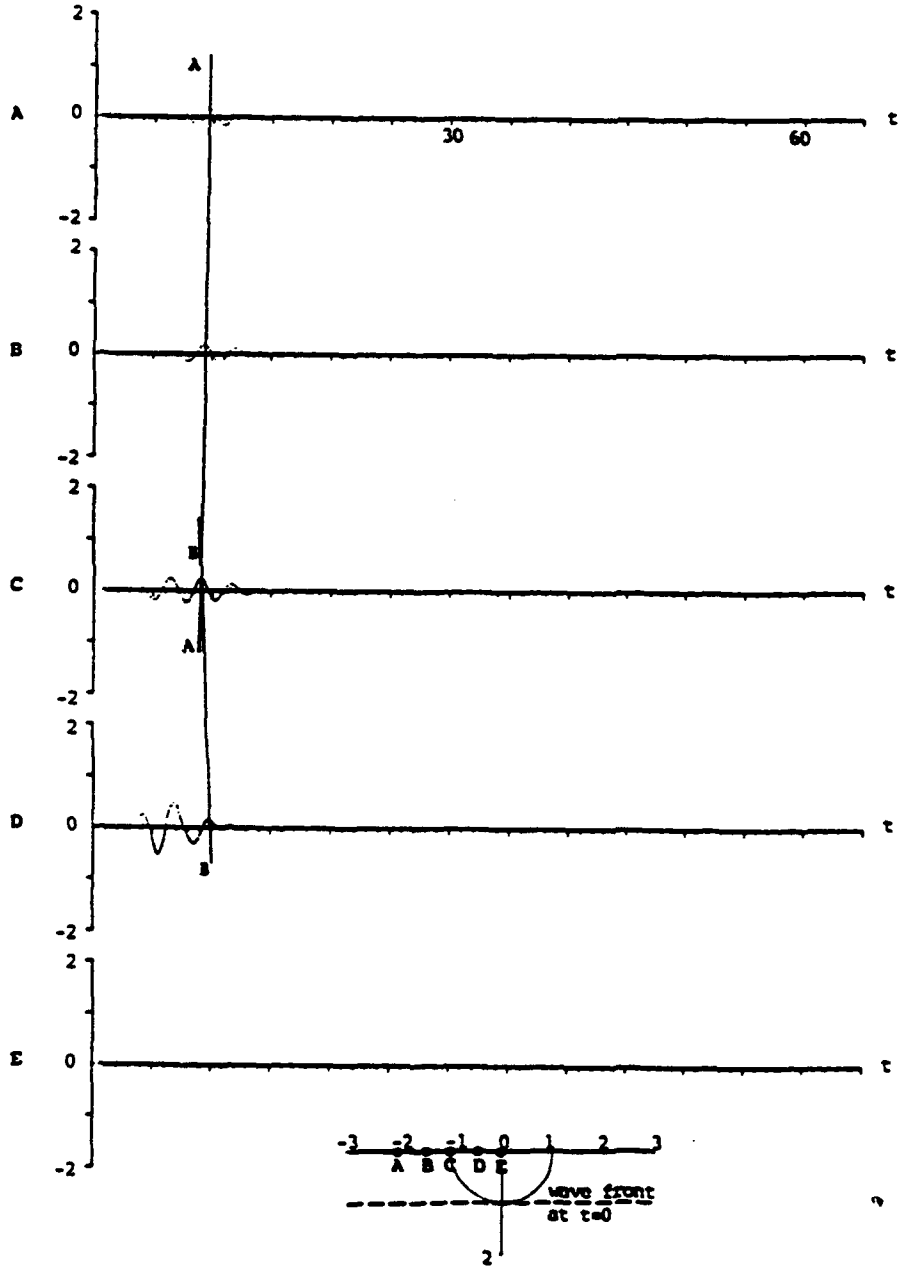

Figure 10. Horizontal component of transient surface reponse of a semicircular dipping layer to a vertically incident P Ricker wavelet with characteristic period $t_0 = 3{\cdot}66$ ($t_s = 4$). $\mu_1 = 0{\cdot}167$, $\beta_1 = 0{\cdot}5$, $\alpha_1 = 1$, $R_1 = 1$, $P = 256$, $\Delta t = 0{\cdot}25$, $\omega_c = 7{\cdot}697$. Throughout Figures 10 to 13, stations A to E are located at $x = -2$, $-1{\cdot}5$, -1, $-0{\cdot}5$ and 0

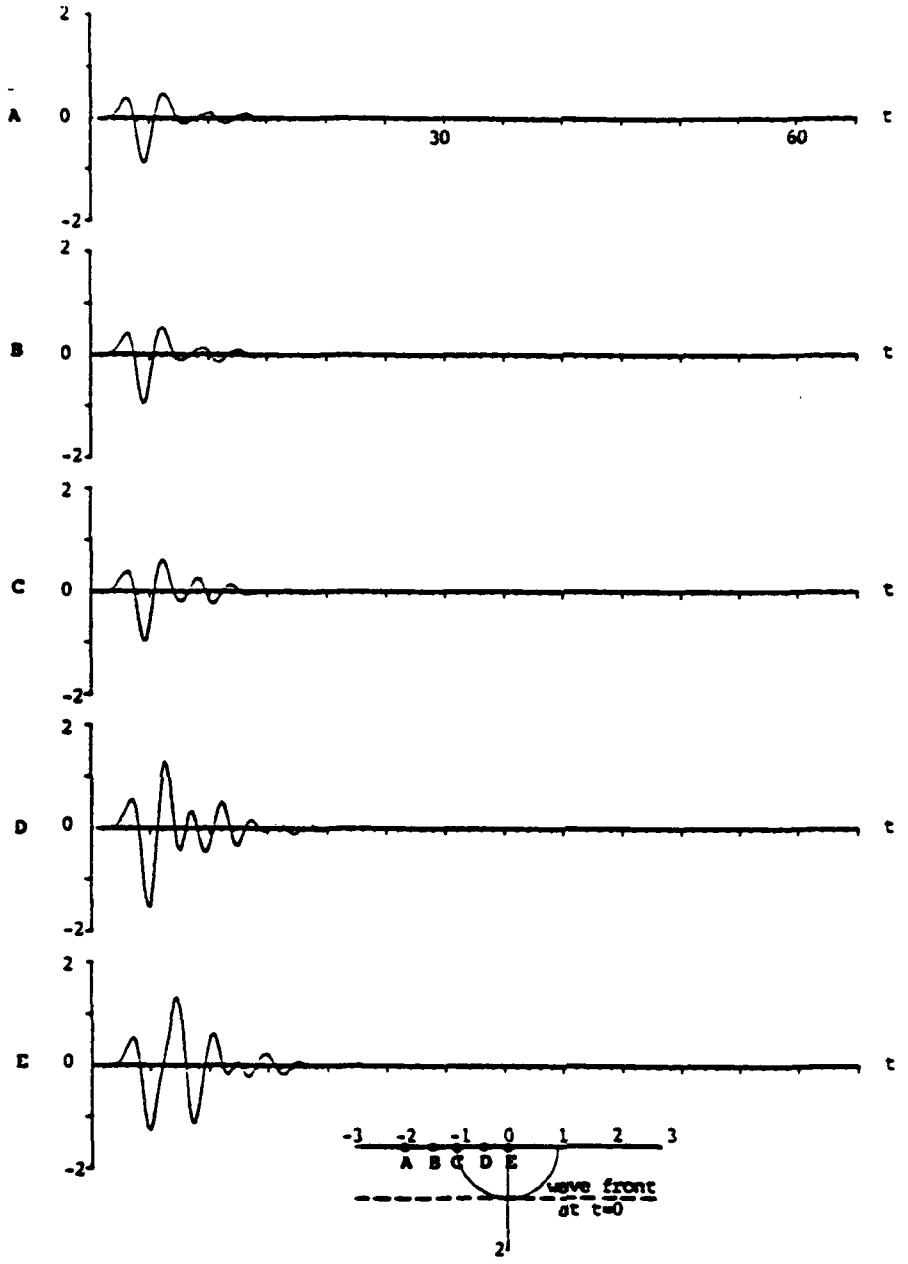

Figure 11. Vertical component of transient surface response of a semicircular dipping layer to a vertically incident P Ricker wavelet with characteristic period $t_p = 3{\cdot}66$ ($t_s = 4$). $\mu = 0{\cdot}167$, $\beta_1 = 0{\cdot}5$, $\alpha_1 = 1$, $R_1 = 1$, $P = 256$, $\Delta t = 0{\cdot}25$, $\omega_c = 7{\cdot}697$

response at the centre of the valley is evident. Figure 10 shows the horizontal component of the scattered field. Again, the amplification of surface motion inside the valley is significant. Generation and propagation of the surface waves at each edge of the valley are clearly displayed on these figures: thus, the positive slope of line AA in Figure 10 shows propagation of disturbances in the half-space away from the valley edge, while the negative slope of line BB indicates wave propagation within the sediments toward the centre of the valley.

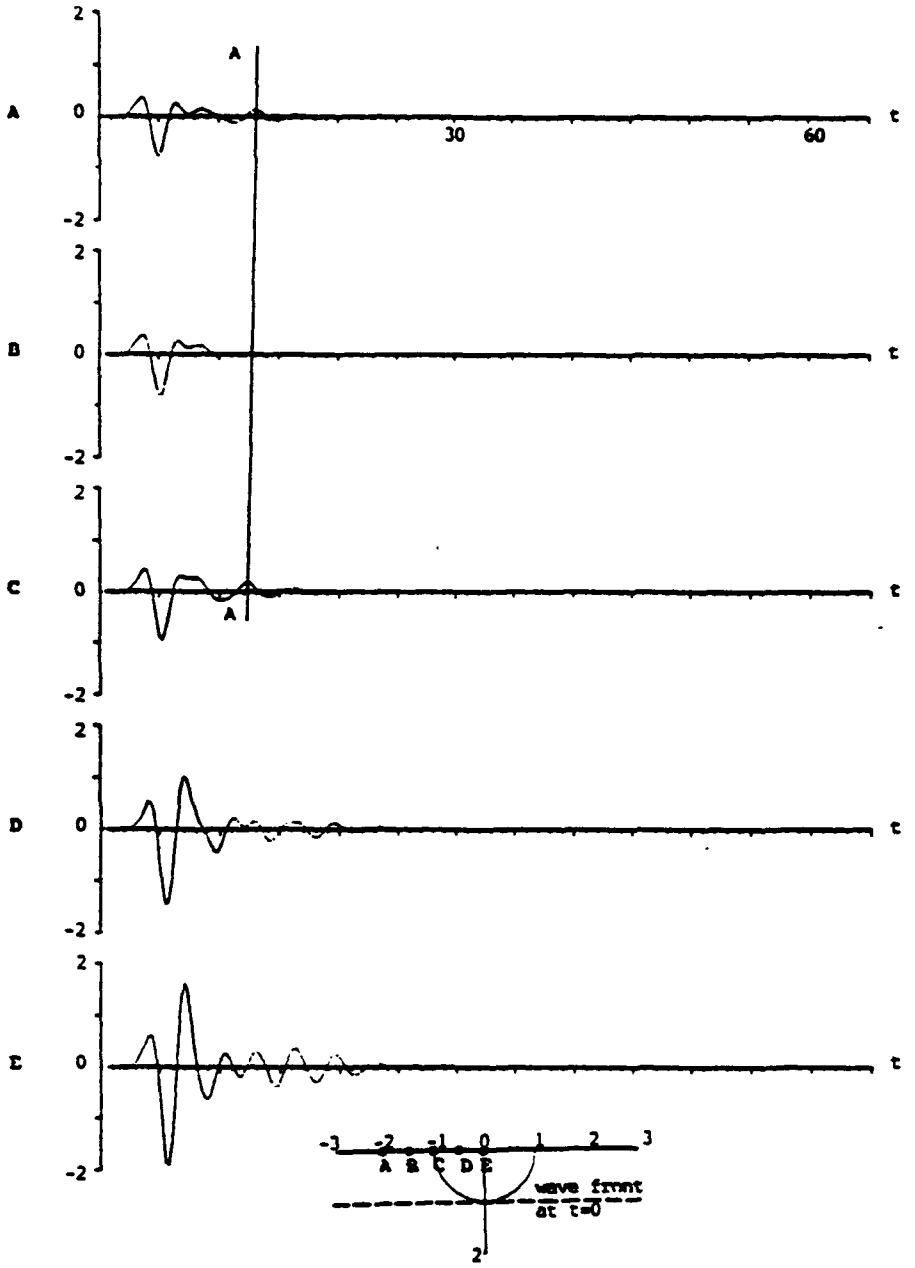

Figure 12. Horizontal component of transient surface response of a semicircular dipping layer to a vertically incident SV Ricker wavelet with characteristic period $t_p = 3{\cdot}66$ ($t_s = 4$). $\mu_1 = 0{\cdot}167$, $\beta_1 = 0{\cdot}5$, $\alpha_1 = 1$, $R_1 = 1$, $P = 256$, $\Delta t = 0{\cdot}25$, $\omega_c = 7{\cdot}697$

Therefore, the edges can be viewed as sources of these surface waves. Similar results are obtained for the incident SV wave displayed by Figures 12 and 13. As in the case of the incident P wave large amplification of the surface displacement field is observed within the sediments. The predominant motion takes place in the horizontal direction, as shown by Figure 12. Figure 13 displays the vertical component of the displacement field for the same model. It is interesting to observe large ground motion amplification for the vertical

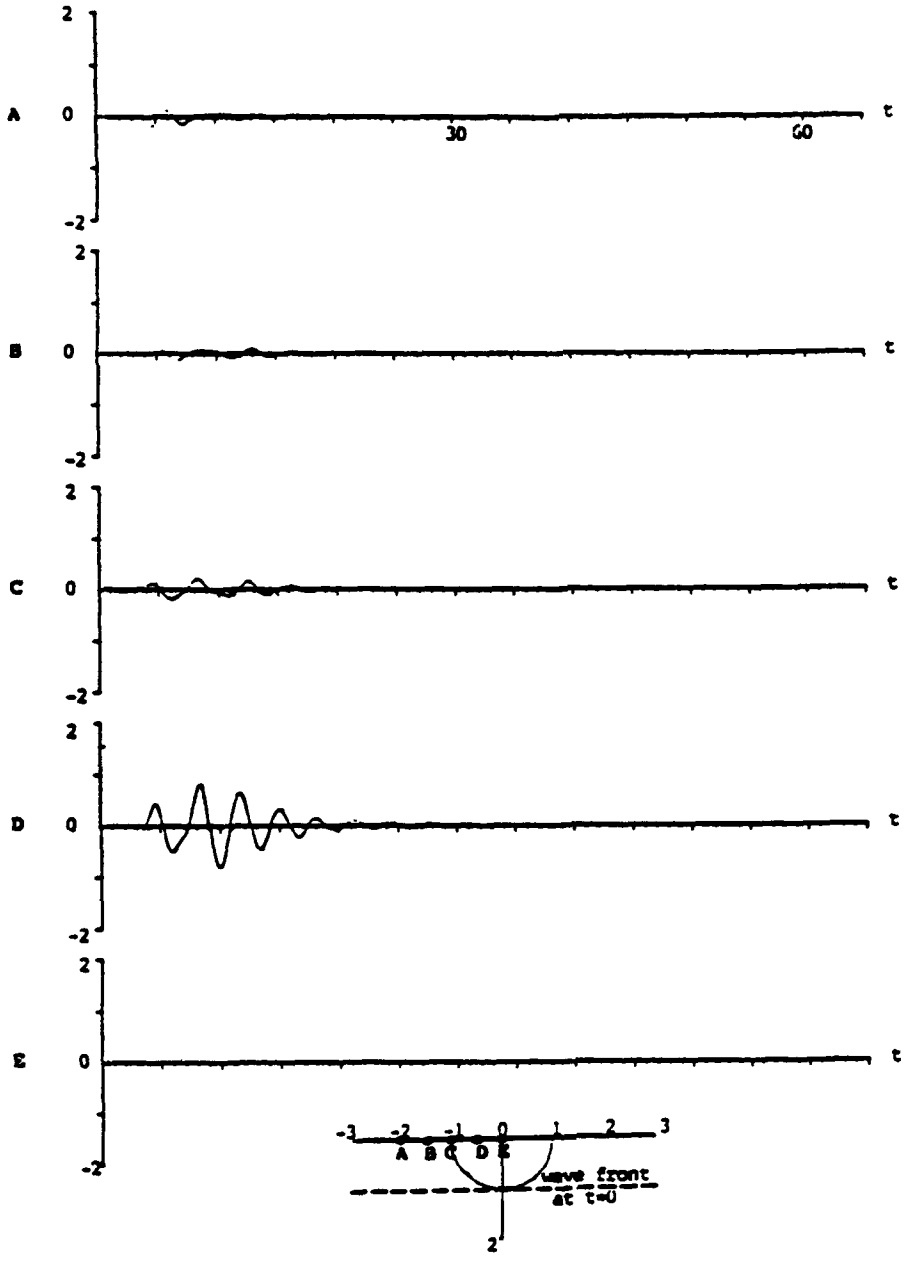

Figure 13. Vertical component of transient surface response of a semicircular dipping layer to a vertically incident SV Ricker wavelet with characteristic period $t_p = 3{\cdot}66$ ($t_s = 4$), $\mu_1 = 0{\cdot}167$, $\beta_1 = 0{\cdot}5$, $\alpha_1 = 1$, $R_1 = 1$, $P = 256$, $\Delta t = 0{\cdot}25$, $\omega_c = 7{\cdot}697$

displacement component at about midpoint between the centre and the edge of the sediment (station D in Figure 13). For the same station and displacement component this phenomenon can be observed in the corresponding frequency spectra (see Figure 3). Analogous observations can be made for the horizontal displacement component. Figure 12 indicates very clearly that the maximum amplification of the surface ground motion for that component of displacement field occurs at the centre of the sediment. The corresponding frequency spectra (see Figure 3) confirm this result. Similar observations can be made for other incident waves as well. However, these are omitted in order to reduce the number of figures.

For the two layer model and a vertically incident P wave the vertical and horizontal components of the splacement field are presented by Figures 14 and 15, respectively. The predominant motion of the valley igure 14) consists of both incident and scattered waves. Amplification of the incident signal is evident for e stations inside the valley. Lines AA and BB track two distinct surface waves as they move atop the half-

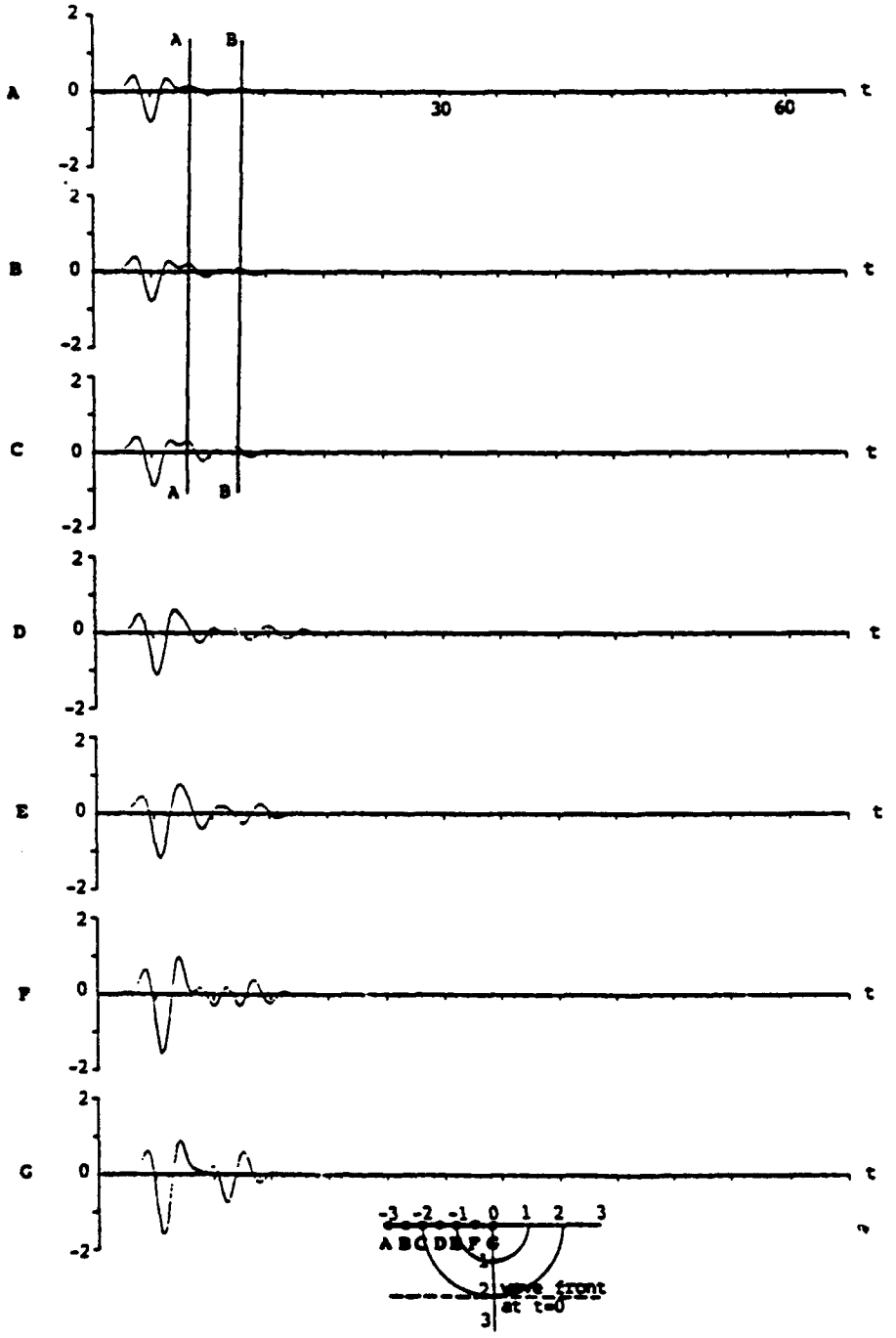

ure 14. Vertical component of transient surface response for two semicircular dipping layers subjected to a vertically incident P ker wavelet with characteristic period $t_p = 3{\cdot}66$ ($t_s = 4$). Material properties and model geometry are the same as in the steady state case of Figure 6

space away from the valley. Amplification of the surface waves inside the valley suggests that most of the energy associated with the scattered field is trapped inside the valley. The propagation pattern of surface waves within the valley is complicated by multiple generation and reflections of surface waves by the edges of the valley. Therefore, it is difficult to track particular waves individually. For the horizontal component of the

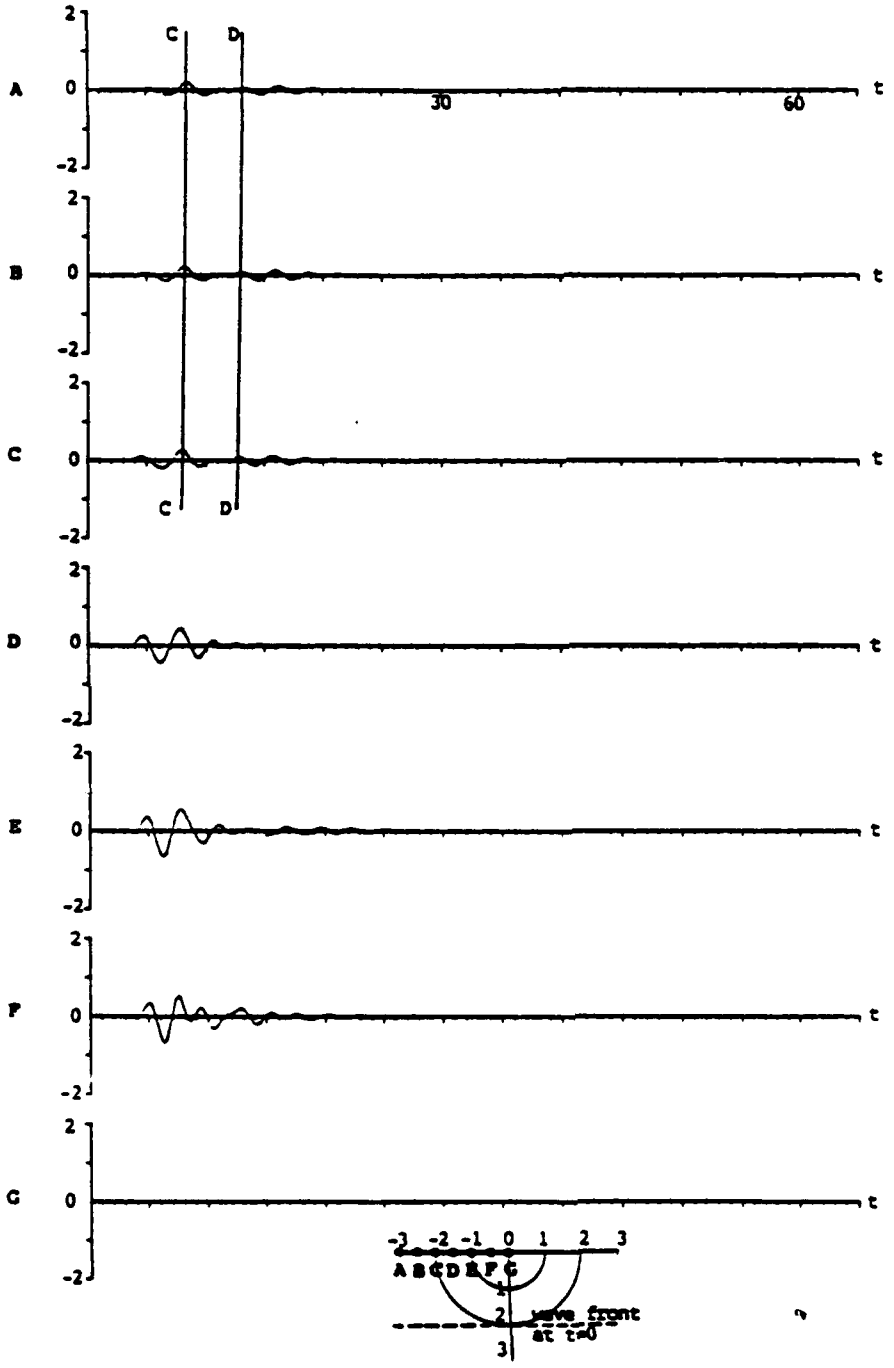

Figure 15. Horizontal component of transient surface displacement response for two semicircular dipping layers subjected to a vertically incident P Ricker wavelet with characteristic period $t_p = 3{\cdot}66$ ($t_s = 4$). Material properties and model geometry are the same as for Figure 14

lacement field (Figure 15) amplification of the scattered waves for stations inside the valley follows a ern similar to that observed in the corresponding steady state model (see Figure 6). Lines CC and DD k two surface waves as they move atop the half-space away from the valley. The slopes and points of rsections with the time axis for lines CC and DD are similar to the ones for lines AA and BB in Figure 14. thermore, the pattern of the local surface waves tracked by lines AA and CC (BB and DD) in Figures 14 15 suggests that these waves are actually two displacement components of the same local surface waves. milar observation can be made for other incident waves.

omparison of strong ground motion amplification for a canyon with one and two dipping layers suggests the presence of sediment may result in very large amplification of the surface displacement field. These parisons demonstrate the importance of the sedimentary deposits in local amplification of the ground ion. Failure to include sediments in the analysis of localized amplification may result in significant erestimation of the resulting strong ground motion. The presented results clearly illustrate the import- : of these phenomena.

iparison with observed earthquake motions

ecently, King and Tucker[13] measured the variation of earthquake motion across a sediment-filled valley. velocity of the ground motion was measured along two sections of the valley and at two adjacent rock . The results of the measurements show that response to earthquake motion of a site depends strongly n frequency and position of the site within the valley and weakly upon the input signal's azimuth and e of incidence. Ratios of the Fourier spectra from soil to spectra from nearby rock sites showed sediment amplification of up to a factor of ten. A clear difference could be observed between the spectra for rent components of the displacement field at the sediment sites. Finally, a larger variation of ground ion was observed over sections of the sediment profile which span larger changes in sediment thickness over the profiles that span sediments of approximately equal thickness. Apparently, with the exception e angle of incidence, all the conclusions of the experimental observations are verified by this theoretical stigation. The discrepancy in angle of incidence may be explained if one considers the response of an vial basin from the resonance point of view.[14] That would require evaluation of ground motion for an mble of incident signals of different periods and then use of the peak surface ground motion for parison with the experiments. Still, the agreement in general features of the response between the retical and experimental investigations for the range of frequencies studied here is very convincing and ific sedimentary basins have to be investigated on a case by case basis. It should be pointed out that the ulations for different impedance contrasts between the dipping layers are not presented here in order to ce the number of figures.

CONCLUSIONS

plification of incident plane P, SV and Rayleigh waves by two dimensional dipping layers of arbitrary e is investigated by using a boundary method. Both harmonic and transient incident wave fields are idered.

he results presented indicate that the presence of sediments may change substantially local amplification e strong ground motion. This amplification is very sensitive to the type and frequency of the incident e, angle of incidence, nature of subsurface irregularity, impedance contrast between the layers, compo- : of displacement field being observed and the location of the observation station at the surface of the vium. It is shown that surface waves generated by the edges of the layers play a very important role in the lting displacement patterns atop the deeper parts of the sediments.

he results of this study and the antiplane strain study[1] show that failure to take into account the presence ubsurface irregularities may greatly underestimate the resulting strong ground motion in a theoretical lelling of sedimentary basins.

ACKNOWLEDGEMENT

material is based upon work supported in part by the National Science Foundation under Grant 53-4519-3792 and in part by the Office of Naval Research under Contract No. N00014-88-K-0157.

REFERENCES

1. H. Eshraghi and M. Dravinski, 'Transient scattering of elastic waves by dipping layers of arbitrary shape. Part I. Antiplane strain model', *Earthquake eng. struct. dyn.* 18, 397–415 (1989).
2. I. Herrera and F. Sabina, 'Connectivity as an alternative to boundary integral equations: Construction of bases', *Proc. natl. acad. sci. U.S.A.* 75, 2059–2063 (1978).
3. I. Herrera, 'Boundary methods: A criterion for completeness', *Proc. natl. acad. sci. U.S.A.* 77, 4395–4398 (1980).
4. F. J. Sanchez-Sesma, I. Herrera and J. Aviles, 'A boundary method for elastic wave diffraction: Application to scattering of SH waves by surface irregularities', *Bull. seism. soc. Am.* 72, 473–490 (1982).
5. F. J. Sanchez-Sesma, M. A. Bravo and I. Herrera, 'Surface motion of topographical irregularities for incident P, SV, and Rayleigh waves', *Bull. seism. soc. Am.* 75, 263–269 (1985).
6. M. Dravinski, H. Eshraghi and F. J. Sabina, 'Scattering of SH waves by an alluvial valley of arbitrary shape: A boundary integral approach', *Proc. 3rd U.S. natl. conf. earthquake eng.* (1986).
7. K. Aki and P. G. Richards, *Quantitative Seismology, Theory and Methods*, Vol. I, W. H. Freeman, San Francisco, 1980.
8. M. Abramowitz and I. A. Stegun, *Handbook of Mathematical Functions*, Dover, New York, 1972.
9. H. L. Wong, 'Diffraction of P, SV, and Rayleigh waves by surface topographies', *Bull. seism. soc. Am.* 72, 1167–1184 (1982).
10. M. Dravinski and T. K. Mossessian, 'Scattering of plane harmonic P, SV, and Rayleigh waves by dipping layers of arbitrary shape', *Bull. seism. soc. Am.* 77, 212–235 (1987).
11. T. K. Mossessian and M. Dravinski, 'Application of a hybrid method for scattering of P, SV and Rayleigh waves by near surface irregularities', *Bull. seism. soc. Am.* 77, 1784–1803 (1987).
12. P.-Y. Bard and M. Bouchon, 'The seismic response of sediment-filled valleys. Part 2. The case of incident P and SV waves', *Bull seism. soc. Am.* 70, 1921–1941 (1980).
13. J. L. King and B. E. Tucker, 'Observed variations of earthquake motion across a sediment-filled valley', *Bull. seism. soc. Am.* 74, 137–151 (1984).
14. P.-Y. Bard and M. Bouchon, 'The two-dimensional resonance of sediment-filled valleys', *Bull. seism. soc. Am.* 75, 519–541 (1985).

EARTHQUAKE ENGINEERING AND STRUCTURAL DYNAMICS, VOL. 18, 983–998 (1989)

CATTERING OF PLANE HARMONIC SH, SV, P AND RAYLEIGH WAVES BY NON-AXISYMMETRIC THREE-DIMENSIONAL CANYONS: A WAVE FUNCTION EXPANSION APPROACH

HOSSEIN ESHRAGHI AND MARIJAN DRAVINSKI

Department of Mechanical Engineering, University of Southern California, Los Angeles, California 90089–1453, U.S.A.

SUMMARY

tering of elastic waves by three-dimensional canyons embedded within an elastic half-space is investigated by using a e function expansion technique. The geometry of the canyon is assumed to be non-axisymmetric. The canyon is ected to incident plane Rayleigh waves and oblique incident SH, SV and P waves. The unknown scattered wavefield is essed in terms of spherical wave functions which satisfy the equations of motion and radiation conditions at infinity, they do not satisfy stress-free boundary conditions at the half-space surface. The boundary conditions are imposed lly in the least-squares sense at several points on the surface of the canyon and the half-space.

hrough a comparative study the validity and limitations of two-dimensional approximations (antiplane strain and e strain models) have been examined. It is shown that scattering of waves by three-dimensional canyons may cause tantial change in the surface displacement patterns in comparison to the two-dimensional models. These results hasize the need for three-dimensional modelling of realistic problems of interest in strong ground motion seismology earthquake engineering.

INTRODUCTION

ecent years, the importance of the site effects in the local amplification of strong ground motion has been established.[1] This led a number of researchers to study more realistic problems of ground motion plification by surface and subsurface irregularities.[2] The complexity of such problems precludes the use of ed form analytical solutions. However, recent advances in computational techniques make numerical roaches more feasible for realistic problems of interest in strong ground motion seismology and hquake engineering. Boundary integral equations (BIE) are one of those approaches. This technique nulates the problem in terms of boundary values and possibly internal sources.[3] Solution at interior points s not need to be considered in order to solve the integral equations. The main advantage of the BIE hods is that the discretization is applied only to the boundaries of the scatterers, thus reducing the number ne unknown variables significantly in comparison to the finite element and finite difference techniques.[4, 5] he BIE techniques the radiation conditions at infinity are satisfied exactly. The main drawback in the BIE hods is the requirement for evaluation of the Green's functions, which often requires a large amount of putational effort.[2] For that reason, another approach in solving the problems of scattering of waves by r surface irregularities appears to be more effective. The method utilizes the wave function expansion roach which does not require evaluation of the Green's functions in the course of solving the problem. se wave functions satisfy the equations of motion and radiation conditions at infinity. However, in general / do not satisfy traction-free boundary conditions on the surface of the half-space which must be imposed lly. These functions can be used to express the scattered fields in complex diffraction problems. Sanchez-na *et al.*[6] used this approach to study scattering of harmonic P, SV and Rayleigh waves by two-ensional irregularities. Eshraghi and Dravinski[7,8] extended this technique to transient problems in the tilayer two-dimensional irregularities for incident SH, SV, P and Rayleigh waves. For three-dimensional blems, except for axisymmetric geometries, the application of this technique has been very limited.

8–8847/89/070983–16$08.00

Received 17 November 1988
Revised 7 March 1989

Sanchez-Sesma[9] used the wave function expansion technique to construct the scattered fields for axisymmetric scatterers and vertically incident P waves. Using a wave function approach, Lee[10] solved similar problems for hemispherical alluvial valleys for incident plane harmonic SH, P and SV waves. Day[11] used the finite element method to study scattering of elastic waves by axisymmetric sedimentary basins. Apsel[12] considered the BIE technique for studying soil–structure interaction for axisymmetric scatterers. Avanessian *et al.*[13] considered the steady state soil–structure interaction. The finite element technique was used to model the structure and some portion of the surrounding soil medium. Beyond the finite element mesh, expansion in terms of the spherical wave functions was employed. This study is limited to axisymmetric scatterers and incident P waves. For an additional review of the literature on scattering of elastic waves by near surface irregularities the reader is referred to recent papers by the present authors.[7,8]

Since irregularities of practical interest are of arbitrary shape, a general non-axisymmetric model is considered in the present paper. The wave function expansion technique is used to express the unknown scattered wave field for such irregularities subjected to obliquely incident SH, SV, P and Rayleigh waves.

STATEMENT OF THE PROBLEM

The geometry of the problem is depicted by Figure 1. The problem consists of a canyon embedded in an elastic half-space. The surface of the canyon is considered to be smooth, without sharp corners. Throughout the paper C_0 denotes the half-space surface, C_1 denotes the surface of the canyon and D corresponds to the domain of the half-space. The medium is assumed to be linearly elastic, homogeneous and isotropic. The half-space is subjected to an incident plane harmonic SH, SV, P or Rayleigh wave.

In the absence of body forces, the steady state equation of motion in three-dimensional media is defined in vector form by

$$\mu\nabla^2\mathbf{u} + (\lambda+\mu)\nabla\nabla\cdot\mathbf{u} + \omega^2\mathbf{u} = 0, \quad \mathbf{x}\in D \tag{1}$$

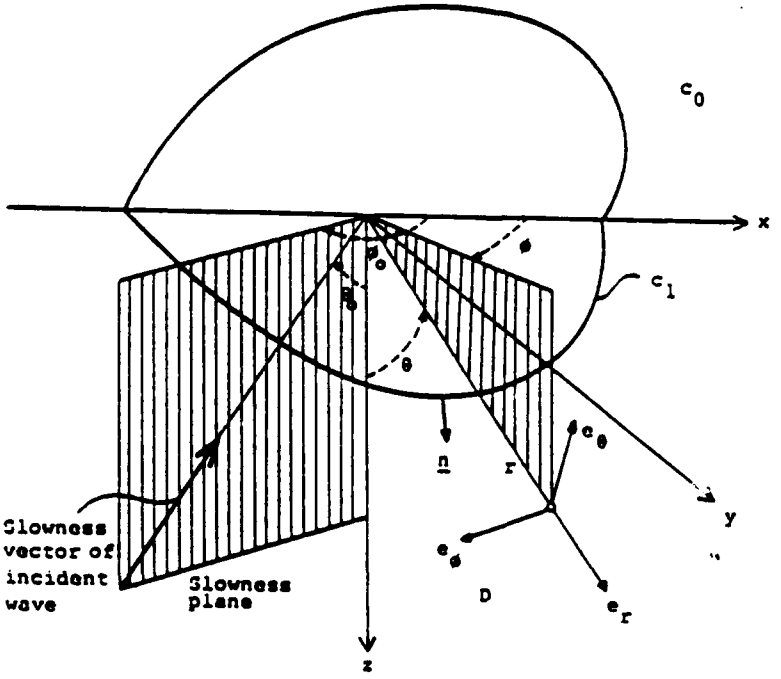

Figure 1. Problem model

x and u are position and displacement vectors, respectively, λ and μ are the Lamé constants and ω es the circular frequency. A system of unit bases $\{\mathbf{e}_r, \mathbf{e}_\theta, \mathbf{e}_\phi\}$ is defined for spherical coordinates (r, θ, ϕ) ding to Figure 1. For the same coordinate system, the displacement vector $\mathbf{u}$ can be expressed in terms of displacement components u_r, u_θ and u_ϕ. Using Helmholtz decomposition the displacement field u can be n as

$$\mathbf{u} = \nabla\Phi + \nabla(r\Psi) \times \mathbf{e}_r + l\nabla \times \nabla \times (r\chi\mathbf{e}_r) \tag{2}$$

Φ, Ψ and χ are the three displacement wave potentials and l is a scalar factor to give the potentials the dimension. Substitution of equation (2) into (1) decomposes the equation of motion in terms of the three tials according to

$$(\nabla^2 + h^2)\Phi(\mathbf{x}, \omega) = 0 \tag{3a}$$

$$(\nabla^2 + k^2)\Psi(\mathbf{x}, \omega) = 0 \tag{3b}$$

$$(\nabla^2 + k^2)\chi(\mathbf{x}, \omega) = 0 \tag{3c}$$

∇^2 denotes the Laplacian in spherical coordinates and h and k are the longitudinal and shear iumbers, respectively.

ındary conditions on the surface of the half-space are given by

$$\sigma_{r\theta} = \sigma_{\theta\theta} = \sigma_{\theta\phi} = 0, \ \theta = \pi/2 \ (z = 0), \ \mathbf{x} \in C_0 \tag{4}$$

$\sigma_{r\theta}$, $\sigma_{\theta\theta}$ and $\sigma_{\theta\phi}$ are components of the stress tensor. Boundary conditions on the surface of the canyon efined by the following equations:

$$T_r = \sigma_{rr}n_r + \sigma_{r\theta}n_\theta + \sigma_{r\phi}n_\phi = 0, \ \mathbf{x} \in C_1 \tag{5a}$$

$$T_\theta = \sigma_{r\theta}n_r + \sigma_{\theta\theta}n_\theta + \sigma_{\theta\phi}n_\phi = 0, \ \mathbf{x} \in C_1 \tag{5b}$$

$$T_\phi = \sigma_{r\phi}n_r + \sigma_{\theta\phi}n_\theta + \sigma_{\phi\phi}n_\phi = 0, \ \mathbf{x} \in C_1 \tag{5c}$$

T_r, T_θ and T_ϕ are the components of the traction vector along the bases $\mathbf{e}_r$, $\mathbf{e}_\theta$ and $\mathbf{e}_\phi$, respectively, and n_r, l n_ϕ correspond to the components of the unit vector normal to the canyon surface C_1. For the slowness r in the xz-plane expressions for the components of displacement field and stress tensor can be found in erature.[14]

incident field consists of Rayleigh waves or oblique incident SH, SV or P waves. For slowness vectors i the xz-plane, expressions describing these incident fields can be found in recent papers by the present rs.[7,8] For slowness vectors located outside the xz-plane, the corresponding incident field is obtained gh rotation about the z-axis.

SOLUTION OF THE PROBLEM

incident wave strikes the surface of the canyon C_1, it is scattered back into the half-space. Therefore, the ield in the half-space consists of the free field and the scattered wavefield. The displacement field can be n in the following form:

$$\mathbf{u} = \mathbf{u}^{ff} + \mathbf{u}^s, \ \mathbf{x} \in D \tag{6}$$

superscripts s and ff denote the scattered and free field, respectively. The scattered wavefield can be ısed as a linear combination of the wave functions

$$\Phi^s = c^{\Phi}_{mn} h^{(2)}_n(hr) P^m_n(\cos\theta)\cos m\phi + s^{\Phi}_{mn} h^{(2)}_n(hr) P^m_n(\cos\theta)\sin m\phi \tag{7a}$$

$$m = 0, 1, \ldots, M, \ n = 0, 1, \ldots, N, \ M \leqslant N$$

$$\Psi^s = c^{\Psi}_{mn} h^{(2)}_n(kr) P^m_n(\cos\theta)\cos m\phi + s^{\Psi}_{mn} h^{(2)}_n(kr) P^m_n(\cos\theta)\sin m\phi \tag{7b}$$

$$m = 1, 2, \ldots, M, \ n = 1, 2, \ldots, N, \ M \leqslant N$$

$$\chi^s = c^x_{nm} h^{(2)}_n(kr) P^m_n(\cos\theta)\cos m\phi + s^x_{nm} h^{(2)}_n(kr) P^m_n(\cos\theta)\sin m\phi \qquad (7c)$$

$$m = 1, 2, \ldots, M,\ n = 1, 2, \ldots, N,\ M \leqslant N$$

where c_{nm} and s_{nm} are unknown coefficients. N and M are the orders of expansions. $h^{(2)}_n(kr)$ are spherical Hankel functions of the second kind and $P^m_n(\cos\theta)$ are associate Legendre polynomials.[15] Summation over repeated indices m and n is understood. The wave functions in equations (7) are solutions of the equation of motion consisting of outgoing waves. Therefore, these functions satisfy the radiation condition at infinity, however, they do not satisfy the stress-free boundary conditions along the surface of the half-space. These conditions must be imposed locally.

Once the scattered wavefield is expressed as a double series of the wave functions, it is necessary to determine the unknown expansion coefficients. Substitution of the scattered wavefield into the boundary conditions on the surface of the canyon [equations 5(a–c)] at L_1 collocation points, and into the boundary conditions on the surface of the half-space [equation (4)] at L_0 collocation points, results in a system of linear equation of the form

$$\mathbf{Gc} = \mathbf{f} \qquad (8)$$

where vector c contains the unknown expansion coefficients, vector f corresponds to the free-field stresses on the boundaries C_0 and C_1, and matrix G contains the wave functions and their derivatives. The size of matrix G is $(L \times K)$, where $L > K$ in order to solve equation (8) in the least-squares sense. Once the expansion coefficients are found, the displacement and stress fields can be evaluated throughout the elastic medium.

NUMERICAL RESULTS

Geometry of the canyon

The response of a non-axisymmetric canyon subjected to incident plane harmonic SH, SV, P and Rayleigh waves is discussed in this section. The canyon is in the form of a semi-ellipsoid defined by

$$C_1: x^2/a_1^2 + y^2/a_2^2 + z^2/a_3^2 = 1,\ z > 0 \qquad (9)$$

where a_1, a_2 and a_3 are the principal axes of the ellipsoid along the Cartesian coordinates x, y and z, respectively. Results are presented for spherical canyons ($a_1 = a_2 = a_3$) and prolates ($a_1 \neq a_2 = a_3$). A spherical canyon is considered in order to test the method with the available results in the literature and also for comparison with non-axisymmetric models. The prolate type of canyon is chosen since it possess non-axisymmetric features of a general three-dimensional model and facilitates comparison with existing two-dimensional models. This serves also as an additional test of the numerical results. Namely, by assigning sufficiently large values to one of the principal axes of the prolate (in the direction normal to the vertical plane containing the slowness vector of an incident wave), it is possible to make a systematic comparison with available solutions in the literature for cylindrical canyons.[7,8] More about that will be discussed later in this section.

Conventions

The slowness vector of the incident wave (referred to hereafter as the slowness vector) is specified by two angles, the azimuthal angle of incidence, ϕ_0, and the off-vertical angle of incidence, θ_0 (Figure 1). A slowness plane is defined as a vertical plane which contains the slowness vector. The out-of-plane direction is referred to as the direction normal to the slowness plane. The in-plane motion is defined as a motion which takes place in a slowness plane.

The following dimensionless variables are introduced. The density ρ and shear wave velocity β for the half-space material are assumed to be equal to unity and, unless stated differently, the longitudinal wave velocity α is taken to be two. All of the distances are normalized with respect to the half-width of the canyon along the y-axis (a_2). In addition to the actual frequency ω, a dimensionless frequency Ω is introduced as the ratio of the maximum width of a cross-section of the canyon (lying in the slowness plane passing through the centre of the

canyon) and the wavelength of the incident shear wave. For convenience, all numerical results for the surface displacement field are displayed in terms of the Cartesian components u, v, and w.

Testing of results

Numerical accuracy of the proposed method is first assessed through comparison with available results in the literature. For a spherical canyon subjected to a vertical plane harmonic P wave the results are compared with those of Sanchez-Sesma.[9] The surface displacement field for stations along the x-axis is depicted by Figures 2(a) and (b) for two different frequencies of incident wave. The present results are in very good agreement with those obtained previously. In order to test the accuracy of the present technique for non-axisymmetric geometries and obliquely incident waves, a prolate type of canyon is considered next. The

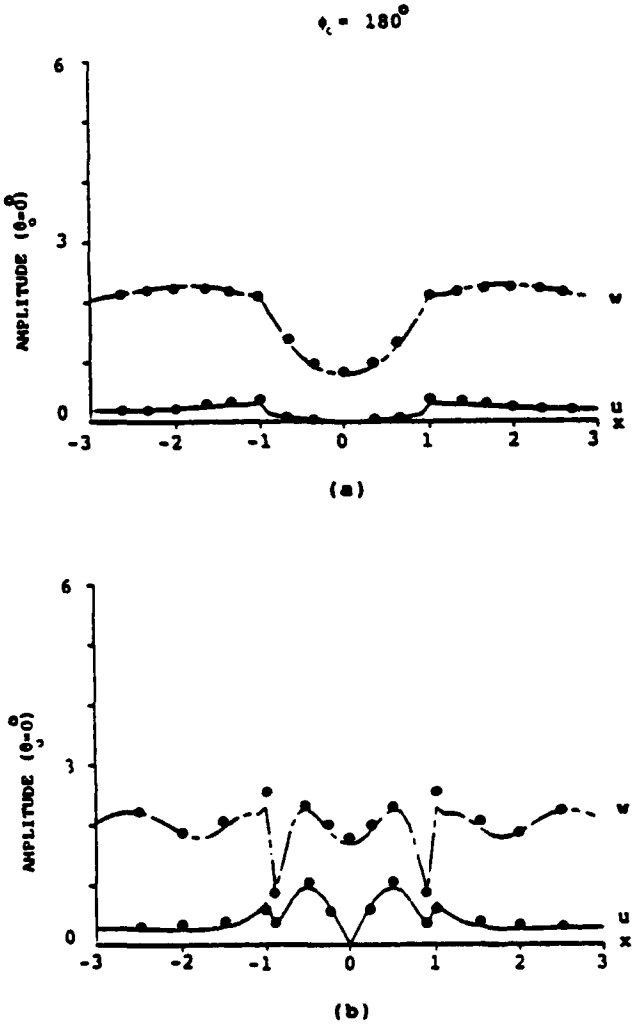

Figure 2. Amplitude of components of the surface displacement field along the x-axis for vertically incident P waves and a hemispherical canyon: (a) dimensionless frequency $\Omega = 0{\cdot}433$; (b) $\Omega = 1{\cdot}299$. Throughout, u, v and w correspond to the component of the displacement field along x-, y- and z-directions, respectively. Solid and dashed lines correspond to the results of this investigation for u- and w-components of the displacement field, respectively, while dots correspond to results of Sanchez-Sesma.[9] The following material properties are assumed: $\beta = \rho = 1$. $\alpha = 1{\cdot}732$. The radius of the canyon is one. The order of the expansion terms M and N, and the number of collocation points on the surface of the canyon L_1 and on the surface of the half-space L_0 are considered to be the following: $M = 0$, $N = 15$, $L_0 = 30$, $L_1 = 56$

canyon is subjected to an incident P wave with a slowness vector in the yz-plane ($\phi_0 = -90°$). The relatively large width of the canyon in the out-of-plane direction ($a_1 = 3, a_2 = a_3 = 1$) allows a comparative study of the results with those of a similar two-dimensional (cylindrical) model. Namely, the attenuated scattered waves from elongated edges reaching the yz-plane may not significantly affect the total scattered wavefield. Figures 3(a)–(c) correspond to the three-dimensional model while Figures 3(d)–(f) correspond to results obtained

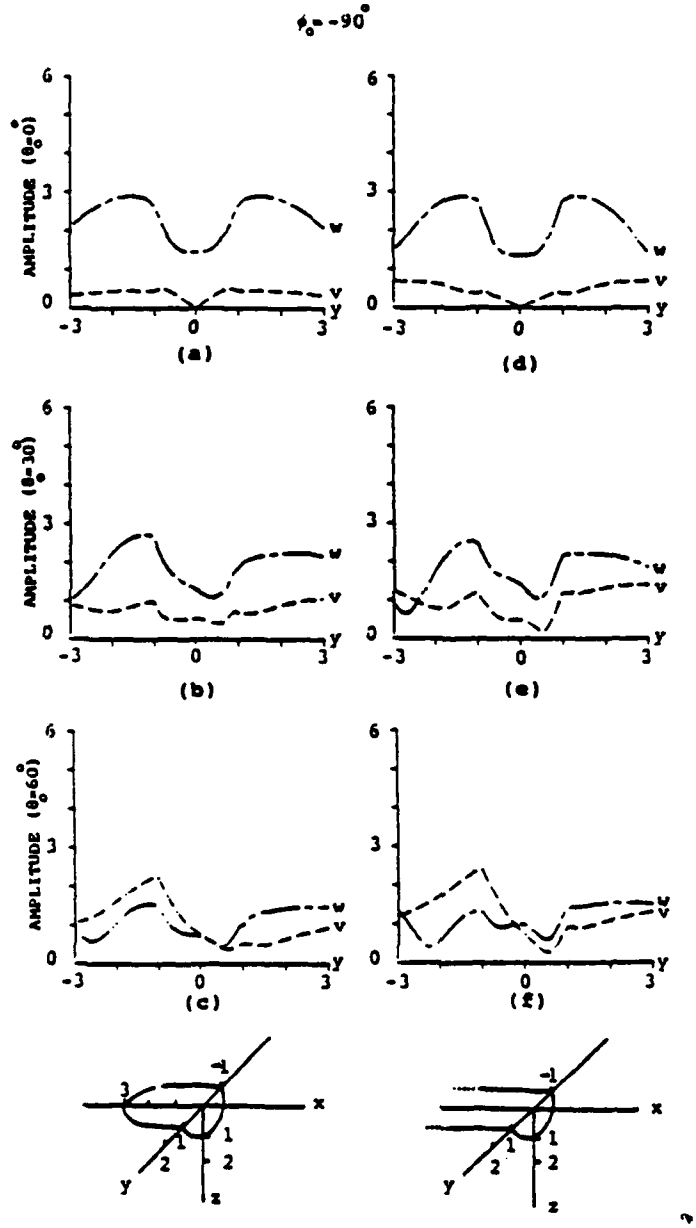

Figure 3. Amplitude of v- and w-components of the surface displacement field for stations along the y-axis. Graphs 3(a)–(c) correspond to the results for a prolate type canyon with principal axes $a_1 = 3$ and $a_2 = a_3 = 1$, while graphs 3(d)–(f) correspond to the results for a cylindrical canyon with unit radius. Both canyons are subjected to the same incident P waves with slowness vectors lying in the yz-plane ($\phi_0 = 90°$). Three off-vertical angles of incidence are considered: $\theta_0 = 0°$, 30° and 60°. The geometry of the canyons (cut by the slowness plane) is shown in the lower section of the figure. $\Omega = 0{\cdot}5$ (relative to a_2). The following parameters are assumed hereafter throughout the figure captions: $\beta = \rho = 1$, $\alpha = 2$, $M = 3$, $N = 9$, $L_0 = 96$, $L_1 = 80$

previously for a two-dimensional model by the present authors using a similar cylindrical wave expansion technique.[7,8] The model geometries (cut by the slowness plane to show the direction of incidence) are illustrated at the bottom of the figure. The results of Figure 3 show that the surface displacement field for the two models is similar for all angles of incidence. This gives further confidence into the accuracy of the present technique in handling the non-axisymmetric models. Such similarity can be observed for incident SH, SV and Rayleigh waves as well.

Response of a prolate canyon

Figures 4 to 8 correspond to the displacement field for a prolate type canyon ($a_1 = 2$, $a_2 = a_3 = 1$). Results are presented for incident SH, P and Rayleigh waves for two azimuthal angles of incidence. In addition, three different off-vertical angles of incidence are assumed for incident SH and P waves. Although the actual frequency of the incident wave is the same for all these figures, the dimensionless frequency is one (normalized relative to a_1) for an azimuthal angle of incidence $\phi_0 = 180°$, while it reduces to one-half for $\phi_0 = -90°$ (normalized relative to a_2). In these figures the graphs on the left-hand side correspond to the displacement field for observation stations along the x-axis and the ones on the right-hand side correspond to stations along the y-axis. For incident SH waves the results for azimuthal angles of incidence ϕ_0 of 180° and −90° are presented in Figures 4 and 5, respectively. For incident SH waves with slowness vectors lying in the xz-plane, the results on the left-hand side of Figure 4 show that the motion in the xz-plane takes place in the y-direction only (out-of-plane direction). This is due to the symmetrical features of the model and is in agreement with what is observed in the two-dimensional approximation (antiplane strain model). However, for stations along the y-axis [Figures 4(d)–(f)] all three components of the displacement field may be present. Apparently, the two displacement components u, w, non-existent in the two-dimensional approximation, could have substantial amplitudes. Results for incident SH waves with slowness vectors lying in the yz-plane are shown in Figure 5. It is interesting to observe how a change of the canyon width in the out-of-plane direction affects the displacement field. It should be noted that the displacement field for stations along the x-axis (the y-axis) of Figure 4 must be compared with the displacement field along the y-axis (the x-axis) of Figure 5. By taking into account that the results of Figure 5 correspond to a much wider canyon in the out-of-plane direction, one sees basically no drastic change in the pattern and amplitude of the main component of the displacement field between the results of Figures 4 and 5. This main component of displacement for incident SH waves is in the out-of-plane direction and is specified in Figures 4 and 5 by the v- and u-components, respectively. However, the results for the narrower (in the out-of-plane direction) canyon show much larger amplitudes for the two non-predominant components of displacement [Figures 4(d)–(f)] than for the wider canyon [Figures 5(a)–(c)]. This is expected, because as the edges of the canyon get further apart in the out-of-plane direction, the model approaches further and further to a cylindrical geometry (antiplane strain model), where the two non-predominant components of displacement are non-existent. This sharp increase in amplitude of the two non-predominant components of displacement for a model with smaller width in the out-of-plane direction is an important characteristic of the three-dimensional models studied here.

Figures 6 and 7 correspond to incident P waves with slowness vectors lying in the xz- and yz-planes, respectively. Similarly to the two-dimensional approximation, for observation stations along the x-axis in Figure 6 and the y-axis in Figure 7, the displacement field consists only of two components which constitute the in-plane motion. However, for stations along the axis in the out-of-plane direction (y in Figure 6 and x in Figure 7) an additional SH mode conversion occurs for oblique incidences. Considering the same rule of comparison between the incidences with azimuthal angles $\phi_0 = 180°$ and $\phi_0 = -90°$, explained for the SH case, we observe that, for incident P waves with slowness vectors lying in the xz-plane, the two in-plane components of displacement (u and w in Figure 6) display characteristics similar to those of their counterparts (v and w in Figure 7) for the incidences with slowness vectors lying in the yz-plane.

Results for incident Rayleigh waves with slowness vectors lying in the xz- and yz-planes are depicted by Figures 8(a), (b) and (8(c), (d), respectively. Considering the same rule of comparison as discussed for two types of incident SH waves with azimuthal angles of incidence $\phi_0 = 180°$ and $\phi_0 = -90°$, one observes similar characteristics between components of displacement for the two incident Rayleigh waves. Analogously to the incident P waves, an additional component of displacement field in the out-of-plane direction appears for the

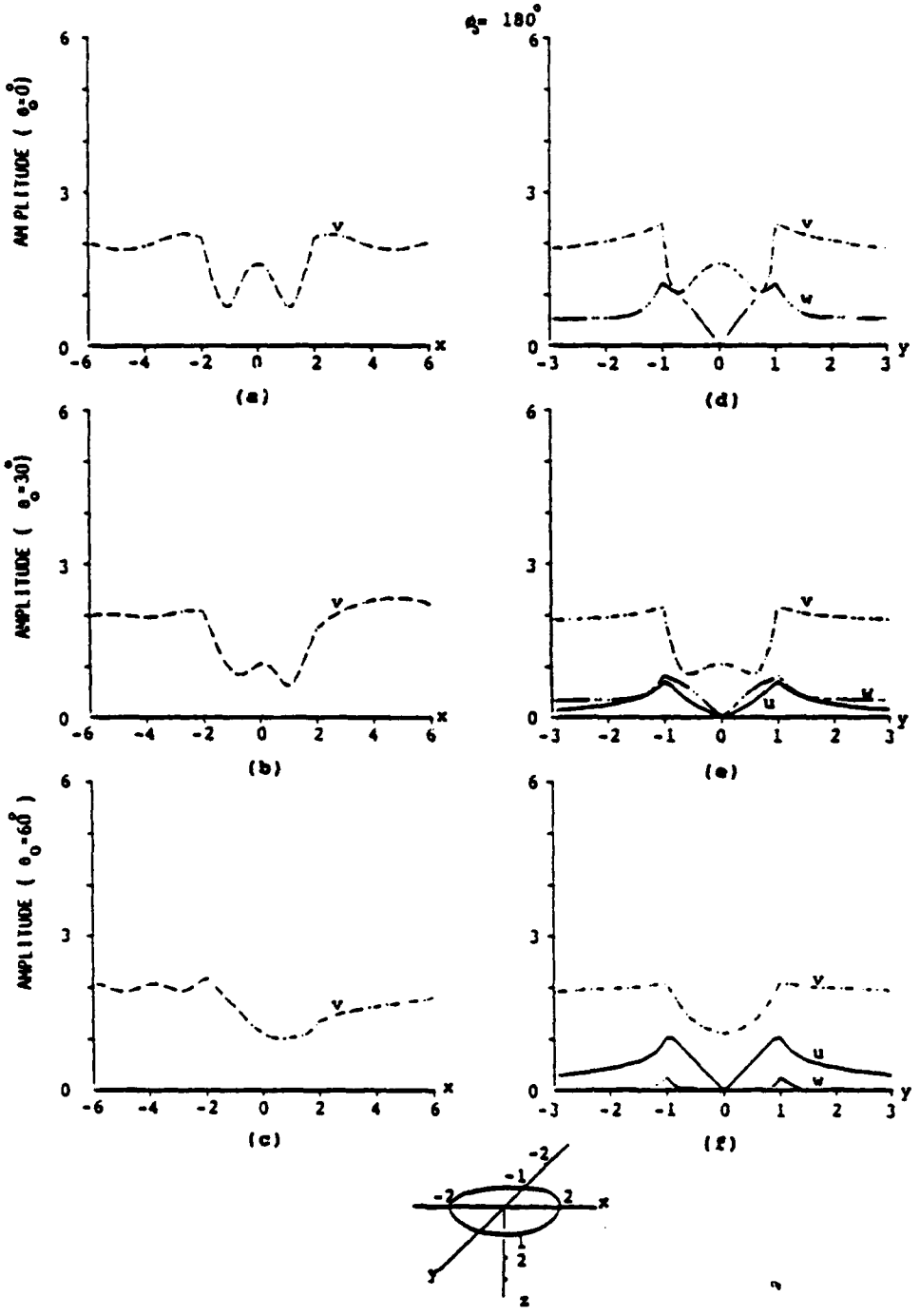

Figure 4. Surface displacement amplitudes at stations along the x- and y-axes for incident SH waves ($\phi_0 = 180°$) and a prolate type canyon ($a_1 = 2, a_2 = a_3 = 1$). Graphs on the left and right-hand sides correspond to the observation stations along the x- and the y-axes, respectively. $\Omega = 1$ (relative to a_1)

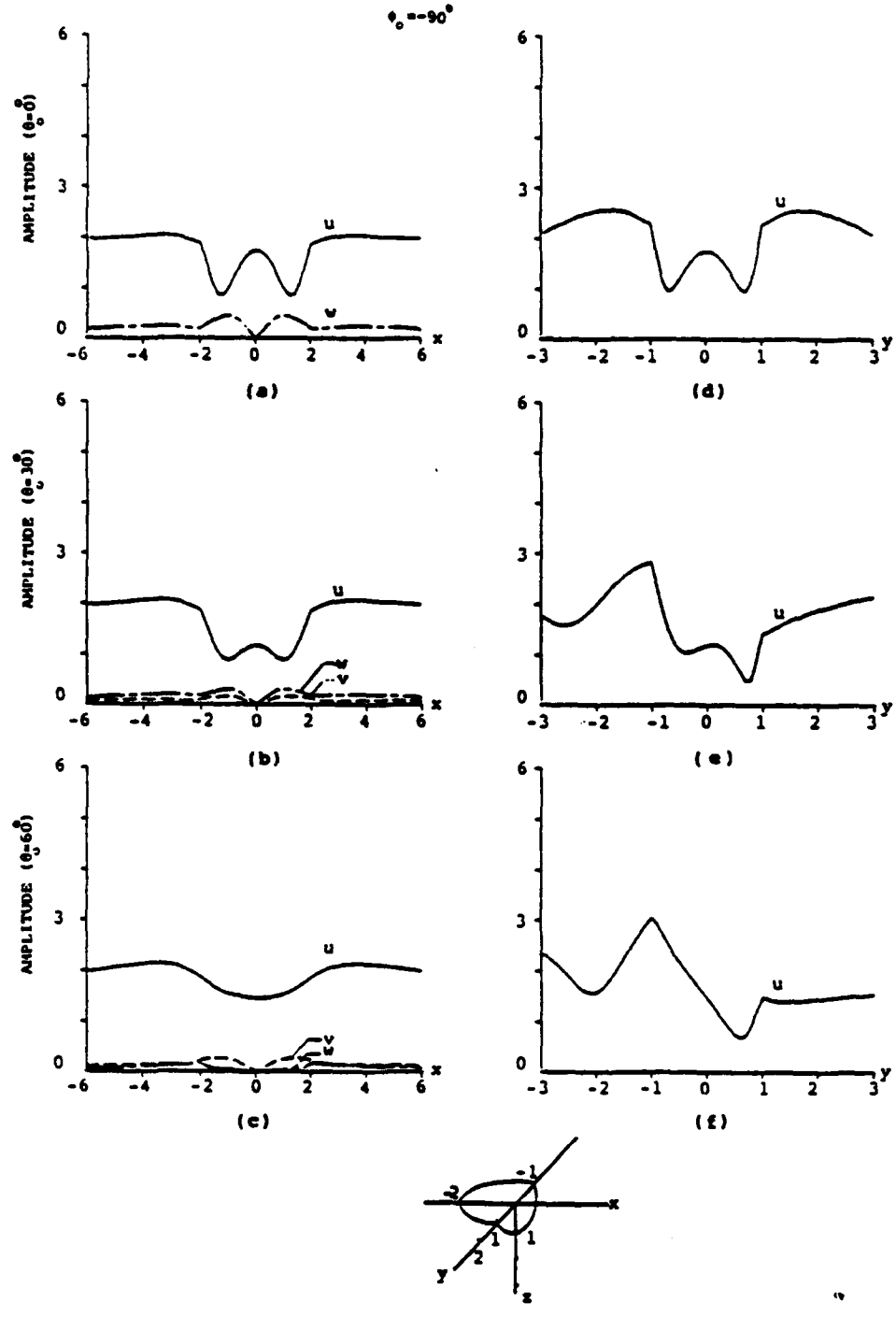

Figure 5. Surface displacement amplitudes at stations along the x- and y-axes for incident SH waves ($\phi_0 = -90°$) and a prolate type canyon ($a_1 = 2$, $a_2 = a_3 = 1$). $\Omega = 0.5$ (relative to a_2)

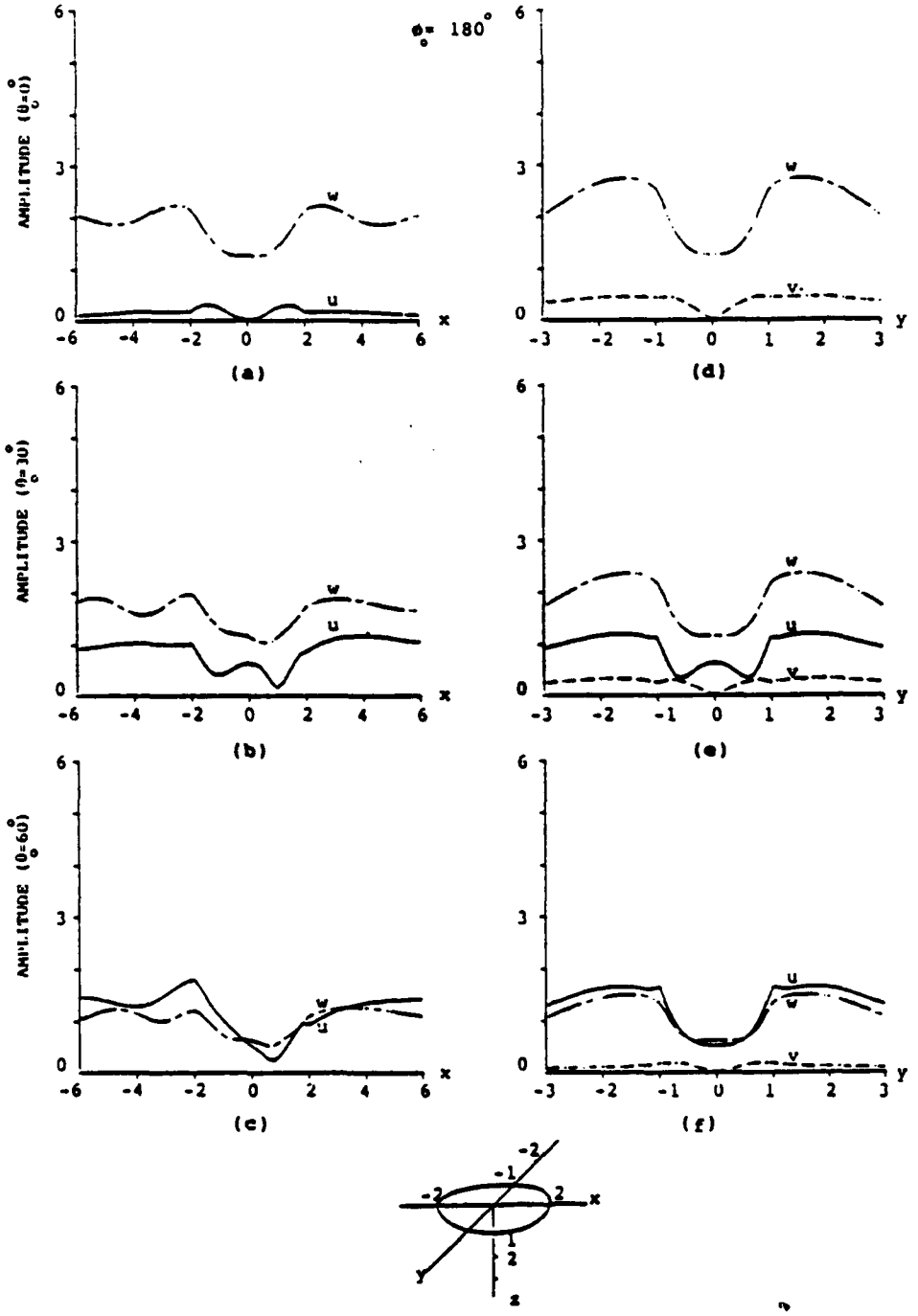

Figure 6. Surface displacement amplitudes at stations along the x- and y-axes for incident P waves ($\phi_0 = 180°$) and a prolate type canyon ($a_1 = 2$, $a_2 = a_3 = 1$). $\Omega = 1$ (relative to a_1)

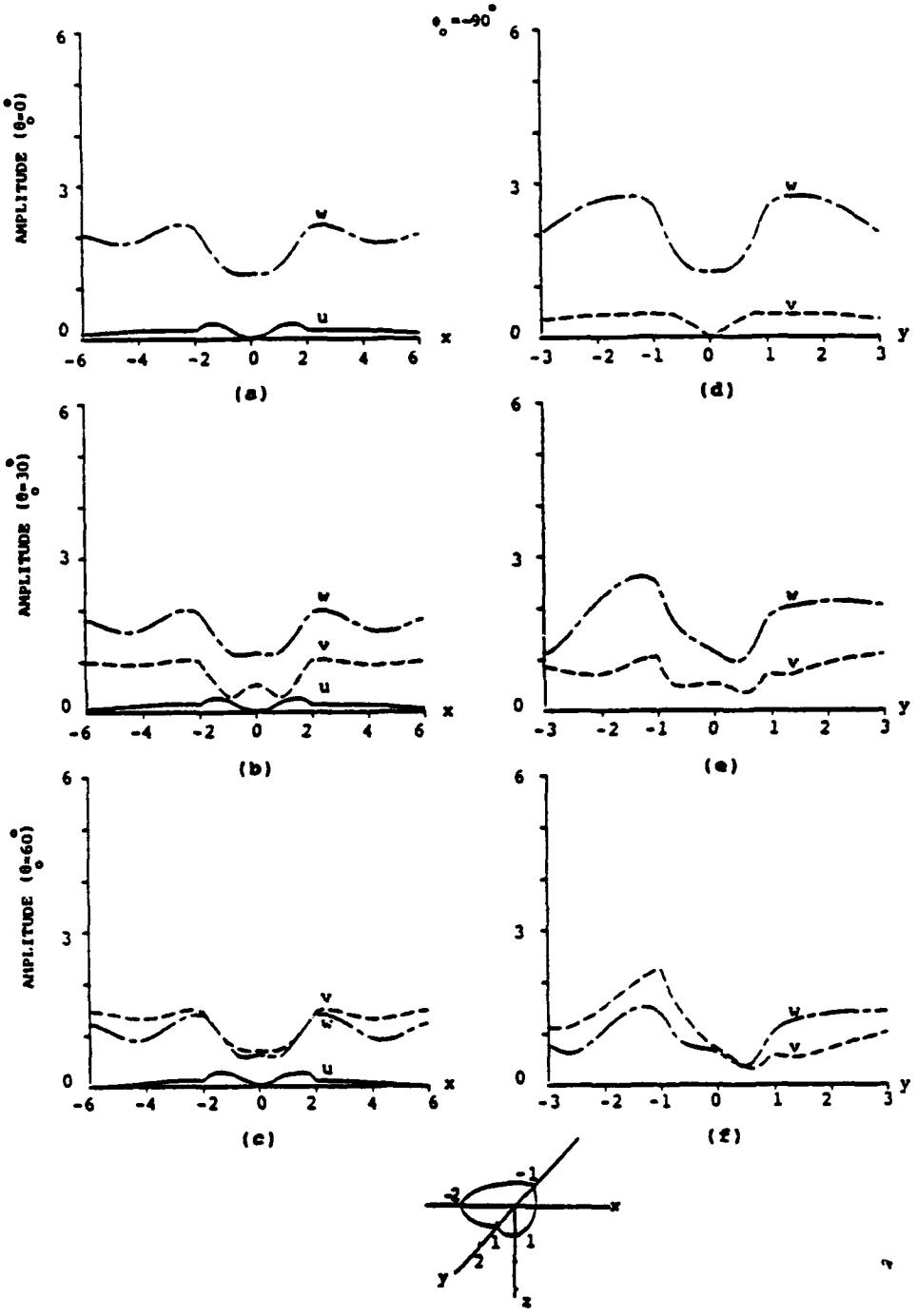

Figure 7. Surface displacement amplitudes at stations along the x- and y-axes for incident P waves ($\phi_0 = -90°$) and a prolate type canyon ($a_1 = 2$, $a_2 = a_3 = 1$), $\Omega = 0{\cdot}5$ (relative to a_2)

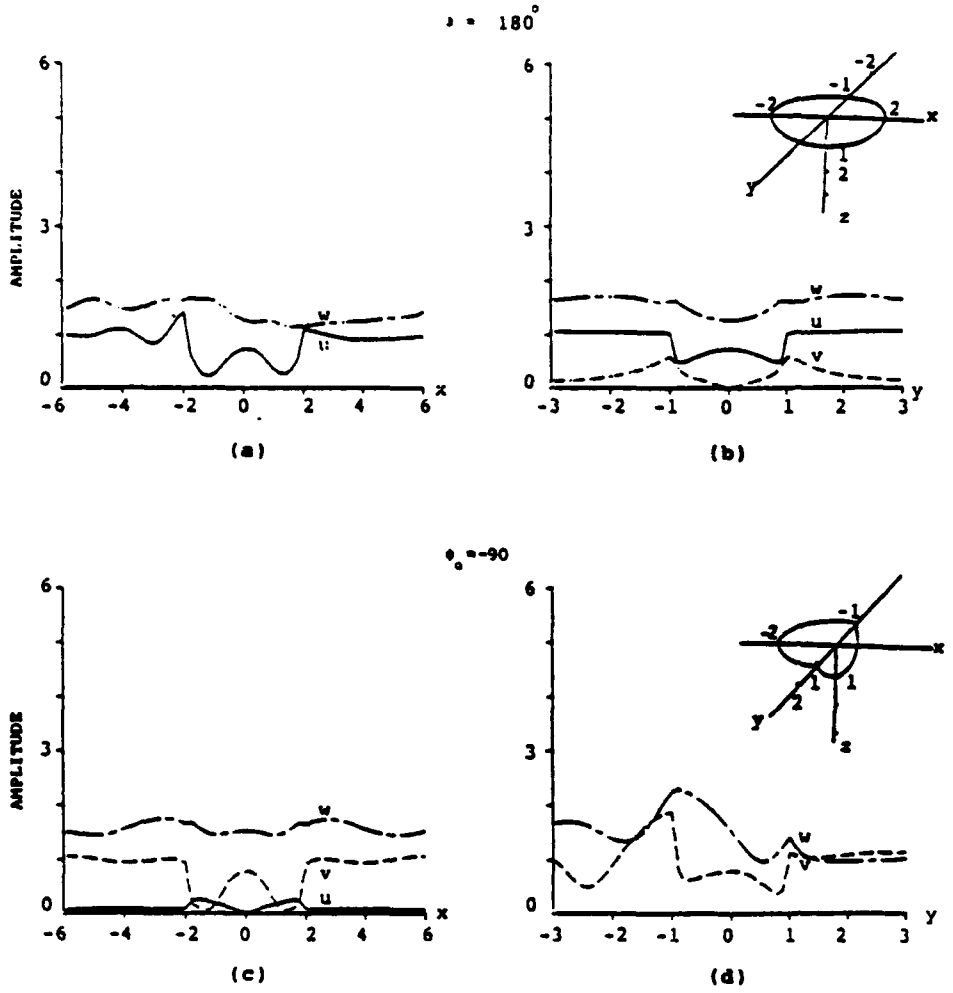

Figure 8. Surface displacement amplitudes at stations along the x- and y-axes for incident Rayleigh waves with slowness vectors lying in the xz-plane [8(a), (b)] and yz-plane [8(c), (d)] for a prolate type canyon ($a_1 = 2$, $a_2 = a_3 = 1$). In Figures 8(a), (b) and 8(c), (d) $\Omega = 1$ (relative to a_1) and $\Omega = 0{\cdot}5$ (relative to a_2), respectively

stations along the y-axis in Figure 8(b) and the x-axis in Figure 8(c). These components of displacement do not exist in the two-dimensional models.

Response comparison for the prolate, spherical, and cylindrical canyons

The results presented so far (Figures 4 to 8) demonstrate that a change in the azimuthal angle of incidence may greatly affect the surface displacement field. This observation emphasizes the need for three-dimensional modelling of actual surface irregularities, since two-dimensional approximations may result in a poor assessment of the actual displacement field. To elaborate further upon this need for a three-dimensional analysis and to find limitations on the application of two-dimensional models, responses for canyons in the form of a prolate and a sphere are compared with those of a cylindrical canyon. The prolate is considered to be narrow in the out-of-plane direction ($a_1 = 0{\cdot}5$, $a_2 = a_3 = 1$). The maximum width of these canyons in the y-direction is the same in order to make realistic comparisons. Figures 9 and 10 correspond to a comparative study of the displacement field response for the three different canyons to incident SH, SV waves, respectively, with slowness vectors lying in the yz-plane. The results corresponding to the cylindrical model are obtained in

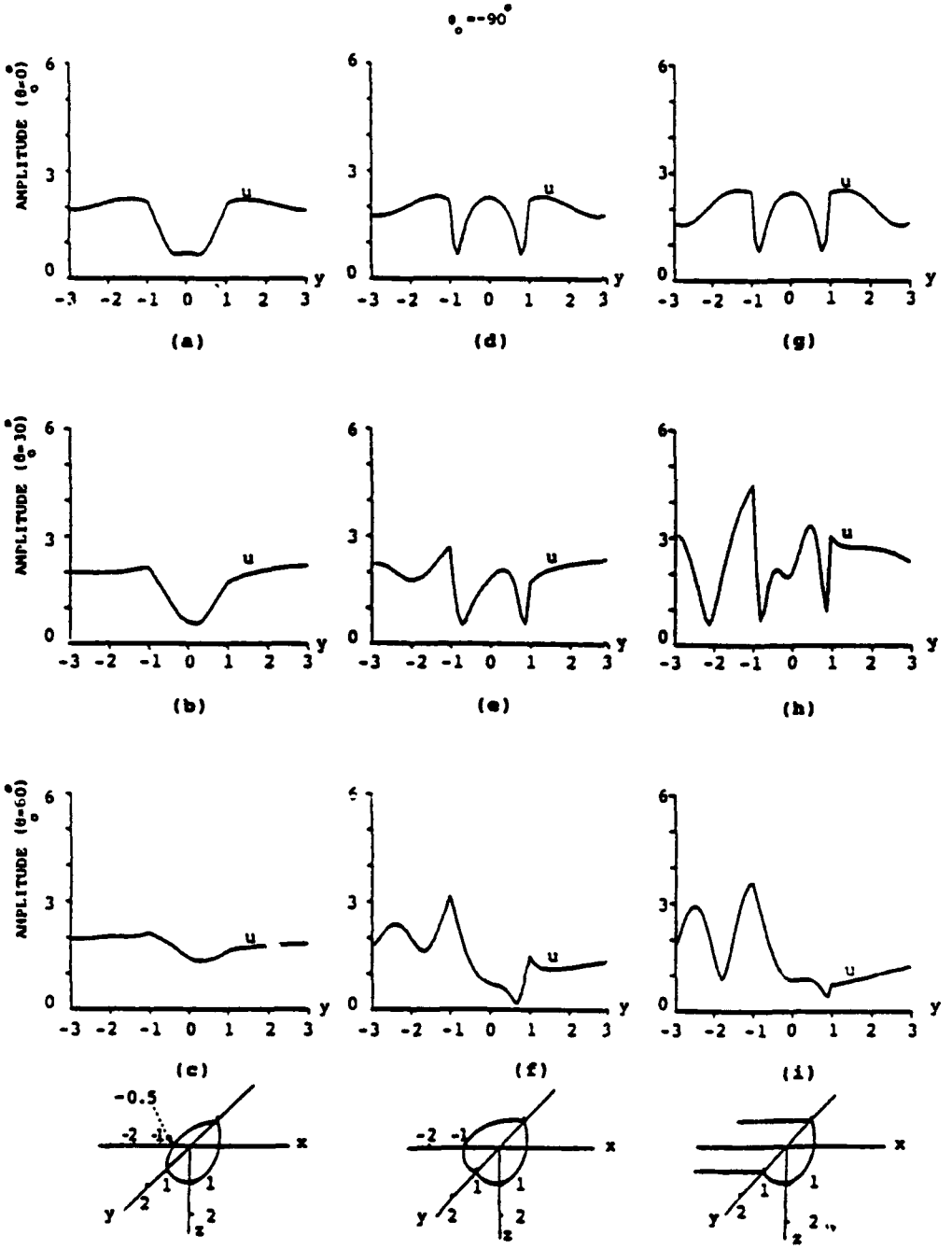

Figure 9. Amplitude of the main component of the surface displacement field (u-component) at stations along the y-axis for incident SH waves ($\phi_0 = -90°$) for a prolate type canyon with principal axis $a_1 = 0{\cdot}5$ and $a_2 = a_3 = 1$ [9(a)–(c)], a spherical canyon [9(d)–(f)] and a cylindrical canyon [9(g)–(i)]. $\Omega = 0{\cdot}75$ (relative to a_2)

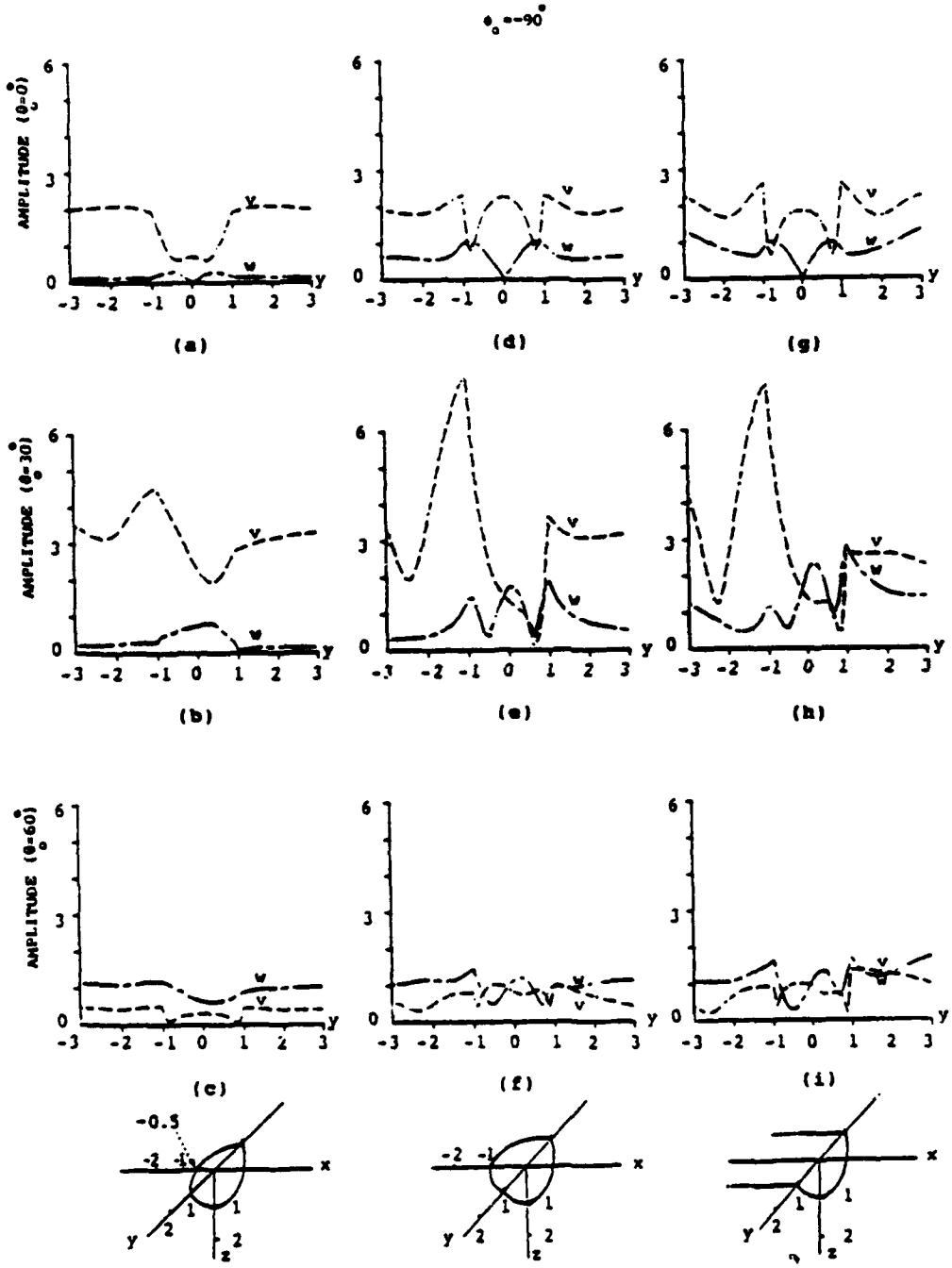

Figure 10. Amplitude of the components of in-plane motion (v- and w-components) along the y-axis for incident SV waves ($\phi_0 = 90°$) and a prolate type canyon with principal axes $a_1 = 0{\cdot}5$, $a_2 = a_3 = 1$ [10(a)–(c)], a spherical canyon [10(d)–(f)] and a cylindrical canyon [10(g)–(i)]. $\Omega = 0{\cdot}75$ (relative to a_2)

n earlier study b; ..e present authors[7,8] using a cylindrical wave function expansion technique. For incident H waves (Figure 9) only the out-of-plane component of displacement is presented to facilitate comparison ith two-dimensional models. Similarity between the results for the spherical and cylindrical models is pparent in Figure 9. However, the narrow canyon exhibits completely different characteristics of the main mponent of the surface displacement field. Results for incident SV waves are depicted by Figure 10. Only ie in-plane motion (in the slowness plane) is considered here. Apparently, similarity between the response of herical and cylindrical canyons is even stronger than in the case of incident SH waves (Figure 9). However, ie difference between the results for the narrow canyon and the other two models is still very pronounced. imilar observations are made for incident P and Rayleigh waves. The results of Figures 9 and 10 show that, r a narrow prolate type canyon, a clear reduction occurs for the in-plane components of the displacement eld in comparison to the other two models.

umerical aspects of the method

At this point it is of interest to elaborate further about some numerical aspects of the solution. It has been bserved that in solving the steady state problem at low and moderate frequencies only a small number of pansion terms and observation points are needed. For the range of frequencies studied here, the results hibit good accuracy with an azimuthal order of expansion $M = 3$. However, the convergence of the results is ore sensitive upon the second order of expansion N. For low and moderate frequencies, say $\Omega < 1{\cdot}5$, nerally $N = 9$ provides acceptable convergence. The number of collocation points L_0 and L_1, and their cations on the surface of the canyon and the half-space, play an important role in the accuracy of the results. ollocation points are distributed on elliptical contours on the surface of the canyon. These contours are ually spaced at different elevations from $z = 0$ to $z = a_3$. For low and moderate frequencies eight contours roduce accurate results. Collcation points are uniformly distributed along these contours. A total of 80 llocation points is distributed in this way on the surface of the canyon. In order to satisfy the traction-free oundary condition on the surface of the half-space, a number of elliptical contours, following the shape of the nyon edge, are considered on the surface of the half-space. These contours are equally spaced from the edge the canyon up to three times the width of the canyon at the surface of the half-space. A total of 96 llocation points uniformly distributed on these contours produced good accuracy of the results. As the equency of the incident wave increases, the number of collocation points and expansion terms needed for nvergence increases as well. This results in a more extensive computation. What makes the computation pensive is the inversion of relatively large matrices in solving the least-squares problem [see equation (8)]. general, the following criterion has been used to establish the convergence of the results: as the number of pansion terms and collocation points increases, the results are accepted as the final ones if the maximum fference between two successive calculations of the surface displacement field is sufficiently small (less than 4 r cent).

CONCLUSIONS

he response of a non-axisymmetric three-dimensional canyon for different angles of incidence of plane rmonic SH, SV, P and Rayleigh waves is investigated by using the wave function expansion technique. The ave functions describe the unknown scattered wavefield. These functions do not satisfy stress-free boundary nditions at the surface of the half-space. These conditions, in addition to the traction-free boundary ndition on the surface of the canyon, are locally imposed at a number of points on the surface of the half- ace and on the surface of the canyon.

The results presented provide a basic understanding of the scattering phenomenon due to non- isymmetric three-dimensional canyons. A comparative study is done to show the validity and limitation of e corresponding two-dimensional approximations (antiplane and plane strain models). For the range of equencies studied here, it is shown that, even for the cases where two- and three-dimensional results match osely for the main components of displacement field, the two-dimensional approximation will ignore an out- -plane displacement component for the case of incident P, SV and Rayleigh waves and an in-plane motion r the case of incident SH waves which may have significant amplitudes. This is particularly evident for the

cases of incident SH waves. Results clearly demonstrate that, when the edges of the canyon in the out-of-plane direction (with respect to the slowness plane) are close to each other, the three-dimensional nature of the problem is essential and it can not be modelled by two-dimensional approximations. Therefore, this strongly suggests that a complete description of the site phenomenon in strong ground motion will require, in general, a three-dimensional modelling of actual irregularities.

ACKNOWLEDGEMENTS

This material is based upon work supported in part by the National Science Foundation under Grant No. 53–4519–3792 and in part by the Office of Naval Research under Contract No. N00014–88–K–0157.

REFERENCES

1. J. L. King and B. E. Tucker, 'Observed variations of earthquake motion across a sediment-filled valley', *Bull. seism. soc. Am.* 74, 137–151 (1984).
2. M. Dravinski and T. K. Mossessian, 'Scattering of plane harmonic P, SV, and Rayleigh waves by dipping layers of arbitrary shape', *Bull. seism. soc. Am.* 77, 212–235 (1987).
3. D. M. Cole, D. D. Kosloff and J. B. Minster, 'A numerical boundary integral equation method for elastodynamics', *Bull. seism. soc. Am.* 68, 1331–1357 (1978).
4. T. K. Mossessian and M. Dravinski, 'Application of a hybrid method for scattering of P, SV and Rayleigh waves by near surface irregularities', *Bull. seism. soc. Am.* 77, 1784–1803 (1987).
5. W. D. Smith, 'The application of finite element analysis to body wave propagation problems', *Geophys. roy. astr. soc.* 42, 747–768 (1975).
6. F. J. Sanchez-Sesma, M. A. Bravo and I. Herrera, 'Surface motion of topographical irregularities for incident P, SV, and Rayleigh waves', *Bull. seism. soc. Am.* 75, 263–269 (1985).
7. H. Eshraghi and M. Dravinski, 'Transient scattering of elastic waves by dipping layers of arbitrary shape. Part 1. Antiplane strain model', *Earthquake eng. struct. dyn.* 18, 397–415 (1989).
8. H. Eshraghi and M. Dravinski, 'Transient scattering of elastic waves by dipping layers of arbitrary shape. Part 2. Plane strain model', *Earthquake eng. struct. dyn.* 18, 417–434 (1989).
9. F. J. Sanchez-Sesma, 'Diffraction of elastic waves by three-dimensional surface irregularities', *Bull. seism. soc. Am.* 73, 1621–1636 (1983).
10. V. W. Lee, 'Three-dimensional diffraction of plane P, SV, and SH waves by a hemispherical alluvial valley', *Soil dyn. earthquake eng.* 3, 133–144 (1984).
11. S. Day, 'Finite element analysis of seismic scattering problem', *Ph.D. Thesis*, UC San Diego, California, 1977.
12. R. J. Apsel, 'Dynamic Green's functions for layered media and applications to boundary value problems', *Ph.D. Thesis*, UC San Diego, California, 1979.
13. V. Avanessian, R. Muki and S. B. Dong, 'Axisymmetric soil–structure interaction by global–local finite elements', *Earthquake eng. struct. dyn.* 14, 355–367, 1986.
14. Y.-H. Pao and C. C. Mow, *Diffraction of Elastic Waves and Dynamic Stress Concentrations*, Crane Russak, New York, 1973.
15. M. Abramowitz and I. A. Stegun, *Handbook of Mathematical Functions*, Dover, New York, 1972.

Scattering of Elastic Waves by Nonaxisymmetric Three-Dimensional Dipping Layer

Hossein Eshraghi and Marijan Dravinski
Department of Mechanical Engineering, University of Southern California, Los Angeles, California 90007

Using a boundary method, we investigated the scattering of elastic plane harmonic SH, SV, P, and Rayleigh waves by three-dimensional nonaxisymmetric dipping layers embedded in an elastic half-space. The valley was subjected to incident Rayleigh wave and oblique incident SH, SV, and P waves. The method utilized spherical wave functions to express the unknown scattered field. These functions satisfy the equation of motion and radiation conditions at infinity but they do not satisfy the stress-free boundary conditions at the surface of the half-space. The boundary and continuity conditions are imposed locally in the least-square-sense at several points on the layer interface and on the surface of the half-space. A comparative study was done to examine the validity and limitations of the two-dimensional approximations (antiplane and plane strain models) of three-dimensional models. It is demonstrated that the two-dimensional approximations may be inadequate to represent actual displacement field for three-dimensional irregularities.

I. INTRODUCTION

In studying the effects of local site upon strong ground motion, researchers mostly directed their efforts to solving the problems of ground motion amplification by using simplified two-dimensional models.* The validity and limitations of these simplified models were always a matter of speculation, since available solutions to the three-dimensional models were limited to only axisymmetric geometries. Recent advances in computational techniques made certain numerical approaches applicable to more realistic problems of local site effects (Eshraghi and Dravinski [3]). The wave expansion method, which we use here, is one of these techniques. This method uses a series of spherical wave functions to represent the scattered wave fields. These wave functions satisfy the equations of motion and radiation conditions at infinity, but they do not satisfy the traction-free boundary condition on the surface of the half-space, which must be imposed locally. The approach originates in the works of Herrera and Sabina [4] and Herrera [5] and has been successfully applied by a number of researchers to two-dimensional diffraction problems of interest in strong ground motion seismology. Only papers dealing with three-dimensional scattering problems are discussed in this paper.

*For a detailed review of such two-dimensional modeling, see the recent two-part paper by Eshraghi and Dravinski [1, 2].

Numerical Methods for Partial Differential Equations, 5, 327–345 (1989)

CCC 0749-159X/89/04327-19$04.00

Sanchez-Sesma [6] used the wave function expansion technique to solve diffraction problems for three-dimensional axisymmetric scatterers and vertically incident P waves. Lee [7, 8] used similar approach to study scattering problems for a hemispherical canyon and alluvium. Apsel [9] considered a boundary integral equation (BIE) method for studying soil-structure interaction for axisymmetric scatterers. Lee and Langston [10] used a ray method to solve the transient problem for amplification of ground motion by an axisymmetric scatterer. In all of these papers the scatterers were assumed to be axisymmetric. Recently, we extended the wave expansion technique to study diffraction of seismic waves by nonaxisymmetric surface irregularities (Eshraghi and Dravinski [3]). In that paper we provided a detailed comparative study between the responses of two- and three-dimensional canyons subjected to incident Rayleigh wave and obliquely incident SH, SV, and P waves. In this paper we extend that work to nonaxisymmetric valleys. We subject the valley to incident Rayleigh wave and obliquely incident SH, SV, and P waves, and, in addition to a parametric study of three-dimensional results, include a comparison between the two- and three-dimensional dipping layers. Validity and limitations of the two-dimensional approximations are also examined for a class of problems at hand.

II. STATEMENT OF THE PROBLEM

Geometry of the problem is depicted by Figure 1. The model consists of a soft dipping layer embedded within an elastic half-space. Throughout the paper C_0 denotes the surface of the half-space and the valley at $z = 0$, while C_1 denotes the interface between the layer and the half-space. Domains D_0 and D_1 correspond to the half-space and the dipping layer, respectively. Summation over repeated indices is understood. *Underlined indices indicate that the summation is being suppressed.* The layer interface C_1 is assumed to be smooth, without sharp corners. Material of the medium is chosen to be linearly elastic, homogeneous, and isotropic. The half-space is subjected to incident plane harmonic SH, SV, P, or Rayleigh waves.

Steady-state equation of motion in a three-dimensional media, in the absence of body forces, is defined in a vector form by

$$\mu_j \nabla^2 \underline{u}_j + (\lambda_j + \mu_j)\nabla\nabla \cdot \underline{u}_j + \omega^2 \underline{u}_j = \underline{0}, \underline{x}_j \in D_j, \qquad (j = 0, 1) \qquad (1)$$

where subscripts $j = 0$ and 1 correspond to the half-space and dipping layer, respectively, $\underline{x}_j$ is a position vector while $\underline{u}_j$ denotes the displacement vector. Lame's constants are denoted by λ_j and μ_j, and ω is the circular frequency. A system of unit basis $\{\underline{e}_r, \underline{e}_\theta, \underline{e}_\phi\}$ is defined for a spherical coordinates (r, θ, ϕ) according to Figure 1. For the same coordinate system the displacement vector $\underline{u}_j$ can be expressed in terms of three displacement components u_r, u_θ, and u_ϕ. Using the Helmholtz decomposition the displacement field $\underline{u}$ can be written as

$$\underline{u}_j = \nabla\Phi_j + \nabla(r\Psi_j) \times \underline{e}_r + \ell_j \nabla \times \nabla \times (r\chi_j \underline{e}_r), \qquad (j = 0, 1) \qquad (2)$$

where Φ_j, Ψ_j, and χ_j are the three displacement wave potentials for the jth layer and ℓ is a scalar factor to give potentials the same dimension. Substitution of Eq. (2) into (1) decomposes the equation of motion in terms of the three po-

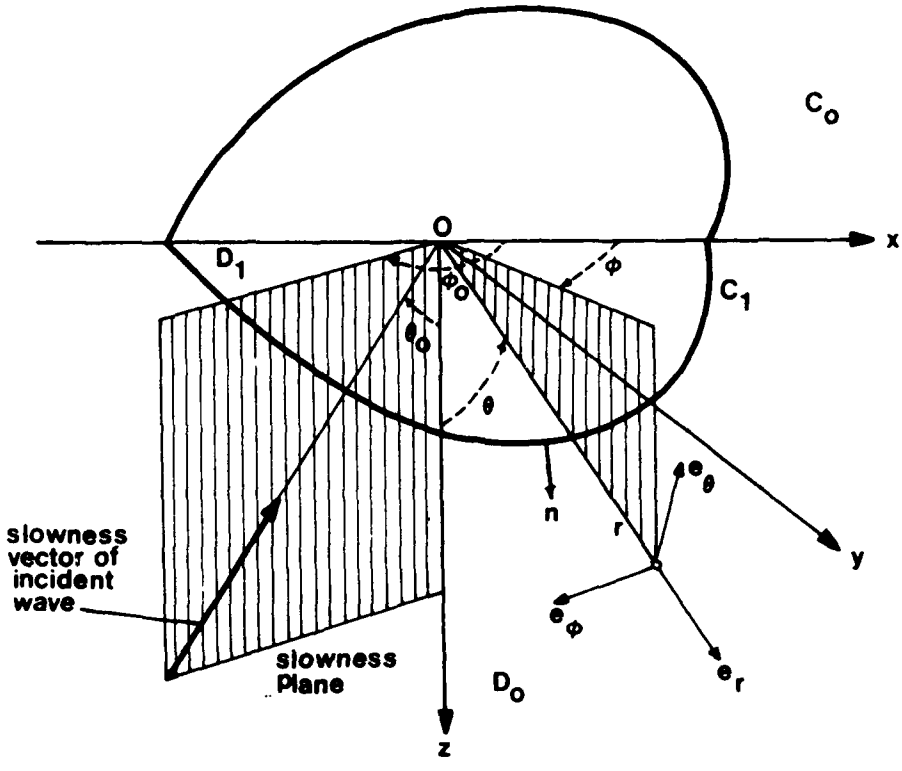

FIG. 1. Problem model.

tentials according to

$$(\nabla^2 + h_j^2)\Phi_j(\underline{x}_j, \omega) = 0 \tag{3a}$$

$$(\nabla^2 + k_j^2)\Psi_j(\underline{x}_j, \omega) = 0 \tag{3b}$$

$$(\nabla^2 + k_j^2)\chi_j(\underline{x}_j, \omega) = 0, \qquad (j = 0, 1) \tag{3c}$$

where h_j and k_j denote the pressure and shear wavenumbers, respectively.

Boundary conditions on the surface $z = 0$ of the half-space and the valley are given by

$$\sigma_{r\theta_j} = \sigma_{\theta\theta_j} = \sigma_{\theta\phi_j} = 0, \qquad \theta = \pi/2 (z = 0), \qquad \underline{x} \in C_0, \qquad (j = 0, 1), \tag{4}$$

where $\sigma_{r\theta}$, $\sigma_{\theta\theta}$, and $\sigma_{\theta\phi}$ are components of the stress tensor. Perfect bonding along the layer interface C_1 requires continuity of displacement and traction fields according to

$$\underline{u}_0^+(\underline{x}, \omega) = \underline{u}_1^-(\underline{x}, \omega) \tag{5a}$$

$$\underline{T}_0^+(\underline{x}, \omega) = \underline{T}_1^-(\underline{x}, \omega) \tag{5b}$$

where $\underline{u}$ and $\underline{T}$ are the displacement field and traction vectors with components along the basis $\underline{e}_r$, $\underline{e}_\theta$, and $\underline{e}_\phi$, respectively. Superscripts + (−) denotes that the

interface is being approached from the outside (inside). The components of the traction vector are defined according to

$$T_r = \sigma_{rr} n_r + \sigma_{r\theta} n_\theta + \sigma_{r\phi} n_\phi \tag{6a}$$

$$T_\theta = \sigma_{r\theta} n_r + \sigma_{\theta\theta} n_\theta + \sigma_{\theta\phi} n_\phi \tag{6b}$$

$$T_\phi = \sigma_{r\phi} n_r + \sigma_{\theta\phi} n_\theta + \sigma_{\phi\phi} n_\phi \tag{6c}$$

Here, σ_{rr}, $\sigma_{r\theta}$, $\sigma_{r\phi}$, $\sigma_{\theta\theta}$, $\sigma_{\theta\phi}$, and $\sigma_{\phi\phi}$ are components of the stress tensor, and n_r, n_θ, and n_ϕ correspond to the components of unit vector normal to the interface C_1 (see Figure 1). Expressions for the components of displacement field and stress tensor in terms of the displacement potentials can be found in literature (Pao and Mow [11]).

Incident field consists of plane harmonic Rayleigh wave or oblique incident SH, SV, or P waves. For slowness vector within the xz-plane, expressions describing these fields can be found in recent papers by the present authors (Eshraghi and Dravinski [1, 2]). For slowness vector located outside the xz-plane, corresponding incident field is obtained through rotation about the z-axis. This completes the statement of the problem. Solution of the problem is considered next.

III. SOLUTION OF THE PROBLEM

As an incident wave strikes the interface C_1, it is partially reflected back into the half-space D_0 and partially transmitted into the top layer D_1. Consequently, the wave field in the half-space consists of the free-field and the scattered wave field, while the wave field inside the dipping layer consists of the scattered wave field only. The displacement field can be written in the following form

$$\underline{u}_0 = \underline{u}^{ff} + \underline{u}_0^s, \qquad \underline{x} \in D_0, \tag{7a}$$

$$\underline{u}_1 = \underline{u}_1^s, \qquad \underline{x} \in D_1, \tag{7b}$$

where $\underline{u} = (u_r, u_\theta, u_\phi)$, $\underline{x} = (r, \theta, \phi)$, and superscripts s and ff denote the scattered and free-field, respectively. The scattered wave field can be expressed as a linear combination of the wave functions according to

$$\Phi_0^s = a_{nm}^{\Phi} h_n^{(2)}(h_0 r) P_n^m(\cos\theta) \cos m\phi + b_{nm}^{\Phi} h_n^{(2)}(h_0 r) P_n^m(\cos\theta) \sin m\phi \tag{8a}$$

$$m = 0, 1, \ldots, M, \qquad n = 0, 1, \ldots, N, \qquad M \le N, \qquad \underline{x} \in D_0.$$

$$\Psi_0^s = a_{nm}^{\Psi} h_n^{(2)}(k_0 r) P_n^m(\cos\theta) \cos m\phi + b_{nm}^{\Psi} h_n^{(2)}(k_0 r) P_n^m(\cos\theta) \sin m\phi \tag{8b}$$

$$m = 1, 2, \ldots, M, \qquad n = 1, 2, \ldots, N, \qquad M \le N, \qquad \underline{x} \in D_0.$$

$$\chi_0^s = a_{nm}^{\chi} h_n^{(2)}(k_0 r) P_n^m(\cos\theta) \cos m\phi + b_{nm}^{\chi} h_n^{(2)}(k_0 r) P_n^m(\cos\theta) \sin m\phi \tag{8c}$$

$$m = 1, 2, \ldots, M, \qquad n = 1, 2, \ldots, N, \qquad M \le N, \qquad \underline{x} \in D_0.$$

$$\Phi_1^s = c_{nm}^{\Phi} j_n^{(2)}(h_1 r) P_n^m(\cos\theta)\cos m\phi + d_{nm}^{\Phi} j_n^{(2)}(h_1 r) P_n^m(\cos\theta)\sin m\phi \tag{8d}$$

$$m = 0, 1, \ldots, M, \quad n = 0, 1, \ldots, N, \quad M \le N, \quad \underline{x} \in D_1,$$

$$\Psi_1^s = c_{nm}^{\Psi} j_n^{(2)}(k_1 r) P_n^m(\cos\theta)\cos m\phi + d_{nm}^{\Psi} j_n^{(2)}(k_1 r) P_n^m(\cos\theta)\sin m\phi \tag{8e}$$

$$m = 1, 2, \ldots, M, \quad n = 1, 2, \ldots, N, \quad M \le N, \quad \underline{x} \in D_1,$$

$$\chi_1^s = c_{nm}^{\chi} j_n^{(2)}(k_1 r) P_n^m(\cos\theta)\cos m\phi + d_{nm}^{\chi} j_n^{(2)}(k_1 r) P_n^m(\cos\theta)\sin m\phi \tag{8f}$$

$$m = 1, 2, \ldots, M, \quad n = 1, 2, \ldots, N, \quad M \le N, \quad \underline{x} \in D_1,$$

where a_{nm}, b_{nm}, c_{nm}, and d_{nm} are unknown coefficients, N and M are the orders of expansions, $h_n^{(2)}(kr)$ are the spherical Hankel functions of the second kind, $j_n(kr)$ are the spherical Bessel functions of the first kind, and $P_n^m(\cos\theta)$ are the associate Legendre polynomials (Abramowitz and Stegun [12]). As indicated earlier, summation over repeated indices is understood. The wave functions in Eqs. (8) are solutions of the equation of motion (Eq. 1). Furthermore, the scattered wave field within the half-space D_0 consists of outgoing waves only, thus satisfying the radiation conditions at infinity. The scattered waves within the dipping layer D_1 consists of standing waves only. It can be seen that these wave functions do not satisfy the stress-free boundary conditions along the surface of the half-space. These conditions must be imposed locally.

To evaluate the scattered wave field and subsequently the total displacement field everywhere within the domain of the problem, it is necessary to determine the unknown expansion coefficients in Eqs. (8). Substitution of the scattered wave field into the continuity conditions on the surface of the layer interface C_1 (Eqs. 5) at L_1 collocation points, and into the boundary conditions (Eq. 4) on the surface $z = 0$ of the half-space and the valley at L_0 collocation points, results in a system of linear equation of the form

$$\underline{G}\,\underline{c} = \underline{f}, \tag{9}$$

where vector $\underline{c}$ contains the unknown expansion coefficients, vector $\underline{f}$ corresponds to the free-field displacements and stresses on the boundaries C_0 and C_1, and matrix $\underline{G}$ contains the wave functions and their derivatives. The size of matrix $\underline{G}$ is $(L \times K)$, where $L > K$ in order to solve Eq. (9) in the least-square-sense. Once expansion coefficients are found, the displacement and stress fields can be evaluated throughout the elastic medium.

This concludes the solution of the problem. Numerical results are presented next.

IV. NUMERICAL RESULTS

In this section, the numerical results are presented for response of non-axisymmetric valleys subjected to plane harmonic Rayleigh waves and oblique incident SH, SV, and P waves.

A. Geometry of the Valley

The shape of the layer interface C_1 is assumed to be in the form of a semiellipsoid defined in the Cartesian coordinate system (x, y, z) according to

$$x^2/a_1^2 + y^2/a_2^2 + z^2/a_3^2 = 1, \qquad z > 0, \tag{10}$$

where a_1, a_2, and a_3 are the principal axis of the ellipsoid along the coordinates x, y, and z, respectively. In particular, the results are presented for spherical valleys ($a_1 = a_2 = a_3$) and prolates ($a_1 \neq a_2 = a_3$). The spherical valley is considered for comparing the results of the present investigation with those available in the literature. On the other hand, prolate type of valley is used to investigate the nonaxisymmetric features of a general three-dimensional model. The choice of these two models allows a comparison between the results of axisymmetric and nonaxisymmetric models. Furthermore, a prolate type valley can be used to test the overall accuracy of the proposed technique. Namely, by assigning sufficiently large values to one principal axis of the prolate, it is possible to make a systematic comparison with available solutions in literature for cylindrical valleys (Eshraghi and Dravinski [1, 2]). This model also can be used to establish the validity and limitations of the corresponding two-dimensional approximations (antiplane and plane strain models).

B. Conventions

Throughout the paper the following conventions are used (Eshraghi and Dravinski [3]). The slowness vector of an incident wave (referred hereafter as the slowness vector) is specified by two angles, azimuthal angle of incidence, ϕ_0, and off-vertical angle of incidence θ_0 (Figure 1). A slowness plane is defined as a vertical plane that contains the slowness vector. In particular, when the slowness vector is contained within the xz-plane (yz-plane) the incidence is defined as an azimuthal (off-azimuthal) one. The out-off plane direction is referred to as a direction normal to the slowness plane. The in-plane motion is defined as a motion that takes place in a slowness plane. In addition to the actual frequency ω, a dimensionless frequency Ω is introduced as the ratio of the maximum width of a cross-section of the dipping layer (lying in the slowness plane passing through the center of valley) and the wavelength of the incident shear wave. Unless stated differently, the density and shear wave speed for the material of the half-space are assumed to be equal unity and corresponding Possion's ratio for all materials is taken to be 1/3. For convenience, all numerical results for surface displacement field are displayed in terms of the Cartesian components u, v, and w.

C. Testing of Results

To assess numerical accuracy of the proposed method, diffraction of a vertically incident P-wave by a spherical dipping layer embedded in a half-space is investigated first. Amplitude of surface displacement field is depicted by Figure 2. The results of Sanchez-Sesma [6] obtained previously for the same

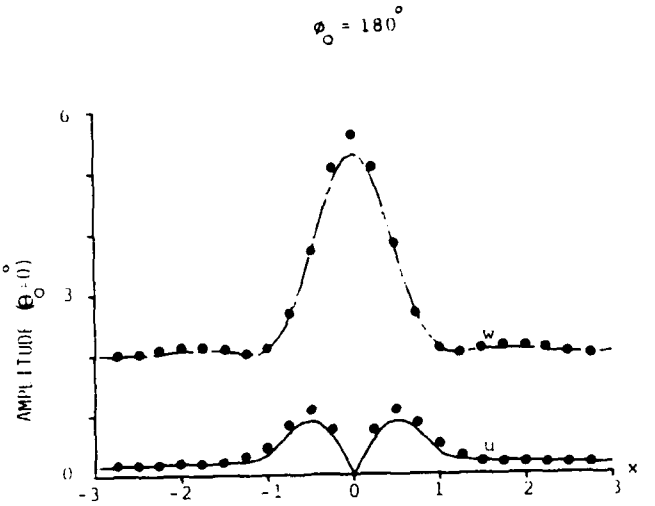

FIG. 2. Surface displacement field amplitudes for stations along the x-axis and a hemispherical valley of unit radius subjected to a vertically incident P wave. The dimensionless frequency Ω of the incident wave is 0.833. The following material properties are assumed: For the half-space, $\beta_0 = \rho_0 = 1$, $\alpha_0 = 1.732$, and for the dipping layer, $\beta_1 = 0.707$, $\rho_1 = 0.6$, $\alpha_1 = 1.414$. The order of expansion terms M and N are assumed to be: $M = 0$, $N = 14$. The number of collocation points on the surface of the layer interface L_1 and on the surface $z = 0$ of the half-space and the valley L_0 are considered to be as following: $L_0 = 24$, and $L_1 = 40$. Throughout, u, v, and w correspond to the three components of the displacement field along the axis x, y, and z, respectively. Solid and dash lines correspond to the results of the present study, while dots correspond to results of Sanchez-Sesma [6].

problem are displayed as well. Very good agreement between the two results can be observed.

To test the accuracy of the present technique for nonaxisymmetric geometries and obliquely incident waves, a prolate type of valley is considered next. The valley is subjected to an off-azimuthal incident P wave (Figure 3). Larger width of the valley in the out-of-plane direction ($a_1 = 2, a_2 = a_3 = 1$) allows a comparative study at low frequency of the results with those of a similar two-dimensional (cylindrical) models studied previously by the same authors (Eshraghi and Dravinski [1, 2]). Namely, the attenuated scattered waves from elongated edges reaching the yz-plane may not significantly affect the total scattered wave field. In Figure 3, the graphs in the first column ($3a$–c) correspond to the results obtained for the prolate, while those in the second column correspond to the results of the cylindrical model. The model geometry (cut by the slowness plane to show the direction of incidence) is illustrated in the bottom of each column. Similarity of the results between these two models are obtained for all angles of incidence studied here. Such similarity can be observed for incident SH, SV, and Rayleigh waves as well. To reduce the number of figures, they are omitted here. This concludes testing of the results. Response of a nonaxisymmetric valley is considered next.

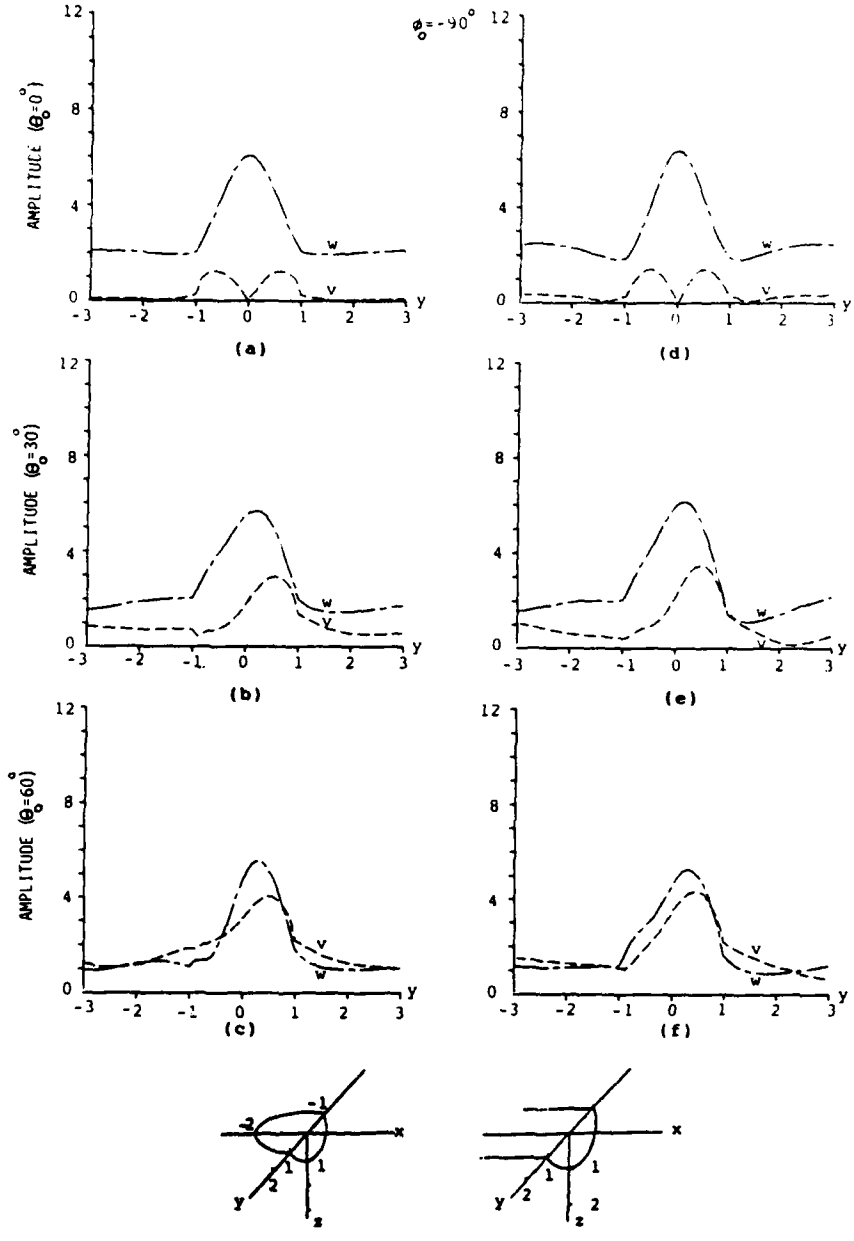

FIG. 3. Comparison of the in-plane components of the surface displacement field (v- and w-components) of a prolate type of valley (a–c) with those of a cylindrical valley (d–f) for stations along the y-axis. For the prolate the principle axis are $a_1 = 2$, $a_2 = a_3 = 1$, while for the cylindrical valley the radius is one. The geometry of the valleys (cut by the slowness plane) are illustrated in the lower section of the figure. Both valleys are subjected to same off-azimuthal incident P waves ($\phi_0 = -90°$). Three off-vertical angles of incidence are considered: $\theta_0 = 0°$, 30°, and 60°. $\Omega = 0.5$ (relative to a_2), $M = 3$, $N = 11$, $L_0 = 104$, and $L_1 = 124$. The following material properties are assumed hereafter: $\beta_0 = \rho_0 = 1$, $\alpha_0 = 2$, $\beta_1 = 0.5$, $\rho_1 = 2/3$, $\alpha_1 = 1$.

D. Response of a Nonaxisymmetric Valley

Surface responses for a prolate type valley ($a_1 = 2, a_2 = a_3 = 1$) are shown in Figures 4 through 7. For stations along the x- and the y-axes displacement field is obtained for three off-vertical incident SH and P waves. Both azimuthal and off-azimuthal incidences are considered. Actual frequency of the incident wave being $\omega = 1.571$ sec^{-1} results in a dimensionless frequency of one (relative to a_1) for the azimuthal incidences and one half (relative to a_2) for the off-azimuthal incidences. For Figures 4 to 7, graphs in the first and second column correspond to the surface response for the observation stations along the x- and y-axes, respectively.

Results for azimuthal and off-azimuthal incident SH waves are depicted by Figures 4 and 5, respectively. For azimuthal incident SH waves and stations along the x-axis the motion occurs in the out-of-plane direction only (Figures 4a–c). This agrees with the two-dimensional antiplane strain model However, for stations along the y-axis (Figures 4d–f) all three components of displacement field may be present. Of interest in these graphs is large amplitude of the vertical component of displacement field. This component, not present in the two-dimensional approximation, can assume values comparable to the amplitude of the predominant component (the v-component) as shown by Figure 4d. At this point it is interesting to observe how change of the valley width perpendicular to the slowness plane affects surface displacement field. For that purpose, the valley considered in Figure 4 is reinvestigated for off-azimuthal incident SH waves as shown by Figure 5. It should be noted that for realistic comparison, displacement field for stations along the x-axis (the y-axis) for azimuthal SH-incidences must be compared with displacement field along the y-axis (the x-axis) for off-azimuthal SH-incidences. Therefore, the results of Figure 5 correspond to a relatively wider valley (in perpendicular direction to the slowness plane) than those of Figure 4. By comparing the main component of displacement fields of Figure 4d–f with Figure 5a–c, one finds very little similarity between the two. This main component of displacement field for incident SH wave is specified in Figures 4 and 5 by v- and u-components, respectively. Better agreement can be observed between results of Figures 4b and c and Figures 5e and f for the main component of displacement field. However, the vertical component of displacement field that has substantial amplitude for the narrower valley (Figure 4d–f) is reduced considerably for the wider valley (Figure 5a–c). Significant amplitude of the vertical displacement component, which is not present in the antiplane strain model, demonstrates clearly the importance of three-dimensional modeling of realistic valleys. It is interesting to note that for geometrically similar three-dimensional canyons (Eshraghi and Dravinski [3]), considerably greater similarity could be observed for predominant displacement components between the narrow and wide canyons than between corresponding valleys studied in this paper. Furthermore, the amplitudes of nonpredominant components of displacement field (the in-plane motion) for the canyon appear to be considerably smaller than those of the valley. This large amplitude of the two nonpredominant components of displacement field (specially for the narrower valley) is an important characteristic of three-dimensional models studied here.

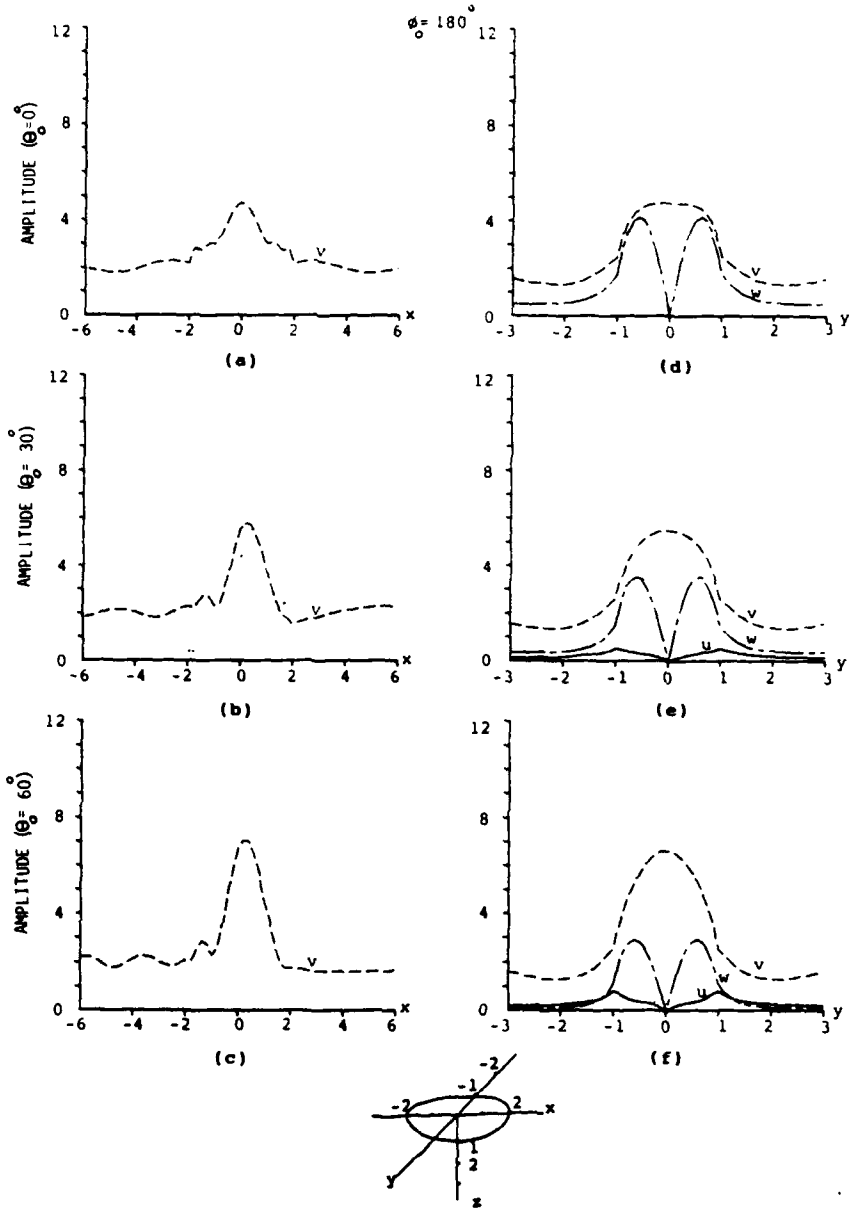

FIG. 4. Surface displacement amplitudes for a prolate type valley ($a_1 = 2$, $a_2 = a_3 = 1$) subjected to azimuthal incident ($\phi_0 = 180°$) SH waves. Stations lie along the x-axis (a–c) and the y-axis (d–f). $\Omega = 1$ (relative to a_1), $M = 3$, $N = 11$, $L_0 = 104$, and $L_1 = 124$.

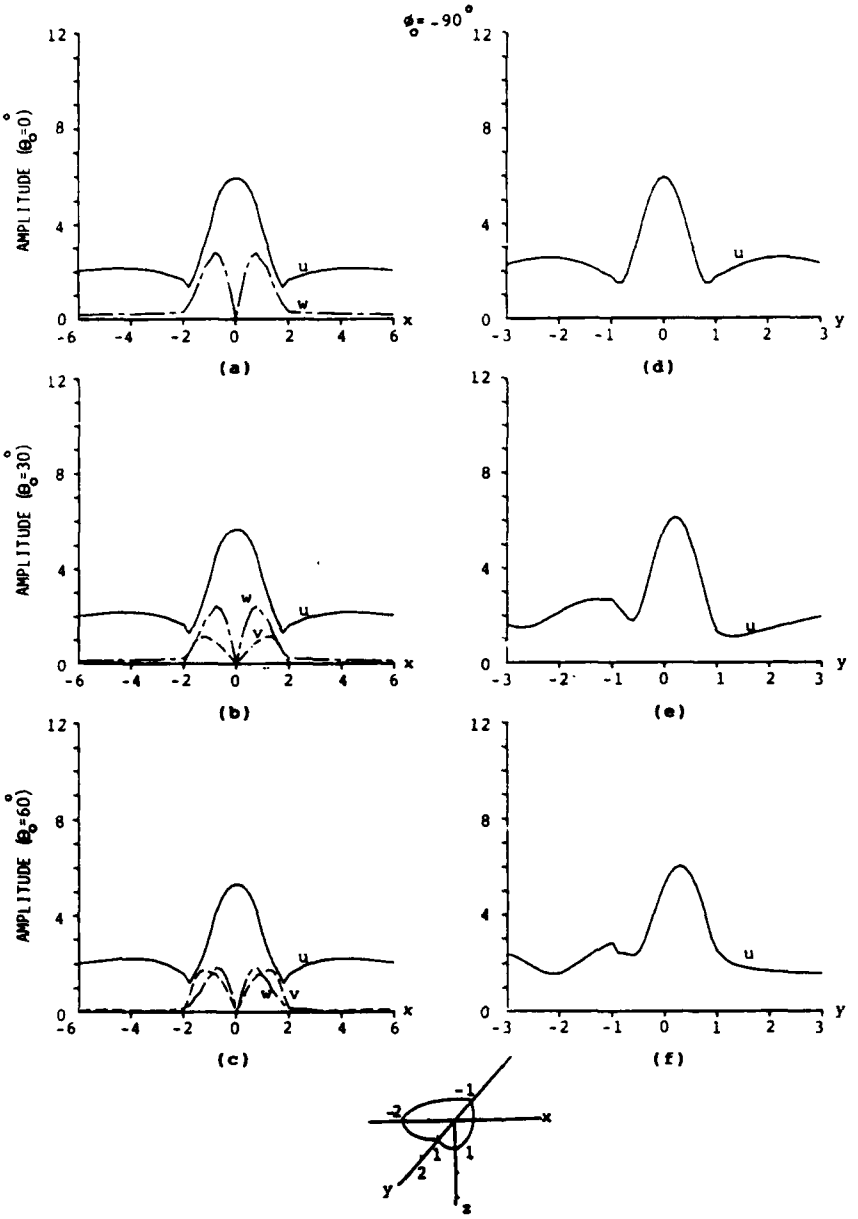

FIG. 5. Surface displacement amplitudes for a prolate type valley ($a_1 = 2$, $a_2 = a_3 = 1$) subjected to off-azimuthal incident ($\phi_0 = -90°$) SH waves. Stations lie along the x-axis (a–c) and the y-axis (d–f). $\Omega = 0.5$ (relative to a_2), $M = 3$, $N = 11$, $L_0 = 104$, and $L_1 = 124$.

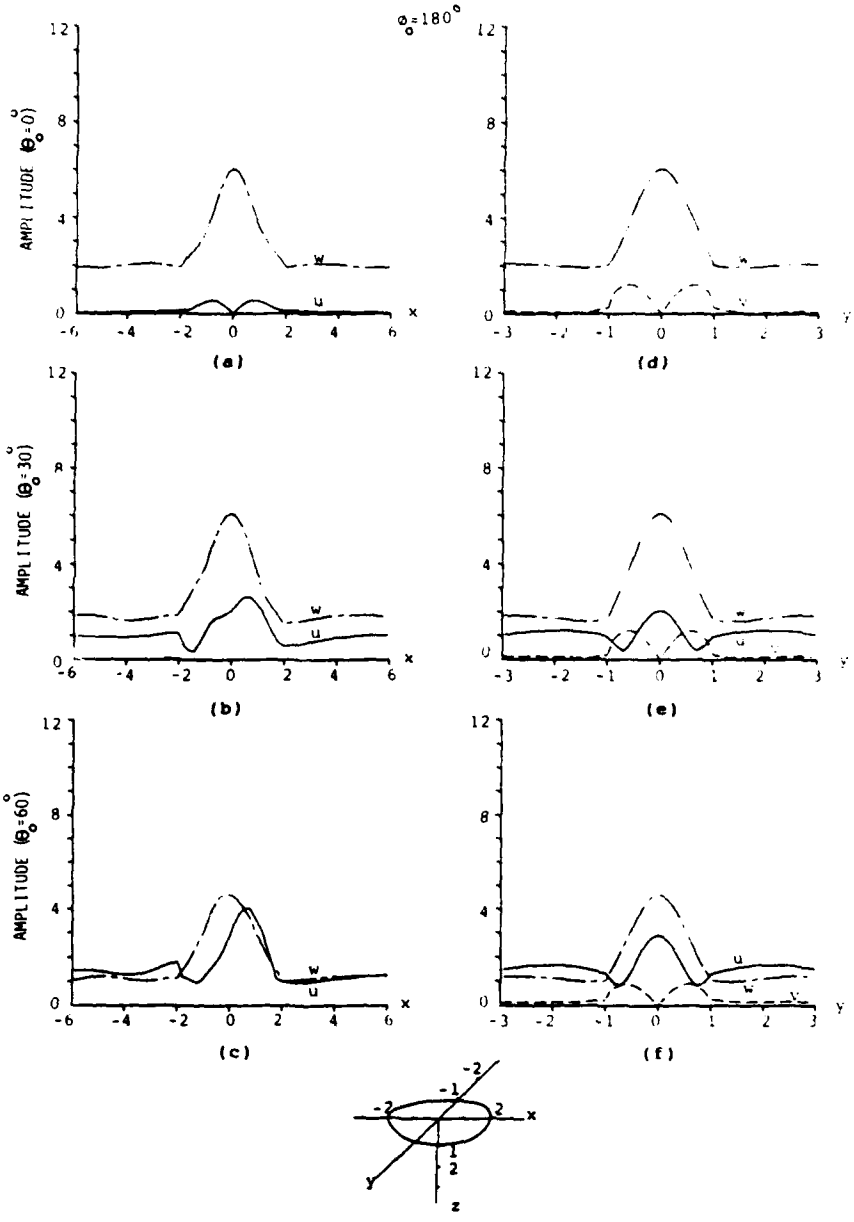

FIG. 6. Surface displacement amplitudes for a prolate type valley ($a_1 = 2$, $a_2 = a_3 = 1$) subjected to azimuthal incident ($\phi_0 = 180°$) P waves. Stations lie along the x-axis (a–c) and the y-axis (d–f). $\Omega = 1$ (relative to a_1). $M = 3$, $N = 11$, $L_0 = 104$, $L_1 = 124$.

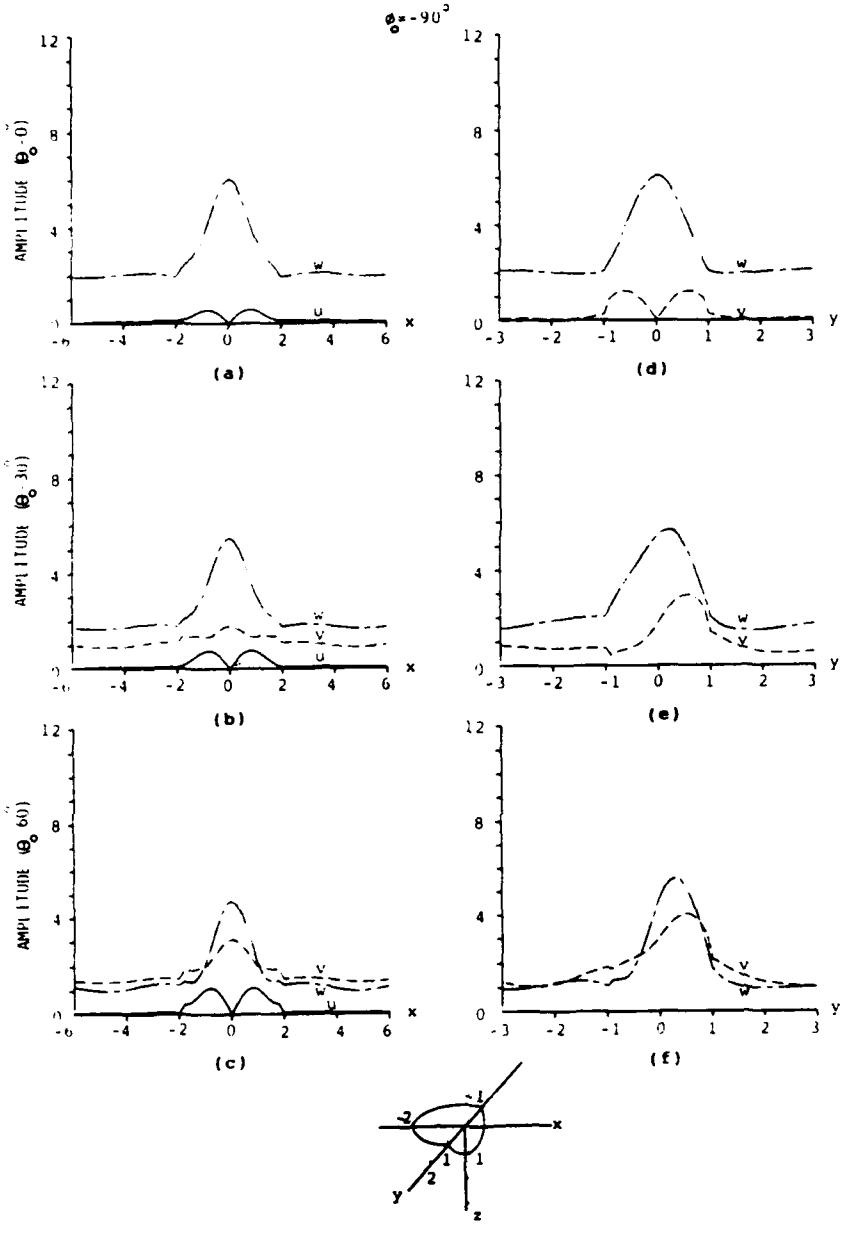

FIG. 7. Surface displacement amplitudes for a prolate type valley ($a_1 = 2$, $a_2 = a_3 = 1$) subjected to off-azimuthal incident ($\phi_0 = -90°$) P waves. Stations lie along the x-axis (a–c) and the y-axis (d–f). $\Omega = 0.5$ (relative to a_2), $M = 3$, $N = 11$, $L_0 = 104$, and $L_1 = 124$.

Figures 6 and 7 correspond to surface response for azimuthal and off-azimuthal incident P waves, respectively. For stations along the axis in the out-off plane direction an additional component of displacement is present in that plane (dash and solid lines in Figure 6d–f and a–c, respectively). Considering the same rule of comparison defined earlier for incident SH case, one observes more similarity between the results for azimuthal and off-azimuthal incident P waves than those for the incident shear waves. As expected, for the vertically incident P waves, the displacement field is identical for both azimuthal and off-azimuthal incidences.

E. Two-Dimensional vs. Three-Dimensional Modeling

Results in the last section illustrate that for nonaxisymmetric valleys a change in azimuthal angle of incidence affects the displacement field substantially. Results for the azimuthal and off-azimuthal incidences display different characteristics in general. This dissimilarity is more pronounced here than in the geometrically similar canyons (Eshraghi and Dravinski [3]). Furthermore, it was observed that the extra components of displacement field that are not present in the two-dimensional approximations (antiplane and plane strain models), may have substantial amplitude. These results emphasize the need for three-dimensional modeling of realistic problems of interest in the strong ground motion seismology and earthquake engineering. To enhance further upon the need for a three-dimensional analysis, response for valleys in the form of a prolate ($a_1 = 0.5, a_2 = a_3 = 1$) and a sphere are compared with those of a cylindrical valley. This comparison should illustrate the limitations of the two-dimensional models in approximating more general three-dimensional problems. Figures 8 through 10 display the surface response for three types of valleys to off-azimuthal incident SH, SV, and Rayleigh waves, respectively. To make realistic comparison, we chose valleys having identical widths along the y-axis. Results for cylindrical valleys are obtained in an earlier study by the present authors using a cylindrical wave function expansion technique (Eshraghi and Dravinski [1, 2]).

Results of Figure 8 correspond to off-azimuthal incident SH waves. To simplify the comparison between the responses of three dimensional and two dimensional models, only the out-of-plane component of displacement field is displayed. Apparently, there are no similarities between the responses for different types of valleys in this figure. For incident SV and Rayleigh waves, only the in-plane motion (in the slowness plane) is considered, i.e., only v- and w-components of displacement field are displayed in Figures 9 and 10. Analogously to the results obtained for incident SH case quite different patterns can be observed for different types of valleys studied here. It is interesting to mention that in the similar study for the canyons (Eshraghi and Dravinski [3]), the surface response for the narrow three-dimensional canyon was completely different from those of spherical and cylindrical canyons. However, in that study very similar results were obtained for the spherical and cylindrical canyons. Therefore, presented results clearly demonstrate that in general the three-dimensional nature of the problem is essential in modeling of the actual

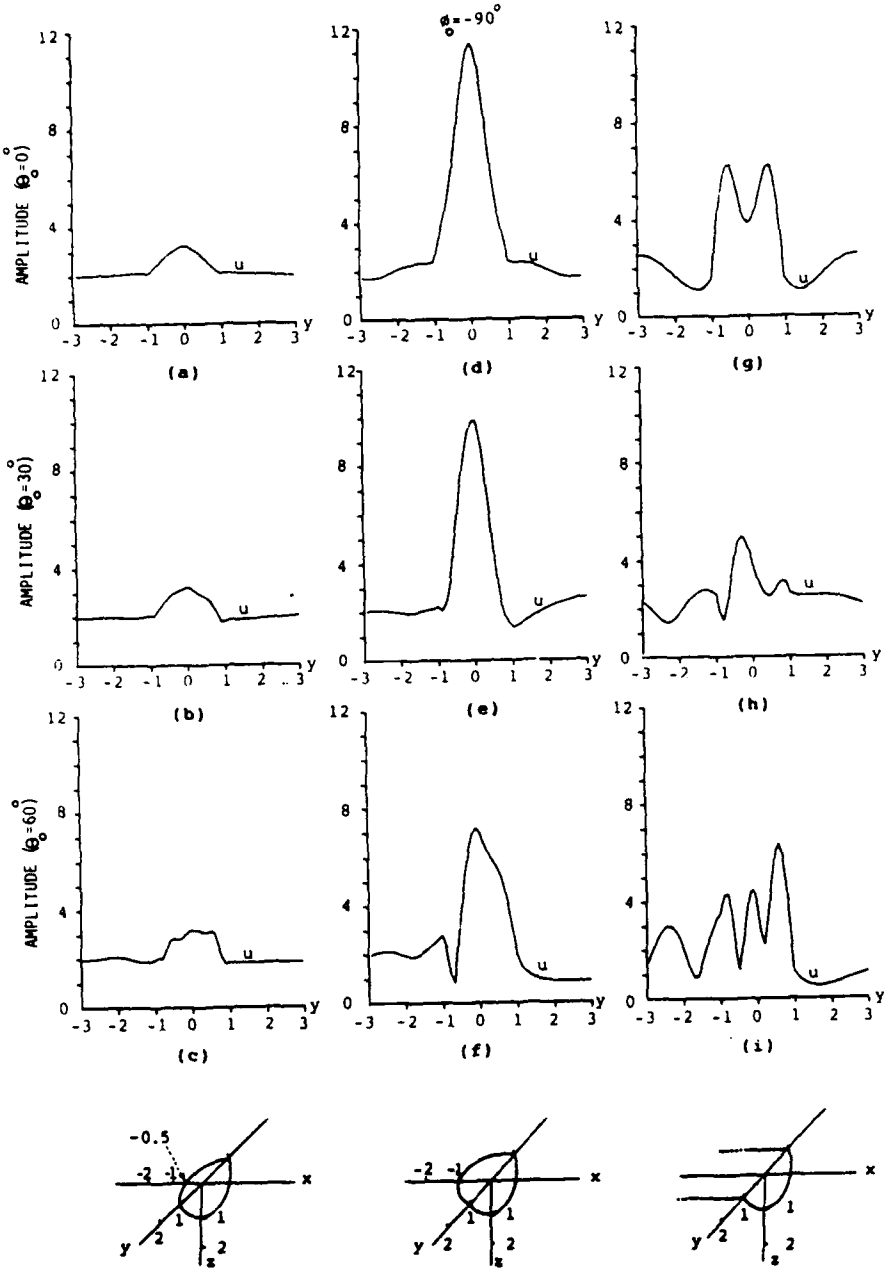

FIG. 8. Amplitude of the predominant component of surface displacement field (u-component) at stations along the y-axis for off-azimuthal incident ($\phi_0 = -90°$) SH waves for a prolate type valley with principal axis $a_1 = 0.5$ and $a_2 = a_3 = 1$ (a–c), a spherical valley of unit radius (d–f), and a cylindrical valley of unit radius (g–i). $\Omega = 0.75$ (relative to a_2). $M = 3$, $N = 11$, $L_0 = 104$, and $L_1 = 124$.

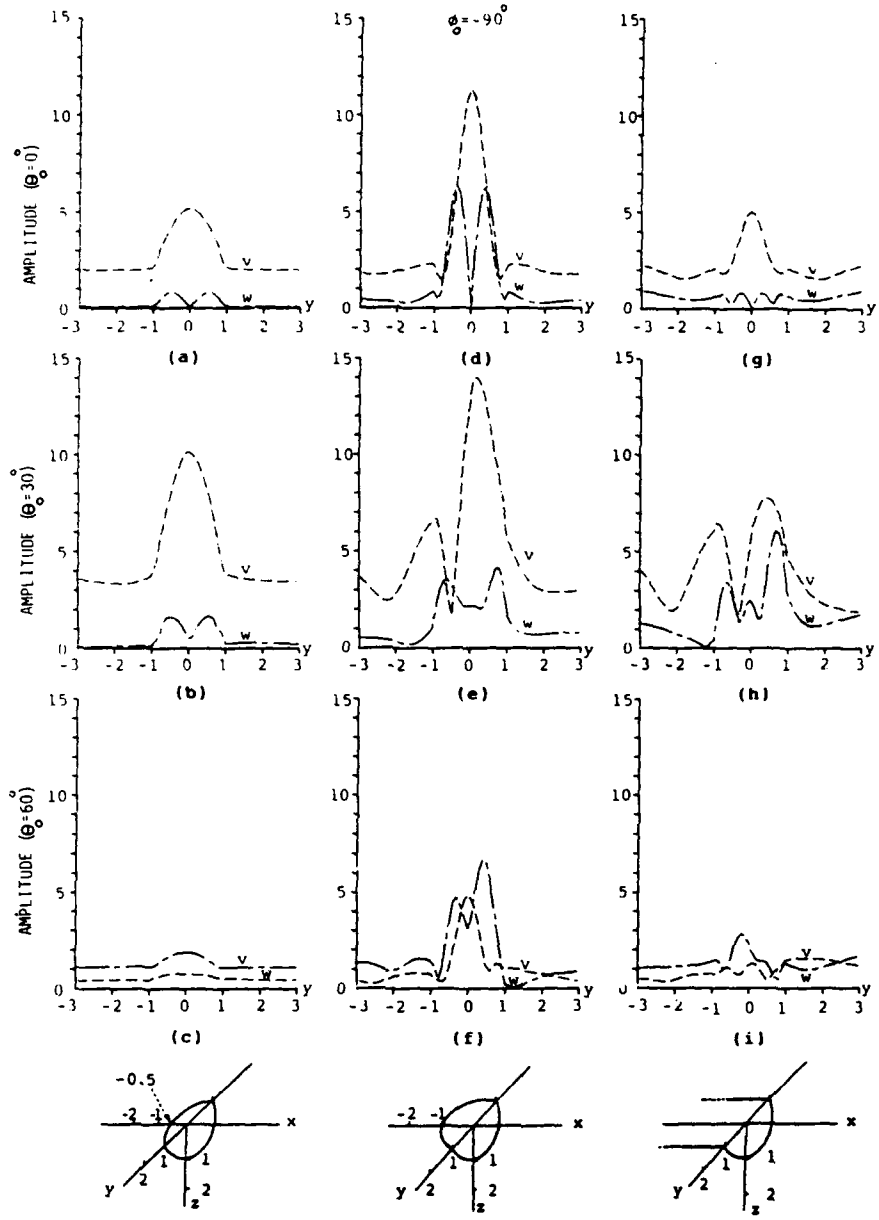

FIG. 9. Amplitude of the components of inplane motion (v- and w-components) along the y-axis for off-azimuthal incident ($\phi_0 = -90°$) SV waves and a prolate type valley with principal axis $a_1 = 0.5$, $a_2 = a_3 = 1$ (a–c), a spherical valley with radius of one (d–f), and a cylindrical valley with the radius of one (g–i). $\Omega = 0.75$ (relative to a_2). $M = 3$, $N = 11$, $L_0 = 104$, and $L_1 = 124$.

irregularities and that two-dimensional models may result in rather inadequate approximations. Furthermore, comparison of the present results with their counterparts for the canyons (Eshraghi and Dravinski [3]) shows that presence

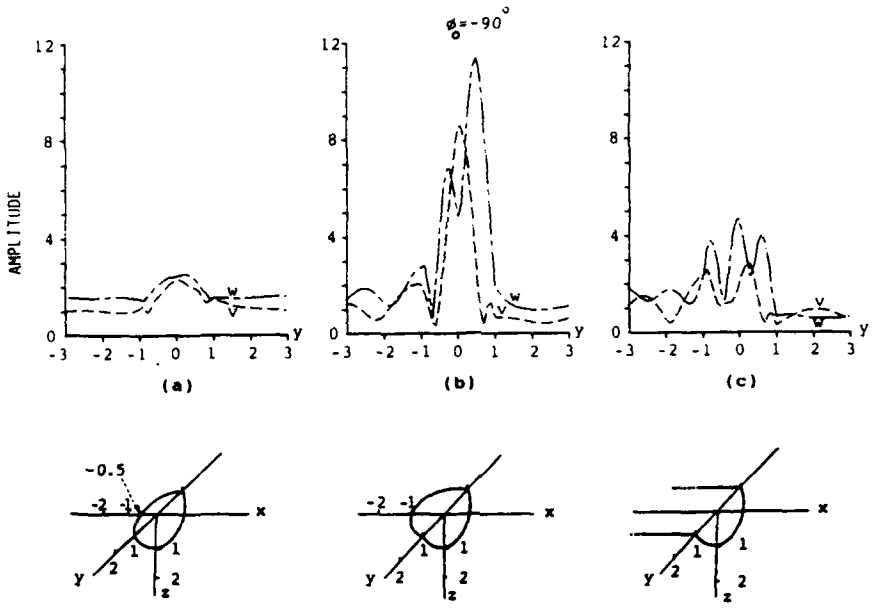

FIG. 10. Amplitude of the components of the inplane motion (v- and w-components) along the y-axis for off-azimuthal incident ($\phi_0 = -90°$) Rayleigh waves and a prolate type valley with principal axis $a_1 = 0.5$, $a_2 = a_3 = 1$ (a), a spherical valley of unit radius (b), and a cylindrical valley of unit radius (c). $\Omega = 0.75$ (relative to a_2). $M = 3$, $N = 11$, $L_0 = 104$, and $L_1 = 124$.

of alluvial valleys results, in general, in a larger amplification of surface ground motion than those observed for the canyons. This amplification appears to be more pronounced for three-dimensional valleys than for their two-dimensional approximations as results in Figures 8 to 10 clearly demonstrate.

F. Numerical Aspects of the Method

It is useful at this point to elaborate in some detail about the numerical aspects of the solutions presented in this paper. First, it should be pointed out that the number of expansion terms and collocation points needed for convergence of the results increase as the frequency of the incident wave increases. For the range of frequencies studied here, good accuracy can be obtained with an azimuthal order of expansion $M = 3$. However, the results are more sensitive upon the second order of expansion N (see Eqs. 8). For low and moderate frequencies, say $\Omega < 1.5$, generally $8 < N < 12$ provides acceptable convergence. It is observed that location and the number of collocation points L_0 and L_1 play a crucial rule in the convergence of the results. These points are distributed on elliptical contours on the surface of the layer interface C_1 and also on the surface C_0 ($z = 0$) of the half-space and the valley. On interface C_1 these contours are equally spaced at different elevations from $z = 0$ to $z = a_3$. For low and moderate frequencies eight to ten contours are sufficient. A total of 82 to 104 collocation points are uniformly distributed along these contours. Similar elliptical contours are considered on the surface of the half-space. These con-

tours follow the shape of the valley edge and are equally spaced from the origin up to three times the width of the valley at the surface of the half-space. Twelve contours equally spaced this way on the surface of the half-space contained a total of 124 uniformly distributed collocation points. The order of expansion and the number of collocation points is determined through the following convergence criteria: First the material properties of the half-space and the dipping layer are assumed to be the same. This should results in the free field for total wave field. The orders of expansion and the number of collocation points are increased until the total wave field is identical to the free field one. Subsequently, for different material properties of the layer and the half-space the order of expansions and the number of collocation terms are further increased until the difference between two successive calculations are judged to be sufficiently small. This concludes the analysis of numerical results.

V. CONCLUSIONS

Amplification of incident plane harmonic SH, SV, P, and Rayleigh waves by nonaxisymmetric three-dimensional valleys of arbitrary shape is investigated by using a boundary method. Different angles of incidence are considered. Scattered wave fields are expanded in terms of spherical wave functions that satisfy the equation of motion and radiation conditions at infinity but they do not satisfy the stress-free boundary conditions at the surface of the half-space. These conditions are imposed locally at a number of points atop the valley and the half-space.

Results presented in this investigation demonstrate the importance of three-dimensional modeling of the actual alluvial valleys. For the range of frequencies studied it is shown that for the valleys with elongation (in the out-of-plane direction) being more than twice that of the corresponding width in the slowness plane, a two-dimensional approximation could results in a fairly similar response for the predominant components of displacement field. It is shown that the two-dimensional models ignore an out-of-plane displacement component for incident P, SV, and Rayleigh waves and an in-plane motion for incident SH wave that may be significant in amplitude. Presented results show that similarity of predominant components of displacement field between the valley and its two-dimensional approximations deteriorates as the elongated width of the valley (in direction perpendicular to the slowness plane) reduces in size. This deterioration reaches a point where no apparent similarity may exist between the results of a spherical valley and its two-dimensional counterpart. For the range of frequencies studied here, this rate of deterioration is significantly faster here than the one observed for the canyons (Eshraghi and Dravinski [3]). Therefore, the results of the present study strongly suggest that complete description of the site phenomenon and corresponding strong ground motion will require a three-dimensional modeling of the actual alluvial valleys.

This material is based on work supported in part by the National Science Foundation under grant 53-4519-3792 and in part by the Office of Naval Research under contract N00014-88-K-0157.

References

[1] H. Eshraghi and M. Dravinski, "Transient scattering of elastic waves by dipping layers of arbitrary shape. Part 1. Antiplane strain model," *Earthquake Eng. Struct. Dyn.*, **18**, 397–415 (1989).

[2] H. Eshraghi and M. Dravinski, "Transient scattering of elastic waves by dipping layers of arbitrary shape. Part 2. Plane strain model," *Earthquake Eng. Struct. Dyn.*, **18**, 417–434 (1989).

[3] H. Eshraghi and M. Dravinski, "Scattering of plane harmonic SH, SV, P, and Rayleigh waves by non-axisymmetric three dimensional canyons: A wave function expansion approach," *Earthquake Eng. Struct. Dyn.*, in press.

[4] I. Herrera and F. J. Sabina, "Connectivity as an alternative to boundary integral equations: Construction of bases," *Proc. Natl. Acad. Sci. USA*, **75**, 2059–2063 (1978).

[5] I. Herrera, "Boundary methods: A criterion for completeness," *Proc. Natl. Acad. Sci. USA*, **77**, 4395–4398 (1980).

[6] F. J. Sanchez-Sesma, "Diffraction of elastic waves by three dimensional surface irregularities," *Bull. Seism. Soc. Am.*, **73**, 1621–1636 (1983).

[7] V. W. Lee, "Displacement near a three dimensional hemispherical canyon subjected to incident plane waves," University of Southern California, Dept. of Civil Engineering, Report No. 78-16, 1978.

[8] V. W. Lee, "Three dimensional diffraction of plane P, SV, and SH Waves by a hemispherical alluvial valley," *J. Soil Dyn. Earthq. Eng.*, **3**, 133–144 (1984).

[9] R. J. Apsel, "Dynamic green's functions for layered media and applications to boundary value problems," PhD thesis, University of California, San Diego, California, 1979.

[10] J. J. Lee and C. A. Langston, "Wave Propagation in a Three Dimensional Circular Basin," *Bull. Seism. Soc. Am.*, **73**, 1637–1653 (1983).

[11] Y-H Pao and C. C. Mow, *Diffraction of Elastic Waves and Dynamic Stress Concentrations*, New York, Crane, Russak, 1973.

[12] M. Abramowitz and I. A. Stegun, *Handbook of Mathematical Functions*, Dover, New York, 1972.

EARTHQUAKE ENGINEERING AND STRUCTURAL DYNAMICS VOL. 19, 667-680 (1990)

AMPLIFICATION OF ELASTIC WAVES BY A THREE DIMENSIONAL VALLEY. PART 1: STEADY STATE RESPONSE

TOMI K. MOSSESSIAN* AND MARIJAN DRAVINSKI

Department of Mechanical Engineering, University of Southern California, Los Angeles, California 90089, U.S.A.

SUMMARY

Steady state scattering of incident P, SV, SH and Rayleigh waves by general non-axisymmetric three dimensional dipping layers is investigated by using an indirect boundary integral equation method. Material of the half-space and the layer is assumed to be linear, weakly anelastic, homogeneous and isotropic.

Systematic comparisons between three dimensional and two dimensional models demonstrate that the validity of a two dimensional approximation for a given basin shape may be affected strongly by changes in azimuthal angle of incidence, type of incident wave and frequency. The discrepancies of two dimensional modelling appear to be much more pronounced for the case of an incident SH wave. Another important feature of the results is the existence of strong coupling between P, SV and SH modes, which has no correspondence in two dimensional models. Such off-azimuthal mode conversions are particularly strong for an incident SH wave.

INTRODUCTION

The importance of local site effects on strong ground motion has been well recognized.[1] The site conditions appear mainly in the form of irregular surface topographies (canyons and ridges) and/or soft subsurface layers (sedimentary basins). The seismic response of sedimentary valleys is especially important since many highly populated areas are located on such basins, e.g. Mexico City[2] and Los Angeles.[3] In recent years the amplification effects of sedimentary basins have been the subject of numerous experimental and theoretical studies. For a detailed review of literature on the subject the reader is referred to articles by Dravinski and Mossessian,[4] Moczo *et al.*[5] and Aki.[1] Most of the recent theoretical investigations have been limited to two dimensional plane strain models.[4-9] Three dimensional studies are few in number and are mostly limited to simple geometries and axisymmetric cases. Lee[10] investigated diffraction of elastic plane harmonic P, SV and SH waves by a hemispherical valley using the method of series expansion. His solution is applicable for basins of spherical shape only. Day[11] used the finite element technique to study the response of a cone-shaped sedimentary basin due to a dislocation source. Sanchez-Sesma[12] considered diffraction of a vertical incident P wave by several types of irregularities including alluvial basins using a wave function expansion approach. Both studies were limited to axisymmetric cases. Lee and Langston[13] studied wave propagation in a three dimensional circular basin subjected to incident plane P and SH waves using a ray technique. Their solution is applicable only in the high frequency range. Very recently, Khair *et al.*[14,15] have considered three dimensional amplification of P and SV waves by cylindrical valleys. However, their model in not a general three dimensional one, and it corresponds to the problem of two dimensional type valleys subjected to a three dimensional plane incident wave field.

In this paper, an indirect boundary integral equation method is applied to study the amplification of elastic waves by a three dimensional dipping layer of arbitrary shape. The present work is an extension of the recent study done by the authors[16] in which they investigated seismic response of canyons of arbitrary shapes. The model used in this study is a general three dimensional one. Incident plane harmonic SH, SV, P and Rayleigh

*Presently at Structural Research and Analysis Corp. 1661 Lincoln Blvd, Suite 200, Santa Monica, CA 90404, U.S.A.

0098-8847/90/050667-14$07.00

Received 10 January 1989
Revised 18 January 1990

waves are considered. A general formulation of the problem is presented. The accuracy of the method is tested through comparison with results of some earlier studies. The effects of different parameters such as basin shapes, types of waves, angles of incidence and frequency are investigated. The validity of two dimensional models is examined through several comparisons between three dimensional and corresponding two dimensional responses.

STATEMENT OF THE PROBLEM

The geometry of the model is depicted by Figure 1. The basin is modelled as a single dipping layer of arbitrary shape perfectly bonded to a half-space. The spatial domain of the half-space is denoted by D_0 and that of the layer by D_1. The interface between the layer and the half-space is denoted by S_1 and it is assumed to be sufficiently smooth without sharp corners. The material of the half-space and the layer is assumed to be weakly anelastic, homogeneous and isotropic. The half-space is subjected to incident plane harmonic P, SV, SH and Rayleigh waves.

The equation of motion for steady state elastic wave propagation is specified by

$$(\lambda_j + \mu_j)\nabla\nabla.\mathbf{u}_j + \mu_j\nabla^2\mathbf{u}_j + \rho_j\omega^2\mathbf{u}_j = \mathbf{0}; \qquad j = 0, 1, \mathbf{x} \in D_0 \cup D_1 \tag{1}$$

(no summation over j)

where $\mathbf{u}_j = (u, v, w)$ is the displacement vector, $\mathbf{x}$ is the position vector, ρ_j is the density and λ_j and μ_j are the Lamé constants. These constants are assumed to be complex numbers to account for anelasticity.[17] Subscripts 0 and 1 correspond to the half-space and the layer, respectively. Throughout the paper the term $\exp(i\omega t)$ is understood. Stress free boundary conditions along the surface of the half-space are specified by

$$\sigma_{xz} = \sigma_{yz} = \sigma_{zz} = 0; \qquad z = 0, \qquad \mathbf{x} \in D_0 \cup D_1 \tag{2}$$

The continuity of the displacements and tractions along the interface S_1 is given by

$$\mathbf{u}_0 = \mathbf{u}_1; \qquad \mathbf{x} \in S_1 \tag{3a}$$

$$\mathbf{t}_0^{\nu} = \mathbf{t}_1^{\nu}; \qquad \mathbf{x} \in S_1 \tag{3b}$$

where $\mathbf{t}_j^{\nu}, j = 0, 1$ are the traction vectors at the surface S_1 with unit normal ν. The usual radiation conditions should be satisfied by the scattered wave field at infinity.

METHOD OF SOLUTION

The total displacement field in the half-space and the dipping layer is specified by

$$\mathbf{u}_0 = \mathbf{u}^{ff} + \mathbf{u}_0^s; \qquad \mathbf{x} \in D_0 \tag{4a}$$

$$\mathbf{u}_1 = \mathbf{u}_1^s; \qquad \mathbf{x} \in D_1 \tag{4b}$$

where the superscripts ff and s denote the free and scattered wave field, respectively. Following an indirect boundary integral equation approach,[4, 18] the scattered field is assumed to be generated from the distribution of unknown forces $\mathbf{f}_0(\mathbf{y})$ and $\mathbf{f}_1(\mathbf{y})$ over auxiliary surfaces S_a^0 and S_a^1, respectively. The auxiliary surfaces S_a^0 and S_a^1 are located inside and outside of the surface S_1, respectively. Hence the scattered displacement field in the half-space and the dipping layer can be written in the form

$$\mathbf{u}_0^s = \int_{S_a^0} \mathbf{G}(\mathbf{x}, \mathbf{y})\mathbf{f}_0(\mathbf{y})\,dS_a^0(\mathbf{y}); \qquad \mathbf{x} \in D_0 \tag{5a}$$

$$\mathbf{u}_1^s = \int_{S_a^1} \mathbf{G}(\mathbf{x}, \mathbf{y})\mathbf{f}_1(\mathbf{y})\,dS_a^1(\mathbf{y}); \qquad \mathbf{x} \in D_1 \tag{5b}$$

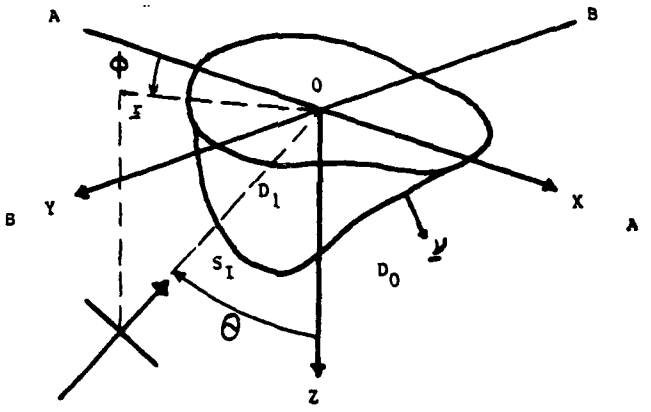

Figure 1. Problem model

where G is a half-space displacement Green's function tensor.[17] The element $G_{ij}(x, y)$ corresponds to the ith component of the displacement vector at x due to a unit harmonic force at y acting in the jth direction. The theoretical development of these Green's functions is rather involved; their complete explicit forms can be found in the article by Mossessian and Dravinski,[16] and also in Mossessian.[19]

Choosing $\mathbf{f}_0(y)$ and $\mathbf{f}_1(y)$ to be distributed at discrete points x_m and x_l on the surfaces S_a^0 and S_a^1, then the total wave field follows from equations (4a, b) and (5a, b)

$$\mathbf{u}_0 = \mathbf{u}^{ff} + \mathbf{G}(x, x_m)\mathbf{f}_0^m, \qquad x \in D_0, \qquad x_m \in S_a^0, \qquad m = 1, 2, \ldots, M \tag{6a}$$

$$\mathbf{u}_1 = \mathbf{G}(x, x_l)\mathbf{f}_1^l, \quad x \in D_1, \; x_l \in S_a^1, \qquad l = 1, 2, \ldots, L \tag{6b}$$

The unknown force magnitudes $\mathbf{f}_0^m$ and $\mathbf{f}_1^l$ are yet to be determined for all m and l. Throughout, summation over repeated indices is understood. Using equations (6a, b), the components of total traction along the surface S_1 become

$$\mathbf{t}_0 = \mathbf{t}^{ff} + \mathbf{T}(x, x_m)\mathbf{f}_0^m; \qquad x \in S_1; \qquad m = 1, 2, \ldots, M \tag{7a}$$

$$\mathbf{t}_1 = \mathbf{T}(x, x_l)\mathbf{f}_1^l; \qquad x \in S_1; \qquad l = 1, 2, \ldots, L \tag{7b}$$

where $\mathbf{t}^{ff}$ is the free-field traction vector and T is the half-space traction Green's function tensor. The component $T_{ij}(x, x_m)$ corresponds to the ith component of the traction vector at x due to unit harmonic force at x_m acting in the jth direction. For simplicity, the superscript v is suppressed. By choosing N observation points along the surface S_1 the corresponding traction field can be stated as follows:

$$\mathbf{t}_0(x_n) = \mathbf{t}^{ff}(x_n) + \mathbf{T}(x_n, x_m)\mathbf{f}_0^m; \qquad x_m \in S_a^0 \tag{8a}$$

$$\mathbf{t}_1(x_n) = \mathbf{T}(x_n, x_l)\mathbf{f}_1^l; \qquad x_l \in S_a^1 \tag{8b}$$

$$x_n \in S_1, \quad n = 1, 2, \ldots, N; \qquad m = 1, 2, \ldots, M; \qquad l = 1, 2, \ldots, L$$

Using equations (8a, b), the continuity conditions given by equations (3a, b) assume the following form:

$$\mathbf{G}_T \hat{\mathbf{f}} = \mathbf{a}; \qquad \hat{\mathbf{f}} = (\mathbf{f}_0^1, \mathbf{f}_0^2, \ldots, \mathbf{f}_0^M, \mathbf{f}_1^1, \ldots, \mathbf{f}_1^L)^T \tag{9}$$

where vector $\hat{\mathbf{f}}$ contains the unknown force magnitudes, and matrix $\mathbf{G}_T$ and vector a are known. Choosing N

greater than M and L, equation (9) is solved in the least square sense. Once the magnitudes of the forces $\tilde{\mathbf{f}}$ are known, the total wave field within the half-space and the valley can be obtained through equations (6a, b).

NUMERICAL RESULTS AND DISCUSSION

The geometry of the valley is assumed to be in the form of a semi-prolate dipping layer. This allows systematic comparison with available two dimensional results, without loss of general three dimensional characteristics of the model. This geometry can be defined in the following parametric form:

$$x = a\cos(t)\cos(s) \tag{10a}$$

$$y = b\cos(t)\sin(s) \tag{10b}$$

$$z = b\sin(t) \tag{10c}$$

$$0 \leqslant t \leqslant \pi/2, \qquad 0 \leqslant s \leqslant 2\pi$$

where a and b are the major and minor axis of the semi-prolate. The minor axis b is chosen to be equal to one throughout the calculations. For different valley shapes only the major axis 'a' is varied. To reduce the number of figures, only the results for cross sections $y = 0$ and $x = 0$ are presented, and they will be referred to as sections A and B, respectively. In addition, two types of planes are distinguished in this paper: an azimuthal plane is defined to be a vertical plane which contains the slowness vector of the incident wave; all other planes are denoted as off-azimuthal planes. For example, if the slowness vector of the incident wave field lies in the xz-plane, section A is an azimuthal plane while section B is an off-azimuthal plane. Incident waves are plane P, SV, SH and Rayleigh waves. The azimuthal angle of incidence ϕ is measured counterclockwise from the negative x-axis (Figure 1). The off-vertical angle of incidence θ is measured from the positive z-axis toward vector r, which defines the azimuthal position on the surface of the half-space. The amplitudes of the incident waves are the same as those used by Dravinski and Mossessian.[4] For convenience, a dimensionless frequency of incident wave Ω is defined as the ratio of the length of the valley along section B (which is equal to 2 for all the valley shapes) and the wavelength of the shear wave in the half-space.

The accuracy of the method is highly dependent on the location of auxiliary surfaces, S_a^0 and S_a^1, the number of sources, M and L, and the number of observation points, N. The auxiliary surfaces are chosen to be in the following form:

$$\mathbf{x}_a^0 = (1 - \xi)\mathbf{x} \tag{11a}$$

$$\mathbf{x}_a^1 = (1 + \xi)\mathbf{x} \tag{11b}$$

$$0 < \xi < 1$$

where the components of x are described in equations (10a–c). Through numerical experiments the value of the parameter ξ is chosen to be between 0·4 and 0·5. The sources and observation points are distributed uniformly along several rings (with constant values of z) on the surfaces S_a^0, S_a^1, and S_1, respectively. The number of sources M and L and observation points vary for different cases, depending on the shape of the scatterer and frequency. In calculations for different frequencies the positions of the auxiliary surfaces are kept the same and only the numbers of sources and observation points are changed. For the examples considered here a typical range for M and L is between 81 and 105 (for all the cases M and L are chosen to be equal), and for N it is between 177 and 245.

Testing of the method

To establish the numerical accuracy of the method, scattering of a vertical incident harmonic plane P wave by a hemispherical valley studied earlier by Sanchez-Sesma[12] is reconsidered. Clearly, this problem is

axisymmetric. The surface displacement field at section A is depicted in Figure 2. It is evident from Figure 2 that the results of the two independent studies are in excellent agreement. Further testing of the method for non-axisymmetric cases has also been conducted through comparisons with the results of a hybrid technique.[19] The results of these comparisons have been shown to be very satisfactory.

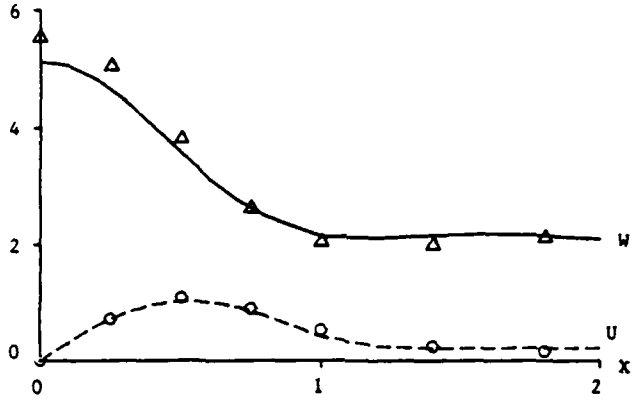

Figure 2. Amplitude of surface displacement spectra for a hemispherical valley and vertical incident P wave and for dimensionless frequency $\Omega = 0{\cdot}866$. Material properties of the half-space and the valley are $\mu_0 = \beta_0 = 1$, $\alpha_0 = 1{\cdot}732$, $\mu_1 = 0{\cdot}3$, $\beta_1 = 0{\cdot}707$, $\alpha_1 = 1{\cdot}323$. Radius of the valley $R = 1$. Dash, dash–dot and solid lines represent x-, y- and z-components (u, v, w) of the displacement vector, respectively obtained in this investigation (this convention is used up to Figure 6). The triangles and open circles denote z- and x-components of the displacement vector by Sanchez-Sesma[12]

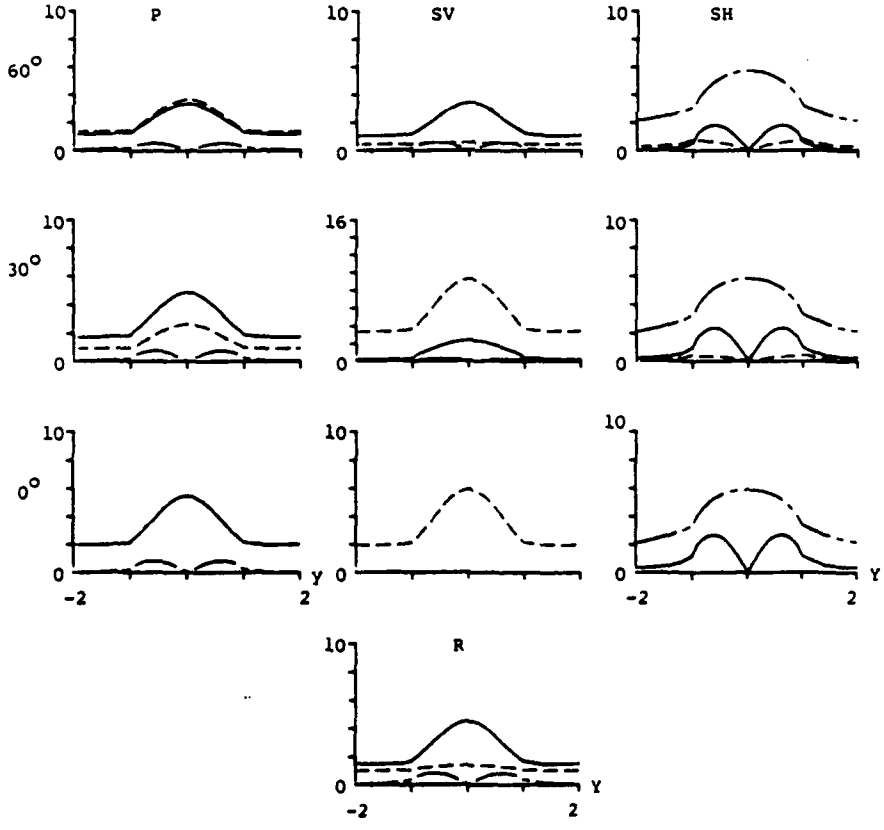

Figure 3. Amplitude of surface displacement spectra for a hemispherical valley of a unit radius $R = 1$ at section B for incident P, SV, SH and Rayleigh waves (denoted by R) with azimuthal angle of incidence $\phi = 0°$ and off-vertical angle of incidence $\theta = 0°, 30°, 60°$. $\Omega = 0{\cdot}5$. Material properties of the half-space and the valley: $\mu_0 = \beta_0 = 1$, $\alpha_0 = 2$, $\mu_1 = 1/6$, $\beta_1 = 0{\cdot}5$, $\alpha_1 = 1$, $Q_\alpha = Q_\beta = 100$. (Unless stated differently, all material properties are kept the same)

Response of hemispherical valleys

Throughout the calculations the intrinsic shear wave velocities of the valley and the half-space are assumed to be equal to one-half and one, respectively. The Poisson ratio ν for all materials is chosen to be 1/3. Figure 3 shows the surface displacements at section B for incident P, SV, SH and Rayleigh waves with azimuthal angle $\phi = 0^\circ$ (an off-azimuthal case). The dimensionless frequency Ω is equal to one-half. For oblique angles of incidence the displacements in the x- and z- directions due to SH waves and in the y-direction due to P, SV and Rayleigh waves are entirely produced by P/SV–SH mode conversions. The coupling between SH and P/SV modes appears to be much stronger for SH incident waves. For example, in the case of SH waves with 30° off-vertical angle of incidence the resulting peak vertical displacement has an amplitude close to that of the free field. This characteristic has also been observed in the case of a canyon.[16] It is interesting to note that for SV waves with 60° angle of incidence and Rayleigh waves the displacement in the x-direction along section B is very insensitive to the presence of the valley.

Increasing the dimensionless frequency to $\Omega = 0{\cdot}75$, the surface displacements at section B for incident P, SV, SH and Rayleigh waves with azimuthal angle $\phi = 0°$ are shown by Figure 4. Comparisons between Figures 3 and 4 reveal a considerable difference in amplification patterns for all the incident waves. In particular, a striking difference takes place in the magnitude of the displacement in the x-direction. In contrast to the results of Figure 3, here the displacement in the x-direction is amplified the most for the case of SV waves with 60° off-vertical angle of incidence and Rayleigh waves. Furthermore, it is evident from Figure 4 that increase in frequency has caused a substantial increase in P/SV and SH mode coupling. For dimensionless frequency $\Omega = 0{\cdot}5$, the peak amplitude of displacement in the x-direction due to incident SH

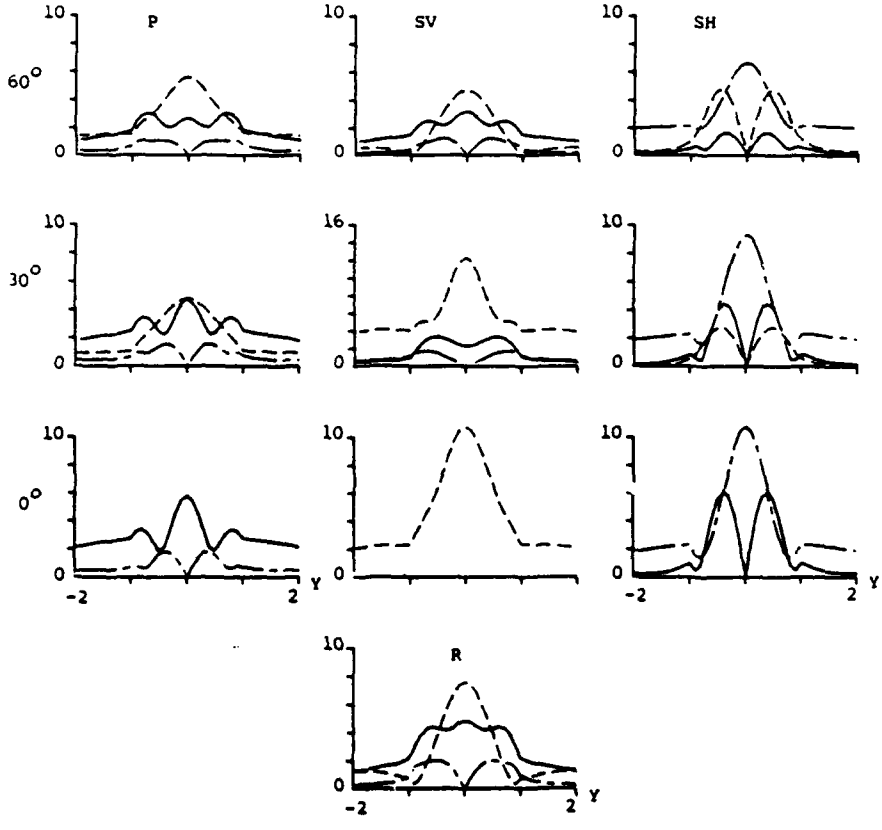

Figure 4. Amplitude of surface displacement spectra for a hemispherical valley at section B and incident P, SV, SH and Rayleigh waves. $R = 1$, $\Omega = 0{\cdot}75$, $\phi = 0°$

waves is less than 50 per cent of the free field, but for $\Omega = 0{\cdot}75$ this amplitude is more than twice that of the free field.

Response of semi-prolate valleys

To study the effect of the valley shape, two types of semi-prolate basin are considered. Type 1 valley has a major to minor axis ratio (a/b) equal to 1·5 and for type 2 valley this ratio is 2. Clearly, these geometries are non-axisymmetric. Figure 5 displays the surface response at section B for different incident waves for type 1 valley. The azimuthal angle of incidence is 0°. The displacement in the x-direction due to incident SV and Rayleigh waves exhibits a remarkable increase in peak amplitude compared to the case of a hemispherical valley (Figure 3). The coupling between SH and P/SV modes also appears to be stronger than in the case of a hemispherical valley. For the same type of valley, Figure 6 shows the surface responses at section A for different incident waves with azimuthal angle of incidence equal to 90°. The amplification pattern for incident P and Rayleigh waves appears to be similar to the case depicted by Figure 5. However, a notable difference is observed for the cases of incident SV and SH waves. Namely, for incident SV waves with an off-vertical angle of incidence of 30° (critical angle), the change in azimuthal angle from 0° to 90° (Figures 5, 6) has reduced the amplification of the predominant motion by 40 per cent at the centre of the valley. For incident SH waves with off-vertical angles of 30° and 60°, this effect is reversed. It should be emphasized that the differences between the results for Figures 5 and 6 occur because of the non-axisymmetric nature of the valley.

For type 2 valley, surface responses at section B for incident SH and Rayleigh waves with azimuthal angle of incidence $\phi = 0°$ are similar[19] to the corresponding cases for type 1 valley. However, for incident P and SV waves the amplitudes of motion in the x-direction for type 2 valley are much smaller than the ones for type 1 valley (the results are omitted for the sake of brevity).

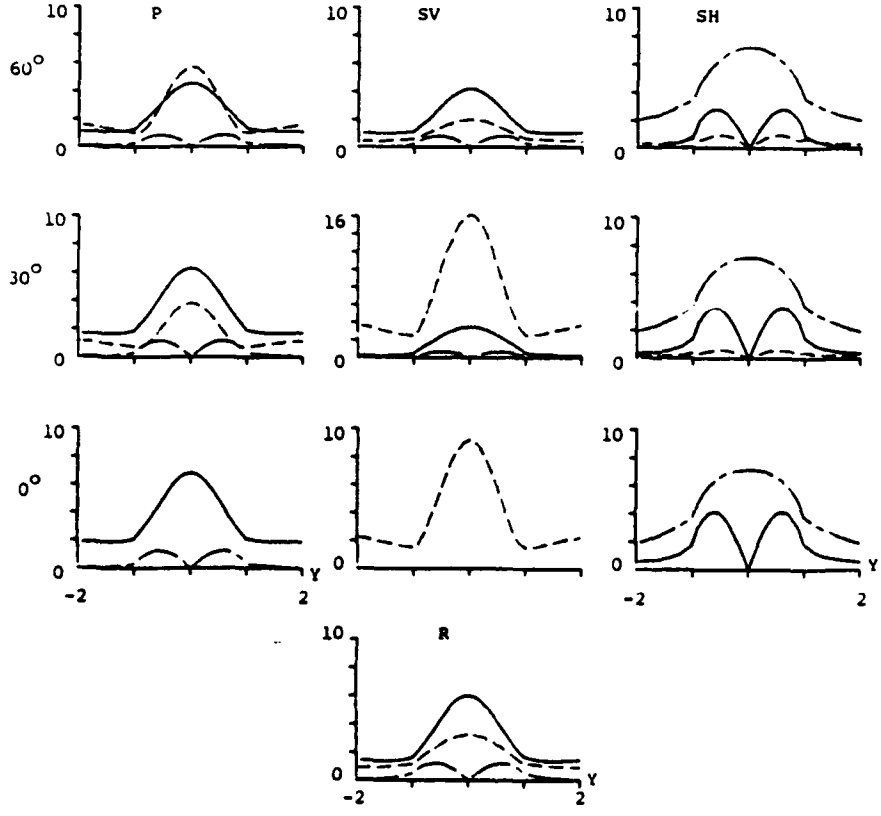

Figure 5. Amplitude of surface displacement spectra for type 1 valley at section B and incident P, SV, SH and Rayleigh waves. Major axis $a = 1{\cdot}5$, minor axis $b = 1{\cdot}$, $\Omega = 0{\cdot}5$, $\phi = 0°$

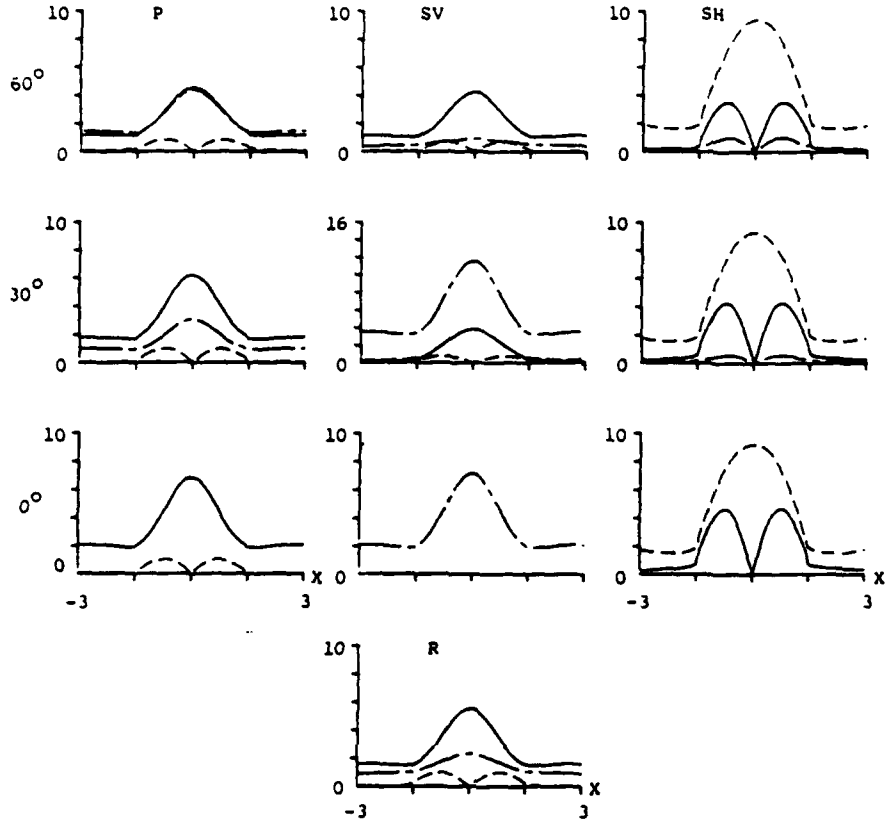

Figure 6. Amplitude of surface displacement spectra for type I valley at section A and incident P, SV, SH and Rayleigh waves. $a = 1{\cdot}5$, $b = 1$, $\Omega = 0{\cdot}5$, $\phi = 90°$

Comparisons with two dimensional models

Since computational efforts are greatly reduced for two dimensional approximations, it is beneficial to use two dimensional models whenever applicable. Therefore, it is of great interest to examine the validity of two dimensional approximations for some three dimensional models. Clearly, for the off-azimuthal cases such comparisons are inadequate since the coupling between P/SV and SH modes cannot be accounted for by using two dimensional models. Here, the azimuthal response of section B for several valley shapes including hemispherical and the type 1 and 2 semi-prolates are compared with the corresponding responses of a two dimensional circular valley. For a plane strain model the responses of circular valleys have been investigated by Dravinski and Mossessian[4] and the accuracy of their results has been verified through several independent studies.[7,9,14] Figure 7 shows the surface responses for horizontal (the y-direction) and vertical displacements due to incident P waves for different types of valleys. The three dimensional results correspond to section B with azimuthal angle of incidence equal to $-90°$. The two dimensional results appear to be in good agreement with type 1 and 2 semi-prolate valleys, and in fair agreement with the case of a hemispherical valley. This agrees with the physical interpretation of the results. As the dimension of the valley in the x-direction increases, the three dimensional model approaches its two dimensional counterpart.

For incident SV and Rayleigh waves the observed similarities and disagreements with the two dimensional results are of the same nature as for the case of incident P waves and therefore are omitted to reduce the number of figures. It should be noted, however, that as the valley becomes more elongated in the x-direction the approach to two dimensional results appears to be particularly uniform for non-predominant components of motion.

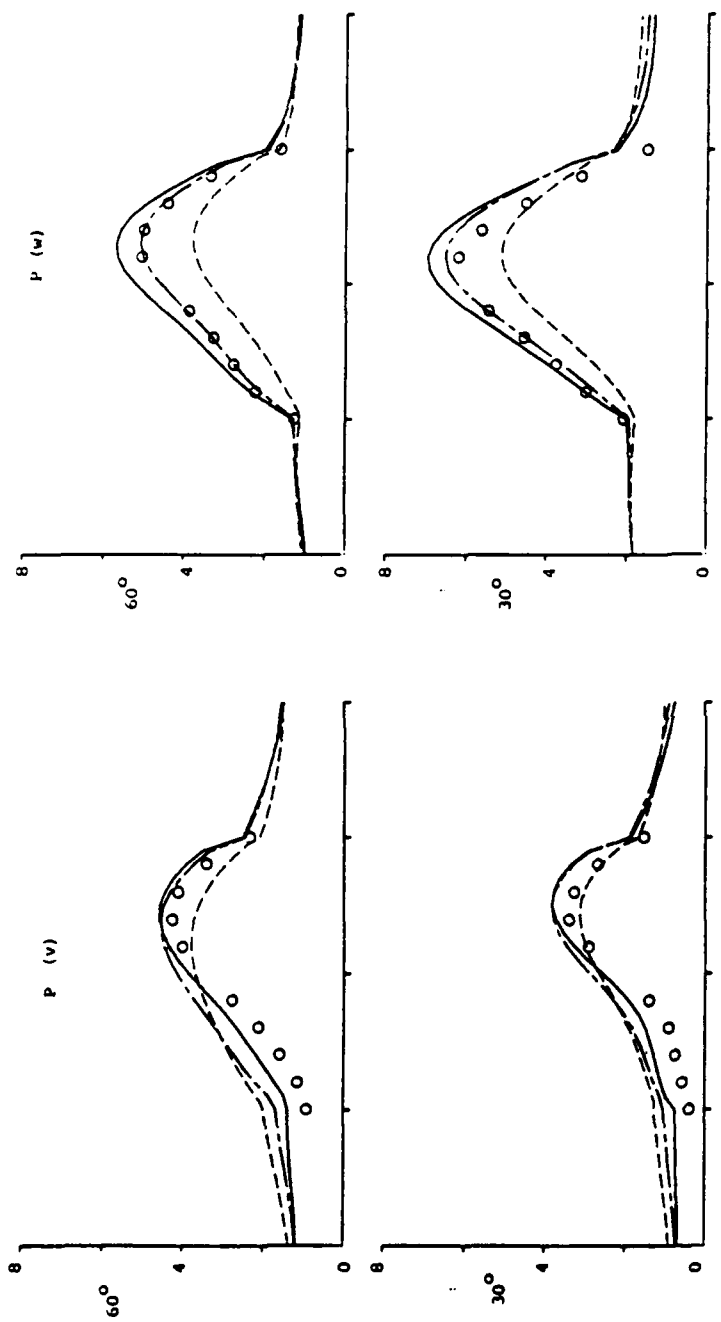

Figure 7. Comparison of surface displacement spectra for horizontal and vertical components of motion (v, w) due to incident P waves for $\phi = -90°$, $\theta = 0°$, 30°, 60°, $\Omega = 0{\cdot}5$. Dash, dash-dot and solid lines represent the results for spherical, type 1 and 2 valleys at section B, respectively. The open circles denote the results for a two dimensional semi-circular valley

Figure 8 shows the surface responses for incident SH waves. For this case the three dimensional results have significant disagreements with the two dimensional ones for all three types of valley, although the differences are still less pronounced for the type 2 valley compared to hemispherical and type 1 valleys. These results suggest that the validity of two dimensional approximations is strongly dependent on the type of incident wave under consideration. For instance, the resulting displacement at the centre of the valley due to vertical incident SH waves is about two to three times (depending on the shape of the valley) greater than the one for the two dimensional case, whereas for the case of incident P wave (Figure 7) the difference for the predominant motion is at most 20 per cent. For the same case, it can be observed that the disagreements with the two dimensional results are greater for type 1 valley compared to the spherical valley, despite the fact that

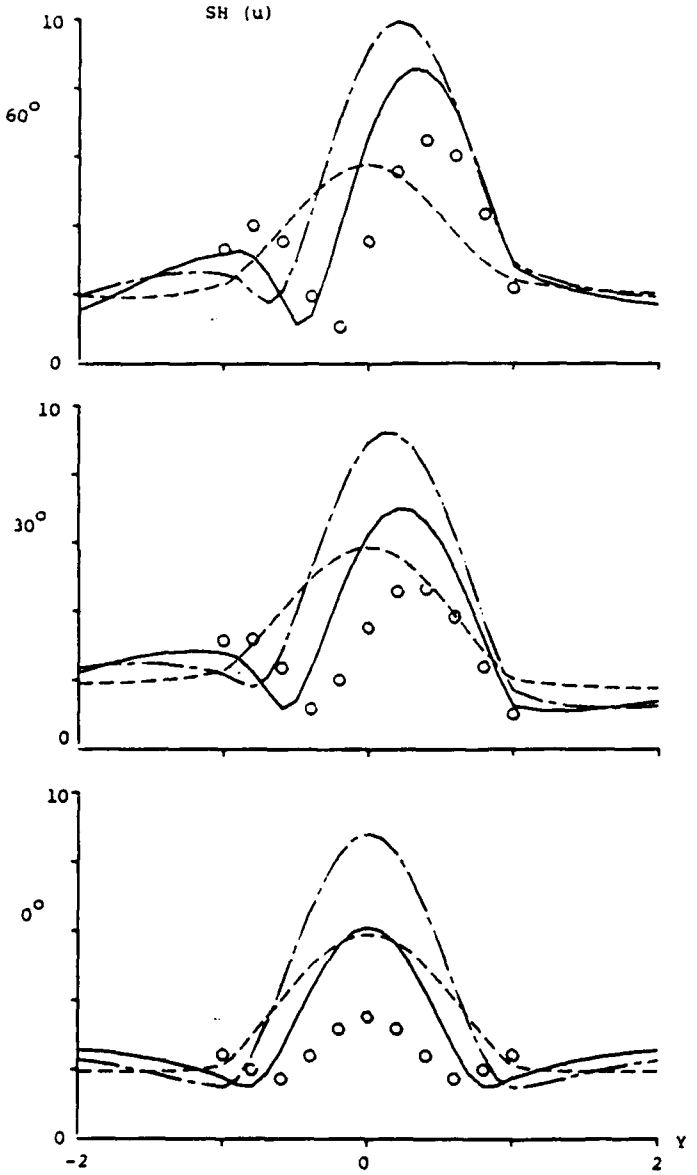

Figure 8. Comparison of surface displacement spectra for incident SH waves (all the parameters and conventions are the same as Figure 7)

type 1 valley is more elongated in the x-direction. These observations indicate that, as the dimension in the x-direction gets longer, the response may not approach the two dimensional results uniformly.

Increasing the dimensionless frequency to $\Omega = 0{\cdot}75$, Figure 9 displays the surface responses for incident P, SV and SH waves (for the sake of brevity the non-predominant motions due to P and SV waves are omitted). It is evident that increase in frequency has caused a considerable increase in discrepancies between two and three dimensional results. For dimensionless frequency $\Omega = 0{\cdot}5$ the results for the spherical valley (Figure 7) are in fairly good agreement with the ones for the two dimensional case; however for dimensionless frequency $\Omega = 0{\cdot}75$ the differences are very significant. This observation demonstrates that a two dimensional

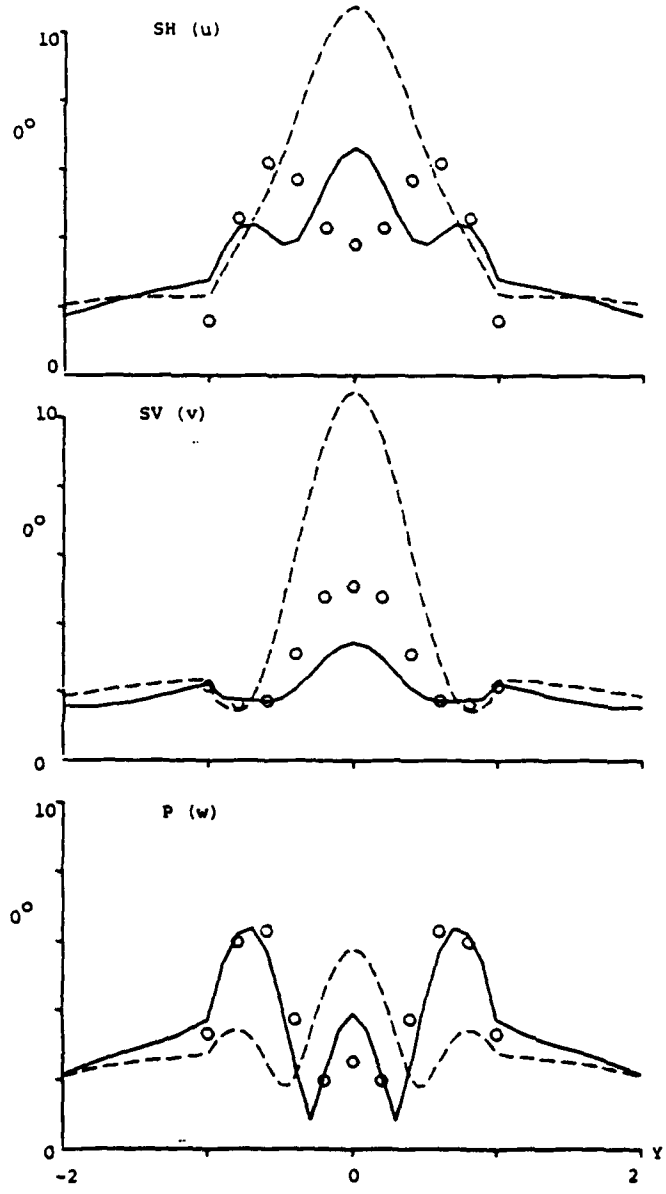

Figure 9. Comparison of surface displacement spectra for predominant components of motion due to vertical incident P, SV and SH waves, $\Omega = 0{\cdot}75$. Dash and solid lines represent the results for spherical and type 1 valleys at section B, respectively. The open circles denote the results for a two dimensional semi-circular valley

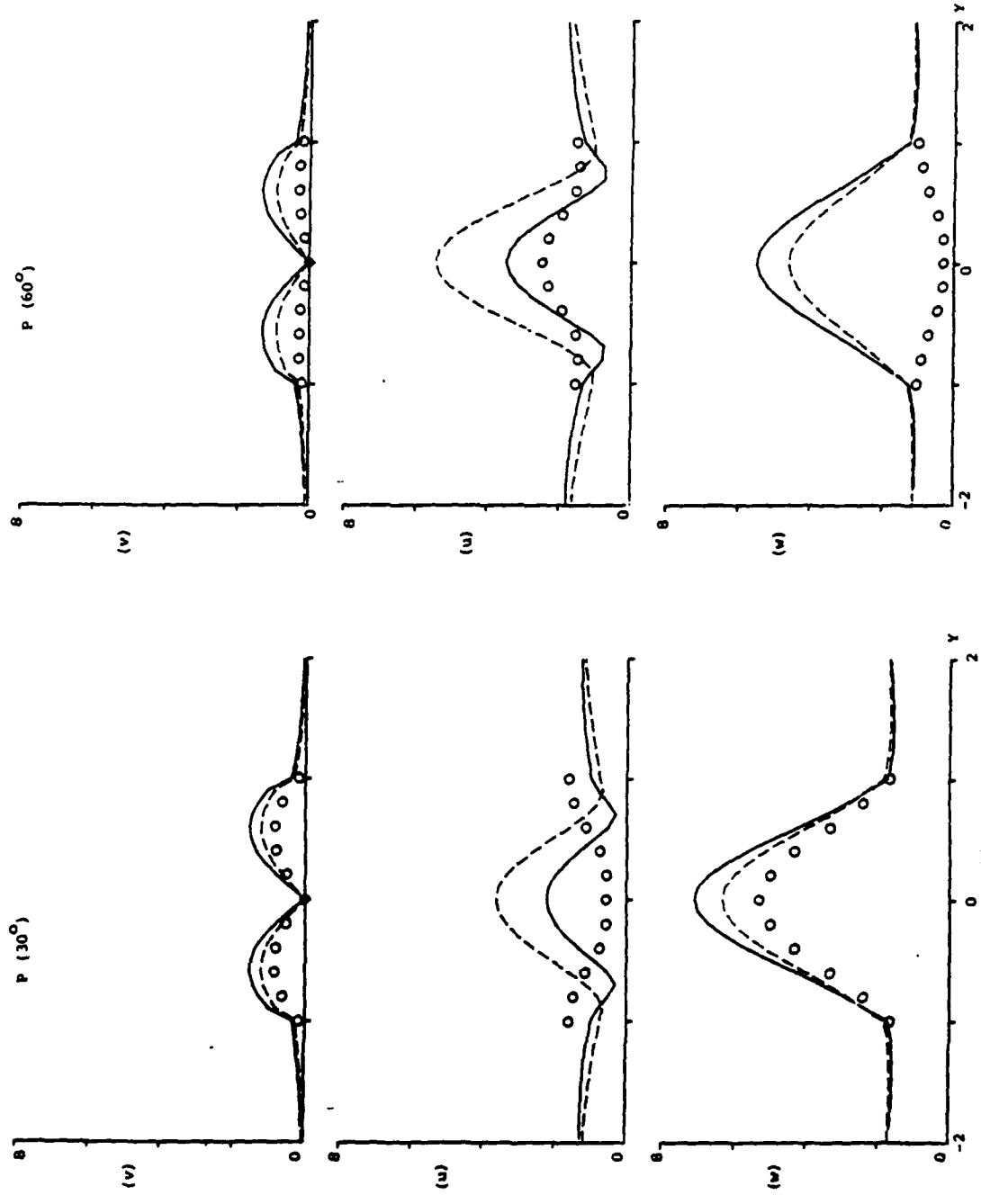

Figure 10. Comparison of surface displacement for incident P wave for $\phi = 0°$. (a) $\theta = 30°$, (b) $\theta = 60°$. $\Omega = 0{\cdot}5$. Dash and solid lines represent the results for type 1 and 2 valleys at section B, respectively. The open circles denote the results for a semi-circular cylindrical valley by Khair *et al.*[14]

approximation of a three dimensional model may produce reasonable results at certain frequencies but become completely inadequate for some other frequencies.

Comparisons with three dimensional responses of cylindrical valleys

Recently Khair *et al.*[14] have considered an interesting model in which the valley is assumed to be in the form of an infinite cylinder and is subjected to a three dimensional incident wave field. This model can account for certain three dimensional features (such as coupling between P/SV and SH modes) and at the same time it retains the computational efficiency of the two dimensional modelling. It is of interest to see how well the results of this model agree with the ones for the semi-prolate valleys. Clearly, if the major axis of the semi-prolate valley is very large compared to its minor axis, the results should be similar to the ones for a cylindrical valley at stations away from the edges in the x-direction. Figure 10(a) shows the surface responses for semicircular cylindrical[14] and semi-prolate valleys (types 1 and 2) due to incident P waves. The three dimensional responses correspond to those at section B. The azimuthal and off-vertical angles of incidence are 0° and 30° respectively. It should be noted that the semi-circular section of the cylinder coincides with section B. It is apparent in Figure 10(a) that reasonable agreements between the three dimensional and cylindrical models exist for the displacements in the y- and z-directions. However, for the displacements in the x-direction there are significant differences between the results. Namely, at the centre of the valley the three dimensional models predict large amplification, but for the cylindrical valley this component of motion is de-amplified.

Figure 10(b) shows the surface responses for incident P waves with off-vertical angle of incidence equal to 60°. The disagreements between the results have a surprisingly different nature from the ones for the case of $\theta = 30°$ [Figure 10(a)]. Here the major discrepancies occur for the y- and z-components of displacements. In particular, for the vertical displacement the differences between three dimensional and cylindrical valleys are remarkable.

In the cases of incident SV waves the disagreements between the amplification patterns are not as great as the ones for incident P waves; however, pronounced differences for non-predominant components of displacement are still present (the results are omitted for the sake of reduction in the number of figures). Overall, these observations suggest that the approximation of fully three dimensional valleys by such a model may in some cases lead to very misleading results.

SUMMARY AND CONCLUSIONS

Scattering of steady state plane P, SV, SH and Rayleigh waves by three dimensional dipping layers of arbitrary shape has been investigated by using an indirect boundary integral equation method. Numerical examples for different parameters such as geometry of basin, and nature and frequency of the incident wave are presented.

Systematic comparison between three dimensional and corresponding two dimensional models demonstrate that the validity of a two dimensional approximation for a given valley shape may be affected strongly by changes in azimuthal angle of incidence, type of incident wave and frequency. The discrepancies of two dimensional modelling appear to be much more pronounced for the case of incident SH waves. Furthermore, it is shown that, as the valley becomes more elongated in the direction perpendicular to the observation plane, the approach to two dimensional results may not take place uniformly. Another important feature of the results is the existence of strong coupling between P/SV and SH modes, which has no correspondence in two dimensional models. Such off-azimuthal mode conversions are particularly strong for incident SH waves. This characteristic has also been observed for the case of a canyon.[15,19] Over all, these features indicate the importance of the three dimensional modelling for studying the seismic response of dipping layers of arbitrary shape.

It should be pointed out that the method can be applied to the case of a layered valley embedded in a layered medium. However, this would require the use of Green's functions for the layered medium (e.g. Apsel and Luco;[20] Kundu and Mal[21]). For two dimensional cases Dravinski and Mossessian[4] have demonstrated

the capability of the method for modelling valleys with several dipping layers embedded in a uniform half-space. Other alternatives such as hybrid techniques appear to be very promising for handling very complex media (e.g. Mossessian and Dravinski;[7, 22] Khair *et al.*[14, 15]).

ACKNOWLEDGEMENT

This work was supported in part by the National Science Foundation under Grant No. 53–4519–3792 and in part by the Office of Naval Research under Contract No. N00014–88–K–0157.

REFERENCES

1. K. Aki, 'Local site effects on strong ground motion', *Proc. earthquake eng. soil dyn. II*, ASCE, Park City, Utah (1988).
2. J. G. Anderson, P. Bodin, J. N. Brune, J. Prince, S. K. Singh, R. Quaas, and M. Onate, 'Strong ground motion from the Michoacan, Mexico, earthquake', *Science* **233**, 1043–1049 (1986).
3. H. Kagami, C. M., Duke, G. C. Liang and Y. Ohta, 'Observation of 1- to 5-second microtremors and their application to earthquake engineering. Part II. Evaluation of site effect upon seismic waves amplification due to extremely deep soil deposits', *Bull. seism. soc. Am.* **72**, 987–998 (1982).
4. M. Dravinski and T. K. Mossessian, 'Scattering of harmonic P, SV, and Rayleigh waves by dipping layers of arbitrary shape', *Bull. seism. soc. Am.* **77**, 212–235 (1987).
5. P. Moczo, P.-Y. Bard and I. Psencik, 'Seismic response of a two dimensional structure by the ray method', *J. Geophys.* **62**, 38–49 (1987).
6. P.-Y. Bard and M. Bouchon, 'The two-dimensional resonance of sediment-filled valleys', *Bull. seism. soc. Am.* **75**, 905–922 (1985).
7. T. K. Mossessian and M. Dravinski, 'Application of a hybrid method for scattering of P, SV, and Rayleigh waves by near surface irregularities', *Bull. seism. soc. Am.* **77**, 1784–1803 (1987).
8. S. Kobayashi, 'Elastodynamics', in *Boundary Element Methods in Mechanics* (Ed. D. E. Beskos), North-Holland, Amsterdam, 1987, Chapter 4.
9. H. Eshraghi and M. Dravinski, 'Transient scattering of elastic waves by dipping layers of arbitrary shape. Part. 2. Plain strain model', *Earthquake eng. struct. dyn.* **18**, 417–434 (1989).
10. V. W. Lee, 'Three-dimensional diffraction of plane P, SV and SH waves by a hemispherical alluvial valley', *Soil dyn. earthquake eng.* **3**, 133–144 (1984).
11. S. Day, 'Finite element analysis of seismic scattering problem', *Ph.D. Thesis*, UC San Diego, CA, 1977.
12. F. J. Sanchez-Sesma, 'Diffraction of elastic waves by three-dimensional surface irregularities', *Bull. seism. soc. Am.* **73**, 1621–1636 (1983).
13. J.-J. Lee and C. A. Langston, 'Wave propagation in a three dimensional circular basin', *Bull. seism. soc. Am.* **73**, 1637–1653 (1983).
14. K. R. Khair, S. K. Datta and A. H. Shah, 'Three dimensional amplification of seismic waves by alluvial valleys of arbitrary shape: Part I. Incident P and SV waves', *Report No. CUMER-88-2*, Department of Mechanical Engineering, University of Colorado at Boulder, 1988.
15. K. R. Khair, S. K. Datta and A. H. Shah, 'Amplification of obliquely incident seismic waves by cylindrical alluvial valleys of arbitrary cross sectional shape', *Bull. seism. soc. Am.* **79**, 610–630 (1989).
16. T. K. Mossessian and M. Dravinski, 'Scattering of elastic waves by three dimensional surface topographies', *Wave motion* **11**, 579–592 (1989).
17. K. Aki and P. G. Richards, *Quantitative Seismology*, Vol. I, Freeman, San Francisco, CA, 1980.
18. R. J. Apsel and J. E. Luco, 'Impedance functions for foundations embedded in a layered medium: An integral equation approach', *Earthquake eng. struct. dyn.* **15**, 213–231 (1987).
19. T. K. Mossessian, 'Diffraction of elastic waves by non-axisymmetric three dimensional subsurface inhomogeneities using a boundary integral equation method and a hybrid technique', *Ph.D. Thesis*, Department of Mechanical Engineering, University of Southern California, Los Angeles, 1990.
20. R. J. Apsel and J. E. Luco, 'On the Green's functions for a layered half space', *Bull. seism. soc. Am.* **73**, 931–951 (1983).
21. T. Kundu and A. K. Mal, 'Elastic waves in multilayered solids due to a dislocation source', *Wave motion* **7**, 459–471 (1985).
22. T. K. Mossessian and M. Dravinski, 'A hybrid technique for scattering of elastic waves by three dimensional irregularities', submitted for publication.

EARTHQUAKE ENGINEERING AND STRUCTURAL DYNAMICS, VOL. 19, 681–691 (1990)

AMPLIFICATION OF ELASTIC WAVES BY A THREE DIMENSIONAL VALLEY. PART 2: TRANSIENT RESPONSE

TOMI K. MOSSESSIAN* AND MARIJAN DRAVINSKI

Department of Mechanical Engineering, University of Southern California, Los Angeles, California 90089, U.S.A.

SUMMARY

Transient response of three dimensional dipping layers of different shapes subjected to incident P, SV, SH and Rayleigh waves is investigated. The time domain response is constructed from steady state solutions through the Fourier synthesis. An indirect boundary integral equation method is applied to calculate the required steady state solutions. The material of the half-space and the layer is assumed to be linear, weakly inelastic, homogeneous and isotropic.

Numerical results show that the maximum amplification of motion is strongly dependent upon the type of incident wave, the shape of the basin and signal frequency. The change in the shape of the valley from hemispherical to semi-prolate causes a significant increase in the amplitude of surface waves near the edges; however, the maximum amplification of motion near the centre of the valley decreases. This phenomenon is especially apparent for the case of an incident P wave. In comparison to the corresponding two dimensional responses, the amplitude of motion near the centre of the valley is in general higher for three dimensional models.

INTRODUCTION

The literature review in the companion paper[1] showed that there are only a few studies that have considered scattering of elastic waves by three dimensional dipping layers. An even fewer number of investigations have addressed the transient responses of three dimensional basins. Among these, only the work of Lee and Langston[2] discusses the time domain solution in studying scattering of P and SH waves by a circular (axisymmetric) three dimensional basin using a ray technique. However, this solution is limited to a high frequency range.

In this paper, the time domain response of three dimensional dipping layers of different shapes is studied. The present work is an extension of the study by Mossessian and Dravinski,[1] in which steady state scattering of elastic waves by three dimensional dipping layers was considered. The transient response is constructed from the steady state solutions through the Fourier synthesis. Incident P, SV, SH and Rayleigh waves are considered. Surface response for several basin shapes, angles of incidence and signal frequencies is presented. The differences and similarities in wave propagation patterns with respect to responses of two dimensional models are discussed.

METHOD OF SOLUTION

The time domain solutions are obtained through the fast Fourier synthesis of steady state responses calculated at discrete frequencies. The indirect boundary integral equation method developed in the companion paper by Mossessian and Dravinski[1] is used to calculate the steady state results. Incident P, SV, SH and Rayleigh waves are assumed. The incident signal is in the form of the Ricker wavelet[3] defined as

$$u(t) = (\pi)^{1/2}/2(a^2 - 0{\cdot}5)\exp(-a^2) \tag{1}$$

$$a = \pi t/t_p$$

*Presently at Structural Research and Analysis Corp. 1661 Lincoln Blvd. Suite 200, Santa Monica, CA 90404, U.S.A.

0098–8847/90/050681–11$05.50

Received 10 January 1989
Revised 18 January 1990

where t_p is the predominant period of the wavelet. The Fourier transform of this wavelet has the following form:

$$U(\omega) = -t_p^3\omega^2/8\pi^2 \exp(-\omega^2 t_p^2/4\pi^2) \tag{2}$$

Clearly, $U(\omega)$ has its maximum at $\omega_p = 2\pi/t_p$ and it decreases very rapidly at frequencies larger than ω_p. For all the results presented here the frequency domain calculations are done for the range $0 < \omega < 3{\cdot}5\omega_p$ at equal increments of frequency. For this range 32 to 50 sample frequencies are used to calculate the transient response.

NUMERICAL RESULTS AND DISCUSSIONS

Spherical and semi-prolate basins considered in this analysis have been defined in equations 10 (a–c) of the paper by Mossessian and Dravinski.[1] To reduce the number of figures only the surface responses for cross sections $y = 0$ and $x = 0$ are presented and they will be referred to as sections A and B, respectively. The conventions for azimuthal and off-vertical angles of incidence are the same as the ones used in the companion paper.[1] Throughout the calculations the shear wave velocities of the basin and the half-space are assumed to be equal to one-half and one, respectively. The Poisson ratio ν for all materials is chosen to be 1/3. For convenience a non-dimensional time $\tau = t\beta_0/b$ is introduced. Therefore the values of τ_p throughout the paper correspond to non-dimensional predominant periods. It should be noted that the response would remain the

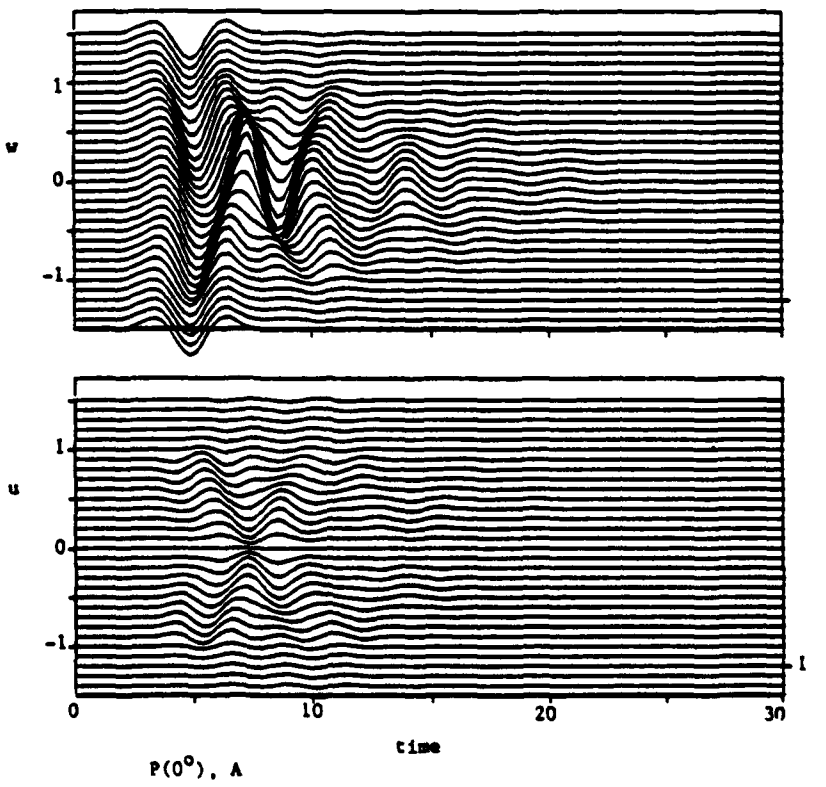

Figure 1. Surface responses (u, w) for a hemispherical valley of radius $R = 1$ at equally spaced stations along section A, for a vertical incident P wave. $\phi = 0°$, $\theta = 0°$, $\tau_p = 4$. Material properties of the half-space and the valley: $\mu_0 = \beta_1 = 1{\cdot}$, $\alpha_0 = 2$, $\mu_1 = 1/6$, $\beta_1 = 0{\cdot}5$, $\alpha_1 = 1{\cdot}$, $Q_\alpha = Q_\beta = 100$ (all material properties are kept the same). The tickmark on the right hand side of each figure gives the scale for the unit magnitude of displacements. τ and τ_p denote dimensionless time and predominant period, respectively

same for any valley of the same shape (same a/b ratio) as long as the non-dimensional time, shear wave velocity ratio β_1/β_0 and Poisson ratios are the same.

Hemispherical valley

Because of the axisymmetric nature of the basin the azimuthal angle of incidence ϕ is taken to be equal to zero for all the results. Surface responses at section A due to an incident P wave are shown in Figure 1. The predominant period of the signal τ_p is 4, which corresponds to the fundamental period of a P wave for a flat layer assumption at the centre of the valley (one-half that of an S wave). In comparison to the corresponding results for two dimensional valleys[4] the peak amplitude of predominant motion is about 50 per cent higher for the three dimensional case. Nevertheless, near the centre of the basin the wave propagation patterns, namely the arrivals and duration of surface waves, are similar to those of a semi-circular valley. However, near the edges, the amplitudes of the surface waves are smaller than the ones for the two dimensional case. This phenomenon is due to the fact that for a spherical type basin the focusing of the surface waves toward the centre and their spreading away from the centre are much stronger than in the two dimensional case. The maximum amplification occurs for the second peak of the Ricker wavelet, which is mainly due to constructive interference of surface waves and the refracted incident wave. The results for a predominant period of $\tau_p = 7$ have also been calculated (to reduce the number of figures these results are omitted). The main difference between these results and the ones for a lower period ($\tau_p = 4$) is that the surface waves completely disappear. This is not surprising since the fundamental period is considerably longer than the fundamental period of an equivalent horizontal layer.

Figure 2 shows the surface responses at section A for a vertical incident SV wave with predominant period $\tau_p = 4$. Similar to the two dimensional cases,[4-6] the amplitude and duration of surface waves are much

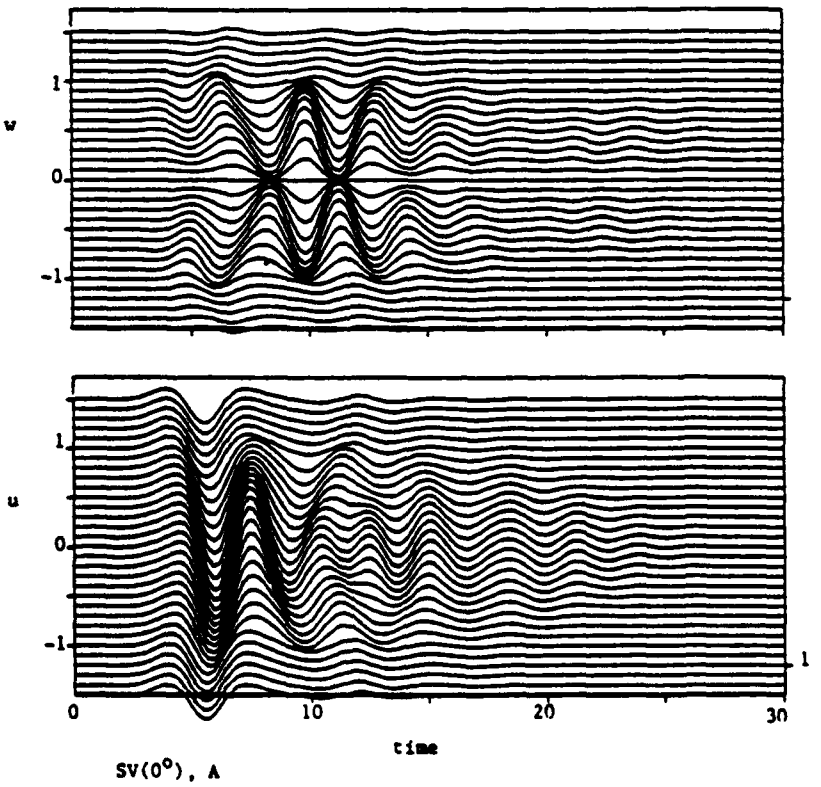

Figure 2. Surface responses (u, w) for a hemispherical valley at section A for vertical incident SV wave. $\phi = 0°$, $\theta = 0°$, $\tau_p = 4$, $R = 1$

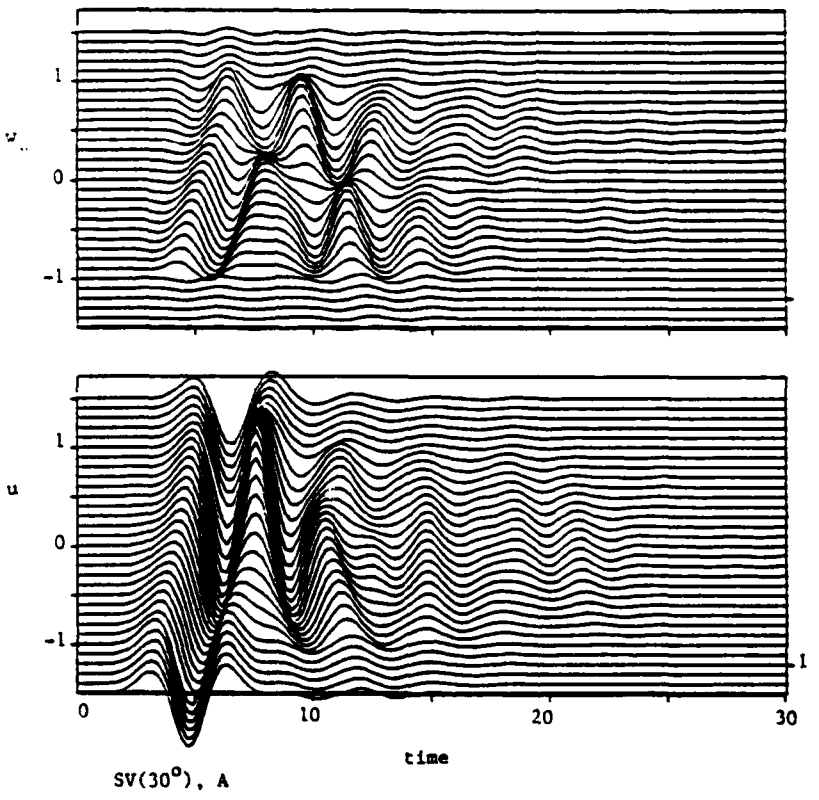

Figure 3. Surface responses (u, w) for a hemispherical valley at section A for incident SV wave with $\phi = 0°$ and $\theta = 30°$. $\tau_p = 4$, $R = 1$

higher for an incident SV wave than the case of an incident P wave (Figure 1). However, the maximum amplification of motion for the incident SV wave is much smaller than the case of the incident P wave. In comparison with two dimensional circular valleys, the peak amplitudes of the predominant motion are about the same but the amplitude of the surface waves is higher for the three dimensional case. The phase velocity of the surface waves is about 0·85 (clearly displayed in the non-predominant component of motion), which compares well with the first higher mode of the Rayleigh waves. Increasing the predominant period of the incident signal to 7 results in a large reduction of surface wave amplitudes (these resuls are omitted for the sake of brevity).

For incident SV waves with off-vertical angle of incidence $\theta = 30°$ (critical angle) the surface responses at section A are shown in Figure 3. Here the location of the peak amplitude is shifted to the right of the centre of the valley and it corresponds to the second peak of the Ricker wavelet. Considering the phase velocities of the surface waves (apparent in the vertical component of motion) and refracted incident wave, it appears that the resulting amplitude of the second peak is mainly due to constructive interference of the reflected surface waves travelling towards left and the refracted incident wave (similar observations have been obtained in the case of two dimensional valleys[6]).

Figure 4 shows the surface responses at section A due to incident SH waves for three different off-vertical angles of incidence. Because of symmetry, the only non-zero component of motion at this section is in the y-direction. It should be noted that for the case of vertical incidence the response of the valley is the same as in the case of the vertical SV wave, provided that the proper switching of the observation planes and the non-zero displacement components is taken into account. Hence, the observed motion at the centre of the valley is exactly the same as the one shown in Figure 2. It is evident from Figure 4 that the changes in the off-vertical

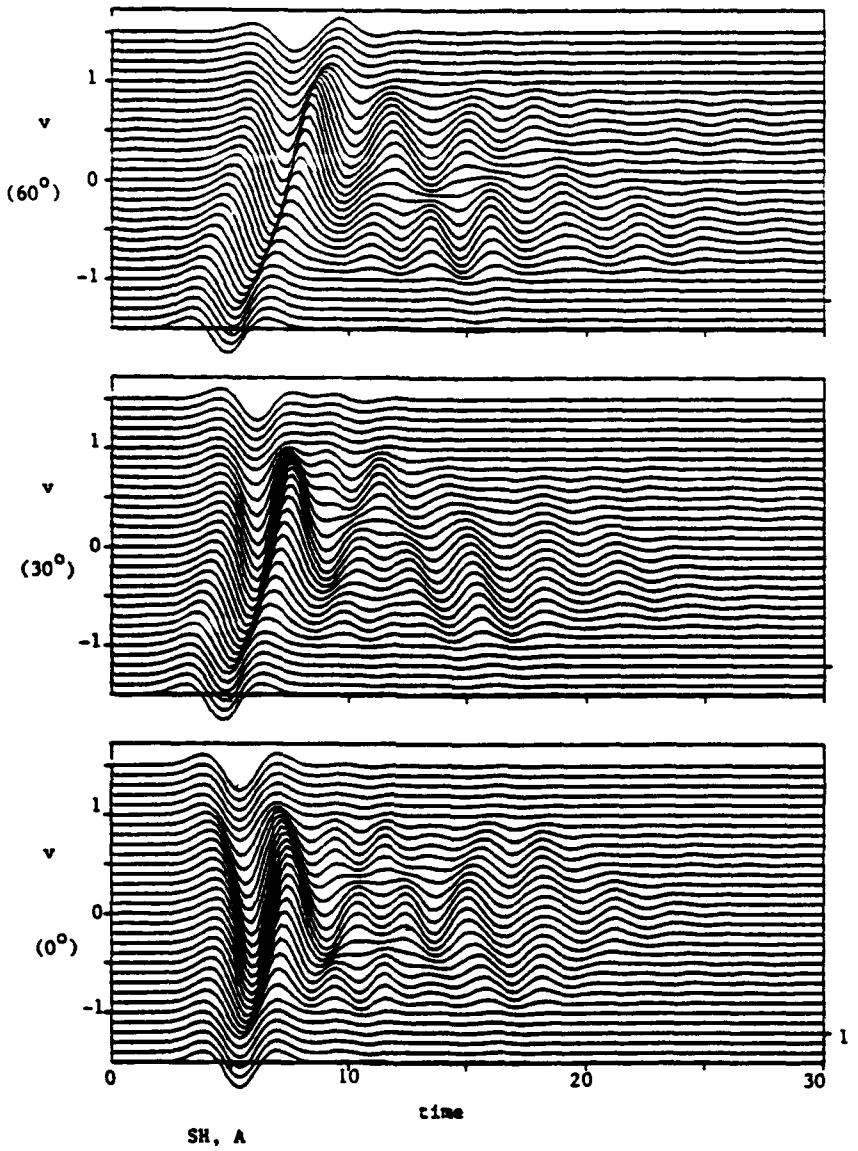

Figure 4. Surface responses (v) for a hemispherical valley at section A for incident SH wave with $\phi = 0°$ and $\theta = 0°, 30°, 60°$. $\tau_p = 4$, $R = 1$

angle of incidence have not affected the peak amplitude of motion; however, its location is shifted to the right side of the centre of the valley. Furthermore, it appears that the duration of motion for the case of $\theta = 60°$ has slightly increased. Owing to the complexity of the motion it is hard to analyse the contribution of Love waves to the observed surface waves.

Figure 5 shows the surface responses at section A due to incident Rayleigh waves. For this case the amplitudes of secondary surface waves generated from the right edges of the valley are larger than the peak amplitude of the refracted incident wave. This is especially apparent for the vertical component of motion. The phase velocities of successive surface waves with dominant vertical motion, generated from the right edges of the valley, are lower than the ones observed for other incident waves.

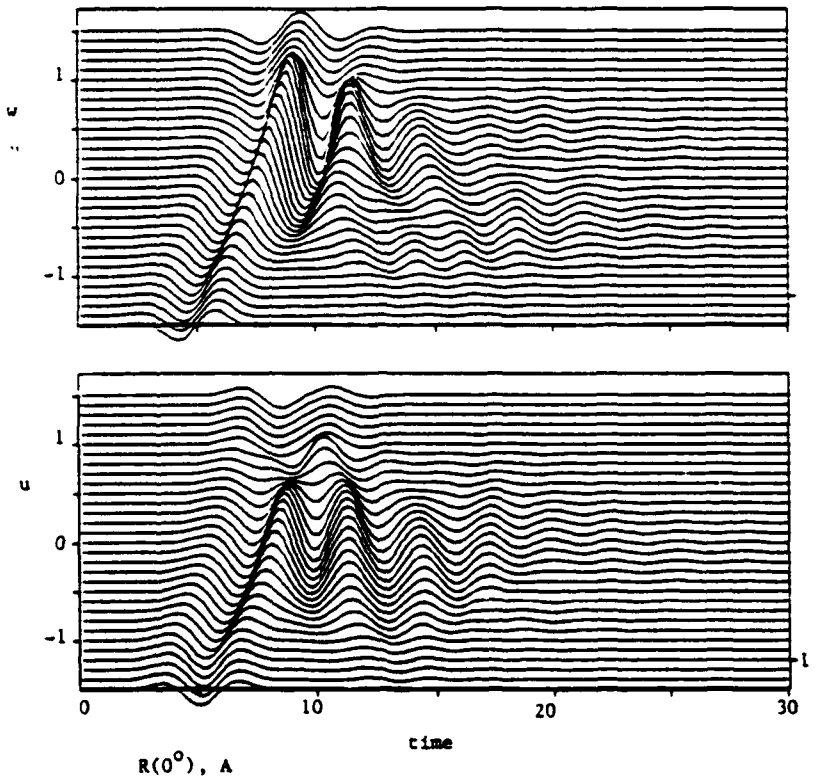

Figure 5. Surface responses (u, w) for a hemispherical valley at section A for incident Rayleigh wave with $\phi = 0°$, $\tau_p = 4$, $R = 1$

Figure 6 shows the surface responses at section B for an incident P wave with off-vertical angle of incidence $\theta = 30°$ (off-azimuthal case). For this case all three components of displacements are non-zero. The displacement component in the y-direction is totally due to P/SV to SH mode conversions. It is interesting to observe that the peak amplitude of the y-component of motion is comparable with the free-field amplitude of the horizontal displacement in the x-direction. The rather low phase velocity for this component of motion may suggest the presence of Love waves. It should be mentioned that the resulting amplitude in the y-component of motion for corresponding cases of incident SV and Rayleigh waves is about the same as the ones for incident P waves (to reduce the number of figures these results are omitted). However, for incident SH waves the resulting displacements in the x- and z-directions, which are products of SH to P/SV mode conversions, are rather large.[7] This agrees well with the observations made for the frequency domain results,[1] namely that the off-azimuthal mode conversions are much stronger for incident SH waves than for the other three types of incident wave.

Semi-prolate valley

A semi-prolate basin with its major to minor axis ratio equal to two is considered. Computational efforts needed for this geometry are much higher than what is required for the hemispherical basin. This is mainly due to the fact that the length of this basin in the x-direction (the major axis) is twice that of the hemispherical basin. Hence, for the same incident signal the dimensionless frequency with respect to the major axis of the semi-prolate is twice that of the hemispherical case. To keep the computational efforts in an affordable range only a few results for shorter periods ($\tau_p = 4$) are obtained. Figure 7 shows the surface response for vertical components of motion at sections A and B for a vertical incident P wave with predominant period $\tau_p = 4$.

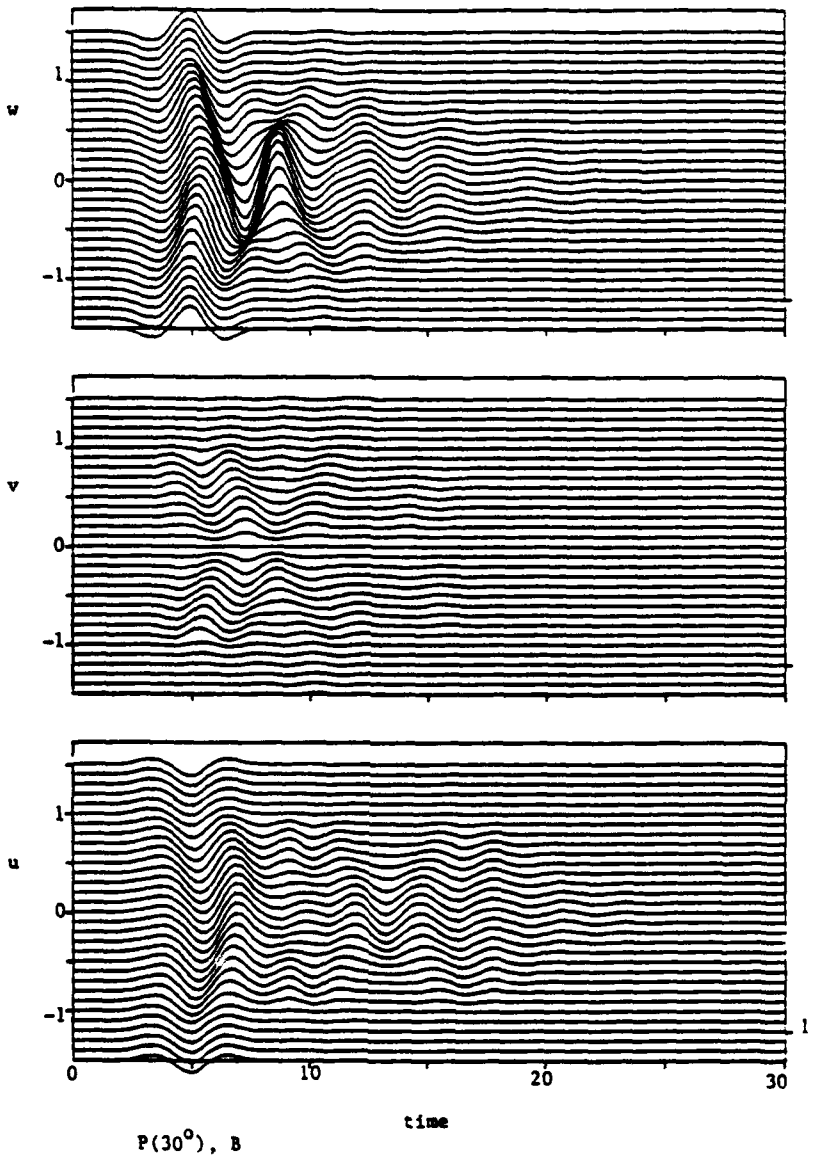

Figure 6. Surface responses (u, v, w) for a hemispherical valley at section B for incident P wave with $\phi = 0°$ and $\theta = 30°$. $\tau_p = 4$, $R = 1$

The maximum amplification of the second peak of the Ricker wavelet is considerably smaller than the one for the corresponding case of the hemispherical basin (Figure 1). This peak amplitude occurs at a later time for the prolate valley than the hemispherical valley. In contrast to the case of a hemispherical valley, here the surface waves generated from the surrounding edges of the prolate have to travel different distances to reach the centre of the valley. Thus the focusing effect near the centre is not as intense as in the case of the hemispherical valley. Near the edges of section B, however, the amplitudes of the surface waves are larger than those for the hemispherical valley, and they have a closer resemblance to the corresponding two dimensional results. The differences in surface wave propagation pattern for the two sections A and B are quite apparent (for the hemispherical case they would be the same). At later times the amplitudes of surface waves near the edges of section A (longer section) are much larger than those for section B; therefore the

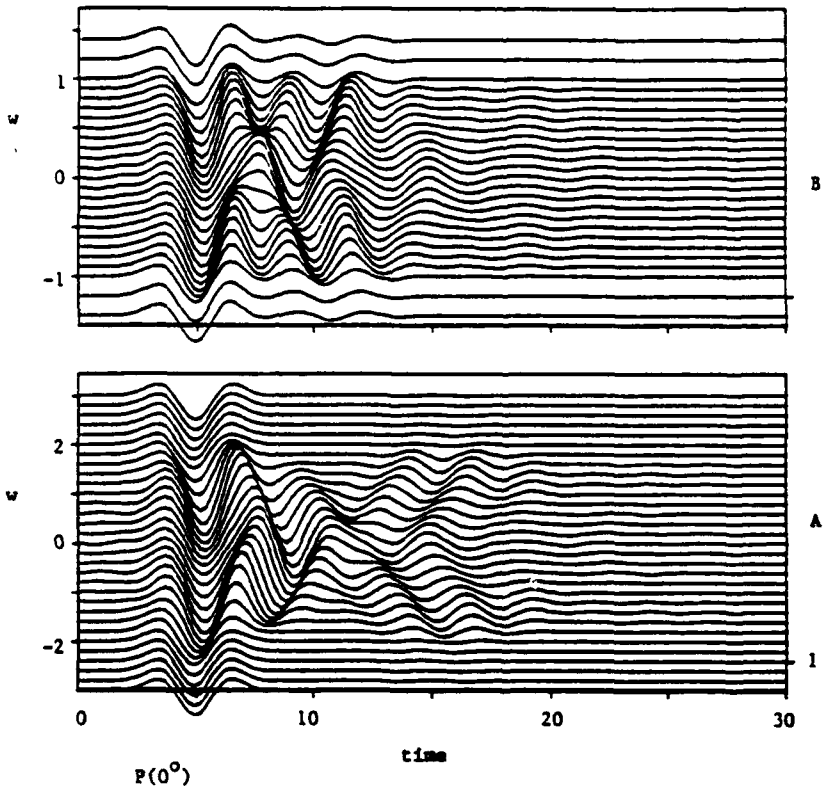

Figure 7. Surface responses (w) for semi-prolate valley at sections A and B for incident P wave with $\phi = 0°$ and $\theta = 0°$. $a = 2$, $b = 1$, $\tau_p = 4$

duration of motion appears to be longer. It should be mentioned that for incident P waves with predominant period $\tau_p = 7$ hardly any surface waves can be observed.[7]

Figure 8 shows the surface responses at section A for a vertical incident SV wave with azimuthal angle of incidence $\phi = 0°$. The predominant period τ_p is 7. In contrast to the corresponding case for incident P waves (not shown here[7]), the surface waves are quite visible here and the duration of motion is much longer. Changing the azimuthal angle of incidence of $\phi = 90°$, the results at section B are depicted by Figure 9. The resulting amplitude and duration of surface waves are much lower than in the case shown by Figure 8. However, in comparison with the corresponding case of the hemispherical valley, the amplitudes of the surface waves are larger. It should be emphasized that the observed differences between the results of Figures 8 and 9 are due to the non-axisymmetric nature of the basin.

Figure 10 shows the surface responses at sections A and B for vertical incident SH waves with azimuthal angle of incidence $\phi = 0°$ and predominant period $\tau_p = 4$. It should be noted that the results for section B in Figure 10 are the same as those for vertical incident SV waves with azimuthal angle of incidence $\phi = 90°$. Comparing the results for section B with the ones for the hemispherical valley (Figure 2), the peak amplitudes are about the same. However, owing to the different arrival times of the surface waves, the wave pattern at later times is slightly different. Comparisons of the results for sections A and B show significant differences in wave propagation pattern at later times. For section A the propagation of the surface waves across the valley appears much more clearly than it does for section B. Also the duration of motion near the edges is much longer for section A than for section B. It should be pointed out that the slight violations of causality at the initial part of the response (more apparent for section A) are mainly due to numerical inaccuracy at higher frequencies.

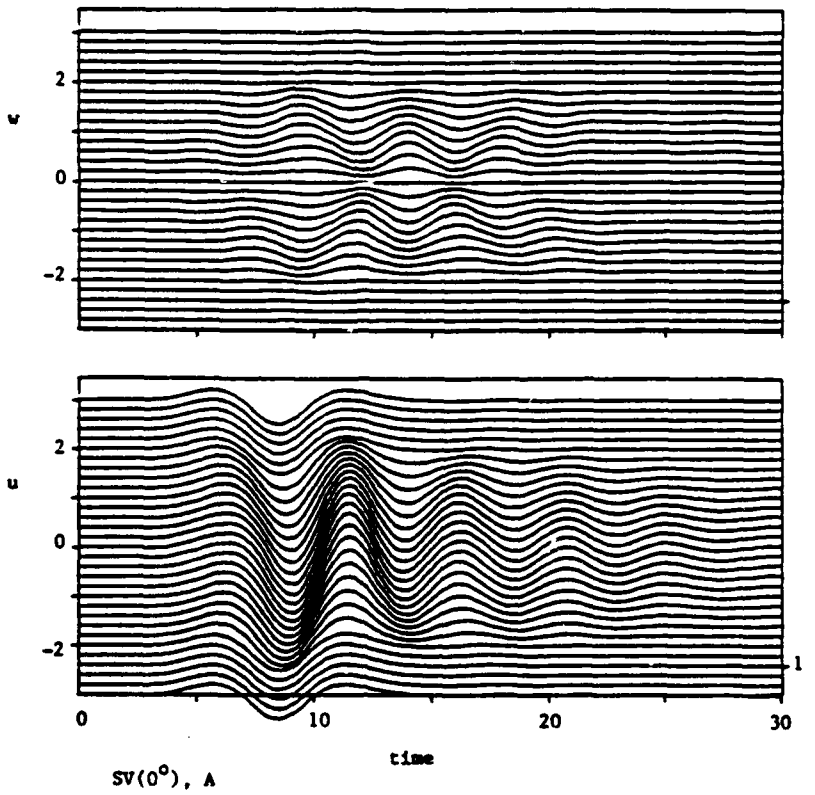

Figure 8. Surface responses (u, w) for semi-prolate valley at section A for incident SV wave with $\phi = 0°$ and $\theta = 0°$. $a = 2$, $b = 1$, $\tau_p = 7$

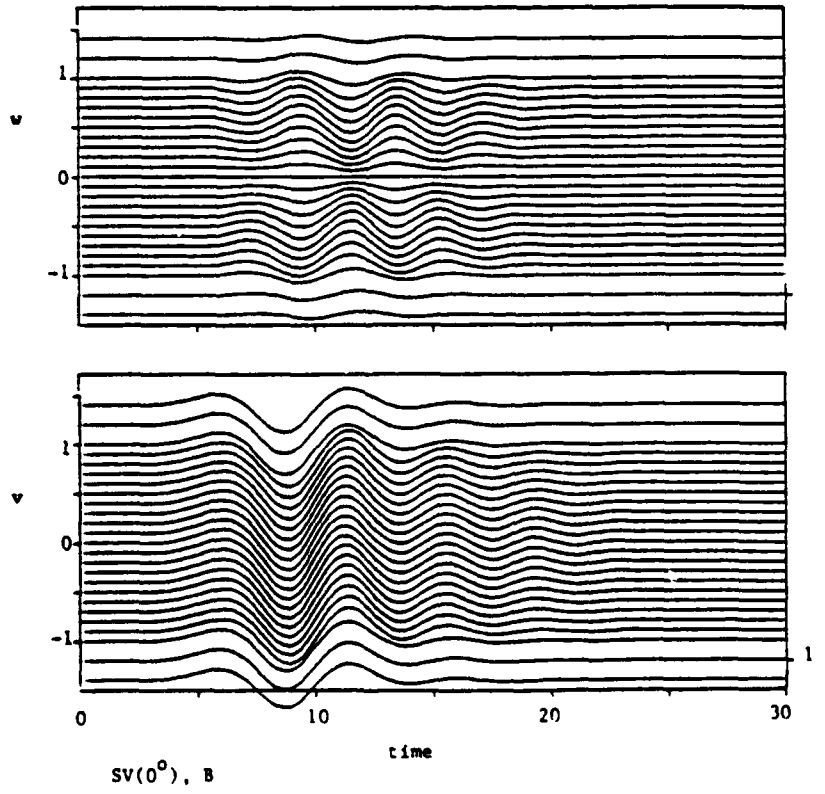

Figure 9. Surface responses (v, w) for semi-prolate valley at section B for incident SV wave with $\phi = 90°$ and $\theta = 0°$. $a = 2$, $b = 1$, $\tau_p = 7$

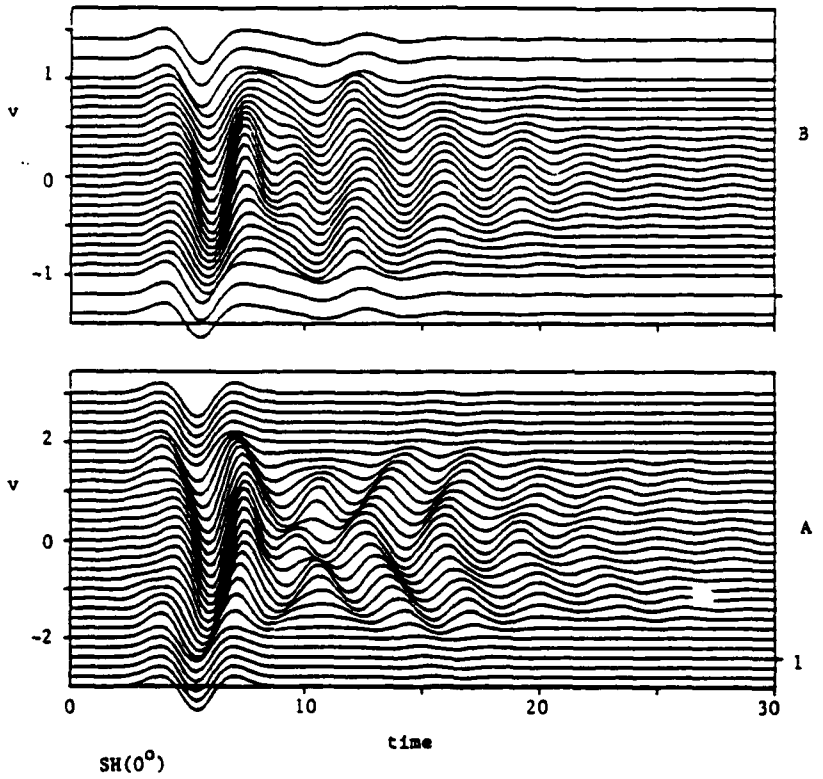

Figure 10. Surface responses (v) for semi-prolate valley at sections A and B for incident SH wave with $\phi = 0°$ and $\theta = 0°$, $a = 2$, $b = 1$, $\tau_p = 4$

SUMMARY AND CONCLUSIONS

Using a boundary integral equation method and Fourier synthesis the transient response of three dimensional valleys of different shapes is investigated. Incident P, SV, SH and Rayleigh waves have been considered.

The nature of observed differences with the corresponding two dimensional responses appears to be highly dependent upon the shape of the basin and the type of incident wave under consideration. The amplitude of motion near the centre of the valley is in general higher for three dimensional basins; this is especially apparent for the case of a hemispherical valley subjected to a vertically incident P wave. However, near the edges of the valley the amplitude of motion decays faster for three dimensional basins than for two dimensional ones. Another important feature of the results is that change in the shape of the valley from spherical to semi-prolate causes a considerable increase in the amplitude of surface waves, especially near the edges of the valley. The maximum amplifications occurring at the time of direct arrivals decrease, since the constructive interferences of refracted incident wave with the surface waves are less focused for the semi-prolate than for a hemispherical basin.

Because of the complexity of the motion in the examples studied here, it is difficult to analyse the specific contributions of different modes of Love and Rayleigh waves in the total motion. From the high phase velocity of the surface waves it appears that Rayleigh waves have been dominant in surface motion for the class of examples considered here. In order to analyse different surface wave packets, one needs to consider more elongated basin geometries and short period incident signals. Such an analysis would require considerable computational efforts which are beyond the scope of the present paper.

ACKNOWLEDGEMENT

The authors would like to thank Hiroshi Kawase and Keiiti Aki for providing a preprint of their paper. This work was supported in part by the National Science Foundation under Grant No. 53-4519-3792 and in part by the Office of Naval Research under Contract No, N00014-88-K-0157.

REFERENCES

1. T. K. Mossessian and M. Dravinski, 'Amplification of elastic waves by a three dimensional valley. Part 1: Steady state response', *Earthquake eng. struct. dyn.*
2. J.-J. Lee, and C. A. Langston, 'Wave propagation in a three dimensional circular basin', *Bull. seism. soc. Am.* 73, 1637-1653 (1983).
3. N. H. Ricker, *Transient Waves in Visco-elastic Media*, Elsevier, Amsterdam, 1977.
4. H. Eshraghi and M. Dravinski, 'Transient scattering of elastic waves by dipping layers of arbitrary shape. Part 2: Plane strain model', *Earthquake eng. struct. dyn.* 18, 417-434 (1989).
5. P.-Y. Bard and M. Bouchon, 'The seismic response of sediment-filled valleys. Part II. The case of incident P and SV waves', *Bull seism. soc. Am.* 70, 1921-1941 (1980).
6. H. Kawase and K. Aki, 'A study on the response of a soft basin for incident S, P, and Rayleigh waves with special reference to the long duration observed in Mexico City', *Bull. seism. soc. Am.* 79, 1361-1382 (1989).
7. T. K. Mossessian, 'Diffraction of elastic waves by non-axisymmetric three dimensional subsurface inhomogeneities using a boundary integral equation method and a hybrid technique', *Ph.D. Thesis*, Department of Mechanical Engineering, University of Southern California, Los Angles, 1990.

INTERNATIONAL JOURNAL FOR NUMERICAL METHODS IN ENGINEERING, VOL. 31, 1009–1026 (1991)

TRANSIENT SCATTERING OF ELASTIC WAVES BY THREE DIMENSIONAL NON-AXISYMMETRIC DIPPING LAYERS

HOSSEIN ESHRAGHI AND MARIJAN DRAVINSKI

Department of Mechanical Engineering, University of Southern California, Los Angeles, California 90089-1453, U.S.A.

SUMMARY

Scattering of elastic plane waves by three dimensional non-axisymmetric multiple dipping layers embedded in an elastic half-space is investigated by using a boundary method. The dipping layer is subjected to incident Rayleigh waves and oblique incident SH, SV and P waves. For the steady state problem, spherical wave functions are used to express the unknown scattered field. These functions satisfy the equation of motion and radiation conditions at infinity but they do not satisfy the stress free boundary conditions on the surface of the half-space. The boundary and continuity conditions are imposed locally in the least-square sense at points on the layer interfaces and on the surface of the half-space. The transient response is constructed from the steady state solution by using Fourier synthesis.

Numerical results are presented for both steady state and transient problems. Steady state problems include solutions for two non-axisymmetric dipping layers in the form of a prolate. Transient responses are presented for one and two dipping layer models subjected to incident wave signals in the shape of a Ricker wavelet. It is shown that change in azimuthal orientation of the incident wave may significantly change the surface response of the dipping layer. For the transient problem, response comparison of one and two dipping layers indicates that the addition of an extra layer may also completely change the response characteristics of the alluvium. In particular, the delay in arrival of much larger amplitude surface waves by two dipping layers in comparison with other geometrically compatible models demonstrates the importance of the detailed three dimensional modelling of layered irregularities.

INTRODUCTION

Details of scattering phenomena near subsurface inhomogeneities are of great importance in many branches of science. The theory of scattering of elastic waves is widely applied in non-destructive testing, in studying the behaviour of composite materials under dynamic loading, in delineating buried geologic formations in petroleum exploration, and in investigation of strong ground motion amplification in seismology and earthquake engineering.[1,2] Although the subject of numerous studies in the past, the analytical complexity of the problem and numerical difficulties in implementing computational techniques have been major obstacles in studying realistic models such as three dimensional problems.[3] With recent advances in computational techniques it is possible now to investigate these type of problems in more detail.

Among the earlier studies of three dimensional scattering of elastic waves, the works of Day,[4] Apsel,[5] Sanchez-Sesma[6] and Lee[7] are of special importance. Day[4] used the finite element technique to study scattering of elastic waves by an axisymmetric sedimentary basin. Apsel[5] used a boundary integral equation (BIE) method to study soil–structure interactions for axisymmetric scatterers. Sanchez-Sesma[6] and Lee[7] used wave expansion techniques to solve similar problems. Recently, Niwa and Hirose[8] formulated a BIE method to solve the scattering problem of elastic

0029–5981/91/051009–18$09.00

Received 17 August 1989
Revised 18 June 1990

waves by a non-axisymmetric cavity or crack in a three dimensional half-space. Eshraghi and Dravinski[9,10] used the wave expansion technique to study scattering of elastic waves by non-axisymmetric near surface irregularities. Recently, Jiang and Kuribayashi[11] investigated three dimensional resonance of axisymmetric sediment-filled valleys. All the papers cited so far dealt with steady state problems. Lee and Langston[12] extended the problem to include the transient solution for an axisymmetric scatterer using the ray method, while Sanchez-Sesma *et al.*[13] considered a similar model through the wave function expansion approach. Still, at the present time the transient solution for scattering of elastic waves by general three dimensional irregularities has not been fully developed. The main reason for that is the prohibitive amount of computation required for solving the problems of interest with non-axisymmetric characteristics. For that reason, a boundary method is used in the present study to formulate the steady state problem for non-axisymmetric irregularities, from which the transient solution is constructed by using Fourier synthesis. The method utilizes the wave function expansion technique which does not require evaluation of the Green functions. These wave functions can be evaluated easily, making it feasible to approach transient problems for more general three dimensional models. For a more detailed review of the literature on scattering of elastic waves, the reader is referred to recent papers by the present authors.[1,2]

STATEMENT OF THE PROBLEM

The geometry of the problem is depicted by Figure 1. The problem model consists of an elastic half-space which contains a finite number of elastic dipping layers of arbitrary shape. The layer interfaces are considered to be smooth, without sharp corners. Throughout this paper subscript j corresponds to either layer domains D_j ($j = 0, 1, \ldots, R$) or to the interface C_j ($j = 1, 2, \ldots, R$). Domain D_0 denotes the half-space while C_1 denotes the interface between the half-space and the first layer, etc. In addition, C_0 corresponds to the surface $z = 0$ of the dipping layer and the half-space. The material of the medium is assumed to be linearly elastic, homogeneous and isotropic. The half-space is subjected to incident plane SH, SV, P or Rayleigh waves. The steady state equation of motion in a three dimensional medium, in the absence of body forces, is defined in terms of the displacement potentials by

$$(\nabla^2 + h_j^2)\Phi_j(\mathbf{x}, \omega) = 0 \tag{1}$$

$$(\nabla^2 + k_j^2)\Psi_j(\mathbf{x}, \omega) = 0 \tag{2}$$

$$(\nabla^2 + k_j^2)\chi_j(\mathbf{x}, \omega) = 0 \tag{3}$$

$$\mathbf{x} \in D_j, \quad j = 0, 1, \ldots, R$$

where $\mathbf{x}$ is a position vector, Φ_j, Ψ_j and χ_j are the three displacement potentials for the jth layer, $h_j (= \omega/\alpha_j)$ and $k_j (= \omega/\beta_j)$ denote the pressure and shear wavenumber, respectively, α_j and β_j are the pressure and shear wave velocities, respectively, ω is the circular frequency, and ∇^2 denotes the Laplacian in spherical co-ordinates. A system of unit basis $\{\mathbf{e}_r, \mathbf{e}_\theta, \mathbf{e}_\phi\}$ is defined for spherical co-ordinates (r, θ, ϕ) according to Figure 1. For the same co-ordinate system the displacement vector $\mathbf{u}_j$ can be expressed in terms of three displacement components u_r, u_θ and u_ϕ according to[14]

$$\mathbf{u}_j = \nabla\Phi_j + \nabla(r\Psi_j) \times \mathbf{e}_r + l_j \nabla \times \nabla \times (r\chi_j \mathbf{e}_r) \tag{4}$$

$$\mathbf{x} \in D_j, \quad j = 0, 1, \ldots, R$$

where l is a scalar factor to give the potentials the same dimension.

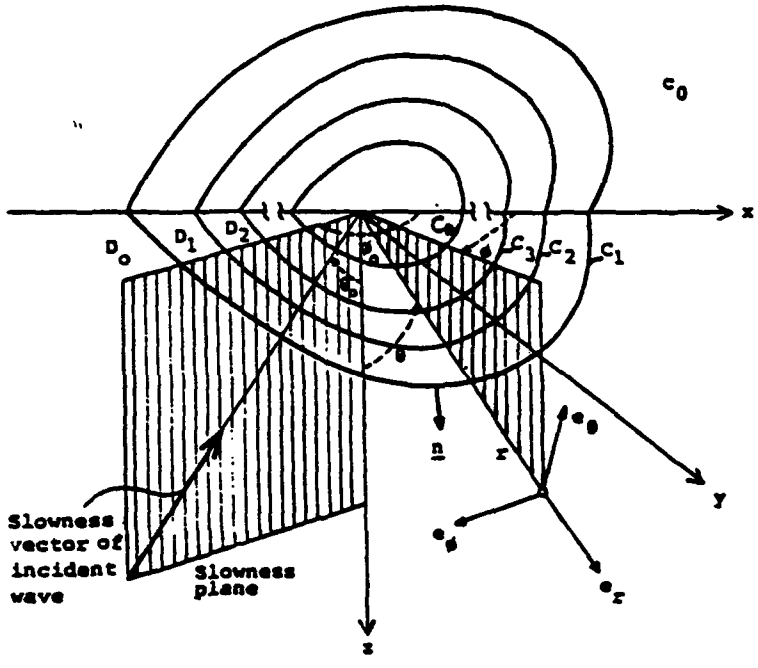

Figure 1. Problem model

Boundary conditions on the surface $z = 0$ of the dipping layers and the half-space are given by

$$\sigma_{r\theta j} = \sigma_{\theta\theta j} = \sigma_{\theta\phi j} = 0 \tag{5}$$

$$\theta = \frac{\pi}{2}(z = 0), \quad \mathbf{x} \in C_j, \quad j = 0, 1, \ldots, R$$

where $\sigma_{r\theta j}$, $\sigma_{\theta\theta j}$ and $\sigma_{\theta\phi j}$ are components of the stress tensor. Perfect bounding on each layer interface requires continuity of displacement and traction fields according to

$$\mathbf{u}_{j-1}^{+}(\mathbf{x}, \omega) = \mathbf{u}_{j}^{-}(\mathbf{x}, \omega) \tag{6}$$

$$\mathbf{T}_{j-1}^{+}(\mathbf{x}, \omega) = \mathbf{T}_{j}^{-}(\mathbf{x}, \omega) \tag{7}$$

$$\mathbf{x} \in C_j, \quad j = 1, 2, \ldots, R$$

where $\mathbf{u}$ and $\mathbf{T}$ are the displacement and traction vectors, respectively. Superscript $+$ $(-)$ denotes that the interface is being approached from the outside (inside). Expressions for the components of displacement field and stress tensor in terms of the displacement potentials can be found in the literature.[14]

For the steady state problem the incident field consists of plane harmonic Rayleigh waves or oblique incident SH, SV or P waves. For slowness vectors within the xz-plane, incident fields are defined in previous works by the present authors.[1-3] For slowness vectors located outside the xz-plane, the corresponding incident field is obtained through rotation about the z-axis. This completes the statement of the problem. Solution of the problem is considered next.

SOLUTION OF THE PROBLEM

As an incident wave strikes interface C_1, it is partially scattered back into the half-space D_0 and partially transmitted into layer D_1. This process continues from one layer to another as the waves propagate throughout the layered medium. Consequently, the wave field in the half-space consists of the free-field and the scattered wave field, while the wave field inside each dipping layer consists of the scattered wave field only. The displacement field can be written in the following form:

$$\mathbf{u}_0 = \mathbf{u}_0^{ff} + \mathbf{u}_0^{s} \tag{8}$$

$$\mathbf{u}_j = \mathbf{u}_j^{s}, \quad \mathbf{x} \in D_j, \quad j = 1, 2, \ldots, R \tag{9}$$

where superscripts s and ff denote the scattered field and free-field, respectively. Scattered wave fields in this model can be expressed as a linear combination of the spherical wave functions.[14] For the half-space, scattered wave fields for the displacement wave potentials are defined according to

$$\begin{aligned}\Phi_0^{s} = \sum_{n=0}^{N}\sum_{m=0}^{M} & a_{nm}^{\Phi_0} h_n^{(2)}(h_0 r) P_n^m(\cos\theta)\cos m\phi \\ & + b_{nm}^{\Phi_0} h_n^{(2)}(h_0 r) P_n^m(\cos\theta)\sin m\phi \\ & m \leqslant n,\ M \leqslant N,\ \mathbf{x} \in D_0\end{aligned} \tag{10}$$

$$\begin{aligned}\Psi_0^{s} = \sum_{n=1}^{N}\sum_{m=1}^{M} & a_{nm}^{\Psi_0} h_n^{(2)}(k_0 r) P_n^m(\cos\theta)\cos m\phi \\ & + b_{nm}^{\Psi_0} h_n^{(2)}(k_0 r) P_n^m(\cos\theta)\sin m\phi \\ & m \leqslant n,\ M \leqslant N,\ \mathbf{x} \in D_0\end{aligned} \tag{11}$$

$$\begin{aligned}\chi_0^{s} = \sum_{n=1}^{N}\sum_{m=1}^{M} & a_{nm}^{\chi_0} h_n^{(2)}(k_0 r) P_n^m(\cos\theta)\cos m\phi \\ & + b_{nm}^{\chi_0} h_n^{(2)}(k_0 r) P_n^m(\cos\theta)\sin m\phi \\ & m \leqslant n,\ M \leqslant N,\ \mathbf{x} \in D_0\end{aligned} \tag{12}$$

For the intermediate layers according to

$$\begin{aligned}\Phi_j^{s} = \sum_{n=0}^{N}\sum_{m=0}^{M} & c_{nm}^{\Phi_j} h_n^{(2)}(h_j r) P_n^m(\cos\theta)\cos m\phi \\ & + d_{nm}^{\Phi_j} h_n^{(2)}(h_j r) P_n^m(\cos\theta)\sin m\phi \\ & + e_{nm}^{\Phi_j} h_n^{(1)}(h_j r) P_n^m(\cos\theta)\cos m\phi \\ & + f_{nm}^{\Phi_j} h_n^{(1)}(h_j r) P_n^m(\cos\theta)\sin m\phi \\ & m \leqslant n,\ M \leqslant N,\ \mathbf{x} \in D_j, j = 1, \ldots, R-1\end{aligned} \tag{13}$$

$$\begin{aligned}\Psi_j^{s} = \sum_{n=1}^{N}\sum_{m=1}^{M} & c_{nm}^{\Psi_j} h_n^{(2)}(k_j r) P_n^m(\cos\theta)\cos m\phi \\ & + d_{nm}^{\Psi_j} h_n^{(2)}(k_j r) P_n^m(\cos\theta)\sin m\phi \\ & + e_{nm}^{\Psi_j} h_n^{(1)}(k_j r) P_n^m(\cos\theta)\cos m\phi \\ & + f_{nm}^{\Psi_j} h_n^{(1)}(k_j r) P_n^m(\cos\theta)\sin m\phi \\ & m \leqslant n,\ M \leqslant N,\ \mathbf{x} \in D_j, j = 1, \ldots, R-1\end{aligned} \tag{14}$$

$$\chi_j^s = \sum_{n=1}^{N} \sum_{m=1}^{M} c_{nm}^{\chi_j} h_n^{(2)}(k_j r) P_n^m(\cos\theta)\cos m\phi + d_{nm}^{\chi_j} h_n^{(2)}(k_j r) P_n^m(\cos\theta)\sin m\phi + e_{nm}^{\chi_j} h_n^{(1)}(k_j r) P_n^m(\cos\theta)\cos m\phi + f_{nm}^{\chi_j} h_n^{(1)}(k_j r) P_n^m(\cos\theta)\sin m\phi \quad (15)$$
$$m \leqslant n, M \leqslant N, \mathbf{x} \in D_j, j = 1, \ldots, R-1$$

and for the innermost layer specified by

$$\Phi_R^s = \sum_{n=0}^{N} \sum_{m=0}^{M} g_{nm}^{\Phi_R} j_n(h_R r) P_n^m(\cos\theta)\cos m\phi + l_{nm}^{\Phi_R} j_n(h_R r) P_n^m(\cos\theta)\sin m\phi \quad (16)$$
$$m \leqslant n, M \leqslant N, \mathbf{x} \in D_R$$

$$\Psi_R^s = \sum_{n=1}^{N} \sum_{m=1}^{M} g_{nm}^{\Psi_R} j_n(k_R r) P_n^m(\cos\theta)\cos m\phi + l_{nm}^{\Psi_R} j_n(k_R r) P_n^m(\cos\theta)\sin m\phi \quad (17)$$
$$m \leqslant n, M \leqslant N, \mathbf{x} \in D_R$$

$$\chi_R^s = \sum_{n=1}^{N} \sum_{m=1}^{M} g_{nm}^{\chi_R} j_n(k_R r) P_n^m(\cos\theta)\cos m\phi + l_{nm}^{\chi_R} j_n(k_R r) P_n^m(\cos\theta)\sin m\phi \quad (18)$$
$$m \leqslant n, M \leqslant N, \mathbf{x} \in D_R$$

where $h_n^{(1)}$ and $h_n^{(2)}$ are spherical Hankel functions of the first and second kind, respectively, j_n are spherical Bessel functions of the first kind, $P_n^m(\cos\theta)$ are associate Legendre polynomials,[18] a_{nm} to l_{nm} are unknown coefficients, and N and M are the orders of expansions. The wave functions in equations (10) to (18) are solutions of the equations of motion (equations (1)–(3)). The scattered wave field within the half-space D_0 (equations (10)–(12)) consists of outgoing waves only, thus satisfying the radiation conditions at infinity. Scattered waves within the layers D_1 to D_{R-1} (equations (13)–(15)) incorporate both incoming and outgoing waves, while scattered waves within the innermost layer D_R (equations (16)–(18)) consist of standing waves only. It can be seen that these wave functions do not satisfy the stress free boundary conditions on the surface $z = 0$ of the valley and the half-space. These conditions must be imposed locally.

Once the scattered field is expressed as a double series of wave functions according to equations (10) to (18), it is necessary to determine the unknown expansion coefficients. Substitution of the scattered wave field into the boundary conditions (equation (5)) on the surface $z = 0$ of the dipping layer and the half-space at L_0 points and into the continuity conditions (equations (6) and (7)) on the surface of layer interfaces at $L_j (j = 1, \ldots, R)$ points results in a system of linear equations

$$\mathbf{Ga} = \mathbf{f} \quad (19)$$

where matrix G and vector f are known and vector a contains all the unknown coefficients. Using QR decomposition, the system of equations (19) is then solved in the least-square sense.[15]

Once these coefficients are found, the displacement and stress fields can be evaluated throughout the elastic medium.

This concludes the steady state solution of the problem. Corresponding transient response is evaluated through the Fourier synthesis.[1, 16]

NUMERICAL RESULTS

The numerical results are presented for steady state and transient responses of non-axisymmetric one and two dipping layer models subjected to oblique incident SH, SV and P waves.

Geometry of the layers

For two dipping layers the model geometry is in the form of semi-ellipsoids defined by

$$C_1: \quad \frac{x^2}{a_1^2} + \frac{y^2}{a_2^2} + \frac{z^2}{a_3^2} = 1, \quad z > 0 \tag{20}$$

$$C_2: \quad \frac{x^2}{b_1^2} + \frac{y^2}{b_2^2} + \frac{z^2}{b_3^2} = 1, \quad z > 0 \tag{21}$$

where a_1 and b_1 are the principal axes of the ellipsoids along the x-axis, a_2 and b_2 are the principal axes along the y-axis, and a_3 and b_3 are the principal axes along the z-axis. For the one dipping layer model only interface C_1, defined in equation (20), is present. Results are shown for spherical dipping layers ($a_1 = a_2 = a_3, b_1 = b_2 = b_3$) and prolates ($a_1 \neq a_2 = a_3, b_1 \neq b_2 = b_3$). There are some advantages associated with these choices of model geometry. Prolate dipping layers possess non-axisymmetric features of a general three dimensional model which facilitate comparison with existing two dimensional models by extending the prolate in one direction. This serves also as a test of numerical results since the authors are not aware of any solutions at the present time for scattering of elastic waves by multiple dipping layers in the literature. A spherical model is considered because of its simplicity and also for comparison with numerical results for non-axisymmetric geometries.

Conventions

The slowness vector of the incident wave is specified by two angles, an azimuthal angle of incidence ϕ_0 and an off-vertical angle of incidence θ_0 (Figure 1). A slowness plane is defined as a vertical plane which contains the slowness vector. Consequently, the in-plane and out-of-plane motions correspond to displacement fields with components in the slowness plane and perpendicular to that plane, respectively. Throughout, u, v and w correspond to the three components of the displacement field along the x-, y- and z-axis, respectively. All distances are normalized in respect to the half-width of the innermost layer along the y-axis (e.g. b_2 for a two dipping layer model), which is assumed to be of unit length. In addition, the following dimensionless variables are introduced. The shear modulus and shear wave velocity of the half-space are assumed to equal unity. The dimensionless shear modulus, shear wave speed and pressure wave speed are denoted by μ_j, β_j and α_j, respectively, for the jth layer. With all velocities normalized with respect to the shear wave speed of the half-space and all distances with respect to the half-width of the innermost layer along the y-axis, the time variable t appears in dimensionless form as well. A dimensionless frequency Ω is defined as the ratio of the total width of the outermost dipping layer along the y-axis to the wavelength of the incident shear wave ($\Omega = 2a_2/\lambda^{inc}$).

Steady state results

In the absence of any available solution in the literature for the scattering of elastic waves by two three dimensional dipping layers, the best alternative to test the proposed technique is through comparison with the results of compatible two dimensional models.[1,2] By assigning relatively large values to the principal axis of the prolates in the direction perpendicular to the slowness plane, it is expected that, for the incidences with slowness vector in the *yz*-plane, the response of the dipping layer for stations along the *y*-axis resembles that of a similar cylindrical model. Figure 2 displays the results of a comparison between these two models for an incident SV wave with slowness vector lying in the *yz*-plane. The geometry of the models cut by the slowness plane is shown at the bottom of the figure. Results are presented for a vertical and an oblique incidence. It is apparent from these results that a strong similarity exists between the responses of the two models. Therefore, this served as a verification of the results. Another verification of the method is through the zero scattering test. Namely, by assuming material properties of the layers

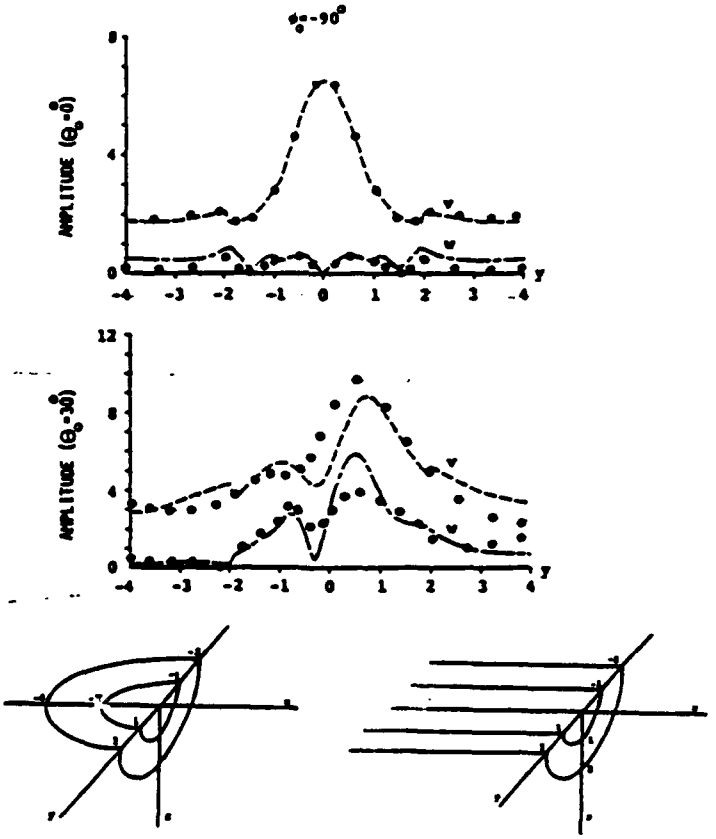

Figure 2. Comparison of the surface displacement field of a prolate type two dipping layer model (dashed lines) with those of a compatible cylindrical two dipping layer model[2] (solid dots) for stations along the *y*-axis. For the prolate type valley the principal axes are ($a_1 = 4$, $a_2 = a_3 = 2$; $b_1 = 2$, $b_2 = b_3 = 1$), while for the cylindrical valley the radii are two and one. Both valleys are subjected to the same incident SV wave with the slowness vector in the *xz*-plane ($\phi_0 = -90°$). Two off-vertical angles of incidence are considered; $\theta_0 = 0°$, 30°. Throughout, *u*, *v* and *w* correspond to the three components of the displacement field along the axes *x*, *y* and *z*, respectively. $\Omega = 1$, $\mu_0 = \beta_0 = 1$, $\alpha_0 = 2$, $\mu_1 = 0{\cdot}4$, $\beta_1 = 0{\cdot}7$, $\alpha_1 = 1{\cdot}4$, $\mu_2 = 0{\cdot}167$, $\beta_2 = 0{\cdot}5$, $\alpha_2 = 1$, $M = 3$, $N = 8$, $L_0 = 160$, $L_1 = L_2 = 72$

to be the same as those of the half-space the resulting model should produce no scattered waves.

Results for incident SH waves with slowness vectors lying in the yz-plane are shown in Figure 3. The model consists of two dipping layers in the form of a prolate. For stations along the x- and y-axis the displacement field is obtained for different off-vertical incidences. Owing to the symmetry, the displacement field for stations along the y-axis consists only of the component in the out-of-plane direction. This is in agreement with the two dimensional antiplane strain model.

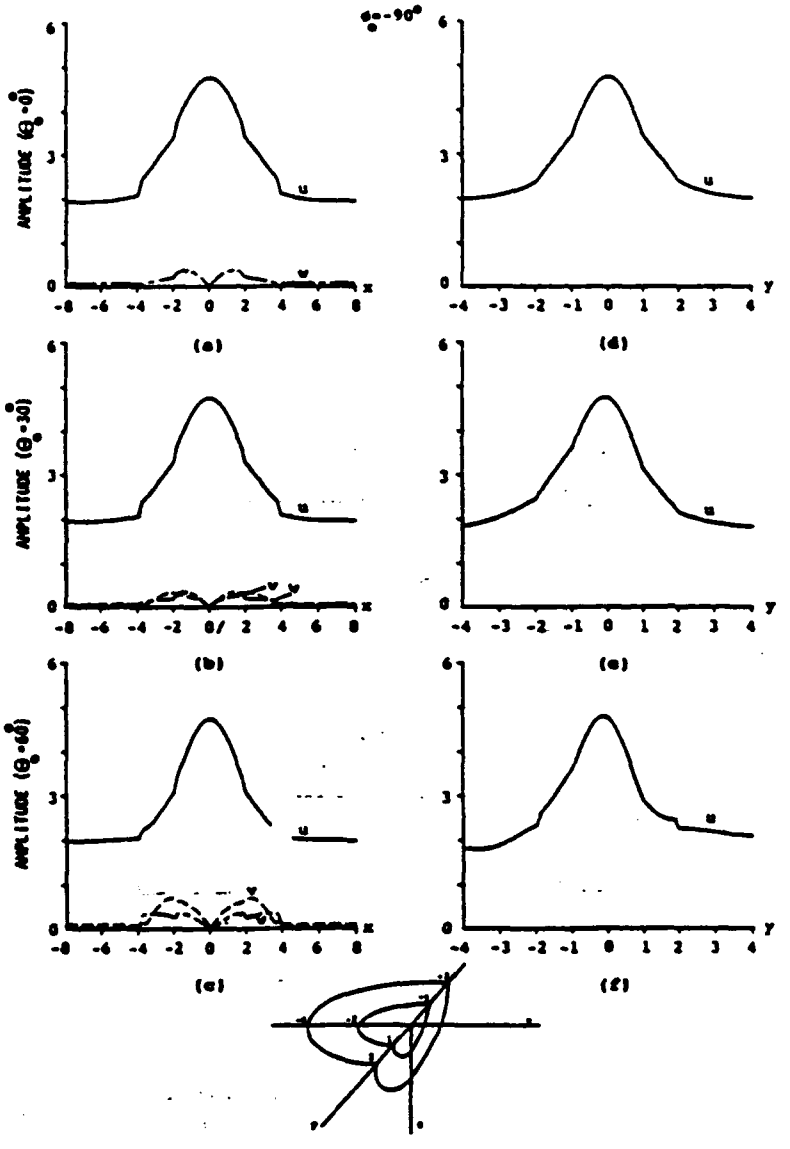

Figure 3. Surface displacement amplitudes for a prolate type two dipping layer model ($a_1 = 4$, $a_2 = a_3 = 2$; $b_1 = 2$, $b_2 = b_3 = 1$) subjected to incident SH waves with the slowness vector in the yz-plane ($\phi_0 = -90°$). Stations lie along the x-axis (a)–(c) and the y-axis (d)–(f). For both models: $\Omega = 0.5$, $M = 3$, $N = 6$, $L_0 = 160$, $L_1 = L_2 = 42$, $\mu_0 = \beta_0 = 1$, $\alpha_0 = 2$, $\mu_1 = 0.4$, $\beta_1 = 0.7$, $\alpha_1 = 1.4$, $\mu_2 = 0.167$, $\beta_2 = 0.5$, $\alpha_2 = 1$

However, for stations along the x-axis all three components of the displacement field may be present (P- and SV-mode conversions).

It is interesting at this point to elaborate further on the numerical aspect of the steady state solution. The method developed here is very sensitive to two sets of parameters. The first one is the orders of expansion considered for the scattered wave field. The second one is the number of collocation points and their locations. For the range of frequency studied here, good accuracy can be obtained with an azimuthal order of expansion $M = 3$. The second order of expansion N requires higher values. Steady state results presented in this paper generally require $5 < N < 8$ for good convergence. The number and locations of the collocation points are very important for accuracy of the results. These points are distributed on elliptical contours on the surface of each layer C_1 and C_2, and also on the surface $z = 0$ of the half-space and the valley C_0. On layer interface C_1 (interface C_2) these contours are equally spaced at different elevations from $z = 0$ to $z = a_3$ ($z = b_3$). For the range of frequency considered here generally six to eight contours are sufficient. A total of 42 to 72 collocation points for each of the layer interfaces is uniformly distributed along these contours. On the surface of the half-space and the valley similar elliptical contours following the shapes of the valley edges are considered. These contours are equally spaced from the origin up to about twice the width of the valley at the surface of the half-space. Fifteen contours placed this way atop the valley contained a total of 160 uniformly distributed collocation points.

In general, the following criteria have been used to establish the convergence of the steady state results. First, through the zero scattering test (all materials are the same) an initial number of expansion terms and collocation points is determined. Subsequently, for the actual material of the half-space and the layers the number of expansion terms and collocation points is increased until the maximum difference of the surface displacement response for two successive calculations is judged to be sufficiently small (e.g. less than 4 per cent). This concludes the analysis of steady state numerical results.

Transient results

The incident signal is assumed to be in the form of a Ricker wavelet defined according to[16]

$$f(t) = \frac{\sqrt{\pi}}{2}(\alpha - 0{\cdot}5)e^{-\alpha}, \quad \alpha = \left(\frac{\pi(t - t_s)}{t_p}\right)^2 \tag{22}$$

where t_s corresponds to the peak amplitude in the time domain and t_p corresponds to the angular frequency $\omega_p (= 2\pi/t_p)$ which is associated with the peak amplitude in the Fourier domain. The transient response is obtained by using Fourier transform techniques.[17] There are several important parameters which are used in applying the fast Fourier transform (FFT), such as Δt, ω_c and N_s, which correspond to sampling time interval, cutoff frequency and number of samples, respectively. In the present study the cut-off frequency ω_c is considered to be about two and half times the characteristic frequency ω_p.

One dipping layer model. The surface response of a prolate type valley at stations along the x- and y-axes is depicted by Figures 4 to 6 for incident P and SH Ricker wavelets. To reduce the number of figures, the results are presented only for the main component of the displacement field. The main component of motion for incident SH waves corresponds to the out-of-plane component of the displacement field. For P wave incidences, the main component of the displacement field is in the direction of propagation of the incident wave. The geometry of the models and locations of equally spaced stations are shown at the bottom of each figure.

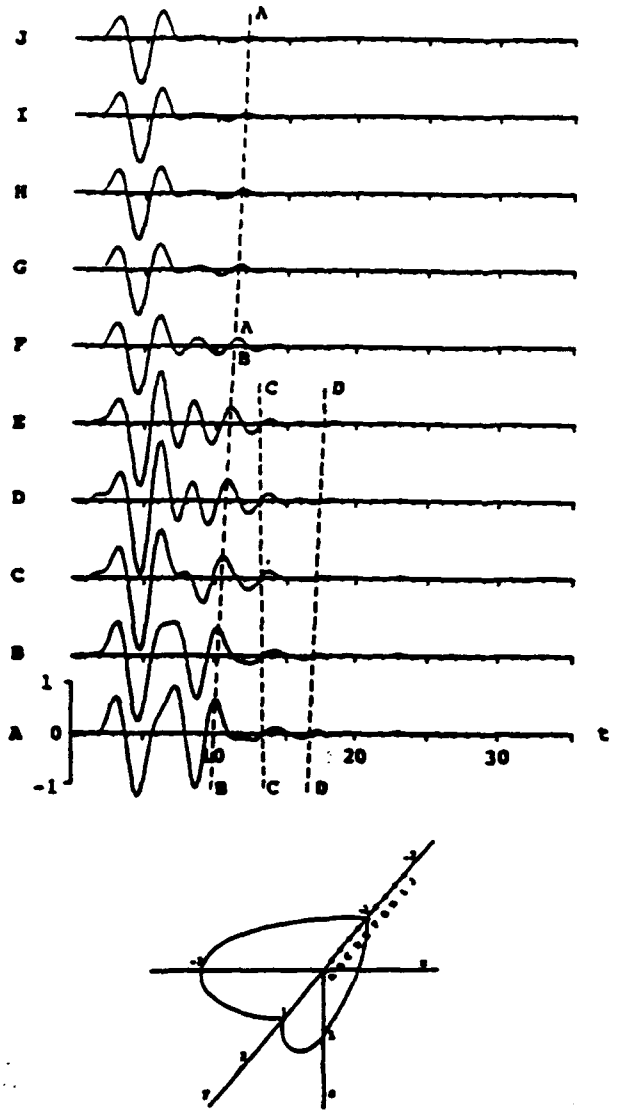

Figure 4. Vertical component of displacement field (w-component) for transient surface response of a prolate type valley with principal axes $a_1 = 2$, $a_2 = a_3 = 1$ to a vertically $\theta_0 = 0°$ incident P Ricker wavelet with characteristic period $t_p = 3{\cdot}66$ ($t_c = 4$). Locations of equally spaced stations A to J are displayed at the lower section of the figure. $\mu_0 = \beta_0 = 1$, $\alpha_0 = 2$, $\mu_1 = 0{\cdot}167$, $\beta_1 = 0{\cdot}5$, $\alpha_1 = 1$, $N_s = 256$, $\Delta t = 0{\cdot}2$

For a vertically incident P Ricker wavelet, the vertical component of the surface response at stations A to J along the y-axis is depicted by Figure 4. Seismographs on the surface of the half-space (G to J) indicate that the incident signal remains essentially undisturbed. However, for stations atop the dipping layer (A to F) significant amplification of the incident signal is evident. On the surface of the half-space there is little disturbance after the passage of the direct incident signal, which can be tracked by line AA as it propagates away from the valley. Lines CC and DD track the propagation of surface waves toward and away from the centre of the valley,

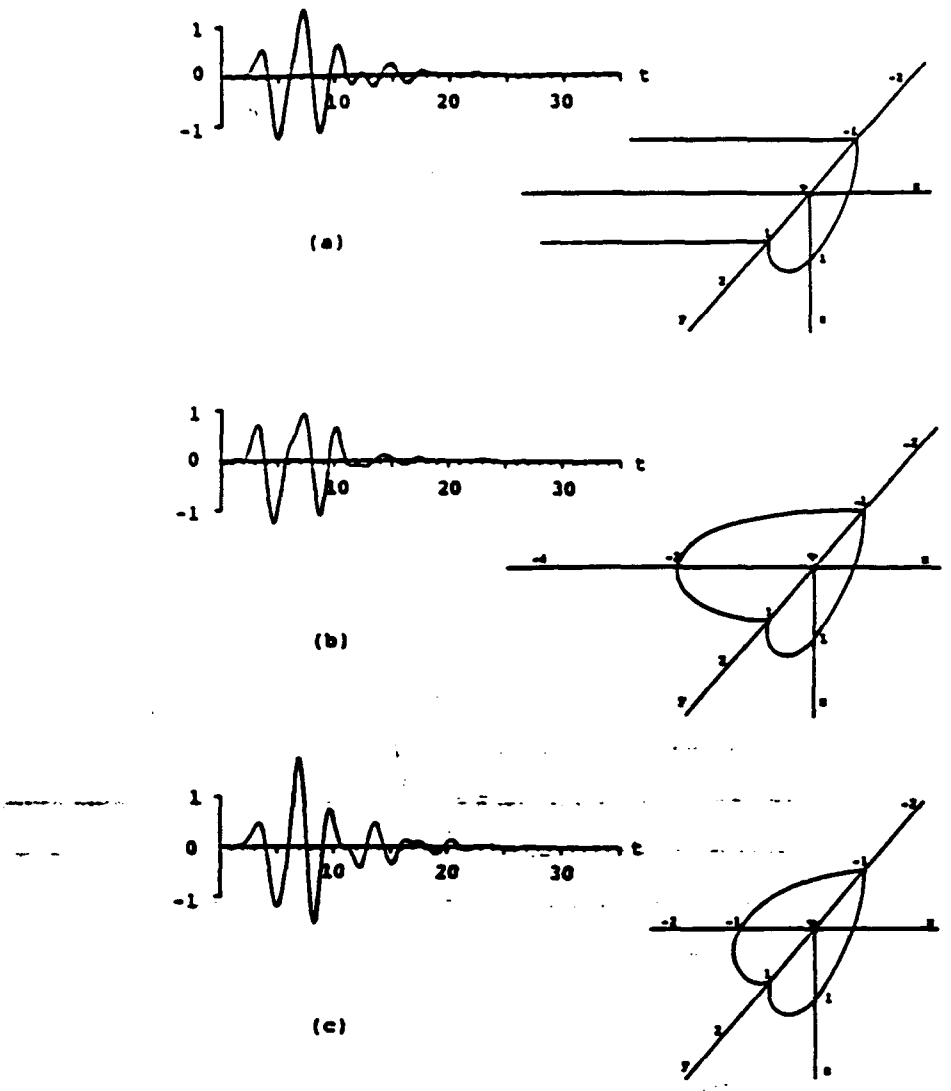

Figure 5. Vertical component of displacement field (w-component) for transient surface response at the centre of a cylindrical valley of unit radius (a), a prolate type valley $a_1 = 2, a_2 = a_3 = 1$ (b), and a spherical valley of unit radius (c), to a vertically $\theta_0 = 0°$ incident P Ricker wavelet. $t_p = 3{\cdot}66$ ($t_s = 4$), $\mu_0 = \beta_0 = 1$, $\alpha_0 = 2$, $\mu_1 = 0{\cdot}167$, $\beta_1 = 0{\cdot}5$, $\alpha_1 = 1$. For spherical and prolate type valleys: $N_s = 256$, $\Delta t = 0{\cdot}2$

respectively. The large width of the valley in the direction perpendicular to the slowness plane allows a comparison between the results of Figure 4 with those of a compatible cylindrical model studied previously.[2] In addition, the response of a compatible spherical valley is included for comparison as well. Consequently, the seismographs for the vertical component of the displacement field located at the centre of these three models are depicted by Figure 5. Apparently, the results for the cylindrical valley (Figure 5(a)) and for the prolate type valley (Figure 5(b)) are very similar. The response of the spherical valley at its centre also resembles those of the other two models. However, the spherical model produces larger amplification at the centre of the valley.

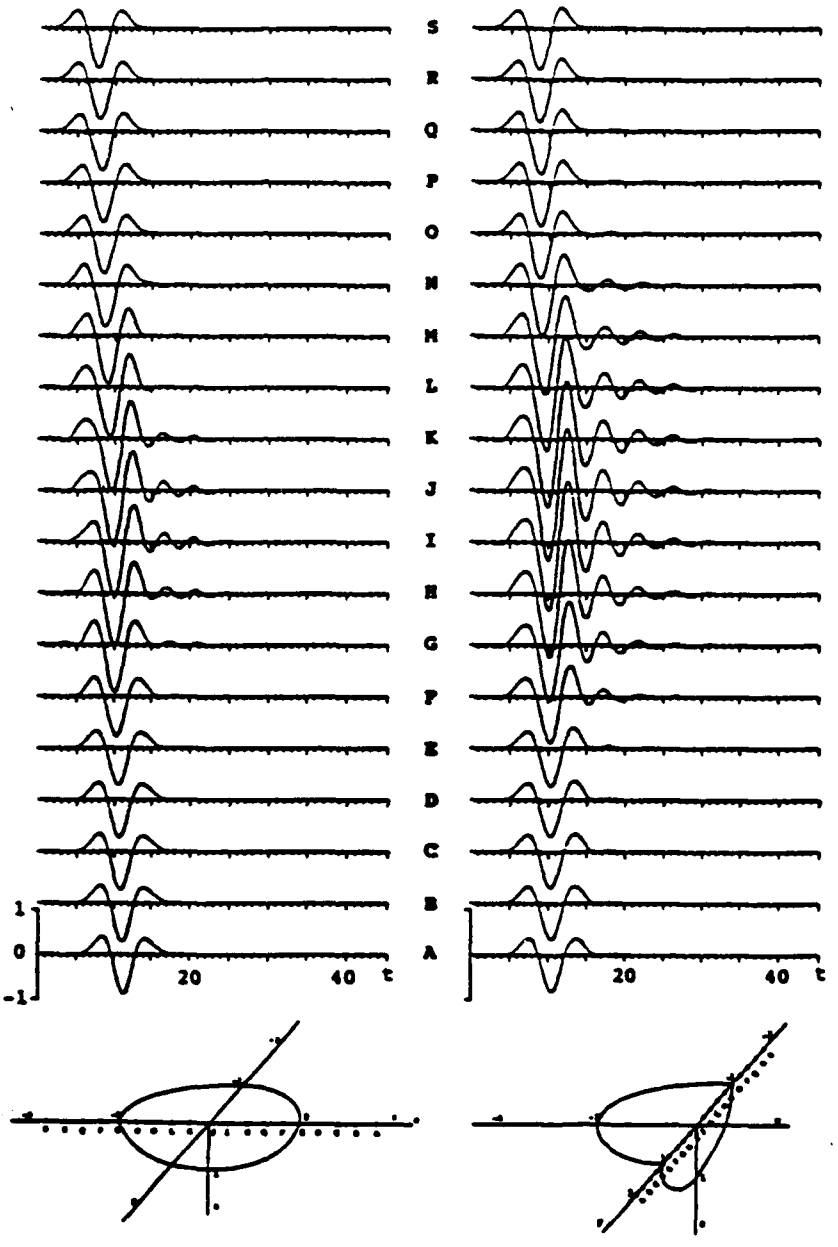

Figure 6. The v-component (u-component) of displacement field for transient surface response of a prolate type valley $a_1 = 2$, $a_2 = a_3 = 1$ to an oblique $\theta_0 = 30°$ incident SH Ricker wavelet with slowness vector in the xz-plane (yz-plane) for stations located along the x-axis (y-axis) is displayed in the first column (second column). $t_p = 7{\cdot}32$ ($t_s = 8$), $\mu_0 = \beta_0 = 1$, $\alpha_0 = 2$, $\mu_1 = 0{\cdot}167$, $\beta_1 = 0{\cdot}5$, $\alpha_1 = 1$, $N_s = 256$, $\Delta t = 0{\cdot}2$

Results for an obliquely incident Ricker SH wavelet are depicted by Figure 6. Seismograms in the first column (second column) are located along the x-axis (y-axis) for the incidence with slowness vector on the xz-plane (yz-plane) and they display the v- (u-) component of the surface displacement field which is the main component of the displacement field. The wavelength of the

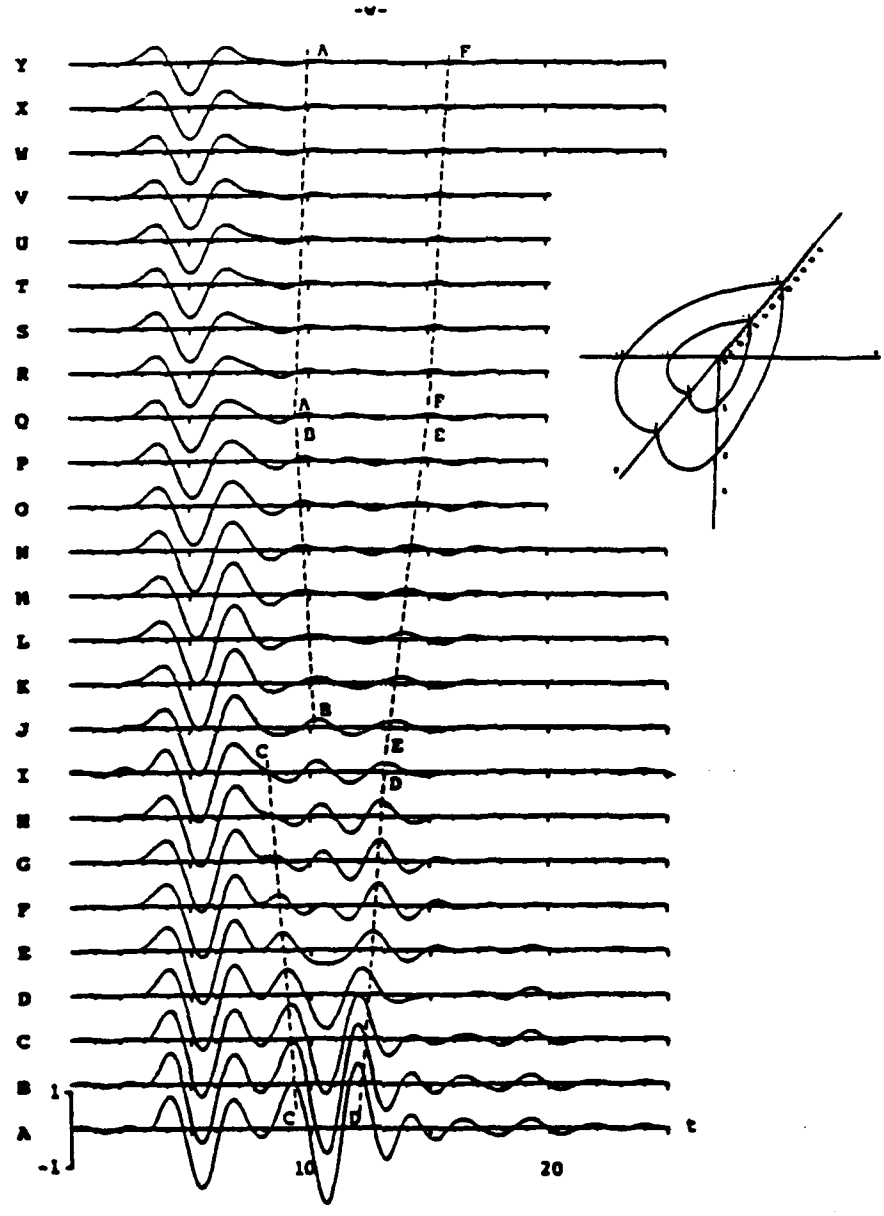

Figure 7. Vertical component of displacement field (w-component) for transient surface response of two spherical dipping layers ($a_1 = a_2 = a_3 = 2$, $b_1 = b_2 = b_3 = 1$) to a vertically incident P Ricker wavelet with characteristic period $t_p = 3{\cdot}66$ ($t_s = 4$), $\mu_0 = \beta_0 = 1$, $\alpha_0 = 2$, $\mu_1 = 0{\cdot}4$, $\beta_1 = 0{\cdot}7$, $\alpha_1 = 1{\cdot}4$, $\mu_2 = 0{\cdot}167$, $\beta_2 = 0{\cdot}5$, $\alpha_2 = 1$, $N_s = 256$, $\Delta t = 0{\cdot}1$

incident signal is the same for both models. Seismographs in the second column display larger amplification of the incident signal than those in the first column. This demonstrates the importance of the azimuthal orientation of incident waves for three dimensional models.

Two dipping layer model. The surface response of two dipping layers subjected to vertically incident Ricker P wavelets at stations along the y-axis is depicted by Figures 7 to 10. The results

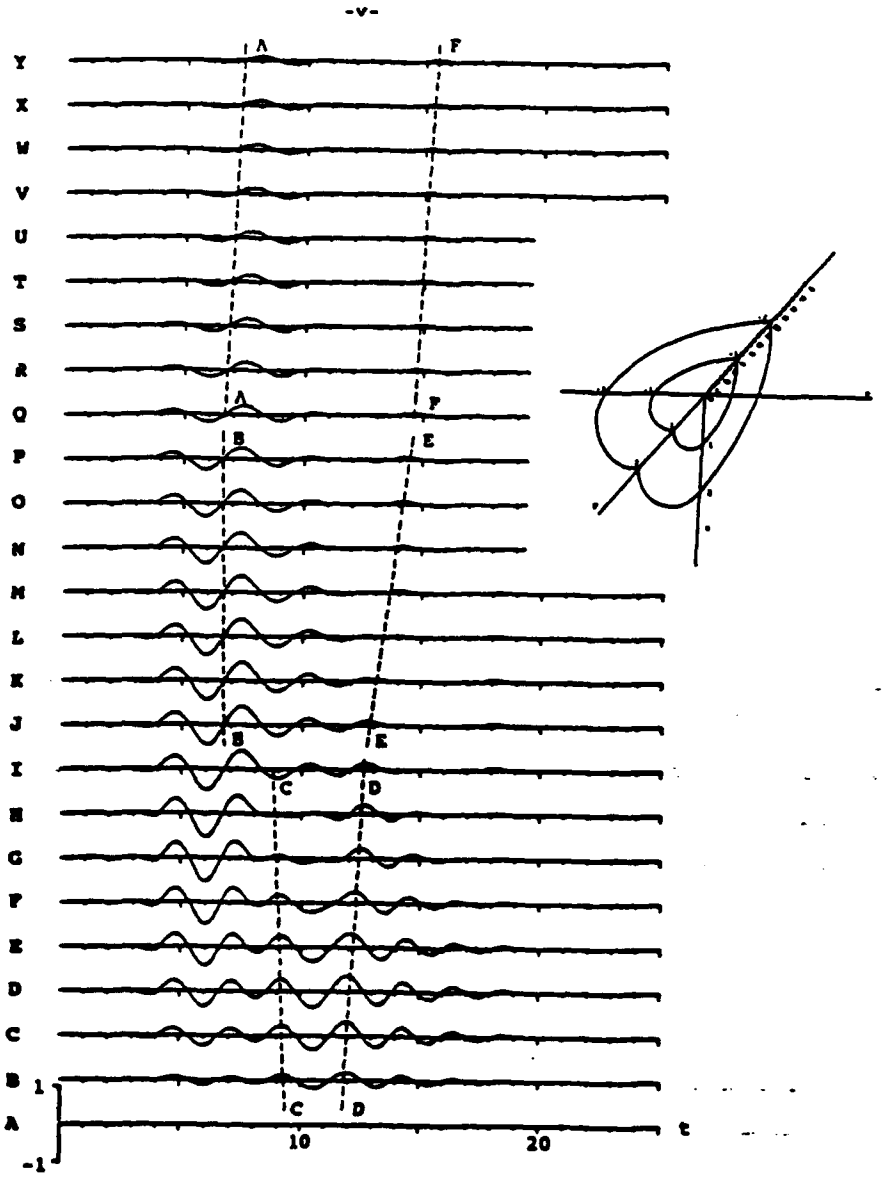

Figure 8. Horizontal component of displacement field (v-component) for transient surface response of two spherical dipping layers ($a_1 = a_2 = a_3 = 2$, $b_1 = b_2 = b_3 = 1$) to a vertically incident P Ricker wavelet with characteristic period $t_p = 3{\cdot}66$ ($t_s = 4$). $\mu_0 = \beta_0 = 1$, $\alpha_0 = 2$, $\mu_1 = 0{\cdot}4$, $\beta_1 = 0{\cdot}7$, $\alpha_1 = 1{\cdot}4$, $\mu_2 = 0{\cdot}167$, $\beta_2 = 0{\cdot}5$, $\alpha_2 = 1$, $N_s = 256$, $\Delta t = 0{\cdot}1$

are presented for two types of valley. The first model consists of two spherical dipping layers and the second model consists of two dipping layers with a circular basin and a relatively shallow depth. The geometry of the models and locations of equally spaced stations along the y-axis are shown in each figure.

For two spherical dipping layers, the vertical (w-) component of surface response is depicted for different stations by Figure 7. Seismographs on the surface of the half-space (Q to Y) indicate that

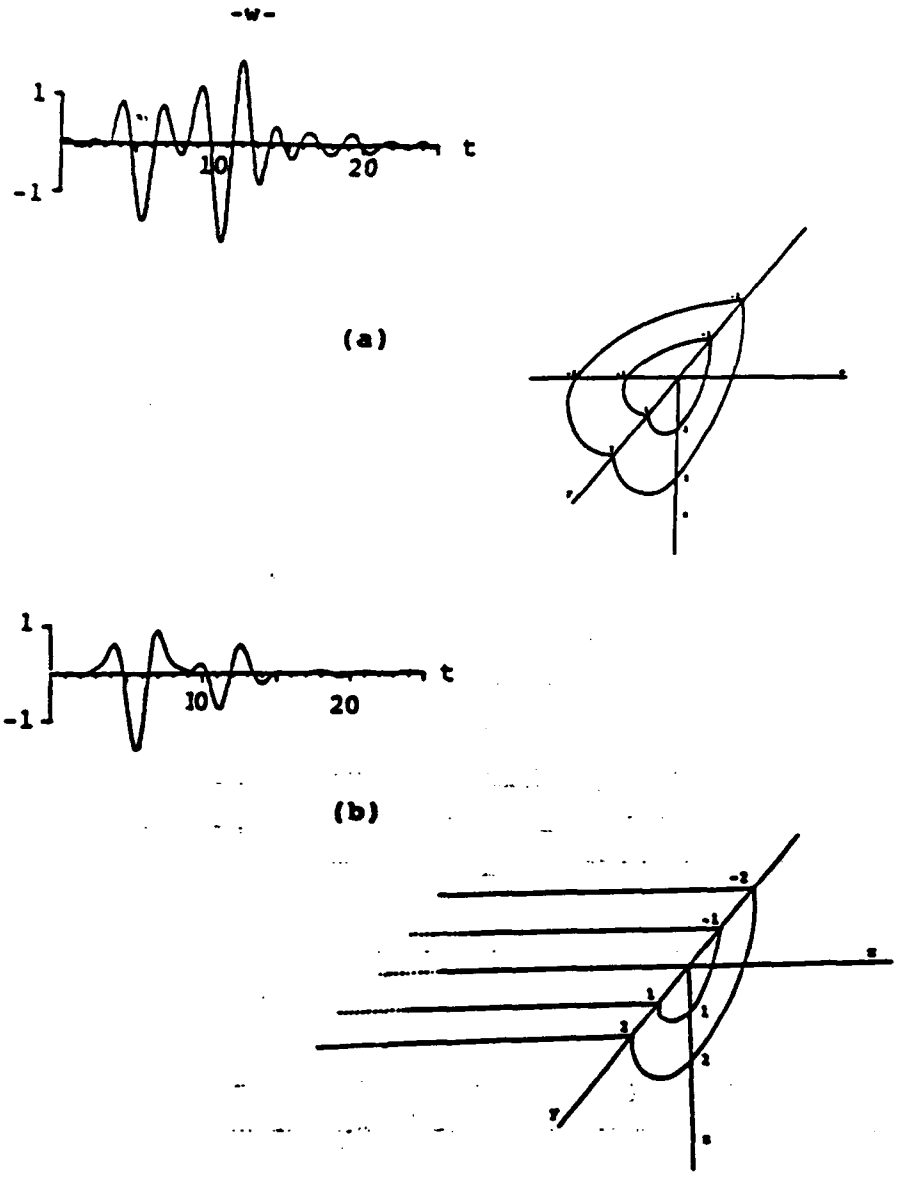

Figure 9. Comparison of the vertical component of displacement field for transient surface response at the centre of two spherical dipping layers $a_1 = a_2 = a_3 = 2$, $b_1 = b_2 = b_3 = 1$ (a) with the response at the centre of two cylindrical dipping layers (b) to a vertically incident P Ricker wavelet. $t_p = 3{\cdot}66$ ($t_s = 4$), $\mu_0 = \beta_0 = 1$, $\alpha_0 = 2$, $\mu_1 = 0{\cdot}4$, $\beta_1 = 0{\cdot}7$, $\alpha_1 = 1{\cdot}4$, $\mu_2 = 0{\cdot}167$, $\beta_2 = 0{\cdot}5$, $\alpha_2 = 1$, $N_s = 256$, $\Delta t = 0{\cdot}1$

the incident signal remains essentially undisturbed (neglecting small disturbances tracked by lines AA and BB). On the surface of the innermost layer seismographs A to I display the formation and propagation of a surface wave at and from the inner edge (station I) toward the centre of the valley as can be tracked by line CC. This surface wave amplifies as it converges toward the centre of the valley. Line DD tracks a surface wave as it propagates away from the valley on the surface of the

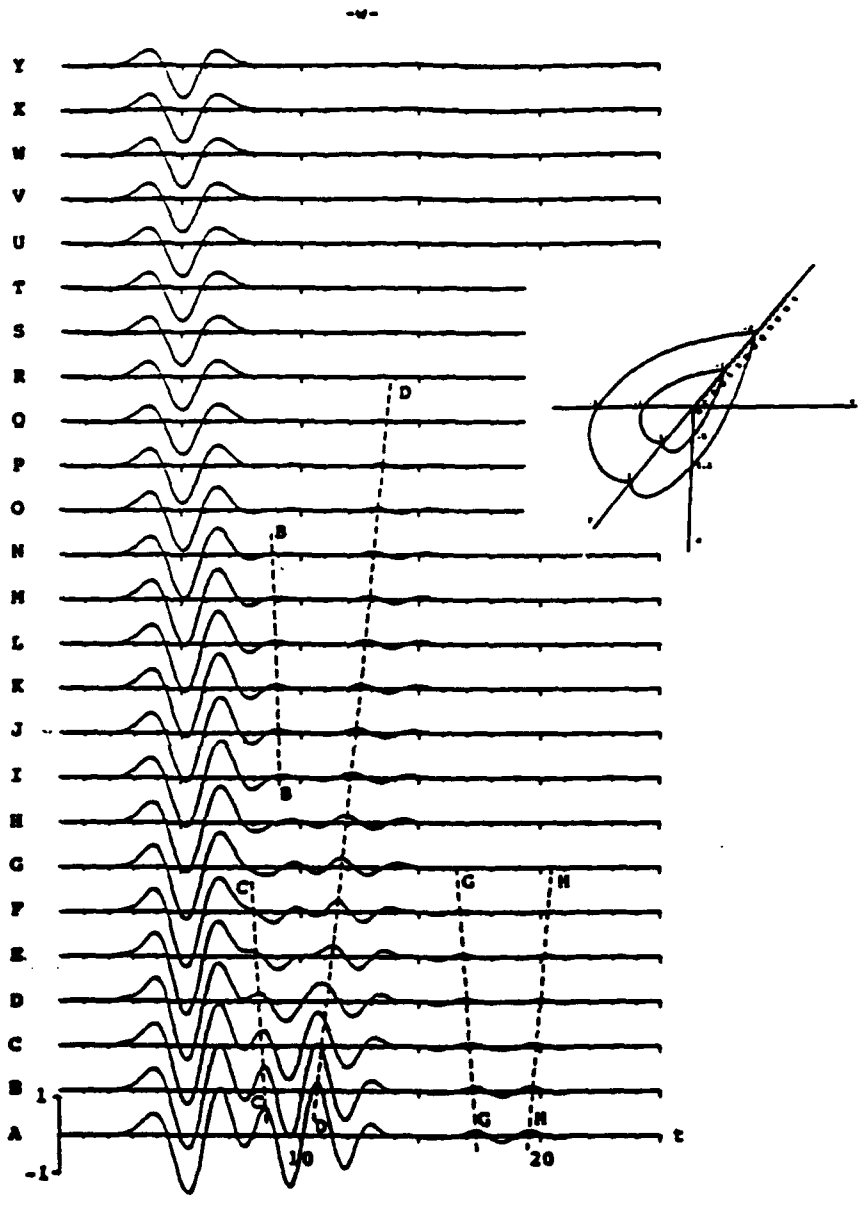

Figure 10. Vertical component of displacement field (*w*-component) for transient surface response of two shallow dippi layers ($a_1 = a_2 = 2$, $a_3 = 1{\cdot}2$; $b_1 = b_2 = 1$, $b_3 = 0{\cdot}6$) to a vertically incident P Ricker wavelet with characteristic peri $t_p = 3{\cdot}66$ ($t_s = 4$). $\mu_0 = \beta_0 = 1$, $\alpha_0 = 2$, $\mu_1 = 0{\cdot}4$, $\beta_1 = 0{\cdot}7$, $\alpha_1 = 1{\cdot}4$, $\mu_2 = 0{\cdot}167$, $\beta_2 = 0{\cdot}5$, $\alpha_2 = 1$, $N_s = 256$, $\Delta t = 0{\cdot}1$

innermost layer. The surface wave reduces in amplitude as it diverges away from the valley centr This surface wave continues to propagate away from the valley on the surface of the first lay (line EE) and then on the surface of the half-space (line FF). It is interesting to observe how t focusing of the surface waves tracked by lines CC and DD contributes to such a lar

amplification at stations around the centre of the valley (e.g. stations A to D for $8 < t < 13$). These surface waves can be better tracked and identified by investigating the horizontal component of the displacement field where the response consists of a scattered field only. Seismographs in Figure 8 display the horizontal (v-) component of the displacement field. Lines AA to FF track the same surface waves as their counterparts in Figure 7 for the vertical component of the displacement field.

It is interesting to compare the vertical component of the displacement field at the centre of these two spherical dipping layers with that of compatible two cylindrical dipping layers subjected to the same type of incidence as in Figure 7. For that purpose, the response of a cylindrical two dipping layer model, studied previously by the present authors,[2] is reconsidered. Figure 9 displays the response at the centre of the two models. Comparison of these two results indicates that the amplification of the incident signal for $0 < t < 9$ is very similar in both models. Even the amplitudes of the main peak at about $t = 5{\cdot}5$ are almost identical. Furthermore, for the cylindrical model a signal develops at the centre and at about the same time ($9 < t < 15$) as in the spherical model, with very similar characteristics but with smaller amplitude. The larger amplitude of this wave signal for the spherical model is due to the constructive interaction and convergence of surface waves at the centre of the valley. The results of Figure 9 demonstrate the importance of three dimensional modelling for scattering of waves by actual irregularities.

It is interesting to compare the main component of the displacement field (w-component) of the two dipping layer model with that of a one dipping layer model studied earlier in Figure 5(c). These two models are compatible in the sense that both include a spherical dipping layer on the top with identical geometries and material properties. However, the two dipping layer model includes an additional layer which results in a smoother transition of the material properties from the soft layer on the top to the hard bed rock (the half-space). Furthermore, the ratios of the wavelength of the incident wavelet to the width of the soft top layer are the same for both models. A comparison between the vertical component of surface response at the centre of these two models indicates that the amplification of an incident signal at early times is more significant for the one dipping layer model than for the two dipping layer one. However, for the two dipping layer model much larger amplification of surface waves is observed at later times ($9 < t < 15$) than for the one dipping layer model. This observation indicates that the presence of sediments may change substantially the local amplification of ground motion.

Finally, Figure 10 displays the vertical component of the surface response of a shallow two dipping layer model, subjected to a vertically incident P Ricker wavelet. The wavelength of the incident signal is considered to be the same as for the spherical model. However, the depth of this valley is reduced, in comparison with the spherical model, in order to study the depth dependency of the surface response. On the surface of the half-space (stations Q to Y) the scattered waves are very insignificant, whereas, for the spherical model (Figure 7) these scattered waves are more pronounced. Similar surface waves (as in Figure 7) propagate on top of the second layer (stations J to Q) with smaller amplitudes. On the surface of the inner layer (stations A to I) both converging and diverging surface waves to and from the centre of the valley can be observed. The converging and diverging surface waves tracked by lines CC and DD resemble those of Figure 7. However, the amplitude of these surface waves is reduced significantly in this model. Reflected converging and diverging surface waves from the edges of the valley can be identified by lines GG and HH.

The geometric complexity of these models precludes a more detailed examination of the corresponding response. Nevertheless, the presented results provide sufficient information to reach a basic understanding of the transient response of a three dimensional multiple dipping layer subjected to different incident waves. These results indicate clearly the importance of the surface waves in the resulting ground motion.

CONCLUSIONS

The amplification of incident plane SH, SV, P and Rayleigh waves by non-axisymmetric three dimensional multiple dipping layers of arbitrary shapes is investigated by using a boundary method. Both harmonic and transient incident wave fields are considered.

The presented results demonstrate the importance of three dimensional modeling of actual irregularities. It is shown that the surface response of a dipping layer is very sensitive to azimuthal orientation of the incident signal. The transient response of the spherical two dipping layer model indicates the significance of the scattered surface waves. These surface waves could have large amplitudes at stations close to the centre of the valley. The large amplitude of these surface waves, in comparison with their counterparts in cylindrical models, further emphasizes the importance of three dimensional modelling of actual near surface irregularities. Furthermore, the comparison of the transient surface response of the compatible spherical one and two dipping layer models indicates that the presence of an additional layer may produce a substantial change in the surface response of the model.

ACKNOWLEDGEMENTS

This material is based upon work supported in part by the National Science Foundation under Grant No. 53–4519–3792 and in part by the Office of Naval Research under Contract No. N00014–88–K–0157.

REFERENCES

1. H. Eshraghi and M. Dravinski, 'Transient scattering of elastic waves by dipping layers of arbitrary shape. Part I. Antiplane strain model', *Earthquake eng. struct. dyn.*, **18**, 397–415 (1989).
2. H. Eshraghi and M. Dravinski, 'Transient scattering of elastic waves by dipping layers of arbitrary shape. Part 2. Plane strain model', *Earthquake eng. struct. dyn.*, **18**, 417–434 (1989).
3. H. Eshraghi, 'Scattering of elastic waves by two and three dimensional near surface irregularities of arbitrary shape', *Ph.D. Dissertation*, Department of Mechanical Engineering, University of Southern California, 1989.
4. S. Day, 'Finite element analysis of seismic scattering problem', *Ph.D. Thesis*, UC San Diego, California, 1977.
5. R. J. Apsel, 'Dynamic Green's functions for layered media and applications to boundary value problems', *Ph.D. Thesis*, UC San Diego, California, 1979.
6. F. J. Sanchez-Sesma, 'Diffraction of elastic waves by three- dimensional surface irregularities', *Bull. Seism. Soc. Am.*, **73**, 1621–1636 (1983).
7. V. W. Lee, 'Three-dimensional diffraction of plane P, SV, and SH waves by a hemispherical alluvial valley', *Soil Dyn. Earthquake Eng.*, **3**, 133–144 (1984).
8. Y. Niwa and S. Hirose, 'Application of the BEM to elastodynamics in a three dimensional half-space', *Recent Applications in Computational Mechanics*, ASCE, 1987, pp. 1–15.
9. H. Eshraghi and M. Dravinski, 'Scattering of plane harmonic SH, SV, P, and Rayleigh waves by non-axisymmetric three dimensional canyons: A wave function expansion approach', *Earthquake eng. struct. dyn.*, **18**, 983–998 (1989).
10. H. Eshraghi and M. Dravinski, 'Scattering of elastic waves by non-axisymmetric three dimensional dipping layer', *Numer. Methods Part. Diff. Eqs.*, **5**, 327–345 (1989).
11. T. Jiang and E. Kuribayashi, 'The three-dimensional resonance of axisymmetric sediment-filled valleys', *Soils Found.*, **18**, No. 4, 130–148 (1988).
12. J. J. Lee and C. A. Langston, 'Wave propagation in a three dimensional circular basin', *Bull. Seism. Soc. Am.*, **73**, 1637–1653 (1983).
13. F. J. Sanchez-Sesma, L. E. Perez-Rocha and S. Chavez-Perez, 'Diffraction of elastic waves by three-dimensional surface irregularities. Part II', *Bull. Seism. Soc. Am.*, **79**, 101–112 (1989).
14. Y.-H. Pao and C. C. Mow, *Diffraction of Elastic Waves and Dynamic Stress Concentrations*, New York, Crane, Russak, 1973.
15. B. Noble and J. W. Daniel, *Applied Linear Algebra*, Prentice-Hall, Englewood Cliffs, N.J., 1977.
16. N. H. Ricker, *Transient Waves in Visco-Elastic Media*, Elsevier, New York, 1977.
17. E. O. Brigham, *The Fast Fourier Transform*, Prentice-Hall, Englewood Cliffs, N.J., 1974.
18. M. Abramowitz and I. A. Stegun, *Handbook of Mathematical Functions*, Dover, New York, 1972.

JOURNAL OF THE GEOLOGICAL SOCIETY OF CHINA
Vol.35, No.2, P.153-172, 11 Figs., Apr., 1992

TRANSIENT RESPONSE PATTERNS FOR A 3D CANYON IN A VISCOELASTIC HALF SPACE FOR DIFFERENT INCIDENT WAVES

T. K. MOSSESSIAN[1] and M. DRAVINSKI[2]

1. Structural Research and Analysis Corp.,
1661 Lincoln Blvd., Santa Monica, California 90404, U.S.A.
2. Department of Mechanical Engineering, University of Southern California,
Los Angeles, California 90089-1453, U.S.A.

ABSTRACT

An indirect boundary integral equation method is applied to study amplification of elastic waves by three dimensional canyons of arbitrary shape. Model investigated in this study is a general three dimensional one. Incident plane SH, SV, P and Rayleigh waves in form of a Ricker wavelet are assumed. Formulation of the problem is outlined first in the frequency domain. Subsequent transient solution is obtained through the Fourier synthesis. Surface displacement fields are presented for several canyon shapes subjected to different types of incident waves. The nature of different scattered waves in the near field is examined. In particular, the waves propagating along the surface of the canyon are identified as creeping P and S-waves.

INTRODUCTION

Amplification of waves by near surface irregularities has been subject of extensive investigations in recent years (Aki, 1988). The importance of this problem has been reinforced through observations of strong ground motion amplification during some recent earthquakes (e.g., Anderson *et al.*, 1986). However, almost the entire theoretical research on this topic has been done for two dimensional models. Studies on diffraction of elastic waves by three dimensional near surface irregularities have been limited to axisymmetric scatterers (e.g., Lee, 1978; Sanchez Sesma, 1983). Only recently, investigations involving nonaxisymmetric models have been made available (Mossessian and Dravinski, 1989; Eshraghi and Dravinski, 1989, Luco *et al.*, 1990).

This work is a continuation of research reported in a paper by Mossessian and Dravinski (1989) in which the steady state solution of the problem has been presented. Transient analysis of the model is differed to this investigation.

STATEMENT OF THE PROBLEM

Geometry of the model is depicted by Figure 1. An anelastic half-space $-\infty \leq x, y \leq \infty, z \geq 0$ contains a canyon of arbitrary shape S_I Surface of the half-space D_H is composed of two parts, flat surface S_F and irregular surface S_I. Surface S_I is defined by equation $z = g(x,y)$ for $z > 0$, where $g(x,y)$ is some arbitrary function. In this study the irregular surface is chosen to be sufficiently smooth with no sharp corners being present. Material of the half-space is assumed to be weakly anelastic, homogeneous and isotropic. The half-space is subjected to incident plane harmonic P, SV, SH and Rayleigh waves.

Equation of motion for steady state elastic wave propagation is specified by

$$(\lambda + \mu)\, \nabla \nabla \cdot \mathbf{u} + \mu \nabla^2 \mathbf{u} + \rho\omega^2 \mathbf{u} = 0;\ \mathbf{x} \in D_H \qquad (1)$$

where $u = (u,v,w)$ is the displacement vector, x is the position vector and λ and μ are the Lame constants. These constants are assumed to be complex numbers to account for anelasticity (e.g. Aki and Richards, 1980). Throughout the paper the term $\exp(i\omega t)$ is understood. Stress free boundary conditions along the flat surface SF are specified by

$$\sigma_{xz} = \sigma_{yz} = \sigma_{zz} = 0;\ z = 0,\ \mathbf{x} \in S_F \qquad (2)$$

On irregular surface S_I boundary conditions are of the form

$$t^{\nu} = 0;\ \mathbf{x} \in S_I \qquad (3)$$

where t^{ν} is the traction vector at the surface S_I with unit normal ν. Usual radiation conditions should be satisfied by the scattered wave field at infinity.

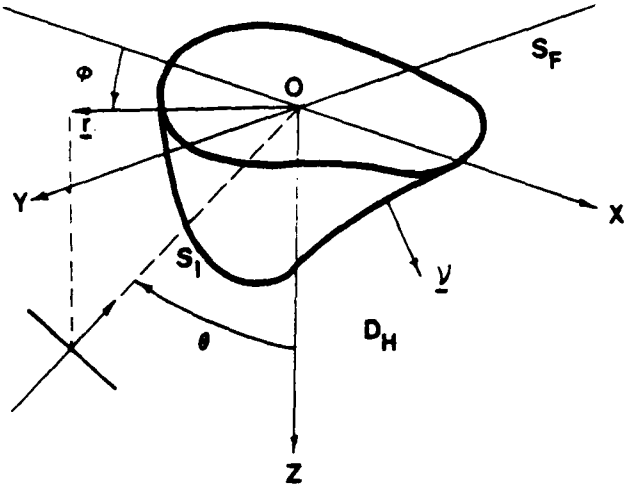

Figure 1. Problem model.

METHOD OF SOLUTION

Steady State Solution

Since the steady state part of the solution has been discussed in the previous paper (Mossessian and Dravinski, 1989) only a brief outline of the solution in frequency domain is presented here.

Total displacement field in the half space D_H is specified by

$$\mathbf{u} = \mathbf{u}^{ff} + \mathbf{u}^{s}; \quad \mathbf{x} \in D_H \tag{4}$$

where the superscripts ff and s denote the free and scattered wave field, respectively. Following an indirect boundary integral equation approach (e.g. Apsel and Luco, 1987; Dravinski and Mossessian, 1987) the scattered field is assumed to be generated from distribution of unknown tractions f(y) over an auxiliary surface S_a inside the surface S_I (Herrera, 1984). Hence, the scattered displacement field in the half-space can be written in the form

$$\mathbf{u}^{s} = \int_{S_a} \mathbf{G}(\mathbf{x}, \mathbf{y})\, \mathbf{f}(\mathbf{y})\, dS_a(\mathbf{y}); \quad \mathbf{x} \in D_H \tag{5}$$

where G is a half-space displacement Green's function tensor (Aki and Richards, 1980). The element $G_{ij}(x,y)$ corresponds to the i-th component of the displacement vector at x due to a unit harmonic force at y acting in the j-th direction. Theoretical development of these Green's functions is rather involved and their complete explicit forms are available in the literature (e.g. Mossessian and Dravinski, 1989).

Choosing f(y) to be distributed at discrete points x_m on the surface Sa, then it follows from equation (5) that the total wave field can be written in the form (Mossessian and Dravinski, 1989)

$$\mathbf{u} = \mathbf{u}^{ff} + \mathbf{G}(\mathbf{x}, \mathbf{x}_m)\, \mathbf{f}^{m}; \quad \mathbf{x}_m \in S_a; \quad m = 1,2,...,M \tag{6}$$

Here f^m are the unknown magnitudes of the point forces. Throughout the paper summation over repeated index m is understood.The unknown force magnitudes f^m are yet to be determined for all m. Using equation (6), the components of total traction along the surface S_I become

$$\mathbf{t} = \mathbf{t}^{ff} + \mathbf{T}(\mathbf{x}, \mathbf{x}_m)\, \mathbf{f}^{m}; \quad \mathbf{x} \in S_I; \quad m=1,2,...,M \tag{7}$$

where t^{ff} is the free-field traction vector and T is the half-space traction Green's function tensor. The component $T_{ij}(x, x_m)$ corresponds to i-th component of the traction vector at x due to unit harmonic force at x_m acting in the j-th direction. For simplicity, the superscript ν is suppressed. By choosing N observation points along the surface S_I the corresponding traction field can be stated as follows

$$t(x_n) = t^{ff}(x_n) + T(x_n, x_m) f^m;\ x_n \in S_I;\ x_m \in S_a, \qquad (8)$$

$$n = 1,2,...,N;\ m = 1,2,...,M$$

Using equation (8), the traction free boundary condition given by equation (3), assumes the following form

$$G_t\ f^t = a;\ f^t = (f^1, f^2, ..., f^m)^T \qquad (9)$$

where, vector f^t contains the unknown force magnitudes and matrix G_t and vector a are known. Choosing N greater than M, equation (9) is solved in the least square sense. Once the magnitudes of the forces f^t are known, the total wave field within the half-space D_H can be obtained through equation (6).

Transient Solution

Transient solution is obtained from the steady state one by using an inverse Fourier transform according to

$$u(x,t) = 1/2\pi \int_{-\infty}^{\infty} u(x,\omega)\, e^{i\omega t}\, d\omega \qquad (10)$$

The temporal part of the incident signal is assumed to be in the form of a Ricker wavelet (Ricker, 1977) defined by

$$f(t) = \sqrt{(\pi)/2}\ \ (a^2 - 0.5)e^{-a^2};\ a = \pi t / t_p \qquad (11)$$

where t_p is the predominant period of the wavelet. The Fourier transform of this wavelet has the following form

$$F(\omega) = -\ t^3_p\, \omega^2/8\pi^2\ e^{-\omega^2 t^2_p/4\pi^2} \qquad (12)$$

It is apparent that $F(\omega)$ has a maximum at $\omega_p = 2\pi/t_p$ and that it decreases very fast for frequencies larger than ω_p. Consequently, the steady state calculations are done for the range of frequencies $0 \leq \omega \leq 3.5\ \omega_p$ at equal frequency intervals. For convenience the time delay $t - t_s$ can be introduced in equation (11) to account for shift in the temporal origin of the input motion.

NUMERICAL RESULTS AND DISCUSSION

The scatterer in the form of a semiprolate canyon is considered. This geometry can be defined in parametric form by

$$x = a\cos(t)\cos(s) \quad y = b\cos(t)\sin(s) \quad z = b\sin(t) \tag{13}$$

$$0 \le t \le \pi/2, \quad 0 \le s \le 2\pi$$

where a and b are the major and minor axis of the prolate, respectively. To reduce the number of figures, only the results for cross sections y=0 and x=0 are presented. Incident waves are plane P, SV, SH, and Rayleigh waves. The azimuthal angle of incidence ϕ_0 is measured counterclockwise (viewed from $z \le 0$) from the negative x-axis (see Figure 1). The off-vertical angle of incidence θ_0 is measured form the positive z axis towards vector r=(x,y), which defines the azimuthal position on the surface of the half-space. The amplitude of the incident waves are the same as those used by Dravinski and Mossessian (1987).

Testing of the method

Since at the present time the authors are not aware of any results pertinent to transient scattering of elastic waves by nonaxisymmetric three dimensional scatterers, validation of the method has been done in the frequency domain. Namely, for steady state results and axisymmetric scatterers there are available results in the literature which can be used for testing of the method. The details of the testing have been reported in the paper on steady state results (Mossessian and Dravinski, 1989) and they can be summarized here as follows. Surface displacement fields obtained by this method are in excellent agreement with those obtained by other researchers using different techniques. This was the case for different incident waves at various frequencies.

For transient results the testing was done in a qualitative manner. This included checking the time arrivals of direct waves as well as verification of the causality principle for observation stations at the surface of the canyon and the half space. All numerical calculations proved to be stable and they could be performed on a standard workstation.

Transient Surface Response of a Canyon

Hemispherical and semiprolate canyons considered in this analysis have been defined by equation (13). Throughout the paper the following normalization procedure is adopted. All distances are normalized with respect the principal axis "a" of the canyon which is chosen to be of a unit length. All velocities are normalized with respect to the shear wave velocity of the half-space which is assumed to be equal one. The dimensionless time is defined as $t\,\beta/a$, where β denotes the half-space S- wave velocity. Poisson ratio ν and the shear modulus of the half-space are taken to be 1/3 and 1, respectively. Consequently, the half-space P-wave velocity is equal 2.

The Fourier integrals are evaluated by using the fast Fourier transform (FFT) algorithm. For that purpose each calculation requires certain sampling rate $\Delta\omega$ and number of samples N. Transient response is evaluated for stations along the surface of the half-spaceand the canyon.

Incident SH-Wave. For a vertically incident SH-wave (θ_0 =0, ϕ_0 = 0) and a hemispherical canyon surface displacement field along the xz-plane is depicted by Figure 2. First trace from the bottom corresponds to the station on the half-space being farthest away from the center of the canyon along the negative x-axis. Similarly, the top trace corresponds to

the station on the half-space which is farthest away from the center of the canyon along the positive x-axis. Intermediate stations are chosen in such a way that the distance between them remains the same regardless whether the stations are along the surface of the half-space or the canyon. Therefore, 21 central traces in each figure correspond to the canyon stations. The remaining traces correspond to the half-space stations. Since the distances between the stations on the surface of the canyon are presented as being rectified it is possible to determine the apparent velocity of the waves propagating along the surface of the half-space and the canyon directly from the figures. Namely, if the time arrivals of wave peaks are marked, then for a wave propagating with a constant phase velocity, the markings will lie on a straight line with a slope corresponding to that phase speed. This convention is being used for the responses evaluated in the the yz-plane as well (with appropriate change of axes).

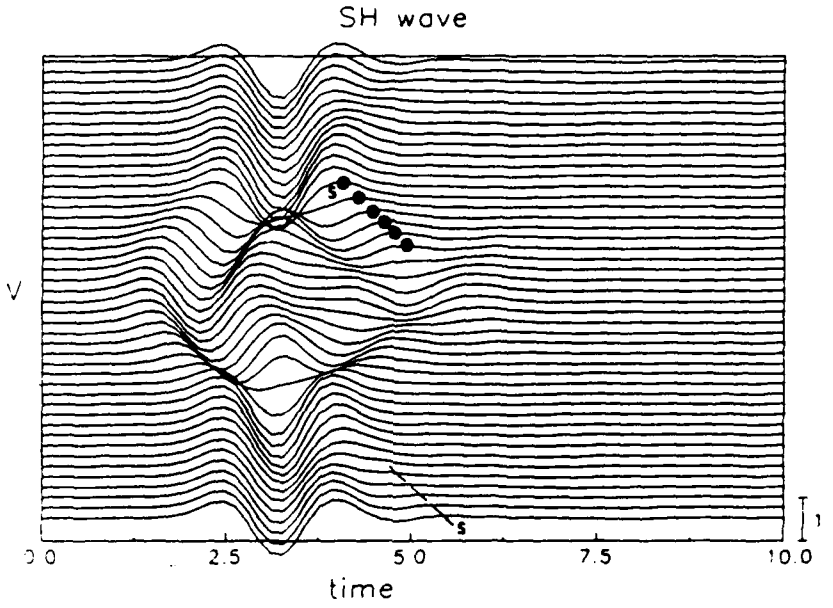

Figure 2. Horizontal component (v) of surface displacement field for a hemispherical canyon of unit radius subjected to a vertical incident SH Ricker wavelet for 45 different observation stations along the surface of the half-space and the canyon in the y=0 plane. The stations are symmetrically spaced at equal distances Δ = 0.157 in the range $-2.884 \leq x \leq 2.884$. The response unit amplitude is marked on the right vertical side of the figure window. If not stated differently the following parameters are kept the same: Incident wave parameters: $t_p = 2$, $t_s = 2.2$, $\theta_0 = 0°$, $\varphi_0 = 0°$. FFT parameters: Number of samples N = 128. Material properties of the half-space: $\beta = \mu = 1$, $\alpha = 2$, attenuation factors for P and S-waves (after Aki and Richards, 1980) $Q_\alpha = Q_\beta = 100$.

Due to symmetry the only non-zero displacement component is along the y-axis. The v-component of displacement is called the predominant one for this incident wave. It is apparent from Figure 2 that presence of the canyon caused great change of the free-field

response which would be present in the half-space in absence of any irregularities. In particular, it should be emphasized increase in duration of the response for stations along the surface of the canyon in comparison to the stations along the surface of the half-space.

Diffracted body S-wave propagating away from the edges of the canyon can be observed as well. The one propagating along the negative x-axis is marked by a dash line. Apparently, the amplitude of the body waves diffracted by the canyon edges is very small in comparison to that of a direct wave.

In addition to the waves traveling along the surface of the half-space one can observe the waves propagating along the surface of the canyon. Their peaks are marked with solid circles. From Figure 2 the apparent speed of the waves along the canyon surface is found to be equal to the shear wave speed β of the half-space.These waves are called the creeping waves. Since the particle motion of the creeping wave in Figure 2 is perpendicular to its direction of propagation the wave is of the S-type. Kawase (1988) observed the creeping waves in studying SH incidence upon a two-dimensional semicircular canyon.

For the same geometry of the canyon and an oblique incident SH-wave surface response in the yz-plane is depicted by Figure 3. To emphasize the importance of mode conversion only the non-predominant components of displacement field (u and w) are displayed. These components are entirely produced by SH to P/SV mode conversions and they are not present in two-dimensional models. Evidently, the non-predominant components of motion may have substantial amplitude. One can detect presence of Rayleigh waves propagating away from the edges of the canyon. The phase shift between horizontal and vertical components of motion, which is characteristic of Rayleigh waves, can be clearly observed. To elaborate upon this further Figure 4 displays a phase plot for observation station (0, -2.884, 0) (bottom traces in Figure 3). The phase plot demonstrates overall the Rayleigh type of motion along the surface of the half-space.

Another important feature exhibited by Figures 2 and 3 is dependence of surface motion amplification upon azimuthal orientation of the observation stations relative to the incident wave. This further emphasizes the need for three dimensional modeling of actual irregularities.

In addition to Rayleigh waves one can observe in Figure 3 the presence of the creeping waves as well. The one marked for the vertical component of motion travels with speed of the half-space P-waves and the one marked for the horizontal component of motion travels with apparent velocity of the half-space S-waves. The former is identified as the creeping P-wave while the latter one is recognized as the creeping S-wave. It should be noted that, since the canyon waves travel along a curved path, the polarization of these waves may not be so obvious. However, near the canyon edge, creeping P-wave results in a vertical predominant motion while creeping S-wave produces horizontal predominant motion. Based on this, and the observed apparent velocity of the creeping waves, it is possible to asses their nature on a case by case basis.

As the shape of the canyon changes from a hemispherical to a semiprolate one expects to see change in surface response patterns. To examine this, transient response for a prolate canyon subjected to a vertical incident SH Ricker wavelet is considered next. Figure 5 displays the predominant component of motion in the xz-plane.

Apparently, reduction in canyon depth (compare Figures 2 and 5) produced reduction in amplitude of the body waves diffracted by the canyon edges. These waves could be clearly detected for the hemispherical canyon (Figure 2) while they are barely visible for a semiprolate canyon.

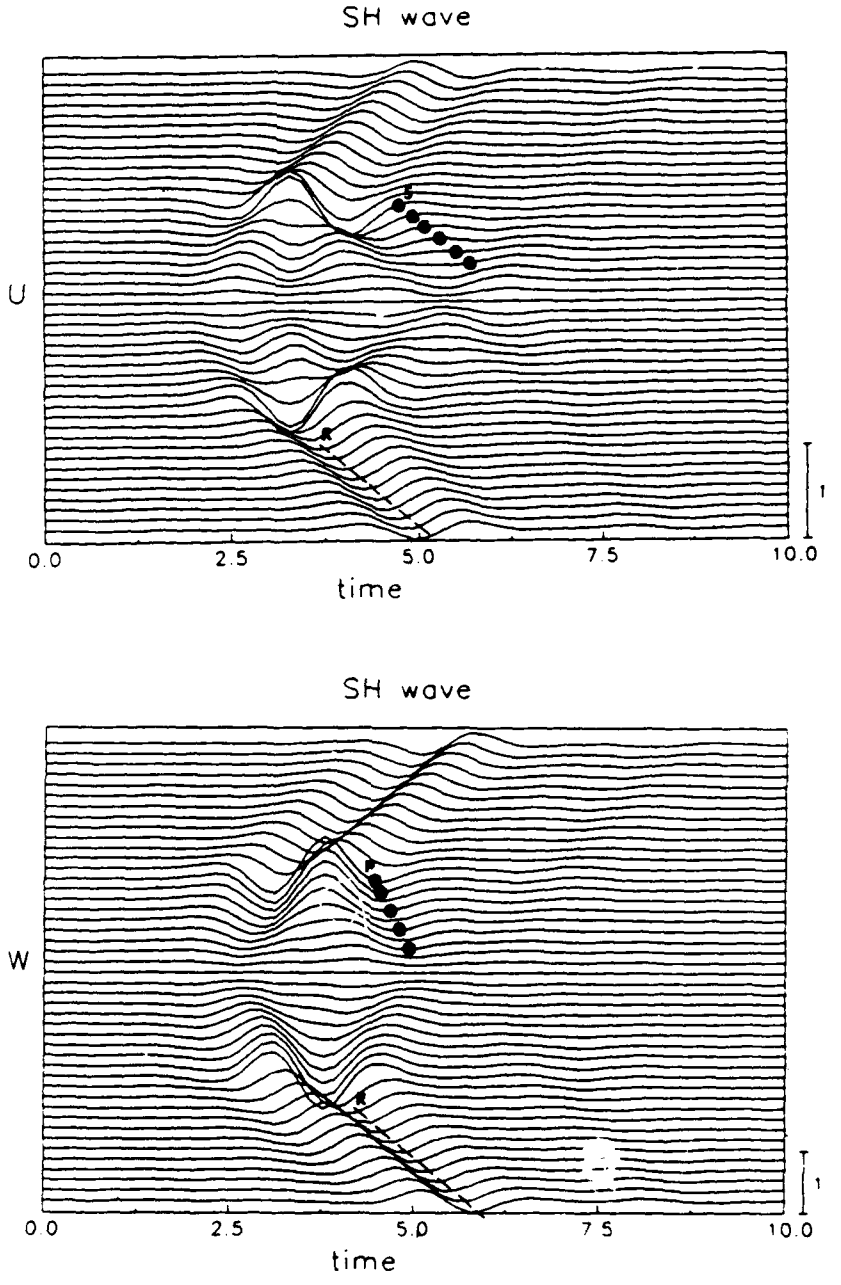

Figure 3. Vertical component (w) and horizontal component (u) of the surface displacement field for a hemispherical canyon of unit radius subjected to an incident SH Ricker wavelet. 45 observation stations are symmetrically spaced in the yz-plane for $-2.884 \leq y \leq 2.884$ ($\Delta = 0.157$). $\theta_0 = 30°$, $\varphi_0 = 0°$.

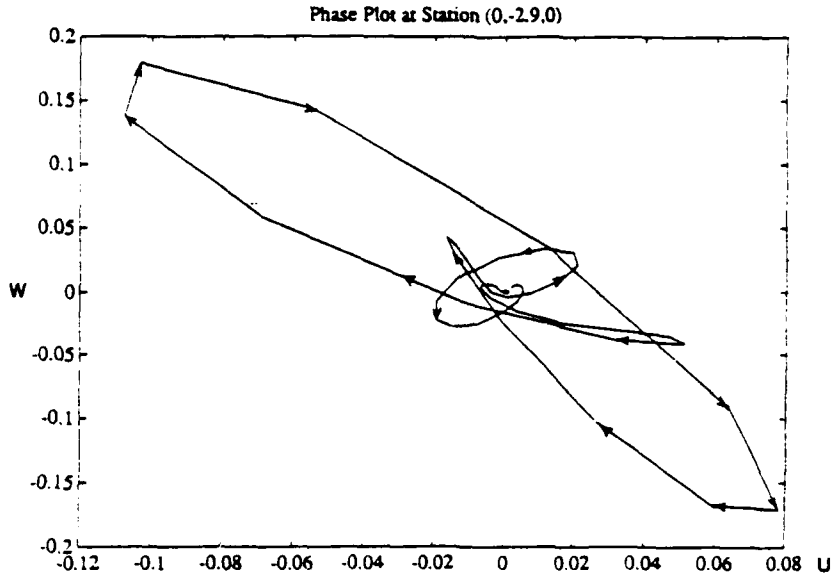

Figure 4. Phase plot for the station (0,-2.884,0), which corresponds to the bottom trace of Figure 3, for a hemispherical canyon and obliquely incident SH Ricker wavelet. θ_0 =30°, ϕ_0 =0. The arrows indicate the evolution of the phase plot with time.

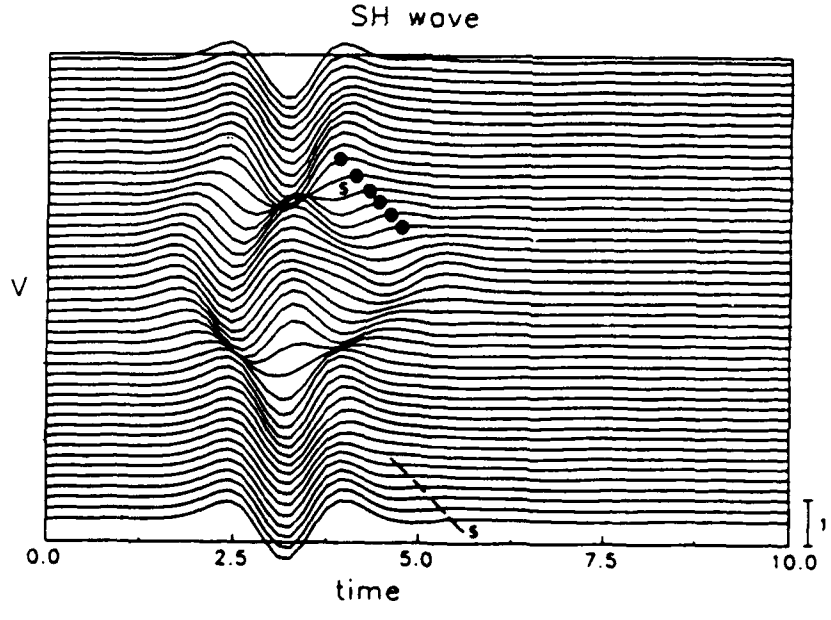

Figure 5. Horizontal component (v) of surface response for a semiprolate canyon in the xz-plane subjected to a vertically incident SH Ricker wavelet. a=1, b=0.7, $-2.614 \leq x \leq 2.614$ for 45 stations (Δ = 0.1345).

Comparison of Figures 2, 3, and 5 suggests that most of the scattered wave energy is converted into Rayleigh waves and considerably less into body waves diffracted by the canyon edges.

In addition to diffracted waves one can observe in Figure 5 the creeping S-waves as well.

Therefore, the results for incident SH-waves can be summarized as follows: Rayleigh waves can be clearly observed. Very strong SH to P/SV mode conversion can be detected and this phenomena does not exist in two-dimensional models. Reduction of canyon depth resulted in decrease of surface wave content of the ground motion. Both P- and S-creeping waves are observed propagating along the canyon surface. Most of the energy radiates away from the scatterer in form of the surface waves rather than body waves diffracted by the canyon edges.

Incident P-Waves. For a vertically incident P-wave and a semiprolate canyon surface displacement field in xz-plane is depicted by Figure 6. Due to symmetry only two components of motion are present. Rayleigh waves can be clearly seen propagating away from the edges of the canyon. They are marked by dash lines. The speed of the surface waves, c_R=0.94, determined from the figure, is in excellent agreement with the theoretical value c_R=0.934. In addition, the appropriate phase shift between the horizontal and vertical component of surface motion can be observed as well. Creeping P-waves are observed for the horizontal component u while the ones of the S-type are not detected.

For a hemispherical canyon and a vertically incident P-wave surface response for xz-plane is very similar to the response of a semiprolate canyon and is therefore omitted. However, as in the case of SH incidence, larger canyon depth produced more pronounced surface waves in the resulting ground motion and greater amplification at the edges of the canyon.

For the same incident wave and geometry of the canyon surface motion in the yz-plane is shown by Figure 7. From comparison of Figures 6 and 7 it is evident that surface wave content of motion is greater along the yz-plane than for the xz-plane. This can be measured in terms of surface waves amplitudes as they propagate away from the canyon which is especially evident for the nonpredominant components of motion u and v.

It is evident from Figure 7 that in the yz-plane only the creeping P-waves are observed with clarity.

Incident SV-Wave. Figure 8 displays surface displacement field for a hemispherical canyon subjected to a vertically incident SV-wave. The motion is evaluated along the xz-plane. Consequently, only two components of motion are present and the predominant motion is along the x-axis. In addition to Rayleigh waves one can detect presence of the creeping waves for both components of motion. These waves are of the P- and of the S-type.

It should be noted that in comparison to SH and P incidence the SV incident wave produced considerably longer duration of surface ground motion for the same shape of the scatterer.

Furthermore, larger amplification of ground motion can be detected near the canyon edges for predominant component of motion for SV incidence than for SH incidence. For an oblique incident SV-wave the results are depicted by Figure 9. Evidently, a much more complicated pattern of surface motion emerges in this case. Thus, surface motion appears to be very sensitive upon the orientation of the incident wave. Change from a vertical to an oblique incidence resulted in significant change of motion pattern for both components of displacement field. Still, the basic features remain the same: Large amplification of motion

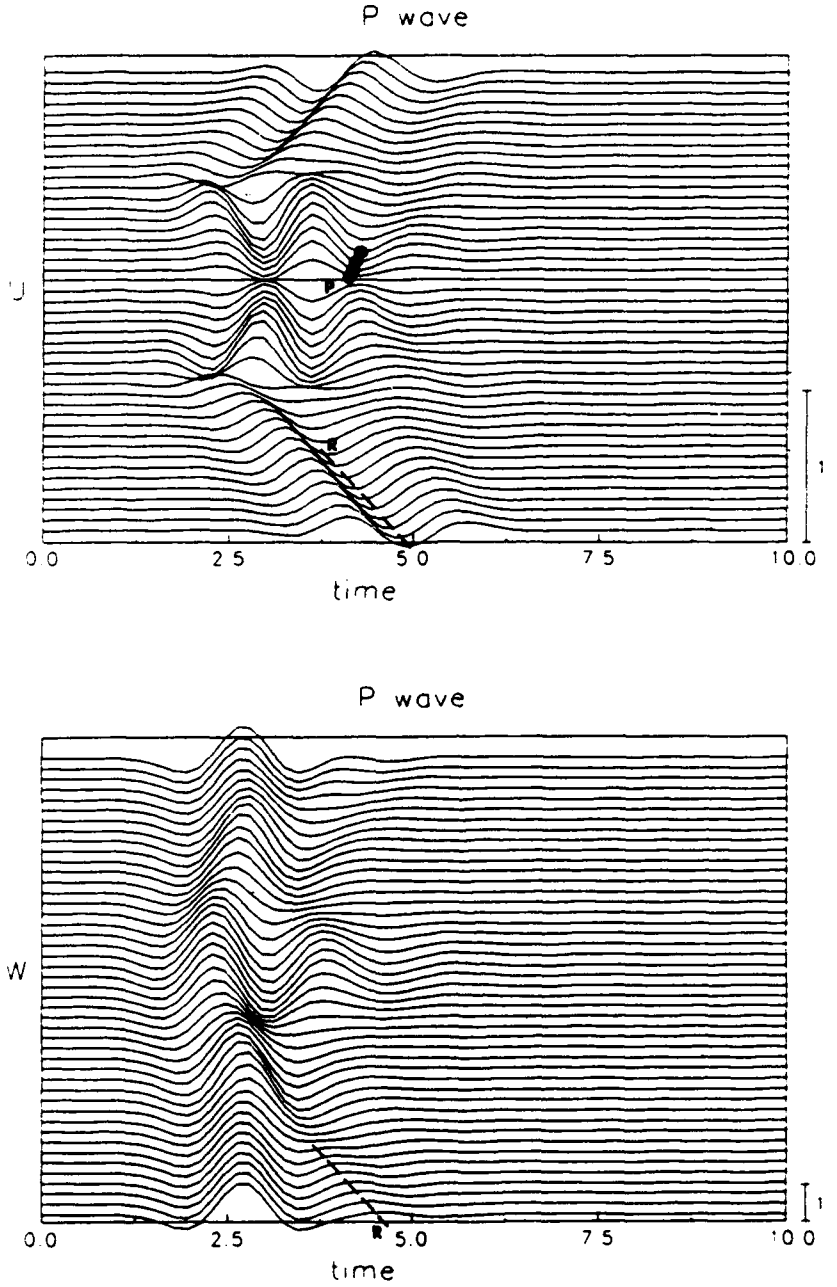

Figure 6. Vertical (w) and horizontal (u) components of surface displacement field in the xz-plane for a vertically incident P Ricker wavelet and a semiprolate canyon a=1, b=0.7. $-2.614 \leq x \leq 2.614$ for 45 stations ($\Delta = 0.1345$).

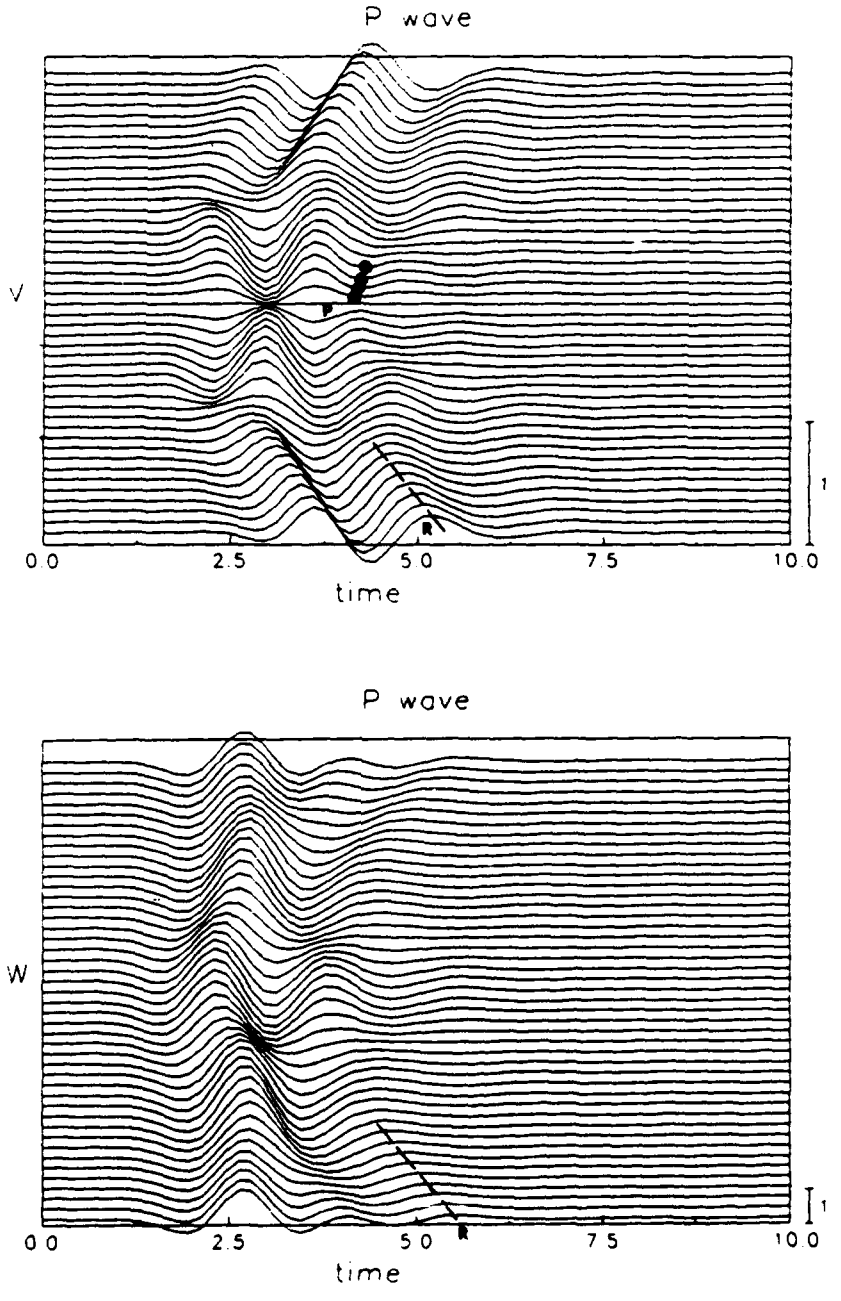

Figure 7. Vertical (w) and horizontal (v) components of surface displacement field in yz-plane for a vertically incident P Ricker wavelet and a semiprolate canyon a=1, b=0.7. $-2.0195 \leq y \leq 2.0195$ at 45 stations ($\Delta = 0.11$).

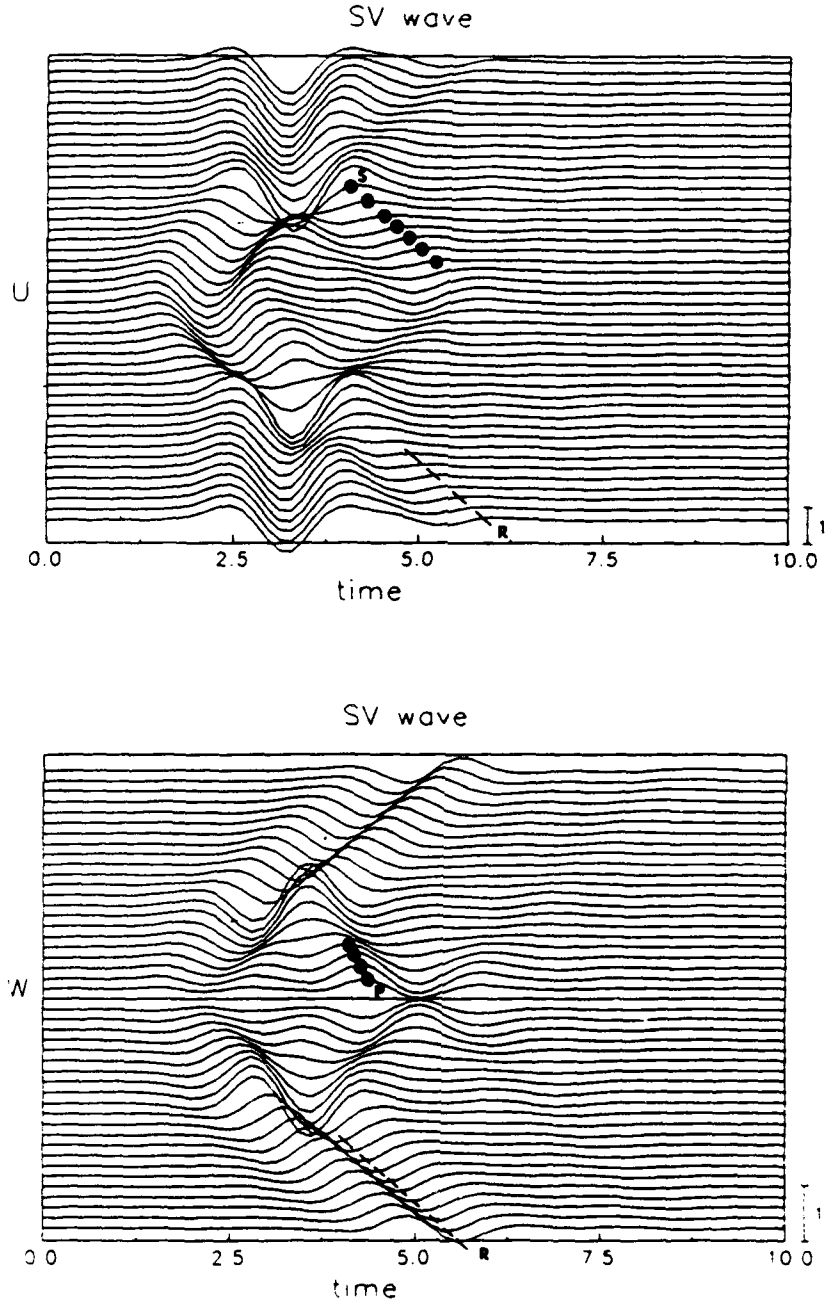

Figure 8. Vertical (w) and horizontal (u) components of surface displacement field in the xz-plane for a vertically incident SV Ricker wavelet and a hemispherical canyon of unit radius. $-2.884 \leq x \leq 2.884$ at 45 stations ($\Delta = 0.157$).

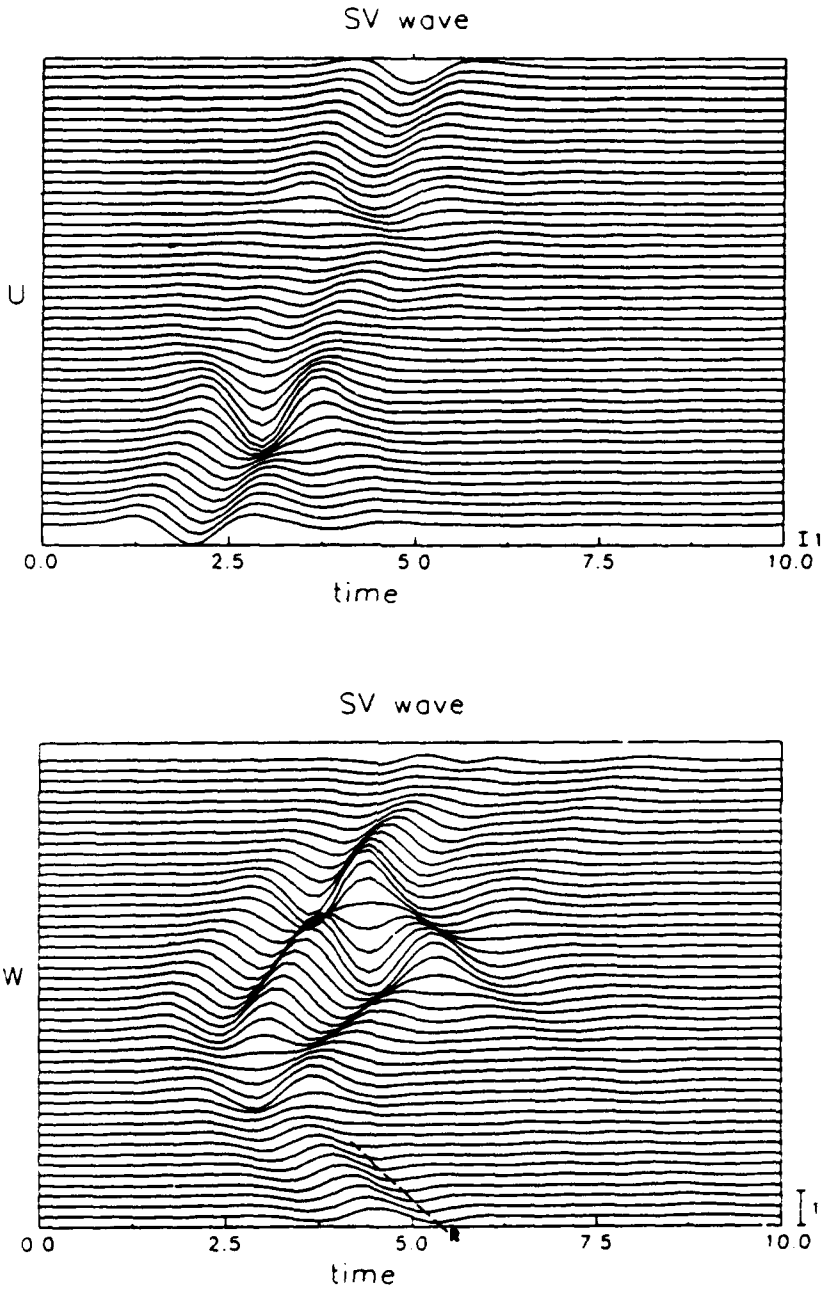

Figure 9. Vertical (w) and horizontal (u) components of surface displacement field in the xz-plane for an oblique incident SV Ricker wavelet ($\theta_0 = 30°$, $\alpha_0 = 0$) and a hemispherical canyon of unit radius. $-2.884 \leq x \leq 2.884$ at 45 stations ($\Delta = 0.157$).

near the canyon edges, significant presence of Rayleigh waves, and large duration of motion atop the canyon in comparison to duration of the free-field motion.

Change from a hemispherical to a semiprolate canyon for SV incidence produced similar results as discussed for SH and P-wave incidence and they are omitted in order to reduce the number of figures.

Incident Rayleigh Waves. For a semiprolate canyon and Rayleigh wave incidence corresponding surface displacement field is presented by Figure 10. Since the wavelength of the incoming wave is fairly large in comparison to the size of the canyon very little blocking effect can be observed due to the canyon. Amplification by the canyon edges is present but it is considerably smaller than for incident SH, P, or SV-waves. If the azimuthal angle of incidence o_0 is changed from zero to 90° and the motion is evaluated in the yz-plane instead in the xz-plane the resulting surface displacement pattern is similar to the one depicted by Figure 10 the only difference being that the amplification by the canyon edges is increased. This result is in agreement with those of Figures 6 and 7 for incident P-waves. Consequently, the results along the yz-plane are omitted.

If the wavelength of the incident Rayleigh wave is reduced to t_p=1 the resulting surface displacement field is displayed by Figure 11. Apparently, as the wavelength of the incident wave becomes shorter the blocking effect of the canyon becomes significant. The results of Figure 10 show practically no blocking effect due to the canyon. However, the results of Figure 11 show that the blocking of the surface waves by the canyon becomes significant. This phenomenon has been observed for two-dimensional models as well (Wong, 1982; Kawase, 1988). For the three dimensional models studied here the blocking effect is smaller than for the two dimensional models.

It is interesting to observe from Figure 11 the waves diffracted by the canyon edges. These waves appear to be diffracted P, SV, and Rayleigh waves. Furthermore, one should note significant amplification of the surface motion near the edges of the canyon which is not observed for Rayleigh wave incidence with larger period t_p (Figure 10).

CONCLUSIONS

Transient response for a three dimensional canyon of arbitrary shape embedded within a viscoelastic half space and subjected to plane SH, P, SV, and Rayleigh waves is investigated by using an indirect boundary integral equation method. Numerical results are presented for incident waves in form of a Ricker wavelet and for a prolate type of canyon. The results demonstrate the importance of three dimensional modeling. This is particularly true for the SH-wave incidence were it is shown that SH to P/SV mode conversion is very important and that this process can result in significant displacement field which is not represented by two dimensional antiplane strain model. Furthermore, it is shown that the results may be very sensitive upon the azimuthal orientation of the incident waves which implies that the nonaxisymmetric nature of the problem must be taken into account in order to model the resulting displacement field accurately.

The scattered P and S-waves generated by the canyon edges are observed propagating along the surface of the canyon. In addition, the scattered Rayleigh waves propagating along the surface of the half-space away from the canyon appear to have significant amplitude in comparison to the scattered body P and SV-waves. Thus it appears that most of the scattered energy dissipates away from the canyon in the form of Rayleigh waves.

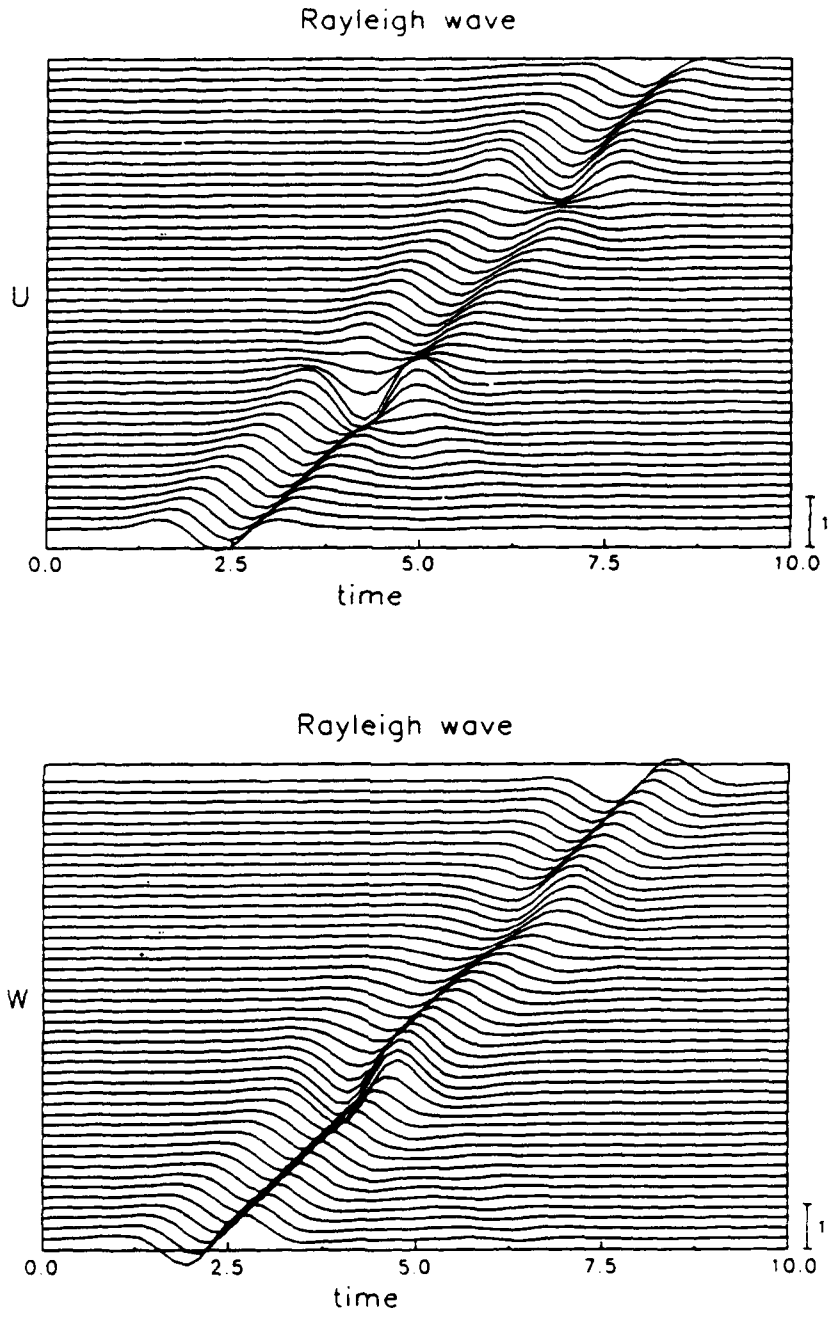

Figure 10. Vertical (w) and horizontal (u) components of surface displacement field in the xz-plane for an incident Rayleigh Ricker wavelet (φ_0 =0) and a semiprolate canyon a=1, b=0.7. $-2.614 \leq x \leq 2.614$ at 45 stations (Δ = 0.1345).

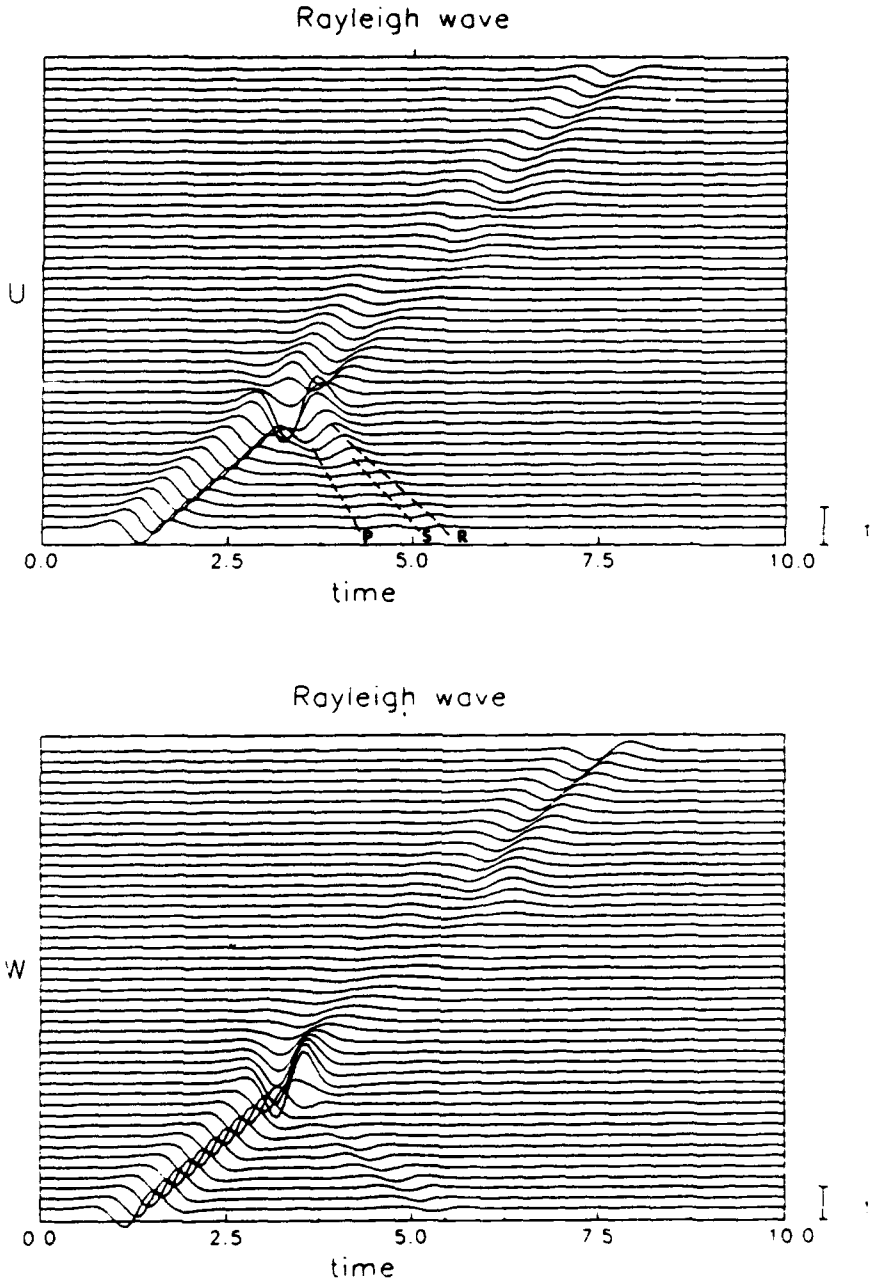

Figure 11. Vertical (w) and horizontal (u) components of surface displacement field in the xz-plane for an incident Rayleigh Ricker wavelet and a hemispherical canyon of unit radius. t_p=1, t_s=1.2. $-2.884 \leq x \leq 2.884$ at 45 stations ($\Delta = 0.157$).

The so called blocking effect of the canyon for incident Rayleigh waves is observed for shorter wavelengths of the incident wave. The blocking effect is judged to be smaller than in the corresponding two dimensional cases. The same effect is not observed for large wavelengths of Rayleigh waves.

Change from a hemispherical canyon to a semiprolate canyon (reduction of the canyon depth) resulted in smaller amplification of the surface ground motion.

Finally, the creeping P and S-waves propagating along the surface of the canyon have been identified.

ACKNOWLEDGMENTS

This research has been completed in part due to support by the Office of Naval Research under Contract No. N00014-88-K-0157. The authors would like to express appreciation to Mr. Isao Yagi for his work in plotting of the figures.

REFERENCES

Aki, K. (1988) Local site effects on strong ground motion, Proc. of "*EarthquakeEngineering and Soil Dynamics II*", Am. Soc. Civil Eng., Park City, Utah, June 27-30, pp. 103-155.

Aki, K. and P. G. Richards (1980) *Quantitative Seismology*, **1**, W. H. Freeman & Co., San Francisco, California.

Anderson, J. G., P. Bodin, J. N. Brune, J. Prince, S. K. Singh, R. Quaas, M. Onate (1986) Strong ground motion from the Michoacan, Mexico, earthquake, *Science*, **233**, pp. 1043-1049.

Apsel, R. J. and J. E. Luco (1987) Impedance functions for foundations embedded in a layered medium: An integral equation approach, *Earthquake Eng. Struct. Dyn.*, **15**, pp. 213-231.

Dravinski, M. and T. K. Mossessian (1987) Scattering of harmonic P, SV, and Rayleigh waves by dipping layers of arbitrary shape, *Bull. Seism. Soc. Am.*, **77**, pp. 212-235.

Dravinski, M. and T. K. Mossessian (1988) On evaluation of the Green functions for harmonic line loads in a viscoelastic half space, *Int. J. Num. Meth. Engin.*, **26**, pp. 823-841.

Eshraghi H. and M. Dravinski (1989) Scattering of Plane Harmonic SH, SV, P, and Rayleigh waves by non-axisymmetric three-dimensional canyons: A wave function expansion approach, *Earthq. Eng. Struct. Dyn.*, **18**, pp. 983-998.

Herrera, I. (1984) *Boundary Methods: An Algebraic Theory*, Pitman Publishing, Inc., Boston.

Kawase, H. (1988) Time-domain response of a semi-circular canyon for incident SV, P and Rayleigh waves calculated by the discrete wavenumber boundary element method, *Bull. Seism. Soc. Am.*, **78**, pp. 1415-1437.

Lee, V. W. (1978) Displacement near a three-dimensional hemispherical canyon subjected to incident plane waves, Univ. of So. Calif., Dept. of Civil Engineering, *Report No. 78-16*.

Luco, J.E., H.L.Wong, and F.C.P. Barros (1990) Three dimensional response of a cylindrycal canyon in a layered half-space, *Earthq. Eng. Struct. Dyn.*, **19**, 799-817.

Mossessian, T. K., and M. Dravinski (1989) Scattering of elastic waves by three dimensional surface topographies, *Wave Motion*, **11**, pp. 579-592.

Ricker, N. H. (1977) *Transient waves in visco-elastic media*, Elsevier publication Co. Amsterdam, Holland.

Sanchez-Sesma, F. J. (1983) Diffraction of elastic waves by three-dimensional surface irregularities, *Bull. Seism. Soc. Am.*, **73**, pp. 1621-1636.

Wong, H. L. (1982) Diffraction of P, SV, and Rayleigh waves by surface topographies, *Bull. Seism. Soc. Am.*, **72**, pp. 1167-1184.

三維粘彈性半無限空間峽谷地形對不同入射波之暫態反應

T.K.Mossessian and M. Dravinski

摘要

本研究採用一般之三維模式，應用間接邊界積分方程法研究任意形狀三維峽谷對彈性波之放大作用，入射之平面SH、SV、P及雷利（Rayleigh）波均假設爲黎克漣波(Ricker Wavelet)。此問題是先在頻率域公式化，然後利用富氏(Fourier)合成得到暫態解。本文展現有數種峽谷形狀在不同入射波入射下之地表位移場，並研究不同散射波在近場之特性，尤其是沿著峽谷表面傳遞之波已確認爲潛移之P和S波。

J. Phys. Earth, 40, 241–261, 1992

A Hybrid Approach for Scattering of Elastic Waves by Three-Dimensional Irregularities of Arbitrary Shape

Tomi K. Mossessian* and Marijan Dravinski

Department of Mechanical Engineering, University of Southern California, Los Angeles, California, U.S.A.

A hybrid technique is developed for studying scattering of elastic waves by non-axisymmetric three-dimensional near-surface inhomogeneities. The technique combines an indirect boundary integral equation method with the finite element approach. Special emphasis is placed on inhomogeneities in the form of dipping layers embedded in a half-space and subjected to plane incident P, SV, SH, and Rayleigh waves.

The accuracy and efficiency of the hybrid technique are examined through several numerical examples. The comparisons with the results obtained by a boundary integral equation method validate the accuracy of the hybrid technique. The versatility of the method is demonstrated by considering several types of inhomogeneous basins containing multiple horizontal and dipping layers. It is found that the numerical efficiency of the hybrid technique becomes much higher than that of the boundary integral equation methods as the structure of the inhomogeneities gets more complex.

1. Introduction

The extent of the damage in the central part of Mexico City due to the Michoacan, Mexico earthquake of September 19, 1985, was remarkably severe considering the long epicentral distance of 350 km (Anderson *et al.*, 1986). Nearly all the buildings that collapsed during the earthquake of September 19, were located in the central portion of Mexico City, while the damage in the surrounding area was minimal. The central part of Mexico City is founded on a lake bed zone formed by clay deposits which are considerably softer than the alluvium of the surrounding hilly zone. In the two second period, the acceleration response at the lake zone was about ten times greater than that of outlying districts (Anderson *et al.*, 1986). Thus, it appears that subsoil structure played an important role in the resulting pattern and extent of damages in Mexico City during the earthquake of September 19, 1985.

Observations from previous earthquakes in the Valley of Mexico (Zeevaert, 1964) show that in spite of differences in source mechanism and epicentral distances, accelerograms at the lake bed zone are similar with the low frequency oscillations known as resonant excitation of the sedimentary basin (Anderson *et al.*, 1986). Analysis of

Received November 20, 1990; Accepted June 30, 1992

* To whom correspondence should be addressed. Presently at Structural Research and Analysis Corp., 1661 Lincoln Blvd., Suite 200, Santa Monica, CA 90404, U.S.A.

earthquake damages at other locations, e.g., Lima, Peru earthquake of 1974 (Repetto *et al.*, 1980), indicates that the areas of intense damage atop alluvium can be highly localized. Since many other highly populated areas are located on sedimentary basins, the study of their response to seismic waves is of great interest in earthquake engineering and strong ground motion seismology (Aki, 1988).

Experimental studies of Kagami *et al.* (1982), Kagami *et al.* (1986), and King and Tucker (1984), as well as theoretical studies by Bouchon and Aki (1977), Bard and Bouchon (1980a, b) and Dravinski (1982a, b, c, 1983) have shown that presence of sediment-filled valley may cause very large localized amplification of surface ground motion. Studies of microtremors and strong ground motion in deep alluvial basins by Kagami *et al.* (1982), Kagami *et al.* (1986), King and Tucker (1984), and Bard and Bouchon (1985) show that there appears to be a resonant-type behavior of the valley. This can be explained only if there are interactions between horizontal and vertical waves within the valley. Thus, for thorough understanding of seismic response of deep alluvial valleys it is necessary to study the problem of amplification of the surface ground motion by subsurface irregularities using two- and three-dimensional models.

Modeling the amplification of seismic waves due to scattering by subsurface irregularities is characterized by considerable complexities. Better understanding of the site amplification effects requires more realistic models, which in turn should account precisely for complex geometry and the material properties of the actual alluvial valley. For that reason, it is necessary to develop methods capable of incorporating these requirements in studying the problems of site amplification effects.

Scattering of seismic waves by an alluvial valley may be solved analytically or numerically. Analytical solutions are limited to very simple geometries and linear materials (e.g., Trifunac, 1971). Most commonly used numerical methods, finite elements and finite differences, on the other hand, require the discretization of the entire solution domain. This makes such procedures inefficient for geotechnical problems which involve very large characteristic length. However, they have the advantage in their applicability to problems with complex geometries and varying material properties (e.g., Smith, 1975; Zahradnik and Hron, 1987).

For the problems of scattering of seismic waves by irregularities with moderately shallow slopes Aki and Larner (1970) have developed a technique using the so-called Rayleigh hypothesis. The method is applicable to wavelengths which are either larger than or of the order of the dimension of the irregularities. Bouchon (1973) and Bard and Bouchon (1980a, b) used this method to study the seismic response of sediment-filled valleys subjected to incident P, SV, and SH waves. Bouchon and Aki (1977) extended the Aki-Larner method to study the near field of a seismic source in a layered medium with irregular interfaces. Bard and Gariel (1986) have developed an extension of the technique to study seismic response of basins with large vertical velocity gradient. They presented results for SH waves only.

Other methods shown to be very effective for studying the wave scattering in geotechnical problems involving unbounded domains are the boundary integral equation methods (BIEM) (Dravinski, 1982a, b, c, 1983; Dravinski and Mossessian, 1987a, b; Rizzo *et al.*, 1985; Sánchez-Sesma and Rosenblueth, 1979; Wong, 1982). These methods require only discretization of the boundary of the scatterers (Cole *et al.*, 1978),

and the rediation conditions at infinity can be modeled exactly. A disadvantage of BIEM is the large computational efforts needed for evaluation of the half-space Green's functions. For plain strain and three-dimensional models the Green's functions cannot be expressed in a simple form. Several alternative techniques have been proposed to avoid this difficulty. One way is to use the full-space Green's functions and then impose the traction-free boundary conditions on part of the free surface (Niwa *et al.*, 1986). This approach has several drawbacks. First, the required size of the free surface to stimulate a half-space is not clear beforehand since it is dependent upon frequency, the shape of the irregularity and the type of incident wave. Therefore, extensive testing is required for each case. Another disadvantage of this approach becomes apparent in the three-dimensional cases (Niwa and Hirose, 1987). Since the required number of boundary elements on the free surface becomes very large (larger than what is required for the scatterer itself), the size of the Green's function matrix needed for this method grows substantially. Therefore, required amount of memory and computation time is greatly increased. Kawase and Aki (1989) have used an alternate approach to study transient responses of two-dimensional sedimentary basin. The technique combines the direct boundary element method with the discrete wavenumber Green's functions. In this approach the infinite integrals are transformed into infinite sums over discrete wavenumbers under the assumption of periodicity (Bouchon and Aki, 1977). Due to periodicity assumption, the solution is valid until the arrival time of scattered waves from adjacent irregularities. Therefore, detailed testing is needed to determine a suitable periodicity length which avoids contamination from neighboring fictitious structures.

Another boundary method suitable for problems of scattering of elastic waves in an infinite media is the wave function expansion approach (Eshraghi and Dravinski, 1988a, b; Sánchez-Sesma, 1983). The method makes use of the C-complete family of wave functions (Herrera and Sabina, 1978) which can be evaluated very efficiently. However, the wave functions in general do not satisfy the traction-free boundary conditions. These boundary conditions have to be imposed on part of the free surface. Therefore, the disadvantages of this method are similar to the case of the BIEM with use of full-space Green's functions mentioned earlier.

For high frequency range, the ray methods and Gaussian beam technique appear to be very effective (e.g., Hong and Helmberger, 1978; Moczo *et al.*, 1987; Nowack and Aki, 1984). These methods are relatively fast and they are applicable to inhomogeneous basins with complex geometries. As demonstrated by Moczo *et al.* (1987) such techniques cannot produce correct results for wavelengths larger than the minimum radius of curvature of the basin boundary. However, in higher frequency range these methods can compliment other low frequency methods mentioned earlier (BIEM, discrete wavenumber method, finite element and finite differences).

In recent years, hybrid techniques which combine the boundary integral equation methods (BIEM) with the finite element approach have proved to be very effective for studying various problems of interest in engineering mechanics, earthquake engineering and seismology (e.g., Beskos and Spyrakos, 1984; Kobayashi *et al.*, 1986; Mossessian and Dravinski, 1987). The main advantage of the hybrid techniques is that it utilizes the versatility of the finite element method for detailed modeling of the near field and the effectiveness of the BIEM in the far field (Berg, 1984; Zienkiewicz *et al.*, 1977). For

extensive review of the literature on the subject the reader is referred to articles by Wong *et al.* (1985), Beskos (1987), and Mossessian and Dravinski (1987). These papers show that at the present time, there are very few studies that have applied the hybrid techniques to problems of scattering of elastic wave by non-axisymmetric three-dimensional near-surface irregularities. One of the most complex models considered in the literature to date is due to Kobayashi *et al.* (1986), who investigated the steady state response of a non-axisymmetric three-dimensional structure embedded in a visco-elastic half-space. They applied a hybrid technique which utilizes a direct BIEM using full-space Green's functions. The advantage of this approach is that it avoids the extensive computational efforts needed for calculation of the half-space Green's functions (Dravinski and Mossessian, 1988). However, one needs to impose the traction-free boundary conditions on part of the free surface, which results in the drawbacks discussed earlier.

In this paper, applicability of a hybrid method to problems of scattering of elastic waves by non-axisymmetric three-dimensional subsurface inhomogeneities is investigated. The present work is an extension of the recent study done by Mossessian and Dravinski (1987) in which they investigated seismic responses of two-dimensional dipping layers of arbitrary shapes. The hybrid method combines an indirect boundary integral equation approach (Dravinski and Mossessian, 1987a; Mossessian, 1989; Mossessian and Dravinski, 1989) with the finite element technique. Incident plane harmonic P, SV, SH, and Rayleigh waves are assumed. General formulation of the method is presented. Testing of the accuracy of the technique is performed through comparisons with the results obtained by the indirect boundary integral equation method (Mossessian, 1989) for a homogeneous dipping layer. The capability of the method is demonstrated by considering several types of inhomogeneous basins containing multiple horizontal and dipping layers. The effects of horizontal and dipping type layering on seismic response of the basin are examined. Finally, the efficiency of the method in comparison to the boundary methods is discussed.

2. Statement of the Problem

Geometry of the problem is depicted by Fig. 1(a). Interior region D_I is assumed to include all the irregularities which may contain inhomogeneous and nonisotropic materials. Material of the exterior region of the half-space D_E is assumed to be linearly elastic, homogeneous and isotropic. Boundary B defines the interface between regions D_I and D_E. Incident wave is assumed to be a plane harmonic P, SV, SH or Rayleigh wave.

Equation of motion for a steady state wave propagation is specified by

$$\operatorname{div} \boldsymbol{\sigma} + \rho\omega^2 \boldsymbol{u} = 0 \; ; \quad \boldsymbol{x} \in D_I \cup D_E \, . \tag{1}$$

where $\boldsymbol{\sigma}$ and $\boldsymbol{u}$ denote the stress tensor and displacement vector, respectively, $\boldsymbol{x}$ is a position vector, ρ is the mass density, and ω is the circular frequency. Stress-free boundary conditions along the surface of the half-space are specified by

$$\sigma_{xz} = \sigma_{yz} = \sigma_{zz} = 0 \; ; \quad z = 0 \quad \text{and} \quad \boldsymbol{x} \in D_I \cup D_E \, . \tag{2}$$

Usual radiation conditions should be satisfied by the scattered wave field at infinity.

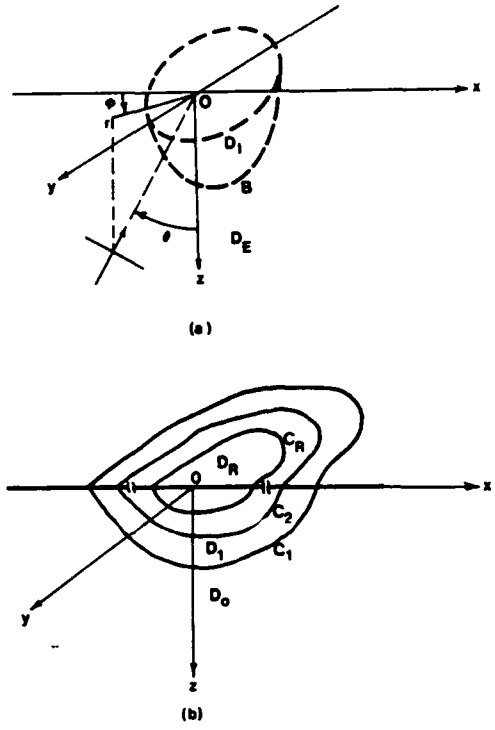

Fig. 1. (a) Geometry of the problem. (b) Basin model.

For this study, we choose region D_1 to consist of several horizontal or dipping layers (D_i, $i=1, \cdots, R$) which are perfectly bonded together, overlaying a half-space D_0 (Fig. 1(b)). Interfaces C_i between the layers need not be smooth. Continuity of the displacement and the traction field along interfaces C_j, $j=1, 2, \cdots, R$ is specified by

$$\boldsymbol{u}_{j-1}^{+}=\boldsymbol{u}_{j}^{-}; \quad \boldsymbol{x}\in C_j \tag{3}$$

$$\boldsymbol{t}_{j-1}^{\nu^+}=\boldsymbol{t}_{j}^{\nu^-}; \quad \boldsymbol{x}\in C_j, \tag{4}$$

where the subscripts + and − denote that the interface is being approached from the outside and the inside, respectively, and $\boldsymbol{t}_j^{\nu}$ denotes the traction vector at a surface C_j with an outward unit normal ν_j.

3. Method of Solution

The interior region D_1, is modeled by using the finite element method and the exterior region D_E is modeled by using an indirect boundary integral equation approach. Complete solution of the problem is then obtained by imposing the continuity conditions along the boundary B.

The finite element analysis of the interior region is considered first.

4. Finite Element Analysis

By discretizing the continuum of the interior region D_1 into a set of finite elements, the equation of motion for each element can be written in the following form (Zienkiewicz, 1977):

$$K_e^* u_e - \omega^2 M_e u_e = r_e^*; \; x \in D_1 , \tag{5}$$

where K_e^* and M_e are the stiffness and mass matrices, respectively, r_e^* is the vector of nodal point forces due to surface tractions, and u_e contains the nodal displacements of the element.

Applying the piecewise-uniform traction approximation (i.e., the tractions are assumed to be constant along the face of each element) at the boundary of an element, r_e^* reduces to

$$r_e^* = R_e t_e^v , \tag{6}$$

where R_e is the matrix which transforms the traction vector t_e^v into the nodal force vector r_e^*. Hence, the equation of motion (5) can be written in the following form:

$$K_e u_e = R_e t_e^v , \tag{7}$$

where the matrix K_e is defined by

$$K_e = K_e^* - \omega^2 M_e . \tag{8}$$

The matrices K_e and R_e are computed for each element and assembled into global matrices K and R. Therefore, the equation of motion becomes

$$Ku = Rt^v; \; x \in D_1 . \tag{9}$$

Here, u and t^v represent all the nodal displacements and tractions in the region D_1, respectively. The nodal displacement u_B at the boundary B can be separated from the interior nodal displacement u_I. Subsequently, the nodal displacement vector u becomes

$$u = (u_I, u_B)^T , \tag{10}$$

where the superscript T denotes the transpose. Partitioning of the matrices in Eq. (9) results in the following equation:

$$\begin{bmatrix} K_{II} & K_{IB} \\ K_{BI} & K_{BB} \end{bmatrix} \begin{bmatrix} u_I \\ u_B \end{bmatrix} = \begin{bmatrix} R_{II} & R_{IB} \\ R_{BI} & R_{BB} \end{bmatrix} \begin{bmatrix} t_I^v \\ t_B^v \end{bmatrix} . \tag{11}$$

Since for the problem at hand only the boundary B would be subjected to surface tractions, there would be no nodal forces of the interior nodes, i.e., $t_I^v = R_{IB} = R_{BI} = 0$. Thus, u_I can be eliminated from Eq. (11) to obtain the following result:

$$Lu_B = R_{BB} t_B^v , \tag{12}$$

where

$$L = -K_{BI} K_{II}^{-1} K_{IB} + K_{BB} . \tag{13}$$

This completes the analysis of the finite element formulation for the interior region D_I. It should be emphasized that Eq. (12) relates the nodal displacements u_B with nodal tractions t_B^v on the boundary B.

Formulation of the problem in the exterior region D_E is considered next.

5. Boundary Integral Equation Analysis

The total displacement field in the exterior region is specified by

$$u_E = u_E^{ff} + u_E^s; \quad x \in D_E, \tag{14}$$

where the superscripts ff and s denote the free and the scattered wave field, respectively. Following an indirect boundary integral equation approach (Dravinski and Mossessian, 1987a; Mossessian and Dravinski, 1989) the scattered field is assumed to be generated from distribution of unknown tractions $f(y)$ on an auxiliary surface S_a inside the surface B. Hence the scattered displacement field in the half-space can be written in the form

$$u_E = \int_{S_a} G(x, y) f(y) \mathrm{d}S_a(y); \quad x \in D_E, \tag{15}$$

where G is a half-space displacement Green's function tensor (Aki and Richards, 1980). The element $G_{ij}(x, y)$ corresponds to the i-th component of the displacement vector at x due to a unit harmonic force at y acting in the j-th direction. Theoretical development of these Green's functions is rather involved and their complete explicit forms can be found in the article by Mossessian and Dravinski (1989).

Choosing $f(y)$ to be concentrated at discrete points of the surface S_a, it can be shown (Mossessian, 1989; Mossessian and Dravinski, 1989) that the total wave field takes the following form:

$$u_E = u_E^{ff} + G(x, x_m) f^m; x_m \in S_a, m = 1, 2, \cdots, M. \tag{16}$$

Here x_m are chosen and the unknown force magnitudes f^m are yet to be determined for all m. Throughout, summation over repeated indices m is understood. Using Eq. (16), the components of total traction along the surface S_t become

$$t_E = t_E^{ff} + T(x, x_m) f^m; x \in B; m = 1, 2, \cdots, M, \tag{17}$$

where t^{ff} is the free-field traction vector and T is the half-space traction Green's function tensor. The component $T_{ij}(x, x_m)$ corresponds to the i-th component of the traction vector at x due to unit harmonic force at x_m acting in the j-th direction. For simplicity, superscript v is suppressed. By choosing N observation points on boundary B (to coincide with the boundary nodes of the finite element model), corresponding displacement and traction fields can be stated as follows:

$$u_E = u_E^{ff} + G_u f^* \tag{18}$$

$$t_E = t_E^{ff} + G_t f^* \tag{19}$$

$$f^* = (f^1, f^2, \cdots, f^M)^T.$$

Here, vector f^* (of order $3M \times 1$) contains all the unknown force magnitudes.

Matrices G_u and G_t (of order $3N \times 3M$), and vectors t_E^{ff} and u_E^{ff} (of order $3N \times 1$) are all known. Continuity of the displacement and traction field along the boundary B requires that

$$u_E = u_B ; \quad x \in B \tag{20}$$

$$t_E = t_B ; \quad x \in B , \tag{21}$$

where t_E and u_E are given by Eqs. (18) and (19). Substituting Eqs. (18) and (19) into Eq. (12), via Eqs. (20) and (21), it follows that

$$L[u_E^{ff} + G_u f^{\wedge}] = R_{BB}[t_E^{ff} + G_t f^{\wedge}] . \tag{22}$$

This last result can be written as

$$G_A f^{\wedge} = a , \tag{23}$$

where

$$G_A = LG_u - R_{BB}G_t \tag{24}$$

$$a = R_{BB}t_E^{ff} - Lu_E^{ff} . \tag{25}$$

By choosing N greater than M, Eq. (23) is solved in the least square sense. Once the magnitude of forces $f^{\wedge}$ are known, the displacement and the stress fields in region D_E can be calculated through use of Eqs. (16) and (17). The displacement field in the interior region D_I is obtained by using Eq. (11).

6. Numerical Results and Discussion

Shape of the linearly elastic dipping layer is chosen to be in the form of a semi-prolate with a flat lower section. This geometry can be defined in the following parametric form:

for $0 < z < c$

$$x = a\cos(t)\cos(s) \quad y = b\cos(t)\sin(s) \quad z = b\sin(t) \tag{26}$$

$$0 < s < 2\pi , \quad 0 < t < t_i, \; t_i = \sin^{-1}(c/b)$$

for $z = c$

$$x = a\cos(t_i)\cos(s) , \quad y = b\cos(t_i)\sin(s) , \tag{27}$$

where a and b are the major and minor axis and c is the maximum depth of the semi-prolate. This shape is chosen to optimize the efforts for mesh generation without loosing the general three-dimensional characteristics of the model. To reduce the number of figures, only the results for cross sections $y = 0$ and $x = 0$ are presented, and they will be referred to as sections A and B, respectively. Incident waves are plane P, SV, SH, and Rayleigh waves. The azimuthal angle of incidence ϕ is measured counterclockwise from negative x axis (Fig. 1(a)). The off-vertical angle of incidence θ is measured from positive z axis toward vector r, which defines the azimuthal position on the surface of the half-space. The amplitude of the incident waves are the same as those used by Dravinski and Mossessian (1987a). For convenience, a dimensionless frequency of incident wave Ω_a is defined as the ratio of the maximum length of the basin $2a$ and the

wavelength of shear waves in the half-space. Throughout the paper μ_j, α_j, β_j; $j=0, 1, \cdots, R$ denote the shear modulus, P- and S-wave velocities, respectively for layer D_j (see Fig. 1). Subscript zero refers to the half-space while nonzero ones denote the dipping layers.

Several parameters may greatly affect the numerical accuracy of the method. These are: i) shape and location of the auxiliary surface S_a; ii) number of sources (point forces) M; iii) number of observation points N; and iv) maximum length of each element. From previous investigations (Dravinski and Mossessian, 1987 b; Mossessian and Dravinski, 1987) it has been determined that a good choice for the auxiliary surface S_a is the one that follows in shape the boundary B. Therefore, the auxiliary surface is chosen to be in the following form:

$$x_a=(1-\xi)x\,, \tag{28}$$

$$y_a=(1-\xi)y\,, \tag{29}$$

$$z_a=(1-\xi)z\,, \tag{30}$$

where x, y, and z are described by Eqs. (26), (27). Through numerical experiments the value of the parameter ξ is chosen to be 0.4. The number of sources is 105 and the number of observation points (same as the boundary nodes at B) is 295. The effect of element size is discussed in later sections.

6.1 Finite element discretization

The finite element mesh form at elliptical cross section $z=0$ is shown in Fig. 2(a). Due to symmetry only a quarter of the mesh plane is displayed. This mesh form is

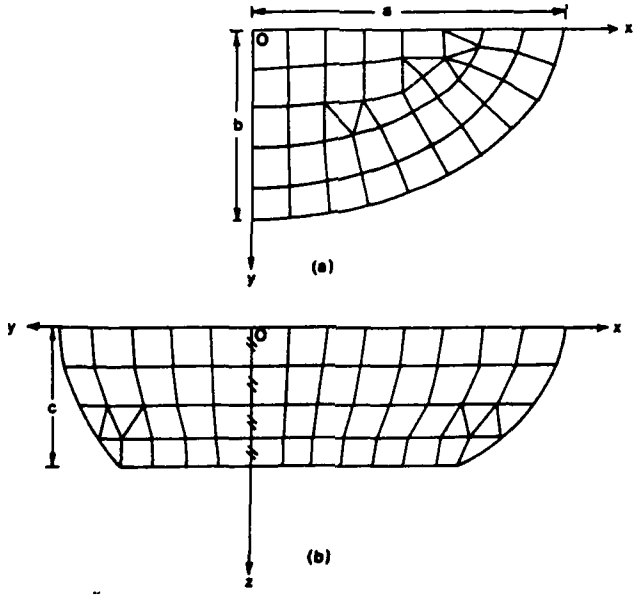

Fig. 2. Finite element meshes for sections x-y, x-z, and y-z of the basin.

repeated for deeper sections following the pattern shown in Fig. 2(b), which displays the view of the mesh distributions along the vertical sections x-z and y-z. Again, due to symmetry only half of each section is displayed. It is apparent from Fig. 2(a) and (b) that this model can easily incorporate planar and nonplanar layering. Throughout volume discretization only eight node cubic and six node triangular prisms are used. The number of elements used is 768, which leads to a total of 835 nodes. The mesh size is kept constant for all the examples presented in this study.

6.2 *Testing of the method*

In order to assess the accuracy of the method the case of a homogeneous dipping layer subjected to various incident wave fields is considered first. For this problem the results of the hybrid technique are compared to the ones obtained through an indirect boundary integral equation method (Mossessian and Dravinski, 1990). Surface response at section A for incident P, SV, SH, and Rayleigh waves with azimuthal angle of incidence $\phi = 0^\circ$ is shown in Fig. 3. It can be seen from these figures that for all incident waves the results of hybrid technique are in excellent agreement with those obtained by the boundary integral equation method. Keeping the element sizes constant and increasing the frequency by 30%, results in displacement fields depicted by Fig. 4. Some differences between the results of the two methods are apparent. These discrepancies are due to the fact that the number of elements per wavelength in the hybrid technique has decreased. For this model the finite element discretization error has been analyzed by considering the case when the material properties of the half-space are the same as the ones for the dipping layer. In this case no scattering takes place, hence the internal nodal displacements are obtained through Eq. (11) by using free-field displacement values for boundary nodes. Therefore, deviation of the internal nodal displacement values from the free-field ones would correspond entirely to the error generated by the finite element discretization. Using this approach, by keeping the mesh size constant and varying the frequency, it is established that 10 elements per wavelength are sufficient for convergence of the results.

In order to show the capability and versatility of the method, numerical results for inhomogeneous basins are presented next.

6.3 *Horizontally stratified basin*

A basin consisting of two homogeneous strata is considered next (see Fig. 5(a)). This model is obtained from the homogeneous dipping layer considered in Figs. 3 and 4 by changing the material properties of the lower section of the basin to fall in between the ones of the top layer and the half-space. The surface displacement at section A for incident P, SV, SH, and Rayleigh waves with azimuthal angle of incidence $\phi = 0^\circ$ are depicted by Fig. 6. Comparison of the results with the ones for homogeneous basin (Fig. 4) reveals that introduction of the intermediate layer has considerably reduced the amplification at the center of the valley. This is not surprising since the "average velocity of the basin" (Bard and Gariel, 1986) has become larger than the case of the homogeneous dipping layer. It is interesting to note that for the Rayleigh waves the horizontal component of displacement has been affected very little by stratification while the changes for vertical component of motion are drastic. For different incident

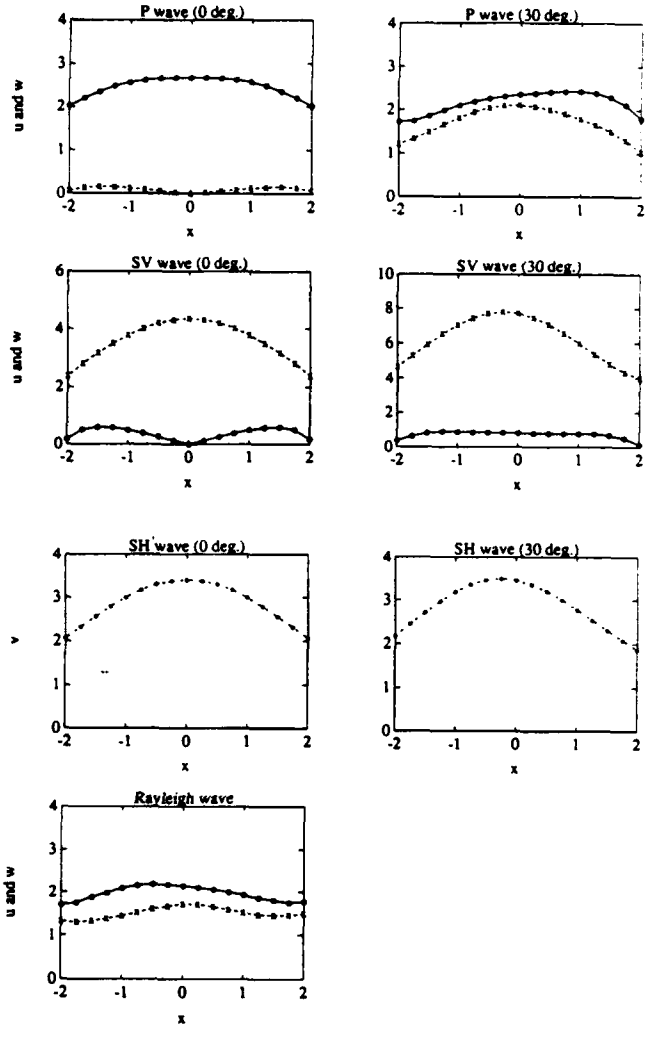

Fig. 3. Amplitudes of surface displacement spectra for a homogeneous valley at section A for incident P, SV, SH, and Rayleigh waves with $\phi = 0°$, $\theta = 0°$, 30°. $a = 2$, $b = 1.2$, $c = 0.88$, $\mu_0 = \beta_0 = 1$, $\alpha_0 = 2$, and $\mu_1 = 1/6$, $\beta_1 = 0.5$, $\ldots = 1$, $\Omega_a = 0.64$ (Unless stated differently these parameters stay the same for other figures). Dash, dash-dot, and solid lines represent x-, y-, and z-components (u, v, w) of the displacement vector, respectively, obtained by the hybrid technique (This convention holds for all the figures). The 'x' signs, stars, and open circles denote x-, y-, and z-components of the displacement vector, respectively, obtained by the boundary integral equation method.

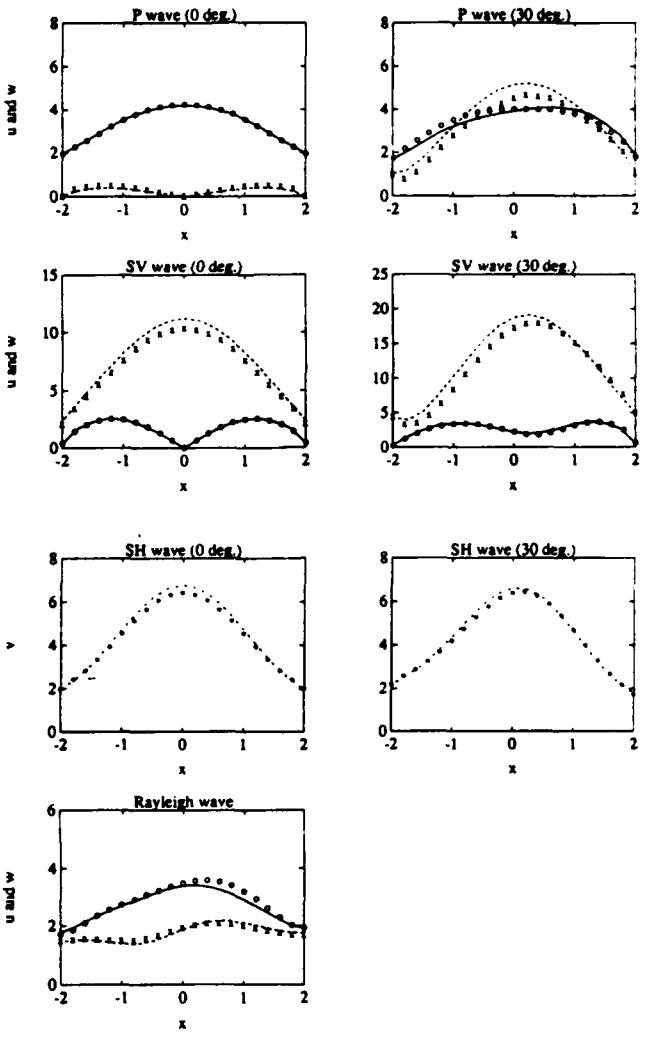

Fig. 4. Amplitudes of surface displacement spectra for a homogeneous valley at section A for incident P, SV, SH, and Rayleigh waves. $\phi = 0°$, $\Omega_a = 0.83$.

waves the surface responses at section B are shown by Fig. 7. Coupling between P/SV and SH modes appear to be much stronger for incident SH wave than the other type of waves.

6.4 *Multiple dipping layer basin*

To further emphasize the versatility of the method, a case of a basin with two dipping layers is considered. This model is obtained from the horizontally layered basin studied earlier. Namely, the lower layer is extended toward the surface of the half-space

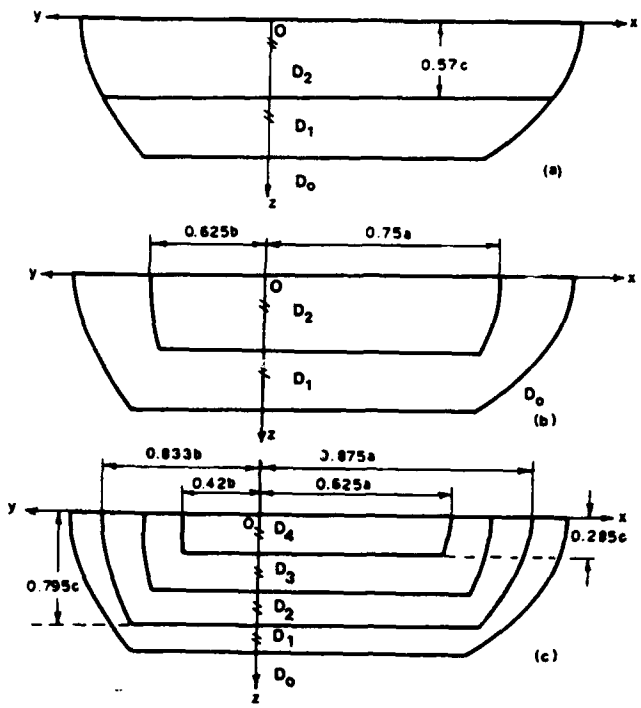

Fig. 5. Three models of inhomogeneous basins.

through a circumferential strip (see Fig. 5(b)). Surface displacements at section A for various incident waves with azimuthal angle of incidence $\phi = 0°$ are displayed by Fig. 8. In comparison with the results of the horizontally stratified basin, here the overall amplifications are smaller. It should be noted that the observed changes in the slopes are due to discontinuity of the material properties at the interface of the two layers. Figure 9 shows the surface response at section B for various incident waves. Here again the amplification of the predominant component of motion is lower than the corresponding case of horizontally stratified basin (Fig. 7), and it is more confined to surface of the top layer. However, the intensity of P/SV-SH mode conversion is about the same. For a four dipping layer basin, Fig. 10 shows the surface response at section A due to various incident waves. This model is obtained through simple extension of the two-layer model. Namely, an intermediate layer is added to each of the two layers (see Fig. 5(c)). In comparison with the case of two dipping layers, here the amplification of predominant motion is higher. However, the changes are rather small. This is partly due to the fact that the average velocity of the four dipping layers is close to that of the two dipping layers and also due to the fact the frequency of incident wave is rather low.

The complexity of the problems discussed here clearly demonstrate the capability of the hybrid technique. Furthermore, it is of interest to note that the computational time needed for the hybrid technique in the case of two and four dipping layers (Figs.

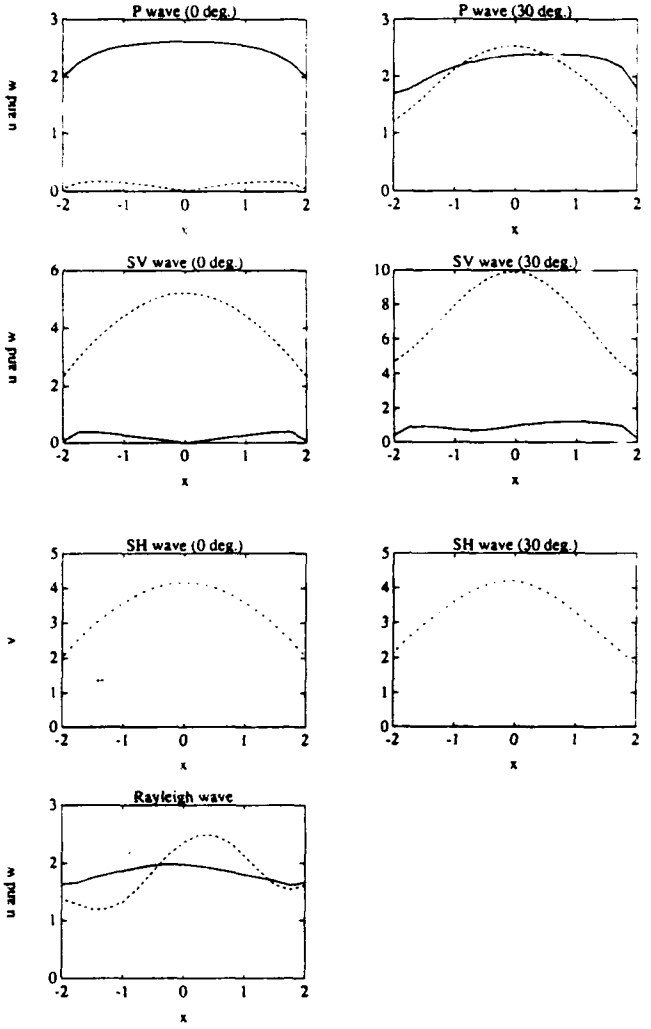

Fig. 6. Amplitudes of surface displacement spectra at section A of a basin with two horizontal layers and incident P, SV, SH, and Rayleigh waves. $\mu_0 = \beta_0 = 1$, $\alpha_0 = 2, \mu_1 = 0.45, \beta_1 = 0.73, \alpha_1 = 1.46, \mu_2 = 1/6, \beta_2 = 0.5, \alpha_2 = 1, \Omega_a = 0.83, \phi = 0^\circ$.

8, 9, and 10) is the same as in the case of homogeneous basin (one dipping layer, Fig. 4). However, for the boundary integral equation method, in going from one to two and four dipping layers (in the analogous model), the required computational time would approximately increase by factors of 8 and 64, respectively. This is caused by increase in size of the Green's functions matrix. This analogy is true for other boundary methods such as wave function expansion approach (Eshraghi and Dravinski, 1988a, b). Such comparisons illustrate that the hybrid technique tends to be more efficient than the boundary integral equation approach as the structure of the inhomogeneity becomes

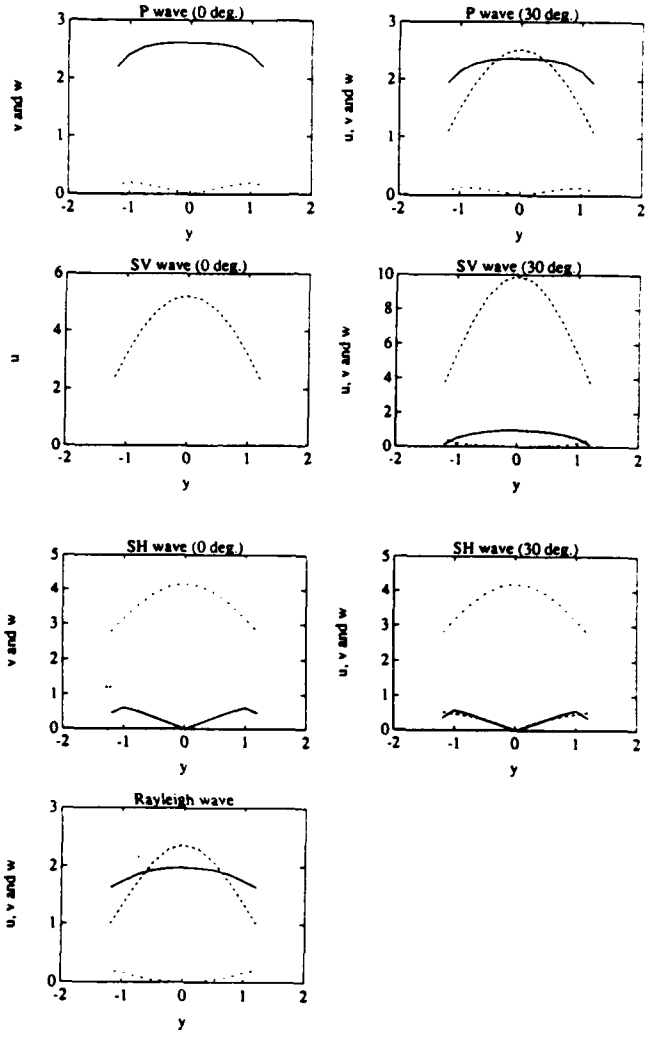

Fig. 7. Amplitudes of surface displacement spectra at section B of the basin with two horizontal layers and incident P, SV, SH, and Rayleigh waves. $\Omega_a = 0.83$, $\phi = 0^\circ$.

more complex. The drawback of the hybrid method is that the required number of nodes grows rapidly as the frequency increases. Therefore it appears that for simple inhomogeneities it may be more beneficial to use boundary integral equation approach (specially for higher frequencies). However, if the inhomogeneity is very complex (e.g., a basin with a number of dipping layers, heterogeneity, or anisotropicity) the hybrid technique becomes much more effective.

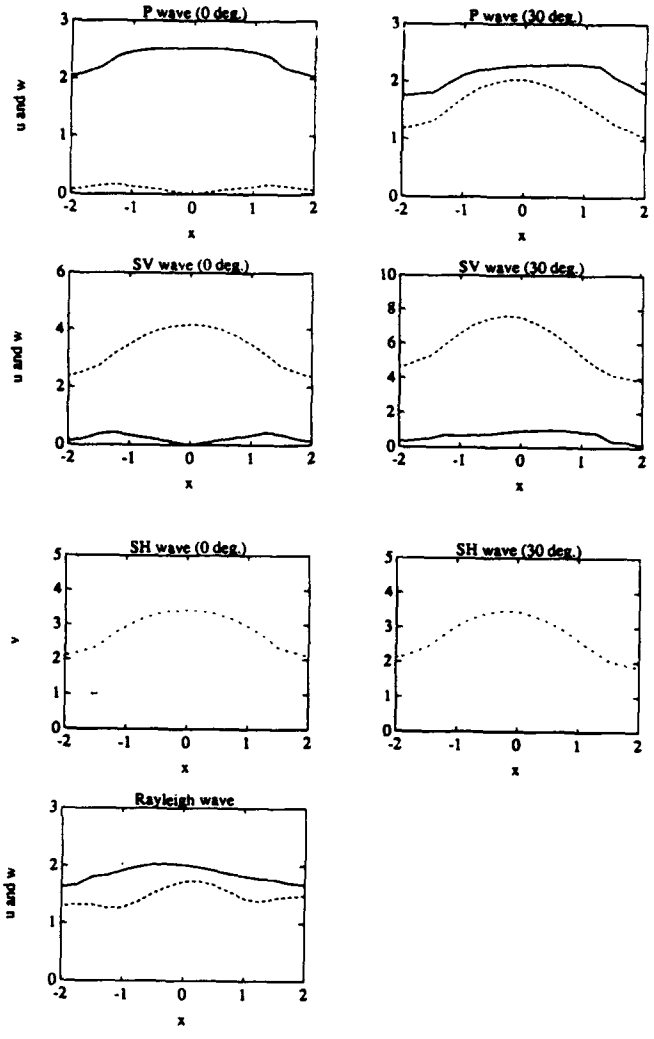

Fig. 8. Amplitudes of surface displacement spectra at section A of the basin with two dipping layers and incident P, SV, SH, and Rayleigh waves. $\Omega_a = 0.83$, $\phi = 0°$.

7. Summary and Conclusion

A hybrid method which combines an indirect boundary integral equation and the finite element techniques, has been developed to study scattering of elastic waves by general three-dimensional subsurface inhomogeneities. The application of the method are demonstrated through studying the surface responses of elastic basins containing several horizontal or dipping layers subjected to P, SV, SH, and Rayleigh waves.

Comparisons of the results obtained by the present method with those obtained by

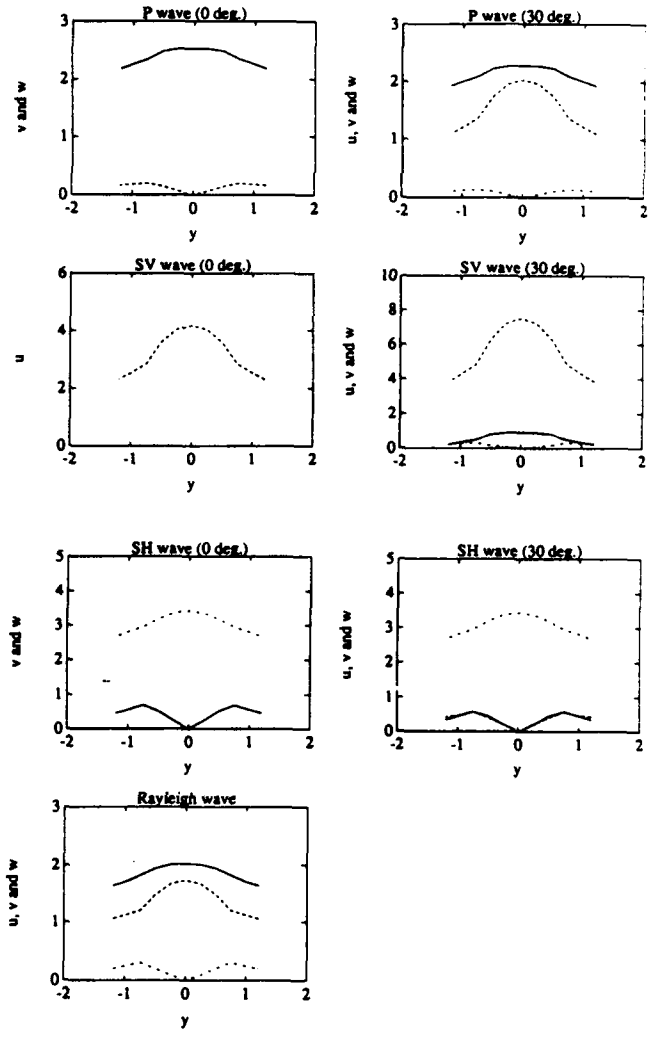

Fig. 9. Amplitudes of surface displacement spectra at section B of the basin with two dipping layers and incident P, SV, SH, and Rayleigh waves. $\Omega_a = 0.83$, $\phi = 0°$.

a boundary integral equation method, clearly show that the proposed technique produces very accurate results, provided that the condition of minimum number of elements per wavelength is satisfied (about 10 elements per wavelength). The types of problems considered here indicate that the method can easily handle dipping layers with very irregular geometries or varying material properties. Furthermore, it is demonstrated that the hybrid technique becomes much more efficient than the boundary integral equation method as the structure of the inhomogeneities becomes very complex. The drawback of the hybrid method is that the memory requirement increases very rapidly

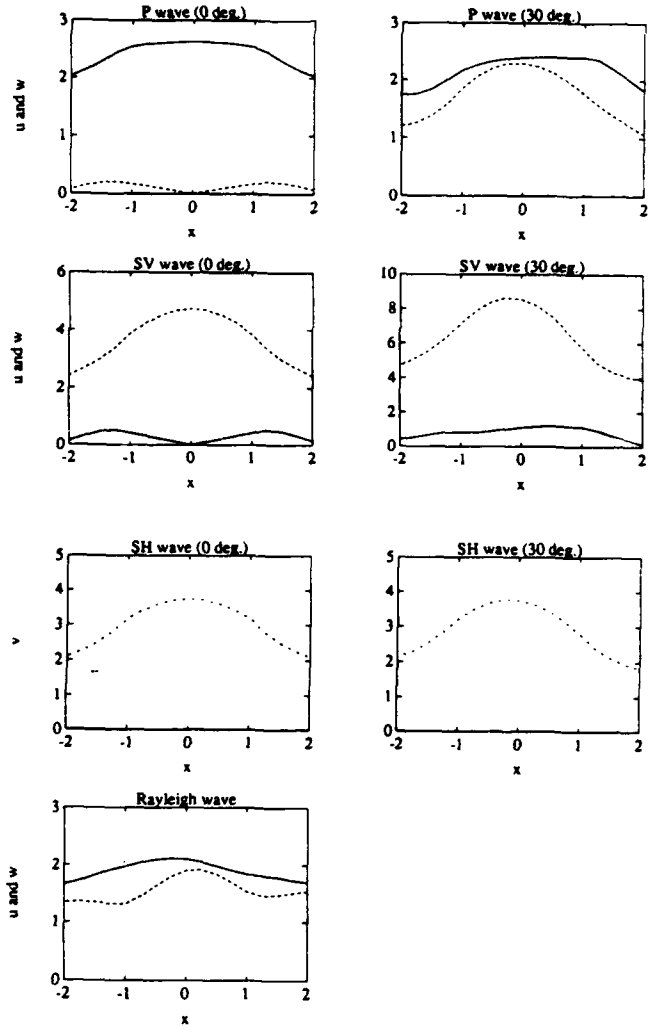

Fig. 10. Amplitudes of surface displacement spectra at section A of the basin with four dipping layers and incident P, SV, SH, and Rayleigh waves. $\Omega_a = 0.83$, $\phi = 0°$, $\mu_0 = \beta_0 = 1$, $\alpha_0 = 2$, $\mu_1 = 0.392$, $\beta_1 = 0.7$, $\alpha_1 = 1.4$, $\mu_2 = 0.284$, $\beta_2 = 0.62$, $\alpha_2 = 1.24$, $\mu_3 = 0.198$, $\beta_3 = 0.54$, $\alpha_3 = 1.08$, and $\mu_4 = 0.131$, $\beta_4 = 0.46$, $\alpha_4 = 0.92$.

(for the finite element part) as the frequency increases. However, with the existing rapid growth in computational facilities this obstacle is expected to be remedied to a great extent in the near future.

This work was supported in part by the National Science Foundation under Grant No. 53-4519-3792 and in part by the Office of Naval Research under Contract No. N00014-88-K-0157.

REFERENCES

Aki, K., Local site effects on strong ground motion, Proceedings of Earthquake Engineering and Soil Dynamics II, American Society Civil Engineering., Park City, Utah, June 27–30, 103–155, 1988.

Aki, K. and K. L. Larner, Surface motion of a layered medium having an irregular interface due to incident plane SH waves, *J. Geophys. Res.*, **75**, 933–954, 1970.

Aki, K. and P. G. Richards, *Quantitative Seismology*, Vol. 1, W. H. Freeman & Co., San Francisco, California, 1980.

Anderson, J. G., P. Bodin, J. N. Brune, J. Prince, S. K. Singh, R. Quaas, and M. Onate, Strong ground motion from the Michoacan, Mexico, earthquake, *Science*, **233**, 1043–1049, 1986.

Bard, P.-Y. and M. Bouchon, The seismic response of sediment-filled valleys. Part I. The case of incident SH waves, *Bull. Seismol. Soc. Am.*, **70**, 1263–1286, 1980 a.

Bard, P.-Y. and M. Bouchon, The seismic response of sediment-filled valleys. Part II. The case of incident P and SV waves, *Bull. Seismol. Soc. Am.*, **70**, 1921–1941, 1980 b.

Bard, P.-Y. and M. Bouchon, The two dimensional resonance of sediment-filled valleys, *Bull. Seismol. Soc. Am.*, **75**, 519–541, 1985.

Bard, P.-Y. and J.-C. Gariel, The seismic response of two-dimensional sedimentary deposits with large vertical velocity gradients, *Bull. Seismol. Soc. Am.*, **76**, 343–346, 1986.

Berg, A. P., A hybrid solution for wave propagation problems in regular media with bounded irregular inclusions, *Geophys. J. R. Astron. Soc.*, **79**, 3–10, 1984.

Beskos, D. E., Boundary element method in dynamic analysis, *Appl. Mech. Rev.*, **40**, 1–23, 1987.

Beskos, D. E. and C. C. Spyrakos, Dynamic response of strip foundations by the time domain BEM-FEM method, Final Report Part B, NSF Grant No. CEE-8024725, Department of Civil and Mineral Engineering, University of Minnesota, Minneapolis MN, Jan., 1984.

Bouchon, M., Effect of topography on surface motion, *Bull. Seismol. Soc. Am.*, **63**, 615–632, 1973.

Bouchon, M. and K. Aki, Near-field of a seismic source in a layered medium with irregular interfaces, *Geophys. J. R. Astron. Soc.*, **50**, 669–684, 1977.

Cole, D. M., D. D. Kosloff, and J. B. Minster, A numerical boundary integral equation method for elastodynamics, *Bull. Seismol. Soc. Am.*, **68**, 1331–1357, 1978.

Dravinski, M., Influence of interface depth upon strong ground motion, *Bull. Seismol. Soc. Am.*, **72**, 596–614, 1982 a.

Dravinski, M., Scattering of SH waves by subsurface topography, *J. Eng. Mech. Div.*, **108**, No. EM1, 1–16, 1982 b.

Dravinski, M., Scattering of elastic waves by an alluvial valley, *J. Eng. Mech. Div.*, **108**, No. EM1, 19–31, 1982 c.

Dravinski, M., Scattering of plane harmonic SH waves by dipping layers of arbitrary shape, *Bull. Seismol. Soc. Am.*, **73**, 1303–1319, 1983.

Dravinski, M. and T. K. Mossessian, Scattering of harmonic P, SV, and Rayleigh waves by dipping layers of arbitrary shape, *Bull. Seismol. Soc. Am.*, **77**, 212–235, 1987 a.

Dravinski, M. and T. K. Mossessian, Amplification of surface ground motion by an inclusion of arbitrary shape for harmonic surface line loading, *Numer. Methods Part. Diff. Eqs.*, **3**, 9–27, 1987 b.

Dravinski, M. and T. K. Mossessian, On evaluation of the Green functions for harmonic line loads in a viscoelastic half space, *Int. J. Numer. Methods Eng.*, **26**, 823–841, 1988.

Eshraghi, H. and M. Dravinski, Transient scattering of elastic waves by dipping layers of arbitrary

shape. Part 1. Antiplane strain model, *Earthq. Eng. Struct. Dyn.*, **18**, 397–415, 1988 a.

Eshraghi, H. and M. Dravinski, Transient scattering of elastic waves by dipping layers of arbitrary shape. Part 2. Plane strain model, *Earthq. Eng. Struct. Dyn.*, **18**, 417–434, 1988 b.

Herrera, I. and F. J. Sabina, Connectivity as an alternative to boundary integral equations: Construction of basis, *Proc. Natl. Acad. Sci. U.S.A.*, **75**, 2059–2063, 1978.

Hong, T. L. and D. V. Helmberger, Glorified optics and wave propagation in nonplanar structure, *Bull. Seismol. Soc. Am.*, **68**, 1313–1330, 1978.

Kagami, H., C. M. Duke, G. C. Liang, and Y. Ohta, Observation of 1- to 5-second microtremors and their application to earthquake engineering. Part II. Evaluation of site effect upon seismic wave amplification due to extremely deep soil deposits, *Bull. Seismol. Soc. Am.*, **72**, 987–998, 1982.

Kagami, H., S. Okada, K. Shiono, M. Oner, M. Dravinski, and A. Mal, Observation of 1- to 5-second microtremors and their application to earthquake engineering. Part III. A two dimensional study of site effect in the San Fernando Valley, *Bull. Seismol. Soc. Am.*, **76**, 1801–1812, 1986.

Kawase, H. and K. Aki, A study on the response of a soft basin for incident S, P, and Rayleigh waves with special reference to the long duration observed in Mexico City, *Bull. Seismol. Soc. Am.*, **79**, 1361–1382, 1989.

King, J. L. and B. E. Tucker, Observed variations of earthquake motion across a sediment-filled valley, *Bull. Seismol. Soc. Am.*, **74**, 137–151, 1984.

Kobayashi, S., N. Nishimura, and K. Mori, Applications of boundary element-finite element combined method to three dimensional viscoelastodynamic problems, in *Boundary Elements*, ed. D. Qinghua, pp. 67–74, Pergamon Press, Oxford, 1986.

Moczo, P., P.-Y. Bard, and I. Pšenčik, Seismic response of a two dimensional structure by the ray method, *J. Geophys.*, **62**, 38–49, 1987.

Mossessian, T. K., Diffraction of elastic waves by non-axisymmetric three dimensional subsurface inhomogeneities using a boundary integral equation method and a hybrid technique, Ph. D. thesis, Department of Mechanical Engineering, University of Southern California, Los Angeles, 1989.

Mossessian, T. K. and M. Dravinski, Application of a hybrid method for scattering of P, SV and Rayleigh waves by near surface irregularities, *Bull. Seismol. Soc. Am.*, **77**, 1784–1803, 1987.

Mossessian, T. K. and M. Dravinski, Scattering of elastic waves by three dimensional surface topographies, *Wave Motion*, **11**, 579–592, 1989.

Mossessian, T. K. and M. Dravinski, Amplification of elastic waves by a three dimensional valley. Part 1: Steady-state response, *Earthq. Eng. Struct. Dyn.*, **19**, 667–680, 1990.

Niwa, Y. and S. Hirose, Application of the BEM to elastodynamics in a three dimensional half space, Recent Applications in Computational Mechanics, ASCE, 1–15, 1987.

Niwa, Y., S. Hirose, and M. Kitahara, Application of the boundary integral equation (BIE) method to transient analysis of inclusions in a half-space, *Wave Motion*, **8**, 77–91, 1986.

Nowack, R. and K. Aki, The two dimensional Gaussian beam synthetic method: Testing and application, *J. Geophys. Res.*, **89**, 7797–7819, 1984.

Repetto, P., I. Arango, and H. B. Seed, Influence of site characteristics on building damage during the October 3, 1974, Lima earthquake, Report No. UCB/EERC 80/41, University of California, Berkeley, California, 1980.

Rizzo, F. J., D. J. Shippy, and M. Rezayat, A boundary integral equation method for radiation

and scattering of elastic waves in three dimensions, *Int. J. Numer. Methods Eng.*, **21**, 115–129, 1985.

Sánchez-Sesma, F. J., Diffraction of elastic waves by three-dimensional surface irregularities, *Bull. Seismol. Soc. Am.*, **73**, 1621–1636, 1983.

Sánchez-Sesma, F. J. and E. Rosenblueth, Ground motion at canyons of arbitrary shapes under incident SH-waves, *Earthq. Eng. Struct. Dyn.*, **7**, 441–449, 1979.

Smith, W. D., The application of finite element analysis to body wave propagation problems, *Geophys. J. R. Astron. Soc.*, **42**, 747–768, 1975.

Trifunac, M. D., Surface motion of semicylindrical alluvial valley for incident plane SH waves, *Bull. Seismol. Soc. Am.*, **61**, 1755–1770, 1971.

Wong, H. L., Diffraction of P, SV, and Rayleigh waves by surface topographies, *Bull. Seismol. Soc. Am.*, **72**, 1167–1184, 1982.

Wong, K. C., A. H. Shah, and S. K. Datta, Diffraction of elastic waves in a half space. II. Analytical and numerical solutions, *Bull. Seismol. Soc. Am.*, **75**, 69–91, 1985.

Zahradnik, J. and F. Hron, Seismic ground motion of sedimentary valleys—example La Molina, Lima, Peru, *J. Geophys.*, **62**, 31–37, 1987.

Zeevaert, L., Strong ground motion recorded during earthquakes of May the 11th and 19th, 1962 in Mexico City, *Bull. Seismol. Soc. Am.*, **54**, 209–231, 1964.

Zienkiewicz, O. C., *The Finite Element Method (3rd ed.)*, McGraw Hill Book Company, London, 1977.

Zienkiewicz, O. C., D. W. Kelly, and P. Bettess, The coupling of the finite element method and boundary solution procedures, *Int. J. Numer. Methods Eng.*, **11**, 355–375, 1977.

Elastic Wave Scattering by an Inclusion in a Multilayered Medium Submerged in Fluid

RAMDASS KESHAVAMURTHY and MARIJAN DRAVINSKI

Department of Mechanical Engineering, University of Southern California, Los Angeles, CA 90089-1453, U.S.A.

Abstract

Response of plane multilayerd media enclosing an elastic inclusion of arbitrary shape and submerged in fluid is investigated. The plane strain model is assumed. The steady-state free-field response is modeled by the Thomson-Haskell method using delta-matrix modification and the scattered wave field by a boundary method. The transient response is evaluated using the Fourier synthesis. Numerical results are presented for a single layer plate with an elliptical inclusion and a single layer with an inclusion bounded by an elastic half-space. For the steady-state fluid-solid interface response the results show that (i) presence of the half-space greatly influences the response; (ii) the response is very sensitive upon the geometry and the embedment depth of the inclusion; (iii) the response is sensitive upon the angle and frequency of incident wave; and (iv) impedance contrast between the plate and inclusion is important for overall response pattern. Transient results for vertical incidence demonstrate that the presence of the inclusion is detected very clearly by both predominant and non-predominant components of motion.

Introduction

Study of wave scattering by inclusions in elastic media submerged in fluid has many practical applications. A few problems of interest are the non destructive evaluation of materials (NDE) and geophysical prospecting at the bottom of the sea. In the NDE , the part to be evaluated is immersed in water and subjected to an acoustic disturbance by a transducer located in water [1]. The reflected signal contains the acoustic signature of the material under investigation which reveals the nature of fault present in the structure.

Theoretical modeling of scattering by inclusion in elastic media immersed in fluid aids in the interpretation of the results obtained by tests like NDE.

The two-dimensional reflection of an acoustic beam from a plane solid-liquid interface at or near the Rayleigh angle has been the subject of study by several investigators in the past. Bertoni and Tamir [2] presented a unified theory of Rayleigh-angle phenomena for acoustic beams at liquid-solid interfaces. The reflection of plane waves from a single layered half-space under water was investigated by Bogy and Gracewski [3], who later extended the analysis to include the bounded beam reflection from a multilayered half-space [4]. Kundu et al. [1] studied the reflection from a multilayered half-space in fluid using the Thomson-Haskell formulation [5,6]. They reformulated the original Thomson-Haskell approach in terms of delta matrices [7]. Schmidt and Jensen [8] studied the Gaussian beam reflection at fluid-solid interfaces for a multilayered viscoelastic media.

So far there have been very few investigations of reflection from a scatterer embedded in an elastic medium immersed in fluid. Varadan et al. [9] studied three dimensional ultrasonic wave scattering by a submerged flaw in joined fluid-solid half-space by the T-matrix approach. They evaluated the back scattered pressures at far fields by making an asymptotic approximation for the scattered field. The two dimensional scattering from an interfacial crack in a layered half-space submerged in fluid for incident plane waves and bounded beams was investigated by Gracewski and Bogy [10,11]. They presented numerical results in the form of stress intensity factors at the crack tip.

Analytical solutions of the scattering problems are generally limited to simple geometries. Hence, numerical methods are employed to study most of the practical problems of interest. The common numerical methods employed are the finite element (FE) and finite difference (FD) methods, the boundary integral equation (BIE) method, and the transition matrix (T-Matrix) method. In addition, investigators have employed many hybrid methods.

Modeling the scattering of waves in infinite media by FE or FD appears to be ineffective for geophysical problems in view of the vast computational grid required for problems with long characteristic lengths [12]. In addition, these methods do not completely satisfy the radiation condition at infinity [13].

The BIE methods formulate the problem in terms of boundary values and possible internal sources [14,15]. The radiation condition is satisfied

exactly. Since the discretization is done only on the boundaries, the number of variables is greatly reduced. But the BIE methods require the evaluation of Green's function which often results in large amount of computational effort [16]. While the FE methods are generally more versatile in handling medium with varying material properties [17], BIE methods are in general not suitable for inhomogeneous media [18]. To overcome the shortcomings of both the methods, some hybrid methods which combine say, FE and BIE approach have been employed [19]. The advantage of such a method is that it uses the versatility of the FE method for detailed modeling of the near field and the effectiveness of the BIE methods in the far field [20]. But the method still requires the evaluation of the Green's function which can be time consuming. To overcome that problem, Shah et al. [21] proposed another hybrid method which combines the finite element method with the wave function expansion technique. The interior region containing the scatterer is modeled by the FE and the wave function expansions are used to represent the field in the exterior homogeneous, isotropic and unbounded medium. The wave functions satisfy the radiation condition at infinity. Another hybrid method combining the BIE method and the Thomson-Haskell method for scattering by plane layered medium is presented by Schuster and Smith [22]. The hybrid method computes the Green's function of the scatterer without the layer by a BIE method and the Green's function of the layer without the scatterer by a Thomson-Haskell method. The coupling between the scatterer and plane-layers is achieved by a combination of Fast Fourier Transforms (FFT) and extrapolation operators and these interactions are finally summed up in a Born series.

The T-matrix approach has been adopted by a number of investigators to study various scattering problems [23,24,25,26]. The essence of the T-matrix method is to express the unknown coefficients of the scattered field in terms of the known coefficients of the incident field by employing the T-matrix. The formation of the T-matrix requires the evaluation of certain integrals which are calculated numerically for arbitrary geometries.

In addition to the above methods, the Aki-Larner technique [27] based on the Rayleigh hypothesis has been applied to the scattering problems where the wave lengths are either larger than or equal to the size of the irregularities. Bouchon [28], Bard and Bouchon [29,30] used this method to study two dimensional seismic response of sediment filled valleys subjected to incident P, SV, and SH waves. Bouchon and Aki [31] extended the Aki-Larner method

to study the near field of a seismic source in a layered medium with irregular interfaces.

For the high frequency wave scattering problems, the ray method is found to be very effective. This method is based on asymptotic techniques in approximating the wave field [32]. The method has been extended to include the moderate frequencies by Moczo et al. [33]

All the methods described so far principally pertain to the steady-state response of the problem. For the numerical solution of the transient problems there are two approaches (i) Direct methods and, (ii) Indirect methods.

In direct methods, solutions to scattering problem is formulated as a function of time. The main difficulty with this method is the accumulation of errors with increase of time [34]. Smith [12] used the FE approach and Boore et al. [35], used the FD technique to solve the antiplane strain problem directly in the time domain. Banerjee et al. [36] applied the BIE technique to solve the three dimensional transient problem for spherical and hemispherical cavities embedded in an infinite or semi-infinite medium subjected to radial pressures. For indirect methods, the transient response is obtained from steady state solution through the use of Fourier or Laplace transform [37]. Manolis and Beskos [38] used the Laplace transform method to solve elastodynamic plane strain problems in infinite media. Niwa et al. [39] used the Fourier transform technique and the BIE approach for calculating the two dimensional transient response for completely embedded irregularities subjected to incident P and SV waves. A comparative study of direct and indirect methods combined with BIE method is presented by Manolis [40]. A detailed review of the BIE method and other boundary techniques (T-Matrix, Born Approximation, Hybrid FE-BIE etc.) in dynamic analysis can be found in the paper by Beskos [41].

In the present study, a hybrid Thomson-Haskell method and boundary method is employed to study the steady-state response of an inclusion in a plane multilayered medium in fluid. The Thomson-Haskell formulation is recast in terms of delta matrices. The transient response is evaluated by using the fast Fourier transforms . The analysis is done for the plane strain case.

The Thomson-Haskell formulation [5,6,7,1] with delta-matrix modification is employed for the free-field evaluation which involves the response of the layered medium in fluid without the inclusion. A boundary method which utilizes the wave function expansion is employed to model the scattered

field. The boundary method originates in the works of Herrera and Sabina [42] and Herrera [43]. The method involves employing the wave functions satisfying the equations of motion in each domain to represent the scattered field. These wave functions, in general, do not satisfy the boundary or continuity conditions. These conditions are satisfied in the least square sense at a finite number of points on the boundary. The advantage of this method over the BIE method is that it does not involve the evaluation of the Green's function. Sanchez-Sesma et al. [44,45] used this approach to solve the scattering of SH, P, SV and Rayleigh waves for two dimensional problems. The elastic wave scattering by two dimensional dipping layers has been solved by this approach by Eshraghi and Dravinski [46,47].

This paper is divided into several parts. After the introduction, the statement of the problem is presented. Then, the steady state solution of the problem is given. Next, numerical results are discussed for both the steady state and transient cases, followed by the conclusions.

Statement of the problem

The geometry of the problem is shown by the Fig. 1. The model consists of a multilayered infinite elastic half-space (or a plate) with an inclusion within a layer. The medium is surrounded by inviscid fluid on one side. The following conventions are understood throughout. The domains are designated by $D_j(j = 0, 1, \ldots, N)$ and the boundaries, $C_j(j = 0, 1, \ldots, N)$. Domain D_0 denotes the fluid half-space while C_0 denotes the interface between the fluid and the first layer. The inclusion domain and boundary in the p^{th} layer are designated by $D_{p'}$ and $C_{p'}$ respectively. Summation over repeated indices is understood. Underlined indices indicate that the summation is being suppressed. Material of the media is assumed to be linearly elastic, homogeneous and isotropic. The fluid half space is subjected to an oblique incident plane harmonic acoustic wave. The problem is of the plane strain type.

The equation of motion in terms of displacement potentials is given by [48]

$$M[k_{\alpha \underline{j}}]\varphi_{\underline{j}}(\mathbf{x}, \omega) = 0; j = 0, 1, 2, \ldots, N, p' \tag{1}$$

$$M[k_{\beta \underline{j}}]\psi_{\underline{j}}(\mathbf{x}, \omega) = 0; j = 1, 2, \ldots, N, p' \tag{2}$$

where

$$M[*] = \nabla^2 + (*)^2$$

$$k_{\alpha j} = \frac{\omega}{\alpha_j}; k_{\beta j} = \frac{\omega}{\beta_j}; \alpha_j^2 = \frac{\lambda_j + 2\mu_j}{\rho_j}; \beta_j^2 = \frac{\mu_j}{\rho_j} \tag{3}$$

Here, φ_j and ψ_j denote the P-wave and SV-wave potentials , respectively , $\mathbf{x}$ is the position vector, and ω is the circular frequency. α_j and β_j denote the dilatational and shear wave velocities, respectively and $k_{\alpha j}$ and $k_{\beta j}$ are the respective wavenumbers. ρ_j, μ_j and λ_j are the density, and Lame's constants of the j^{th} layer, respectively. For convenience, the wavenumber in fluid $k_{\alpha 0}$ is sometimes denoted by k_f.

The displacement field in the j^{th} layer is then represented by

$$\mathbf{u}_j = \nabla\varphi_j + \nabla \times (0, 0, \psi_j) \tag{4}$$

where, $\mathbf{u}_j$ has components $(u_{rj}, u_{\theta j}, 0)$ and $(u_j, 0, w_j)$ in the polar and rectangular coordinate systems respectively.

The boundary conditions on the free surface of the plate are given by

$$\sigma_{nt} = 0; \sigma_{nn} = 0; z = z_N \tag{5}$$

where σ_{nn} and σ_{nt} are the normal and tangential components of the traction vector, respectively. For the multilayer half-space, instead of Eqn.(5) radiation condition is applied for the half space. The continuity conditions along the solid-fluid interface C_0 are specified to be [7]

$$w_0^+(\mathbf{x}, \omega) = w_1^-(\mathbf{x}, \omega) \tag{6}$$

$$\sigma_{nn\,0}^+(\mathbf{x}, \omega) = \sigma_{nn\,1}^-(\mathbf{x}, \omega) \tag{7}$$

$$\sigma_{nt\,1}^-(\mathbf{x}, \omega) = 0. \tag{8}$$

The continuity conditions along the interfaces $C_j (j = 1, \ldots, N-1)$ are given by

$$u_{j-1}^+(\mathbf{x}, \omega) = u_j^-(\mathbf{x}, \omega) \tag{9}$$

$$w_{j-1}^+(\mathbf{x}, \omega) = w_j^-(\mathbf{x}, \omega) \tag{10}$$

$$\sigma_{nn\,j-1}^+(\mathbf{x}, \omega) = \sigma_{nn\,j}^-(\mathbf{x}, \omega) \tag{11}$$

$$\sigma_{nt\,j-1}^+(\mathbf{x}, \omega) = \sigma_{nt\,j}^-(\mathbf{x}, \omega) \tag{12}$$

where u_j, w_j are the components of the displacement along the x and z directions, respectively. The '+' and '-' signs refer to the interface C_j being approached from below and above, respectively.
The continuity conditions along the inclusion boundary $C_{p'}$ are taken to be

$$u_p^+(\mathbf{x},\omega) = u_{p'}^-(\mathbf{x},\omega) \tag{13}$$

$$w_p^+(\mathbf{x},\omega) = w_{p'}^-(\mathbf{x},\omega) \tag{14}$$

$$\sigma_{nn\,p}^+(\mathbf{x},\omega) = \sigma_{nn\,p'}^-(\mathbf{x},\omega) \tag{15}$$

$$\sigma_{nt\,p}^+(\mathbf{x},\omega) = \sigma_{nt\,p'}^-(\mathbf{x},\omega) \tag{16}$$

Here, the '+' and '-' signs refer to the interface being approached from outside and inside the inclusion, respectively.

The incident field is a plane wave in the fluid given by

$$\varphi^{inc} = (-i/k_f)e^{i(k_f x \sin\theta_0 + k_f z \cos\theta_0 - \omega t)} \tag{17}$$

where θ_0 is the off-vertical angle of incidence (see Fig. 1). The factor $(-i/k_f)$ is introduced for convenience.

Steady state solution of the problem

The solution is sought as a superposition of the free-field and scattered wave fields according to

$$\mathbf{u}_j = \mathbf{u}_j^{ff} + \mathbf{u}_j^s;\ \mathbf{x} \in D_j; j = 0, 1, \ldots, N \tag{18}$$

$$\mathbf{u}_{p'} = \mathbf{u}_{p'}^s;\ \mathbf{x} \in D_{p'} \tag{19}$$

where the superscripts 'ff' and 's' denote the free-field and scattered wave fields, respectively.

Free-field solution

In the absence of the inclusion, the Thomson-Haskell method for multilayer plate is employed for the free-field solution [5,6,1]. Delta-matrix approach [7] is incorporated to overcome the precision problem. For the free-field, Cartesian coordinate system with the origin located at the solid-fluid interface is employed (see Fig. 1).

The incident wave of Eqn.(17) can be written as

$$\varphi^{inc} = (-i/k_f)e^{i\eta_f z}e^{i(kx-\omega t)} \tag{20}$$

where

$$\eta_f = \begin{cases} (k_f^2 - k^2)^{1/2} & k \leq k_f \\ i(k^2 - k_f^2)^{1/2} & k \geq k_f \end{cases} \tag{21}$$

Here the horizontal P-wavenumber is defined by,

$$k = k_f sin\theta_0. \tag{22}$$

The reflected wave is given by

$$\varphi^{ref} = R(-i/k_f)e^{-i\eta_f z}e^{i(kx-\omega t)} \tag{23}$$

where R is the reflection coefficient [1] . Hence the total free-field in the fluid is

$$\varphi^{ff} = (-ie^{i(kx-\omega t)}/k_f)(e^{i\eta_f z} + Re^{-i\eta_f z}). \tag{24}$$

Scattered wave field solution

For the scattered field evaluation, the origin is shifted inside the inclusion with the polar coordinate system (r,θ) used for the stress and displacement field evaluations (see Fig.1). The scattered field for the fluid is taken to be of the form

$$\varphi_0^s = a_{m\,0}H_m^{(1)}(k_{\alpha 0}r)cosm\theta + a_{m\,0}^* H_m^{(1)}(k_{\alpha 0}r)sinm\theta \tag{25}$$

$$\begin{aligned} \psi_0^s &= 0. \\ & m = 0, \ldots, M_0. \end{aligned} \tag{26}$$

For the j^{th} layer the scattered waves are assumed to be of the form,

$$\begin{aligned} \varphi_j^s = {} & b_{m\,j}H_m^{(2)}(k_{\alpha j}r)cosm\theta + b_{m\,j}^* H_m^{(2)}(k_{\alpha j}r)sinm\theta + \\ & c_{m\,j}H_m^{(1)}(k_{\alpha j}r)cosm\theta + c_{m\,j}^* H_m^{(1)}(k_{\alpha j}r)sinm\theta \end{aligned} \tag{27}$$

$$\begin{aligned} \psi_j^s = {} & d_{m\,j}H_m^{(2)}(k_{\beta j}r)cosm\theta + d_{m\,j}^* H_m^{(2)}(k_{\beta j}r)sinm\theta + \\ & e_{m\,j}H_m^{(1)}(k_{\beta j}r)cosm\theta + e_{m\,j}^* H_m^{(1)}(k_{\beta j}r)sinm\theta \\ & j = 1, \ldots, N; m = 0, \ldots, M_j. \end{aligned} \tag{28}$$

If an elastic half space is present, we have,

$$\varphi^s_N = c_m \underset{N}{} H^{(1)}_m(k_\alpha \underset{N}{} r) cosm\theta + c^*_m \underset{N}{} H^{(1)}_m(k_\alpha \underset{N}{} r) sinm\theta \quad (29)$$

$$\psi^s_N = e_m \underset{N}{} H^{(1)}_m(k_\beta \underset{N}{} r) cosm\theta + e^*_m \underset{N}{} H^{(1)}_m(k_\beta \underset{N}{} r) sinm\theta \quad m = 0, \ldots, M_N. \quad (30)$$

Within the inclusion we have,

$$\varphi^s_{p'} = f_m \underset{p'}{} J_m(k_\alpha \underset{p'}{} r) cosm\theta + f^*_m \underset{p'}{} J_m(k_\alpha \underset{p'}{} r) sinm\theta \quad (31)$$

$$\psi^s_{p'} = g_m \underset{p'}{} J_m(k_\beta \underset{p'}{} r) cosm\theta + g^*_m \underset{p'}{} J_m(k_\beta \underset{p'}{} r) sinm\theta. \quad m = 0, \ldots, M_{p'}. \quad (32)$$

Here, a_m to g^*_m are the unknown coefficients, J_m is the Bessel function of the first kind, $H^{(1)}_m$ and $H^{(2)}_m$ are the Hankel functions of the first and second kind, respectively and M is the order of expansion in each domain. All the wave functions in the Eqns.(25-32) are solutions of the equations of motion. In addition, the scattered wave field in the fluid and the half space consists of the outgoing waves only while the scattered field in the plate consists of both incoming and outgoing waves. Inside the inclusion the wave field consists of standing waves. As indicated earlier, in Eqns.(25-32), summation over repeated index 'm' is assumed.

At this point more about the nature of the wave functions used to formulate the scattered waves should be stated. These functions belong to a class of functions known as the c-complete functions. The theory of these functions has been developed by Herrera and Sabina [42] and Herrera [43] using algebraic theory. The concept of c-completeness allows constructing systems of solutions which are complete with respect to general boundary values independently of the specific region of consideration. The boundary method employing these c-complete functions grants convergence of the approximating sequence when a least-squares fitting of the boundary conditions is used [44]. Sanchez-Sesma et al. [44] demonstrated the applicability of this method for the problem of diffraction of SH waves by surface irregularities. They later extended the study to the diffraction of plane P, SV and Rayleigh waves by surface irregularities [45]. This method has been used by Eshraghi and Dravinski [46,47] to study the scattering by multiple dipping layers for

the antiplane and plane strain models. Details of the theory concerning the boundary method can be found in the paper by Herrera [43].

Evaluation of expansion coefficients

The unknown coefficients of the scattered wave field are determined by imposing the boundary and the continuity conditions given by Eqns.(5-16). These conditions are imposed at the N_j points along the boundaries $C_{p'}$ and $C_j, j = 0, 1 \ldots N(N-1$, for the half-space) resulting in a system of linear equations of the form

$$\mathbf{Ga} = \mathbf{f}. \tag{33}$$

Here **a** contains all the unknown expansion coefficients, vector **f** involves the free-field displacements and tractions, and **G** consists of the wave functions and their derivities evaluated along the boundaries. The size of the matrix **G** is (S×K), where S>K. Hence Eqn.(33) is solved in the least square-sense [49]. Once the expansion coefficients are known, the displacement and the stress fields can be evaluated throughout the medium.

Numerical results

This section describes the steady state and transient response for a single layered plate and a single layered half-space with an elliptical inclusion.

These models are chosen to incorporate most of the physical characteristics of the problem while keeping the computation to a minimum. The geometry of the model is shown for a single plate in Fig. 2. Half-space is added to the plate when present. The fluid domain is designated by D_0 and that of the plate and inclusion by D_1 and $D_{1'}$, respectively. Half-space is denoted by D_2. The plate thickness and the inclusion depth are denoted by 'h' and 'd', respectively. The principal axes of the elliptical inclusion are denoted by 'a' and 'b'. The lengths on the top and bottom plate boundaries, along which the continuity and boundary conditions are imposed, are taken to be to be 'C0' and 'C1', respectively (see Fig.2). The orders of expansion for the fluid, plate, inclusion and the half-space are denoted by M_0, M_1, $M_{1'}$ and M_2, respectively. Number of collocation points along the solid-fluid interface and the free surface of the plate (or plate-half-space interface when present) are taken to be N_0 and N_1, respectively. For the inclusion boundary it is denoted

by N_1'. The density, shear modulus and shear wave velocity of the plate are taken to be unity. When half-space is present, the density, shear modulus and shear wave velocity of the half-space are taken to be unity. All spatial variables are normalized with respect to the major principal axis of the elliptical inclusion which is assumed to be unity. For convenience, dimensionless frequency Ω is defined as the ratio of the maximum width of the inclusion to the wavelength of the shear wave in the layer enclosing the inclusion. Horizontal and vertical steady-state amplitudes are denoted by $|Ux|$ and $|Uz|$, respectively. The total free-field displacement used for normalization is defined as $|Ufft| = \sqrt{(|Uffx|^2 + |Uffy|^2)}$, where $|Uffx|$ and $|Uffy|$ are the free-field horizontal and vertical displacement amplitudes, respectively.

Steady state response

This section describes the steady state response of the plate and layered half-space models. First, convergence tests are conducted to fix various problem parameters. Subsequently, the formulation is verified for the zero-scattering condition and symmetric response. Finally, the steady state results for a single plate and layered half-space models are discussed.

Convergence and testing of results

First, tests are conducted to evaluate the orders of expansion required for convergence of results in each domain. Similar tests are conducted to determine the number of collocation points along each interface at which the continuity and boundary conditions are imposed. In addition, studies are done to determine the lengths of the plate boundary along which the continuity and boundary conditions are imposed. The convergence of results has been established by observing the change in scattered wave displacement amplitudes at the solid-fluid interface with change in the value of the parameter under consideration. The numerical results are accepted as the final ones if the difference between two successive calculations is judged to be sufficiently small for the increase in the value of the parameter of interest.

In the absence of a test case to compare the results with, the formulation was first tested for zero-scattering condition in which the material of the inclusion was taken to be the same as that of the plate. As expected,

the contribution of the scattered field was found to be zero. In addition, the formulation is verified for symmetry for a vertical incidence. Both the horizontal and vertical displacement amplitudes are found to be symmetric thus lending further confidence in the validity of the calculated results.

The parameters chosen for convergent results are indicated in the respectively figures. Further details of the convergence studies and testing of the results are given in [50].

Response of a plate with inclusion

Response of a plate with an inclusion is studied for different impedance contrasts. Two cases are considered: Inclusion being stiffer than the plate and the plate being stiffer than the inclusion.

Figure 3 summarizes the results for the case of a stiff inclusion for different aspect ratios of the inclusion i.e., circular, elliptical with horizontal and vertical major axes. The vertical and horizontal displacement amplitudes of the plate are normalized with respect to the total free-field displacement. From the vertical component of displacement in Fig. 3, the scattered field is found to interfere destructively with the free-field near the inclusion. This appears as a dip in the total field indicating the presence of the scatterer. As to be expected, the scattered field has the greatest influence when the geometry is circular (aspect ratio=1) and least when the elliptical major axis is in the horizontal direction (aspect ratio=2). Away from the scatterer, the displacement field approaches the free-field value. Figure 3 also shows the influence of the scatterer on the horizontal component of motion. The effect of the inclusion depth on the surface displacements is shown in the Fig. 4. As expected, the effect of the scattered field on the vertical displacement is found to diminish with increase in depth.

Figure 5 depicts the response of a plate with a stiffer inclusion as a function of frequency and spatial variable 'x' for a vertical incidence. The three dimensional plots show the total horizontal and vertical displacement amplitudes of the plate along the solid-fluid interface for different frequencies of the incident wave. The peaks of the vertical displacement correspond to the natural frequencies of a free-free plate without the inclusion for a vertical incidence. The analytical values of these are given by

$$\omega = n\pi\alpha/h; n = 0, 1, 2, \ldots \tag{34}$$

where α and h are the P-wave velocity and the thickness of the plate, respectively. As seen from Fig.5, the natural frequencies for the plate considered are at ω=0.0, 2.60, 5.20, etc. In view of the very low density of the fluid, the natural frequencies of the plate in fluid are found to almost coincide with the natural frequencies of the free-free plate. The horizontal displacement is found to peak at these frequencies as well. This is due to the fact that the horizontal displacement, which is entirely due to the scatterer, is dependent on the free-field response. The free-field response in turn, peaks at the natural frequencies of the plate thus resulting in large response at the fluid-solid interface.

Figure 6a shows the response due to a very small off-vertical incidence for the case discussed above. The free-field horizontal displacement is significantly higher than the vertical displacement for this case (compare Figs.3 and 6a). The effect of the scattered wave field can be observed on both the horizontal and vertical free-field displacements. Above the inclusion, the scattered field interferes constructively for the vertical displacement and destructively for the horizontal displacement.

Figure 6b refers to the case of a soft inclusion inside a hard medium . The vertical component of displacement shows a peak atop the center of the scatterer indicating constructive interference of the scattered field with the free-field as opposed to the destructive interference for the case of hard inclusion inside a soft medium (compare Figs. 6b and 3).

Based on the presented results, it is found that the steady state response at the fluid-solid interface is sensitive upon the shape and embedment depth of the scatterer, location of the observation points, angle of incidence, and the frequency of excitation. In addition, the impedance contrast between the plate and the inclusion has significant influence on the response.

Response of a layer with inclusion on an elastic half-space

In this model, the inclusion is embedded in a layer atop an elastic half-space. The inclusion is taken to be softer than the surrounding layer which in turn is softer than the elastic half-space below it.

The response of the model to a vertical incidence is shown in Fig. 6c. The vertical displacement shows a peak inside a valley indicating the presence of the scatterer. The presence of the valley below the free-field value indicates the destructive interference of the scattered field with the free-field. The

peak inside the valley shows smaller destructive interference over the scatterer up to a distance of twice the width of the scatterer. Comparison of the vertical displacement with that of the plate with a softer inclusion (Figs. 6c and 6b) shows that the presence of the half-space changes the response at the fluid-solid interface considerably.

Transient response

This section deals with the transient response of plate with a hard inclusion. The transient response is obtained from the steady state response by Fourier synthesis [46] Here, the response is studied for a vertically incident Ricker wavelet [51]. The Ricker wavelet is defined as

$$f(t) = (\sqrt{\pi}/2)(\tau - 0.5)e^{-\tau}, \tau = (\pi(t - t_s)/t_p)^2 \tag{35}$$

where t_s corresponds to the peak amplitude in the time domain and t_p corresponds to the angular frequency $\omega_p(= 2\pi/t_p)$ which is associated with the peak amplitude in the Fourier transform domain .

The Fourier transform of the Ricker wavelet is given by

$$F(\omega) = (-t_p/2)(\omega/\omega_p)^2 e^{-(\omega/\omega_p)^2} e^{i\omega t_s}. \tag{36}$$

Figure 7 displays the total horizontal and vertical displacement components of the fluid at the plate-fluid interface for a vertically incident Ricker wavelet (t_s=25.0 secs. and t_p=6.0 secs.). Total of 41 equally spaced observation stations are chosen. The bottom trace depicts the motion at (X=-10,Z=0), while the top trace corresponds to the station at (X=10,Z=0). The impedance contrast corresponds to that of a very hard inclusion in a soft plate. From the Fig. 7, it is found that the displacements are quiescent over a time required for the initial disturbance to reach the surface of the plate. The vertical displacement is mostly due to the superposition of the incident wave and the waves reflected at the top and the bottom surfaces of the plate. The vertical displacement, though dominated by the free-field, clearly indicates the presence of the scatterer. This is evident from the fact that , near the scatterer, the vertical displacement field is different from that observed at farther distances from the scatterer. The horizontal displacement, which is entirely due to scattering , shows the presence of the inclusion clearly. The horizontal disturbance is found to be anti-symmetric about the middle

observation point. A little distance from the inclusion, the scattered wave field is found to assume a uniform shape traveling with a constant velocity. This is indicated by the line 'A-B' in Fig.7. Based on the time arrivals at 'A' and 'B', the scattered wave found in the horizontal component of interface motion is found to be traveling along the interface with the P-wave velocity of the fluid. The amplitude of the horizontal disturbance is found to be decreasing very slowly with increasing distance from the scatterer over the observed range.

Figure 8 shows the vertical displacement for the same inclusion in a stiffer plate than that of Fig.7. The vertical displacement field, which is dominated by the free-field, displays waviness which decays with time. This waviness is due to the multiple reflection of the incident wave between the plate surfaces. This phenomena is observed only when the density of the plate is much higher than that of the fluid, so that incident energy is trapped in the plate for a longer period (compare Figs. 7 and 8). As the contrast between the inclusion and plate becomes smaller, the effect of the scatterer is found to be very small on the predominant component of the displacement.

Figure 9 displays the vertical response of the plate described above when the inclusion is much harder than the plate. The effect of the inclusion is strongly felt in the vicinity of the inclusion. This is evident through the lack of waviness in the response above the inclusion. The effect of the scatterer is found to be very local as opposed to the case described in Fig. 7.

Conclusions

In the present study, fluid-solid interface response of the plate with inclusion submerged in fluid is investigated. It is found that the steady-state fluid-solid interface response is very sensitive upon the geometry and embedment depth of the inclusion as well as the frequency and the angle of the incident wave. In addition, the impedance contrast between the plate and the inclusion influences greatly the response. Finally, the presence of the half-space greatly changes the response.

From the transient response of a plate with a very hard inclusion and for vertical incidence, it is found that the presence of the inclusion is indicated very clearly by both the predominant and the non-predominant components of displacement. In the predominant component this is evident from the altered free-field near the inclusion and the scattered waves traveling away from

the inclusion. In the non-predominant component of the displacement, the scattered field is observed as the waves traveling at the plate-fluid interface with the P-wave velocity of the fluid. These waves are found to attenuate very slowly with increased distance from the scatterer. When the density of the fluid is significantly lower than that of the plate, the effect of multiple reflection at the plate surfaces is observed in the transient response. For this case, the effect of the scattering from the inclusion is observed only when the inclusion is significantly harder than the plate. Due to the significant presence of the free-field waves trapped in the plate, the effect of the scattered wave field is felt only locally and is not visible at farther distances from the inclusion.

Acknowledgments

This material is based upon work supported by the Office of Naval Research under Contract No. N00014-88-K-0157. The computations were done through a grant by the San Diego Super Computer Center at UC, San Diego. The authors would like to express their appreciation to Hossein Eshraghi for his critical comments in numerous discussions during the research on this paper.

References

[1] T. Kundu, A. K. Mal and R. D. Weglein, 'Calculation of the acoustic material signature of a layered solid', *J. Acoust. Soc. Am.*, **77**, 353-361 (1985).

[2] H. L. Bertoni and T. Tamir, 'Unified theory of Rayleigh-angle phenomena for acoustic beams at liquid-solid interfaces', *Appl. Phys.*, **2**, 157-172 (1973).

[3] D. B. Bogy and S. M. Gracewski, 'On the plane-wave reflection coefficient and nonspecular reflection of bounded beams for layered half-spaces underwater', *J. Acoust. Soc. Am.*, **74**, 591-599 (1983).

[4] D. B. Bogy and S. M. Gracewski, 'Nonspecular reflection of bounded acoustic beams from the liquid-solid interface of two elastic layers on a halfspace under water', *Int. J. Sol. Struct.*, **20**, 747-760 (1984).

[5] W. T. Thomson, 'Transmission of elastic waves through a stratified solid medium', *J.Appl. Phys.*, **21**, 89-93 (1950).

[6] N. A. Haskell, 'The dispersion of surface waves on multilayered media', *Bull. Seism. Soc. Am.*, **43**, 17-34 (1953).

[7] J. W. Dunkin, 'Computation of modal solutions in layered elastic media at high frequencies', *Bull. Seism. Soc. Am.*, **55**, 335-358 (1965).

[8] H. Schmidt and F. B. Jensen, 'A full wave solution for propagation in multilayered viscoelastic media with application to Gaussian beam reflection at fluid-solid interfaces', *J. Acoust. Soc. Am.*, **77**, 813-825 (1985).

[9] V. V. Varadan, T. A. K. Pillai and V. K. Varadan. 'Ultrasonic wave scattering by a subsurface flaw in joined fluid-solid half spaces', *J. Appl.Mech.*, **50**, 802-806 (1983).

[10] S. M. Gracewski and D. B. Bogy, 'Elastic wave scattering from an interface crack in a layered half space submerged in water: Part I:Applied tractions at the liquid-solid interface', *J. Appl. Mech.*, **53**, 326-332 (1986).

[11] S. M. Gracewski and D. B. Bogy, 'Elastic wave scattering from an interface crack in a layered half space submerged in water: Part II:Incident plane and bounded beams', *J. Appl. Mech.*, **53**, 333-338 (1986).

[12] W. D. Smith, 'The application of finite element analysis to body wave propagation problems', *Geophys. J. R. Astr. Soc.*, **42**, 747-768 (1975).

[13] A. Mita and W. Takanashi, 'Dynamic soil-structure interaction analysis by hybrid method', in *Boundary elements*, Proc. Fifth Int. Conf., Hiroshima, C. A. Brebbia, T. Futgami, and M. Tanaka, eds., Springer-Verlag, New York, 785-794 (1983).

[14] D.M. Cole, D.D. Kosloff and J.B. Minster. 'A numerical boundary integral equation method for elastodynamics. I', *Bull. Seism. Soc. Am.*, **68**, 1311-1357 (1978).

[15] Y. Niwa, T. Fukui and S. Hirose, 'An application of the integral equation method to two dimensional elastodynamics', in *Theoretical and Applied Mechanics* **28**, University of Tokyo Press, Tokyo, 281-290 (1980).

[16] M. Dravinski and T. K. Mossessian, 'On evaluation of the Green functions for harmonic line loads in a viscoelastic half-space', *Int. J. Num. Meth. Eng.*, **26**, 823-841 (1988).

[17] O. C. Zienkiewicz, D. W. Kelly and P. Bettess. 'The coupling of the finite element method and boundary solution procedures', *Int. J. Num. Meth. Eng.*, **11**, 355-375 (1977).

[18] Y. Niwa, M. Kitahara and S. Hirose. 'Elastodynamic problems for inhomogeneous bodies', *Boundary Elements*, Springer, Berlin, 751-763 (1983).

[19] A. P. Berg , 'A hybrid solution for wave propagation problems in regular media with bounded irregular inclusions, *Geophys. J. R. Astr. Soc.*, **79**, 3-10 (1984).

[20] T. K. Mossessian and M. Dravinski, 'Application of a hybrid method for scattering of P, SV and Rayleigh waves by near surface irregularities', *Bull. Seism. Soc. Am.*, **77**, 1784-1803 (1987).

[21] A. H. Shah, K. C. Wong and S. K. Datta, 'Single and multiple scattering of elastic waves in two dimensions', *J. Acoust. Soc. Am.*, **74**, 1033-1043 (1983).

[22] G. T. Schuster and L. C. Smith, 'Modeling scatterers embedded in plane-layered media by a hybrid Haskell-Thomson and boundary integral equation method', *J. Acoust. Soc. Am.*, **78**, 1387-1394 (1985).

[23] P. C. Waterman, 'New formulation of acoustic scattering', *J. Acoust. Soc. Am.*, **45**, 1417-1429 (1969).

[24] V. Varatharajulu (V. V. Varadan) and Y. H. Pao, 'Scattering matrix for elastic waves I. Theory', *J. Acoust. Soc. Am.*, **60**, 556-566 (1976).

[25] V. V. Varadan, 'Scattering matrix for elastic waves. II. Application to elliptic cylinders', *J. Acoust. Soc. Am.*, **63**, 1014-1024 (1978).

[26] V. V. Varadan and V. K. Varadan, 'Scattering matrix for elastic waves. II. Application to spheroids', **65**, 896-905 (1979).

[27] K. Aki and K. L. Larner, 'Surface motion of a layered medium having an irregular interface due to incident plane SH waves', *J.Geophys. Res.*, **75**, 933-954 (1970).

[28] M. Bouchon, 'Effect of topography on surface motion', *Bull. Seism. Soc. Am.*, **63**, 615-632 (1973).

[29] P-Y. Bard and M. Bouchon, 'The seismic response of sediment filled valleys. Part 1. The case of incident SH waves', *Bull. Seism. Soc. Am.*, **70**, 1263-1286 (1980).

[30] P-Y. Bard and M. Bouchon, 'The seismic response of sediment filled valleys. Part 2. The case of incident P and SV waves', *Bull. Seism. Soc. Am.*, **70**, 1921-1941 (1980).

[31] M. Bouchon and K. Aki, 'Near field of a seismic source in a layered medium with irregular interfaces', *Geophys. J. R. Astron. Soc.*, **50**, 669-684 (1977).

[32] V. Cerveny and R. Ravindra, *Theory of seismic head waves*, University of Toronto Press, Toronto (1971).

[33] P. Moczo, P-Y. Bard and I. Psenick, 'Seismic response of a two dimensional structure by the ray method', *J. Geophys.*, **62**, 38-49 (1987).

[34] F. J. Rizzo, D. J. Shippy and M. Rezayat, 'A BIE method for radiation and scattering of elastic waves in three dimensions', *Int. J. Num. Meth. Eng.* , **21**, 115-129 (1985).

[35] D. M. Boore, K. L. Larner and K. Aki. 'Comparasion of two independent methods for the solution of wave-scattering problems: Response of a sedimentary basin to vertically incident SH waves', *J. Geophys. Res.*, **76**, 558-559 (1971).

[36] P. K. Banerjee, S. Ahmad and G. D. Manolis. 'Transient elastodynamic analysis of three-dimensional problems by boundary element method', *Earthquake Eng. Struct. Dyn.*, **14**, 933-946 (1986).

[37] S. Kobayashi, 'Some problems of the boundary integral equation method in elastodynamics', in *Boundary Elements*, Springer, Berlin, 775-784 (1983).

[38] G. D. Manolis and D. E. Beskos, 'Dynamic stress concentration studies by boundary integrals and Laplace transform', *Int. J. Num. Meth. Eng.*, **17**, 573-599 (1981).

[39] Y. Niwa, S. Hirose, and M. Kitahara, 'Application of the boundary integral equation (BIE) method to transient response analysis of inclusions in a half-space', *Wave Motion*, **8**, 77-91 (1986).

[40] G. D. Manolis, 'A comparative study on three boundary element method approaches to problems in elastodynamics', *Int. J. Num. Meth. Eng.*, **19**, 73-91 (1983).

[41] D. E. Beskos, 'Boundary element methods in dynamic analysis', *Appl. Mech. Rev.*, **40**, 1-23 (1987).

[42] I. Herrera and F. J. Sabina, 'Connectivity as an alternative to boundary integral equations: Construction of bases', *Pro. Natl. Acad. Sci. U.S.A.*, **75**, 2059-2063 (1978).

[43] I. Herrera, 'Boundary methods: A criterion for completeness', *Pro. Natl. Acad. Sci. U.S.A.*, **77**, 4395-4398 (1984).

[44] F. J. Sanchez-Sesma, I. Herrera and J. Aviles, 'A boundary method for elastic wave diffraction: Application to scattering of SH waves by surface irregularities', *Bull. Seism. Soc. Am.*, **72**, 473-490 (1982).

[45] F. J. Sanchez-Sesma, M. A. Bravo and I. Herrera, 'Surface motion of topographical irregularities for incident P, SV and Rayleigh waves', *Bull. Seism. Soc. Am.*, **75**, 263-269 (1985).

[46] H. Eshraghi and M. Dravinski, 'Transient scattering of elastic waves by dipping layers of arbitrary shape', Part 1: Antiplane strain model', *Earthquake Eng. Struct. Dyn.* **18**, 397-415 (1989).

[47] H. Eshraghi and M. Dravinski, 'Transient scattering of elastic waves by dipping layers of arbitrary shape', Part 2: Plane strain model', *Earthquake Eng. Struct. Dyn.* **18**, 417-434 (1989).

[48] K. Aki and P. G. Richards, *Quantitative Seismology Theory and Methods*, W.H. Freeman and Company, San Francisco, 1 (1980).

[49] G. Dahlquist and A. Björck, *Numerical Methods*, Prentice-Hall, Inc., New Jersey (1974).

[50] R. Keshavamurthy, *Ph. D. Thesis*, Dept. of Mech. Eng., University of Southern California, Los Angeles (1992).

[51] N. H. Ricker, *Transient waves in visco-elastic media*, Elsevier Scientific Publishing Co., Amsterdam, Holland (1977).

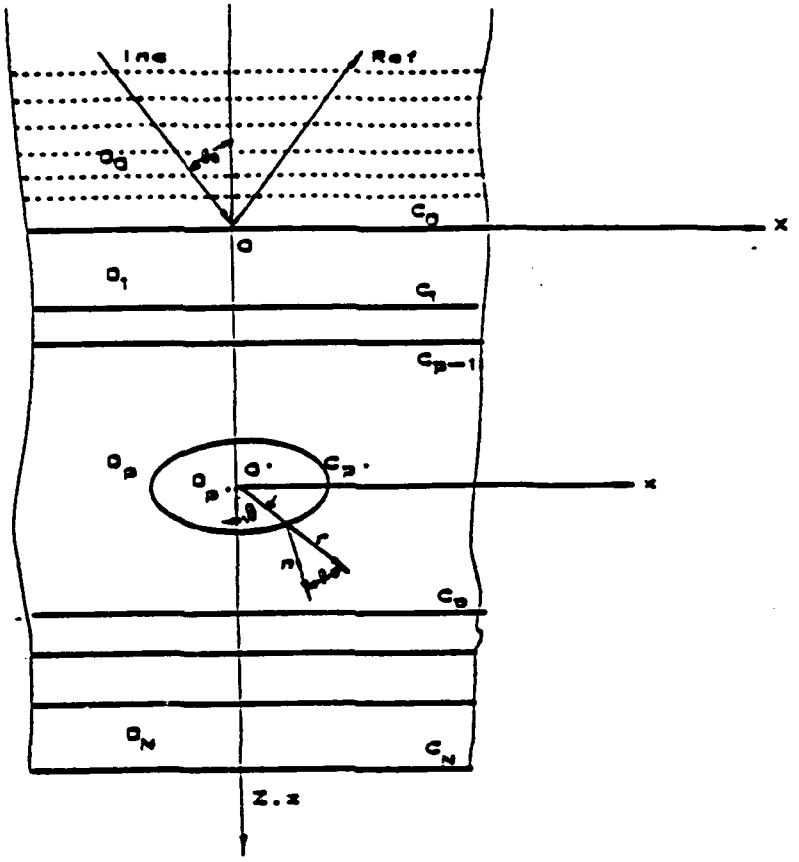

Figure 1:

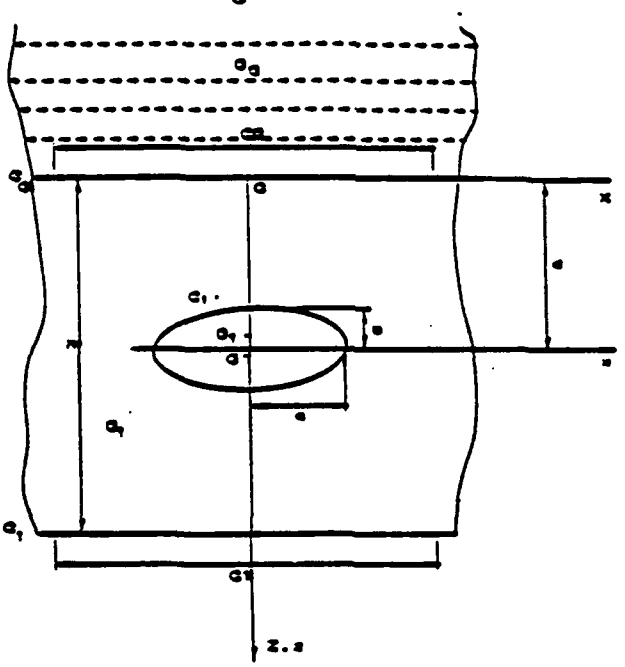

Figure 2:

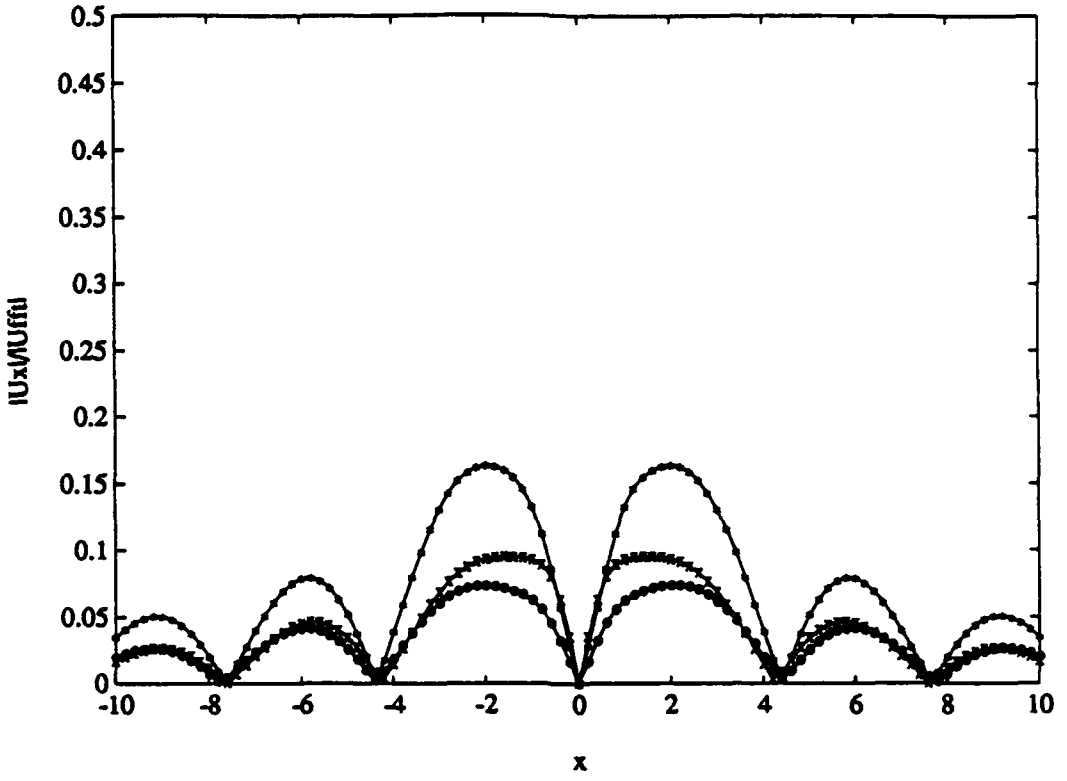
0.5
0.45
0.4
0.35
0.3
0.25
0.2
0.15
0.1
0.05
0
|Ux|/|Uffi|
-10
-8
-6
-4
-2
0
2
4
6
8
10
x

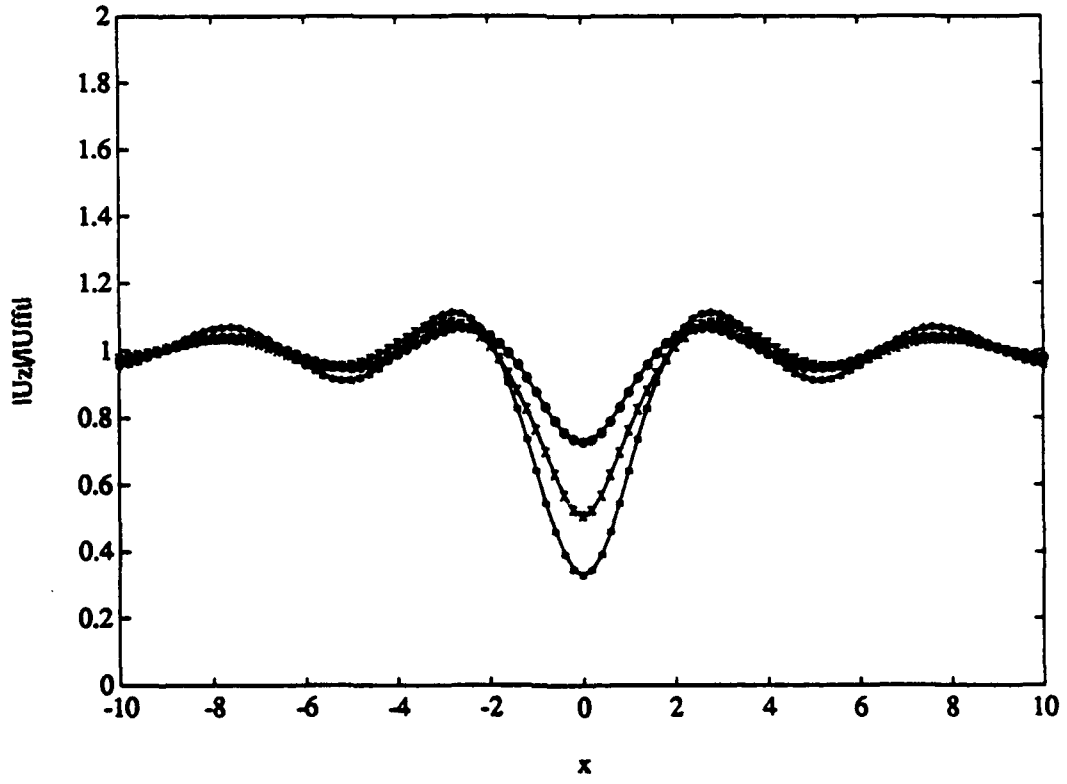
2
1.8
1.6
1.4
1.2
1
0.8
0.6
0.4
0.2
0
|Uz|/|Uffi|
-10
-8
-6
-4
-2
0
2
4
6
8
10
x

Figure 3:

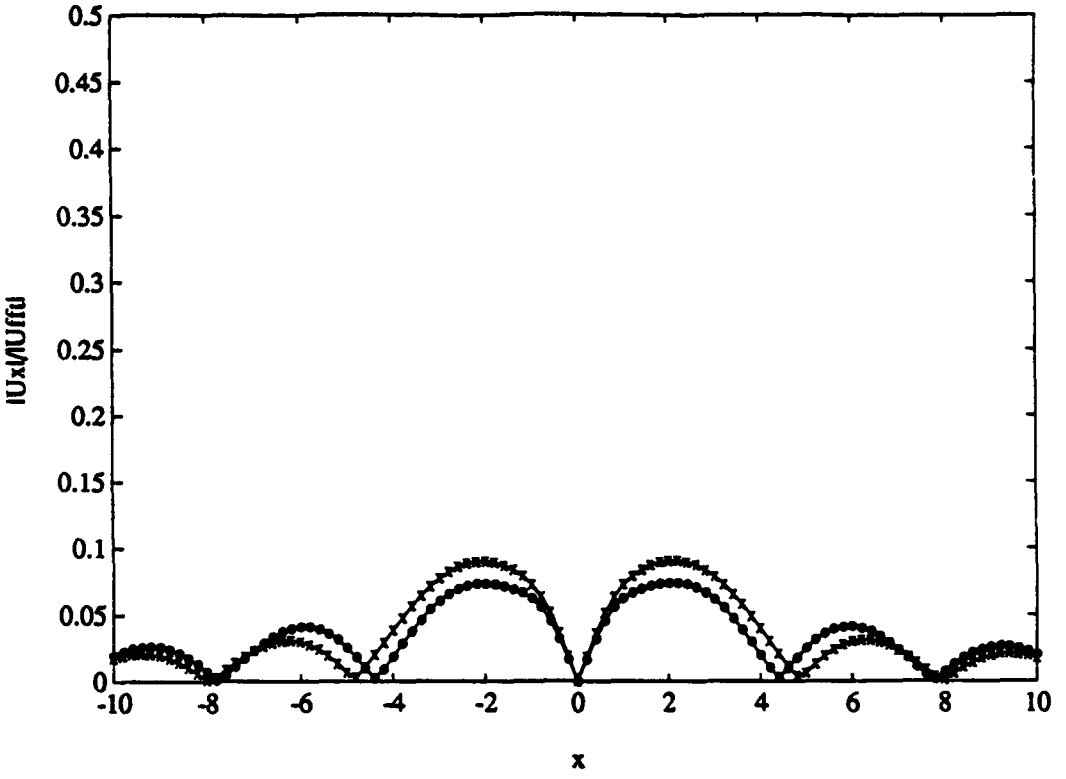
0.5
0.45
0.4
0.35
0.3
0.25
0.2
0.15
0.1
0.05
0
-10
-8
-6
-4
-2
0
2
4
6
8
10
x
|Ux|/|Uffl|

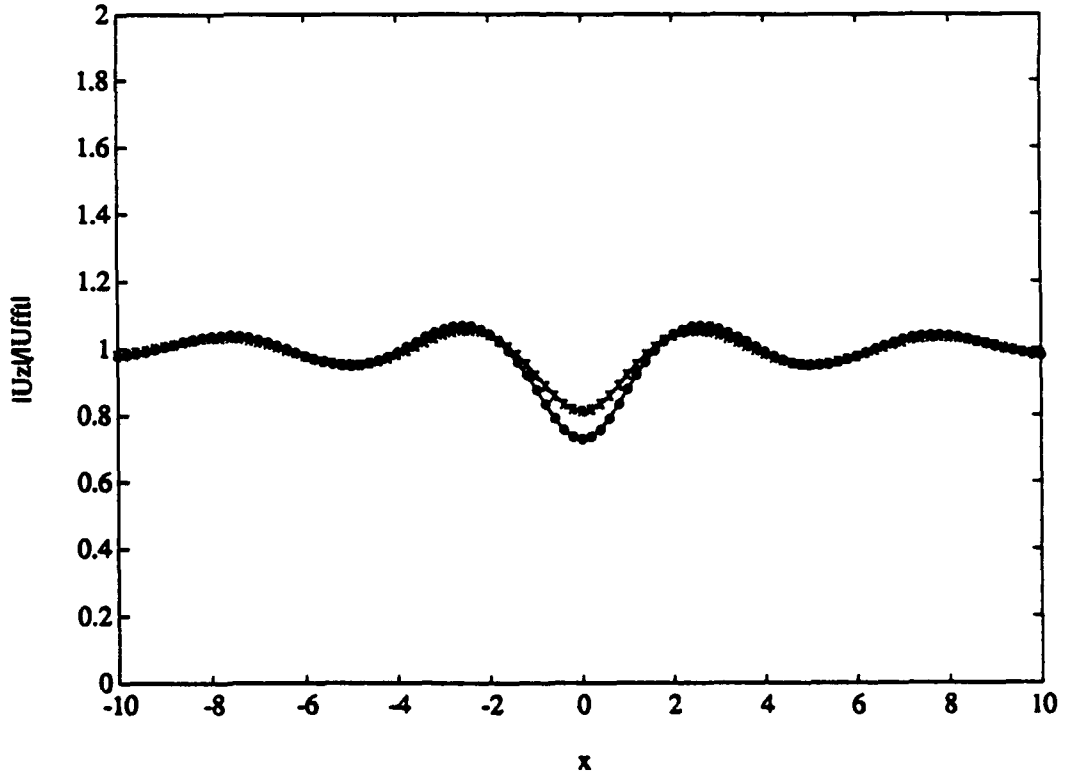
2
1.8
1.6
1.4
1.2
1
0.8
0.6
0.4
0.2
0
-10
-8
-6
-4
-2
0
2
4
6
8
10
x
|Uz|/|Uffl|

Figure 4:

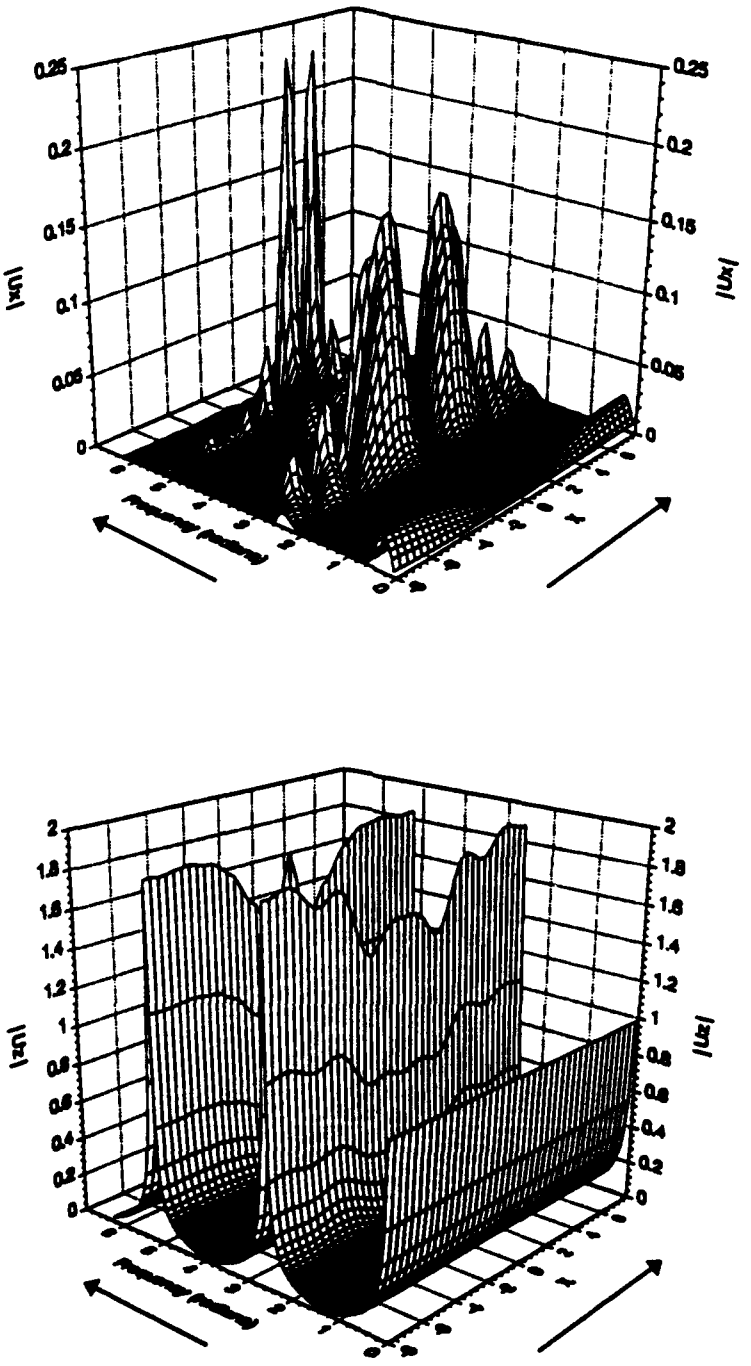

Figure 5:

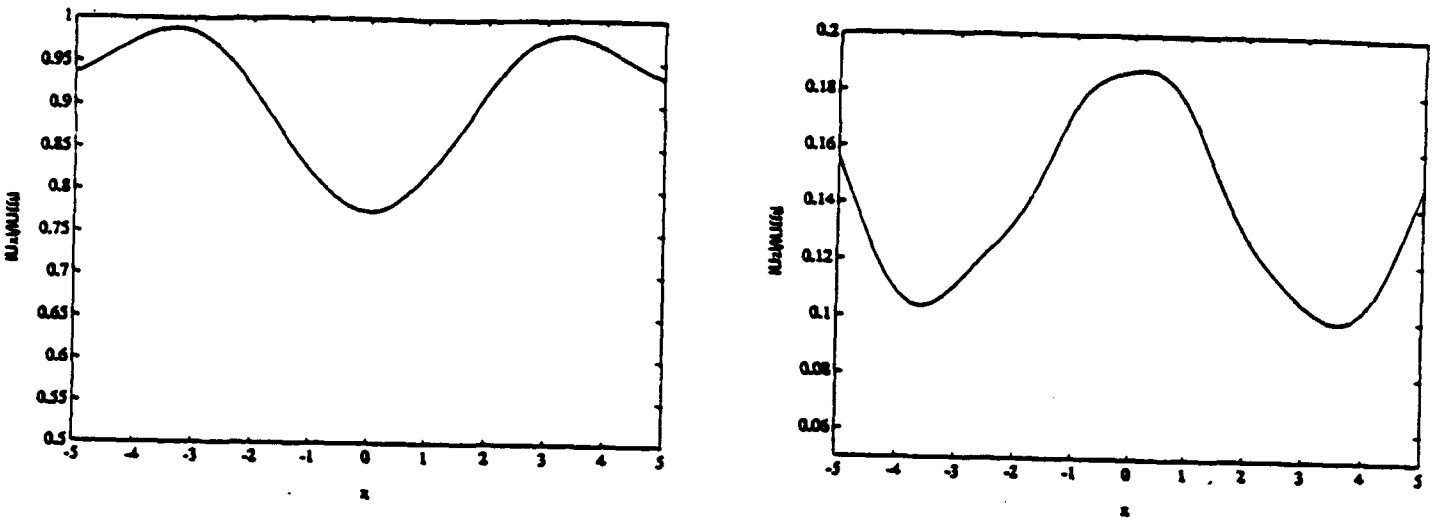

(a)

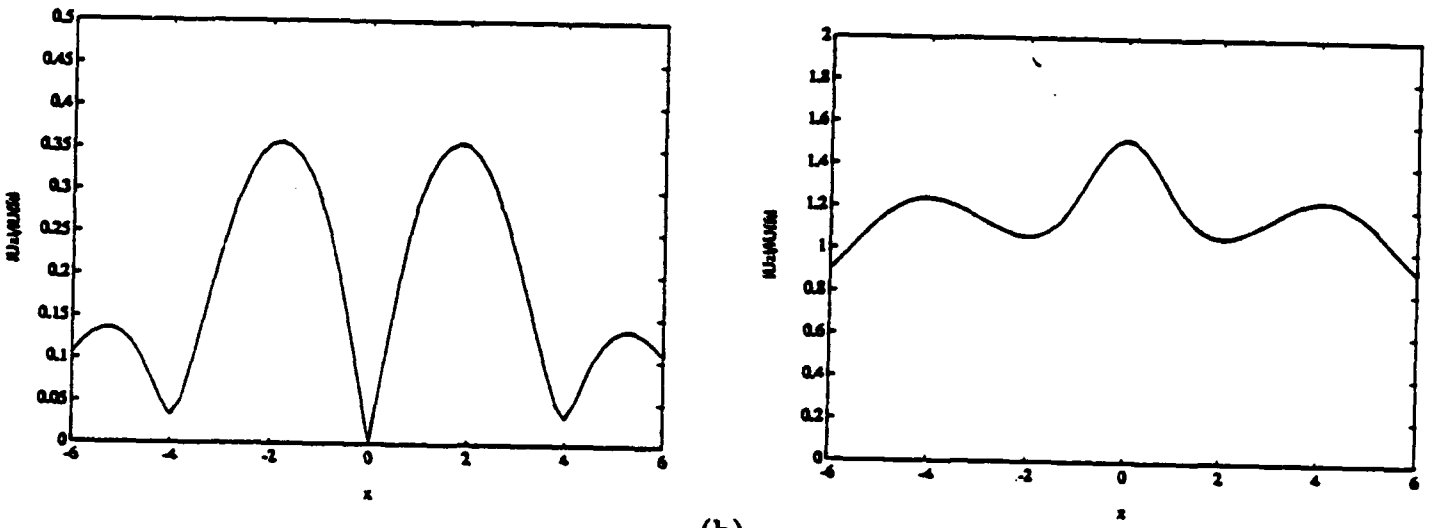

(b)

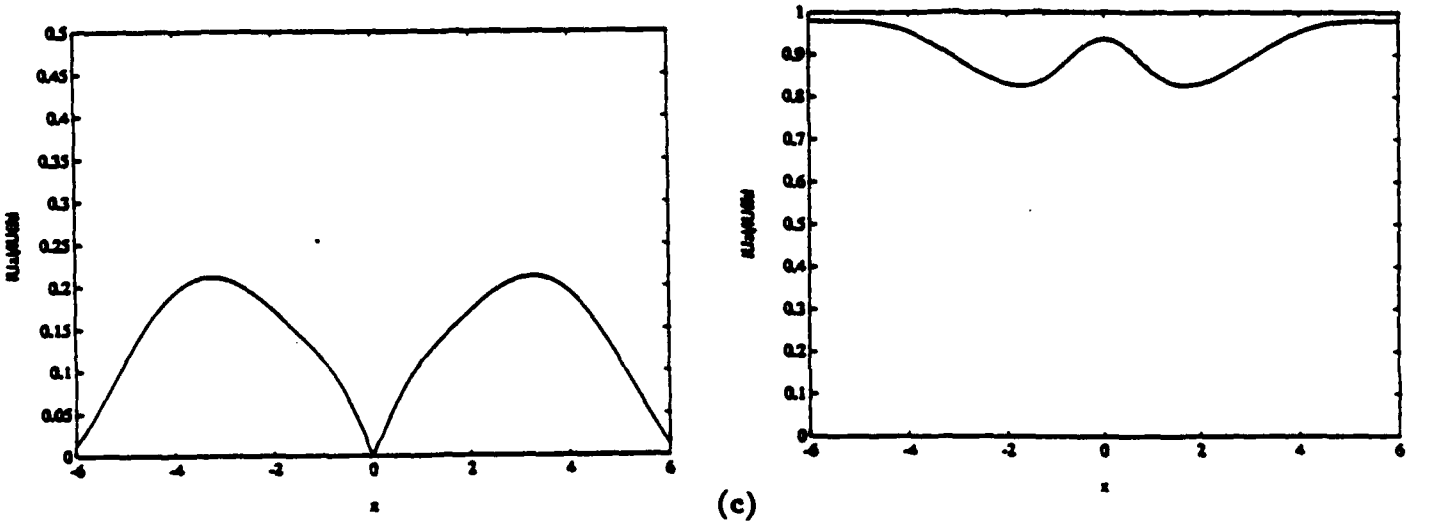

(c)

Figure 6:

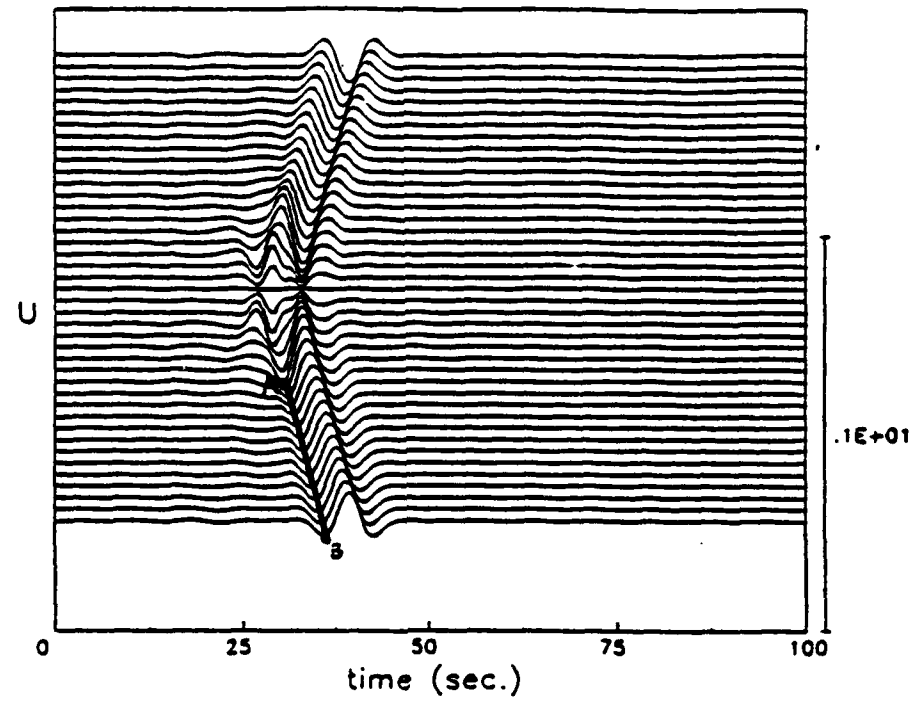

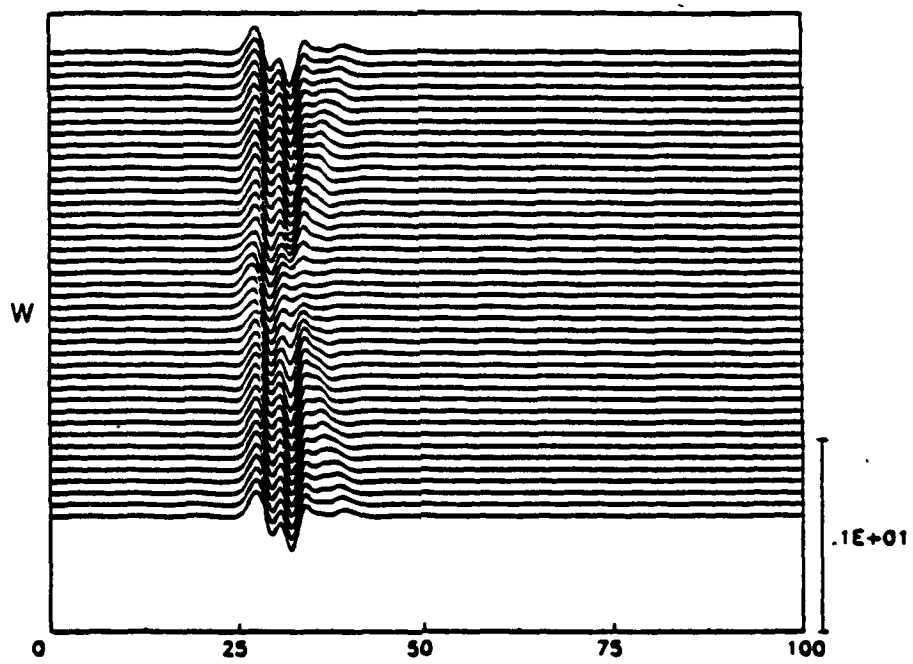

Figure 7:

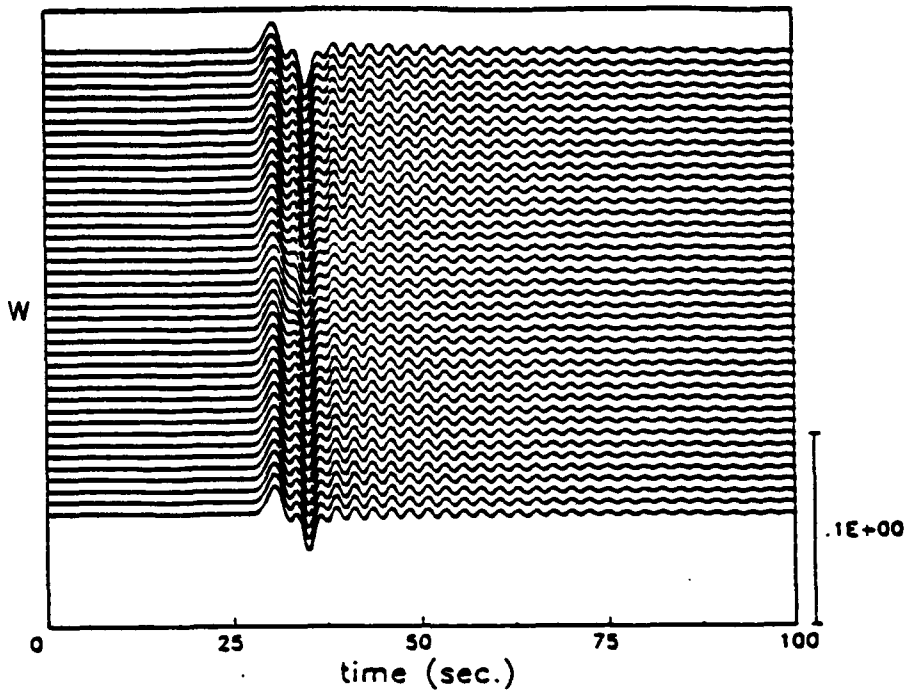

Figure 8:

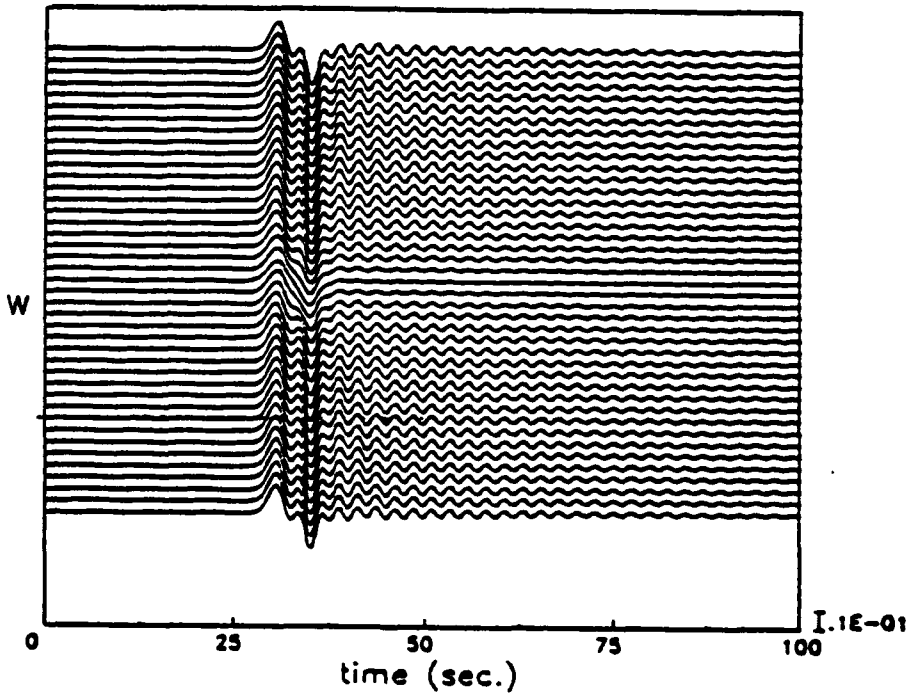

Figure 9:

List of Figures

Elastic Wave Scattering by an Inclusion in a Multilayered Medium Submerged in Fluid-Three Dimensional Model

RAMDASS KESHAVAMURTHY and MARIJAN DRAVINSKI

Department of Mechanical Engineering, University of Southern California, Los Angeles, CA 90089-1453, U.S.A.

Abstract

Three dimensional response of plane multilayerd media enclosing an elastic inclusion of arbitrary shape and submerged in fluid is investigated. The steady-state free-field response is modeled by the Thomson-Haskell method using delta-matrix modification and the scattered wave field by a boundary method. The transient response is evaluated using the Fourier synthesis. Numerical results are presented for a single layer plate with an ellipsoidal inclusion.

The steady-state results show that the response along the fluid-solid interface is sensitive to the aspect ratio and location of the inclusion, impedance contrast and the angle of incidence. In addition, the results of the 3D analysis for the non-axisymmetric problem indicate significant variation of the radial and azimuthal displacement components with the change in the azimuthal angle. Comparison of the 2D and 3D models indicates that for the harder inclusion, both the models show similar qualitative trends in the transient and steady state responses. However, for a softer inclusion, the steady state responses of the two models are found to differ significantly from each other. The transient studies clearly indicate the horizontal wave traveling at the solid-fluid interface with the acoustic wave velocity of the fluid. The effect of the scatterer on the vertical displacement is found to be significant only in the vicinity of the inclusion.

Introduction

This paper is an extension of a similar study for a plain strain model by Keshavamurthy and Dravinski [1]. A detailed literature review of the works relating to the two dimensional scattering can be found in the paper [1].

The literature review in the present paper is concerned only with the three dimensional elastic wave scattering problems.

Among the earlier studies of three dimensional scattering of elastic waves, the works of Day [2], Aspel [3], Sanchez-Sesma [4] and Lee [5] are of special importance. Day [2] used a finite element (FE) technique to study the scattering of seismic waves by an axisymmetric cone-shape sedimentary basin. Aspel [3] used a boundary integral equation (BIE) method to study soil-structure interactions for axisymmetric scatterers. Sanchez-Sesma [4] studied the diffraction of elastic waves by three dimensional surface irregularities by the boundary method. Lee [5] used the wave function expansion method to study three-dimensional diffraction of plane P, SV and SH waves by a hemispherical alluvial valley. Niwa and Hirose [6] formulated a BIE method to solve the scattering problem of elastic waves by a non-axisymmetric cavity or crack in a three dimensional half-space. Paskaramoorthy et al. [7] employed the hybrid FE-wave function expansion method to study scattering of elastic waves by an axisymmetric scatterer embedded in an isotropic elastic medium. All the papers cited so far deal with steady state problems. Lee and Langston [8] studied the transient response of a circular basin using the ray method, while Sanchez-Sesma et al. [9] studied the response of a 3D axisymmetric valley by the boundary method. Eshraghi and Dravinski [10] used the boundary method to solve the transient scattering by three dimensional non-axisymmetric dipping layers. Mossessian and Dravinski [11] employed the hybrid FE-BIE method to study the elastic scattering by three dimensional irregularities of arbitrary shape. Boström and Karlsson [12] studied three dimensional response to point-force excitation of elastic plate with an embedded cavity by the T-matrix approach. Varadan et al. [13] studied the three dimensional ultrasonic wave propagation by a submerged flaw in joined fluid-solid half-space by the T-matrix approach.

In the present study, a hybrid Thomson-Haskell and boundary method is employed to study the steady state response of an inclusion in a plane multilayered medium in fluid. The Thomson-Haskell formulation is recast in terms of delta matrices. The transient response is evaluated by using the fast Fourier transforms. Details of the procedure can be found in the paper [1].

This paper is divided into several parts. After the introduction, the statement of the problem is presented. Then, the steady state solution of the problem is given. Next, numerical results are discussed for both the steady state and transient cases, followed by the conclusions.

Statement of the problem

The geometry of the problem is shown by the Fig. 1. The model consists of a multilayered infinite elastic half-space (or a plate) with an inclusion within a layer. The medium is surrounded by inviscid fluid on one side. The Cartesian and spherical coordinate systems with the origin at O' are denoted by (x,y,z) and (r, θ, ϕ), respectively. The Cartesian coordinate system with origin at O is represented by (X, Y, Z). The domains are designated by $D_j (j = 0, 1, \ldots, N)$ and the boundaries by $C_j (j = 0, 1, \ldots, N)$. Domain D_0 denotes the fluid half-space while C_0 denotes the interface between the fluid and the first layer. The inclusion domain and the boundary in the p^{th} layer are designated by $D_{p'}$ and $C_{p'}$, respectively. Summation over repeated indices is understood. Underlined indices indicate that the summation is being suppressed. Material of the media is assumed to be linearly elastic, homogeneous and isotropic. The fluid half-space is subjected to an oblique incident plane harmonic wave. The off vertical and azimuthal angles of incidence are denoted by θ_0 and ϕ_0, respectively (see Fig. 2a). The equation of motion in terms of displacement potentials is given by [14]

$$M[k_{\alpha \underline{j}}]\varphi_{\underline{j}}(\mathbf{x}, \omega) = 0; j = 0, 1, 2, \ldots, N, p' \tag{1}$$

$$M[k_{\beta \underline{j}}]\psi_{\underline{j}}(\mathbf{x}, \omega) = 0; j = 1, 2, \ldots, N, p' \tag{2}$$

$$M[k_{\beta \underline{j}}]\chi_{\underline{j}}(\mathbf{x}, \omega) = 0; j = 1, 2, \ldots, N, p' \tag{3}$$

where

$$\begin{aligned} M[*] &= \nabla^2 + (*)^2 \\ k_{\alpha j} &= \frac{\omega}{\alpha_j}; k_{\beta j} = \frac{\omega}{\beta_j}; \alpha_j^2 = \frac{\lambda_{\underline{j}} + 2\mu_{\underline{j}}}{\rho_{\underline{j}}}; \beta_j^2 = \frac{\mu_{\underline{j}}}{\rho_{\underline{j}}}. \end{aligned} \tag{4}$$

Here, φ_j denotes the P-wave potential while ψ_j and χ_j denote the shear wave potentials, x is the position vector, and ω is the circular frequency. In addition, α_j and β_j denote the dilatational and shear wave velocities, respectively while $k_{\alpha j}$ and $k_{\beta j}$ are the corresponding wavenumbers. Finally, ρ_j, and μ_j, λ_j are the density, and Lame's constants of the j^{th} layer, respectively. For

convenience, the wavenumber in fluid $k_{\alpha 0}$ is sometimes denoted by k_f.

A system of unit basis ($\mathbf{e_r}, \mathbf{e_\theta}, \mathbf{e_\phi}$) is defined for spherical coordinates (r, θ, ϕ) according to Fig. 2b. For the same coordinate system the displacement vector in the j^{th} layer $\mathbf{u}_j$ can be expressed in terms of three displacement components $(u_{rj}, u_{\theta j}, u_{\phi j})$ according to

$$\mathbf{u}_j = \nabla\varphi_j + \nabla(r\psi_j) \times \mathbf{e_r} + \ell\nabla \times \nabla \times (r\chi_j \mathbf{e_r}) \qquad (5)$$

$$\mathbf{x} \in D_j,\ j=0,1,\ldots,N,p'.$$

where ℓ is a scalar factor to give potentials the same dimension. The Cartesian displacement components of vector $\mathbf{u_j}$ are denoted by (u_j, v_j, w_j). Similarly, the traction vector $\mathbf{T_j}$ has components (T_{xj}, T_{yj}, T_{zj}) and $(T_{rj}, T_{\theta j}, T_{\phi j})$ in the Cartesian and spherical coordinate systems, respectively.

The boundary conditions on the free surface of the plate are given by

$$\mathbf{T}_N^+(\mathbf{x}, \omega) = 0; \quad z = z_N \qquad (6)$$

For multilayer half-space, instead of Eqn. (6), radiation condition should be applied for the half-space. The continuity conditions along the solid-fluid interface C_0 are specified to be

$$w_0^+(\mathbf{x}, \omega) = w_1^-(\mathbf{x}, \omega) \qquad (7)$$

$$T_{z1}^-(\mathbf{x}, \omega) = 0 \qquad (8)$$

$$T_{y1}^-(\mathbf{x}, \omega) = 0 \qquad (9)$$

$$T_{z0}^+(\mathbf{x}, \omega) = T_{z1}^-(\mathbf{x}, \omega) \qquad (10)$$

The continuity conditions along the interfaces $C_j (j = 1, \ldots, N-1)$ are given by

$$\mathbf{u}_{j-1}^+(\mathbf{x}, \omega) = \mathbf{u}_j^-(\mathbf{x}, \omega) \qquad (11)$$

$$\mathbf{T}_{j-1}^+(\mathbf{x}, \omega) = \mathbf{T}_j^-(\mathbf{x}, \omega) \qquad (12)$$

In the Eqns. (6-12), '+' and '-' signs refer to the interface being approached from below and above, respectively.

The continuity conditions along the inclusion boundary $C_{p'}$ are given by

$$\mathbf{u}_{p'}^+(\mathbf{x}, \omega) = \mathbf{u}_{p'}^-(\mathbf{x}, \omega) \qquad (13)$$

$$\mathbf{T}_p^+(\mathbf{x},\omega) \;=\; \mathbf{T}_{p'}^-(\mathbf{x},\omega) \tag{14}$$

where '+' and '-' signs refer to the interface $C_{p'}$ being approached from outside and inside the inclusion, respectively.

The incident field is a plane wave in the fluid given by

$$\varphi^{inc} = (-i/k_f)e^{i(k_f(\mathbf{n}.\mathbf{x})-\omega t)} \tag{15}$$

where n is the unit normal to the plane of the incident wave and x is the position vector, respectively (see *Fig. 2a*). The factor $(-i/k_f)$ is introduced for convenience.

Steady state solution of the problem

The solution is sought as a superposition of the free-field and scattered wave fields according to

$$\mathbf{u}_j = \mathbf{u}_j^{ff} + \mathbf{u}_j^{s};\ \mathbf{x} \in D_j; j = 0, 1, \ldots, N \tag{16}$$

$$\mathbf{u}_{p'} = \mathbf{u}_{p'}^{s};\ \mathbf{x} \in D_{p'} \tag{17}$$

where the superscripts 'ff' and 's' denote the free-field and scattered wave fields, respectively.

Free-field solution

The free-field problem is solved by the Thomson-Haskell method with delta matrix modification. The problem is initially solved for the off-vertical angle of incidence of θ_0 in the coordinate system (X', Y', Z') shown in the Fig. 1a. The procedure is outlined in [1]. The displacement and stress fields are then transformed to the coordinate system (X,Y,Z) shown in Fig. 2a by rotating about the Z-axis by the azimuthal angle of incidence ϕ_0.

Scattered wave field solution

For the scattered field evaluation, the origin is shifted inside the inclusion with the spherical coordinate system (r, θ, ϕ) used for the stress and displacement field evaluations (see Fig. 2b). The scattered field for the fluid is taken

to be of the form

$$\begin{aligned}\varphi_0^s &= a_{nm}^{\varphi 0}\, h_n^{(1)}(k_{\alpha 0} r)\, P_n^m(\cos\theta)\cos m\phi \\ &+ b_{nm}^{\varphi 0}\, h_n^{(1)}(k_{\alpha 0} r)\, P_n^m(\cos\theta)\sin m\phi \end{aligned} \tag{18}$$

$m \le n,\ M_0 \le N_0,\ \mathbf{x} \in D_0.$

$$\psi_0^s = 0 \tag{19}$$

$$\chi_0^s = 0. \tag{20}$$

For the j^{th} layer the scattered waves are assumed to be of the form

$$\begin{aligned}\varphi_j^s &= c_{nm}^{\varphi j}\, h_n^{(2)}(k_{\alpha j} r)\, P_n^m(\cos\theta)\cos m\phi \\ &+ d_{nm}^{\varphi j}\, h_n^{(2)}(k_{\alpha j} r)\, P_n^m(\cos\theta)\sin m\phi \\ &+ e_{nm}^{\varphi j}\, h_n^{(1)}(k_{\alpha j} r)\, P_n^m(\cos\theta)\cos m\phi \\ &+ f_{nm}^{\varphi j}\, h_n^{(1)}(k_{\alpha j} r)\, P_n^m(\cos\theta)\sin m\phi \end{aligned} \tag{21}$$

$m \le n,\ M_j \le N_j,\ \mathbf{x} \in D_j,\ j = 1,\ldots,N (N-1, \text{for the half-space}).$

$$\begin{aligned}\psi_j^s &= c_{nm}^{\psi j}\, h_n^{(2)}(k_{\beta j} r)\, P_n^m(\cos\theta)\cos m\phi \\ &+ d_{nm}^{\psi j}\, h_n^{(2)}(k_{\beta j} r)\, P_n^m(\cos\theta)\sin m\phi \\ &+ e_{nm}^{\psi j}\, h_n^{(1)}(k_{\beta j} r)\, P_n^m(\cos\theta)\cos m\phi \\ &+ f_{nm}^{\psi j}\, h_n^{(1)}(k_{\beta j} r)\, P_n^m(\cos\theta)\sin m\phi \end{aligned} \tag{22}$$

$m \le n,\ M_j \le N_j,\ \mathbf{x} \in D_j,\ j = 1,\ldots,N (N-1, \text{for the half-space}).$

$$\chi_j^s = c_{nm}^{\chi j}\, h_n^{(2)}(k_{\beta j} r)\, P_n^m(\cos\theta)\cos m\phi$$

$$+ d_{nm}^{x_j} h_n^{(2)}(k_{\beta j} r) P_n^m(\cos\theta) \sin m\phi$$

$$+ e_{nm}^{x_j} h_n^{(1)}(k_{\beta j} r) P_n^m(\cos\theta) \cos m\phi$$

$$+ f_{nm}^{x_j} h_n^{(1)}(k_{\beta j} r) P_n^m(\cos\theta) \sin m\phi \qquad (23)$$

$m \le n$, $M_j \le N_j$, $x \in D_j$, $j = 1,\ldots,N(N-1, \text{for the half-space})$.

If an elastic half-space is present, we have,

$$\varphi_N^s = e_{nm}^{\varphi N} h_n^{(1)}(k_{\alpha N} r) P_n^m(\cos\theta) \cos m\phi + f_{nm}^{\varphi N} h_n^{(1)}(k_{\alpha N} r) P_n^m(\cos\theta) \sin m\phi \qquad (24)$$

$m \le n$, $M_N \le N_N$, $x \in D_N$.

$$\psi_N^s = e_{nm}^{\psi N} h_n^{(1)}(k_{\beta N} r) P_n^m(\cos\theta) \cos m\phi + f_{nm}^{\psi N} h_n^{(1)}(k_{\beta N} r) P_n^m(\cos\theta) \sin m\phi \qquad (25)$$

$m \le n$, $M_N \le N_N$, $x \in D_N$.

$$\chi_N^s = e_{nm}^{\chi N} h_n^{(1)}(k_{\beta N} r) P_n^m(\cos\theta) \cos m\phi + f_{nm}^{\chi N} h_n^{(1)}(k_{\beta N} r) P_n^m(\cos\theta) \sin m\phi \qquad (26)$$

$m \le n$, $M_N \le N_N$, $x \in D_N$.

Within the inclusion we have,

$$\varphi_{p'}^s = g_{nm}^{\varphi p'} j_n(k_{\alpha p'} r) P_n^m(\cos\theta) \cos m\phi + h_{nm}^{\varphi p'} j_n(k_{\alpha p'} r) P_n^m(\cos\theta) \sin m\phi \qquad (27)$$

$m \le n$, $M_{p'} \le N_{p'}$, $x \in D_{p'}$.

$$\psi_{p'}^s = g_{nm}^{\psi p'} j_n(k_{\beta p'} r) P_n^m(\cos\theta) \cos m\phi + h_{nm}^{\psi p'} j_n(k_{\beta p'} r) P_n^m(\cos\theta) \sin m\phi \qquad (28)$$

$m \leq n, \quad M_{p'} \leq N_{p'}, \quad \mathbf{x} \in D_{p'}.$

$$\chi^s_{p'} = g^{\mathbf{x}\mathbf{p}'}_{nm}\, j_n(k_\beta \mathbf{p}' r)\, P^m_n(cos\ \theta)\, cos\ m\phi + h^{\mathbf{x}\mathbf{p}'}_{nm}\, j_n(k_\beta \mathbf{p}' r)\, P^m_n(cos\ \theta)\, sin\ m\phi \tag{29}$$

$m \leq n, \quad M_{p'} \leq N_{p'}, \quad \mathbf{x} \in D_{p'}$

where $h^{(1)}_n$ and $h^{(2)}_n$ are the spherical Hankel functions of the first and second kind, respectively, j_n is the spherical Bessel function of the first kind, $P^m_n(cos\ \theta)$ is the associate Legendre polynomial, a_{nm} through h_{nm} are unknown coefficients, and N and M are the orders of expansions. The wave functions in Eqns. (18-29) are solutions of the equations of motion (Eqns. (1-3)). In addition, the scattered wave field in the fluid and the elastic half-spaces consists of the outgoing waves only while the scattered field in the plate consists of both incoming and outgoing waves. Inside the inclusion, the wave field consists of standing waves. As indicated earlier, in Eqns. (18-29), summation over repeated indices 'm' and 'n' is understood.

Evaluation of expansion coefficients

The unknown coefficients of the scattered wave field are determined by imposing the boundary and the continuity conditions given by Eqns. (6-14). These conditions are imposed at the L_j points along the boundaries $C_{p'}$ and $C_j, j = 0, 1 \ldots N (N-1$, for the half-space) resulting in a system of linear equations of the form

$$\mathbf{Ga} = \mathbf{f}. \tag{30}$$

Here **a** contains all the unknown expansion coefficients, vector **f** involves the free-field displacements and tractions, and **G** consists of the wave functions and their derivities evaluated along the boundaries. The size of the matrix **G** is (S×K), where S>K. Hence Eqn. (30) is solved in the least square-sense. Once the expansion coefficients are known, the displacement and the stress fields can be evaluated throughout the media.

Numerical results

This section describes the steady state and transient response for a single layered plate with an ellipsoidal inclusion. The steady state response is presented for both axisymmetric and non-axisymmetric case. The transient response is shown for the axisymmetric case.

These models incorporate most of the physical characteristics of the problem while keeping the computation to a minimum. The geometry of the model is shown for a single plate in Fig. 3a. The plate thickness and the inclusion depth are denoted by 'h' and 'd', respectively. The principal axes of the ellipsoidal inclusion are denoted by 'a', 'b' and 'c'. The radii on the top and bottom plate boundaries, along which the continuity and boundary conditions are imposed, are taken to be to be 'R0' and 'R1', respectively (see Fig. 3a). The orders of expansion of the spherical Hankel functions for the fluid, plate, and the inclusion are denoted by N_0, N_1 and $N_{1'}$, respectively. The azimuthal orders of expansion for the fluid, plate, and the inclusion are denoted by M_0, M_1 and $M_{1'}$, respectively. Number of collocation points along the solid-fluid interface and the free surface of the plate are taken to be L_0 and L_1, respectively. For the inclusion boundary the number of collocation points is denoted by $L_{1'}$. The density, shear modulus and shear wave velocity of the plate are taken to be unity. All spatial variables are normalized with respect to the major principal axis of the ellipsoidal inclusion which is assumed to be unity. For convenience, dimensionless frequency Ω is defined as the ratio of the maximum width of the inclusion to the wavelength of the shear wave in the layer enclosing the inclusion. The displacement field at the surface is referred to in the cylindrical (r, ϕ, z) coordinate system with the origin at (X=Y=Z=0) (see Fig. 3b.). The radial, azimuthal and vertical displacement amplitudes are denoted by $|Ur|$, $|U\phi|$ and $|Uz|$, respectively. The total free-field displacement used for normalization is defined as $|Ufft| = \sqrt{(|Uffx|^2 + |Uffy|^2 + |Ufz|^2)}$, where $|Uffx|$, $|Uffy|$ and $|Ufz|$ are the free-field displacement amplitudes in the x,y and z directions, respectively. The scattered wave field radial and vertical displacement amplitudes are denoted by $|Ur(scatt)|$ and $|Uz(scatt)|$, respectively.

Steady state response

This section describes the steady state vertical response of the plate with an ellipsoidal inclusion. First, convergence tests are conducted to fix various problem parameters. Finally, the steady state results for the single plate model are discussed.

Convergence and testing of results

Tests are conducted in order to determine the orders of expansion 'M' and 'N' (see Eqns. (18-29)) required for convergence of results in each domain. In addition, maximum radii of the plate boundary along which the continuity and boundary conditions are imposed are also determined. The convergence of results has been established by observing the change in scattered wave displacement amplitudes at the solid-fluid interface with change in the value of the parameter under consideration. The numerical results are accepted as the final ones if the difference between two successive calculations is judged to be sufficiently small for an increase in the parameter under consideration.

In addition to the convergence studies, the formulation was verified for the zero scattering condition where the material of the inclusion is the same as that of the plate. The model was also tested for axisymmetric response. Here the azimuthal orders of expansion $M > 0$ are also included even though M=0 is sufficient for axisymmetric problems. The response was found to be perfectly axisymmetric.

The details of convergence and testing can be found in [15]. Only the final parameters chosen for convergent results have been indicated in the respective figures.

Axisymmetric response

Axisymmetric response of a plate with an inclusion is studied for different impedance contrasts. As in the two dimensional problem, two cases are considered: Inclusion being stiffer than the plate and the plate being stiffer than the inclusion. Figure 4 summerizes the steady state response of a stiff ellipsoidal inclusion to a vertical incidence for different sizes of the inclusion. The geometry is always axisymmetric about the vertical axis. The vertical and radial displacement amplitudes of the plate are normalized with respect to

the total free-field displacement. From the vertical component of displacement in Fig. 4, the scattered field is found to interfere destructively with the free-field near the inclusion. This is indicated by the dip in the total field above the inclusion. As to be expected, the vertical scattered field has the greatest influence when a=b=c=1 and least when a=b=1,c=0.5. Figure 4 also shows the influence of the scatterer on the radial component of motion. The study concerning the effect of the inclusion depth on the surface displacements is shown in the Fig. 5. As expected, the effect of the scattered field on the vertical displacement is found to diminish with increase in depth.

Figure 6 refers to the case of a soft inclusion in a stiff medium. The vertical displacement shows a dip near the scatterer indicating a destructive interference. The effect of the scatterer on the vertical displacement is found to be a little less pronounced than in the case of stiffer inclusion. The radial displacement on the other hand is significantly higher than for the stiffer inclusion (Compare Figs. 6 and 4).

Non-axisymmetric response

The non-axisymmetric response of a plate with a stiff inclusion is studied for two cases: Off vertical incidence with an axisymmetric inclusion and vertical incidence with a non-axisymmetric inclusion.

Figure 7 depicts the response of a stiff spherical inclusion in a softer plate to an off vertical angle of incidence. The response is shown along the mutually perpendicular x and y-axes, respectively. The radial components of displacement along these axes are indicated by subscripts 'x' and 'y', respectively. Fig. 7a shows the response along the x-axis. From the figure, along the x-axis, the radial scattered wave field is found to interact destructively over the inclusion. The vertical scattered wave displacement, on the other hand, indicates constructive interference. This is in contrast to the response to a vertical incidence (compare Figs. 4 and 7a). Due to the off-vertical incidence, a strong free-field is present in the radial component of the displacement. The displacement field is nearly identical on either side of the mid point for small off vertical angle of incidence. Similar trend was observed for the 2D case (compare Figs. 6a of [1] and 7a). Fig. 7b shows the response along the y-axis. The problem is symmetric about the x-axis as ϕ_0=0. Hence the radial and vertical displacement amplitudes are found to be symmetric about the mid point. In addition, the radial displacement, which is entirely

due to scattering, is found to be zero at the mid point. Along the y-axis, the vertical scattered wave field is found to interfere constructively with the free-field over the inclusion. These studies indicate that the off-vertical incidence and the azimothal orientation of the observation point, relative to the incident wave, greatly influence the motion at the solid-fluid interface.

Figure 8 shows the steady state response of a stiff ellipsoidal inclusion for a vertical incidence. In the Fig. 8, the variations of the radial, azimuthal and vertical displacements are plotted against the surface coordinates over the first quadrant of the solid-fluid interface. Due to the bi-axial symmetry of the problem about x and y-axes, the displacement amplitudes are similar over the other quadrants. The radial lines on the mesh surface of the Fig. 8 correspond to ϕ increments of 10°. Hence the figure displays variation of the displacements with change in the azimuthal angle of observation ϕ. From the Fig. 8c, the vertical displacement is found to vary little with ϕ. This indicates that the vertical displacement does not show the non-axisymmetric nature of the problem very clearly. On the other hand, radial and azimuthal displacements (see Figs. 8a and 8b) are found to vary significantly with ϕ. Due to the bi-axial symmetry of the problem, the azimuthal component is observed to be zero along the x and y-axes. The azimuthal displacement is found to increase towards $\phi = 45°$ from both the axis. The radial displacement, on the other hand, decreases from either of the two axes.

Based on the presented results, the axisymmetric steady state response is found to be sensitive upon the shape and embedment depth of the scatterer, location of the observation points, the impedance contrast between the plate and the inclusion, and the angle of incidence. In addition, the response of a non-axisymmetric inclusion for a vertical incidence showed significant variation in the non-predominant components of displacement with the change in the azimothal angle.

Transient response

This section deals with the 3D transient response of plate with a stiff inclusion. The transient response is obtained from the steady state one by the Fourier synthesis. Here, the response is studied for a vertically incident Ricker wavelet. Only axisymmetric problems have been considered to keep the computations at a minimum. For convenience, the displacement components Ux, Uy, and Uz are denoted by U, V, and W, respectively. Dis-

placements U and W are plotted in order to facilitate comparison with the corresponding 2D-problems.

Figure 9 displays horizontal and vertical displacement components of the fluid at the plate-fluid interface for a vertically incident longer wavelength Ricker wavelet. Total of 20 equally spaced observation stations are chosen on either side of (X=Y=Z=0) along the X-axis. Therefore, the bottom trace depicts the motion at (X=-10,Y=0,Z=0), while the top trace corresponds to the station at (X=10,Y=0,Z=0). The trace corresponding to (X=Y=Z=0) is not shown. The impedance contrast corresponds to that of a very stiff inclusion in a soft plate. Due to the longer wavelength of the incident wave and dominant free-field, the scattered wave influence on the vertical displacement is found to be very small. The effect of the scattered field, however, is visible from the altered free-field near the inclusion. The horizontal displacement, which is entirely due to scatterer, is found to assume uniform shape. A wave traveling with the P-wave velocity of the fluid is observed moving away from the origin. This is indicated by the slope of the straight line 'AB', which corresponds to the P-wave velocity α_f in the fluid. The amplitude of the horizontal disturbance is found to be almost constant over the observed range.

Figure 10 shows the transient response for the case when the incident wave has shorter wavelength. The vertical displacement is mainly composed of the incident wave and the waves reflected at the bottom and top surfaces of the plate. This is clearly visible due to the shorter wavelength of the incident wave. In the Fig. 10, presence of the scatterer is visible from the changed free-field vertical displacement field near the inclusion. In addition, scattered waves are observed traveling away from the inclusion.

Figure 11 shows the vertical displacement for the same inclusion in a stiffer plate than that of Fig. 10. The vertical displacement field, which is dominated by the free-field, displays waviness which decays with time. As indicated for the plane strain problem, this phenomena is observed only when the density of the plate is much higher than that of the fluid, so that incident energy is trapped in the plate for a longer period (compare Figs. 10 and 11). As the contrast between the inclusion and plate becomes smaller, the effect of the scatterer is found to be very small on the predominant component of motion.

Figure 12 displays the vertical response of the plate described above when the inclusion is much stiffer than the plate. The effect of the inclusion is

strongly felt in the vicinity of the inclusion. This is evident through the lack of waviness in the response above the inclusion. The effect of the scatterer is found to be very local as opposed to the case described in Fig. 10.

Comparison with 2D

The following observations can be made from the study of 3D and 2D problems with analogous geometry and property contrasts.

Comparison of the 2D and 3D responses for different aspect ratios (compare Fig. 3 of [1] and Fig. 4), indicates that the vertical displacement shows similar qualitative trends for both the 2D and 3D problems. That is, the effect of the scatterer on the vertical response is found to be most pronounced when the inclusion is spherical (circular for 2D) and least when the minor axis of the inclusion is in the vertical(z) direction for ellipsoidal(3D) and elliptical(2D) inclusions. The effect of the scattered field on the vertical displacement is found to be higher for the 3D problem in comparison with the 2D problem. The horizontal displacement on the other hand is found to be higher for the 2D problem.

Comparison of the vertical displacements in Fig. 6b of [1] and Fig. 6 for a softer inclusion shows that the scattered field interferes destructively for the 3D case in contrast to constructive interference observed for the 2D-case. This change is significant. The horizontal displacement for this case is found to be of the same order for both the 2D and 3D models.

Comparison of the transient response for 2D and 3D models for a stiff inclusion indicates that the qualitative features of the response are preserved for both the models. The vertical displacement is found to be dominated by the free-field with the effect of the scatterer strongly visible near the inclusion. Horizontal scattered wave displacement is observed to be traveling at the fluid-solid interface with the P-wave velocity of the fluid. The amplitude of the horizontal scattered wave was found to be almost constant over the observed range.

From the above comparison, it is observed that for the stiff inclusion, the 2D problem is found to give qualitatively similar results to that of the 3D problem. For the soft inclusion, on the other hand, the vertical response is found to differ qualitatively for the two models.

Conclusions

In the present study, fluid-solid interface response of the plate with inclusion submerged in fluid is investigated for a 3D model. As in the 2D model, it is found that the steady state fluid-solid interface response is very sensitive upon the geometry and embedment depth of the inclusion and the off vertical and azimuthal angles of incidence. In addition, the impedance contrast between the plate and the inclusion greatly influences the response. Moreover, the response of a non-axisymmetric inclusion for a vertical incidence showed significant variation in the non predominant displacement components with change in the azimuthal angle. The vertical displacement field showed only small variation with the azimuth.

Transient response shows similar features observed for the 2D model. From the transient response of a plate with a very stiff inclusion and for vertical incidence, it is found that the presence of the inclusion is indicated very clearly by both the predominant and the non-predominant components of displacement. In the predominant component this is evident from the altered free-field near the inclusion and the scattered waves traveling away from the inclusion. In the non-predominant component of the displacement, the scattered field is observed as the waves traveling at the plate-fluid interface with the P-wave velocity of the fluid. These waves are found to be almost constant with increased distance from the scatterer. When the density of the fluid is significantly lower than that of the plate, the effect of multiple reflection at the plate surfaces is observed in the transient response. For this case, the effect of the scattering from the inclusion is strongly felt only when the inclusion is significantly stiffer than the plate. Due to the significant presence of the free-field waves trapped in the plate, the effect of the scattered wave field is felt only locally and is not visible at farther distances from the inclusion.

Comparison of the 2D and 3D responses indicates that for the stiff inclusion, the 2D problem is found to give qualitatively similar results as that of the 3D problem. But for the soft inclusion the vertical steady state response is found to significantly differ for the two models. The 2D model showed constructive interference of the scattered wave field over the inclusion as opposed to the destructive interference observed for the 3D model. This illustrates the importance of the 3D modeling of the scattered wave problem.

Acknowledgments

This material is based upon work supported by the Office of Naval Research under Contract No. N00014-88-K-0157. The computations were done through a grant by the San Diego Super Computer Center at UC, San Diego. The authors would like to express their appreciation to Hossein Eshraghi for his critical comments in numerous discussions during the research on this paper.

References

[1] R. Keshavamurthy and M. Dravinski. 'Elastic wave scattering by an inclusion in a multilayered medium submerged in fluid', *Wave Motion*, (submitted).

[2] S. Day. 'Finite element analysis of seismic scattering problem', *Ph.D. Thesis* , UC San Diego, California (1977).

[3] R. J. Aspel. 'Dynamic Green's functions for layered media and applications to boundary value problems', *Ph.D. Thesis*, UC San Diego, California (1979).

[4] F. J. Sanchez-Sesma. 'Diffraction of elastic waves by three dimensional surface irregularities', *Bull. Seism. Soc. Am.*, **73**, 1621-1636 (1983).

[5] V. W. Lee. 'Three-dimensional diffraction of plane P, SV and SH waves by a hemispherical alluvial valley', *Soil Dyn. Earthquake Eng.*, **3**,133-144 (1984).

[6] Y. Niwa, S. Hirose. 'Application of the BEM to elastodynamics in a three dimensional half-space', *Recent Applications in Computational Mechanics*, ASCE, 1-15 (1987).

[7] R. Paskaramoorthy, S. K. Datta and A. H. Shah. 'Effect of Interface Layers on Scattering of Elastic Waves', *J. Appl. Mech.*, **55**, 871-878 (1988).

[8] J. J. Lee and C. A. Langston. 'Wave propagation in a three dimensional circular basin', *Bull. Seism. Soc. Am.*, **73**, 1637-1653 (1983).

[9] F. J. Sanchez-Sesma, L. E. Perez-Rocha and S. Chavez-Perez. 'Diffraction of elastic waves by three-dimensional surface irregularities. Part II', *Bull. Seism. Soc. Am.*, **79**, 101-112 (1989).

[10] H. Eshraghi and M. Dravinski. 'Transient scattering of elastic waves by three dimensional non-axisymmetric dipping layers', *Int. J. Num. Meth. Eng.*, **31**, 1009-1026 (1991).

[11] T. K. Mossessian and M. Dravinski. 'A hybrid approach for scattering of elastic waves by three dimensional irregularities of arbitrary shape', *J. Phys. Earth.*, **40**, 241-261 (1992).

[12] A. Boström and A. Kristensson. 'Elastic wave scattering by a three-dimensional inhomogeneity in an elastic half space', *Wave Motion*, **2**, 335-353 (1985).

[13] V. V. Varadan, T. A. K. Pillai and V. K. Varadan. 'Ultrasonic wave scattering by a subsurface flaw in joined fluid-solid half spaces', *J. Appl. Mech.*, **50**, 802-806 (1983).

[14] K. Aki and P. G. Richards, *Quantitative Seismology Theory and Methods*, W.H. Freeman and Company, San Francisco, 1 (1980).

[15] R. Keshavamurthy, *Ph. D. Thesis*, Dept. of Mech. Eng., University of Southern California, Los Angeles (1992).

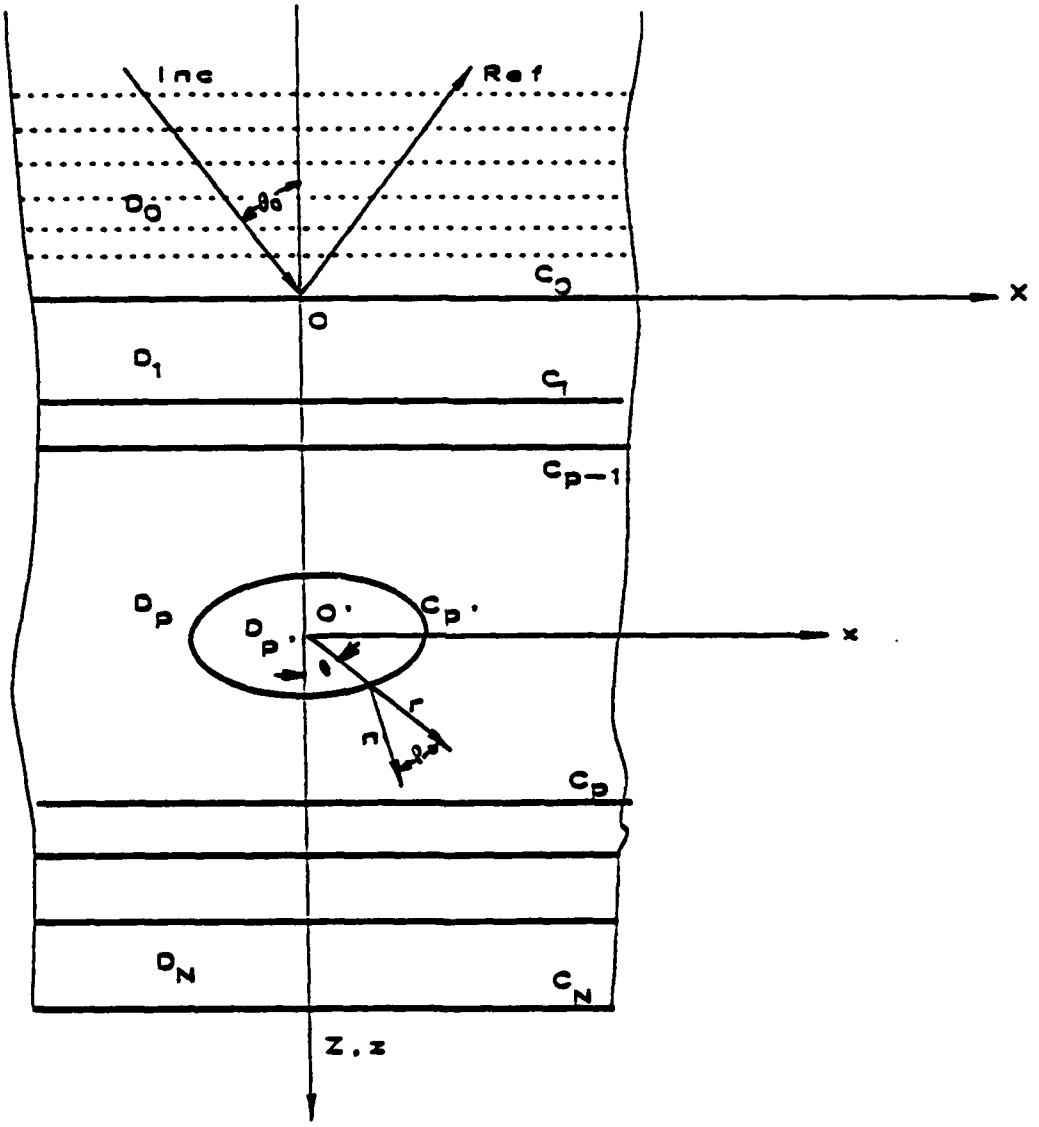

Figure 1:

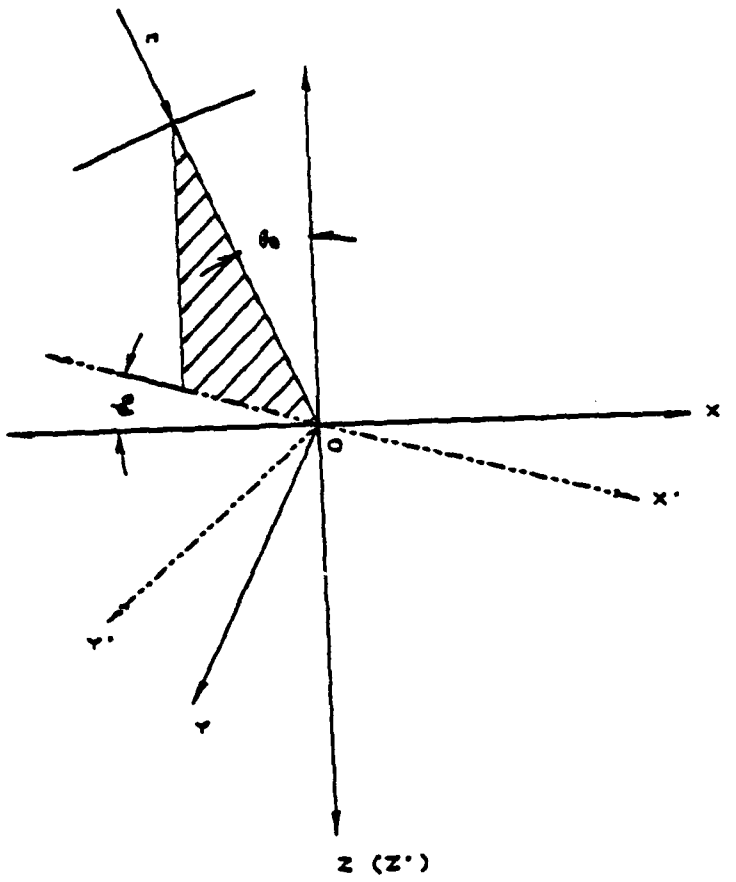

(a)

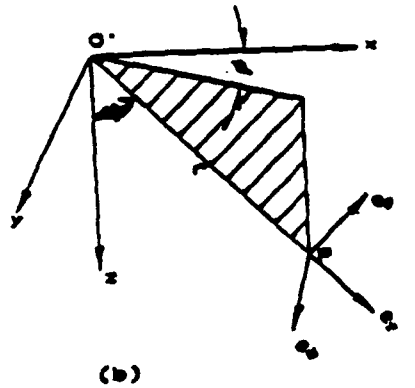

(b)

Figure 2:

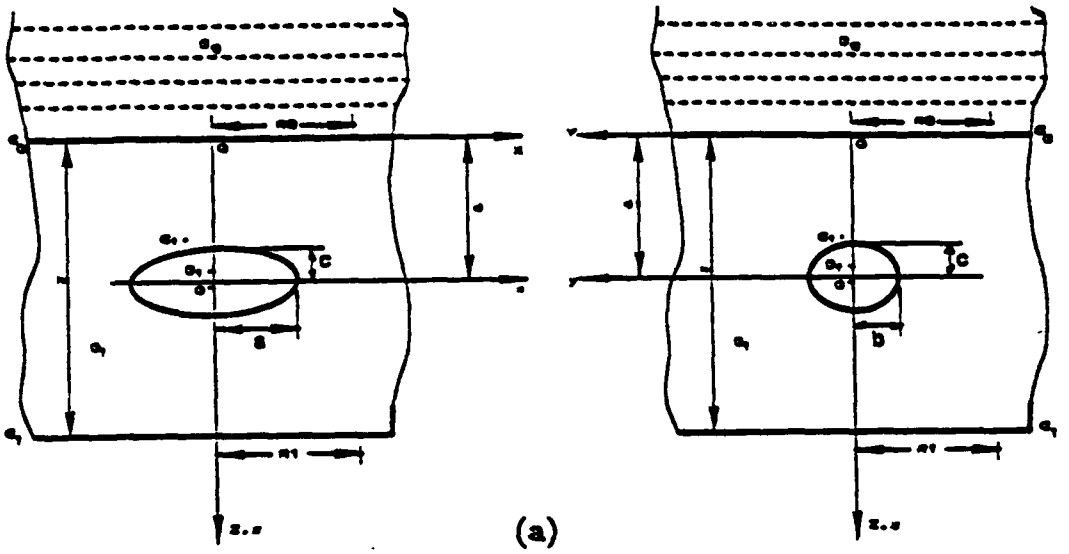

(a)

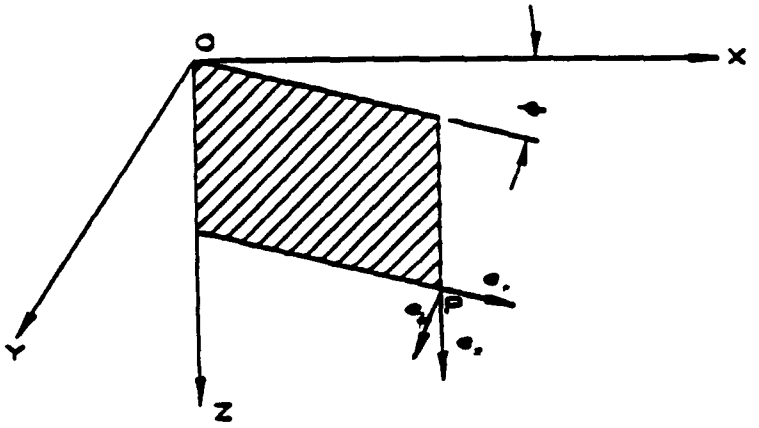

(b)

Figure 3:

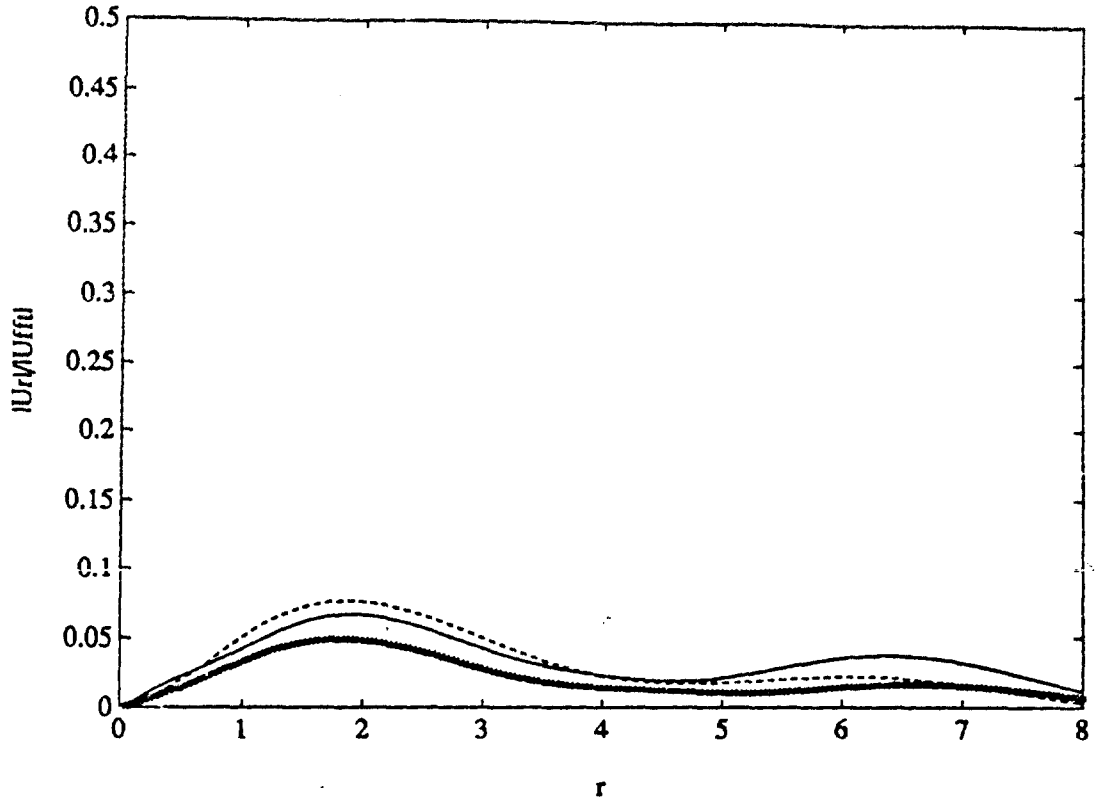
0.5
0.45
0.4
0.35
0.3
0.25
0.2
0.15
0.1
0.05
0
0
1
2
3
4
5
6
7
8
r
|Ur|/|Uffd|

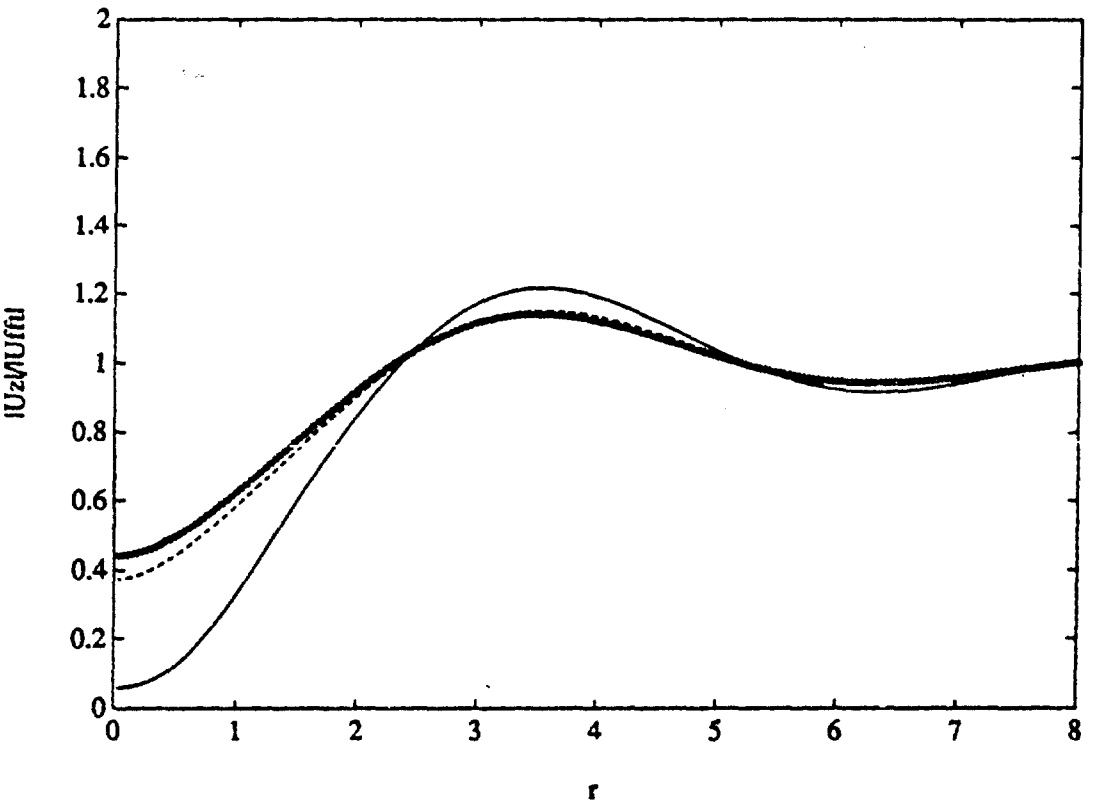
2
1.8
1.6
1.4
1.2
1
0.8
0.6
0.4
0.2
0
0
1
2
3
4
5
6
7
8
r
|Uz|/|Uffd|

Figure 4:

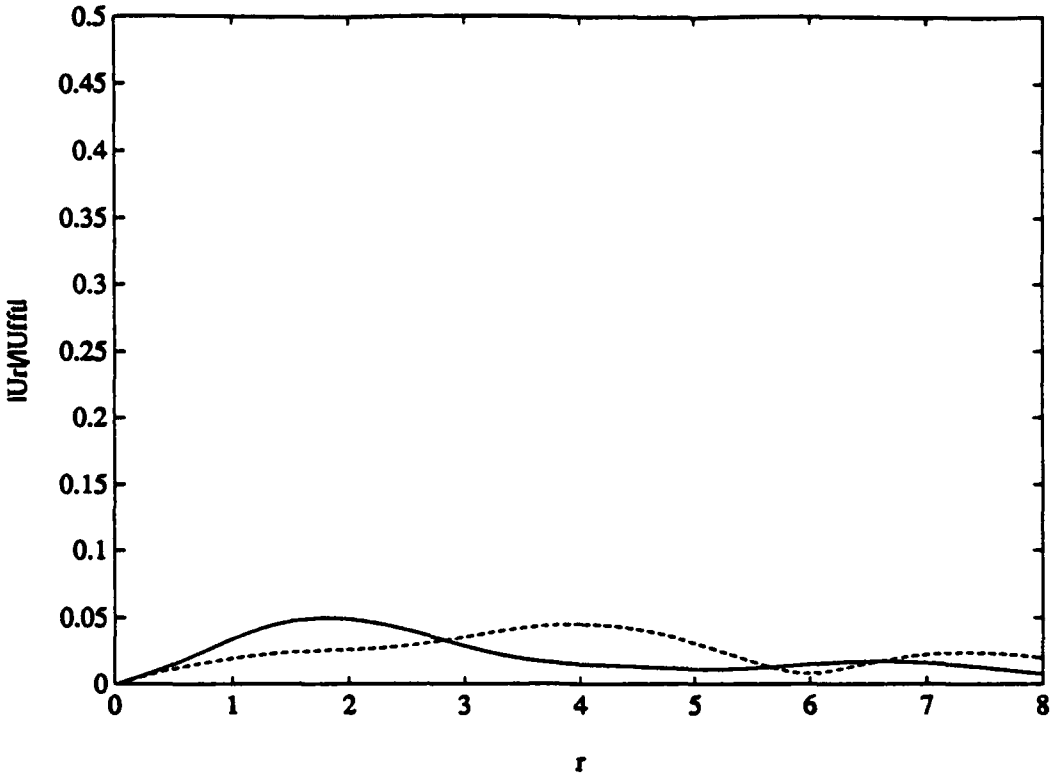
0.5
0.45
0.4
0.35
0.3
0.25
0.2
0.15
0.1
0.05
0
0 1 2 3 4 5 6 7 8
r

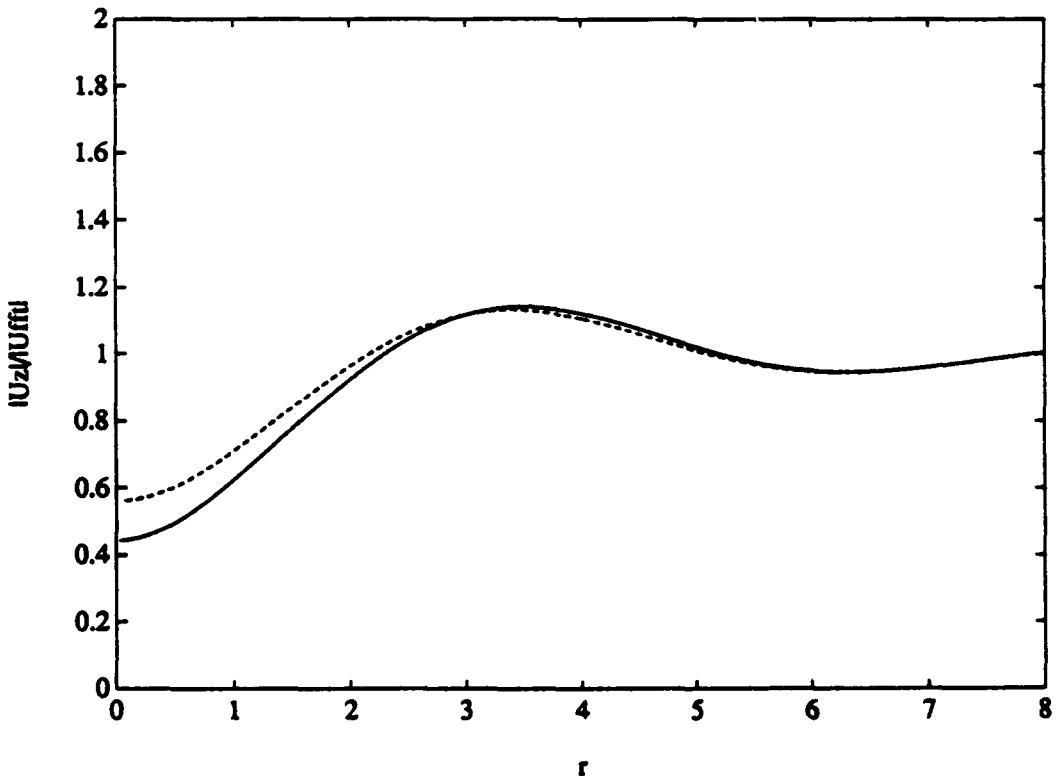
2
1.8
1.6
1.4
1.2
1
0.8
0.6
0.4
0.2
0
0 1 2 3 4 5 6 7 8
r

Figure 5:

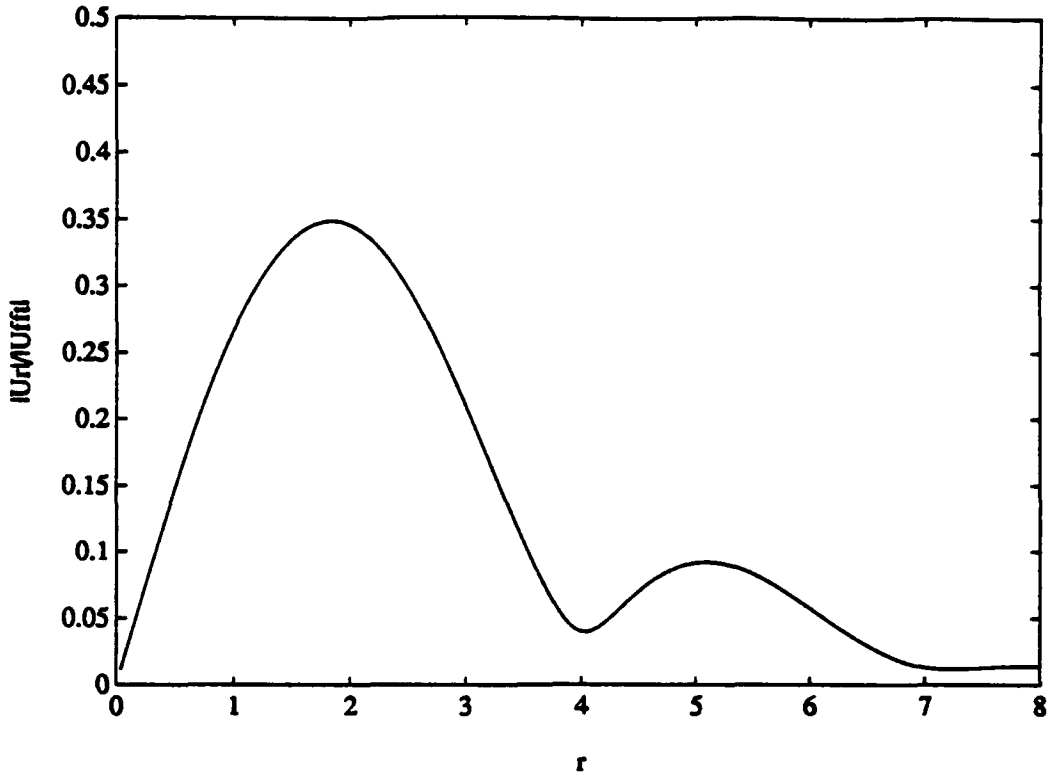
0.5
0.45
0.4
0.35
0.3
0.25
0.2
0.15
0.1
0.05
0
0
1
2
3
4
5
6
7
8
r

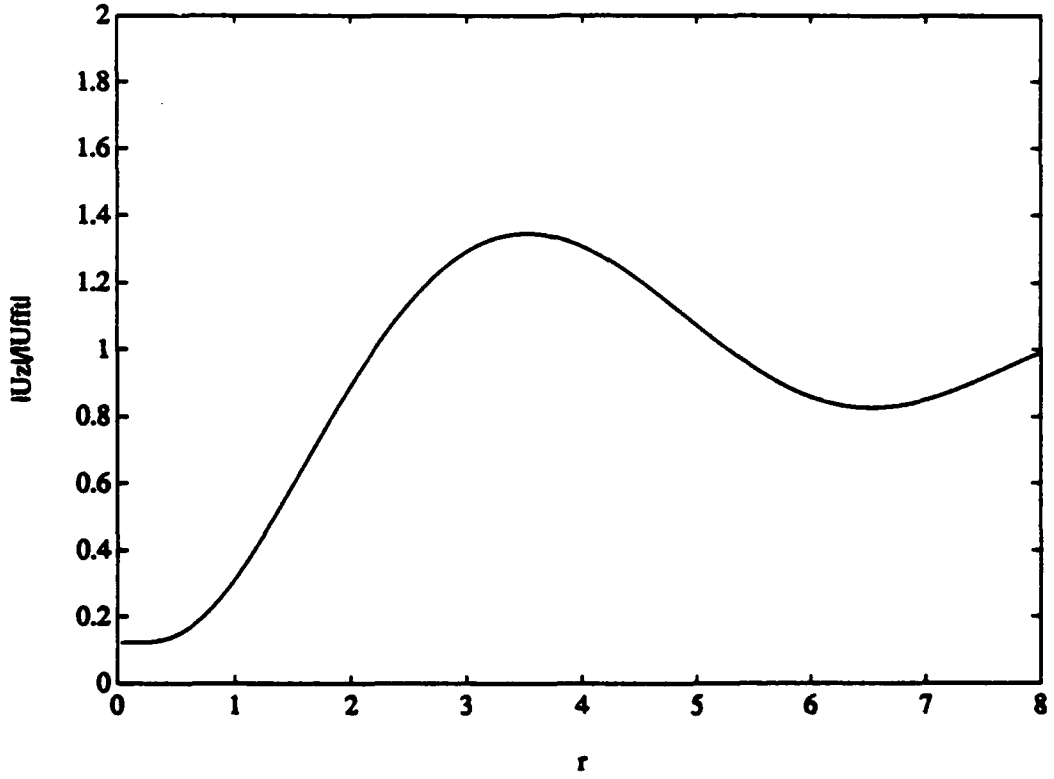
2
1.8
1.6
1.4
1.2
1
0.8
0.6
0.4
0.2
0
0
1
2
3
4
5
6
7
8
r

Figure 6:

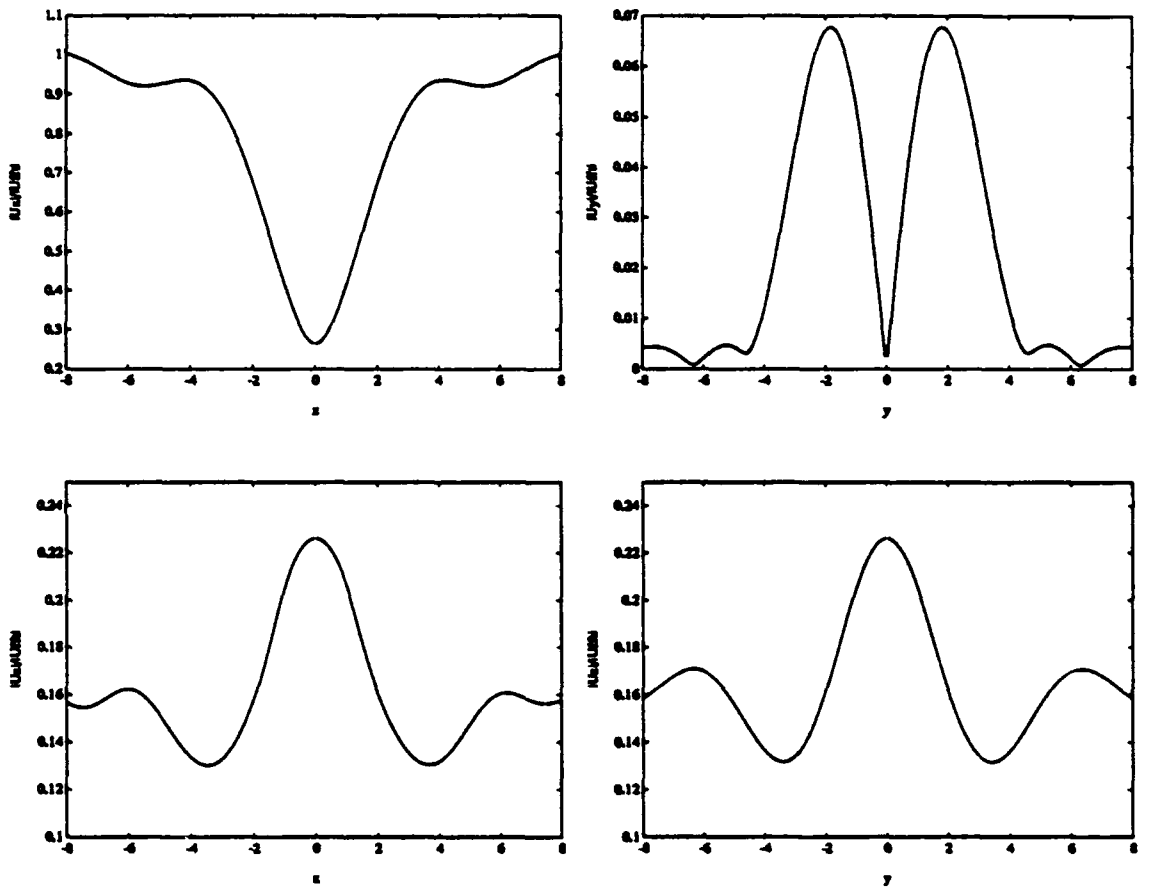

(a) Figure 7: (b)

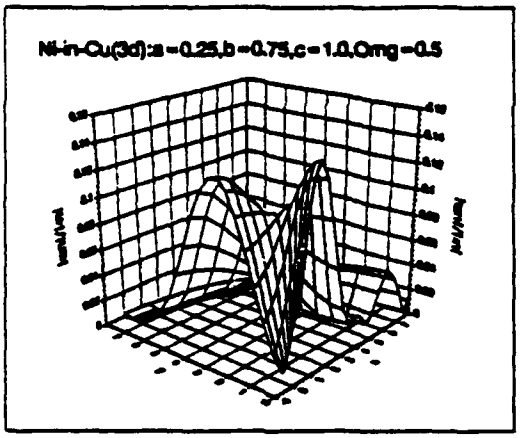
Ni-in-Cu(3d):a=0.25,b=0.75,c=1.0,Omg=0.5

(a)

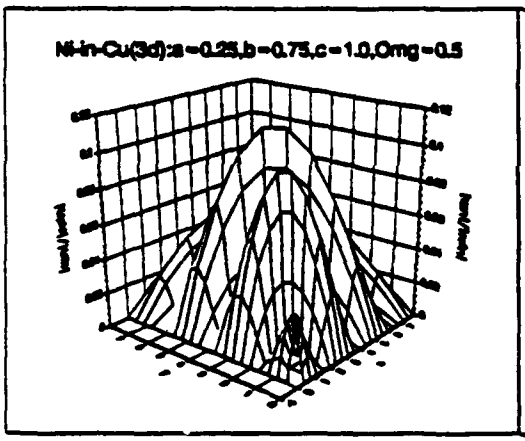
Ni-in-Cu(3d):a=0.25,b=0.75,c=1.0,Omg=0.5

(b)

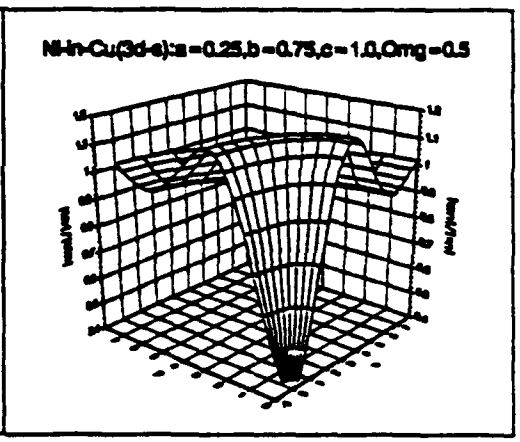
Ni-in-Cu(3d-e):a=0.25,b=0.75,c=1.0,Omg=0.5

(c)

Figure 8:

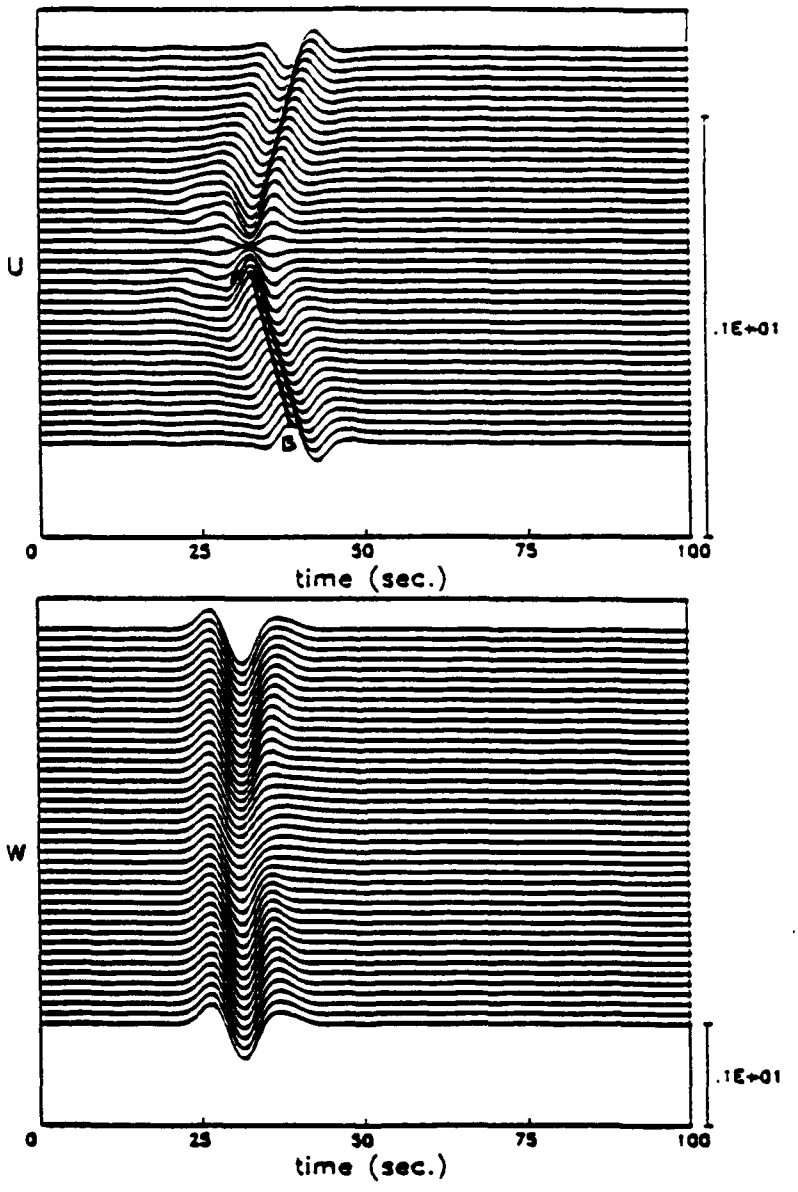

Figure 9:

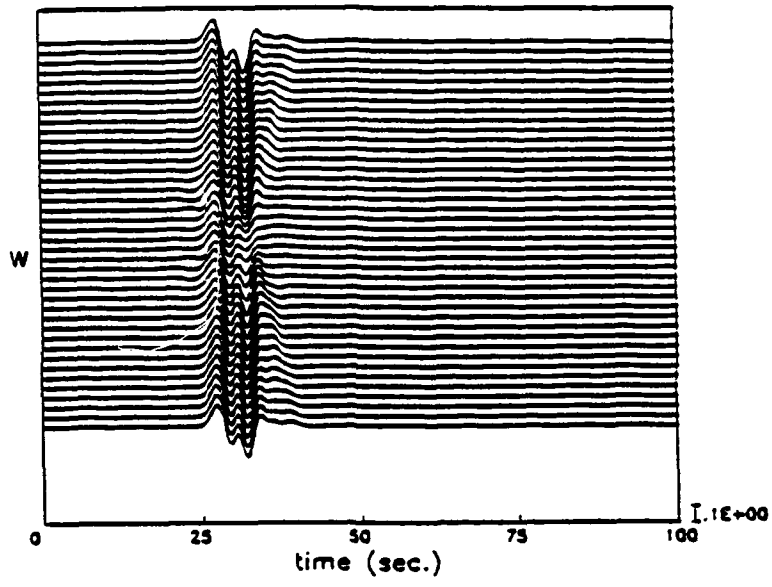

Figure 10:

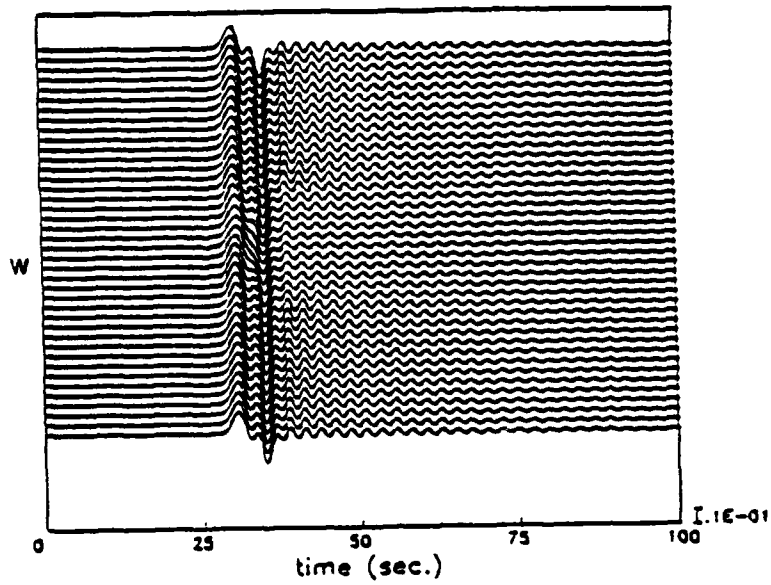

Figure 11:

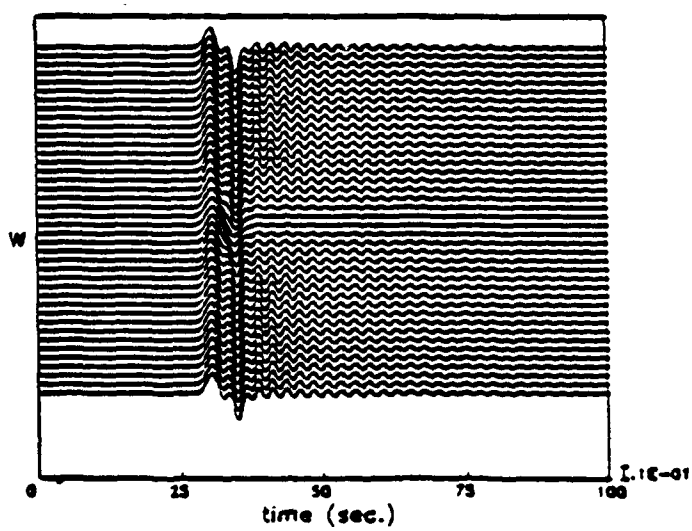

Figure 12:

List of Figures